Journal of the ICRU Vol 5 No 1 (2005) Report 73
Oxford University Press
doi:10.1093/jicru/ndi002

STOPPING OF IONS HEAVIER THAN HELIUM

CONTENTS

PREFACE 1

GLOSSARY 3

ABSTRACT 7

EXECUTIVE SUMMARY 9

GUIDE TO THE REPORT 11

1 INTRODUCTION 13

2 DEFINITIONS 15

2.1 Stopping 15
2.1.1 Mean energy loss 15
2.1.2 Energy-loss fluctuation 16
2.1.3 Impact-parameter dependence 16
2.2 Range 17
2.3 Radiation effects 17
2.4 Angular scattering 18
2.5 Units, fundamental constants and conversion factors 18
2.5.1 Units 18
2.5.2 Examples 18
2.5.3 Conversion 19
2.5.4 Notation 19

3 THEORY 21

3.1 Introductory survey 21
3.2 Stopping processes 22
3.2.1 Classification 22
3.2.2 Thomas–Fermi estimates 22
3.2.3 Regimes of heavy-ion stopping 22
3.2.4 Target excitation 23
3.2.5 Interaction range 24
3.2.6 Role of projectile electrons 24
3.2.7 Nuclear stopping 24

3.3 Electronic stopping of point charges . . . 24
3.3.1 Classical theory . . . 24
3.3.2 Quantal perturbation theory . . . 25
3.3.3 Bloch theory . . . 25
3.3.4 Barkas–Andersen effect . . . 27
3.3.5 Fermi density effect . . . 29
3.3.6 I-values and oscillator-strength spectra . . . 29
3.3.7 Z_2 structure . . . 30
3.4 Electronic stopping of dressed ions . . . 30
3.4.1 Equilibrium and non-equilibrium stopping . . . 30
3.4.2 Screening and antiscreening . . . 31
3.4.3 Effective charge and quantal perturbation theory . . . 31
3.4.4 Screened potential . . . 33
3.4.5 Classical perturbation theory . . . 33
3.4.6 Charge-dependent stopping . . . 33
3.4.7 Projectile excitation and charge exchange . . . 34
3.4.8 Z_2 structure . . . 35
3.5 Aggregation effects . . . 35
3.5.1 Stopping in compounds and alloys, and phase effects . . . 35
3.5.2 Stopping of molecules and aggregates . . . 37
3.6 Low-velocity electronic stopping . . . 37
3.6.1 General considerations . . . 37
3.6.2 Free target electrons . . . 37
3.6.3 Bound target electrons . . . 38
3.6.4 Z_1 structure: modified-Firsov models . . . 39
3.6.5 Z_1 structure: Lindhard–Finnemann model . . . 40
3.6.6 Self-consistent nonlinear models . . . 40
3.6.7 Z_2 structure . . . 41
3.6.8 Conclusions . . . 41
3.7 Survey of current theoretical schemes . . . 41
3.7.1 Unitary-convolution approximation . . . 42
3.7.2 Binary theory . . . 42
3.7.3 Nonlinear electron-gas model . . . 43
3.7.4 CKT and related theories . . . 44
3.8 Nuclear stopping . . . 44
3.8.1 Introductory remarks . . . 44
3.8.2 Binary elastic scattering . . . 44
3.8.3 Scaling properties . . . 45
3.8.4 Power-law cross sections . . . 47
3.8.5 Concluding remarks . . . 47
3.9 Nuclear reactions . . . 48
3.10 Channeling, and stopping at surfaces . . . 48
3.11 Statistics of particle penetration . . . 49
3.11.1 Qualitative survey . . . 49
3.11.2 Stripped ions . . . 49
3.11.3 Partially stripped ions . . . 51
3.11.4 Transport equations and simulation . . . 52
3.11.5 Non-Poisson statistics . . . 52
3.12 Straggling . . . 53
3.12.1 General survey . . . 53
3.12.2 Point charge . . . 54
3.12.3 Dressed ions . . . 55
3.12.4 Low-speed ions . . . 56
3.13 Multiple scattering . . . 57

3.14 Restricted nuclear stopping . . . 59
3.14.1 Bohr–Williams theory . . . 59
3.14.2 Bothe–Landau theory . . . 60
3.14.3 Scaling laws . . . 60
3.14.4 Predictions . . . 61
3.15 Range and range straggling . . . 62
3.15.1 Introductory remarks . . . 62
3.15.2 Transport equations . . . 63
3.15.3 Simulation codes . . . 64
3.15.4 csda range . . . 64
3.15.5 Influence of angular deflection on projected range . . . 65
3.15.6 Range straggling . . . 65
3.15.7 Extraction of electronic-stopping cross sections from range measurements . . . 66
3.15.8 Ranges of low-energy ions . . . 66
3.16 Summary . . . 66

4 EXPERIMENT . . . 69

4.1 Introductory survey . . . 69
4.2 Projectiles . . . 69
4.2.1 Recoil ions and fission fragments . . . 69
4.2.2 Stable beams from accelerators . . . 69
4.2.3 Scattered beams and target recoils from elastic scattering . . . 70
4.2.4 Radioactive beams from accelerators . . . 70
4.3 Target characterization and requirements . . . 71
4.3.1 General . . . 71
4.3.2 Solids . . . 71
4.3.3 Gases . . . 71
4.4 Target thickness and uniformity . . . 71
4.4.1 Solids . . . 71
4.4.2 Gases . . . 72
4.5 Charge states and charge exchange . . . 72
4.5.1 Experimental methods . . . 72
4.5.2 Equilibrium . . . 73
4.5.3 Non equilibrium . . . 74
4.6 Methods of energy-loss measurement . . . 74
4.6.1 General . . . 74
4.6.2 Calorimetric detection . . . 75
4.6.3 Secondary-particle detection . . . 76
4.6.4 Time-of-flight spectrometers . . . 76
4.6.5 Doppler-shift attenuation . . . 77
4.6.6 Electrostatic and magnetic spectrometers . . . 77
4.7 Aspects of data analysis and interpretation . . . 78
4.8 Stopping of stripped ions . . . 79
4.8.1 Light ions . . . 79
4.8.2 Heavy ions . . . 79
4.9 Charge-dependent stopping . . . 80
4.10 Equilibrium stopping . . . 81
4.10.1 General considerations . . . 81
4.10.2 Screening in high-velocity stopping . . . 83
4.10.3 Gas–solid effect in high-velocity stopping . . . 84
4.10.4 Stopping in plasmas . . . 84
4.11 Energy-loss straggling . . . 85
4.11.1 Stripped and few-electron ions . . . 85
4.11.2 Heavily screened ions . . . 86

4.12 Angular deflection . . . 86
4.12.1 Experimental techniques . . . 86
4.12.2 Multiple scattering . . . 87
4.13 Range and range straggling . . . 89
4.14 Summary . . . 89

5 DATA COMPILATIONS, TABLES, PROGRAMS AND COMPARISONS WITH EXPERIMENTAL DATA . . . 91

5.1 Introductory survey . . . 91
5.2 Scaling procedures . . . 91
5.2.1 General . . . 91
5.2.2 Effective charge . . . 92
5.2.3 Z_1 structure . . . 93
5.2.4 Z_2 structure . . . 93
5.2.5 Gas–solid difference . . . 96
5.3 Tables and computer codes . . . 96
5.3.1 Tables of Steward . . . 96
5.3.2 Tables of Northcliffe and Schilling . . . 96
5.3.3 Brice formula . . . 101
5.3.4 SRIM (TRIM) program package . . . 102
5.3.5 Tables of Hubert and coworkers . . . 103
5.3.6 Formula of Xia and Tan . . . 103
5.3.7 Code of Tai and coworkers . . . 103
5.3.8 Formula of Konac and coworkers . . . 103
5.3.9 Geant4 program package . . . 103
5.3.10 CasP code . . . 103
5.3.11 Tables of Hiraoka and Bichsel . . . 104
5.3.12 MSTAR code . . . 104
5.3.13 PASS code . . . 104
5.3.14 Formula of Weijers et al. . . . 105
5.4 Further comparisons . . . 105
5.5 Discussion . . . 107
5.5.1 General . . . 107
5.5.2 Nuclear stopping . . . 107
5.5.3 Deviations between tabulations and experimental data . . . 109
5.6 Summary . . . 110

6 TABLES . . . 113

6.1 Introductory Survey . . . 113
6.1.1 Choice of procedure . . . 113
6.1.2 Choice of projectiles and targets . . . 113
6.1.3 Range of beam energies . . . 113
6.2 Computational procedure . . . 114
6.2.1 The basic scheme . . . 114
6.2.2 Energy loss to target atom . . . 116
6.2.3 Shell correction . . . 117
6.2.4 Quantum correction . . . 117
6.2.5 Relativity . . . 117
6.2.6 Projectile excitation . . . 117
6.2.7 Charge exchange . . . 118
6.3 Input . . . 118
6.3.1 Frequency spectra . . . 118
6.3.2 Shell correction . . . 119

6.3.3 Options for shell correction . . . 120
6.3.4 Subshell binding energies . . . 120
6.3.5 Equilibrium ion charge . . . 120
6.3.6 Computational aspects . . . 121
6.3.7 Sensitivity studies . . . 121
6.4 Tables: input data . . . 121
6.5 Tables: electronic stopping force for 16 ions in elemental materials . . . 122
Hydrogen . . . 122
Helium . . . 124
Beryllium . . . 126
Amorphous carbon . . . 128
Nitrogen . . . 130
Oxygen . . . 132
Neon . . . 134
Aluminium . . . 136
Silicon . . . 138
Argon . . . 140
Titanium . . . 142
Iron . . . 144
Nickel . . . 146
Copper . . . 148
Germanium . . . 150
Krypton . . . 152
Molybdenum . . . 154
Silver . . . 156
Tin . . . 158
Xenon . . . 160
Tungsten . . . 162
Platinum . . . 164
Gold . . . 166
Lead . . . 168
Uranium . . . 170
6.6 Tables: electronic stopping force for iron ions in 16 elemental materials . . . 172
Iron . . . 172
6.7 Tables: electronic stopping force for 16 ions in compound materials . . . 174
A-150 tissue-equivalent plastic . . . 174
Adipose tissue (ICRP) . . . 176
Air, dry, sea level . . . 178
Aluminium oxide . . . 180
Bone, compact (ICRU) . . . 182
Bone, cortical (ICRP) . . . 184
C-552 air-equivalent plastic . . . 186
Calcium fluoride . . . 188
Carbon dioxide . . . 190
Glass, borosilicate (Pyrex) . . . 192
Kapton polyimide film . . . 194
Lithium fluoride . . . 196
Lithium tetraborate . . . 198
Methane . . . 200
Muscle striated (ICRU) . . . 202
Nylon, type 6 and type 6/6 . . . 204
Photographic emulsion . . . 206
Plastic scintillator (vinyltoluene based) . . . 208
Polycarbonate (makrolon, lexan) . . . 210
Polyethylene . . . 212
Polyethylene terephtalate (Mylar) . . . 214

Polymethyl methacrylate (lucite, perspex) 216
Polystyrene 218
Polytetrafluoroethylene (Teflon) 220
Propane 222
Silicon dioxide 224
Sodium iodide (modelled by NeXe) 226
Tissue-equivalent gas (methane based) 228
Tissue-equivalent gas (propane based) 230
Liquid water 232
Water vapor 234
6.8 Tables: Ranges of 16 ions in liquid water 236
Liquid water 236

REFERENCES 239

doi:10.1093/jicru/ndi001

STOPPING OF IONS HEAVIER THAN HELIUM

Report Committee

R. Bimbot, Institut de Physique Nucléaire, Orsay, France
H. Geissel, Gesellschaft für Schwerionenforschung, Darmstadt, Germany
H. Paul, Johannes-Kepler Universität, Linz, Austria
A. Schinner, Johannes-Kepler Universität, Linz, Austria
P. Sigmund (Chairman), University of Southern Denmark, Odense, Denmark

Commission Sponsors

R. Caswell, National Institutes of Standards and Technology, Gaithersburg, Maryland, USA
M. Inokuti, Argonne National Laboratory, Argonne, Illinois, USA
S. M. Seltzer, National Institutes of Standards and Technology, Gaithersburg, Maryland, USA

Consultants to the Report Committee

N. R. Arista, Centro Atomico, Bariloche, Argentina
H. H. Mikkelsen, University of Southern Denmark, Odense, Denmark
A. H. Sørensen, University of Aarhus, Denmark
D. I. Thwaites, University of Edinburgh, United Kingdom

The Commission wishes to express its appreciation to the individuals involved in the preparation of this report, for the time and efforts which they devoted to this task and to express its appreciation to the organisations with which they are affiliated.

All rights reserved. No part of this book may be reproduced, stored in retrieval systems or transmitted in any form by any means, electronic, electrostatic, magnetic, mechanical photocopying, recording or otherwise, without the permission in writing from the publishers.

British Library Cataloguing in Publication Data. A Catalogue record of this book is available at the British Library.

ISBN 0198570120

Journal of the ICRU Vol 5 No 1 (2005) Report 73
Oxford University Press
doi:10.1093/jicru/ndi004

PREFACE

The interaction of charged particles with matter is at the very core of all radiation effects including essentially all biological and physical phenomena important to radiation damage and radiation dosimetry. The interaction process results in energy loss by the bombarding particle, largely through interactions with atomic electrons. Interactions with the screened field of the nucleus are the dominant cause of changes in the particle trajectory, and as well give rise to energy loss, particularly the so-called nuclear stopping that is important at low speeds. The rate of particle energy loss, that is, the stopping power or the stopping force, for various charged particles moving in different media, constitutes information essential for radiation research and applications such as medical diagnosis or therapy.

From its inception the ICRU assumes as a fundamental responsibility the assembly, publication, and promulgation of carefully evaluated atomic and nuclear data useful for a broad range of radiation applications. Such publications have permeated the history of the ICRU. For the interaction of charged particles with matter, an early comprehensive effort was ICRU Report 37, *Stopping Powers for Electron and Positrons*, published in 1984. This volume is to this day widely accepted as the primary source of such particle energy loss values, particle range values, and a comprehensive discussion of the underlying physics. This publication also includes a thorough review of the literature and a detailed description of the underlying theory and experimental literature. Report 37 is nearly complete for electrons and positrons stopping in matter at essentially any energy. Report 37 also included recommended values for the mean excitation energy, I, for numerous elements and some compounds. More recently, ICRU Report 49, *Stopping Powers and Ranges for Protons and Alpha Particles*, published in 1993, extends the ICRU publication of fundamental stopping power data to light-mass nuclear particles, namely protons and alpha particles. For the first time, the ICRU included a data disk with the publication that provides fundamental data as well as software to generate stopping power and range values for numerous elements, compounds, and mixtures. For both volumes, the ICRU was most fortunate to have as the lead author and scientific director Martin Berger of the National Institute of Standards and Technology. Berger's scholarship perfuses these documents and clearly contributed to the superb level of science and readability.

Following Robert R. Wilson's suggestion in 1947, energetic protons are now increasingly being used for radiation therapy. Proton radiation therapy is driven by the improved physical selectivity of the energy depositions due to the finite and well-defined proton range as well as the modest proton lateral scattering that yields minimal beam penumbra. As predicted by Wilson, high-energy protons are especially useful for small irregular radiation sites. No substantive increase in biological effectiveness can be attributed to protons; they are low-LET beams. Swift particles heavier than helium ions, such as carbon and silicon ions, exhibit even greater beam definition, namely, less lateral scattering and range straggling along the ion trajectory. In addition, the large increase in energy-loss rate introduces a strong biological effect especially near the end of range; they are high-LET beams. As a result, they exhibit a selective biological effectiveness for the treatment of some tumors resistant to conventional photon therapy. The interest in ion-beam therapy is dramatically increasing. Following the pioneer work of Berkeley where helium and neon ions were used clinically, carbon ions are now used in two Japanese centers, Chiba and Hyogo, and in Germany at the GSI-Darmstadt. Several other projects are in preparation worldwide.

Other applications for which information on stopping and range of ions heavier than helium is essential include radiation protection for shielding calculations and risk estimates as well as deep space exploration programs. At lower ion energies, another widespread application of heavier particles is in ion implantation for surface preparation and for semiconductor fabrication.

The proper application of ions heavier than helium for radiation therapy, ion implantation, or the other mentioned applications requires a comprehensive knowledge of particle energy loss and range. This

© International Commission on Radiation Units and Measurements 2005

was the basis for pursuing the present report. Compared to protons or heliumions, energy loss by heavier charged particles is considerably more complex. The particle charge state is a complex function of the surrounding media and the speed of the particle. Present Report on *Stopping of Heavier Ions* provides a detailed discussion of the underlying theory, the rich experimental history, and comprehensive tables of energy-loss values for a large range of elements, compounds and mixtures. The volume is organized into six chapters, with the last providing substantial tabular information.

ACKNOWLEGMENT

The ICRU is delighted to dedicate this comprehensive volume to the memory of Martin Berger, who contributed so strongly to this area of science. Regrettably, Martin Berger died on November 6, 2004.

André Wambersie
Paul M. DeLuca, Jr.
Stephen M. Seltzer

February 6, 2005

Journal of the ICRU Vol 5 No 1 (2005) Report 73
Oxford University Press
doi:10.1093/jicru/ndi007

GLOSSARY

a	adiabatic radius v/ω
a	screening radius of interatomic potential
a_0	Bohr radius
A_1	mass number of projectile ion
A_2	mass number of target atom
a_{sc}	atomic screening radius
B_j	Bethe parameter $2mv^2/\hbar\omega_j$
B_ρ	magnetic rigidity
c	speed of light
C	constant 1.1229 in Bohr logarithm
CKT	convergent kinetic theory
csda	continuous-slowing-down approximation
$-\mathrm{d}E/\rho\mathrm{d}\ell$	mass stopping force
$-\mathrm{d}E/\mathrm{d}\ell$	stopping force, stopping power
$-\mathrm{d}E/\mathrm{d}x$	stopping force, stopping power
$\mathrm{d}\mathcal{P}$	probability
DSA	Doppler-shift attenuation
$\mathrm{d}\sigma$	differential cross section
E	kinetic energy of projectile
E_0	initial energy of projectile
E/A_1	specific energy
ECR	electron cyclotron resonance
$F(\alpha,\ell)$	multiple-scattering profile
$F(\Delta E,\ell)$	energy-loss profile
$f(\eta)$	function determining differential cross section in Lindhard units
f_j	oscillator strength of frequency ω_j
GANIL	Grand Accelérateur National d'Ions Lourdes
$\hbar$	Planck's constant divided by 2π
I	mean excitation energy
I_1	I-value entering straggling
IDSA	Inverted Doppler-shift attenuation
Im	imaginary part
J_n	Bessel function of the first kind
k	absorption coefficient
ℓ	angular momentum quantum number
ℓ	path length
L	stopping number
L_0	stopping number omitting shell correction
L_j	stopping number for j'th shell
LSS	Theory of ion ranges by Lindhard, Scharff and Schiøtt
m	rest mass of electron
m	exponent entering power cross section
M_0	reduced mass
M_1	rest mass of projectile ion
M_2	rest mass of target atom

© International Commission on Radiation Units and Measurements 2005

MCP	multi-channel plate
n	number of target atoms per volume
n	refractive index
n_{e}	electron density
$f(\omega), f'(\omega)$	oscillator-strength spectrum
P	projectile momentum
p	impact parameter
p	exponent in low-velocity stopping force
P_ℓ	Legendre polynomial
$P(v, q_1)$	charge fraction
q	exponent entering nuclear scattering cross section
q_1	ion charge number
$q_{1,\mathrm{eff}}$	effective-charge number
Q3D	Magnetic spectrograph with a quadrupole lens and three dipole magnets
$\mathbf{Q}$, Q_{IJ}	matrix governing charge fractions
R	range, range along the path
$\boldsymbol{R}$	vector range
R	Rydberg energy
$\boldsymbol{r}$	position vector
R	internuclear distance
R	nuclear radius
Re	real part
$R_\perp$	lateral range
$r_{\min}$	distance of closest approach
R_{p}	projected range
R_{p}/R	projected-range correction, detour factor
r_{s}	Wigner–Seitz radius
S	stopping cross section
S_{e}	electronic stopping cross section
$s(\varepsilon)$	stopping cross section in Lindhard dimensionless units
$\mathbf{S}$, S_{IJ}	stopping matrix
S_{n}	nuclear stopping cross section
t	time
T_{c}	transition temperature for superconductor
TOF	time of flight
u	atomic mass unit
U	ionization energy
u	screening function
UCA	unitary convolution approximation
v	projectile speed
$\boldsymbol{v}$	projectile velocity
v_0	Bohr velocity
$\boldsymbol{v}_{\mathrm{e}}$	velocity of target electron
W	straggling parameter
w	energy transfer in single event
w_1	limiting energy loss between multiple- and single-collision regime
w_J	energy transfer to J'th loss channel
$w_{\max}$	maximum energy loss in single event
$W_{\mathrm{n}}(E)$	nuclear-straggling parameter
x	penetration depth
Z_1	atomic number of projectile ion
Z_2	atomic number of target atom
ΔE_{peak}	most probable energy loss
α	total deflection angle
α	fine structure constant 1/137
$\langle \ldots \rangle$	beam average

β	v/c
ΔE	energy loss at given pathlength
$\langle \Delta E \rangle$	mean energy loss
$\Delta E_{\pm 1/2}$	right and left halfwidth of energy-loss spectrum
δ_ℓ	phase shift
$\Delta L_{\mathrm{Bloch}}$	Bloch correction to stopping number
$\Delta L_{\mathrm{invBloch}}$	inverse-Bloch correction to stopping number
$\Delta \boldsymbol{u}$	velocity change in single collision
$\Delta \boldsymbol{v}$	velocity change after penetration
ϵ_0	vacuum permittivity
$\varepsilon(\boldsymbol{k}, \omega)$	Lindhard function
ϵ	Lindhard dimensionless energy unit
η	scaled nuclear energy loss
η	$\kappa/2$
γ	Euler's constant $= 0.5772$
γ	$1/\sqrt{1 - v^2/c^2}$
γ^2	effective-charge fraction
γ	energy-transfer factor $4M_1M_2/(M_1 + M_2)^2$
κ	Bohr's kappa parameter $2Z_1v_0/v$
λ	coefficient entering nuclear scattering cross section
ν	species index
ϕ	scattering angle in single event
ψ	digamma function, $\psi(x) = \mathrm{d} \ln \Gamma(x)/\mathrm{d}x$
ρ	curvature radius in magnetic spectrometer
ρ	Lindhard dimensionless range unit
ρ	mass density of medium
σ_J	cross section for energy loss w_J
$\sigma^{(1)}$	transport cross section determining stopping force
$\sigma_B(k, \kappa)$	transport cross section determining energy loss and angular deflection
σ, σ_{IJ}	cross-section matrix
$\sigma(s)$	transport cross section determining energy-loss spectrum
ω	resonance frequency
ω_p	Plasma frequency
Ω^2	straggling, energy-loss straggling, variance of energy-loss profile
Ω_B^2	Bohr's result for Ω^2
ω_j	resonance frequency of j'th shell
Ω_R^2	range straggling, variance of range profile
ξ	Bohr parameter $mv^3/Z_1v_0\hbar\,\omega$

Journal of the ICRU Vol 5 No 1 (2005) Report 73
Oxford University Press
doi:10.1093/jicru/ndi003

ABSTRACT

Following up on ICRU Reports 37 (Stopping powers for electrons and positrons) and 49 (Stopping powers and ranges for protons and alpha particles), this report presents a critical survey on measurements and calculations of quantities governing the penetration of heavy ions through condensed and gaseous matter over an energy range from 1 keV/u upward. The focus is on the electronic stopping force (or stopping power) for ions from lithium to argon ($Z_1 = 3 - 18$), but attention is also given to energy-loss straggling and, to a lesser degree, multiple scattering and ranges. Stopping tables are given for 17 ions on 25 elemental and 34 compound materials covering energies from 0.025 to 1000 MeV/u.

© International Commission on Radiation Units and Measurements 2005

Journal of the ICRU Vol 5 No 1 (2005) Report 73
Oxford University Press
doi:10.1093/jicru/ndi005

EXECUTIVE SUMMARY

Accelerators for charged particles with a very wide range of masses and charge states have an increasing application range in fundamental physics research, in medical radiology, in materials science and engineering, in micro- and nanoscience and technology, in nuclear fission and fusion technology, and in mass spectrometry. The range of kinetic energies reached at existing accelerators spans from a few electron volts per particle into the 10^{12} electron volt regime. Effective and successful application of such particle beams requires detailed quantitative knowledge of the penetration of charged particles through matter, a field commonly categorized under the discipline of atomic physics.

Early studies of charged-particle penetration were stimulated by experimental work with gas discharges toward the end of the 19th century, but experimental possibilities were greatly enhanced after the discovery of radioactivity, in particular in pioneering work by E. Rutherford and coworkers in the beginning of the 20th century. Fundamental theoretical studies of particle penetration in particular by J. J. Thomson and N. Bohr date back to the same time. Subsequently, after the development of quantum mechanics, the quantum theory of particle stopping was developed by H. Bethe, C. Møller, F. Bloch and others.

Prime parameters characterizing the penetration of charged particles are the mean energy loss per unit path length, *i.e.*, the stopping power or stopping force, and its fluctuation, called energy-loss straggling. These quantities determine the penetration depth (range) and its fluctuation (range straggling) as well as the energy-deposition profile. Since particles are more or less deflected from their initial direction of motion, also the spatial and directional distribution, the multiple-scattering profile, is of interest.

With the exception of a very small part of the available parameter space, the dominating process leading to energy loss of a penetrating charged particle is electronic excitation of the atoms or molecules of the penetrated medium. Additional contributing effects are momentum transfer to recoiling nuclei and, depending on the type and energy of the penetrating particle, electronic excitation of the projectile and charge exchange with the atoms of the penetrated medium. At high velocities, radiational processes and nuclear reactions have to be considered. Angular deflection is mainly connected to momentum transfer to recoiling nuclei.

Until the mid-1960s, experimental activities in the area focused on the penetration of light charged particles such as electrons and positrons, protons and alpha particles. This was motivated by the needs of nuclear and particle physics. Moreover, options for experimental research on the penetration of particles heavier than helium were very limited in terms of available species and beam energies. This situation changed rapidly with new generations of ion sources and accelerators becoming available.

Until the early 1990s, theoretical research on particle stopping likewise focused on light penetrating particles, with the exception mainly of low-energy ion implantation. The relatively weak Coulomb interaction of such particles with the electrons of the stopping medium allowed the application of well-developed concepts from quantum mechanical perturbation theory. As the stopping force on a light charged particle is proportional to the square of its charge, the range of validity of quantal perturbation theory must rapidly deteriorate with increasing atomic number of the penetrating particle.

Numerous measurements have been performed on heavy-particle stopping during the past half century. The scatter between comparable data is usually considerably larger than for light particles in the same velocity range for a number of reasons. The coverage with experimental data of the entire parameter space in terms of the atomic number Z_1 and the energy of the projectile, and the atomic number Z_2 of the stopping medium, is necessarily fragmentary. Nevertheless, attempts have been made regularly to collect available experimental data and to systematize them by empirical scaling relations so as to allow predictions of stopping forces for systems not covered by existing data. Data compilations by Northcliffe and Schilling (1970), Ziegler (1980), Zeigler *et al*. (1985), and by Hubert *et al*. (1980, 1990) have had a lasting impact on the development of research around heavy-ion accelerators. The accuracy of specific predictions of these tables is limited as use is made of scaling laws that

© International Commission on Radiation Units and Measurements 2005

lack theoretical justification and as erroneous data are not necessarily identified as such and hence enter as input. However, no feasible alternative was available until recently.

This situation changed during the 1990s, when several new theoretical approaches were developed which did not hinge on quantal perturbation theory to the lowest order. An important step was made with the understanding of the Barkas–Andersen effect, sometimes called Z_1^3 effect, in the stopping of light particles. This had been considered until then as a major hurdle that had to be overcome before a feasible theoretical approach to heavy-ion stopping.

At present, four promising theoretical approaches are available, all of which go beyond or even avoid quantal perturbation theory (Arista, 2002; Grande and Schiwietz, 2002; Maynard *et al*., 2002b, 2001b; Sigmund and Schinner, 2000, 2002b). In order to allow predictions of stopping forces, a number of significant physical processes must be incorporated into the basic schemes, such as projectile screening and equilibrium charge state, charge exchange and projectile excitation, low- and high-speed corrections of various kinds, and reliable input on electronic properties of the penetrated material. This process has not been finished on any of the four schemes. Despite this, successful predictions have been made by all of them.

With regard to straggling, the situation is quite different. Very few measurements with heavy ions have been done altogether. The number of physical processes affecting straggling exceeds those affecting stopping forces. While most of them have been identified and understood theoretically as isolated phenomena, several of them interfere, making quantitative predictions a complex task requiring further study.

Angular deflection (multiple scattering), on the other hand, is well described by existing scaling laws, and despite only few systematic experiments, there is consensus that predictions on the basis of those scaling laws are reliable and accurate.

The present report addresses penetrating ions heavier than helium. Extensive reviews are given of pertinent theory and experiment. Although much progress has been made in light-particle stopping since the appearance of previous ICRU reports on stopping of electrons and positrons (ICRU Report 37) and of protons and alpha particles (ICRU Report 49), no attempt has been made of an update of those areas in the present report. Despite an extensive bibliography,[1] no claim is made of completeness.

A large collection of experimental data on heavy-ion stopping was established which proved to be a valuable tool both within and outside the work of the report committee. The majority of experimental data shown on graphs in this report is quoted from that database (Paul, 2003), whether stated or not. This collection was also employed in a scaling procedure similar to that of Northcliffe and Schilling (1970) allowing the prediction of stopping forces for ions with $Z_1 \leqslant 18$ (Paul and Schinner, 2001, 2002; Paul, 2003).

Comparisons between predictions of codes based either on theory or empirical interpolation were performed for a large number of ion–target combinations. An overall agreement of about 10% is found for the best available codes of both kinds. A somewhat higher accuracy is generally found in the energy range above 10 MeV/u, while at energies below 0.1 MeV/u, uncertainties increase due to increasing scatter of experimental data, increasing deficiencies in available theory and breakdown of simple scaling relationships.

Tables of stopping forces listed in this report were computed by the PASS code (Sigmund and Schinner, 2002b) based on the binary stopping theory of Sigmund and Schinner (2000). The parameter range covered includes 16 ions with atomic numbers from 3 to 18 as well as iron; the range of materials covered is essentially that of ICRU reports 37 and 49 except for a single element and a few compounds, and the tabulated energy range goes from 25 keV/u to 1 GeV/u.

It is planned to make updates accessible on the Internet. Such updates will report errors, improved and extended tables as well as tables for a wider variety of ion–target combinations.

[1]The bibliography was closed on 1 October, 2003.

Journal of the ICRU Vol 5 No 1 (2005) Report 73
Oxford University Press
doi:10.1093/jicru/ndi006

GUIDE TO THE REPORT

While it is hoped that this report will be found useful for a multitude of purposes, there are two main goals:

1. A detailed introduction to the physical processes governing heavy-ion penetration and their quantification in terms of measurement and theory, and
2. providing data that are needed in the user community.

The reader who is primarily interested in the second item may be tempted to go directly to Section 6, which, after a specification of theoretical and numerical input, presents stopping tables for ions and materials specified above. Nevertheless, it is strongly recommended to have a look at Section 5, which is essential for any assessment of the accuracy of the numbers quoted in the tables. Although Section 5 contains a few references to earlier parts of the report, those references are not essential for understanding the main conclusions to be drawn. The reader may find it useful to read Section 2 for definitions, notation and units and to consult the glossary whenever an unknown symbol occurs.

The reader who is interested in the first item may wish to read the report from the beginning. However, some readers may be more interested in experiment than theory, or vice versa. Again, Section 4 on experiments contains only a small number of references to Section 3 which should not prevent the experimentally oriented reader from going directly from Section 2 to Section 4 if so desired. While the theoretical Section 3 is intended to provide a comprehensive survey of pertinent theory on heavy-ion stopping, it has nevertheless more review than textbook character. For explicit derivations of quoted results the reader is advised to consult literature references given in context.

Parts of this report are based on material previously published. The contents of Sections 2 and 3 have been published as a monograph (Sigmund, 2004). Much of the material presented in Section 4 has been extracted from a major review (Geissel *et al*., 2002). Section 5 represents a revised and expanded version of a paper by Paul and Schinner (2003a).

© International Commission on Radiation Units and Measurements 2005

Journal of the ICRU Vol 00 No 00 (2005) Report 73
Oxford University Press
doi:10.1093/jicru/ndi008

1 INTRODUCTION

Quantitative information on the stopping of swift ions in matter is of considerable interest in basic science, in medicine and in technology (see Table 1.1). Following the quest for critical data tabulations, the International Commission on Radiation Units and Measurements has issued tables on stopping powers and ranges for electrons, ICRU Report 37 (ICRU, 1984) and for protons and alpha particles, ICRU Report 49 (ICRU, 1993). The present report is a follow-up on stopping of heavier ions from lithium upward.

The task of issuing such a report has been all but easy. Data are potentially needed for approximately 8000 elemental ion–target combinations and a virtually unlimited number of compound materials. To this is added a recent interest in data for penetrating molecules and clusters. Finally, the range of projectile energies of potential interest covers almost ten orders of magnitude.

It is strictly impossible to adequately support such a parameter range by experimental data alone. At the same time, a comprehensive theory allowing absolute predictions has not been available until recently, and the range of validity of existing scaling relations has been limited and, by and large, unknown. Only a few ion–target combinations have been studied in sufficient detail to allow interpolation and extrapolation on purely experimental grounds. Except for the rare case where direct measurements exist, options available to the user until a few years ago may roughly be classified into two groups:

1. Theoretical predictions valid over limited energy ranges such as Firsov (1959) or Lindhard and Scharff (1961) at low speed and Bethe (1930) or Lindhard and Sørensen (1996) at high speed;
2. Empirical or semi-empirical scaling relationships given in analytical or tabular form (Steward and Wallace, 1966; Northcliffe and Schilling, 1970; Brice, 1972; Ziegler, 1980; Hubert *et al*., 1980; Ziegler *et al*., 1985; Hubert *et al*., 1990; Konac *et al*., 1998a; Paul and Schinner, 2001).

Table 1.1. Application areas for stopping data.

Physics and chemistry	Cosmic radiation, radioactivity, accelerators, detectors, etc
Materials science and technology	Analysis, modification, radiation damage
Fusion technology	High energy density
Microelectronic devices	Development, fabrication, control
Radiation medicine	Diagnostics, therapy, radiation damage
Bio-, geo-, environmental sciences	Mass spectrometry

More generally applicable theoretical schemes are under development (Maynard *et al*., 1996, 2001b; Sigmund, 1997; Sigmund and Schinner, 2000, 2002b; Grande and Schiwietz, 1998, 2002; Lifschitz and Arista, 1998; Arista, 2002). The PASS code of Sigmund and Schinner (2002b) is currently the most powerful and versatile of the four schemes and has been utilized to generate stopping tables in this report. However, unlike the code of Grande and Schiwietz (2001) it is not yet accessible to the general user.

The passage of a heavy ion through a solid or gaseous material represents a strong intrusion that cannot generally be expected to be described adequately as a weak perturbation of the medium, as it is common in the quantification of electron and proton penetration. Moreover, heavy ions are composite particles carrying electrons except at high speed, and their interaction with bound and free electrons in the stopping medium is a problem of considerable complexity involving a number of processes that are absent or less significant in the case of light projectiles.

The task of arriving at a reliable scheme for predicting stopping parameters is by no means straightforward, and strategies adopted in the report committee have undergone some development during the course of this project.

- It was clear from the beginning that scaling procedures currently used in heavy-ion stopping lack theoretical justification.
- Conversely, objections on theoretical grounds concerning the role of projectile screening, Bloch and Barkas corrections severely called into question the validity of all empirical procedures mentioned above.

© International Commission on Radiation Units and Measurements 2005

- A purely theoretical approach was handicapped by a near-complete lack of knowledge of the role of the Barkas–Andersen effect (cf. Sect. 3.3.4) in heavy-ion stopping.

By and large, the work proceeded along three independent lines:

1. Compilation of a large database with experimental stopping data, limited initially to projectiles with atomic numbers $3 \leqslant Z_1 \leqslant 18$;
2. Development of a comprehensive theoretical scheme based on the stopping theory of Bohr (1913, 1915);
3. Providing new experimental data especially in the relativistic regime.

The restriction to atomic numbers $\leqslant 18$ was motivated by the significance of those ions in radiation therapy but has been relaxed somewhat in view of the availability of reliable data also for larger Z_1 and the need for heavier-ion data in numerous applications.

The energy range aimed at initially was defined as going from $\sim$1 keV/u upward. However, in view of major uncertainties in low-velocity stopping, tabulations presented in this report start at 25 keV/u.

This report presents basic definitions (Section 2) and reviews of pertinent theory (Section 3) on stopping and straggling, charge states, ranges and multiple scattering. Section 4 reviews experimental methods and tools and reports selected experimental results and comparisons to theoretical predictions. Section 5 presents available data compilations and computer programs and their ability to predict stopping data, as well as tests of underlying scaling relationships against theoretical predictions.

Stopping tables presented in Section 6 have been produced with the PASS code which implements the binary stopping theory of Sigmund and Schinner (2000, 2001b). This section also presents a concise description of the applied procedure.

Journal of the ICRU Vol 5 No 1 (2005) Report 73
Oxford University Press
doi:10.1093/jicru/ndi009

2 DEFINITIONS

2.1 STOPPING

2.1.1 Mean energy loss

The central quantity characterizing particle stopping is the *stopping force* or *stopping power*.[2] For a point particle it is defined as the average loss of kinetic energy[3] E per path length ℓ, $-\mathrm{d}E/\mathrm{d}\ell$. The minus sign defines the stopping force as a positive quantity.

The stopping force is related to the average change in momentum per path length according to

$$\frac{\mathrm{d}E}{\mathrm{d}\ell} = v\frac{\mathrm{d}P}{\mathrm{d}\ell}, \tag{2.1}$$

where v is the projectile speed, $P = M_1\gamma v$ the momentum, M_1 the projectile mass,

$$\gamma = \frac{1}{\sqrt{1-\beta^2}}, \tag{2.2}$$

$$\beta = \frac{v}{c} \tag{2.3}$$

and c the speed of light.[4]

For composite projectiles such as molecules and clusters for which energy can be transferred into internal degrees of freedom, the stopping force is defined by generalizing Eq. (2.1):

$$\frac{\mathrm{d}E}{\mathrm{d}\ell} = \sum_i v_i\left(\frac{\mathrm{d}P}{\mathrm{d}\ell}\right)_i, \tag{2.4}$$

where the sum extends over all constituents of the projectile.

Equation (2.4) in principle also applies to dressed atomic ions, *i.e.*, ions carrying electrons for which the definition of the stopping force becomes ambiguous due to projectile excitation and charge exchange. However, currently accessible experimental and theoretical accuracy is below the level where terms of order m/M_1 (m = electron rest mass) would be significant. Therefore, the stopping force on a dressed ion may safely be related to the momentum change of the *projectile nucleus*,

$$\frac{\mathrm{d}E}{\mathrm{d}\ell} = \left(v\frac{\mathrm{d}P}{\mathrm{d}\ell}\right)_{\text{nucleus}}. \tag{2.5}$$

The definitions (2.4) and (2.5) allow the inclusion of contributions from all significant energy-loss channels.

The stopping force is related to the velocity change in time — a quantity measured by some techniques — through

$$\frac{\mathrm{d}E}{\mathrm{d}\ell} = \frac{\mathrm{d}P}{\mathrm{d}t} = M_1\gamma^3\frac{\mathrm{d}v}{\mathrm{d}t}. \tag{2.6}$$

It is common practice to tabulate *mass stopping forces*

$$-\frac{1}{\rho}\frac{\mathrm{d}E}{\mathrm{d}\ell}, \tag{2.7}$$

where ρ is the mass density of the target.

A parameter of fundamental significance on the atomic or molecular scale is the *stopping cross section* S, defined by

$$S = \sum_J w_J\sigma_J, \tag{2.8}$$

where the sum extends over all energy-loss channels and where w_J and σ_J denote the energy loss and pertinent cross section per target atom or molecule for the J'th channel.

The stopping cross section is related to the stopping force through

$$S = -\frac{1}{n}\frac{\mathrm{d}E}{\mathrm{d}\ell}, \tag{2.9}$$

where n is the number of target atoms or molecules per volume. The relation to the mass stopping force

[2]The two terms will be used synonymously. While 'stopping power' is the offical nomenclature, 'stopping force' is more precise (Sigmund, 2000b).
[3]Use of the symbol E for kinetic energy is just the first of a series of cases where notation in this report deviates from ICRU Reports 37 and 49.
[4]The symbol γ has at least four well-established functions in the context of heavy-ion penetration. In addition to Eq. (2.2), it characterizes the maximum energy transfer in an elastic binary collision, the effective-charge fraction of a dressed ion and Euler's constant. Established notation will be maintained here, but proper specification will be added whenever ambiguities could arise.

© International Commission on Radiation Units and Measurements 2005

reads

$$\frac{1}{M_2}S = -\frac{1}{\rho}\frac{\mathrm{d}E}{\mathrm{d}\ell}, \tag{2.10}$$

where M_2 is the mass of a target atom (or molecule) if the target consists of only one type of atom or molecule. For polyatomic and polymolecular targets, Eq. (2.10) remains valid if S and M_2 are replaced by averages in accordance with the respective atomic or molecular abundances.

2.1.2 Energy-loss fluctuation

The energy loss ΔE at a given pathlength ℓ is a stochastic variable which obeys a statistical distribution $F(\Delta E, \ell)$ depending on ion–target combination, initial energy and travelled path length.

The mean energy loss is connected to the stopping force by

$$\langle \Delta E \rangle = \int \mathrm{d}(\Delta E)\Delta E\, F(\Delta E, \ell) = -\frac{\mathrm{d}E}{\mathrm{d}\ell}\ell, \tag{2.11}$$

provided that ℓ is small enough so that the variation of $\mathrm{d}E/\mathrm{d}\ell$ across the pathlength segment can be neglected.

The notation $\langle \ldots \rangle$ introduced in Eq. (2.11) denotes an average over a beam, *i.e.*, a large number of trajectories. This includes all relevant parameters characterizing individual projectiles such as energy, charge and excitation state and position in space.

The fluctuation in energy loss ('energy-loss straggling') after a given path length ℓ is described primarily by the variance

$$\Omega^2 = \left\langle (\Delta E - \langle \Delta E \rangle)^2 \right\rangle. \tag{2.12}$$

Ω^2 is proportional to ℓ if individual energy-loss events are statistically independent. The *straggling parameter* W is then defined by

$$W = \frac{1}{n}\frac{\mathrm{d}\Omega^2}{\mathrm{d}\ell}, \tag{2.13}$$

and W may be expressed in atomic-scale parameters by

$$W = \sum_J w_J^2 \sigma_J \tag{2.14}$$

Despite the similarity to Eq. (2.8), the range of validity of Eq. (2.14) is more restricted. It does not describe *charge-exchange straggling*, and since it is based on Poisson statistics, limitations occur especially in crystals and quite generally in dense media (Sigmund, 1978, 1991).

The question of the *shape* of an energy-loss spectrum deserves special attention. For very thin layers the spectrum must reflect the cross sections governing individual scattering events with a pronounced peak at small energy transfers and a tail at the high-energy end. Skewness decreases with increasing thickness, and eventually the spectrum reaches gaussian shape when (Bohr, 1948)

$$\Omega \gg w_{\max}, \tag{2.15}$$

where $w_{\max}$ is the maximum energy loss in an individual event. At thicknesses for which the total energy loss amounts to a sizable fraction of the initial energy, the spectra skew again.

As the rate of energy loss is governed by the speed, the range of thicknesses within which the gaussian approximation is valid widens for heavy ions because of increasing energy at constant speed. The opposite trend is observed when the projectile is an electron. There the gaussian limit of an energy-loss profile is hardly ever reached.

2.1.3 Impact-parameter dependence

The *impact parameter* in a collision denotes the distance between the incoming (straight-line) trajectory and the target when the latter is initially at rest (Figure 2.1). While this is an inherently classical concept, it retains physical significance in the context of heavy-ion penetration. An impact parameter may refer to a target nucleus or a target electron. Unless stated otherwise, reference will be made here to the target nucleus. This is consistent with the so-called semiclassical picture where trajectories of nuclei participating in a collision are characterized by classical orbits, while electronic motion obeys the laws of quantum mechanics.

Beam averages defined in Section 2.1.2 can be interpreted as integrations over the *impact plane*, *i.e.*, a plane perpendicular to the beam direction with the impact parameter being the radial coordinate.

The dependence on the impact parameter of the energy loss must be considered whenever the stopping medium is inhomogeneous or anisotropic or when finite geometric dimensions cannot be ignored. Prominent examples are the stopping of a beam under grazing incidence on a flat surface, or of a beam incident on a single crystal under *channeling* conditions (cf. Section 3.10). Angular scattering of heavy ions — being governed by interactions with

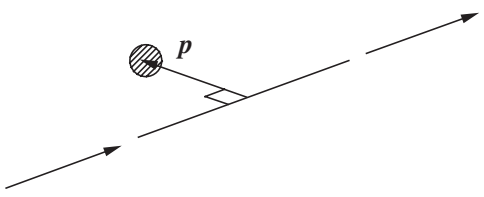


Figure 2.1. Definition of impact parameter.

target nuclei and the associated process of stopping by energy loss to recoil nuclei is another area for which knowledge of impact-parameter dependencies is vital.

2.2 RANGE

The *pathlength* ℓ specifies the length of a segment of the trajectory measured along the path. The pathlength between two points 1 and 2 is related to the stopping force by

$$\ell = \int_1^2 \mathrm{d}\ell = \int_{E_1}^{E_2} \frac{\mathrm{d}E}{\mathrm{d}E/\mathrm{d}\ell} = \int_{E_2}^{E_1} \frac{\mathrm{d}E}{nS(E)}, \tag{2.16}$$

provided that energy-loss fluctuations can be neglected. In the presence of small fluctuations, Eq. (2.16) is an approximate measure of the mean path length with the limits of integration specifying the end points of the path segment. In particular, the *range* or *range along the path* or csda (*continuous-slowing-down approximation*) range is given by

$$R = \int_0^{E_0} \frac{\mathrm{d}E}{nS(E)}, \tag{2.17}$$

where E_0 is the initial energy (Figure 2.2). Eq. (2.17) approximates the mean range along the path when straggling is small.

The variance in range or *range straggling* Ω_R^2 may be estimated from the formula of Bohr (1948)

$$\Omega_R^2 = \int_0^{E_0} \mathrm{d}E \frac{nW(E)}{[nS(E)]^3}, \tag{2.18}$$

again in the limit of low straggling.

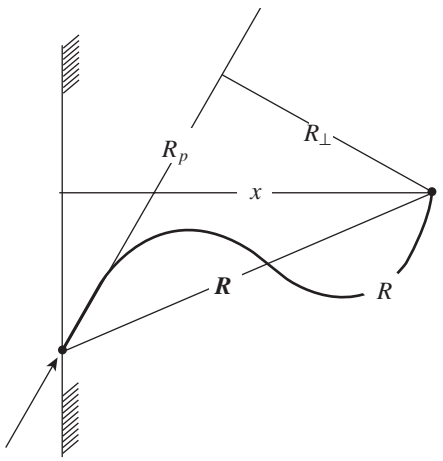


Figure 2.2. Range concepts illustrated schematically.

In addition, the following range parameters (Lindhard *et al*., 1963b) are of interest (cf. Figure 2.2)

- The *vector range* $\boldsymbol{R}$, specifying the vector distance from the starting point to the end point of a trajectory,
- The *projected range* R_p, representing the component of the vector range in the initial direction of motion,
- The *lateral range* $R_\perp$, representing the component of the vector range perpendicular to the initial direction of motion, and
- The *penetration depth* x, representing the component of the vector range along a given direction, *e.g.* the surface normal of a target with a plane surface.
- A useful dimensionless parameter R_p/R, the *projected-range correction* or *detour factor*, which is always $\leqslant 1$.

Range profiles as well as average ranges and variances can be associated with each of the range concepts defined above. These definitions override the approximate relationships (2.17) and (2.18) in the presence of significant straggling and /or angular scattering.

2.3 RADIATION EFFECTS

Radiation effects such as damage and ionization are characterized primarily by *energy deposition profiles*. Both one- and three-dimensional profiles are of interest, *i.e.*, the energy deposited per depth or per volume by the ion and by all secondary particles such as recoiling target atoms and secondary electrons. It is necessary to distinguish between different modes of energy deposition (Lindhard *et al*., 1963a). Unlike range distributions which govern the statistical distribution of a single point, *i.e.*, the end point of the ion trajectory, damage distributions characterize a collision or ionization cascade determined by the fate of a multitude of moving particles. Nevertheless, in the average over a large number of trajectories, damage and ionization profiles are governed by distribution functions analogous to and quantitatively not too different from the corresponding range distributions.

Figure 2.3 shows the simplest estimate of an energy deposition profile, found by ignoring straggling and angular scattering. Integration of Eq. (2.9) specifies the projectile energy $E = E(\ell)$ as a function of pathlength as the inverse of the relation

$$\ell = \ell(E) = \int_E^{E_0} \frac{\mathrm{d}E'}{nS(E')}. \tag{2.19}$$

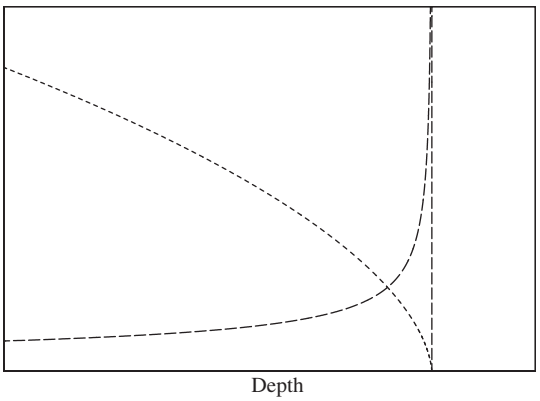


Figure 2.3. Beam energy (short-dashed line) and deposited energy (long-dashed line) *versus* penetration depth in the absence of energy-loss straggling (schematic).

The energy deposited in ionization per pathlength $F_{\mathrm{ioniz}}(\ell)$ may then be expressed as a function of pathlength by

$$F_{\mathrm{ioniz}}(\ell) = nS_{\mathrm{ioniz}}(E(\ell)), \tag{2.20}$$

where S_{inoniz} symbolizes the contribution of ionization processes to the total stopping cross section (*Bragg curve*). Similar relations may be written down for other radiation effects.

2.4 ANGULAR SCATTERING

Angular scattering affects stopping measurements mainly in two ways:

1. Beam particles deflected away from the detecting device may give rise to distortion of the measured energy-loss spectrum and of all averages.
2. Differences between travelled path length and penetration depth through a layer give rise to a detour factor in energy loss and, more seriously, in range.

While the second feature is a key ingredient in standard range theory, consideration of the first one plays a role in all analysis of stopping data. At this point, pertinent notation is introduced.

The probability for angular deflection into a solid angle $\mathrm{d}^2\phi$ is given by

$$\mathrm{d}\mathcal{P} = n\ell K(\phi)\mathrm{d}^2\phi, \tag{2.21}$$

for sufficiently small travelled pathlength ℓ, where $K(\phi)$ is the differential scattering cross section and ϕ the deflection angle in the laboratory frame of reference.

With $\mathrm{d}\mathcal{P}$ increasing, multiple angular deflections become increasingly important. The distribution in total scattering angle α is then described by a distribution $F(\alpha, \ell)\mathrm{d}^2\alpha$ which typically approaches the single-scattering profile Eq. (2.21) at large angles but takes on a gaussian-like shape around $\alpha = 0$.

Complications arise from the fact that angular deflection and energy loss are correlated (cf. Section 3.14).

Table 2.1. Fundamental constants entering stopping parameters: numerical values (IUPAP 1987) and expressions in three systems of units.

Name	Symbol	Value	SI	Gaussian	a. u.
Bohr radius	a_0	0.052917 nm	$4\pi\epsilon_0\hbar^2/me^2$	$\hbar^2/me^2$	1
Rydberg energy	R	13.6057 eV	$e^2/8\pi\epsilon_0 a_0$	$e^2/2a_0$	0.5
Bohr velocity	v_0	$c/137.036$	$e^2/4\pi\epsilon_0\hbar$	$e^2/\hbar$	1

2.5 UNITS, FUNDAMENTAL CONSTANTS AND CONVERSION FACTORS

2.5.1 Units

While the use of gaussian units is most common in the theoretical literature on particle stopping, the SI system of units is clearly preferrable from a user's point of view. A third option, atomic units, is frequently encountered. This section serves to provide pertinent expressions for key parameters in these three systems of units and suitable conversion factors. Table 2.1 specifies expressions for three key parameters, Bohr radius, Rydberg energy and Bohr velocity.

2.5.2 Examples

The use of different units is illustrated on the Coulomb factor in the standard expression for the electronic stopping cross section of a point charge which, in gaussian units, reads

$$S = \frac{4\pi Z_1^2 Z_2 e^4}{mv^2} L, \tag{2.22}$$

where L denotes the dimensionless *stopping number* (which would read $L = \ln(2mv^2/I)$ in case of the Bethe formula) and Z_1 and Z_2 denote the atomic numbers of projectile and target, respectively.

The same relation in SI units reads

$$S = \frac{Z_1^2 Z_2 e^4}{4\pi\epsilon_0^2 mv^2} L \tag{2.23}$$

but is rarely if ever encountered in the literature. In terms of fundamental constants (IUPAP,

1987; NIST, 2001) listed in Table 2.1 the same relation reads

$$S = 4\pi Z_1^2 Z_2 \left(\frac{v_0}{v}\right)^2 L 2\mathsf{R}a_0^2. \tag{2.24}$$

In atomic units this reduces to

$$S = 4\pi Z_1^2 Z_2 \frac{L}{v^2}. \tag{2.25}$$

The atomic unit of S is equivalent to[5] 27.2 eV $\times$ $(0.0529\ \text{nm})^2$.

2.5.3 Conversion

In practical applications the kinetic energy per nucleon or per atomic mass unit E/A_1, or *specific energy* is more convenient than the velocity variable.[6]

Mass stopping forces [Eq. (2.7)] will be reported in units of MeV cm^2/mg and stopping cross sections in units of eVcm^2 per atom or molecule.

Pertinent relations for the most frequently occurring conversions are listed here. The specific energy is related to the projectile speed by

$$\frac{E}{A_1} = uc^2(\gamma - 1) = 931.49\left(\frac{1}{\sqrt{1 - v^2/c^2}} - 1\right), \quad E/A_1 \text{ in MeV}, \tag{2.26}$$

where u is the atomic mass unit 1.6605×10^{-27} kg. The inverse relation reads

$$\frac{1}{2}M_1 v^2 = E\frac{1 + E/2M_1c^2}{(1 + E/M_1c^2)^2}. \tag{2.27}$$

The mass stopping force relates to the stopping number as

$$-\frac{\mathrm{d}E}{\rho \mathrm{d}\ell} = 3.0705 \times 10^{-4}\frac{Z_1^2 Z_2}{A_2\beta^2}L, \quad \mathrm{d}E/\rho\mathrm{d}\ell \text{ in MeVcm}^2/\text{mg}, \tag{2.28}$$

and to the stopping cross section as

$$S = 1.6605A_2\left(-\frac{\mathrm{d}E}{\rho \mathrm{d}\ell}\right), \quad S \text{ in } 10^{-15}\text{eVcm}^2, \quad \mathrm{d}E/\rho\mathrm{d}\ell \text{ in MeVcm}^2/\text{mg}. \tag{2.29}$$

The stopping cross section relates to the stopping number as

$$S = 5.0991 \times 10^{-4}\frac{Z_1^2 Z_2}{\beta^2}L, \quad S \text{ in } 10^{-15}\text{eVcm}^2, \tag{2.30}$$

and the stopping force in atomic units is related to the mass stopping force as

$$\frac{\mathrm{d}E}{\mathrm{d}\ell} = 0.36749\rho\left(\frac{\mathrm{d}E}{\rho \mathrm{d}\ell}\right), \quad \rho \text{ in g/cm}^3,\ \mathrm{d}E/\rho\mathrm{d}\ell \text{ in MeV cm}^2/\text{mg}. \tag{2.31}$$

Alternatively,

$$\frac{\mathrm{d}E}{\mathrm{d}\ell} = 100\rho\frac{\mathrm{d}E}{\rho \mathrm{d}\ell}, \quad \mathrm{d}E/\mathrm{d}\ell \text{ in keV}/\mu\text{m}, \quad \rho \text{ in g/cm}^3,\ \mathrm{d}E/\rho\mathrm{d}\ell \text{ in MeVcm}^2/\text{mg} \tag{2.32}$$

in atomic and modified SI units, respectively.

Finally, the specific energy of an ion at the Bohr velocity v_0 is given by

$$\left(\frac{E}{A_1}\right)_{v = v_0} = 0.02480\,\text{MeV}. \tag{2.33}$$

2.5.4 Notation

In the stopping literature, the symbol S may be found to denote both stopping cross section, stopping force and mass stopping force, and the symbol $-\mathrm{d}E/\mathrm{d}x$ may be found to denote either stopping force or mass stopping force.

[5] Caution is indicated with respect to energy unit which is set to 2R here. This is consistent with the common practice of setting $\hbar = m = e = 1$. However, also the straight R may be encountered as the energy unit, and this is not always noted explicitly in the pertinent literature.

[6] In general, no distinction will be made between energy per nucleon and energy per atomic mass unit because the numerical difference amounts to at most 0.25 % for stable isotopes of all elements from lithium upward.

Journal of the ICRU Vol 5 No 1 (2005) Report 73
Oxford University Press
doi:10.1093/jicru/ndi010

3 THEORY

3.1 INTRODUCTORY SURVEY

Early theoretical efforts on heavy-ion stopping date back to Bohr (1940), who pointed out the importance of screening due to projectile electrons in the slowing-down of fission fragments, and to Lamb (1940) and Knipp and Teller (1941), who studied the problem of charge equilibrium for penetrating heavy particles. The central role of the projectile charge as well as charge exchange in conjunction with stopping phenomena was discussed by Bohr and Lindhard (1954).

Since the appearance of the LSS theory (Lindhard *et al*., 1963b) it has been common to divide heavy-ion stopping into three regimes (Figure 3.1),

- a low-speed regime where the electronic-stopping force is taken to be proportional to the projectile speed v and given roughly by the estimates of Lindhard and Scharff (1961) or Firsov (1959),
- a high-speed regime characterized by the Bethe (1930) formula, and
- an intermediate regime around and above the stopping maximum which has most often been characterized by a Bethe-type formula in conjunction with some effective ion charge (Northcliffe, 1963).

While this picture has been of some help in attempts to scale experimental data, the process of theoretical understanding and quantitative description in particular of the intermediate regime has been slow. Amongst a variety of reasons are the notorious problem of understanding the relation between ion charge and energy loss, in particular in connection with the density effect to be discussed in Section 3.4, uncertainty about the role of the Barkas–Andersen effect (cf. Section 3.3.4), and lack of knowledge about the contribution of charge exchange and projectile excitation at intermediate velocities.

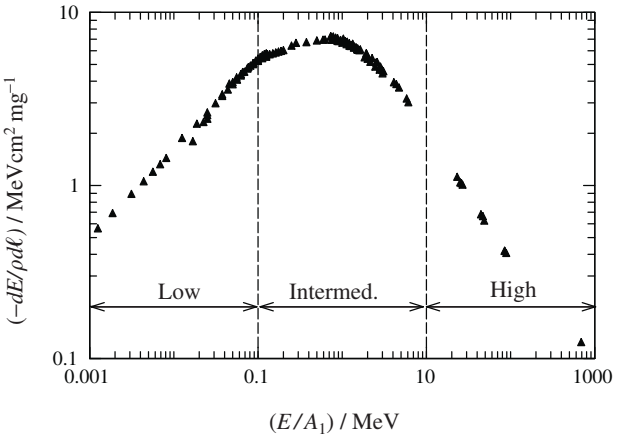


Figure 3.1. Regimes of heavy-ion stopping illustrated by oxygen in aluminium. Data compiled by Paul (2003).

An important step forward was made by Brandt and Kitagawa (1982), who established an explicit connection between ion charge and stopping force. Several details of this theory are either too restrictive or obsolete, but its central feature, to let the ion charge enter *via* a partially screened Coulomb potential as suggested originally by Bohr (1948) in his famous review of particle penetration, has been common to all subsequent theoretical attacks on this problem.

In the quoted paper, Bohr pointed at the fact that the regimes of validity of classical-orbit models and of quantal perturbation theory are roughly complementary: The stopping of low-charge particles like electrons and protons at high speed, *i.e.*, well above the Bohr velocity $v_0 = c/137$, is accurately described by the Bethe theory which treats projectile–target interaction by quantal perturbation theory to the lowest order. Since the accuracy of this scheme deteriorates with increasing projectile charge and decreasing speed, it seemed appropriate in an alternative approach to start at the opposite end, *i.e.*, the classical limit, in an attempt to find a comprehensive theory of heavy-ion stopping. This led to the binary theory of stopping (Sigmund and Schinner, 2000) and various extensions.

Parallel developments in the theory of heavy-ion stopping include the so-called CKT model by Maynard *et al*. (2001b) and the convolution approximation by Grande and Schiwietz (1998, 2002), both geared toward intermediate-to-high velocities. A model by Lifschitz and Arista (1998) based on a generalization of the Friedel sum rule, initially designed for low-speed light ion and antiproton stopping, has

© International Commission on Radiation Units and Measurements 2005

been extended to heavy ions (Arista, 2002). It is geared toward low and intermediate velocities and appears particularly promising for the low-speed range.

3.2 STOPPING PROCESSES

3.2.1 Classification

Energy-loss processes for charged particles may be classified roughly into five groups,

1. Electronic excitation and ionization of the target,
2. Projectile excitation and ionization,
3. Electron capture,
4. Recoil loss ('nuclear stopping'),
5. Electromagnetic radiation.

For electrons only processes 1, 4, and 5 are of interest (ICRU, 1984). For light ions (ICRU, 1993) electromagnetic radiation (process 5) is negligible up to very high energies and process 1 dominates except at the low-speed end. This simple picture changes for heavier ions, where processes 2 and 3 cannot be neglected in general and, moreover, nuclear stopping becomes relatively more important at low and moderate velocities. Radiative processes become dominating at extremely high velocities.

Energy may also be transferred into

6. Nuclear reactions and
7. Chemical reactions.

It is debatable whether or not such processes should be categorized under stopping as projectiles may change identity. While chemical reactions do not affect the stopping process significantly in the energy range of interest in this report, caution is indicated with regard to nuclear reactions. Although it makes little sense to relate the stopping force on the fragments of a disintegrated projectile to that on the mother nucleus, the energy-deposition profile in the stopping medium hinges on all these quantities. Thus, the preferred — and certainly most rigorous — strategy must be to incorporate nuclear reactions that change the identity of the projectile into an appropriate theory of radiation effects and to omit them from the stopping force.

3.2.2 Thomas–Fermi estimates

The Thomas–Fermi model of the atom (Gombas, 1956) ignores the shell structure but provides useful estimates for the qualitative dependence of parameters characterizing an atom as a function of atomic number. Thomas–Fermi parameters read;

- $Z^{-1/3}\, a_0$ for length,
- $Z^{2/3}\, v_0$ for speed,
- $Z^{4/3}$ R for energy per electron, and
- Z R/$\hbar$ for frequency,

for a neutral atom with atomic number Z. Estimates involving these parameters will be applied to quantities characterizing target (Z_2) and projectile (Z_1) in the following.

3.2.3 Regimes of heavy-ion stopping

Figure 3.2 shows a qualitative survey of stopping regimes for a heavy (gold) and a light (carbon) target. Lines indicate rough limits between various regimes.

The thin horizontal line labelled 'Slow' at $E/A_1 =$ 25 keV corresponding to $v = v_0$, the Bohr velocity, roughly delimits the regime of low-speed stopping where the ion speed is lower than the orbital velocities of all but the outermost target electrons.

The horizontal line labelled 'Shell corr.' marks the instance where the projectile speed equals the Thomas–Fermi velocity $Z_2^{2/3} v_0$ of the target electrons. Below this line the motion of target electrons cannot be ignored.

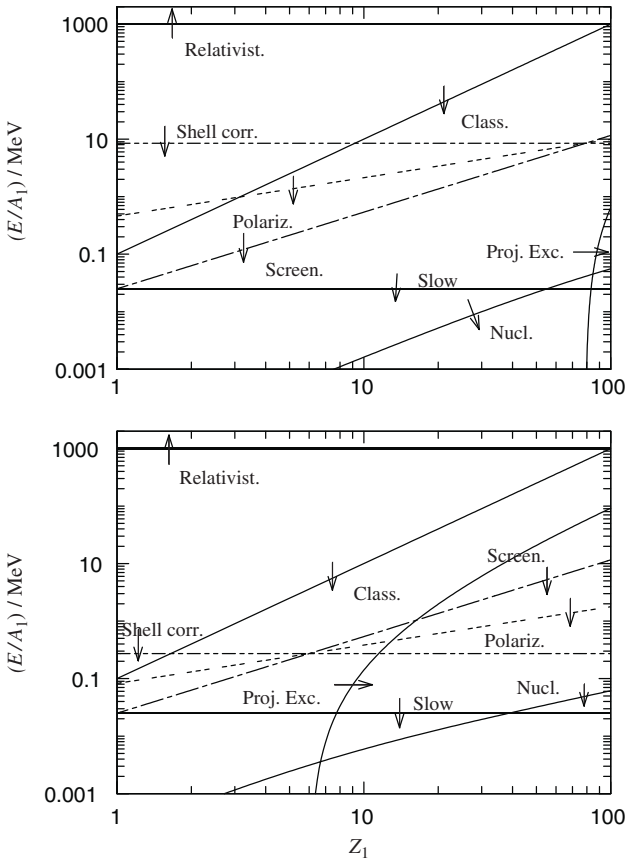


Figure 3.2. Approximate limits between regimes of ion stopping. Arrows cross borderlines and point into a regime where the respective effect is dominating or significant. Upper graph: Gold target. Lower graph: Carbon target.

A third horizontal line labelled 'Relativist.' at $E/A_1 = 1$ GeV, close to the rest energy of the projectile, indicates the transition from the moderately relativistic to the highly relativistic velocity range.

According to Bohr (1948), a moving ion in charge equilibrium carries electrons with orbital velocities exceeding the projectile speed v. This defines a rough borderline labelled 'Screen.' at the Thomas–Fermi velocity $v = Z_1^{2/3} v_0$ of the projectile. Projectiles are expected to be stripped of the majority of their electrons at energies exceeding that limit.

Processes involving excitation or ionization of the projectile must become competitive whenever the number of electrons accompanying the projectile is comparable to or greater than that on the target atom. The lines labelled 'Proj. Exc.' indicate that this effect must be insignificant for gold except for the heaviest ions. Conversely, the effect must be expected to be noticeable for carbon except for the lightest projectile ions.

The line labelled 'Nucl.' marks the transition from dominating electronic to dominating nuclear stopping. It has been estimated very roughly on the basis of the Lindhard and Scharff (1961) formula for velocity-proportional electronic stopping and the so-called Nielsen formula (Lindhard *et al.*, 1963b) for energy-independent nuclear stopping, to be discussed in Section 3.8.4.

The two remaining lines, 'Class.' and 'Polariz.' express fundamental aspects of Coulomb excitation that deserve special attention and will be discussed in the following section.

3.2.4 Target excitation

The dominating contribution to the stopping of light charged particles is excitation and ionization of target electrons ('electronic stopping') over a very wide energy/velocity range. The process is well described by the Bethe theory and its extensions (ICRU, 1993) which treat the Coulomb interaction between the projectile and the target electrons by quantal scattering theory in the first Born approximation. This results in a strict proportionality between the stopping force and the square of the projectile charge, Z_1^2. A lower limit for the range of validity of the first Born approximation is set by the requirement on the Sommerfeld parameter $Z_1 v_0/v$ to be <1, or

$$v > Z_1 \alpha\, c, \tag{3.1}$$

where $\alpha = v_0/c \simeq 1/137$ is the fine structure constant, or

$$E/A_1 > Z_1^2 \times 25 \text{ keV}. \tag{3.2}$$

The Sommerfeld criterion is not a *necessary* criterion, *i.e.*, nothing is said about the accuracy of the first Born approximation when the criterion is not fulfilled. It is roughly complementary to the Bohr criterion which delimits the range of validity of a description of Coulomb collisions in terms of classical orbits by the requirement that the Bohr parameter

$$\kappa = \frac{2Z_1 v_0}{v} > 1, \tag{3.3}$$

i.e.,

$$E/A_1 < Z_1^2 \times 100 \text{ keV}. \tag{3.4}$$

When this criterion is fulfilled, characteristic dimensions of a classical Kepler orbit exceed the de Broglie wavelength so that construction of a wave packet is possible which follows approximately the classical orbit. The Bohr criterion is a *sufficient* criterion.

The fact that there is an overlap regime between the two criteria promises a smooth transition between the classical and the Born regime. Only the line specified by Eq. (3.4), labelled 'classical', has been included in Figure 3.2.

In addition to the Bohr parameter κ, a second dimensionless parameter can be constructed,[7]

$$\frac{1}{\xi} = \frac{Z_1 v_0 \hbar\omega}{m v^3}, \tag{3.5}$$

which limits the range of validity of the Born approximation. Here ω is the frequency of a characteristic target resonance, *e.g.*, $\omega = I/\hbar$ where I is the *mean excitation energy*, the 'I-value' of a target atom. Eq. (3.5) determines the order of magnitude of the leading correction term in the Born series, the Barkas–Andersen effect that depends on the sign of the projectile charge and will be discussed in Section 3.3.4, where also an alternative interpretation of the effect is discussed which does not make reference to the Born series. This correction becomes substantial for

$$v \lesssim (Z_1 Z_2)^{1/3} v_0 \tag{3.6}$$

and is included under the label 'polarization'.

It is seen in Figure 3.2 that for the lightest ions there is a wide energy range in which the uncorrected Bethe formula is valid, particularly for a light target. Conversely, for the heaviest ions an even wider range of validity is expected for

[7] It is emphasized that despite the occurrence of $\hbar$, the parameter specified in Eq. (3.5) is a purely classical quantity since $v_0\hbar\omega = e^2\omega/4\pi\epsilon_0$ is independent of Planck's constant. This notation — which does not distinguish between gaussian and SI units — is used in order to facilitate reference to the original literature that utilizes gaussian units.

a classical model. However, the range of applicability of the pure Bohr model without screening and other corrections is quite narrow, in particular for light targets for which projectile excitation contributes.

The relative significance of screening, polarization and shell correction is reversed at $Z_1 = Z_2$. Going from high to low velocities, the shell correction comes first for $Z_1 < Z_2$ while screening does so for $Z_1 > Z_2$.

The main conclusion to be drawn from Figure 3.2 is the fact that corrections to the simplest models (uncorrected Bethe and uncorrected Bohr formula) are required over a substantial portion of the parameter space, and that one single dominating correction is an exception rather than the rule. Taking due care of simultaneously acting effects in a nonlinear theory is a nontrivial task that, however, is facilitated if one takes the starting point in a classical-orbit description of the scattering process.

3.2.5 Interaction range

Both the classical theory and the Born approximation predict the Coulomb interaction of a projectile moving with a speed v to be effectively limited to within the adiabatic radius

$$a = \frac{v}{\omega}, \tag{3.7}$$

where ω is the resonance frequency of the respective electronic-excitation channel. This quantity is useful to consider in an assessment of the contribution to stopping from individual target shells as well as in estimates of the significance of collective effects.

In the classical regime the energy transfer to a target electron increases with decreasing impact parameter up to the limit defined by the conservation laws of energy and momentum. In the Born regime an effective upper limit is reached at an impact parameter of the order of the de Broglie wavelength. This has the consequence that hard electronic interactions are more important in the classical than in the Born regime. Taken together with Eq. (3.7) this implies that excitation of inner shells increases in significance with increasing Z_1 at constant v.

3.2.6 Role of projectile electrons

A distinct feature of heavy-ion stopping is the presence of electrons on the projectile at all but the highest velocities. Projectile screening due to these electrons tends to reduce the Coulomb interaction between the projectile and the target electrons, but at the same time projectile excitation may become a noticeable energy-loss channel. Moreover, the very processes of electron capture and loss cost energy, and fluctuations in charge state give rise to energy-loss straggling (*charge-exchange straggling*).

Projectile excitation and ionization have usually been treated by, roughly speaking, inverting the roles of target and projectile. This approach is problematic, and attention will be given to a revised procedure.

3.2.7 Nuclear stopping

Energy loss to recoiling nuclei ('nuclear stopping')[8] is insignificant in the region of weakly screened Coulomb interaction with target electrons but increases in relative significance as electronic excitation channels close with decreasing projectile speed. Electronic stopping depends on projectile *speed* while nuclear stopping depends on projectile *energy*. Therefore the point of crossover between nuclear and electronic stopping depends on Z_1 (and, less sensitively, Z_2), as is seen in Figure 3.2.

3.3 ELECTRONIC STOPPING OF POINT CHARGES

3.3.1 Classical theory

The prediction of the Bohr (1913, 1915) theory may be expressed in terms of the stopping number L defined by Eq. (2.22),

$$L = \sum_j f_j L_j(\xi_j, \beta) \tag{3.8}$$

with

$$L_j(\xi_j,\beta) = L_{\text{Bohr}} = \ln(C\xi_j) - \ln(1-\beta^2) - \frac{\beta^2}{2}, \quad \beta = \frac{v}{c} \tag{3.9}$$

and

$$\xi_j = \frac{mv^3}{Z_1 v_0 \hbar \omega_j}, \tag{3.10}$$

i.e., the reciprocal of the expression given in Eq. (3.5), where ω_j and f_j are the resonance frequency and weight factor for the j'th target resonance such that

$$\sum_j f_j = 1. \tag{3.11}$$

[8] In order to avoid confusion with processes on the nuclear scale, this atomic process has occasionally been denoted 'elastic stopping'. This notion is avoided here because the chance for confusion would become considerably greater, cf. footnote 23 on page 52.

Moreover,

$$C = 2e^{-\gamma} = 1.1229, \tag{3.12}$$

where $\gamma = 0.5772$ is Euler's constant.[9] The logarithmic form of Eq. (3.9) originates in an asymptotic expansion for large values of ξ_j. For $\xi_j \lesssim 1$, when Eq. (3.9) turns negative, alternative expressions are available (Sigmund, 1996; Lindhard and Sørensen, 1996; Sigmund, 1997), the simplest of which can be extracted from Lindhard and Sørensen (1996),

$$L_j(\xi) = \tfrac{1}{2}\ln[1 + (C\xi)^2]. \tag{3.13}$$

Eq. (3.9) ignores the intrinsic motion of target electrons. Repairing this defect necessitates shell corrections, the importance of which increases from outer to inner shells.

The shell correction to the Bohr theory has been determined by Sigmund (2000a) *via* re-evaluation of the Bohr theory allowing for initial motion of the target electron. The main outcome from that work is a clear dominance of small-impact-parameter collisions in the shell correction, *i.e.*, collisions in which the effect of binding on the energy transfer is insignificant. This implies that the computation of shell corrections reduces to a binary-collision problem where both collision partners are in motion initially. The appropriate transformation to a coordinate frame in which the target particle is at rest, is well known (Sigmund, 1982) and reads

$$L_j(v) = \left\langle \frac{\boldsymbol{v}\cdot(\boldsymbol{v}-\boldsymbol{v}_e)v}{|\boldsymbol{v}-\boldsymbol{v}_e|^3} L_{0j}(|\boldsymbol{v}-\boldsymbol{v}_e|) \right\rangle_j \tag{3.14}$$

at all nonrelativistic velocities, where L_j and L_{0j} are the shell-corrected and uncorrected stopping numbers, respectively, for the j'th shell.

Eq. (3.14) has been extended to the relativistic regime by Tofterup (1983).

3.3.2 Quantal perturbation theory

Bethe stopping theory for point charges has been discussed extensively in previous reports (ICRU, 1984, 1993). The focus here is on aspects specific to higher values of Z_1 as well as more recent issues.

Eq. (3.8) remains valid, but Eq. (3.9) is replaced by the familiar form

$$L_j(B_j,\beta) = L_{\text{Bethe}} = \ln B_j - \ln(1-\beta^2) - \beta^2 \tag{3.15}$$

with

$$B_j = \frac{2mv^2}{\hbar\omega_j}. \tag{3.16}$$

Figure 3.2 shows that the shell correction is the leading add-on, particularly so for high-Z_2 targets where also the Barkas–Andersen effect may become substantial.

The intrinsic motion of target electrons is taken fully into account in the Bethe theory but is ignored in the derivation of Eq. (3.15). Shell corrections to the Bethe theory have been discussed extensively in ICRU Report 49. With a few exceptions (McGuire, 1983; Bichsel, 2002), existing evaluations have been based on model systems for the target. ICRU Report 49 focused on hydrogenic wave functions whereas the electron-gas model (Lindhard and Winther, 1964) has been most frequently employed in the literature (Bonderup, 1967; Chu and Powers, 1972b; Ziegler *et al.*, 1985). Alternative approaches include the harmonic-oscillator model (Sigmund and Haagerup, 1986) as well as the kinetic theory (Sigmund, 1982; Oddershede and Sabin, 1984).

A very efficient method for computing shell corrections in the Born regime, making use of the binary theory to be described below, has been explored by Sigmund and Schinner (2002c).

3.3.3 Bloch theory

The theory of Bloch (1993b) connects Bohr's classical with Bethe's quantal perturbation theory. A transparent formulation of this theory has been presented by Lindhard and Sørensen (1996). The essential feature of this approach is the replacement of a classical impact parameter by quantized angular momentum. This does not affect distant collisions — where the Bethe theory reproduces Bohr's result — but delivers different results for close collisions when the Bohr parameter κ, Eq. (3.3), is not $\ll 1$.

In the nonrelativistic limit the Bloch term was determined by Lindhard and Sørensen (1996) on the basis of the transport cross section

$$\sigma^{(1)} = 4\pi\left(\frac{\hbar}{mv}\right)^2 \sum_{\ell=0}^{\infty} \sin^2(\delta_\ell - \delta_{\ell+1}), \tag{3.17}$$

where δ_ℓ is the ℓ'th phase shift for elastic binary scattering of a free target electron on a point projectile. $\sigma^{(1)}$ is related to the stopping cross section *via*

$$S = mv^2\sigma^{(1)}. \tag{3.18}$$

Evaluation on the basis of free-Coulomb scattering of target electrons is meaningful because only the *difference* between Eq. (3.17) and the perturbation limit of the same relation is evaluated. Binding is central for distant interactions where the perturbation limit delivers the exact result.

[9] Cf. footnote 4 on page 23.

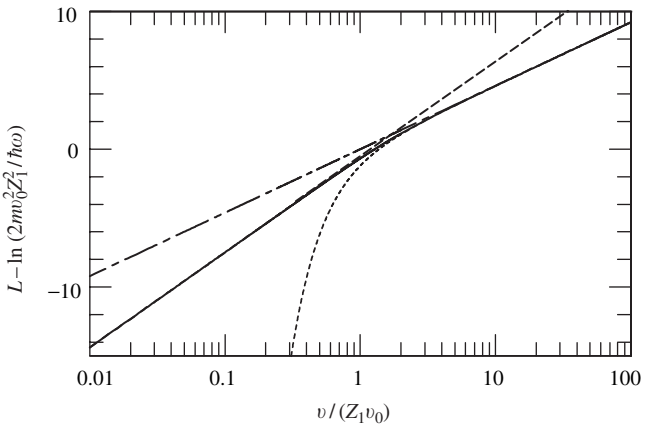


Figure 3.3. Universal plot of simple Bohr and Bethe formulae for swift bare ions. Plotted is the stopping number L versus a scaled projectile speed. Shell, polarization, screening and relativistic corrections are neglected. Solid line: Bloch formula; dot-dashed and dashed lines: Bethe and Bohr logarithm $L_{\rm Bethe}$ and $L_{\rm Bohr}$ respectively; thin short-dashed line: Bethe logarithm plus high-speed approximation of Bloch correction ($\propto Z_1^4$). Figure from Sigmund (1997).

This procedure leads to the Bloch correction

$$\Delta L_{\rm Bloch} = \psi(1) - {\rm Re}\,\psi\left(1 + i\frac{Z_1 v_0}{v}\right), \tag{3.19}$$

where ψ represents the logarithmic derivative of the gamma function, $\psi(\zeta) = d\,\ln\Gamma(\zeta)/d\zeta$, and Re denotes the real part. When added to the Bethe logarithm (Eq. 3.15), the fulldrawn curve in Figure 3.3 is obtained which approaches the Bohr logarithm at low velocities.

The Bloch correction vanishes in the limit of large velocities[10] and behaves like $\ln(Cv/Z_1 v_0)$ at low velocities.

Therefore, Bloch's stopping formula may be rewritten in the form

$$\begin{aligned} L_{\rm Bloch} &= L_{\rm Bethe} + \Delta L_{\rm Bloch} \\ &= \ln\frac{Cmv^3}{Z_1 v_0 \hbar\omega} + \ln\frac{2Z_1 v_0}{v} - {\rm Re}\,\psi\left(1 + i\frac{Z_1 v_0}{v}\right) \\ &= L_{\rm Bohr} + \Delta L_{\rm invBloch}, \end{aligned} \tag{3.20}$$

defining an *inverse-Bloch* correction $\Delta L_{\rm invBloch}$ which vanishes at low speed but becomes substantial in the Bethe regime (de Ferrariis and Arista, 1984; Sigmund, 1996).

[10]The Bloch correction Eq. (3.19) reduces to a power law $\propto Z_1^2$ at high speed. This has led to the terminology of a Z_1^4 correction to the Bethe formula which is frequently identified with the Bloch correction. This is evidently justified when the Bloch correction is small but leads to absurd results in the opposite limit, as is seen from the thin dashed line in Figure 3.3.

An accurate approximation to the Bloch stopping number was found by Ferrariis and Arista (1984),

$$\begin{aligned} L_{\rm Bloch} &= L_{\rm Bethe} + \Delta L_{\rm Bloch} \\ &\simeq \ln\frac{2mv^2/\hbar\omega}{\sqrt{1 + (Z_1 v_0 e^\gamma/v)^2}} \\ &\equiv \ln\frac{Cmv^3/Z_1 v_0 \hbar\omega}{\sqrt{1 + (Cv/2Z_1 v_0)^2}}. \end{aligned} \tag{3.21}$$

Explicit evaluations of shell corrections to the Bloch formula are unexplored. However, since the Bloch correction Eq. (3.19), originates in close collisions, feasible shell corrections may be found by applying Eq. (3.14), which is exact for binary collisions.

While Bloch's calculation has not been extended to include terms of uneven order in Z_1, the magnitude of the Z_1^3 correction to the Bloch term can be estimated by comparison of calculations within classical and quantal perturbation theory. A Z_1^3 correction to the classical theory calculated for lithium on carbon (Schinner and Sigmund, 2000) was found to agree accurately with the corresponding result from quantal perturbation theory in the oscillator approach (Mikkelsen and Sigmund, 1989). To the extent that this finding may be generalized to other systems one may expect that a separate evaluation of Barkas– Andersen corrections to the Bloch term is of minor importance.

An extension of Bloch's theory to relativistic velocities was presented by Lindhard and Sørensen (1986) on the basis of the nonrelativistic approach sketched above, but employing relativistic scattering kinematics and the Dirac equation. This theory replaces earlier, more approximate treatments of corrections to the relativistic Bethe formula (Ahlen, 1978, 1980) as well as the Mott correction (Jackson and McCarthy, 1972; Scheidenberger *et al*., 1994). The result may be summarized as a correction to the relativistic form of the Bethe stopping number,

$$\begin{aligned} \Delta L_{\rm LS} = &\sum_{\varkappa=-\infty(\neq 0)}^{\infty}\left(\frac{|\varkappa|}{\eta^2}\frac{\varkappa-1}{2\varkappa-1}\sin^2(\delta_\varkappa - \delta_{\varkappa-1}) - \frac{1}{2|\varkappa|}\right) \\ &+ \frac{1}{\eta^2}\sum_{\varkappa=1}^{\infty}\frac{\varkappa}{4\varkappa^2-1}\sin^2(\delta_\varkappa - \delta_{-\varkappa}) + \frac{v^2}{2c^2}, \end{aligned} \tag{3.22}$$

where $\eta = Z_1 v_0/v = \kappa/2$, $\varkappa$ is an angular-momentum quantum number, and the phase shifts $\delta_\varkappa$ emerge from the Dirac equation.

This result is shown in Figure 3.4, which represents a correction to the relativistic Bethe formula (Eq. 3.15) including, if necessary, shell, screening, Barkas–Andersen and Fermi density-effect corrections. At very high velocities, deviations from pure Coulomb scattering in electron–nucleus

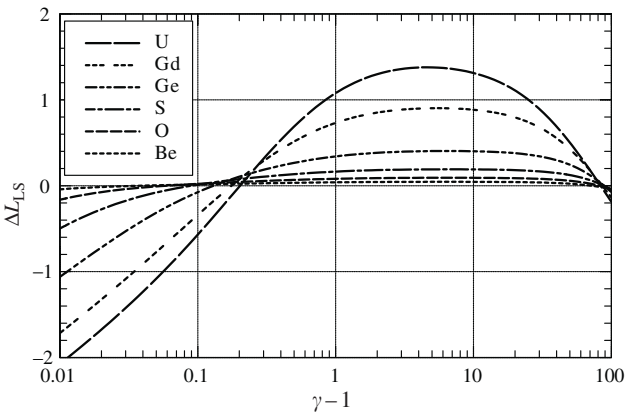


Figure 3.4. Total relativistic correction according to Lindhard and Sørensen (1996), including correction for finite size of the projectile nucleus. The abscissa variable is $\gamma - 1 = 1/\sqrt{1 - v^2/c^2} - 1$.

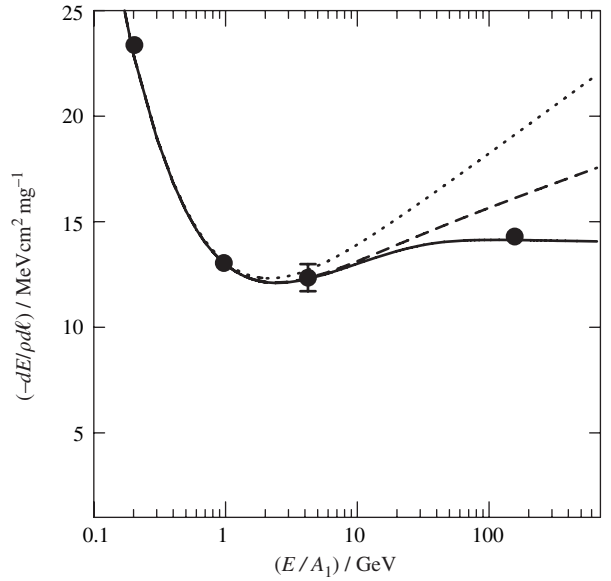


Figure 3.5. Stopping of highly relativistic ions: Experimental data for Pb in Al from Geissel and Scheidenberger (1998), Datz *et al*. (1996) and three theoretical curves based on Lindhard and Sørensen (1996). Dotted line: Point charge. Dashed line: Fermi density effect added. Solid line: Fermi density and nuclear-size effect added.

scattering need to be considered ('finite-size effect') in the evaluation. Figure 3.5 indicates the magnitude of this correction for lead in aluminium. Good agreement with experimental data is found provided that also the Fermi density effect (ICRU, 1984) is included.

For ultrarelativistic projectiles, Lindhard and Sørensen (1996) derived the asymptotic expression

$$L \sim \ln \frac{1.62c}{R\omega_{\mathrm{P}}} \tag{3.23}$$

for the stopping number,[11] where R is the nuclear radius and ω_{P} the plasma frequency reflecting the total electron density in the target.

Sørensen (2003, 2004) demonstrated that energy losses to pair creation and bremsstrahlung dominate over target excitation for $\gamma \gtrsim 10^3$ ($E \gtrsim 10^6$ MeV/u) in heavy materials.

3.3.4 Barkas–Andersen effect

The Barkas effect denotes the difference in stopping between a particle and its antiparticle. The effect was discovered in the analysis of experiments aiming at determining meson masses (Smith *et al*., 1953) and was ascribed to higher-order contributions to the Born series by Barkas *et al*. (1963) which cause deviations from the strict Z_1^2 dependence of the stopping force predicted by the Bethe theory [cf. Eqs. (2.22) and (3.15)].

The fact that this observation could become significant for ion stopping was not recognized until systematic high-precision measurements by Andersen *et al*. (1969) revealed that

- stopping forces on bare helium ions were *higher* than four times those on bare protons,
- that the difference increased with decreasing projectile speed and
- the effect could be quantified in terms of a term proportional to Z_1^3 contributing to the stopping force.

Even though the effect was small — at a level of several per cent for proton energies in the MeV range — it was these measurements that triggered several theoretical studies aiming at an understanding of this 'Z_1^3 effect'. The fact that the two types of measurement track the same physical phenomenon has led to the terminology of the *Barkas effect* (Lindhard, 1976). However, this terminology does not give justice to the seminal character of the measurements of Andersen *et al*. (1969) especially for heavy-ion stopping. Hence, the notion of the *Barkas–Andersen effect* is recommended in the present report.

The existence of a Z_1^3-proportional correction must evidently be the cause of serious concern in any theory of stopping for high-Z_1 ions. Indeed, the lack of a theory of the Barkas–Andersen effect going beyond the first correction term in a series valid for small Z_1 was a major obstacle for a long time toward a theory of heavy-ion stopping at intermediate velocities.

[11] The value 1.62 is more accurate than the one given in the original paper (private communication by A. H. Sørensen).

Ashley *et al*., (1972) presented a theoretical evaluation of the Z_1^3 correction within classical perturbation theory for large impact parameters. An equivalent quantal evaluation by Hill and Merzbacher (1974) confirmed their results. Those authors also proposed the notion of 'polarization effect'.[12] Both models left open the question of a possible higher-order correction from close collisions. That aspect was considered by Lindhard (1976), who analyzed the Barkas–Andersen effect in terms of a deviation from pure Coulomb scattering instead of a deviation from first-order perturbation theory.

Ashley *et al*. (1972) derived an expression for the energy loss $w(p)$ versus impact parameter p in an individual interaction. While the validity of their expression has been confirmed by all subsequent calculations, estimates of the Z_1^3-contribution to the *stopping cross section* have varied considerably, dependent on input. Ashley *et al*. (1972), asserting that there was no Z_1^3-term for close collisions, introduced a cutoff impact parameter. The choice of this parameter is crucial since $w(p)$ determined in this manner diverges strongly at small p. Jackson and McCarthy (1972) followed the same scheme although with a different choice of cutoff, and ICRU Report 49 treats the cutoff as a fitting parameter to measured stopping forces. The estimate by Lindhard (1976) avoided the impact-parameter picture and led to an estimate of the Z_1^3 correction to the stopping cross section about twice the one proposed by Jackson and McCarthy (1972). Dimensional arguments based on characteristic length parameters demonstrated that the parameter (3.5) — which already emerged from the calculation of Ashley *et al*. (1972) — is the dominating characteristic of the Barkas–Andersen effect.

Complete evaluations of the Z_1^3 correction in the stopping cross section were based on the electron-gas model (Esbensen, 1976; Esbensen and Sigmund, 1990) and the harmonic-oscillator model (Mikkelsen and Sigmund, 1989), with a considerable follow-up literature.

According to Eq. (3.5) the Barkas–Andersen correction increases with decreasing speed. This has drastic consequences in antiproton stopping where the correction is negative and thus eventually gives rise to a change of sign in the stopping force. This marks the breakdown of a description of the Barkas–Andersen effect in terms of a series expansion in Z_1 and indicates the need for nonlinear stopping theory.

Much of the existing literature on this item — listed by Arista and Lifschitz (1999) — is based on the electron-gas model, makes reference to Echenique *et al*. (1981), and is geared toward the low-speed (velocity-proportional) regime. Approaches valid also at intermediate velocities were proposed by Mikkelsen and Flyvbjerg (1992) for the harmonic-oscillator model (although not applied in practice), by Schiwietz (1990) (applied mostly to H and He ions), by Lifschitz and Arista (1998), and by Sigmund and Schinner (2001a).

Scaling properties of the Barkas–Andersen effect have been studied by Sigmund and Schinner (2003). It was found that for bare ions the Barkas ratio, *i.e.*, the ratio L_+/L_- of the stopping numbers for an ion and its anti-ion, was almost independent of the atomic number Z_1 when plotted versus the Bohr variable $\xi = mv^3/Z_1 v_0 \hbar\omega$, [cf. Eq. (3.10)], while a more complex dependence was found on Z_2. For ions in charge equilibrium, the magnitude of the Barkas ratio was found to *decrease* with increasing atomic number Z_1 because of increasing screening at constant ξ.

Figure 3.6 shows a comparison of theoretical predictions with measurements on antiproton stopping in silicon. It is seen that, while five theoretical predictions differ in details, the good overall agreement indicates that the Barkas–Andersen effect is well described at least for light ions.

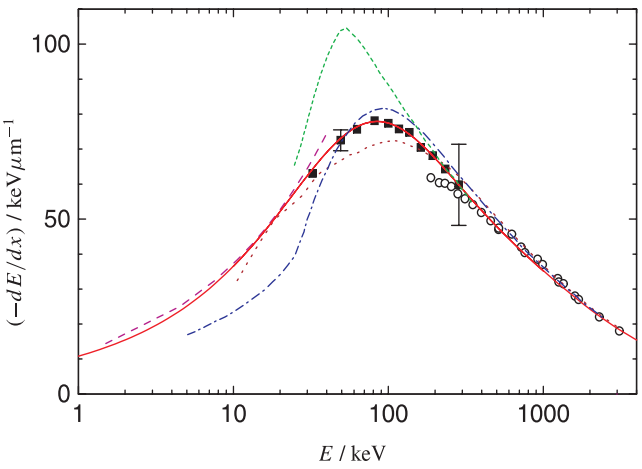


Figure 3.6. Stopping of antiprotons in Si: Comparison of theoretical predictions by Sørensen (1990) (long-dashed line), Møller *et al*. (1997) (dotted line), Arista and Lifschitz (1999) (dot-dashed line), Arbó *et al*. (2000) (short-dashed line) and Sigmund and Schinner (2002c) (solid line) with experimental data from Andersen *et al*. (1989), Medenwaldt *et al*. (1991) (open circles) and Møller *et al*. (1997) (filled squares). From Sigmund and Schinner (2001a).

[12]In this report the terms 'Barkas–Andersen correction' and 'polarization correction' will be used synonymously, while the term Z_1^3 correction will be reserved to the leading correction in Z_1 to the Bethe theory.

3.3.5 Fermi density effect

It was seen in Figure 3.5 that a Fermi density correction needs to be allowed for at extreme relativistic velocities. For a detailed exposition of this effect, reference is made to ICRU Report 37.

3.3.6 *I*-values and oscillator-strength spectra

The excitation spectrum of the target as expressed by data sets (ω_j, f_j) is the main numerical input into both quantal and classical stopping formulae, as is seen from Eqs. (3.8), (3.10) and (3.15). Within the range of validity of the logarithmic expressions (3.9) and (3.15), only the mean excitation energy I defined by

$$\ln I = \sum_j f_j \ln(\hbar\omega_j) \tag{3.24}$$

is of interest, but at lower projectile speed more detailed knowledge is required.

An extensive discussion of the determination of I-values was given in ICRU Reports 37 and 49. I-values given there are mainly extracted from stopping measurements with protons.

Precision measurements on proton stopping have been performed in a velocity range where shell corrections are not negligible and where a Z_1^3 correction is found necessary. Therefore, I-values given in ICRU Report 49 depend to a significant extent on theory available in 1984. Shortcomings of this procedure have become increasingly clear. Therefore, the ICRU has started preparations for a re-evaluation of key data including total I-values.

In the context of the present report, characterizing the excitation spectrum by a single I-value would be inadequate. Therefore, a closer inspection of available data on oscillator strengths was found appropriate.

In general the sum over f_j is replaced by an integral over a continuous spectrum of dipole oscillator strengths $f'(\omega)$ which is related to the long-wavelength dielectric function $\varepsilon(\omega)$ through

$$f'(\omega) = -\frac{2\varepsilon_0 m}{\pi n_e e^2}\omega \,\mathrm{Im}\frac{1}{\varepsilon(\omega)}, \tag{3.25}$$

where Im denotes the imaginary part,

$$\int_0^\infty \mathrm{d}\omega f'(\omega) = 1, \tag{3.26}$$

and $n_e = nZ_2$ is the number of electrons per volume. Since $\varepsilon(\omega)$ can be expressed by the complex refractive index $\mathsf{n}(\omega) + i\mathsf{k}(\omega)$, the oscillator-strength spectrum may also be written in the form

$$f(\hbar\omega) = 1.5331 \times 10^{-3}\frac{A_2}{\rho}\frac{\hbar\omega\,\mathsf{nk}}{(\mathsf{n}^2+\mathsf{k}^2)^2}$$
$$\hbar\omega \text{ in eV}; \quad f(\hbar\omega) \text{ in eV}^{-1} \tag{3.27}$$

with the normalization

$$\int_0^\infty \mathrm{d}(\hbar\omega) f(\hbar\omega) = Z_2. \tag{3.28}$$

The function f differs from f' only by the normalization.

Oscillator-strength spectra have been determined theoretically on the basis of Slater orbitals (Dehmer *et al.*, 1975). These spectra have been discretized into subshell frequencies and oscillator strengths and tabulated by Oddershede and Sabin (1984) for $1 \le Z_2 \le 36$.

Optical constants for numerous solids including covalent and ionic compounds have been tabulated over a wide frequency range (Palik, 1985, 1991, 1996, 2000). Equivalent information may be extracted from a compilation of x-ray scattering and absorption data (Henke *et al.*, 1993). Similar data for atomic and molecular gases may be extracted from Berkowitz (1979, 2002).

The procedure employed in the present report to determine (f_j, ω_j) for determining stopping forces will be described in Section 6.3.1. The resulting data sets specify I-values for all elements and compounds entering the present tables. However, those I-values do not enter directly as input.

Table 3.1 compares selected I-values so determined with values recommended in ICRU Report 49. Quite good agreement is found in most cases where recommended values were based on measurements, taking into account the above reservations.

Table 3.1. Selected *I*-values calculated from oscillator-strength spectra employed in this report (cf. Table 6.2) compared with recommended values from ICRU Report 49.

Element	Present	ICRU49	Element	Present	ICRU49
Be	64.7	63.7 ± 3	Ge	399.1	350 ± 11
C (amorphous)	86.0	81.0	Kr	390.6	352 ± 26
N_2	78.5	82.0 ± 2	Mo	424.0	424 ± 15
O_2	94.6	95.0 ± 2	Ag	447.5	470 ± 10
Ne	135.5	137 ± 4	Sn	457.8	488 ± 15
Al	158.3	166 ± 2	Xe	511.9	482
Si	169.5	173 ± 3	W	719.0	727 ± 30
Ar	182.5	188 ± 10	Pt	751.6	790 ± 30
Ti	241.8	233 ± 5	Au	741.9	790 ± 30
Fe	291.1	286 ± 9	Pb		823 ± 30
Ni	301.1	311 ± 10	U		890 ± 30
Cu	326.3	322 ± 10			

An alternative description of excitation spectra, applied frequently in stopping theory, is the dielectric theory by Lindhard and Scharff (1953) — often called local-density or local-plasma approximation — where the summation over frequencies is replaced by an integration over space such that

$$L = \frac{1}{Z_2}\int d^3\boldsymbol{r} n_e(\boldsymbol{r}) L\left(\frac{2mv^2}{\hbar\omega_P(\boldsymbol{r})}\right). \tag{3.29}$$

Here $n_e(\boldsymbol{r})$ is the electron density in a target atom ($\int d^3\,\boldsymbol{r}\, n_e(\boldsymbol{r}) = Z_2$),

$$\omega_P = \sqrt{\frac{n_e e^2}{\epsilon_0 m}} \tag{3.30}$$

the plasma frequency of a free-electron gas with a density n_e, and $L(2mv^2/\hbar\omega_P)$ the stopping number evaluated for a free-electron gas including shell and (possibly) other corrections. The occurrence of the Bethe factor in the stopping number L is related to the fact that this picture has only been applied within quantal perturbation theory.[13]

3.3.7 Z_2 structure

According to the Thomas–Fermi estimate of the frequency mentioned in Section 3.2.2, the mean excitation energy should vary as $I \simeq Z_2 I_0$ with some universal constant I_0. This behavior, predicted by Bloch (1933a), is well confirmed as a first approximation, but superimposed on this monotonic increase is an oscillatory behavior as a function of Z_2, called Z_2 structure, which is well documented experimentally for protons and helium ions (ICRU, 1984, 1993); more precisely, one sees an oscillatory dependence of the stopping cross section at constant speed on the atomic number Z_2 of the stopping medium. Both effects have been explained within the framework of dielectric theory (Chu and Powers, 1972a,b).

Inspection of Eq. (3.16) shows that within the range of validity of the Bethe theory the amplitude of observable oscillations in the stopping cross section must increase with decreasing speed. This has several reasons,

- The effect of a variation of $\hbar\omega_j$ with Z_2 becomes the more pronounced the smaller the numerator $2mv^2$.

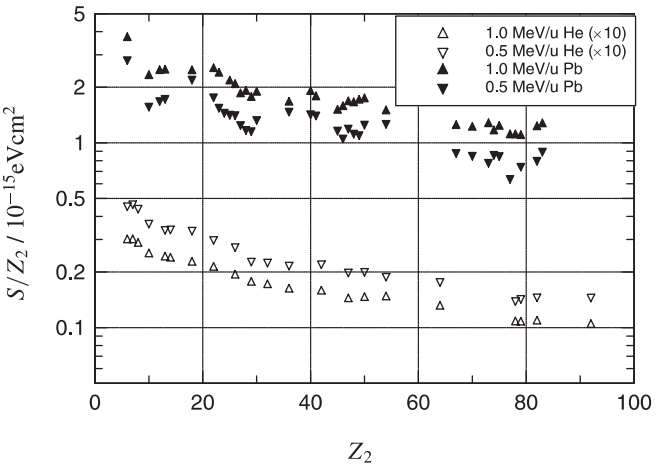


Figure 3.7. Comparison of stopping cross sections per target electron for bombardment with Pb ions (closed symbols) (Geissel, 1982) and He ions (open symbols) (ICRU, 1993).

- Such variations are most pronounced in outer target shells. Since inner-shell excitation channels close one by one with decreasing projectile speed, only those shells that produce the most pronounced oscillations contribute at low speed.
- Shell corrections tend to amplify Z_2 structure caused by the variation of ω_j with Z_2: A low value of ω_j is accompanied by a low orbital speed and hence by a low (negative) shell correction, and vice versa (Oddershede *et al.*, 1983).

Below the classical limit, Eq. (3.9) replaces the Bethe logarithm and the Z_2 structure tends to be enhanced further by the factor Z_1^{-1} under the Bohr logarithm. This is illustrated in Figure 3.7, which compares stopping cross sections *per target electron* measured for Pb ions at 0.5 and 1.0 MeV/u with the corresponding values for He. The respective screening limits lie at 0.47 and 0.040 MeV/u. Even though the measurements with lead ions do not pertain to completely stripped ions, the Z_2 structure is clearly more pronounced than for He in this velocity range.

3.4 ELECTRONIC STOPPING OF DRESSED IONS

3.4.1 Equilibrium and non-equilibrium stopping

Figure 3.2 indicates that screening by electrons accompanying the projectile increases in importance with increasing Z_1. The same statement applies to projectile excitation. These, as well as related effects, are charge-state dependent.

The charge state of the projectile is well-defined and readily measurable as long as the target material

[13] In practice, Eq. (3.29) is usually (Bonderup, 1967; Chu and Powers, 1972b) evaluated by employing a shell correction expansion (Lindhard and Winther, 1964) of the stopping number in powers of v^{-2}. The first term in that expansion is the Bethe logarithm where a numerical factor $1/\chi$ is added to the argument with $\chi \simeq \sqrt{2}$, accounting approximately for atomic binding which is neglected in a Fermi-gas model (Lindhard and Scharff, 1953).

is a gas, while the matter is more delicate for a solid stopping material (Betz, 1972). Charge states of ions penetrating solids are typically measured *after emergence*, and most often ions are allowed to travel over macroscopic distances before detection, with the possibility of electron loss by Auger emission. This problem is avoided in measurements of the charge state *during emergence* (Brunelle *et al*., 1997), but the experimental method involved, making use of hydrogen emission from the target surface and to be discussed in Section 4.5.2, is indirect and not yet understood in detail.

Theoretically the specification of a charge state for an ion moving in a dense medium requires a clear distinction between electrons moving with the projectile and electrons that do not. One complication in this context is the existence of convoy (or cusp) electrons which are emitted downstream with a velocity close to that of the emerging projectile. An operative definition of a charge state is possible in principle by measurement of x-ray satellites (Knudson *et al*., 1974), but this is not part of the standard routine.

This report aims at equilibrium stopping, *i.e.*, stopping under charge-state equilibrium. This is a dynamic equilibrium characterized by probabilities (*charge fractions*) $P(v, q_1)$ for an ion to have a charge $q_1 e$ at speed v. One may then define an average equilibrium charge

$$\langle q_1 \rangle = \sum_{q_1} P(v, q_1) q_1 \tag{3.31}$$

and an equilibrium stopping cross section

$$\langle S \rangle = \sum_{q_1} P(v, q_1) S(v, q_1), \tag{3.32}$$

where the *frozen-charge stopping cross section* $S(v, q_1)$ characterizes the average stopping between two charge-changing events.[14] Energy losses due to charge exchange need to be added to Eq. (3.32) when significant. $S(v, q_1)$ may be determined experimentally under pre-equilibrium conditions, *i.e.*, in measurements of the energy loss in thin targets, differential in entrance and/or exit charge state.

It is well established experimentally that equilibrium charge states of swift heavy ions are higher in solids than in gases (Lassen, 1951a,b). This has been ascribed to a density effect by Bohr and Lindhard (1954): Free-flight times are too short to allow excited ions to decay into their ground states. This results in enhanced electron-loss rates and thus in a shifted charge equilibrium. Although the matter has been the subject of intense debate, increasing evidence appears to support this model (Maynard *et al*., 2000).

Equilibrium charge states for heavy ions have been studied intensely. Results for solids have been summarized by an analytical formula for the mean charge measured after emergence (Shima *et al*., 1982)[15] as well as a comprehensive tabulation for amorphous carbon (Shima *et al*., 1992). A simple Thomas–Fermi estimate

$$\langle q_1 \rangle = Z_1 (1 - e^{-v/Z_1^{2/3} v_0}) \tag{3.33}$$

tends to represent the same data very well for projectiles at least up to argon. An example is given in Figure 3.8. Following Nikolaev and Dmitriev (1968), Shima *et al*. prefer a scaling variable $\propto Z_1^{0.45} v_0$. More involved scaling procedures, allowing for gas–solid differences, have been examined by Schiwietz and Grande (2001).

3.4.2 Screening and antiscreening

The influence on target excitation of electrons accompanying the projectile may be roughly classified into screening and antiscreening. Screening denotes the electrostatic effect of the reduction in electric field strength. This depends on the distance from the projectile nucleus and tends to reduce the stopping force. The concept of antiscreening arises from viewing the projectile as an aggregate of particles, each of them interacting individually with the target electrons, thus giving rise to enhanced stopping.

Antiscreening is a relevant concept for projectile electrons with orbital radii that are not small compared to characteristic interaction distances. A noticeable effect has been found for neutral hydrogen (Kabachnik, 1993). The effect is intimately connected to electron loss and/or projectile excitation. The significance of the effect decreases rapidly with increasing Z_1 (Sigmund, 1997).

3.4.3 Effective charge and quantal perturbation theory

Initially the effect of screening was incorporated into stopping theory *via* introduction of an effective charge which was thought to be close to the

[14] Eq. (3.32) remains valid also when $P(v, q_1)$ describes a non-equilibrium charge distribution.

[15] The analytical formula of Shima *et al*. (1982) has both explicit and implicit limitations. The authors state its range of validity as $Z_1 \geqslant 8$ and $4 \leqslant Z_2 \leqslant 79$. Cases have been found where $\langle q_1 \rangle$ slightly exceeds its maximum value Z_1 for heavy ions like iodine.

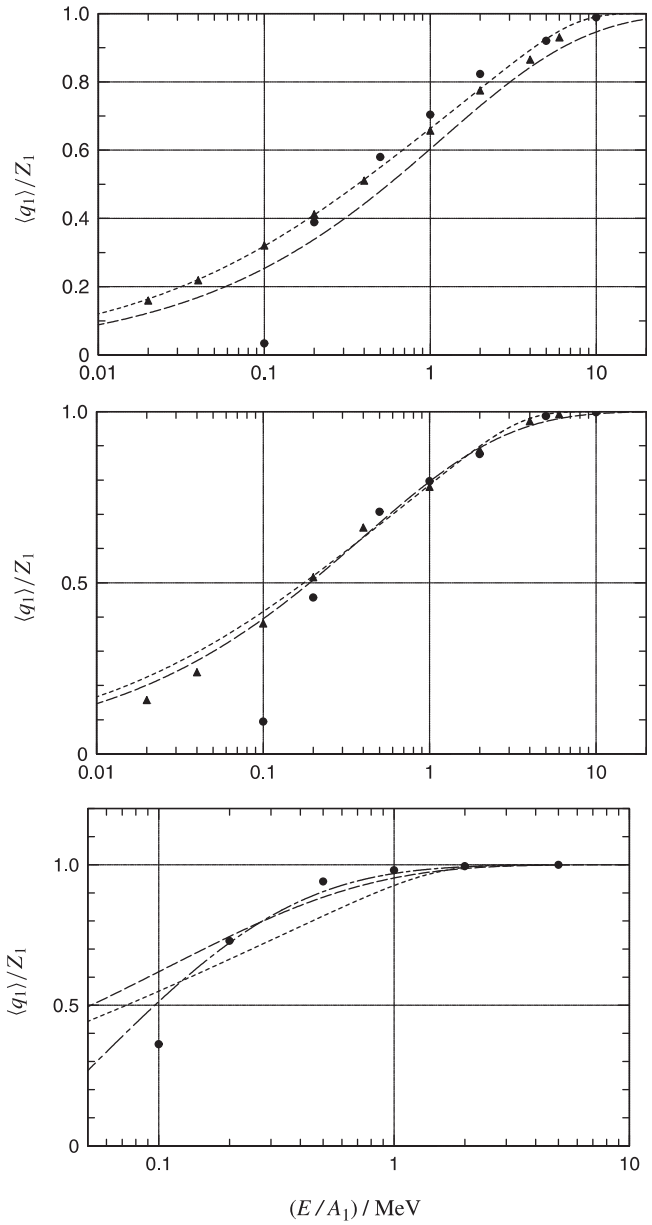


Figure 3.8. Comparison between mean charge numbers $\langle q_1 \rangle$ for Ar, O and Li in Si (top to bottom) predicted by Eq. (3.33) (dashed lines), interpolation formula by Shima *et al*. (1982) (dotted lines), tabulation by Shima *et al*. (1992) (triangles), measurements by Itoh *et al*. (1999) (dot-dashed line) and prediction from ETACHA code by Rozet *et al*. (1996) (circles).

equilibrium ion charge (Bohr, 1940, 1941; Knipp and Teller, 1941). Later on, Northcliffe (1960, 1963) *defined* an effective charge

$$q_{1,\mathrm{eff}} e = \gamma Z_1 e \tag{3.34}$$

via the ratio between the stopping force on a heavy ion and that on a proton at the same speed. Traditionally the effective-charge fraction γ^2 is determined empirically[16] by comparison of measured equilibrium stopping forces with stopping forces on protons or alpha particles, the latter originally being considered as point charges. Attempts of theoretical support to this concept were made by Yarlagadda *et al*. (1978), Brandt and Kitagawa (1982) and others.

It is recalled from Figure 3.2 that the regime of significant screening lies entirely within the classical regime for both light and heavy targets. Thus, treating screening on the basis of quantal perturbation theory necessitates application of the Bloch correction. However, the Bloch correction has been evaluated only for bare ions.[17] In the absence of an evaluation for substantial screening, the atomic number Z_1 in the Bloch correction has usually been identified with the effective ion charge $\langle q_1 \rangle$. Arguments in favor of this choice have been brought forward (Northcliffe, 1960; Arista, 2002). However, the Bloch correction originates in close collisions. Hence, replacing Z_1 by γZ_1 is likely to underestimate the Bloch correction.

The above problem is avoided in a classical treatment: Within the classical regime, screening can be incorporated *via* a suitably chosen interaction potential, and the inverse-Bloch correction ensuring a smooth transition into the Born regime becomes substantial only at velocities where screening is of minor significance.

Figure 3.9 shows the effective-charge ratio γ^2 of oxygen in carbon, calculated theoretically from the ratio of stopping numbers for O–C and He–C, both calculated for charge equilibrium according to Eq. (3.33). Also included is the corresponding curve for completely stripped oxygen and helium ions. If γZ_1 were an effective charge, the latter curve (dashed line) would have to be $= 1$ at all velocities. The fact that the curve falls off to about 0.2 reflects the transition from the Bethe to the Bohr regime which lies at a higher speed for oxygen than for helium. The point corresponding to $\kappa = 1$ for oxygen has been marked in the graph ('classical limit').

The topic has been discussed in considerable detail by Sigmund and Schinner (2001b). One may conclude from their discussion that

- the velocity dependence of the effective charge does not reflect that of the ion charge, and
- there is no reason to expect scaling properties in Z_1 and Z_2 similar to those of the ion charge.

[16]Concerning the *effective-charge ratio* γ^2 as defined by Eq. (3.34) cf. footnote 4 on page 23.

[17]An exception is a study by Sørensen (2002) — utilized by Weick *et al*. (2002) — of the influence of weak screening (one electron per projectile ion) on the Lindhard–Sørensen term in the relativistic regime.

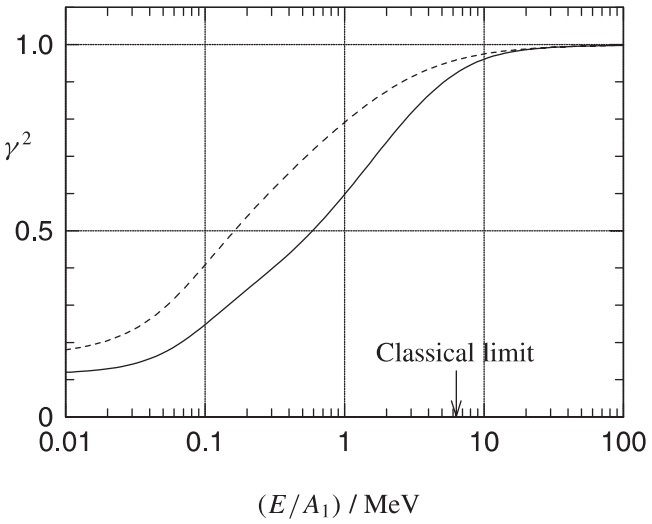


Figure 3.9. Effective-charge ratio for oxygen in carbon, defined as $\gamma^2 = L_{\mathrm{O-C}}/L_{\mathrm{He-C}}$, calculated from binary theory. Solid curve: charge equilibrium assumed for both oxygen and helium; dashed curve: both oxygen and helium assumed to be completely stripped. From Sigmund and Schinner (2001b).

These considerations indicate that there is no theoretical basis for scaling relations involving relative stopping forces. Further objections against the effective-charge postulate will be discussed in connection with Z_2 structure in Section 3.6.7. Empirical findings will be discussed in Section 5.2.

3.4.4 Screened potential

Brandt and Kitagawa (1982) established an explicit connection between ion charge and stopping force by invoking a potential

$$V(r) = -\frac{q_1 e^2}{r} - \frac{(Z_1 - q_1)e^2}{r} e^{-r/a_{\mathrm{sc}}} \tag{3.35}$$

in a quantal perturbation theory for a free-electron gas within the Lindhard (1954) scheme. The screening radius a_{sc} was determined on the basis of a modified Thomas–Fermi model. No Bloch correction was considered.

Eq. (3.35), in combination with Eq. (3.29) and the effective-charge model described above, forms the basis of the tabulation of Ziegler *et al*. (1985), where a_{sc} has been treated as a fitting parameter.

Similar schemes but involving more general screening functions have been explored (Kaneko, 1999; Grande and Schiwietz, 2002; Arista, 2002).

3.4.5 Classical perturbation theory

Screening was incorporated into Bohr's classical theory *via* Eq. (3.35) (Sigmund, 1997) but with a charge-dependent screening radius

$$a_{\mathrm{sc}} = 0.8853 a_0 Z_1^{-1/3}\left(1 - \frac{q_1}{Z_1}\right), \tag{3.36}$$

based on the model of Fermi and Amaldi (1934) of atomic ions. More general screening functions have been applied in classical theory by Maynard *et al*., (1996, 2001b).

The combined effect of projectile screening and a polarization correction was considered by Schinner and Sigmund (2000) in a classically based perturbation approach. The occurrence of unrealistically high Z_1^3 corrections (up to 100 %) indicated the need for an alternative, nonperturbative approach. This led to the binary theory (Sigmund and Schinner, 2000) which is described in more detail below.

3.4.6 Charge-dependent stopping

Several theoretical schemes to be discussed in the following deliver *partial stopping cross sections* or *frozen-charge stopping cross sections*, $S(v, q_1)$, which can be utilized to estimate the energy loss of a beam characterized by charge fractions $P(v, q_1)$ according to Eq. (3.32). Partial stopping cross sections have also been measured, and comparisons with theory will be presented in Section 4. The statistical description of energy-loss spectra in the presence of charge exchange will be described in Section 3.12.

A question of practical significance is to what extent the equilibrium stopping cross section, Eq. (3.32), may be replaced by the stopping cross section taken at the equilibrium charge, Eq. (3.31), *i.e.*,

$$\langle S(q_1)\rangle \stackrel{?}{\simeq} S(\langle q_1\rangle). \tag{3.37}$$

Figure 3.10 shows an estimate of stopping cross section versus ion charge, based on modified Bohr theory allowing for screening (Sigmund, 1997) but disregarding shell and Barkas–Andersen correction as well as projectile excitation. Curves are shown for a series of values of the parameter

$$s = \left(\frac{Z_1 m v_0^2}{I}\right)^{2/3} \simeq 2\left(\frac{Z_1}{Z_2}\right)^{2/3}, \tag{3.38}$$

which was found to characterize the importance of screening.[18] For perfect screening, all curves would coincide with the parabola $(q_1/Z_1)^2$, the lowermost (thin full–drawn) curve in the figure. It is seen that such a behavior is only found for $Z_1 \gg Z_2$. For all other ion–target combinations the dependence of the partial stopping cross section on the instantaneous ion charge is weaker than the q_1^2 dependence that would be expected from complete screening in conjunction with the Bethe formula, and for $Z_1 \ll Z_2$ only a weak charge dependence is found.

[18]The last part of this relation implies the Bloch relation $I \propto Z_2$.

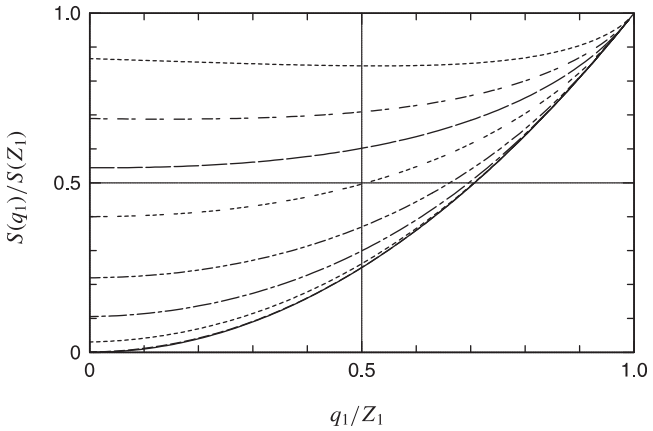


Figure 3.10. Calculated ratio of stopping cross sections for frozen charge q_1 and bare ion, versus charge fraction. Curves for values 0.2, 0.5, 1, 2, 10, 20, 50 (top to bottom) of the parameter $2(Z_1/Z_2)^{2/3}$ (see text). The thick solid line represents a straight q_1^s dependence. Very rough estimate from Sigmund (1997) (see text).

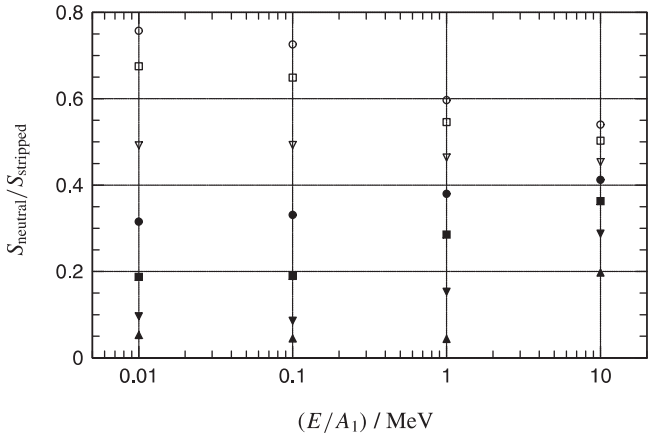


Figure 3.11. Reduction factor in stopping from stripped to neutral projectile versus beam energy. Points for values 0.2, 0.5, 1, 2, 10, 20, 50 (top to bottom) of the parameter $2(Z_1/Z_2)^{2/3}$ (see text). Calculated from binary theory.

Figure 3.11 shows related information but now predicted by the binary theory. Only data for neutral projectiles are shown, as a function of beam energy. Qualitative results are very similar: For $Z_1 \gg Z_2$ stopping is very much reduced for the neutral projectile, except at the high-energy end where collision diameters get below the screening radius. Conversely, with decreasing ratio Z_1/Z_2, the reduction of the stopping force by screening decreases monotonically. On the other hand, even the pronounced decrease for $Z_1 \gg Z_2$ will be counteracted to some extent by projectile excitation at low velocities. Thus, in most cases the overall dependence of the stopping cross section on q_1 must be less than quadratic. Based on these arguments one may give an upper bound on the error,

$$\frac{\langle S\rangle - S(\langle q\rangle)}{S(\langle q\rangle)} < \frac{\langle q_1^2\rangle - \langle q_1\rangle^2}{\langle q_1\rangle^2}. \tag{3.39}$$

The quantity on the right-hand side may be extracted from tabulations by Shima *et al*. (1992). In general terms it is large for low-Z_1 ions — where only few charge states are involved — and falls off rapidly with increasing Z_1.

3.4.7 Projectile excitation and charge exchange

Very roughly speaking, projectile excitation can be treated by inverting the roles of target and projectile. However, both practical and conceptual problems arise here that need careful consideration.

Consider first differences between target and projectile excitation:

- The projectile is charged. This implies that atomic data are needed not only for neutral atoms but also for a wide variety of ionic states.
- Whether neutral or charged, the projectile need not be in its ground state.
- Little systematics is known about the state of a penetrating ion or associated oscillator strengths.

These problems were addressed in terms of simple estimates by Sigmund and Schinner (2002b). Uncertainties associated with the state of the projectile were found to be small in practice. Moreover, two options were considered:

1. the number of electrons in every shell is reduced by a common factor q_1/Z_1, or
2. projectile states are filled up from the bottom,

although shifts in the excitation frequencies were ignored. The difference between the two options was found to be small in general.

For projectile ionization special considerations apply:

- Projectile ionization is a form of charge exchange. In equilibrium stopping the number of electron-loss events is equal to the number of electron-capture events in the average. Including only one of them in the formalism is not meaningful in general.
- The energy loss in an event leading to projectile ionization does not necessarily exceed that of projectile excitation because the speed of an ejected electron in the laboratory frame of reference may well be lower than that of the projectile.

As pointed out by Sigmund and Glazov (2003), the second item implies that energy loss due to projectile

excitation/ionization has, when considered at all, been overestimated in the theoretical literature.

A further problem arises from the fact that an ion emerging from a penetrated layer in a charge state different from the incident one has changed its internal energy. Hence, the value of the measured energy loss depends on the chosen technique (Sigmund and Glazov, 1998): Uncritical analysis of energy losses measured by time-of-flight, magnetic or electrostatic analysis, or energy-dispersive detectors may provide different numerical values when converted to energy loss. This, however, is only significant in measurements of energy loss as a function of incident and/or exit charge.

Glazov (2002a) presented a thorough theoretical analysis, based on the Born approximation, of projectile excitation under frozen-charge conditions. This continues earlier work by Kim and Cheng (1980) with the important difference that ionization is explicitly omitted. This complicates the analysis because of missing sum rules.

Electron capture is a more delicate issue, not only with regard to pertinent cross sections but also the definition of energy loss. Here, nonradiative electron capture is considered which is the dominating process at nonrelativistic velocities.

For a fast ion — with a speed substantially above the initial orbital speed of a captured electron — one may approximate the energy loss $w_{\rm capt}$ in a capture event by

$$w_{\rm capt} \simeq U_{\rm init} - U_{\rm capt} + \frac{mv^2}{2}, \qquad (3.40)$$

where $U_{\rm init}$ is the ionization energy of the bound target electron, $U_{\rm capt}$ the ionization energy of the state into which capture takes place, and $mv^2/2$ the energy needed to accelerate the captured electron to the projectile speed v.

Electrons are typically captured into a high-angular-momentum state, *i.e.*, an excited state of the projectile. In a gas target, such a state may decay into the ground state radiatively or *via* Auger emission. These processes do not lead to significant momentum changes of the projectile and, therefore, have to be omitted from Eq. (3.40).

For high-speed projectiles the dominating contribution in Eq. (3.40) is the last term. At the same time, cross sections for electron capture decrease rapidly with increasing speed. Therefore, equilibrium stopping forces are typically unaffected by capture. On the other hand, $mv^2/2$ may well exceed the average energy loss of a frozen charge in a foil and hence cause the energy-loss spectrum to be split into discrete portions reflecting the number of capture events encountered over a trajectory. Examples will be discussed in Section 3.11.3. If no distinction is made between target electrons excited into the continuum or a bound projectile state, energy loss to electron capture may be considered as being included in target excitation/ionization.

Cross sections for electron capture in the nonrelativistic as well as the relativistic velocity range have been tabulated by Ichihara *et al*. (1993). For comparisons with experimental results, see Geissel *et al*. (2002).

3.4.8 Z_2 structure

It was observed in Section 3.3.7 that for bare ions Z_2 structure gets increasingly pronounced with decreasing beam energy. For dressed ions Z_2 structure is also influenced by projectile screening. To appreciate this, recapitulate that Z_2 structure is generated primarily by variations of the outer-shell frequency ω_j with Z_2, which enters *via* the adiabatic radius v/ω_j: If ω_j is small, the effective interaction range and hence the stopping cross section is large, and vice versa. Now, in the presence of screening the screening radius $a_{\rm sc}$ of the interaction also needs to be considered. Screening is only effective for $a_{\rm sc} < v/\omega_j$, and, if so, the interaction range and hence the stopping force is increasingly determined by $a_{\rm sc}$, which is only weakly dependent on the medium and hence tends to suppress Z_2 structure.

Figure 3.12 shows these trends for argon and proton bombardment. In either case structure increases with decreasing energy but seems to saturate below 100 keV/u. At the same time, structure is considerably more pronounced for proton than for argon bombardment. This has the implication that Z_2 structure is more pronounced in the effective-charge ratio $\gamma^2 = S({\rm Ar})/S({\rm H})$ than in the stopping cross section $S({\rm Ar})$ itself. This is rather surprising, as the original motivation for introducing the effective-charge concept was the assumption that the effective charge was independent of or only weakly dependent on the stopping material.

The importance of projectile screening is further elucidated by a comparison of Figure 3.12 with Figure 3.7, where Z_2 structure was found to *increase* with increasing Z_1 and increasing beam energy. This behavior is characteristic of the regime of small-to-negligible screening.

3.5 AGGREGATION EFFECTS

3.5.1 Stopping in compounds and alloys, and phase effects

While stopping in elemental materials has been the dominating object of both experimental and

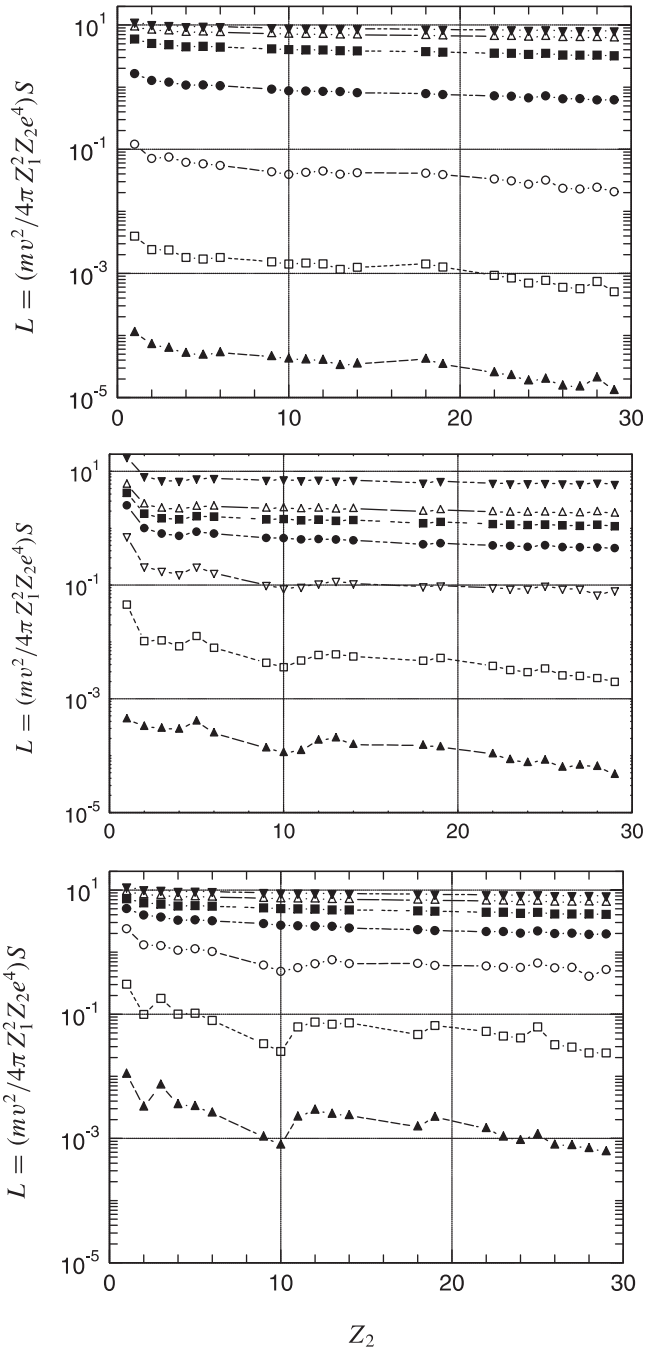


Figure 3.12. Z_2 structure according to the binary theory of stopping for argon (upper graph) and helium (middle graph) ions in charge equilibrium, including projectile excitation, and bare protons (lower graph). Beam energy decreases by factors of 10 from 10^3 MeV/u (top curve) to 10^{-3} MeV/u (bottom curve). From Sigmund *et al*. (2003).

theoretical studies, stopping in compounds and alloys is of prime interest in numerous applications.

A common reference standard is *Bragg's additivity rule*, which can be written in the form

$$-\frac{\mathrm{d}E}{\mathrm{d}\ell} = \sum_\nu n_\nu S_\nu, \tag{3.41}$$

where n_ν and S_ν are the number of atoms per volume and the stopping cross section, respectively, of the νth species of target atoms. This assumes that the stopping cross section of each species is unaffected by the state of aggregation. Hence the rule, when valid, pertains to both chemical and phase effects.

Deviations from additivity have received much attention. Systematic experimental studies for penetrating protons date back to the 1950s (Reynolds *et al*., 1953), and extensive reviews have been given by Thwaites (1983, 1984, 1987, 1992), by Ziegler and Manoyan (1988) and in ICRU Report 49. The vast majority of available experimental data refers to He bombardment, especially by Powers *et al*. (1973) and numerous follow-up papers by Powers's group (Powers *et al*., 1984), and to Li bombardment by Pietsch *et al*. (1976) and follow-up papers by Neuwirth's group (Neuwirth and Both, 1985).

In particular, schemes were proposed for incorporating such deviations in a manner so that Eq. (3.41) can be maintained with a modified stopping cross section depending on the class of compound (ICRU, 1984, 1993).

In the high-velocity regime, as long as shell, Barkas–Andersen and screening corrections are unimportant, stopping forces are governed by the oscillator-strength spectrum. Here, Eq. (3.41) follows from Eq. (3.8) provided that optical oscillator strengths are additive,

$$f_j = \frac{\sum_\nu Z_\nu f_{j,\nu}}{\sum_\nu Z_\nu}, \tag{3.42}$$

where Z_ν and $f_{j,\nu}$ denote the atomic number and optical oscillator strength of the νth species. Since significant deviations from Eq. (3.42) can be expected mainly for valence and conduction electrons, deviations from Bragg's additivity rule are then governed by

- the variation of the oscillator-strength spectrum for valence electrons between the atomic and a compound state and
- the relative significance of those electrons in the total stopping force.

This situation is quite analogous to the Z_2 structure discussed in Sections 3.3.7 and 3.6.7. In particular, one expects deviations from additivity to become increasingly pronounced with decreasing speed because of more rapid variation of the Bethe or Bohr logarithm with ω_j.

This trend is enhanced as shell corrections become important because of the closing of inner-shell excitation channels. However the increasing significance of projectile screening with decreasing projectile speed will tend to wipe out this effect for heavier ions.

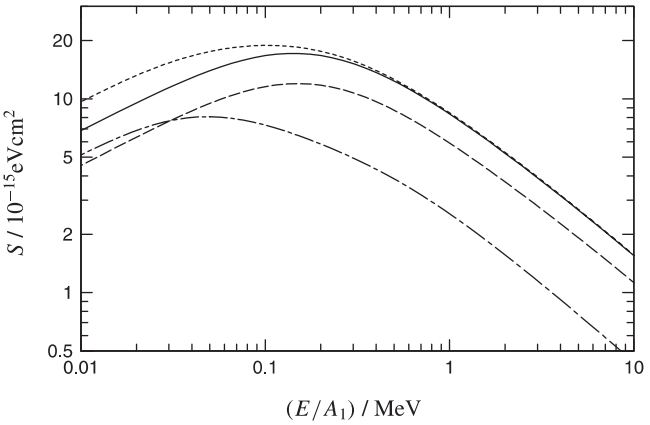


Figure 3.13. Stopping cross section of lithium fluoride (solid line), lithium (dot-dashed line) and fluorine (dashed line) for antiprotons, calculated from binary theory. Also included is the sum of the elemental stopping cross sections (Bragg rule, dotted line). From Sharma *et al*. (2004a).

Figures 3.13 and 3.14 illustrate these features in the case of LiF. This substance has been chosen because from a theoretical point of view it must be expected to show the most pronounced deviations from additivity:

- very large difference in binding energy of the outermost electron between metallic Li and LiF and
- a high fraction of outer electrons because of the low-Z_2 materials involved.

In Figure 3.13 it is seen that for antiproton bombardment, in the complete absence of projectile screening, the predicted deviation from Bragg additivity reaches a factor of about 1.5 at low velocities. This is considerably more than what has been measured experimentally for any system. A direct experimental test would be of interest. Stopping measurements on metallic lithium have been shown to be possible (Eppacher *et al*., 1995).

Conversely, Figure 3.14 shows that the effect decreases in importance and becomes insignificant from carbon upwards. In all cases it decreases rapidly above the stopping maximum.

On the basis of these estimates one may expect Bragg's rule to be adequate for estimating stopping forces on ions with $Z_1 \gtrsim 6$ above the Bohr velocity. However, application of Bragg's rule requires knowledge of the stopping cross sections of all constituent elements. In some cases where those are not known, stopping cross sections of compounds may still be estimated provided that adequate knowledge is available of the optical properties of the material.

3.5.2 Stopping of molecules and aggregates

As a first approximation the stopping force on a molecule, aggregate or cluster is given by the sum of stopping forces on its constituent atoms,

$$\left(\frac{\mathrm{d}E}{\mathrm{d}\ell}\right)_{\mathrm{mol}} = \sum \left(\frac{\mathrm{d}E}{\mathrm{d}\ell}\right)_{\mathrm{atom}} \tag{3.43}$$

at the same speed for both electronic and nuclear stopping.[19] Deviations from strict additivity have been found mainly in the electronic stopping of hydrogen molecules and clusters (Brandt *et al*., 1974; Ray *et al*., 1992). Similar effects for aggregates of heavier ions have been looked for experimentally and theoretically but were found to be only a few per cent (Baudin *et al*., 1994; Tomaschko *et al*., 1995; Ben-Hamu *et al*., 1997).

A theoretical analysis by Jensen and Sigmund (2000) showed that these findings are in agreement with stopping theory.

3.6 LOW-VELOCITY ELECTRONIC STOPPING

3.6.1 General considerations

The regime of low-energy electronic stopping has been defined by

$$v \lesssim v_0 \quad \text{or} \quad E/A_1 \lesssim 25 \text{ keV} \tag{3.44}$$

in Figure 3.2. The fact that the projectile speed is not large compared to even the lowest orbital speeds of the target electrons implies that 'sudden' Coulomb excitation underlying Bohr or Bethe theory ceases to be an effective energy-loss channel. Moreover, projectiles tend to be predominantly neutral in charge equilibrium [see Eq. (3.33)].

While Bohr (1948) asserted that electronic-stopping cross sections would drop rapidly to zero for $v < v_0$, subsequent theoretical considerations led to a predicted friction-like behavior of the stopping force at low projectile speed. Such a behavior emerged from very different and mutually independent arguments.

3.6.2 Free target electrons

Fermi and Teller (1947), estimating slowing-down and capture of negative muons in matter, pointed out that the *rate* of energy loss, $-\mathrm{d}E/\mathrm{d}t$ of a slow heavy particle in a Fermi gas becomes proportional to its kinetic energy. This is equivalent to Stokes' law of a velocity-proportional stopping force.

The origin of this result is most easily identified by viewing the interaction in a reference frame moving along with the (heavy) projectile: When such

[19] Although Eq. (3.43) is formally similar to Eq. (2.4), there is an essential difference. Eq. (2.4) *defines* the energy loss of a composite particle *via* the energy loss experienced by its constituents, while Eq. (3.43) assumes that the energy loss of each constituent is equal to that experienced under *isolated* slowing-down.

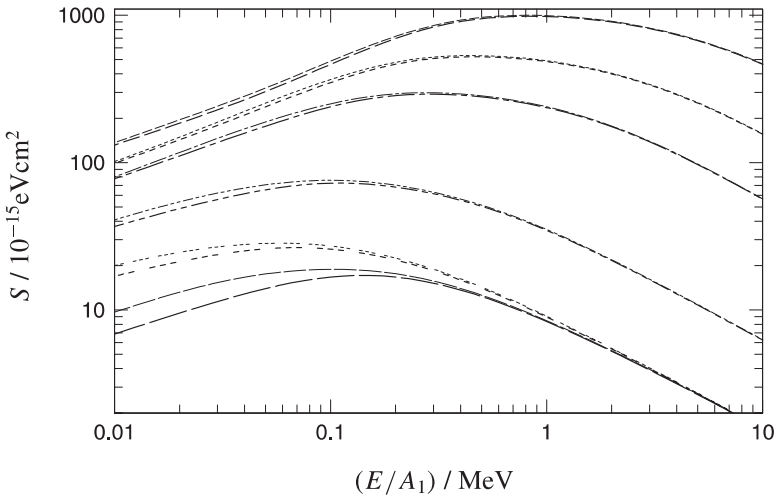


Figure 3.14. Stopping cross section of lithium fluoride for argon, neon, carbon, helium, hydrogen ions and antiprotons (top to bottom, solid lines) calculated from binary theory. Also included are the sums of the elemental stopping cross sections (Bragg rule, thin lines). From Sharma *et al*. (2004a).

a projectile is hit by a target electron, an amount of momentum is transferred that is proportional to the electron velocity. For an isotropic velocity distribution of target electrons these momentum transfers will cancel, but the small anisotropy induced by viewing the system from a slowly moving reference frame causes a net momentum transfer proportional to and directed opposite to the projectile velocity.

A more quantitative version of this finding emerges from Lindhard's comprehensive treatment of the stopping of a point charge in a Fermi gas (Lindhard, 1954). In this formalism electronic properties of a material are described in terms of a frequency- and wavenumber-dependent dielectric function $\epsilon(k,\omega)$. This allows for a self-consistent description of the response of an electron gas to a high degree of rigor, at least to the lowest order in the electric field induced by the projectile. The theory reproduces results of the Bethe (1930) theory at high projectile speeds — with the plasma frequency replacing $I/\hbar$ — and a velocity-proportional, density-dependent stopping force at low speed (Lindhard and Winther, 1964).

An important observation of Lindhard (1954) is the fact that it is not necessary to explicitly take into account the Pauli principle in the collision kinematics for a homogeneous electron gas, because for every scattering event that is forbidden by the Pauli principle there is another event with an equal but oppositely directed momentum transfer at the same probability.[20] This is a key point in attempts to characterize the stopping behavior of inhomogeneous systems like atoms and molecules in terms of free-electron models and Thomas–Fermi-type arguments.

3.6.3 Bound target electrons

Independently and almost simultaneously, two qualitative approaches were developed that led to predictions of velocity-proportional stopping cross sections also for electrons bound in atoms. Firsov (1959) viewed the ion–atom collision system as a quasi-molecule with a flow of electrons between the collision partners. Energy loss is determined by the momentum needed to accelerate target electrons to the projectile velocity, and the number of electrons involved is determined by simple geometric considerations in combination with Thomas–Fermi-type arguments.

The goal of this work was to provide a qualitative explanation of the inelastic energy loss in low-energy ion–atom collisions. The mean inelastic energy loss w per collision at a given impact parameter p was given in the form

$$w(v,p) = 0.35\frac{\hbar v}{a_0}\frac{(Z_1+Z_2)^{5/3}}{[1+0.16(Z_1+Z_2)^{1/3}r_{\min}/a_0]^5} \quad \text{for } 1/4 \le Z_1/Z_2 \le 4, \tag{3.45}$$

where $r_{\min} = r_{\min}(v,\ p)$ is the closest distance of approach between the colliding nuclei.

Firsov was aware of the dominating role of electron promotion between quasimolecular orbitals in the process of electron excitation in slow ion–atom collisions, formulated in more explicit terms several years later by Fano and Lichten (1965). However, Firsov's theory did not aim at particle stopping.

[20]The Pauli principle does enter implicitly through the velocity distribution of the target electrons (Lindhard, 1954), and it cannot be neglected in straggling (Sigmund, 1982).

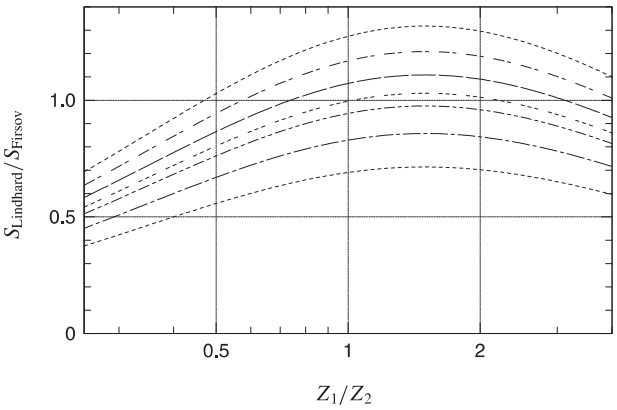


Figure 3.15. Ratio between low-speed electronic-stopping cross sections due to Lindhard and Scharff (1961) and Firsov (1959) for $Z_2 = 79, 47, 26, 18, 13, 6, 2$ (top to bottom). ξe has been set to $Z_1^{1/6}$. The interval covered for Z_1/Z_2 is limited by the range of validity of Eq. (3.46).

Application to this area dates back to Teplova *et al*. (1962), who integrated Eq. (3.45) over the impact parameter — (re)identifying $r_{\min}$ with p so that

$$S = \int_0^\infty 2\pi p \mathrm{d}p w(p) = 2.3\pi a_0^2 (Z_1 + Z_2) m v_0 v. \quad (3.46)$$

A slightly modified version of the Firsov theory that, amongst other features, does not impose the above limitation on the range of Z_1/Z_2, is due to Kishinevskii (1962).

An alternative approach is due to Lindhard and Scharff (1961).[21] This model determines momentum transfer in a quasi-molecule formed during collision on the basis of the Fermi-gas model mentioned above. This, in conjunction with a Thomas–Fermi description of the orbits of the scattering nuclei, leads to a stopping cross section of the form

$$S = \xi_e 8\pi a_0^2 \frac{Z_1 Z_2}{\left(Z_1^{2/3} + Z_2^{2/3}\right)^{3/2}} m v_0 v, \quad (3.47)$$

where $\xi_e \simeq Z_1^{1/6}$ is an empirical parameter added to improve agreement with stopping measurements on fission fragments — the only pertinent data available at the time when the formula was established.

Figure 3.15 shows the ratio of the two expressions, indicating pronounced differences depending on the atomic numbers involved.

[21]This work was part of a pioneering project on low-energy ion implantation. Publication of this series of papers was heavily delayed by external circumstances, but with the exception of the stopping formula (3.47), all major findings eventually appeared in full papers (Lindhard *et al*., 1963a,b, 1968). A major reason for the missing published derivation of the stopping formula was the experimental discovery of Z_1 structure in low-energy stopping. Arguments in support of Eq. (3.47) were published by Sigmund (1975) and Tilinin (1995).

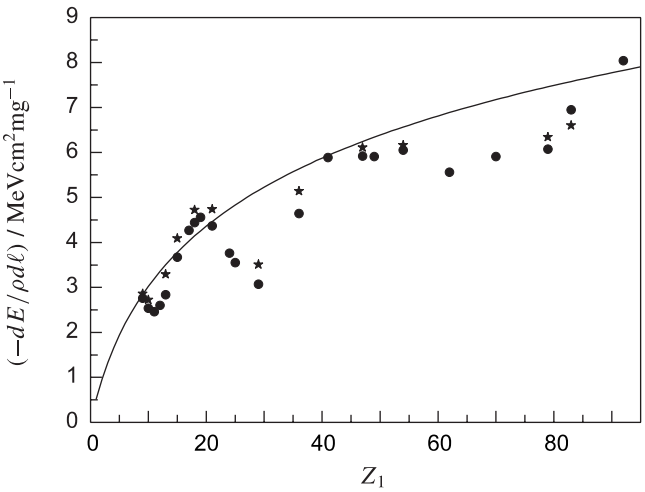


Figure 3.16. Measured Z_1 oscillations in carbon at $0.8v_0$. Solid line: Eq. (3.47). Data from Lennard *et al*. (1986a). Filled circles: thickness 9 μg/cm^2; stars: thickness 29 μg/cm^2.

Eq. (3.47) has been successfully applied in the analysis of ion implantation profiles at keV and low-MeV energies, typically with a significant nuclear-stopping component.

3.6.4 Z_1 structure: modified-Firsov models

Direct measurements of low-speed stopping on thin films and gas targets were performed by Teplova *et al*. (1962), Ormrod and Duckworth (1963), Ormrod *et al*. (1965), Fastrup *et al*. (1966), Ormrod (1968), Hvelplund and Fastrup (1968), Hvelplund (1971), Bierman *et al*. (1972), Hoffmann *et al*. (1976), Ward *et al*. (1979), Lennard *et al*. (1986a), and Lennard and Geissel (1987). Pertinent experimental aspects in these and later measurements will be discussed in the following section. While these measurements confirmed the general behavior predicted by Eqs. (3.46) and (3.47), a distinct nonmonotonic behavior, 'Z_1 oscillations' or 'Z_1 structure' was found which had not been predicted theoretically.

Figure 3.16 shows data for a wide range of ions on amorphous carbon. Similar, less comprehensive data exist on aluminium, silicon, nickel, silver, gold, neon, argon and air. Maxima and minima, where identifiable, lie at approximately the same values of Z_1 for these targets, and oscillation amplitudes range up to 15–20 %.

Much more pronounced Z_1 structure was found in the stopping of well-channeled ions in single crystals of tungsten (Eriksson *et al*. 1967), silicon (Eisen, 1968) and gold (Bøttiger and Bason, 1969), where a narrower range of impact parameters is sampled.

Initial attempts to explain these oscillations were based on the models of Firsov (El-Hoshi and Gibbons, 1968; Winterbon, 1968; Cheshire *et al*., 1968) or Lindhard (Bhalla and Bradford, 1968)

with modified electron densities, electron fluxes and projectile charge states. Most of these and numerous subsequent approaches along similar lines (Bhalla *et al*., 1970; Cheshire and Poate, 1970; Kessel'man, 1971a,b; Bierman *et al*., 1972; Baklitsky *et al*., 1973; Komarov and Kumakhov, 1973) were reasonably successful in the prediction of the positions of maxima and minima, and some of them also matched the amplitudes, although usually with the help of adjustable parameters.

None of these approaches has been utilized to systematically produce *theoretical predictions*, and none of them has been capable of explaining observed deviations from strictly velocity-proportional stopping. The latter feature is usually summarized in an empirical power law, $S \propto v^{\mathrm{p}}$, where p was found to oscillate around 0.5 as a function of Z_1 at considerable amplitudes, *e.g.*, between 0.3 and 0.9 for stopping along the ⟨110⟩ channel in silicon (Eisen, 1968). Numerical results were found to be sensitive to detailed input, a feature that has given rise to some discussion (Cruz *et al*., 1979; Komarov, 1979).

3.6.5 Z_1 structure: Lindhard–Finnemann model

An alternative approach proposed by Lindhard[22] explains the Z_1 structure as a quantum effect. Stopping is described in terms of the transport cross section (3.17), which is governed by the phase shifts for scattering of low-energy electrons ($v < v_0$) on the screened Coulomb potential of a neutral or nearly neutral projectile atom. In this velocity range, low values of ℓ dominate the scattering amplitude. This leads to maxima and minima in the stopping cross section near the point where δ_0 approaches uneven or even multiples of $\pi/2$. In addition to the scattering potential, phase shifts also depend on electron speed. This is known as the Ramsauer– Townsend effect in the scattering of free electrons on gas atoms.

The evaluation by Finnemann (1968) of WKB (Wentzel–Kramers–Brillouin) phase shifts on a Lenz–Jensen potential predicted stopping maxima at $Z_1 = 6$, 20, 41, and 72 and minima at $Z_1 = 12$, 29, and 55 for $v = v_0$. At $v = v_0/2$, maxima were found at $Z_1 = 7$, 18, 37, and 68 and minima at $Z_1 = 3$, 11, 26, 51, and 89, in fair agreement with experimental data shown in Figure 3.16.

Briggs and Pathak (1974) found similar results on the basis of a Molière potential and numerically evaluated phase shifts. Further calculations on the basis of Hartree–Fock atomic densities produced additional structure which was asserted to be sensitive to projectile speed and likely to be wiped out in a more realistic treatment of electron scattering in a solid medium.

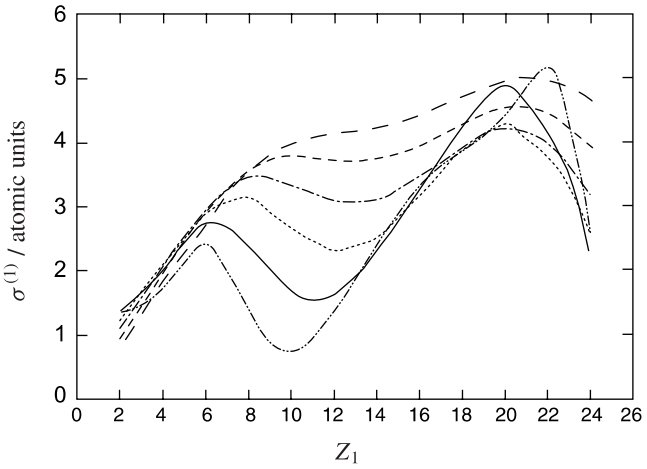


Figure 3.17. Predicted velocity dependence of transport cross section $\sigma^{(1)}$, Eq. (3.17) in a Fermi gas according to Pathak (1980). $v/v_0 = 0.75$, 1.0, 1.25, 1.5, 1.75, 2.0 (bottom to top).

The scheme was analysed in a considerable number of follow-up studies (Briggs and Pathak, 1974; Pathak, 1974a; Ali and Gallahar, 1974; Pathak, 1980; Kumar and Pathak, 1993), with applications mostly to channeling data on Si, W, and Au. Good agreement has been reached with experimental results in particular by Kumar and Pathak (1993). The velocity dependence of Z_1 structure was studied in this model by Pathak (1980). Figure 3.17 shows the transport cross section for a free-electron gas as a function of Z_1 for a speed ratio v/v_0 increasing from 0.75 to 2.0. It is seen that the oscillation amplitude decreases rapidly. Moreover, the position of maxima and minima moves toward higher Z_1 with increasing speed, in accordance with the prediction of Finnemann (1968) mentioned above.

3.6.6 Self-consistent nonlinear models

A key parameter in the calculations discussed above is the screening potential accompanying the projectile, which was determined from a more or less sophisticated atomic-charge distribution in all cases. At low projectile speeds this potential is modified by the presence of a sea of target electrons. A self-consistent theoretical description requires taking into account the relaxation of the electron system due to the presence of the penetrating ion. Scattering phase shifts then need to be calculated with the resulting self-consistent potential as input. One test for self-consistency is the Friedel sum rule, which reads

$$\frac{2}{\pi}\sum_{\ell}(2\ell+1)\delta_\ell(E_{\mathrm{F}}) = Z_1 \qquad (3.48)$$

[22]Lindhard's work dates back to 1968 but was never published. A written record is available in an M.Sc. thesis (Finneman, 1968). The first published record is by Briggs and Pathak (1974).

for a static impurity atom Z_1 embedded into a Fermi gas with Fermi energy E_F.

The dielectric description of Lindhard (1954) satisfies the requirement of self-consistency up to the first order in the electric field. The density-functional theory of Hohenberg and Kohn (1964) and Kohn and Sham (1965) goes significantly beyond this approximation. The use of this scheme in the evaluation of low-speed stopping in a homogeneous electron gas was initiated by Echenique *et al*. (1981) for protons and helium ions. Z_1-dependent stopping was studied by Echenique *et al*. (1986). A considerable number of follow-up studies (Ashley *et al*., 1986; Arnau *et al*., 1988; Arnau and Echenique, 1989; Echenique *et al*., 1991; Peñalba *et al*., 1992) was devoted to the analysis of Z_1 structure. Estimates by Ashley *et al*. (1986) and Echenique *et al*. (1991) — who modelled the undisturbed target as a homogeneous Fermi gas — reproduced observed trends for amorphous carbon and channeling in silicon and gold. Estimates by Peñalba *et al*. (1992), based on more realistic electron distributions in the target, were in good agreement with measurements for ⟨110⟩ Si.

A much simpler approach was presented by Calera-Rubio *et al*. (1994), where a Yukawa-type screening function was adopted with a screening radius determined recursively by the Friedel sum rule using calculated scattering phase shifts. This approach was further developed by establishing a generalized Friedel sum rule (Lifschitz and Arista, 1998). The resulting theory of heavy-ion stopping that summarizes much of the development described in this section (Arista, 2002) will be described in Section 3.7.3.

3.6.7 Z_2 structure

Unlike Z_1 structure, Z_2 structure is present at all velocities, although most pronouncedly so in the low-v regime as discussed in Section 3.3.7. It is of interest, therefore, to explore what genuine low-speed stopping theory can contribute to this topic.

Although all theoretical models discussed above allow predictions on Z_2 structure, systematic studies are scarce. Attempts by Pathak (1974b) and Ali and Gallaher (1974) addressed channeled ions, directed at range measurements by Whitton (1974). Latta and Scanlon (1976) made predictions on the basis of a modified-Firsov model, aiming at experimental results by Broude *et al*. (1972). Pietsch *et al*. (1976), in analyzing their measurements of low-speed stopping of Li, applied a modification to the Lindhard–Scharff formula (3.47). This model and two modified-Firsov models were employed in the analysis of data on low-speed stopping by Land *et al*. (1977), with moderate success. Systematic studies on low-speed Z_2 structure on the basis of the quantum model would be desirable. While predictions are possible on the basis of binary theory, there are clear limitations in view of the fact that Z_1 structure is unaccounted for.

3.6.8 Conclusions

A number of conclusions may be drawn from this fairly large body of theoretical studies:

- Unlike the modified-Firsov models, the quantal model leads to deviations from velocity-proportional stopping. These deviations have not been studied quantitatively, and it is not known whether calculated velocity dependences match those measured.
- Models described above have been successfully utilized in estimates of Z_1 structure in energy losses of channeled ions. Particularly good agreement with measurements has been obtained with the quantal model both in the linear and the nonlinear version. This may be due to the fact that pertinent measurements concern 'best-channeled' ions which move in rather well-defined trajectories in regions with a fairly constant electron density described well by a homogeneous-electron-gas model.
- For *random* slowing-down, really good agreement with existing measurements on Z_1 structure is not found for any of these models, at least as far as amplitudes are concerned. 'Best' estimates were presented by Komarov and Kumakhov (1973) and Calera-Rubio *et al*. (1994) for carbon, and by Calera-Rubio *et al*. (1994) for aluminium. However, unlike Komarov and Kumakhov (1973), Calera-Rubio *et al*. (1994) as well as Echenique *et al*. (1986) predicted oscillation amplitudes that are *larger* than those measured. This leaves open the possibility that oscillation amplitudes are underestimated in the analysis of experimental data, *e.g.*, due to uncertainties in the nuclear-stopping correction.
- In addition to a pronounced dependence on projectile speed of predicted maximum and minimum positions, predicted Z_1 structure also depends on the target material according to Calera-Rubio *et al*. (1994), although the difference between the two cases studied (C and Al) is small.

3.7 SURVEY OF CURRENT THEORETICAL SCHEMES

Owing to the growing interest in heavy-ion stopping, theoretical schemes have been developed over

the past few years aimed at calculating stopping forces more or less from first principles. This section presents four currently available schemes, all of which are still under development (Table 3.2).

3.7.1 Unitary-convolution approximation

The guiding principle behind the unitary-convolution approximation (UCA) by Grande and Schiwietz (1988) is to provide an impact-parameter-dependent version of the Bloch theory. The energy loss of bare ions is determined by interpolation between close and distant interactions, where the latter are described by the standard scheme (dipole approximation) while close collisions are characterized by free-Coulomb interaction with an effective minimum impact parameter dependent on the Bohr parameter $\kappa = 2Z_1 v_0/v$. Interpolation is performed such as to reproduce the Bloch function after integration.

The scheme was extended by Azevedo *et al*. (2000) to screened ions by the introduction of a screened potential, which in turn was found from Hartree–Fock type atomic and ionic projectile wave functions.

In its present stage (Grande and Schiwietz, 2002) the theory is geared to cover the transition from the Born to the classical regime. In addition to projectile screening, also projectile excitation and ionization are allowed for, although the contribution from projectile ionization is likely to be overestimated (see the remarks in Section 3.4.7). Shell and Barkas–Andersen as well as relativistic corrections are omitted. For oxygen on aluminium this would suggest the theory to be valid within the range 0.5 MeV $\ll E/A_1 \ll$ 1 GeV. This is confirmed in Figure 3.18. The excellent agreement with experiment around 0.1 MeV must be assumed to be accidental (Grande and Schiwietz, 2002).

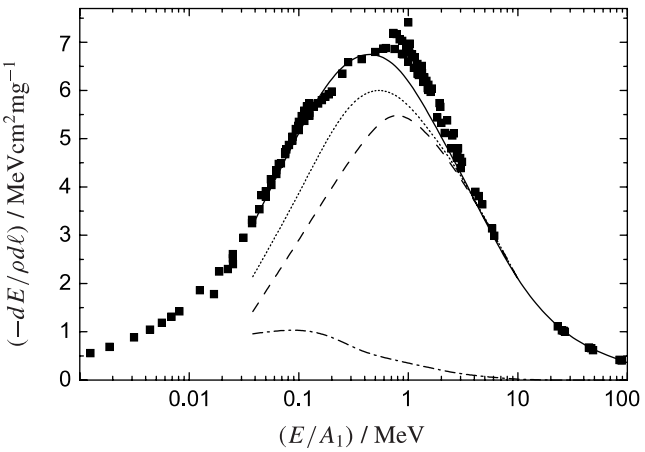


Figure 3.18. Equilibrium stopping force for O–Al predicted from the unitary-convolution approximation, compared with experimental values from Figure 3.1. Dashed line: target excitation assuming mean ion charge. Dotted line: target excitation averaged over ionic charge spectrum. Dot-dashed line: projectile excitation. Solid line: total stopping force averaged over ionic charge spectrum. From Grande and Schiwietz (2002).

The model provides impact-parameter-dependent energy losses that must be expected to have comparable accuracy as the corresponding stopping cross sections. The potential of the theory has been explored mainly for He and Li bombardment (Azevedo *et al*., 2001; Grande *et al*., 2002), although the major issue of those studies, the Barkas–Andersen effect, was treated as input rather than output.

Also charge-dependent ('frozen-charge') stopping cross sections were evaluated and these compared favorably with experiment (Grande and Schiwietz, 2002).

The theory has been implemented in the program CasP, a somewhat reduced version of which — not allowing for projectile excitation/ionization — is available on the Internet (Grande and Schiwietz, 2001).

3.7.2 Binary theory

The physical model underlying binary stopping theory by Sigmund and Schinner (2000) is very close to that of Bohr (1913), but application of perturbation theory and a formal distinction between close and distant interactions have been avoided. This has been achieved by treating the effect of electron binding as screening of the interaction. In this way, a complex many-body problem (involving as a minimum the projectile and target nuclei and a target electron) has been replaced by a binary scattering problem involving the projectile and a target electron.

An estimate of the Barkas–Andersen effect is inherent in the picture, and shell corrections have been incorporated separately (Sigmund and Schinner, 2001c) by means of the transformation (3.14) that is rigorous for binary collisions. An essential ingredient is the inverse-Bloch correction mentioned in Section 3.3.3, which extends the range of validity into the Born regime. The theoretical scheme has been implemented in the program PASS which includes the standard relativistic correction in Eq. (3.15), as well as the correction by Lindhard and Sørensen (1996), and allows for projectile excitation/ionization. Details of the binary theory have been specified by Sigmund and Schinner (2002b), and an up-to-date account will be given in Section 6.

Since optical oscillator-strength spectra form the main input into the theory, the accuracy of its predictions hinges on the quality of available optical properties (refraction indices and attenuation coefficients) over an energy range from about 1 eV to 10–100 keV, dependent on atomic number.

Table 3.2. Summary of theoretical schemes discussed in Section 3.7. Columns 3–10 list options for impact-parameter dependence (p), dependence on ion charge (q_1), Barkas-Andersen effect, shell correction, screening, projectile excitation and ionization (PE), Z_1 structure, and Z_2 structure.

	v regime	p	q_1	Barkas–Andersen	Shell	Screening	PE	Z_1	Z_2
UCA	$v_0 < v \ll c$	Yes	Yes	No	No	Yes	yes[a]	No	Yes
Binary	$v_0 \lesssim v$	Yes	Yes	Yes	Yes	Yes	Yes	No	Yes
Nonlinear	$v \ll c$	No	Yes	Yes	Yes	Yes	No	Yes	Yes[b]
CKT	$Z_2\, v_0 < v < Z_1\, v_0$	No	Yes	Yes	No	Yes	No	No	No

[a]Contribution from projectile ionization likely to be overestimated, see remarks in Section 3.4.7.
[b]Within limitations of the electron-gas model.

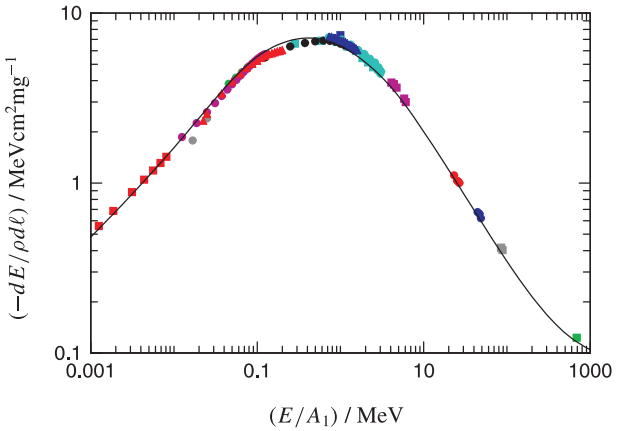


Figure 3.19. Stopping of oxygen in aluminium: comparison of experimental data with prediction from binary theory. From Sigmund and Schinner (2002b).

Extensive tests on the sensitivity to various types of input and comparisons with experimental data were presented by Sigmund and Schinner (2002b). Figure 3.19 shows the case of O–Al with the experimental data also shown in Figure 3.18. Also charge-dependent stopping cross sections were evaluated and compared favorably with experiment (Sigmund and Schinner, 2001c).

Evidence presented by Sigmund and Schinner (2000) indicated that the estimate of the Barkas–Andersen effect inherent in the binary theory can be quite accurate. This conclusion has been strengthened by an evaluation of antiproton stopping forces where excellent agreement has been achieved with numerous experimental results (Sigmund and Schinner, 2001a, 2002c). An example is shown in Figure 3.6.

Although the theory is geared toward beam velocities exceeding v_0, Figure 3.19 shows that good agreement with experimental results can be achieved at lower velocities. However, the theoretical scheme does not incorporate a model of the type described in Sections 3.6.4–3.6.6 to predict Z_1 structure.

3.7.3 Nonlinear electron-gas model

Stopping models based on the transport-cross-section approach in conjunction with scattering phase shifts, Eq. (3.17), have been common in low-speed stopping as discussed in Section 3.6. The approach has also been highly successful in relativistic heavy-ion stopping (see Section 3.3.3).

An attempt to extend the range of validity of a low-speed scheme toward intermediate velocities was initiated by Lifschitz and Arista (1998). The scheme operates with a Fermi gas as a target, and its main ingredient is a generalized Friedel sum rule that takes into account the motion of the projectile through the medium. Apart from this, the ingredients of the theory — when applied to the stopping of point charges — are essentially the same as in the low-speed approach by Calera-Rubio *et al*. (1994). The scheme was applied to estimate antiproton stopping (Arista and Lifschitz, 1999, 2002). Results shown in Figure 3.6 confirm that the theory incorporates a reasonable estimate of the Barkas–Andersen effect.

An extension to heavier ions was presented by Arista (2002). Particular attention was given to projectile screening, for which a variety of screening functions was explored. Being based on a Fermi gas, the scheme incorporates shell corrections from the outset while projectile excitation has not been included.

Figure 3.20 shows a general behavior very similar to Figure 3.17 and confirms the fading away of predicted Z_1 oscillations with increasing projectile speed.

Electron-gas models are powerful in the description of low-speed stopping in normal metals, where stopping is predominantly due to quasi-free electrons. With increasing projectile speed, bound target electrons contribute to stopping. This requires separate attention. The problem gets accentuated for insulators. The problem was solved for antiproton stopping by application of some simplified linear model to inner shells (Arista and Lifschitz, 1999) or

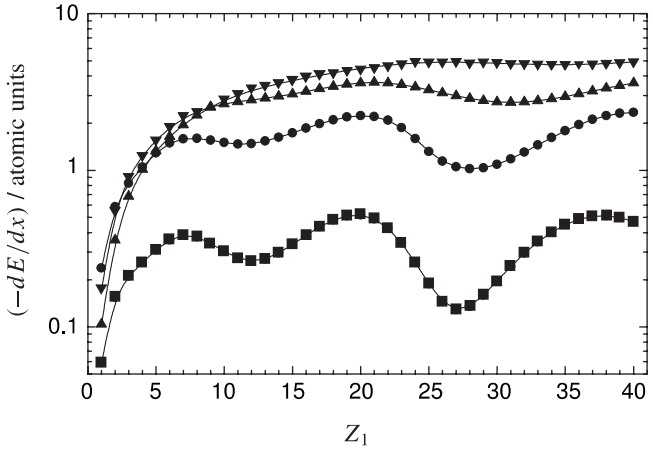


Figure 3.20. Z_1 oscillation in stopping power as a function of projectile speed according to Arista (2002), calculated for homogeneous electron gas with a Wigner-Seitz radius $r_s = a_0(3/4\pi n_e)^{1/3} = 1.6$ representing carbon (n_e = electron density) for $v/v_0 = 3, 2, 1, 0.2$ (top to bottom).

by application of the local-density approximation (Arista and Lifschitz, 2002).

3.7.4 CKT and related theories

Convergent kinetic theory (CKT) is a label for a number of extensions to the Bethe theory that allow stopping calculations for partially ionized ions in partially ionized targets. The theory is geared toward stopping in plasmas but reference is extensively made to cold matter, in particular in the work of Maynard *et al*. (1996, 1998a,b, 2000, 2001a,b, 2002b) summarized by Maynard *et al*. (2002a).

Owing to the emphasis on applications to fusion plasmas, particular attention has been given to projectile processes, especially charge states and the correlation between charge exchange and energy loss. A high degree of symmetry has been aimed at with regard to the description of target and projectile atoms. Close-collision corrections to the Bethe stopping formula are treated on the basis of the transport cross section (3.47) much like the derivation of the Bloch correction by Lindhard and Sørensen (1996) but on the basis of a screening potential incorporating the adiabatic radius, thus providing an estimate of the Barkas–Andersen effect. Shell corrections for close collisions are incorporated *via* kinetic theory [Eq. (3.14)]. Static projectile screening is characterized by a screening function composed of a sum of exponentials.

This model differs from the binary theory mainly by the use of an average-atom model for target and projectile (Maynard *et al*., 1996; Mabong *et al*., 1996) which avoids the use of empirical or semi-empirical oscillator strengths. The range of validity of the theory is asserted to be

$$Z_2 < \frac{v}{v_0} < Z_1. \tag{3.49}$$

Explicit applications of the theory have focused on hydrogen gas targets (Chabot *et al*., 1998; Gardès *et al*., 1998) but also include a study of the density effect in carbon (Maynard *et al*., 2000).

3.8 NUCLEAR STOPPING

3.8.1 Introductory remarks

Nuclear stopping, *i.e.*, energy transfer to recoiling nuclei, accounts for < 0.05 % of all energy loss at projectile speeds above the orbital velocities of the majority of target electrons. Conversely the effect becomes dominating when the majority of electronic excitation channels is closed. Figure 3.2 indicates that the regime of dominating nuclear stopping typically lies within the velocity range $v < v_0$ except for rather heavy ions ($Z_1 \geq 60$ and 40 for $Z_2 = 79$ and 6, respectively). Therefore, nuclear stopping is of minor importance in numerous situations considered in this report. On the other hand, unlike electronic collisions, recoil events are accompanied by angular deflection of the projectile that affects range and energy-deposition profiles as well as the analysis of stopping measurements.

The strong coupling between nuclear energy loss and angular deflection implies that nuclear stopping can only be measured with great difficulty in transmission measurements (Sidenius, 1974). Experimental evidence emerges more indirectly, mainly from measurements of angular scattering on gas targets and, to some extent, solid surfaces. Theory plays a key role in this area.

3.8.2 Binary elastic scattering

The conventional starting point for a theoretical treatment of recoil loss as well as angular scattering is the classical theory of binary elastic scattering[23] on a central force that is standard textbook material.

[23]The term 'elastic scattering' has different meanings in different disciplines. In the fields of x-ray, electron and neutron scattering on solids, elastic scattering means scattering without loss of translational energy, where the momentum change of the projectile is taken up by a macroscopic target. Scattering between heavy particles may be elastic with respect to the sum of the translational energies of the collision partners or, in other words, may be elastic in the center-of-mass system.

This implies

1. decoupling of electronic from nuclear collisions,
2. negligible quantum effects,
3. existence of a spherically symmetric potential and
4. negligible many-body effects.

A brief discussion of these items is given below.

Decoupling. Clearly, recoil and electronic losses are coupled. Indeed, electronic energy losses in individual collisions can be determined experimentally from measurements of the energies of particles scattered into a given direction[24] in conjunction with the law of momentum conservation. Both types of loss tend to decrease in magnitude with increasing impact parameter.

However, the maximum energy transfer from a heavy ion to a recoil atom far exceeds that to an electron. This causes recoil losses to dominate in close collisions. Conversely, at not-too-low projectile speeds, the effective range of electronic interaction exceeds that of the (screened) ion–atom interaction. This implies an approximate separation of nuclear and electronic energy loss in impact-parameter space as far as the contribution to the stopping cross section is concerned (Lindhard *et al.*, 1963a,b).

As a rule of thumb, the significance of this type of correlation increases with decreasing energy down to the crossover of nuclear and electronic stopping. Quantitative estimates require knowledge of the dependence on impact-parameter of the mean nuclear energy loss and pertinent electronic-transition probabilities.

Quantum effects. The Bohr criterion for applicability of a classical-orbit description of binary scattering may be written in the form of Eq. (3.2) with an additional factor Z_2^2. This implies that the curves labelled 'classical' in Figure 3.2 are shifted upward by a factor Z_2^2. Except for hydrogen targets this change is significant. It ensures a very wide regime of validity of classical-scattering theory.

Theoretical treatments based on classical descriptions of nuclear motion but quantal treatment of electronic excitation are common in atomic- and molecular-collision physics and go under the label 'semiclassical'.

Potential. Classical binary-scattering theory makes explicit use of angular-momentum conservation. Therefore the assumption of a central force is essential. Screened-Coulomb interaction potentials of the type of

$$V(R) = \frac{Z_1 Z_2 e^2}{4\pi\epsilon_0 R} u\left(\frac{R}{a}\right) \tag{3.50}$$

are most common. Here R is the distance between the interacting nuclei, u some screening function and a a screening radius. Both u and a depend on Z_1, Z_2, and the charge state q_1. These dependencies are frequently expressed in terms of Thomas-Fermi type scaling relations to be discussed below.

Many-body effects. It is appropriate to distinguish between many-body collisions and many-body potentials. Many-body collisions occur in dense (solid) media at energies so low that the dimensions of a scattering trajectory are of the order of or exceed the internuclear distance in the medium. This is typically the case at particle energies well below 1 keV, *i.e.*, below the range of heavy-ion energies addressed in this report. In practice, collision problems in this energy range are treated by molecular-dynamics or alternative types of computer simulation (Eckstein, 1991).

Many-body potentials describe the interaction between two particles embedded in a medium. The medium is typically characterized as a Fermi gas of constant density, and the interaction between embedded atoms takes into account the relaxation of the electron gas around the intruders. This type of interaction, called 'embedded medium' (Jacobsen *et al.*, 1987) or 'embedded-atom' (Daw and Baskes, 1984) potentials, is elastic but non-binary and hence needs to be treated by some molecular-dynamics computer code. The theoretical formalism behind the embedded-medium theory is closely related to the density-functional approach that also enters the theory of low-speed electronic stopping discussed in Section 3.6.6.

An extensive survey on interatomic potentials in radiation physics has been given by Dedkov (1995).

3.8.3 Scaling properties

For elastic scattering on a central potential of the form of Eq. (3.50), a rigorous scaling relation follows from conservation laws and classical scattering theory (Lindhard *et al.*, 1968):

$$\theta = \theta\left(\frac{p}{a}, \epsilon\right), \tag{3.51}$$

where θ is the center-of-mass scattering angle, p the impact parameter, and ϵ a dimensionless

[24] The same is true for inelastic losses in nuclear reactions.

parameter[25] proportional to the energy defined as

$$\epsilon = \frac{4\pi\epsilon_0 M_0 v^2 a}{2Z_1 Z_2 e^2}, \tag{3.52}$$

where $M_0 = M_1M_2/(M_1 + M_2)$ is the reduced mass.

The energy transfer w to a target atom initially at rest is known to be given by

$$w = \gamma E \sin^2\frac{\theta}{2}, \tag{3.53}$$

with[26] $\gamma = 4M_1M_2/(M_1 + M_2)^2$. From this follows the differential cross section

$$\mathrm{d}\sigma(w) = \pi a^2 g\left(\epsilon, \frac{w}{\gamma E}\right)\frac{\mathrm{d}w}{\gamma E}, \tag{3.54}$$

with the function g determined by the screening function u, and the stopping force

$$-\frac{\mathrm{d}E}{\mathrm{d}\ell} = nS = \int_0^{\gamma E} w\mathrm{d}\sigma(w) = N\pi a^2\gamma E s(\epsilon), \tag{3.55}$$

where $s(\epsilon) = \int_0^1 \mathrm{d}t\, tg(t)$ is a function determined by u. The latter relation is commonly written in the form

$$-\frac{\mathrm{d}\epsilon}{\mathrm{d}\rho} = s(\epsilon), \tag{3.56}$$

where ρ is a dimensionless measure of pathlength

$$\rho = n\pi a^2\gamma\ell. \tag{3.57}$$

While these relations are quite general, they become particularly useful when the screening function u and the screening radius a themselves show simple scaling properties with Z_1 and Z_2. Frequently, universal screening functions are adopted (Bohr, 1948; Firsov, 1957; Lindhard *et al*., 1968; Ziegler *et al*., 1985) and screening radii like those shown in Table 3.3. If u is a universal screening function, $s(\epsilon)$ also becomes a universal function.

In addition to these exact scaling properties, approximate scaling has been demonstrated for repulsive screening functions by Lindhard *et al*. (1968), where the dependence on two variables in Eq. (3.54) is replaced by one variable

$$\eta = \epsilon\sin\frac{\theta}{2}, \tag{3.58}$$

[25]The symbol ϵ occurs with different meanings in the stopping literature, such as beam energy, stopping force, stopping cross section and stopping number. In the present report, ϵ denotes consistently the quantity defined by Eq. (3.52).

[26]For symbol γ, see footnote 4 on page 23.

Table 3.3. Common scaling relations for screening radius a.

Bohr (1948)	$a_0(Z_1^{2/3} + Z_2^{2/3})^{-1/2}$
Lindhard *et al*. (1968)	$0.885a_0(Z_1^{2/3} + Z_2^{2/3})^{-1/2}$
Firsov (1957)	$0.885a_0(Z_1^{1/2} + Z_2^{1/2})^{-2/3}$
Ziegler *et al*. (1985)	$0.885a_0(Z_1^{0.23} + Z_2^{0.23})^{-1}$

Table 3.4. Coefficients entering scaling function $f(\eta)$ for differential scattering cross section, Eq. (3.61).

Screening function u	m	q	λ
Thomas–Fermi	0.333	0.667	1.309
Thomas–Fermi–Sommerfeld	0.311	0.588	1.70
Lenz–Jensen	0.191	0.512	2.92
Molière	0.216	0.570	2.37
Bohr	0.103	0.570	2.37

so that

$$\mathrm{d}\sigma(w) = \pi a^2\frac{\mathrm{d}\eta}{\eta^2}\, f(\eta), \tag{3.59}$$

$$s(\epsilon) = \frac{1}{\epsilon}\int_0^\epsilon \mathrm{d}\eta\, f(\eta), \tag{3.60}$$

and $f(\eta)$ is determined by the adopted screening function.

Convenient analytical approximations for $f(\eta)$ were given by Winterbon *et al*. (1970) and Winterbon (1972),

$$f(\eta) \simeq \frac{\lambda\eta^{1-2m}}{\left(1 + [2\lambda\eta^{2(1-m)}]^q\right)^{1/q}} \tag{3.61}$$

with coefficients m, q and λ given in Table 3.4.

Plots of the functions $f(\eta)$ and $s(\epsilon)$ for these potentials are shown in Figures 3.21 and 3.22. There is general agreement that the Thomas–Fermi screening function overestimates the potential at large distances and hence the stopping cross sections at low energies, and that the opposite is the case for the Bohr screening function. The difference between Lenz–Jensen and Molière, although noticeable especially in the low-energy range, reflects the inherent uncertainty of this type of potentials. Figure 3.22 also includes the reduced stopping cross section in the form favored by Ziegler *et al*. (1985) — denoted by ZBL — which may be written in the form

$$s(\epsilon) = \frac{\ln(1 + a\epsilon)}{2(\epsilon + b\epsilon^c + d\sqrt{\epsilon})}, \tag{3.62}$$

with $a = 1.1383$, $b = 0.01321$, $c = 0.21226$, and $d = 0.19593$. An additional source of uncertainty lies in the choice of screening radius. Common choices are shown in Table 3.3.

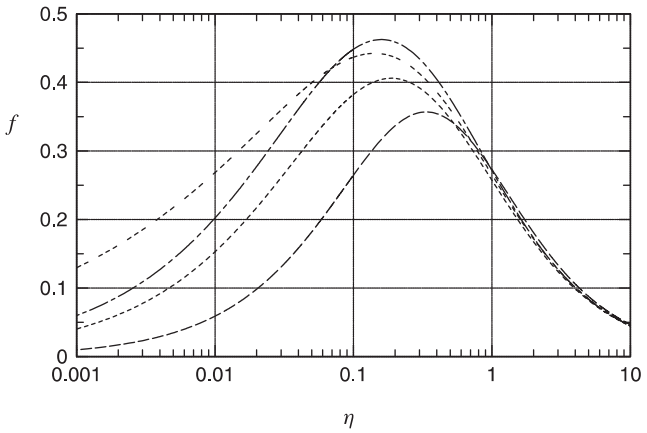


Figure 3.21. Function $f(\eta)$, Eq. (3.61), determining scaled differential scattering cross section for Thomas–Fermi, Molière, Lenz–Jensen and Bohr potentials (top to bottom at the left edge of the graph). Screening functions are specified in Table 3.4.

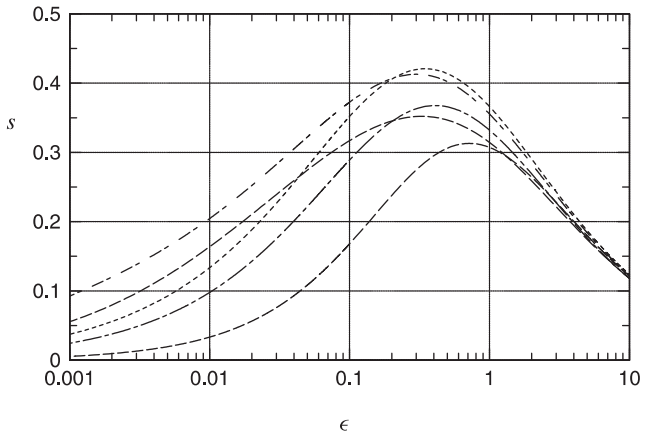


Figure 3.22. Function $s(\epsilon)$, Eq. (3.60), determining scaled nuclear-stopping cross section for Thomas–Fermi, ZBL, Molière, Lenz–Jensen and Bohr potential (top to bottom on left edge of the graph). Screening functions are specified in Table 3.4.

The choice of Ziegler *et al*. (1985), which differs noticeably from the others, was generated by an averaging process involving numerically computed interaction potentials for a very large number of atom–atom pairs. These potentials were computed on the basis of the Thomas–Fermi method with atomic charge distributions as the main input. The value of a screening radius extracted from such potential functions clearly depends on the weights assigned to different regimes of interatomic distance. The procedure by Bohr (1948), followed also by Lindhard *et al*. (1968) and Firsov (1957), refers to the regime of weak screening, $R \lesssim a$, while the averaging process adopted by Ziegler *et al*. (1985) involves the range $R \lesssim 25a$, *i.e.*, far beyond the range of validity of the Thomas–Fermi model.

Although interaction potentials unquestionably depend on the charge states of the collision partners, this dependence is usually neglected, the main reason being that in the low-energy region, where the outer parts of the interaction potential play a most significant role, collision partners are most often neutral. For distant collisions, a simple way to approximately account for the charge state of the ion is to replace Z_1 by q_1 in the expression for the screening radius (Amsel *et al*., 2003).

3.8.4 Power-law cross sections

According to Eq. (3.61), the function $f(\eta)$ approaches power form at low arguments,

$$f(\eta) \simeq \lambda \eta^{1-2m}, \quad \text{for } \eta \ll 0.1. \tag{3.63}$$

At large values of η, on the other hand, all curves approach a common asymptotic form

$$f(\eta) \sim \frac{1}{2\eta}, \quad \text{for } \eta \gg 1 \tag{3.64}$$

reflecting Rutherford scattering and $m = 1$. In the intermediate regime, a constant equivalent with the choice $m = 1/2$ may be employed in rough estimates. The function adopted by Bohr (1948) assumes $m = 1/2$ and $\lambda = 0.327$.

Stopping cross sections following from Eq. (3.63) take the form

$$s(\epsilon) = \frac{\lambda}{2(1-m)} \epsilon^{1-2m}. \tag{3.65}$$

In particular, for $m = 1/2$, a constant stopping cross section $s = 0.327$ was found (Bohr, 1948).

Power-law cross sections are convenient for rough analytical estimates and have been employed extensively in the theory of radiation effects. Their general form is

$$\mathrm{d}\sigma(E, w) = C \frac{\mathrm{d}w}{E^m w^{1+m}}, \tag{3.66}$$

with

$$C = \frac{\pi}{2} \lambda a^2 \left(\frac{M_1}{M_2}\right)^m \left(\frac{2Z_1 Z_2 e^2}{4\pi\epsilon_0 a}\right)^{2m}, \tag{3.67}$$

and parameters m and λ depending on the range of η and/or ϵ where the expression is going to be used.

Power-law cross sections were originally derived by approximating the screening function u by an inverse-power form (Bohr, 1948; Lindhard *et al*., 1968).

3.8.5 Concluding remarks

It is emphasized that the treatment of nuclear stopping offered in this section addresses situations for which the effect is of minor importance.

Moreover, using scaling relations is a matter of convenience and by no means necessary. Computation of classical-scattering integrals is a routine matter which, at least for purely repulsive interaction potentials, does not require excessive computation times. Therefore, when a good estimate of an interaction potential is available, a reliable scattering law ought to be generated by direct integration rather than by scaling.

Finally it is emphasized that, dependent on the experimental setup, only a restricted nuclear-stopping cross section might contribute to the measured energy loss. For the frequently used transmission technique, this aspect will be considered in Section 3.14.

3.9 NUCLEAR REACTIONS

Cross sections for nuclear reactions leading to a change in mass and/or identity of the projectile are much smaller than for atomic processes except for relativistic heavy ions with more than several hundred MeV/u, at which energies they may become comparable. This is illustrated in Figure 3.23, where the nuclear reaction probability is calculated for different ions in carbon, aluminum and lead. The total nuclear-reaction cross section applied in this calculation consists of a pure nuclear part calculated according to Shen *et al*. (1989) and a component due to electromagnetic dissociation (Bertulani and Baur, 1988), which contributes mainly for large Z_1 and/or Z_2. The comparison demonstrates that for lighter projectiles and lighter stopping media the losses due to nuclear reactions are severe. This is the reason why light materials like beryllium are preferred as production targets in high-energy fragmentation reactions. Conversely, for electromagnetic dissociation of relativistic projectiles, lead targets are used successfully in studies and applications of exotic nuclei (Geissel, 1997).

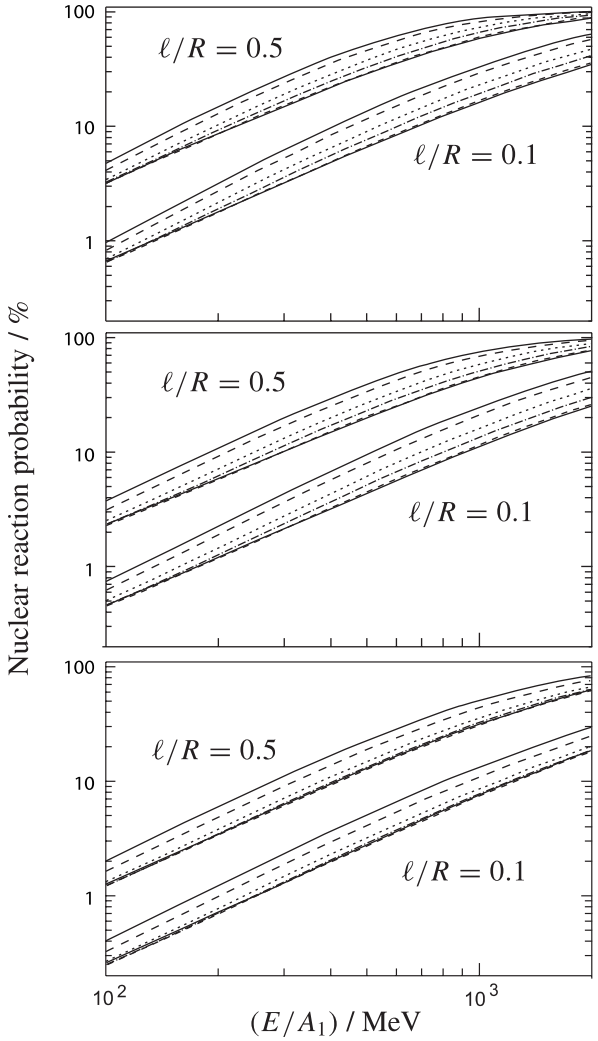


Figure 3.23. Nuclear reaction probability during the slowing down of heavy ions in carbon, aluminum, and lead (top to bottom graph). ℓ is the path length and R the total range. Lines for ^{20}Ne, ^{40}Ar, ^{86}Kr, ^{132}Xe, ^{208}Pb and ^{238}U (top to bottom in each group (From Geissel *et al*., 2002).

3.10 CHANNELING, AND STOPPING AT SURFACES

Although energy loss under channeling conditions is a problem of considerable complexity, the number of application areas is narrower than that of stopping in random media. Therefore the present section is intended mainly to give a brief survey of complicating features. For a general introduction to channeling the reader is referred to a review by Gemmell (1974).

An ion beam penetrating through a medium with a regular crystalline structure can be considered as being split into two components, a random and an aligned beam (Lindhard, 1965). The aligned beam is guided by the collective action of closely spaced atoms making up rows or planes of atoms and hence avoids close encounters with the target nuclei. This gives rise to dramatic reductions in the rates of wide-angle Rutherford scattering, nuclear reactions, inner-shell excitation and multiple angular scattering. Energy loss is also reduced, but that effect is less dramatic because of the long range of electronic interactions in the high-energy range where channeling phenomena are most pronounced.

Theoretical descriptions of energy loss in channeling are traditionally based on electron-gas models (Lindhard, 1965), the underlying reason being the dominance of outer target shells in the energy-loss process. The equipartion rule of Lindhard and Winther (1964) — valid for light ions penetrating

through a homogeneous Fermi gas — suggests reduction by roughly a factor of two of the mean energy loss at not too low projectile speeds. An extensive body of literature is devoted to this topic, based on more or less sophisticated models of homogeneous and inhomogeneous Fermi gases.

More quantitative estimates are now possible on the basis of impact-parameter-dependent energy-loss functions for covalent and ionic materials, supplemented by electron-gas estimates for conduction electrons in metals. This requires impact-parameter distributions that, typically, are found from binary-collision or molecular-dynamics simulation of pertinent trajectories. Energy-loss functions $w(v, p)$ dependent on impact parameter may be determined from schemes discussed in Section 3.7, especially the binary theory and the unitary-convolution approximation. Initial steps have been made (Sigmund and Schinner, 2001d; Azevedo *et al*., 2001), but a considerable effort lies ahead in analyzing a large body of unexplained experimental data.

In addition to target thickness and projectile speed, the energy-loss spectrum for a given beam depends on the orientation of the target and the angle between the beam and the closest crystal chain or plane. For heavy ions, charge equilibration has been found to be dramatically affected (Datz *et al*., 1972). This provides the possibility of measurements with ions in 'frozen-charge states' (Datz *et al*., 1977; Golovchenko *et al*., 1981).

Separation of measured energy-loss spectra into a random and a channeled fraction is frequently possible. In addition, the energy loss of 'best-channeled' particles can occasionally be identified by extrapolation of the low-loss or high-penetration tail. This is in contrast to random slowing-down in which Poisson statistics does not allow this distinction.

With appropriate modifications the present considerations also apply to measurements of scattering and energy loss of well-collimated beams on flat surfaces (Kimura *et al*., 1987; Winter, 2002).

3.11 STATISTICS OF PARTICLE PENETRATION

3.11.1 Qualitative survey

The importance of statistical considerations in the physics of particle penetration has been emphasized in particular by Bohr (1948). An extensive review of the subject matter — including outline for work to be done — was given by Sigmund (1991). The present section serves to summarize central results that affect the analysis of energy-loss measurements and the relation between measured and calculated stopping parameters.

It is useful to distinguish between measurements on

- *thin targets* in which a beam particle can interact with only a small number of target atoms,
- *thick targets* in which the number of interactions is large enough to make fluctuations small, and
- *very thick targets* in which the number of interactions is so large that beam particles lose a significant fraction of their energy, thus giving rise to non-negligible variations in pertinent cross sections.

For thin targets, the energy-loss spectrum and angular distribution of an initially monochromatic and well-collimated beam are modified in accordance with the cross section for energy loss and angular deflection, respectively. This implies a pronounced peak around zero energy loss and a tail extending toward the maximum energy loss or scattering angle in a single collision.

For thick targets the energy-loss spectrum has a trend toward gaussian shape centered around the average energy loss, while the angular distribution tends toward a gaussian centered around the initial beam direction.

For very thick targets pronounced changes in pertinent cross sections cause deviations from gaussian shape that need special consideration.

These differences are highly visible for charged-particle interactions since cross sections for Coulomb scattering are power-like and thus differ dramatically from gaussian shape. This, at the same time, makes it possible to operationally distinguish between the thin- and thick-target regime for a given region in the (Z_1, Z_2, v) parameter space by mere inspection of measured or calculated spectra.

Although Coulomb scattering is the predominant factor in collision statistics for light penetrating particles, charge exchange enters as a complicating phenomenon in case of heavier ions. This influence is two fold:

- cross sections for energy loss and angular deflection may depend on charge state, and
- charge-exchange events may themselves give rise to significant energy loss and/or angular scattering.

In addition to these intrinsic and unavoidable sources of fluctuations, observed fluctuation phenomena are affected by experimental factors like target nonuniformity, beam instabilities, and counting statistics.

3.11.2 Stripped ions

Fluctuation phenomena are well-investigated for penetrating point charges, *i.e.*, for ions with

velocities $v \gg Z_1^{2/3} v_0$ (Figure 3.2). Energy-loss statistics for both thin and thick targets — but not for very thick targets — is governed by the Bothe–Landau formula (Landau, 1944) for the energy-loss spectrum,

$$F(\Delta E, \ell)\mathrm{d}(\Delta E) = \frac{\mathrm{d}(\Delta E)}{2\pi} \int_{-\infty}^{\infty} \mathrm{d}s e^{is\Delta E - n\ell\sigma(s)}, \qquad (3.68)$$

for random slowing down, *i.e.*, uniform distribution of scattering events in space and time. Here, s is a variable in Fourier space, ΔE the total energy loss, ℓ the path length, n the number of target atoms per volume, $\sigma(s) = \int \mathrm{d}\sigma(w)(1 - e^{-isw})$ a transport cross section, w the energy loss in an individual event and $\mathrm{d}\sigma(w)$ the differential cross section per target atom for energy loss in an interval $(w, \mathrm{d}w)$.

One may derive Eqs. (2.8)–(2.14) from (3.68) by taking first- and second-order moments over ΔE. The main question of interest is how these averages relate to peak value and halfwidth of the spectrum, which are often more accessible to measurement.

When ℓ is large, all penetrating particles experience large energy losses so that the integral (3.68) receives contributions mainly from small values of s. Expansion of $\sigma(s)$ up to second order in s and subsequent integration then yields the gaussian

$$F(\Delta E, \ell) \simeq \frac{1}{\sqrt{2\pi n\ell W}} e^{-(\Delta E - n\ell S)^2 / n\ell W}, \qquad (3.69)$$

with the stopping cross section $S = \int w\mathrm{d}\sigma(w)$ and straggling parameter $W = \int w^2 \mathrm{d}\sigma(w)$.

For thin targets Landau (1944) presented the solution

$$F(\Delta E, \ell) = \frac{w_{\max}}{\Omega_B^2} \frac{1}{2\pi i} \int_{c-i\infty}^{c+i\infty} \mathrm{d}s e^{s\ln s + \lambda s} \quad (c > 0), \qquad (3.70)$$

$$w_{\max} = 2mv^2/(1-\beta^2),$$

$$\Omega_B^2 = 4\pi Z_1^2 Z_2 e^4 n\ell,$$

which expresses the spectrum by a single variable

$$\lambda = \frac{w_{\max}(\Delta E - \langle \Delta E \rangle)}{\Omega_B^2} - \ln \frac{\Omega_B^2}{w_{\max}^2} - 1 + \gamma, \qquad (3.71)$$

$\gamma = 0.5772 =$ Euler's constant. Note that unlike (3.69), Eq. (3.70) implies Coulomb scattering specifically.

Eq. (3.71) suggests that the peak position does not normally lie at $\Delta E = \langle \Delta E \rangle$ and is governed by the ratio $\Omega_B^2 / w_{\max}^2$.

The range of validity of these approximations is given by $\Omega_B / w_{\max} \gg 1$ for the gaussian and $\Omega_B / w_{\max} \ll 1$ for the Landau solution. Attempts to reduce the large intermediate regime where neither approximation is applicable include the schemes of Vavilov (1957), Symon (1948) and Sigmund and Winterbon (1985) to expand the high-ℓ regime downward and of Lindhard (1985) to expand the Landau regime upward.

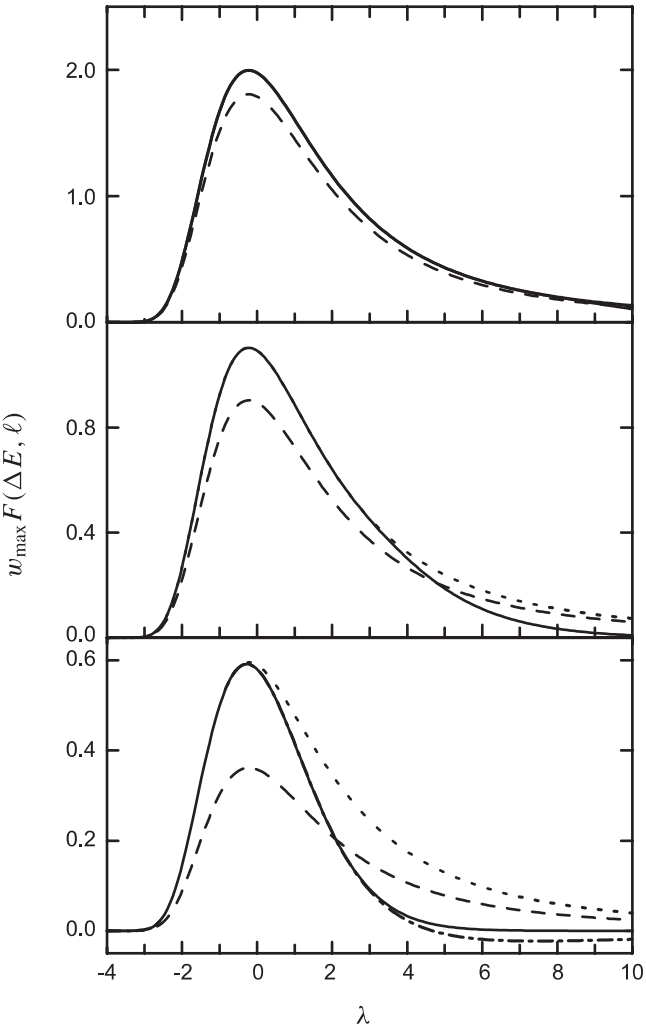


Figure 3.24. Approximations to the energy-loss spectrum of a swift point charge in dimensionless units. Dashed line: Eq. (3.70): Successive approximations to an expanded Landau formula are shown by dotted, dash-dotted and solid lines. The solid line is indistinguishable from a numerical evaluation of Eq. (3.68); $\Omega_B^2/w_{\max}^2 = 0.1$, 0.2 and 0.5 (top to bottom). From Glazov (2000).

Most successful has been a dual approach by Glazov (2000) that extends the Landau scheme toward larger thicknesses and utilizes the steepest-descent method (Sigmund and Winterbon, 1985) at larger thicknesses, with a comfortable overlap regime at sufficiently high energies. An example is shown in Figure 3.24.

Extraction of stopping parameters from measured spectra can be simplified if the mean energy loss $\langle \Delta E \rangle$ is close to the peak value ΔE_{peak}, and if the relation between standard deviation and halfwidth is the one familiar from the gaussian. As long as

deviations are small, the following relations, derived by Sigmund and Winterbon (1985) for the large-thickness limit, may be useful,

$$\Delta E_{\rm peak} = \langle \Delta E \rangle - \frac{mv^2}{2} + \mathcal{O}\left\{\frac{1}{n\ell}\right\}, \tag{3.72}$$

and

$$\Delta E_{\pm 1/2} = \Delta E_{\rm peak} \pm 1.177\Omega_{\rm B} + 0.231 mv^2 \mp 0.098\frac{(mv^2)^2}{\Omega_{\rm B}} + \mathcal{O}\left\{\frac{1}{n\ell}\right\}, \tag{3.73}$$

where $\mathcal{O}\{1/n\ell\}$ indicates the order in $n\ell$ of the leading neglected term.

The range of applicability of the above tools can be extended into the range of very thick targets by replacing the initial energy E by an effective energy

$$E_{\rm eff} = E - \langle \Delta E \rangle/2, \tag{3.74}$$

or by replacing the true pathlength ℓ by an effective pathlength

$$\ell_{\rm eff} = \ell\left(1 + \frac{\alpha}{2}\frac{\langle \Delta E \rangle}{E}\right), \tag{3.75}$$

where α is a numerical coefficient characterizing the energy dependence of the transport cross section ($\sigma(s) \propto E^{-\alpha}$) (Sigmund, 1991). A useful relation for straggling was derived by Symon (1948),

$$\Omega^2 = (NS(E_1))^2 \int_{E_1}^{E_0} {\rm d}E' \frac{nW(E')}{(nS(E'))^3}, \tag{3.76}$$

where E_1 is the exit energy.

Depending on the specific system and desired accuracy, such schemes may be adequate up to pathlengths of half the range. For larger thicknesses and/or high-accuracy estimates, recourse has been made to tools from range theory (Symon, 1948; Tschalär, 1968).

3.11.3 Partially stripped ions

For partially stripped ions the above formalism is applicable as it stands only as long as charge exchange is insignificant, *i.e.*, for *frozen charges*. In the presence of charge exchange several complications arise:

- The effective *collisional stopping force* becomes a weighted mean of *frozen-charge stopping forces*.
- The variation in the frozen-charge stopping force is a source of straggling (*charge-exchange straggling*).
- Energy loss in electron capture and loss is a separate contribution to the total energy loss.
- Electronic processes on the projectile such as excitation, deexcitation or Auger decay may contribute to the energy balance, affect pertinent cross sections and occur on a separate time scale that is only indirectly related to the projectile speed.

A formalism that, if slightly modified, can allow for the above features, was presented by Winterbon (1977). It is based on a linear transport equation and hence applicable to the entire range of target thicknesses. The formalism proposed by Sigmund (1992) is equivalent in physical content, but being based on an extension of Eq. (3.68) it relates more directly to well-known standard results for point charges. Moreover, notation was chosen such as to allow for explicit incorporation of all effects mentioned above to the extent that pertinent atomic parameters are available.

The scheme operates with states I, $J\ldots$ of the ion, which may denote charge and/or excitation states. One then introduces an energy-loss spectrum $F_{IJ}(\Delta E, \ell)\,{\rm d}(\Delta E)$, where I denotes the initial state and J the state after pathlength ℓ. The matrix $\mathbf{F}(\Delta E, \ell)$ obeys the generalized Bothe–Landau formula (Sigmund, 1991, 1992)

$$\mathbf{F}(\Delta E, \ell) = \frac{1}{2\pi}\int_{-\infty}^{\infty} {\rm d}s\, e^{is\Delta E + n\ell\mathbf{Q} - n\ell\sigma(s)}, \tag{3.77}$$

where $\mathbf{Q}$, σ and $\sigma(s)$ represent matrices with elements Q_{IJ} and σ_{IJ}, respectively,

$$Q_{IJ} = \sigma_{IJ} - \delta_{IJ}\sum_L \sigma_{IL}, \tag{3.78}$$

$$\sigma_{IJ} = \int {\rm d}\sigma_{IJ}(w), \tag{3.79}$$

$$\sigma(s) = \int {\rm d}\sigma_{IJ}(w)\left(1 - e^{-isw}\right), \tag{3.80}$$

and ${\rm d}\sigma_{IJ}(w)$ the differential cross section for energy loss $(w, {\rm d}w)$ in a collision with the ion in incident and final states I and J, respectively. In this notation only collision-induced processes are assumed active. In the presence of spontaneous processes such as Auger decay a notation based on transition rates is more convenient (Sigmund, 1992).

Integration of Eq. (3.77) over the energy loss yields the probability

$$P_{IJ}(\ell) = \left(e^{n\ell\mathbf{Q}}\right)_{IJ} \tag{3.81}$$

for an ion in the initial state I to be in state J after a pathlength ℓ. Eq. (3.81) is a compact solution of the familiar rate equations that are normally used to describe the approach to charge equilibrium (Allison, 1958).

The occurrence of a matrix in an exponential is a complication which can be overcome by standard

mathematical tools such as eigenvalue expansion for the approach to equilibrium (Sigmund, 1992; Glazov and Sigmund, 1997) or Taylor expansion when the number of charge exchanges is small (Sigmund, 1994; Glazov, 2002b).

In the present context, prime quantities are stopping force and straggling in charge equilibrium and information about the approach to equilibrium from a given initial charge state. Such information is given in the form of asymptotic expansions in terms of $1/n\ell$ similar to Eqs. (3.72) and (3.73). If only the equilibrium value and the first correction term are given, the latter produces an intercept for the straight lines $\langle \Delta E \rangle$ or Ω^2 versus ℓ.

General expressions for equilibrium and intercept were presented by Sigmund (1992) and Närmann and Sigmund (1994). For equilibrium stopping, Eq. (3.32) is obtained. Straggling is made up by a term analogous to Eq. (3.32) accounting for collisional straggling and another one that vanishes in the absence of charge exchange. The latter can be written in a particularly transparent way for the specific case of a two-state system for which (Sigmund, 1992)

$$\Omega^2_{\text{chex}} = 2n\ell \frac{(S_1 - S_2)}{(\sigma_{12} + \sigma_{21})^3} \times [\sigma_{12}\sigma_{21}(S_{11} - S_{22}) + (\sigma_{12}^2 S_{21} - \sigma_{21}^2 S_{12})], \tag{3.82}$$

$$S_{IJ} = \int w \mathrm{d}\sigma_{IJ}(w),$$

$$S_I = \sum_J S_{IJ}.$$

If energy loss in charge exchange is negligible, only the first term in the square brackets remains, and Ω_{chex} reduces to the well-known expression (Efken *et al.*, 1975)

$$\Omega^2_{\text{chex}} \simeq 2n\ell \frac{(S_1 - S_2)^2}{(\sigma_{12} + \sigma_{21})^3} \sigma_{12}\sigma_{21}. \tag{3.83}$$

For a three-state system, energy loss in charge exchange being neglected, the corresponding expression reads

$$\Omega^2_{\text{chex}} = \frac{n\ell}{\beta^3} \sum_{JK} (S_J - S_K)^2 \mu_J (\alpha\mu_K - \beta\sigma_{JK}), \tag{3.84}$$

$$\alpha = \sum_{KL} \sigma_{KL},$$

$$\mu_1 = \sigma_{32}\sigma_{21} + \sigma_{23}\sigma_{31} + \sigma_{21}\sigma_{31},$$

$$\mu_2,\ \mu_3 = \text{cyclical permutations},$$

$$\beta = \sum_J \mu_J.$$

3.11.4 Transport equations and simulation

To the extent that the assumption of random slowing down is satisfied, linear transport equations constitute a convenient and accurate analytical tool for problems that cannot be handled efficiently on the basis of the Bothe–Landau formula (3.68) or its expanded version (3.77). This includes in particular

- very thick targets allowing substantial energy loss, including complete slowing down,
- problems involving secondary particles such as recoil atoms and ejected electrons,
- complex geometries, including composite targets.

The original derivation of Eq. (3.68) by Landau (1944) started off from

$$\frac{\partial}{\partial \ell} F(E, \ell) = n \int \mathrm{d}w (K(E + w, w) F(E + w, \ell) - K(E, w) F(E, \ell)), \tag{3.85}$$

where $F(E, \ell)$ is the *energy spectrum* at pathlength ℓ and $K(E, w) = \mathrm{d}\sigma(w)/\mathrm{d}w$ at the energy E. Eq. (3.85) is a *forward transport equation* for the energy spectrum versus pathlength. Additional spectral variables like direction of motion and charge state are easily incorporated. This complex has been summarized by Sigmund (1991), where also backward equations are discussed.

For thin and thick targets the most appropriate way to solve transport equations is *via* the Bothe–Landau scheme. For targets that are too thick to allow this procedure, the traditional way of solving the equations goes over moments either of the energy or the pathlength. Reconstruction of a spectrum from its moments is notoriously difficult (Symon, 1948; Winterbon *et al.*, 1970). With easy access to present-day computers this route does not any longer reflect the state-of-the-art. Numerical solutions of transport equations or direct Monte Carlo simulation may easily be superior in both efficiency and accuracy.

3.11.5 Non-Poisson statistics

When the probability for collision processes is distributed uniformly in space and time, their frequency distribution is governed by Poisson statistics. Two configurations are known where pronounced deviations from Poisson behavior can occur:

- In a dense medium atoms are arranged in close packing rather than at random. This means that processes governed by large cross sections, *i.e.*, with a mean free path not much larger than the interatomic distance, do not obey Poisson's law but are more or less correlated.

- For penetration through crystals under channeling conditions, impact parameters are typically not selected at random; in particular, the frequency of close collisions is drastically reduced.

Two examples illustrate the first type of behavior. Consider stopping in a diatomic molecular gas and assume Bragg's additivity rule to be strictly fulfilled. Physically this implies that all changes in the electronic structure of the atoms in the molecule compared to isolated atoms can be ignored in evaluating stopping parameters, and the only molecular property left over is their mutual spatial correlation that may be assumed fixed at a distance D, while the orientation may be assumed random.

For such a system the following results were derived by Sigmund (1976) for mean energy loss and straggling,

$$\langle \Delta E \rangle = n\ell(S_1 + S_2), \tag{3.86}$$

$$\Omega^2 = n\ell\left(W_1 + W_2 + \frac{S_1 S_2}{2\pi D^2}\cdots\right), \tag{3.87}$$

if the interaction range is limited to $\ll D$, where S_1 and S_2 are stopping cross sections and n is the number of molecules per volume. Since W_1 and W_2 are almost constant as a function of the beam energy, the correlation term in Eq. (3.87) is most significant around the stopping maximum, at which the assumption of a short interaction range may not be far from being fulfilled.

In physical terms, the correlation in space of the target atoms implies that ion–target interactions come in pairs, which is in clear contradiction with Poisson statistics. While the average energy loss is unaffected, fluctuations become enhanced. Note that this violation of Poisson statistics is caused by adopting target *atoms* as the basic unit. The problem evaporates if the basic entity is taken to be the target *molecule*.

A molecular gas may serve as a model for a solid since interatomic distances have comparable magnitudes. For a monoatomic medium, Sigmund (1978) found

$$\langle \Delta E \rangle = n\ell S, \tag{3.88}$$

$$\Omega^2 = n\ell\left(W + 2nS^2 \int_0^\infty \mathrm{d}r[g(r) - 1]\cdots\right), \tag{3.89}$$

where $g(r)$ is the pair correlation of the material, normalized according to

$$n \int \mathrm{d}^3\boldsymbol{r}[g(r) - 1] = 1. \tag{3.90}$$

Again the assumption enters that the range of the interaction be smaller than the internuclear distance.

Unlike in (3.87), Eq. (3.89) yields *reduced* fluctuations because of the greater regularity of the atomic arrangement in a closely packed solid than in a random gas.

More quantitative evaluations of correlation effects have been reported by Sigmund (1991) and, for a specific system, by Grande and Schiwietz (1991).

3.12 STRAGGLING

3.12.1 General survey

Statistical aspects of energy-loss straggling have been considered in Section 3.11. The present section is devoted to atomistic aspects, *i.e.*, the contributions of various stopping processes to straggling and appropriate input into numerical evaluations. Attention will be paid primarily to the straggling parameter $W = \int w^2 \mathrm{d}\sigma(w)$ for a frozen charge and the evaluation of the variance Ω^2. Results will also be reported on predicted energy-loss spectra mainly for thin targets.

It was pointed out in Section 2 that Eq. (2.14) is less comprehensive than Eq. (2.8). One reason for this is the correlation effect discussed in the previous section. In addition there is a significant difference between classical and quantal evaluations that is not present in the case of the stopping cross section. Expressed as integrations over the impact parameter, Eqs. (2.8) and (2.14) read

$$S = \int 2\pi p \mathrm{d}p \langle w \rangle(p), \tag{3.91}$$

$$W = \int 2\pi p \mathrm{d}p \langle w^2 \rangle(p). \tag{3.92}$$

In a classical calculation, the fluctuation in energy loss at a given impact parameter can be set equal to zero so that $\langle w^2 \rangle\,(p) \equiv [\langle w \rangle\,(p)]^2$. Hence, in the presence of significant quantal fluctuations at a given impact parameter, a classical calculation will tend to underestimate straggling.

The occurrence of the factor w^2 has the consequence of a greater significance of large energy losses in straggling than in the stopping cross section, *i.e.*, close collisions tend to dominate (Bohr, 1915). Since the stopping cross section for unscreened Coulomb interaction diverges only logarithmically at small energy transfers, this means that the role of binding of target electrons is much less important in straggling than in stopping.

At the same time, more attention needs to be paid to nuclear energy losses. Reference is made to work by Glazov and Sigmund (2003).

3.12.2 Point charge

A general reference is the result of Bohr (1915),

$$W_{\rm B} = 4\pi Z_1^2 Z_2 e^4, \tag{3.93}$$

which is found for unrestricted Coulomb scattering. It is easily verified that binding gives rise to a correction term of the relative order $(Z_1 e^2\omega/mv^3)^2$ within the Bohr theory, *i.e.*, a term that is negligible compared to shell and Barkas–Andersen corrections.

In view of the dominance of close collisions, the shell correction may reliably be evaluated from kinetic theory (Sigmund, 1982),

$$W(v) = \left\langle \frac{3[\boldsymbol{v}\cdot(\boldsymbol{v}-\boldsymbol{v}_e)]^2 - (\boldsymbol{v}-\boldsymbol{v}_e)^2 v^2}{2v|\boldsymbol{v}-\boldsymbol{v}_e|^3} W_0(|\boldsymbol{v}-\boldsymbol{v}_e|) - m\frac{[\boldsymbol{v}\cdot(\boldsymbol{v}-\boldsymbol{v}_e)]^2 - (\boldsymbol{v}-\boldsymbol{v}_e)^2 v^2}{v|\boldsymbol{v}-\boldsymbol{v}_e|} S_0(|\boldsymbol{v}-\boldsymbol{v}_e|) \right\rangle_{\boldsymbol{v}_e}, \tag{3.94}$$

where W_0 and S_0 denote the uncorrected straggling parameter and stopping cross section, respectively.

Evaluations have focused on asymptotic expansions in powers of $\langle v_e^2\rangle/v^2$ where, according to Sigmund (1982),

$$W(v) = W_0(v) + \frac{\langle v_e^2\rangle}{v^2}\left[-W_0(v) + \frac{1}{6}v^2\frac{{\rm d}^2}{{\rm d}v^2}W_0(v) + \frac{2}{3}mv^2 S_0(v)\cdots\right]. \tag{3.95}$$

After insertion of $W_{\rm B}$ for W_0 this reduces to

$$W(v) = W_{\rm B}\left[1 + \frac{\langle v_e^2\rangle}{v^2}\left(\frac{2}{3}L_0(v) - 1\right)\cdots\right], \tag{3.96}$$

where L_0 is the uncorrected stopping number. A correction of this type, with the factor 2/3, was first derived by Livingston and Bethe (1937).

Extension of Bohr's estimate (Bohr, 1915) into the relativistic regime adds a factor of $\gamma^2 = 1/(1 - v^2/c^2)$ to Eq. (3.93). The Born approximation, on the other hand, leads to (Fano, 1963)

$$\Omega^2 = n\ell W_{\rm B}\left[\frac{1 - v^2/2c^2}{1 - v^2/c^2} + \frac{2}{3}\frac{\langle|\sum\boldsymbol{v}_e|^2\rangle}{Z_2 v^2}\ln\frac{2mv^2}{I_1}\right], \tag{3.97}$$

where the sum goes over all electrons of a target atom. The factor $\langle|\sum\boldsymbol{v}_e|^2\rangle/Z_2\, v^2$ reduces to $\langle v_e^2\rangle/v^2$ if correlations between target electrons can be neglected. Moreover,

$$\ln I_1 = \frac{\sum_j f_j\hbar\omega_j \ln(\hbar\omega_j)}{\sum_j f_j\hbar\omega_j}. \tag{3.98}$$

Eq. (3.97) contains an additional relativistic correction factor and an I-value under the Bethe logarithm that is distinct for straggling. Inokuti *et al.* (1981) estimated

$$I_1 \simeq Z_2^{1.6364} \times 33.1 \text{ eV} \tag{3.99}$$

for $Z_2 \le 38$.

In view of the dominance of close collisions, the Bloch correction deserves special attention. Lindhard and Sørensen (1996) showed that there is no Bloch correction to Eq. (3.97) within nonrelativistic theory. Their estimate disregarded the shell correction. Titeica (1937), on the basis of Bloch's formalism, found an additional term so that

$$W(v) = W_{\rm B}\left[1 + \frac{\langle v_e^2\rangle}{v^2}\left(\frac{2}{3}\left[L_0(v) + \psi(1) - {\rm Re}\left(1 + i\frac{Z_1 v_0}{v}\right)\right] - 1\right)\right], \tag{3.100}$$

to replace Eq. (3.96). This expression was confirmed by Sigmund (1982) on the basis of Eq. (3.94). Thus, Titeica's term is to be regarded as a shell correction that is entirely compatible with the conclusion of Lindhard and Sørensen (1996).

A substantial correction was found by Lindhard and Sørensen (1996) for the relativistic regime. An expression was derived for the straggling parameter following the lines that led to Eq. (3.22). Figure 3.25 shows that pronounced deviations from relativistic Bohr straggling as well as from the perturbational expression may be expected for $v/c \gtrsim 0.1$ and that the sign of the deviations from the Bohr value depends on Z_1.

Nonrelativistic model calculations based on the dielectric theory (Bonderup and Hvelplund, 1971;

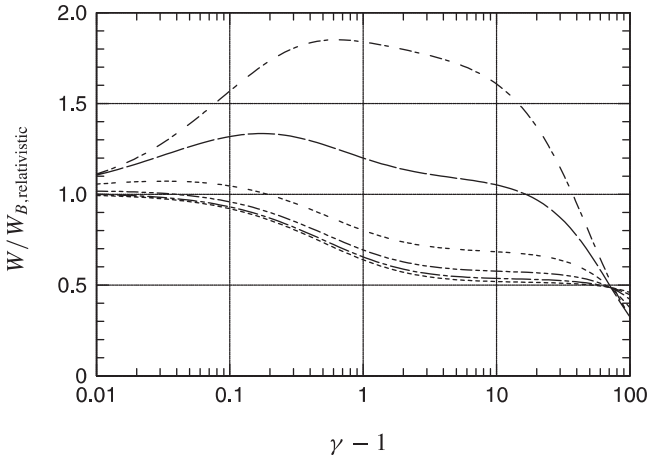


Figure 3.25. Straggling for stripped heavy ions at relativistic velocities. Plotted is the ratio between the result of Lindhard and Sørensen (1996) and the relativistic expression by Bohr (1915), $W_{B,\ \rm relativistic} = 4\pi\, Z_1^2\, Z_2 e^4\, \gamma^2$ for U, Gd, Ge, Si, O and Be (top to bottom).

Chu, 1976; Sigmund and Fu, 1982) and the harmonic-oscillator model (Sigmund and Haagerup, 1986) were geared toward light ions. The range of validity of the numerical results of those evaluations must be quite restricted in case of heavy ions (cf. Figure 3.2). The same statement applies to calculations of impact-parameter-dependent straggling by Kabachnik (1993).

Estimates of the Barkas–Andersen correction to straggling have now become available. First indications of a shoulder of the Bethe–Livingston type were found by Glazov *et al*. (2002), and a detailed study is due to Sigmund and Schinner (2002c). Figure 3.26 shows straggling calculated for protons and antiprotons as well as the average between the two. It is seen that in the absence of a shell correction, a pronounced shoulder forms for protons, while the average curve, representing protons or antiprotons in the absence of a Barkas–Andersen correction, has the form that is familiar from standard theory (Bonderup and Hvelplund, 1971). However, the shoulder is efficiently wiped out by the shell correction.

The influence of the Fermi density effect on straggling is expected to be insignificant because of its collective nature.

3.12.3 Dressed ions

For dressed ions a contribution from charge-exchange straggling needs to be added to 'collisional straggling', *i.e.*, due to excitation of target atoms (Flamm and Schumann, 1916). A comprehensive statistical scheme (Sigmund, 1992) to treat these processes — also incorporating projectile excitation/deexcitation — was mentioned in Section 3.11.3.

Qualitative trends on collisional straggling for dressed ions may be extracted from studies by Kaneko (1990) (U in C and O in Al), Yang (1994) (C in C) and Glazov *et al*. (2002) (O in C). The models differ in detail but none of them makes full use of the theoretical schemes discussed in Section 3.7.

A more systematic theoretical study has been performed by Sigmund and Schinner (2002c) on the basis of the binary theory.

Figure 3.27 shows relative straggling for frozen-charge Li ions in carbon. It is seen that screening

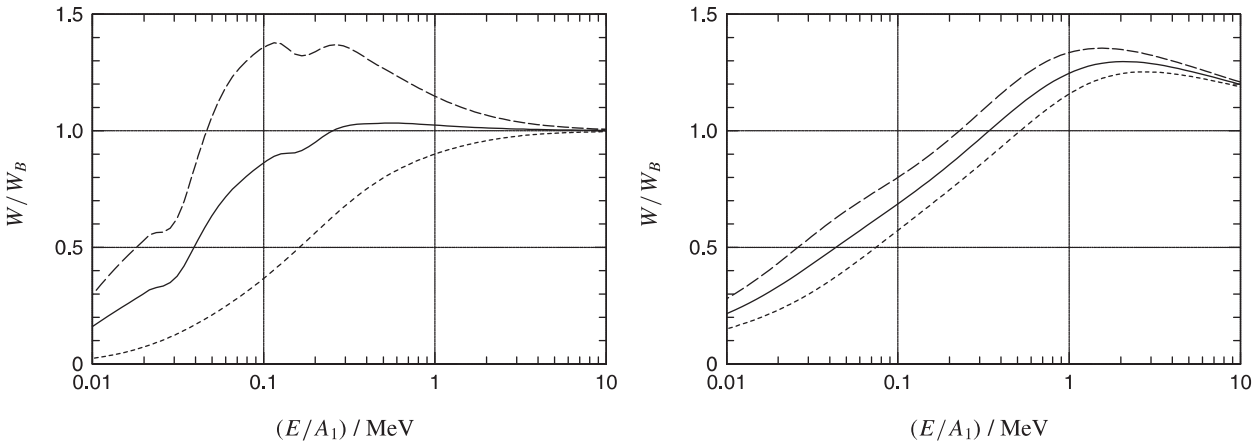


Figure 3.26. Relative straggling W/W_B for protons (dashed lines) and antiprotons (dotted lines) in silicon, and average (solid lines). Without (left) and with (right) shell correction.

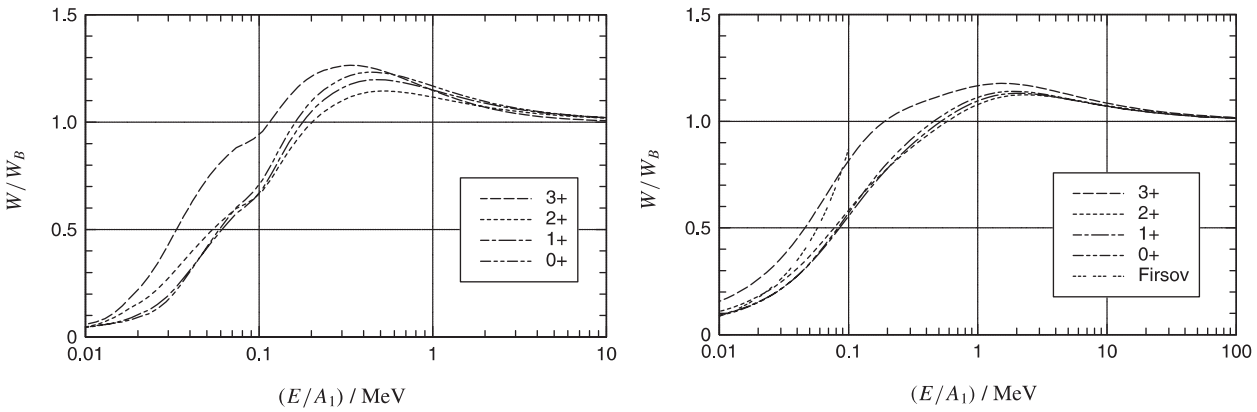


Figure 3.27. Relative straggling for lithium in carbon for frozen-charge state 3+ to 0. Without (left) and with (right) shell correction. The label 'Firsov' refers to Eq. (3.101).

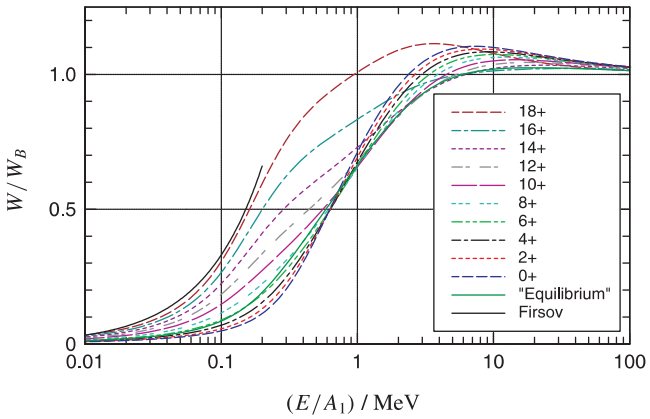


Figure 3.28. Same as Figure 3.27 for argon in carbon. The label 'equilibrium' refers to the equilibrium charge.

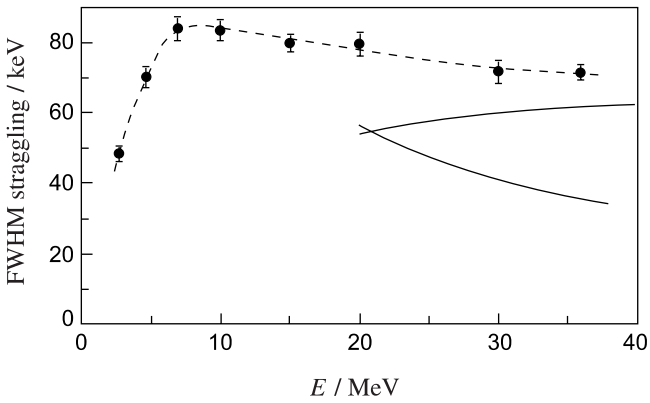


Figure 3.29. Energy-loss straggling for ^{12}C in 217 μg/cm^2 Al. Experimental data and theoretical estimates. Upper solid line: FWHM from Bethe–Livingston formula (estimated from variance). Lower solid line: contribution from charge exchange, estimated by use of cross sections extracted from the same series of experiments. Dashed line: $\Omega_{\rm tot} = \sqrt{\Omega^2_{\rm coll} + \Omega^2_{\rm chex}}$. From Cowern *et al*. (1979).

affects the shape of the straggling parameter below the shoulder region, both for the shoulder generated by the Barkas–Andersen effect in the left graph and by the shell correction in the right one. The actual degree of screening appears to have surprisingly little influence. Figure 3.28 shows a more gradual variation for a heavier ion (Ar in C).

The effect of intra-atomic correlation on straggling was first studied by Besenbacher *et al*. (1980) for He ions. This effect goes roughly with the square of the stopping force. Preliminary estimates by Sigmund and Schinner (2002c) indicate a maximum correction by correlation of ∼40% of the Bohr value for He–Si and less for helium in lighter materials. These values are somewhat higher than those of Besenbacher *et al*. (1980) based on a free-electron gas model. Corresponding values for argon ions were found to be about a factor of two higher. Experimental data that could confirm or reject such high corrections for correlation are desirable.

A systematic effort has been made to determine the charge-exchange contribution to straggling. Estimates have been based either on solutions of the transport equation for energy loss in the presence of charge exchange presented by Winterbon (1977) or on Monte Carlo simulations involving cross sections for capture and loss. While numerous studies were devoted to helium ions, heavier ions were addressed by Vollmer (1974), Efken *et al*. (1975), Cowern *et al*. (1979), Kaneko (1988), and Yang and MacDonald (1993) in the analysis of experiments. Figure 3.29 from Cowern *et al*. (1979) shows the case of carbon on aluminium, for which collisional and charge-exchange straggling are comparable in magnitude.

Ogawa *et al*. (1992b,1993,1996a) measured energy-loss spectra for carbon, oxygen and lithium ions, respectively, penetrating through thin carbon foils at high speed in which the majority of the ions is fully stripped in charge equilibrium. Especially the lithium experiments at 10 MeV/u attracted theoretical attention. Foil thicknesses can be varied in these experiments such as to identify individual capture-loss cycles in the measured spectra. The shape of those individual peaks must then be governed by collisional straggling. In accordance with an earlier analysis (Glazov and Sigmund, 1997) of measurements on helium (Ogawa *et al*., 1991), it was found that experimental energy resolution did not allow information to be extracted about collisional straggling. Claims to the contrary by Balashov *et al*. (1997) were demonstrated to be in error (Glazov and Sigmund, 2000).

3.12.4 Low-speed ions

The theoretical schemes discussed in Section 3.6 could in principle be applied to straggling, but only few studies have been made. In particular, the theory underlying formula (3.47) by Lindhard and Scharff (1961) has never been applied to straggling.

Integration of Eq. (3.45) from the theory of Firsov (1959) yields

$$W = \int 2\pi p \mathrm{d}p w^2(v,p) = 0.133\pi\hbar^2 v^2 (Z_1 + Z_2)^{8/3}. \tag{3.101}$$

Hvelplund (1971), measuring straggling in gases, found a rough overall agreement with this prediction as indicated in Figure 3.30, but significant deviations are observed both from the predicted v^2-dependence and in absolute magnitude. However,

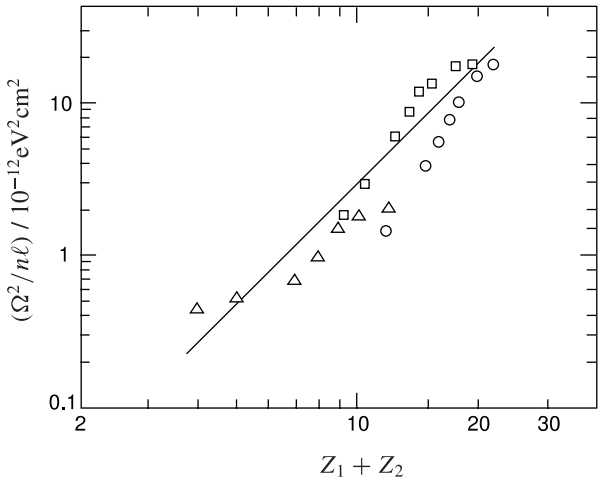


Figure 3.30. Energy-loss straggling in He (triangles), air (squares) and neon (circles) at $v = 0.9v_0$ compared with Eq. (3.101) according to Hvelplund (1971).

near-perfect agreement was found for Li–He from 100 to 500 keV.

Kaneko (1990) derived an expression for straggling at low speed from the dielectric theory combined with a model for screening in an electron gas,

$$W = 12\pi v^2 \hbar^2 Z_1^{4/3} z_{\text{free}} A^2, \tag{3.102}$$

where z_{free} is the number of conduction electrons per target atom,

$$A^2 = \frac{0.56}{1 - 0.51/Z_1^{2/3} r_s}, \tag{3.103}$$

and r_s the Wigner–Seitz radius. Figure 3.31 shows a comparison with the data of Hvelplund (1971) for neon targets, but now at all velocities. Discrepancies up to more than a factor of 2 are found. Figure 3.32 shows calculations on the basis of the binary theory by Sigmund and Schinner (2002c) compared with measurements for lithium ions in He, Ne and Ar by Andersen *et al*. (1978). Tolerable agreement is found for Li–Ar and Li–Ne above v_0, while the theory appears to overestimate straggling for the Li–He system.

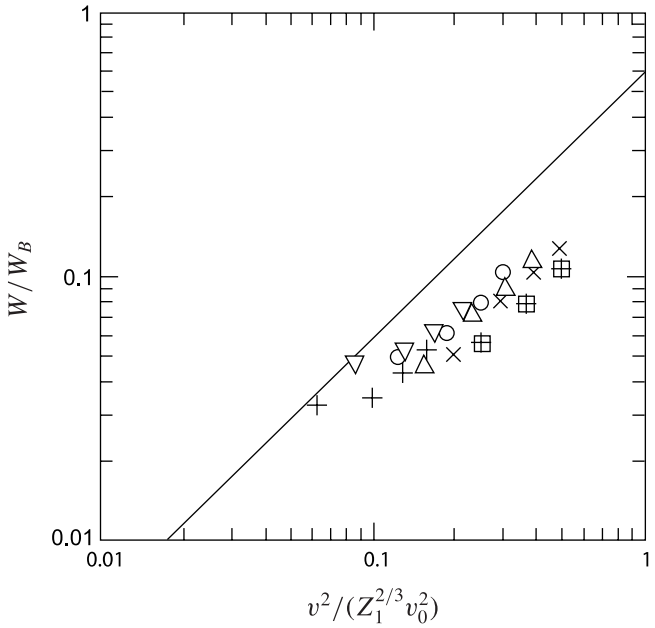


Figure 3.31. Comparison of straggling data for B (○), C (×), N (△), O (□), Ne (▽) and Mg (+) ions in neon with Eq. (3.102). From Kaneko (1990).

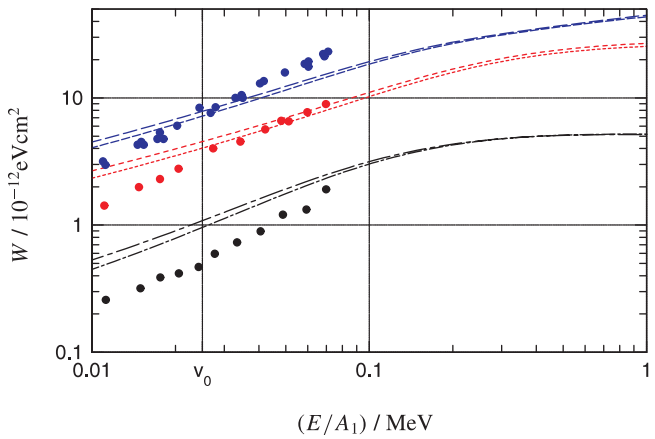


Figure 3.32. Straggling for Li ions in noble gases: Calculations by binary theory disregarding correlation effect compared with measurements of Andersen *et al*. (1978) on Ar, Ne and He (top to bottom). Thick lines: ion in mean equilibrium charge. Thin lines: neutral ion.

3.13 MULTIPLE SCATTERING

The statistical scheme outlined in Section 3.11 also applies to multiple angular deflection, or 'multiple scattering', except that one deals with a two-dimensional problem. Moreover, energy loss is a one-way process in the experimental configurations considered in this report, but that aspect is of minor significance in the general formalism. Multiple scattering was first studied along these lines by Bothe (1921). The theory was developed subsequently by Molière (1948), Bethe (1953), Meyer (1971), Sigmund and Winterbon (1974) and Amsel *et al*. (2003).

Consider a monochromatic, well-collimated beam penetrating through a foil of uniform thickness x that is small enough so that variations of the scattering cross section because of decreasing beam energy can be neglected. Individual scattering events are characterized by a differential scattering cross section $\mathrm{d}\sigma(\phi) = K(\phi)\mathrm{d}^2\phi$, where ϕ is a scattering angle in the laboratory frame of reference.

For heavy ions, multiple-scattering distributions are typically of interest for angular cones with

opening angles of a few degrees. Hence the small-angle approximation, $\sin\phi \simeq \tan\phi \simeq \phi$, will be justified for many purposes. This approximation is implied here except where stated otherwise.

Let $F(\alpha,x)2\pi\alpha d\alpha$ be the probability per beam particle to be scattered into a solid angle $(\alpha,d\alpha)$ after penetrating a foil thickness x. Then the Bothe–Landau formula (3.68) may be rewritten in terms of scattering angles and reads (Bothe, 1921; Sigmund and Winterbon, 1974)

$$F(\alpha,x) = \frac{1}{2\pi}\int_0^\infty k\mathrm{d}k J_0(k\alpha)e^{-nx\sigma(k)}, \qquad (3.104)$$

where n denotes the density of scattering centers, J_0 a Bessel function in standard notation, and

$$\sigma(k) = \int_0^\infty \mathrm{d}\sigma(\phi)[1 - J_0(k\phi)]. \qquad (3.105)$$

Alternatively one may write (Goudsmit and Saunderson, 1940)

$$F(\alpha,\ell) = \frac{1}{4\pi}\sum_{\mu=0}^{\infty}(2\mu+1)P_\mu(\cos\alpha)e^{-n\ell\sigma_\mu}, \qquad (3.106)$$

where $P_\mu(\cos\phi)$ are Legendre polynomials,

$$\sigma_\mu = \int \mathrm{d}\sigma(\phi)\big[1 - P_\mu(\cos\phi)\big], \qquad (3.107)$$

and ℓ denotes the travelled pathlength which, within the small-angle approximation, is equal to the foil thickness.[27]

For heavy ions, multiple angular deflection is due to nuclear collisions with the exception of the case of channeling in which nuclear interactions are strongly suppressed.

Computation of multiple-scattering profiles is simplified substantially by the use of scaling laws of the type discussed for nuclear stopping in Section 3.2.7. Convenient variables for scattering and target thickness are (Molière, 1948; Meyer, 1971; Sigmund and Winterbon, 1974)

$$\tilde{\alpha} = \frac{Ea}{2Z_1Z_2e^2}\alpha; \quad \tau = \pi a^2 n x, \qquad (3.108)$$

where a is the screening radius of the interatomic potential. Within the small-angle approximation the multiple-scattering distribution as expressed by Eq. (3.104) reduces to a universal function of $\tilde{\alpha}$ and τ that is determined by the adopted interatomic potential. This function has been tabulated for

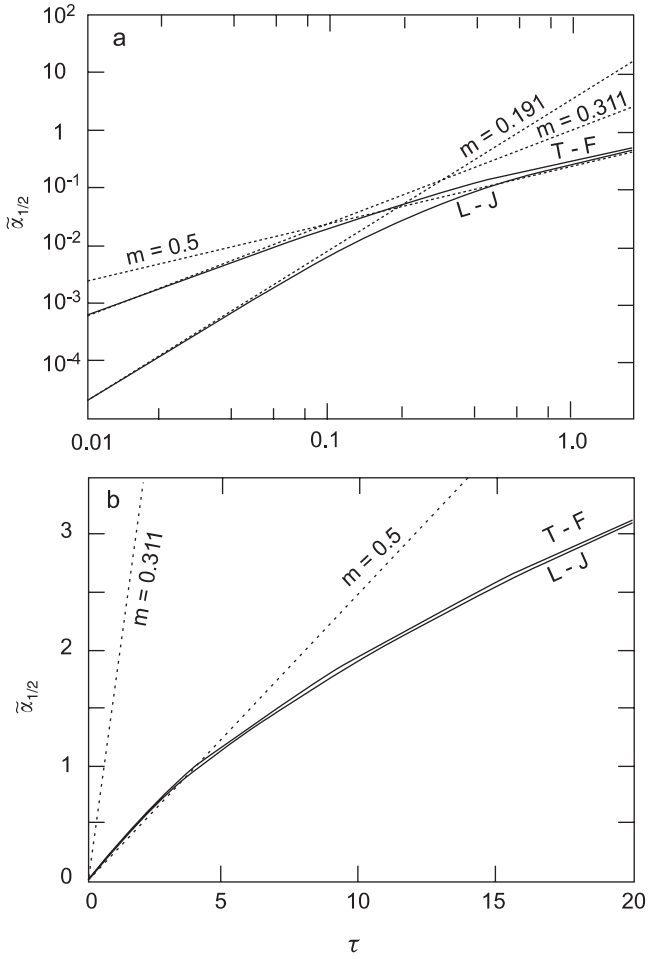


Figure 3.33. Multiple-scattering halfwidth *versus* thickness in dimensionless units according to Sigmund and Winterbon (1974); Thomas–Fermi and Lenz–Jensen interaction and power laws. The two graphs cover different thickness ranges.

$0.001 \leq \tau \leq 2000$ by Sigmund and Winterbon (1974).[28]

Within the small-angle approximation, the multiple-scattering half-width likewise obeys a scaling law, *i.e.*,

$$\tilde{\alpha}_{1/2} = g(\tau), \qquad (3.109)$$

where g is a universal function determined by the interatomic potential. This relation is shown in Figure 3.33 for Lenz–Jensen and Thomas–Fermi interaction specified by Table 3.4. Also included are results for power-law scattering governed by Eq. (3.63).

Comments made at the end of section 3.11.2 in connection with energy-loss straggling on the transition from thick to very thick targets, in particular Eq. (3.74), also apply to small-angle multiple

[27]Unlike Eq. (3.104), which assumes small angles α, Eq. (3.106) holds for all angles in principle. However, the pathlength itself is not necessarily measurable. Therefore, Equation (3.106) also may be limited to small angles where the pathlength ℓ is close to the foil thickness.

[28]With an important erratum for $\tau = 0.05$ and 0.10 by Sigmund and Winterbon (1975).

scattering. The point has been studied in more detail by Valdes and Arista (1994).

In addition to angular deflection, also the lateral spread of an initially narrow beam can be of interest. Lateral and angular distributions are closely related and can be mapped upon each other. This mapping invokes power-law scattering with $m = m(\tau)$. For details the reader is referred to Marwick and Sigmund (1975).

A code for calculating multiple-scattering angular profiles according to Sigmund and Winterbon (1974) has become available (Eyeberger, 1999). A more extensive code, also providing lateral distributions and profiles projected on a plane and based on slightly different physical input is available from Amsel *et al*. (2003).

The prime modification of the above scheme in the relativistic regime is the replacement of the kinetic energy E in Eq. (3.108) by (Bohr, 1948)

$$E \to \frac{1}{2}\gamma M_1 v^2; \quad \gamma = \frac{1}{\sqrt{1 - v^2/c^2}}. \tag{3.110}$$

In addition, screening might not be described adequately by Thomas–Fermi interaction (Schwab *et al*., 1990), and deviations from Coulomb scattering due to the finite size of the nucleus can become relevant (Williams, 1939; Bohr, 1948).

3.14 RESTRICTED NUCLEAR STOPPING

This section addresses the central question of experimentally separating nuclear from electronic stopping. Reference is made specifically to transmission experiments in which the energy-loss spectrum of ions emerging downstream from the target is measured over a narrow angular interval around the initial beam direction. Ions that have undergone a violent nuclear collision will typically be deflected outside the acceptance angle of the detector. Therefore the full (unrestricted) nuclear-stopping cross section will not contribute to the observed energy-loss spectrum. Conversely, ions exiting in the forward direction will typically have undergone a series of small-angle nuclear-scattering events. Hence some nuclear-stopping will be recorded. The corresponding *restricted nuclear-stopping cross section* can be expected to vary slowly with angle within the multiple-scattering cone. More importantly, it will depend sensitively on the penetration depth.

Above the shell-correction limit, where the majority of the target electrons contribute to electronic stopping, nuclear stopping accounts for less than 0.1 % of the total stopping. In fact, Figure 3.2 indicates that nuclear stopping becomes a serious problem mainly for slow ions. Therefore, pertinent theoretical schemes to correct for nuclear stopping refer to the velocity regime in which nuclear and electronic stopping have comparable magnitudes. This is the regime in which Z_1 and Z_2 structure are observed and where noticeable phase effects and deviations from Bragg additivity can be expected.

Following Ormrod and Duckworth (1963), it has been customary in this range to measure peak rather than mean energy losses. This is motivated by the fact that observed energy-loss spectra are skewed with a pronounced high-loss tail that was asserted to be caused by nuclear stopping. Operating with the peak energy loss had been expected to provide more reliable stopping forces due to a smaller nuclear-stopping correction. On the other hand, this generates uncertainties due to the mean-to-peak ratio in pure electronic stopping, which is largely unknown in the energy range in question.

Existing theoretical or numerical schemes (Ormrod and Duckworth, 1963; Fastrup *et al*., 1966; Skoog, 1975; Geissel *et al*., 1984; Krist *et al*., 1984; Lennard *et al*., 1986a; Glazov and Sigmund, 2003) address the behavior of the peak energy loss as a function of target thickness and emission angle. The standard scheme used by most experimental groups was developed by Fastrup *et al*. (1966) on the basis of the Bohr–Williams theory of energy straggling and multiple scattering (Bohr, 1948; Williams, 1939, 1940). The scheme is intuitive rather than quantitative but has proven very efficient and surprisingly accurate when compared with a more rigorous scheme based on the Bothe–Landau theory, which treats both peak and mean energy losses.

3.14.1 Bohr–Williams theory

The Bohr–Williams theory divides trajectories into one group made up by ions that have undergone a single violent collision at a scattering angle ϕ exceeding some limiting angle ϕ_1, and another one made up by ions that have undergone a large number of small-angle events $\phi < \phi_1$. The limiting angle is defined by

$$\phi_1^2 = nx \int_{\phi<\phi_1} \phi^2 \mathrm{d}\sigma(\phi). \tag{3.111}$$

For elastic collisions, the relation between energy loss and scattering angle is unique if the projectile mass M_1 is smaller than the target mass M_2, *i.e.*,

$$w = \frac{M_1}{M_2} E\phi^2 \tag{3.112}$$

at small angles. Thus, the energy-loss spectrum recorded at angles $\phi > \phi_1$ will be sharply peaked around the value given by Eq. (3.112).

Conversely, the energy-loss spectrum recorded within the cone $\phi<\phi_1$ will vary slowly with ϕ and can be approximated by a gaussian centered around

$$w_1 = \frac{M_1}{M_2} E\phi_1^2. \tag{3.113}$$

Rewriting Eq. (3.111) in terms of the energy-loss crosssection $\mathrm{d}\sigma(w)$ one finds

$$w_1 = nx \int_0^{w_1} w \mathrm{d}\sigma(w). \tag{3.114}$$

Dependent on foil thickness, w_1 may be significantly smaller than the maximum recoil loss[29] $w_{\max} = \gamma E$. Hence, the mean energy loss observed in the forward direction will appear reduced.

The width w_1^* of the peak in the nuclear-energy-loss spectrum integrated over all angles was estimated from

$$w_1^{*2} = Nx \int_0^{w_1^*} w^2 \mathrm{d}\sigma(w). \tag{3.115}$$

It was argued that energy losses exceeding w_1^* contribute to the tail of the energy-loss spectrum, while a gaussian peak is generated by collisions with w. These collisions give rise to a total energy loss

$$\Delta E_{\mathrm{nucl}} = Nx \int_0^{w_1^*} w \mathrm{d}\sigma(w), \tag{3.116}$$

which may be identified with the peak of the energy-loss spectrum. It was then demonstrated that $w_1^*<w_1$, *i.e.*, collisions that contribute to the peak energy loss do not give rise to loss of beam particles out of the multiple-scattering cone. Hence, it was concluded that the peak energy loss at zero angle can be identified with the peak energy loss of the angular-integrated spectrum.

This assumes negligible skewness in the electronic-stopping itself.

3.14.2 Bothe–Landau theory

Glazov and Sigmund (2003) describe the joint distribution in energy loss and deflection angle in terms of a Bothe–Landau-type formula

$$F(\Delta\boldsymbol{v}, t)\mathrm{d}^3\Delta\boldsymbol{v} = \frac{\mathrm{d}^3\Delta\boldsymbol{v}}{(2\pi)^3} \int \mathrm{d}^3\boldsymbol{k} e^{i\boldsymbol{k}\cdot\Delta\boldsymbol{v} - nvt\sigma(\boldsymbol{k})}, \tag{3.117}$$

where $\Delta\boldsymbol{v}$ is the accumulated velocity change undergone by the projectile while moving at a speed v through the medium over a time interval t, where

$$\sigma(\boldsymbol{k}) = \int \mathrm{d}\sigma(\Delta\boldsymbol{u})\left(1 - e^{-i\boldsymbol{k}\cdot\Delta\boldsymbol{u}}\right) \tag{3.118}$$

is a transport cross section and $\mathrm{d}\sigma(\Delta\boldsymbol{u})$ the differential cross section for an individual collision resulting in a velocity change $(\Delta\boldsymbol{u}, \mathrm{d}^3\Delta\boldsymbol{u})$. This expression is rigorous for random scattering in a thin or moderately thick target, *i.e.*, when the variation with energy of the cross section is negligible.

In terms of total energy loss ΔE and overall deflection angle α, Eq. (3.117), reads

$$F(\Delta E, \alpha, \ell) = \frac{1}{8\pi^2} \sum_{\mu=0}^{\infty} (2\mu+1) P_\mu(\cos\theta) \times \int_{-\infty}^{\infty} \mathrm{d}k e^{ik\Delta E - n\ell\sigma_\mu(k)}, \tag{3.119}$$

where $\ell = vt$ is the travelled pathlength, $F(\Delta E, \alpha, \ell)\, \mathrm{d}(\Delta E)\, 2\pi \sin\alpha\, \mathrm{d}\alpha$ the joint distribution in energy loss and deflection angle normalized to 1, P_μ a Legendre polynomial and

$$\sigma_\mu(k) = \int \mathrm{d}\sigma(w)\left[1 - P_\mu(\cos\phi) e^{-ikw}\right]. \tag{3.120}$$

Within the small-angle approximation one may alternatively write

$$F(\Delta E, \alpha, x) = \frac{1}{4\pi^2} \int_{-\infty}^{\infty} e^{i\varkappa\Delta E} \mathrm{d}\varkappa \times \int_0^{\infty} k\, \mathrm{d}k\, J_0(k\alpha) e^{-nx\sigma_B(k,\varkappa)} \tag{3.121}$$

and

$$\sigma_B(k,\varkappa) = \int \mathrm{d}\sigma(w)\left[1 - J_0(k\phi(w)) e^{-i\varkappa w}\right]. \tag{3.122}$$

The two descriptions (3.119) and (3.121) are equivalent at small angles and energy losses but have different merits. Eq. (3.119) is formally valid at all deflection angles, although a practical upper limit is set by the fact that the pathlength ℓ is not measurable in general. Eq. (3.121) is more useful at small pathlengths where the μ-series in Eq. (3.119) converges slowly. Eq. (3.119) is computationally more economical in the evaluation of moments in terms of both angle and energy, again with the exception of small pathlengths. Eq. (3.121), on the other hand, allows analytic estimates and has favorable scaling properties.

3.14.3 Scaling laws

Table 3.5 shows that scaling relations obeyed by peak and mean energy losses invoke dimensionless Lindhard units for energy loss ϵ and ρ as well as for multiple scattering τ and $\tilde{\alpha}$. It is worth noting that neither the peak and the mean energy loss at zero scattering angle nor the angle-integrated peak energy loss show the simple proportionality

[29] Concerning γ, see footnote 4 on page 23.

Table 3.5. Scaling relations obeyed by peak energy loss (first row), effective stopping cross section (second row) and stopping cross section (third row). Functions carrying a tilde stand for functions determined uniquely by the interatomic potential within Lindhard scaling.

Angle-dependent	Unrestricted
$\Delta\epsilon_{\rm p} = \frac{\gamma}{\epsilon}\tilde{g}(\tau,\tilde{\alpha})$	$\Delta\epsilon_{\rm p} = \frac{\gamma}{\epsilon}\tilde{g}(\tau)$
$\frac{\Delta\epsilon_{\rm p}}{\rho} = \frac{1}{\epsilon}\tilde{f}(\tau,\tilde{\alpha})$	$\frac{\Delta\epsilon_{\rm p}}{\rho} = \frac{1}{\epsilon}\tilde{f}(\tau)$
$\frac{\langle\Delta\epsilon\rangle}{\rho} = \tilde{h}(\tau,\tilde{\alpha}), \tau\to 0$	$\frac{\langle\Delta\epsilon\rangle}{\rho} = \tilde{h}(\epsilon)$

with target thickness that is found for the angle-integrated mean energy loss.

3.14.4 Predictions

Figure 3.34 shows energy-loss spectra evaluated for Thomas–Fermi and Lenz–Jensen interactions for three representative values of the dimensionless thickness variable τ. All spectra are skewed, although skewness decreases with increasing thickness. The sensitivity to the atomic interaction potential is considerable, especially around and below the peak.

The lower part of Figure 3.35 shows the peak energy loss in Thomas–Fermi units divided by the multiple-scattering target thickness τ. This quantity can be compared with the stopping cross section multiplied by ϵ. That is shown in the upper graph of Figure 3.35. Although the different abscissa scales do not allow a meaningful quantitative comparison, it is evident that the peak energy loss is much more sensitive to the interaction potential than the angle-integrated mean energy loss. This is due to the lack of a contribution by violent collision events to the peak energy loss.

Figure 3.36 shows the calculated mean energy loss for three values of the foil thickness compared to the single-scattering energy transfer. As expected, the single-scattering prediction underestimates the energy loss at small angles of emergence. This is compensated at larger angles. Inspection of the multiple-scattering half-widths $\alpha_{1/2}$ — which have also been included in the graph — reveals that the point of crossover lies at $\sim 2\alpha_{1/2}$. The variation of the calculated mean energy loss within $\alpha_{1/2}$ is considerable albeit less than a factor of 2. In relative terms, the unrestricted nuclear energy loss is reduced by factors 0.150 (0.134), 0.226 (0.211), and 0.277 (0.262) for the three target thicknesses, with Lenz–Jensen values in brackets.

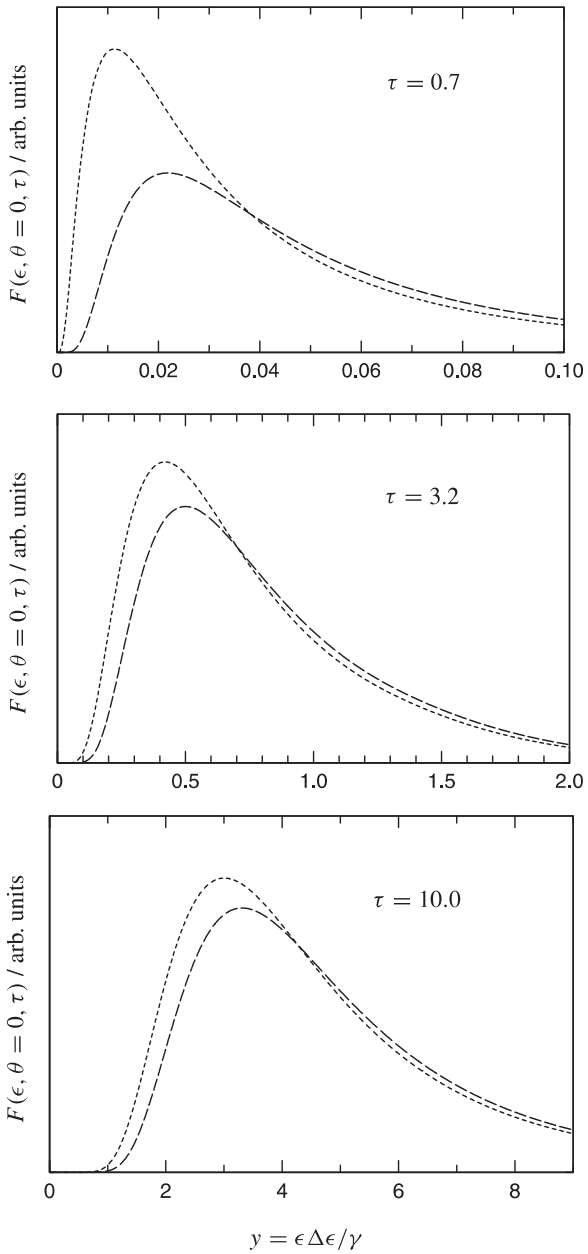


Figure 3.34. Energy-loss spectra due to nuclear stopping at zero angle to incident-beam direction in dimensionless variables. Three values of dimensionless thickness τ. For Thomas–Fermi (dashed lines) and Lenz–Jensen (dotted lines) interaction. From Glazov and Sigmund (2003).

Figure 3.37 shows the variation with target thickness of mean energy loss and straggling at zero emergence angle. These quantities decrease faster with decreasing target thickness than the corresponding unrestricted (angle-integrated) quantities that also have been included in the graph.

Glazov and Sigmund (2003) also discussed the validity of the nuclear-stopping correction applied in several central experimental papers. It was concluded that, where corrections were applied systematically, the adopted procedures were correct from a

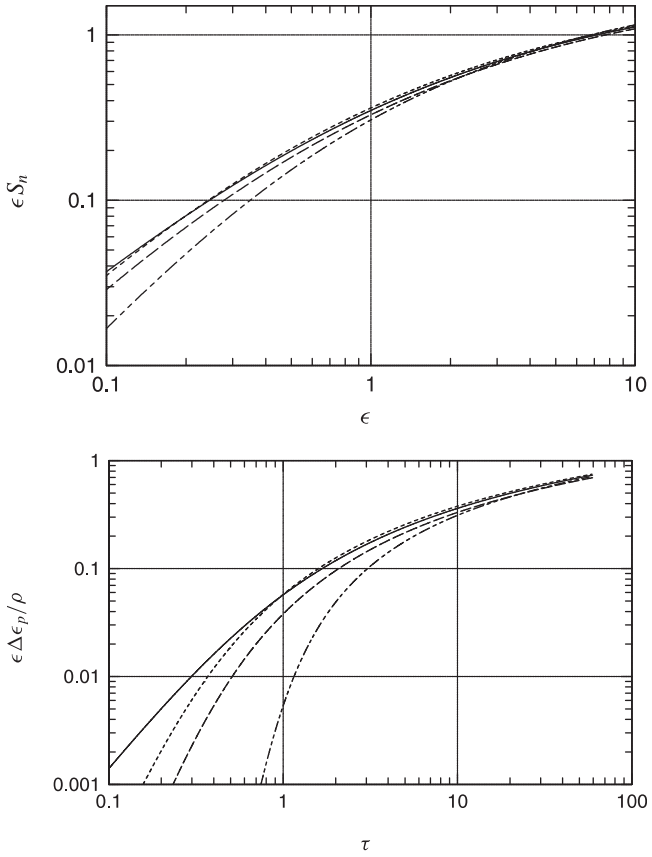


Figure 3.35. Upper graph: stopping cross section in dimensionless Thomas–Fermi units multiplied by ϵ, versus dimensionless energy ϵ. Lower graph: same quantity except for replacement of mean by peak energy loss, and τ replacing ϵ as the abscissa variable. Thomas–Fermi (solid lines), Molière (dotted lines), Lenz–Jensen (dashed lines) and Bohr (dot-dashed lines) screening. From Glazov and Sigmund (2003).

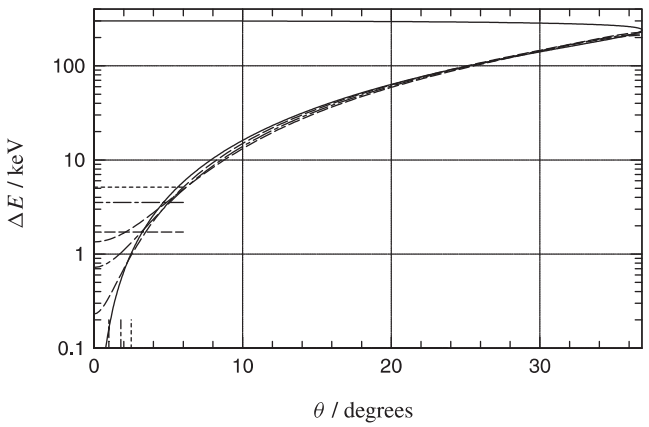


Figure 3.36. Comparison of restricted with unrestricted nuclear energy loss for 0.8 v_0 Ne in C for foils of thickness 4.5, 9.0 and 13.5 μg/cm^2 (dashed, dot-dashed and dotted lines, respectively). Lenz–Jensen interaction assumed. Horizontal lines: unrestricted nuclear energy loss. Broken curved lines: calculated mean nuclear energy loss *versus* deflection angle. Thin solid line: single scattering, upper and lower branch. Vertical lines: multiple-scattering halfwidths. Extracted from Glazov and Sigmund (2003).

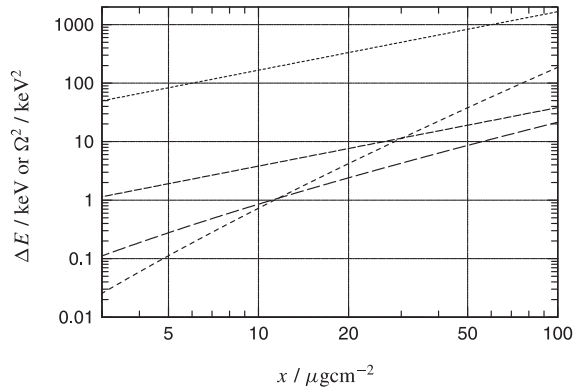


Figure 3.37. Mean energy loss (thick dashed line) and straggling (thick dotted line) at $\theta = 0$ *versus* target thickness for 320 keV ^{20}Ne ions in carbon for Lenz–Jensen interaction. Thin lines show unrestricted mean energy loss and straggling.

theoretical point of view, but that the adopted scattering law, based on the LSS Thomas–Fermi interaction, was likely to overestimate the correction and hence to underestimate electronic stopping in the low-speed range where the correction is sizable.

Analyzing peak energy losses has the advantage of a comparatively small nuclear-stopping correction. In particular, the high-loss peak for $M_1 > M_2$ is of no concern, and the range of validity of scaling laws is wider than for average energy losses. On the other hand, peak energy losses are more sensitive to the elastic-scattering law and to foil inhomogeneities, and corrections for nuclear scattering are harder to determine theoretically. Moreover, it has been mentioned that measuring peak energy losses imposes high requirements on the monochromaticity of the incident beam.

Measuring average energy losses, while implying bigger nuclear-stopping corrections, is more directly related to the quantity sought. After all, it is the mean electronic energy loss, not the peak loss, that is the quantity of interest in most experiments. Moreover the correction is less sensitive to the scattering law. The high-loss peak should be of little concern if a suitable upper limit is introduced for averaging. However, accurate measurements require reasonably low noise levels.

3.15 RANGE AND RANGE STRAGGLING

3.15.1 Introductory remarks

The basic range concepts have been defined in Section 2.2. For not-too-low-energy ions, central quantities are the range along the path R and range straggling Ω_R^2 specified in Eqs. (2.17) and (2.18). The focus of this report is on the regime of dominating electronic stopping. It is tempting, therefore, to evaluate the integrals on the basis of

stopping cross sections and straggling parameters that ignore nuclear stopping altogether. This approach is justified at high beam energies. The main purpose of this section is to specify limitations to this simple approach and to provide suitable corrections to cover the energy regime in which they are comparatively small. Items of concern are

- the influence of nuclear stopping on pathlength,
- the detour factor, *i.e.*, the ratio between projected range and pathlength,
- the validity of the gaussian approximation for the range profile,
- the relative significance of nuclear and electronic energy loss and of angular deflection to range straggling and
- the effect of fluctuating charge states on ranges.

In addition, attention will be paid to

- the extraction of electronic-stopping cross sections from range measurements and
- the difference between range and energy-deposition profiles.

Recourse will be made to comprehensive transport equations that also remain valid in the regime of dominating nuclear stopping.

A rough estimate of the importance of nuclear stopping can be found from Table 3.6 which expresses the dimensionless energy variable Eq. (3.52) in terms of the mass numbers A_1, A_2 at three characteristic beam velocities. To arrive at these simple expressions one approximates $Z_{1,2} \simeq A_{1,2}/2$ and $Z_1^{2/3} + Z_2^{2/3} \sim (Z_1 + Z_2)^{2/3}$. According to Figure 3.22 the nuclear-stopping cross section has its maximum at $\epsilon \simeq 0.3$. Hence, at 1 keV/u, nuclear stopping is of central importance for $A_1 + A_2 > 100$ and is a significant correction also below this limit. At the Bohr velocity, on the other hand, the corresponding limit is given by $A_1 + A_2 > 1000$, implying that nuclear stopping is just a correction and never dominating. Maximum electronic stopping is found at $\sim v_0 Z_1^{2/3}$. This corresponds to an even higher value of ϵ especially for $Z_1 \gg 1$.

Table 3.6. Values of dimensionless energy variable ϵ governing nuclear stopping at characteristic beam energies.

Beam energy or speed	ϵ, Eq. (3.52)
$E/A_1 = 1$ keV	$\frac{130}{(A_1+A_2)^{4/3}}$
$v = v_0$	$\frac{3.2\times10^3}{(A_1+A_2)^{4/3}}$
$v = v\,Z_1^{2/3}$	$\frac{1.3\times10^3}{(1+A_2/A_1)^{4/3}}$

3.15.2 Transport equations

The fundamental equation for the distribution $F(E, R)\mathrm{d}R$ in total pathlength (range along the path) R for an ion with an initial energy E is (Lindhard *et al.*, 1963b)

$$-\frac{\partial}{\partial R}F(E,R) = n\int \mathrm{d}\sigma(E,w)\times[F(E,R) - F(E-w,R)]. \quad (3.123)$$

In contrast to Eq. (3.85) this is a transport equation of the backward type, where E and R refer to different points in space and time. This type of equation is more suitable for range calculations than are forward equations, but there are limitations, *e.g.*, for layered media for which recourse to forward equations has to be made.

From Eq. (3.123) and the normalization $\int_0^\infty \mathrm{d}R F(E,R) = 1$ one obtains an integral equation for the average path length $R(E) = \int_0^\infty \mathrm{d}R R F(E,R)$,

$$n\int \mathrm{d}\sigma(E,w)[R(E) - R(E-w)] = 1. \quad (3.124)$$

From this one can get back to Eq. (2.17) under the assumption of small energy loss per collision, *i.e.*, continuous slowing-down, $w \ll E$.

The corresponding equation for the mean projected range $R_\mathrm{p}(E)$ reads

$$1 = n\int \mathrm{d}\sigma(E,w)\left[R_\mathrm{p}(E) - \cos\phi R_\mathrm{p}(E-w)\right], \quad (3.125)$$

where ϕ is the scattering angle in the laboratory system in a collision specified by an energy loss w. The relation between $R(E)$ and $R_\mathrm{p}(E)$ and other range quantities has been discussed by Lindhard *et al.* (1963b) and Winterbon *et al.* (1970). In general, relations between range quantities may be derived from the distribution in vector range $F(\boldsymbol{v}, \boldsymbol{r})\mathrm{d}^3\boldsymbol{r}$ which also obeys a transport equation of the backward type,

$$-\frac{\boldsymbol{v}}{v}\cdot\nabla F(\boldsymbol{v},\boldsymbol{r}) = n\int \mathrm{d}\sigma(\boldsymbol{v},\boldsymbol{v}')\times[F(\boldsymbol{v},\boldsymbol{r}) - F(\boldsymbol{v}',\boldsymbol{r})]. \quad (3.126)$$

Finally, if the initial charge state I of the beam is of significance, the distribution in vector range $F_I(\boldsymbol{v}, \boldsymbol{r})$ obeys the transport equation

$$-\frac{\boldsymbol{v}}{v}\cdot\nabla F_I(\boldsymbol{v},\boldsymbol{r}) = n\sum_J \int \mathrm{d}\sigma_{IJ}(\boldsymbol{v},\boldsymbol{v}') \times [F_I(\boldsymbol{v},\boldsymbol{r}) - F_J(\boldsymbol{v}',\boldsymbol{r})] \quad (3.127)$$

in the notation of Section 3.11.3. Eq. (3.127) was first given by Burenkov *et al.* (1992a).

3.15.3 Simulation codes

Range profiles can alternatively be determined by computer simulation codes. Existing codes differ from each other in the statistical method and input (Eckstein, 1991). Trajectory simulation codes are conventionally classified into molecular-dynamics, binary-collision and Monte Carlo codes.

Molecular-dynamics codes solve Newton's equation of motion (or its quantal analog). This technique requires considerable computing power and is not much in use for range calculations in the energy range covered by this report.

Binary-collision codes operate on a given — normally non-random — target structure. The prime input is a table of scattering angles and energy losses *versus* energy and impact parameter. The domain of this type of code is the slowing down in a regular crystal lattice, in particular under channeling conditions. Examples are the MARLOWE code (Robinson and Torrens, 1974), ACAT (Yamamura and Misuno, 1985) and CRYSTAL TRIM (Posselt, 1994).

Monte Carlo codes for particle penetration assume a random medium. The prime input is a table of differential cross sections for elastic nuclear scattering and a table of electronic-stopping cross sections and, possibly, electronic straggling. In principle the output of such codes should be equivalent with the solutions of transport equations discussed in Section 3.15.2. Minor differences originate in the treatment of soft (distant) interactions. Monte Carlo codes for gaseous targets as well as early codes for solids operate with a distribution of pathlengths between collisions governed by a mean free path. This mean free path is ill-defined for a cross section that becomes singular at zero scattering angle because of the need for truncation. This problem is circumvented in the TRIM code by Wilson *et al.* (1977) by operating with a fixed pathlength that is approximately equal to the internuclear distance in the structure. Truncation of the cross section then becomes unnecessary. Nevertheless, cross sections are always truncated. The choice of cutoff angle or energy is less critical for range calculations than for multiple scattering and other phenomena that are sensitive to soft collisions.

3.15.4 csda range

The total path length in the csda approximation, Eq. (2.17), is given by

$$R(E) = \int_0^E \frac{\mathrm{d}E'}{n[S_\mathrm{e}(E') + S_\mathrm{n}(E')]}. \tag{3.128}$$

Attention needs to be paid to the low-energy portion of the integrand where both S_e and S_n become small. It would seem tempting to approximate $R(E)$ by the 'electronic path length'

$$R_\mathrm{e}(E) = \int_0^E \frac{\mathrm{d}E'}{nS_\mathrm{e}(E')}. \tag{3.129}$$

One would then have to define a correction for nuclear stopping,

$$\begin{aligned}\Delta R(E) &= R_\mathrm{e}(E) - R(E) \\ &= \int_0^E \mathrm{d}E' \frac{S_\mathrm{n}(E')}{nS_\mathrm{e}(E')[S_\mathrm{e}(E') + S_\mathrm{n}(E')]}\end{aligned} \tag{3.130}$$

and note that nuclear stopping is unimportant in the Bethe regime where it constitutes less than 0.1% of the total stopping. This holds approximately down to the maximum of electronic stopping, which according to Table 3.6, lies far above the maximum of nuclear stopping.

Figure 3.38 shows a rough estimate of the correction to the electronic range based upon the approximations

$$S_\mathrm{e} \propto E^{1/2} \quad \text{and} \quad S_\mathrm{n} = \text{const.} \tag{3.131}$$

While the correction evidently decreases with increasing ratio S_e/S_n, the approach to zero appears slow. Therefore, a range calculation in the energy regime below the stopping maximum should never ignore nuclear stopping.

A related problem deals with the fact that stopping forces are tabulated only down to $E_0 = 25$ keV/u in this report. Figure 3.39 gives an indication of the error made if the lower integration limit in Eq. (3.129) is set to this energy. It is seen that the error becomes negligible only above ~ 1 MeV/u.

A table of such ranges for 16 ions in liquid water is shown on page 238.

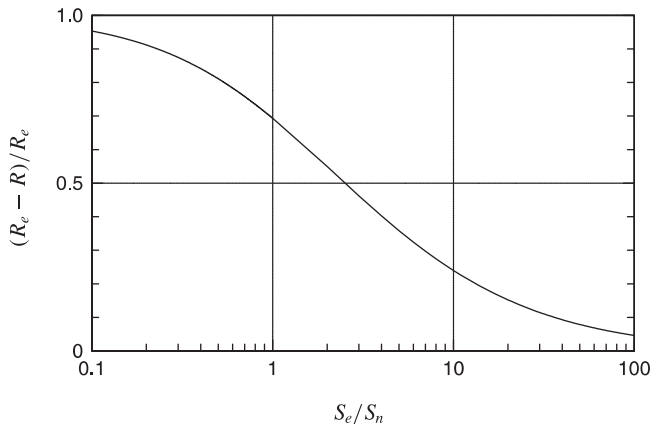


Figure 3.38. Rough estimate of the effect of nuclear stopping on path length below the electronic-stopping maximum on the basis of Eq. (3.131).

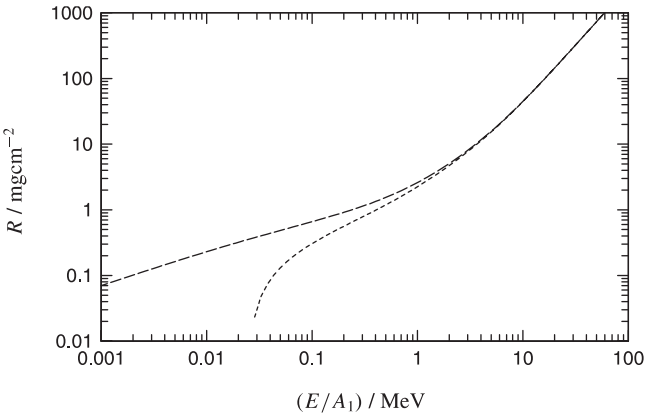


Figure 3.39. csda range for O–Al. Long-dashed line: electronic range defined by Eq. (3.129), determined from electronic-stopping force extrapolated by power law down to zero energy. Short-dashed line: electronic range determined by integration from 25 keV/u upward.

3.15.5 Influence of angular deflection on projected range

Even though energy loss may be well characterized by the continuous-slowing-down approximation, angular deflection might not be negligible. This has an influence on the projected range and can be estimated on the basis of Eq. (3.125), which assuming $w \ll E$ reduces to

$$1 = n[S_e(E) + S_1(E)]\frac{dR_p(E)}{dE} + n\sigma_1(E)R_p(E), \tag{3.132}$$

where

$$\sigma_1(E) = \int d\sigma(E, w)(1 - \cos\phi), \tag{3.133}$$

$$S_1(E) = \int d\sigma(E, w) w \cos\phi \tag{3.134}$$

and

$$\cos\phi = \left(1 - \frac{w}{E}\right)^{1/2} + \frac{M_1 - M_2}{2M_1}\frac{w}{E}\left(1 - \frac{w}{E}\right)^{-1/2}. \tag{3.135}$$

Eq. (3.132) was introduced by Schiøtt (1966) to describe ranges of low-energy protons, but the underlying assumptions are well-fulfilled for swift ions in general. It has the general solution

$$R_p(E) = \int_0^E \frac{dE'}{nS'(E')} \exp\left(-\int_{E'}^E dE'' \frac{\sigma_1(E'')}{S'(E'')}\right), \tag{3.136}$$

where

$$S'(E) = S_e(E) + S_1(E). \tag{3.137}$$

This may be written in the form

$$R(E) - R_p(E) = \int_0^E \frac{dE'}{nS'(E')} \times \left[1 - \exp\left(-\int_{E'}^E dE'' \frac{\sigma_1(E'')}{S'(E'')}\right)\right]. \tag{3.138}$$

For not-too-small mass ratios M_1/M_2, one may expand the exponential function in Eq. (3.138) and approximate

$$\sigma_1(E) \simeq \frac{M_2}{2M_1}\frac{S_n(E)}{E}, \tag{3.139}$$

$$S_1(E) \simeq S_n(E) - \frac{M_2}{2M_1}\frac{W_n(E)}{E}, \tag{3.140}$$

where $W_n(E)$ is the nuclear-straggling parameter,

$$W_n(E) = \int_0^{\gamma E} w^2 d\sigma_n(w). \tag{3.141}$$

Then Eq. (3.138) reduces to

$$\frac{R(E) - R_p(E)}{R(E)} \simeq \frac{M_2}{2M_1}\int_0^E \frac{dE'}{E'}\frac{S_n(E')}{S'(E')}\frac{R(E')}{R(E)}, \tag{3.142}$$

which determines the detour factor $R_p(E)/R(E)$.

3.15.6 Range straggling

Figure 3.40 shows results for csda range straggling corresponding to Figure 3.39 for the mean range. However, widths of range profiles can be quite sensitive to nuclear straggling and angular scattering at comparatively low energies.

The effect of fluctuating charge deserves attention in high-energy ion ranges. Most important are effects on range straggling. If energy-loss straggling is taken into account, the variance of the range profile may be estimated on the basis of Eq. (2.18).

Burenkov *et al*. (1992c) solved Eq. (3.127) numerically for B in Si and found straggling to be increased by 30–40 % over an energy range from ∼10 to 100 MeV/ion. Burenkov *et al*. (1992b) performed Monte Carlo simulations and found very pronounced differences from results of the TRIM code that neglects the effect of charge fluctuation.

Transient effects on the mean range in the case of pronounced deviations of the initial charge state from equilibrium are possible. However, for heavy ions, fairly thin foils are needed to detect such effects in stopping experiments. Equivalent effects in range must be even harder to identify.

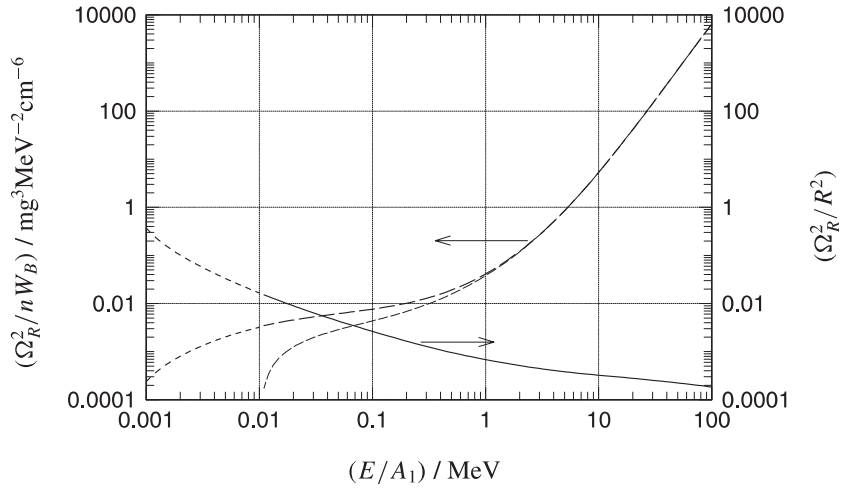


Figure 3.40. Range straggling evaluated from Eq. (2.18) taking into account only electronic stopping and straggling. Thin dashed line: integration from 0.01 MeV upward. Thick lines based on integration of curves extrapolated to lower energy.

3.15.7 Extraction of electronic-stopping cross sections from range measurements

Stopping data for heavy ions have frequently been determined on the basis of ion ranges. If an $R(E)$ dependence is measured over an adequate energy interval, the stopping force can be found by differentiation. In the simplest form, such a procedure does not take into account nuclear scattering and stopping. Eq. (3.132) offers an operational procedure to explicitly take into account this effect in the energy range where it is small. Indeed, rewriting it in the form

$$n[S_e(E) + S_1(E)] = \frac{1 - n\sigma_1(E)R_p(E)}{dR_p(E)/dE}, \qquad (3.143)$$

one finds the standard form

$$nS_e(E) = \frac{1}{dR_p(E)/dE} \qquad (3.144)$$

in the limit of negligible nuclear scattering, but Eq. (3.143) offers explicit corrections for both angular deflection and nuclear energy loss. As in Section 3.14 the resulting electronic-stopping force depends on the adopted input describing nuclear collisions.

3.15.8 Ranges of low-energy ions

In the regime of dominating nuclear stopping, theoretical treatments need to make recourse to transport equations. In accordance with the discussion in Section 3.8.2, it is common — and most frequently justified — to decouple electronic from nuclear collisions. Ignoring angular deflection in electronic collisions, this leads to

$$1 = nS_e(E)\frac{dR_p(E)}{dE} + n\int d\sigma_n(E,w)\left[R_p(E) - \cos\phi\, R_p(E-w)\right] \qquad (3.145)$$

and similar relations for other range quantities.

Numerous alternative statistical formulations of the range problem may be found in the literature, and a variety of tools are available for their solution. Most of them have been developed with applications in ion implantation in mind, *i.e.*, within the energy regime in which the simple estimates mentioned above are not necessarily valid. Efficient methods are available to determine averages, especially of first and second order, on the basis of analytical estimates and numerical evaluation of some integrals. Reliable estimates of range profiles are commonly performed either by numerical solution of the transport equation or by Monte Carlo simulation with equivalent input.

3.16 SUMMARY

With reference to Figure 3.1 one may first note that significant progress has been made over the past few years in the understanding of heavy-ion stopping over the entire velocity range covered in the graph. A fairly comprehensive survey has been given in a recent conference (Andersen and Sigmund, 2002). The highly relativistic regime is well-covered by the theory of Lindhard and Sørensen (1996). Further down in speed lies the domain of the binary theory and of the CasP code. While the range of validity of the binary theory reaches well below

the stopping maximum, that of the CasP code is more restricted because of the lack of shell and Barkas–Andersen corrections. The theory of Arista (2002) has been geared toward low projectile speeds but is becoming successful also around and above the stopping maximum. The theory of Maynard *et al*. (2001b) is particularly successful in connection with hot (plasma) targets.

Key elements in this area are proper account of the Bloch theory and an understanding of the Barkas–Andersen effect as well as projectile screening. At the same time, several features familiar from the Bethe theory are less prominent for heavy ions. This is particularly true for deviations from Bragg additivity, which become less pronounced as one leaves the Bethe regime.

Some clarification has been achieved regarding oscillatory effects, *i.e.*, Z_1 and Z_2 structure, in particular with regard to behavior as a function of speed, but more attention is needed to the quantitative behavior. Arista's theory comes close to Z_1 oscillations, but it applies to free-electron systems only and hence does not make statements about gases and insulators. Binary theory elucidates Z_2 structure, but that structure is most pronounced in the low-speed range for which predictions of the binary theory become uncertain.

Significant progress has also been achieved in understanding and quantifying energy-loss straggling with and without charge exchange, although much more work is needed. Less progress has been reported in more traditional areas such as the analytic theory of nuclear scattering, multiple scattering and range profiles. Efficient tools and computer codes handling these aspects have been available for many years.

Journal of the ICRU Vol 5 No 1 (2005) Report 73
Oxford University Press
doi:10.1093/jicru/ndi011

4 EXPERIMENT

4.1 INTRODUCTORY SURVEY

Measurements of heavy-ion slowing down in matter differ in many aspects from experiments with light particles such as protons and α-particles. This section presents an overview of special experimental requirements, methods, data analysis, experimental results and interpretation for heavy-ion stopping powers, energy and angular straggling, and ranges in the energy domain from the keV/u up to the GeV/u regime. A more detailed account has been given by Geissel *et al*. (2002).

4.2 PROJECTILES

4.2.1 Recoil ions and fission fragments

Monoenergetic heavy ions with low energies can be obtained from radioactive α and γ recoils. The latter emitters are used to study the domain of elastic collisions in the eV region (Falcone *et al*., 1981; Stritt *et al*., 1999). Kinetic energies from α recoils are in the keV range. The practical importance of these sources is now limited since conventional ion implanters are widely available for this energy range (Ryssel and Ruge, 1986).

In spontaneous fission, or in a low-energy binary fission process induced by thermal neutrons, an energy of about 200 MeV is released that is mainly converted into kinetic energy of the fragments. However, nuclear fission is a statistical process that results in fairly wide distributions in energy, angle and mass of the reaction products. This is not favorable for measuring penetration parameters without the use of special experimental methods such as event-by-event coincidences.

Despite this, fission sources were widely used for atomic-collision studies before the advent of heavy-ion accelerators, as the mean kinetic energy of an actinide fission fragment is in the interesting range of 0.4–1.2 MeV/u depending on the mass.

In particular, Lassen (1951a,b) measured charge-state distributions of fission fragments after penetration through gaseous and solid matter. These early measurements were of crucial significance and will be discussed in Section 4.5.

Even now, this source of fragments in the mass region around $A_1 = 100$ remains useful, in particular for detector tests and calibrations.

4.2.2 Stable beams from accelerators

Much progress has been achieved in atomic-collision physics with the invention of particle accelerators providing monoenergetic and monoisotopic beams characterized by a small emittance. For recent reviews of this well-established field, the reader is referred to Andersen (1991) and Schopper (1993).

Electrostatic machines, in which the ions were accelerated by a potential of a few megavolts, drift tube linear accelerators and cyclotrons were invented in the years 1930–1940, but these early machines accelerated only light particles. It was only 20 years later that heavy ions could be produced in high charge states, by using multicharged-ion sources and by a clever and extensive use of the stripping process. This second method consisted in introducing a thin foil — or a gas jet — between two successive sections of the accelerator. The charge state of the ions traversing such strippers was considerably increased and this resulted in a much higher energy of the heavy ion beams. This technique was first used in heavy-ion linear accelerators, the HILAC machines, built around 1955 in Berkeley and Yale, but also in Kharkov and Manchester.

These machines accelerated ions up to argon to 10 MeV/u but were mainly devoted to nuclear physics. Only a few atomic-physics experiments were performed during this period.

In the late 1950s came the electrostatic tandem accelerators, in which negative heavy ions are accelerated from the ground to the positive high voltage V (typically 13 MV), where they go through a stripper. At the exit of this stripper, those ions which have lost n electrons may be accelerated from the high voltage to the ground to the energy $(n + 1)$ eV, *i.e.*, typically $13(n + 1)$ MeV.

Tandem accelerators have been used extensively to measure heavy-ion stopping powers mostly in the range 0.5–3 MeV/u. At the same time, heavy-ion facilities coupling two accelerators, with an

© International Commission on Radiation Units and Measurements 2005

intermediate stripping, were built. The first machine of this type, in which a small linear accelerator was used as a pre-accelerator for a cyclotron, was the ALICE device, built at Orsay in 1970, that accelerated ions up to krypton to energies above the Coulomb barrier for all targets (Bimbot, 1999). Until 1985 this machine was used to measure many stopping powers in solids and gases for ions from Ne to Ag.

The next step — which opened the way to the acceleration of all stable nuclei up to uranium — was the building of two giant linear accelerators, the Berkeley SuperHilac in 1972 and the Universal Linear Accelerator UNILAC in Darmstadt in 1976. With this last machine, stopping powers of solids and gases for ions up to uranium were studied at 1.4 MeV/u and in the energy range 6–10 MeV/u. During these studies, the so-called 'gas–solid effect' was discovered, which will be discussed in Section 4.10.3. After 1980, the development of heavy-ion accelerators was primarily oriented toward higher energies. Most important in connection with the present report is GANIL (Grand Accélerateur National d'Ions Lourds) in Caen that couples two giant cyclotrons, and where systematic measurements of heavy ion stopping powers have been performed in solids and gases between 20 and 100 MeV/u. Other facilities are the RIKEN accelerator, the superconducting cyclotron at Michigan State University, accelerators at Dubna, and the synchrotron SIS which uses the UNILAC as an injector. The present high-energy record in the field of atomic collision studies is achieved with atomic collision measurements of 160 GeV/u ^{208}Pb ions at CERN-SPS.

Finally, after pioneering work on the irradiation of human tumors at the Berkeley BEVALAC, two heavy-ion synchrotrons are presently used for cancer therapy, the SIS machine in Germany and an 800 MeV/u device at Chiba, Japan.

4.2.3 Scattered beams and target recoils from elastic scattering

The intensity of a heavy ion beam can be reduced by several orders of magnitude by using a scattering target. The energy of these scattered ions can easily be varied by changing the scattering angle and the chemical nature of the target. Such 'secondary' beams can then be used for stopping measurement purposes (Bimbot *et al*., 1989a,b).

In the same spirit, an original method for producing low-intensity beams of various projectiles at low energy was recently indicated (Nath *et al*., 1994). These projectiles are recoil ions from targets made of the elements of interest. They are ejected by elastic collisions induced by the primary heavy ions. The nature of the secondary beam is that of the target, and its energy can be varied by modifying the detection angle. This is very convenient in the scope of stopping power measurements. For example, an 80 MeV gold beam, impinging onto targets of Si, Fe, Ni and Cu was used by Harikumar *et al*. (1997) to produce beams of these elements in the energy range 0.1–1 MeV/u and to measure their stopping powers in a carbon foil.

This technique seems very promising for future experiments aiming at completing the stopping power data base at low energy.

4.2.4 Radioactive beams from accelerators

The latest generation of heavy-ion facilities can also provide beams of radioactive isotopes of elements up to uranium. Such beams can be produced through two complementary methods, 'in-flight separation' and 'isotope separation on-line' (ISOL) (see, for example, Geissel *et al*., 1995). The in-flight method mainly uses projectile fragmentation and uranium fission to produce beams of radioactive nuclei at 30–1000 MeV/u. Reaction products are separated in-flight and have practically the velocity of the projectile. In this way one has access to all exotic nuclei down to half-lives in the μs range and below. The ISOL method uses proton or deuteron beams with energies up to 1000 MeV/u or intense neutron beams from reactors and spallation sources which induce target fragmentation and fission. Radioactive ions are created basically at rest and then released from the thick target into an ion-source system. After extraction and electromagnetic mass separation they are post-accelerated in a small accelerator.

As an example, the SPIRAL facility (Villari, 2001), which has been installed at GANIL, uses projectile fragmentation of primary beams from the two large GANIL cyclotrons to produce radioactive fragments that are ionized in an ECR (electron cyclotron resonance) ion-source, extracted, and accelerated to a few MeV/u by another cyclotron (CIME). Secondary nuclear beam facilities at Louvain la Neuve and REX-Isolde at CERN provide post-accelerated radioactive ion beams for nuclear and atomic physics studies (Habs *et al*., 1996).

Heavy-ion beams of stable or radioactive isotopes can be stored and cooled in heavy-ion storage-cooler rings (Pollock, 1991; Franzke, 1987; Bryant and Johnsen, 1993) for precision experiments. For radioactive beams, a magnetic separator is used to select nuclear-reaction products and inject them into storage-cooler rings (Geissel *et al*., 1992b) and ion traps (Scheidenberger *et al*., 2000). Several cooling techniques such as stochastic, laser or electron

cooling can be applied. Electron cooling is particularly attractive in the context of atomic-collision studies. After interaction with a merged electron beam in the ultra-high vacuum of a storage ring, energetic heavy ions adopt the temperature and the velocity of the cooler electrons and in this way can reach a relative momentum spread of less than 10^{-6}.

4.3 TARGET CHARACTERIZATION AND REQUIREMENTS

4.3.1 General

Reliable experimental results require selected and well-known target properties. Key parameters are mean target thickness, chemical structure and composition. Physical properties such as density, temperature and geometrical structure are likewise important. For energy- and angular-straggling experiments, knowledge of the distribution in target thickness (nonuniformity) becomes essential. Preferably the effect of target nonuniformity on the measured energy distribution should be negligible or small compared to that of collision statistics.

4.3.2 Solids

Self-supporting targets are highly preferable for transmission experiments with solids, avoiding corrections due to backing materials. Monoatomic targets have commonly been used in fundamental studies. Techniques used for producing such targets depend on chemical nature and thickness (Folger, 1989, 1999). Pertinent thicknesses range from a few μg/cm^2 for projectiles of a few keV/u to several g/cm^2 for relativistic heavy ions. The most frequent production techniques are rolling and evaporation under vacuum conditions. A special form of evaporation can be achieved by laser-plasma-ablation deposition, which provides very thin and rigid amorphous carbon foils (Maier-Komor *et al*., 1999) suitable for studies of pre-equilibrium effects in heavy-ion stopping. These carbon targets are characterized by a perfectly random orientation of the nanocrystallites, good thickness uniformity and long lifetime under heavy-ion irradiation.

4.3.3 Gases

Gas targets need special cells, either sealed with thin solid windows or differentially pumped with very small apertures. Closed gas cells are applied in measurements on thick targets exceeding several hundred μg/cm^2 (Geissel, 1982; Bimbot *et al*., 1989a,b) for which corrections due to windows are small.

Windowless gas cells are used preferentially if very thin targets are required or as internal targets in storage-cooler rings (Folger, 1989). The density in such gas cells can be kept constant by automatic controllers equipped with precise pressure sensors and a reference gas volume. It is a disadvantage that large-angle scattering events may not be recorded in conventional analyzer systems behind the gas cell because of the small exit aperture. Special techniques have been developed based on pulsed fast valves synchronized with the beam pulse. This system limits the gas leak to several milliseconds and allows investigations of high-pressure targets or plasma discharges. Several versions of translating or rotating devices have been used during the past ten years (Fleurier *et al*., 1991; Chabot *et al*., 1998; Gardès *et al*., 2001).

4.4 TARGET THICKNESS AND UNIFORMITY

4.4.1 Solids

A common technique for measuring the thickness of solid, self-supporting targets is the combination of area and mass measurements. Relative uncertainties of about 3–5 % for the mean value of the ratio between mass and area are obtained for thin targets in the 50–200 μg/cm^2 range by the use of high-precision electronic scales (microbalance) and optical methods to determine the area. The absolute precision of modern microbalances is about 1 μg. Overall uncertainties can be improved to 1 % and better for targets in the mg/cm^2 range and above.

The thickness of self-supporting targets may also be determined by Rutherford backscattering or by measuring the energy loss of a reference beam. Most commonly used are radioactive sources such as the 5.3 MeV α from ^{210}Po or the 8.78 MeV α from ^{211}Po. Mixed sources are advantageous for calibration and redundancy. Proton or helium beams from accelerators may also be used. The accuracy of a target thickness measured by this method is generally a few percent. The use of thin beams or of collimated sources gives the possibility of scanning the target area, thus providing a thickness profile in addition to an average value (Bimbot *et al*., 1978).

Interference measurements (*e.g.*, the Tolanski method) (Geissel *et al*., 1977) and the absorption of light may be used for very thin targets. Such methods require an independent absolute calibration. Measurements of mean target thickness and surface roughness can be performed by laser interferometry. This elegant and precise experimental technique is practical only if the target area does not exceed a few cm^2. Examples are shown in Figure 4.1. Target nonuniformity has also been determined by atomic-force microscopy (Brière and Biersack, 1992).

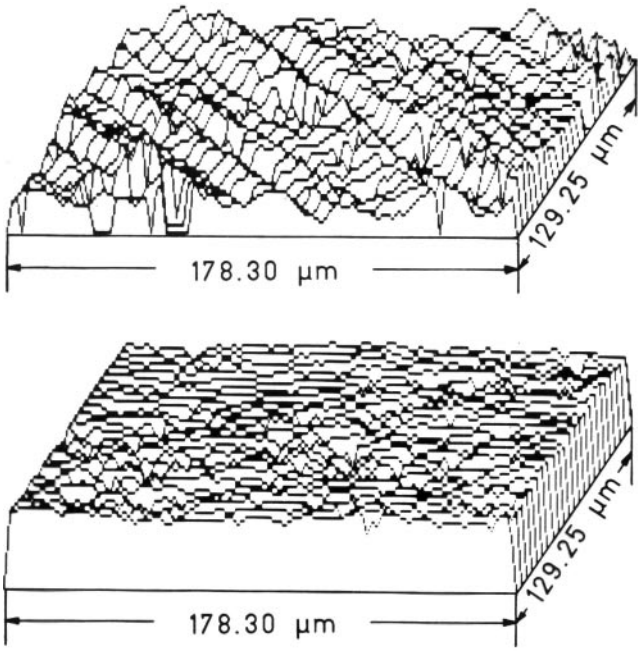


Figure 4.1. Target surface investigation with laser interferometry. Upper graph: large surface roughness ($\Delta_{rms} = 68$ nm); lower graph: target well suited for studying energy-loss straggling ($\Delta_{rms} = 15$ nm). Ordinate scales are identical in the two graphs. From Schwab *et al*. (1990).

4.4.2 Gases

For gas targets the determination of the number of atoms/cm^2 relies on the measurement of cell length, gas pressure and absolute temperature. With the commercial availability of small but very precise probes that can be introduced into the cell, pressure and temperature measurements have become easy, and these quantities can be read and recorded continuously during the experiment. The thickness can then be determined assuming an ideal gas or by using the Van der Waals equation of state (Herault *et al*., 1991). Uncertainties are currently between 0.1 and 1 % for pressure and about 0.1 % for temperature.

It is preferable to keep the density of the gas target constant during the measurement. This can be achieved by a motor-controlled valve driven by a precise pressure controller providing an output signal proportional to the pressure difference of the actual gas-cell volume and a suitable reference volume (Geissel, 1982).

For a window-sealed gas cell, the distance between the two windows is determined by the cell geometry and should be known in principle with an accuracy of the order of 0.1 % (0.1 mm for a 10 cm long cell). However, a correction must be applied to this distance to take into account the window deformation due to the pressure difference between inside and outside the cell. Thus, the resulting accuracy on the gas-target thickness is generally of the order of 3–6%.

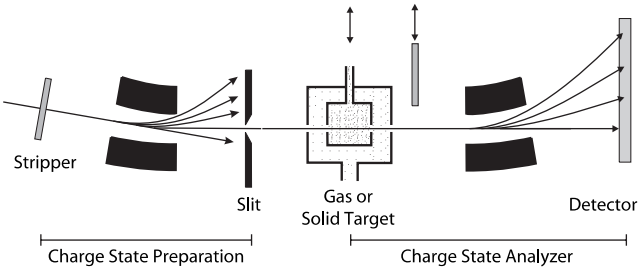


Figure 4.2. Schematic of an experimental setup for charge-exchange studies in gaseous and solid targets. In front of the target station is a preparation stage to select the incident charge state.

Window problems are absent in a differentially pumped windowless cell, but precise knowledge of the gas density profile remains an experimental challenge. A static regime of high-pressure gas flow through apertures was investigated by recording fluorescence light from gas atoms excited by a carbon beam (Gardès *et al*., 2001).

4.5 CHARGE STATES AND CHARGE EXCHANGE

4.5.1 Experimental methods

Measuring charge-exchange cross sections requires selecting the incident ions in a given charge state and measuring their fluence rate and the emerging charge fractions. A typical device used for that purpose is shown in Figure 4.2. It is composed of three sections. In the first section, a monoenergetic and monoisotopic beam extracted from an accelerator penetrates a stripper medium followed by a dispersive element associated with a slit that selects the incident ions in a given charge state. The second section is the target. The beam emerging from this target is analyzed in the third section of the device which has another dispersive stage followed by a position-sensitive detector. Magnetic or electric sector fields associated with focusing systems are used as dispersive stages. The charge-exchange target setup can be a solid foil, a gas cell or a plasma target. The intensity of the beam impinging on the stripper can be determined during the whole experiment with a monitor that does not intercept the beam, and the (constant) fraction of this beam exiting the stripper in the charge state of interest is measured by the position-sensitive detector, the target being removed or the gas cell being empty.

At energies up to a few MeV/u, achieving single-collision conditions requires target thicknesses of

1 μg/cm^2 or less. This is not practical for self-supporting solid foils. Therefore only very few experiments of this type have been performed in solids. Lennard *et al*. (1980) overcame this difficulty by working with very thin carbon foils that had been formed by cracking of carbon compounds by the beam in the residual gas of the acceleration chamber. In this experiment the pressure in the chamber was a few hPa (1 hPa = 1 mbar). In case of gaseous targets, the medium is provided in a gas cell that is differentially pumped, with strict requirements on target thickness and homogeneity.

4.5.2 Equilibrium

The equilibrium charge of an ion traversing matter results from a competition between the loss and capture of electrons. Progress in understanding this competition has been slow because of an apparent paradox:

1. Mean charge states measured upon emergence from solids tend to be higher than from gases.
2. Differences in measured stopping cross sections between solid and gaseous materials, when detectable at all, tend to be smaller than what would be expected from a q_1^2 dependence on the ion charge.
3. Attempts to estimate equilibrium ion charges from stopping measurements by adopting a q_1^2 dependence lead to an effective charge which differs distinctly from the ion charge measured upon emergence.

The first observation goes back to Lassen (1951a,b) who found that the mean charge state of emerging fission fragments increased slightly with density when the target was a gas, and drastically for passage through a solid target. This observation was attributed by Bohr and Lindhard (1954) to the evolution of the charge state within the target: The higher collision frequency in a solid or dense gas target favors excited projectile states and hence increases the frequency of ionizing collisions.

Measured equilibrium charge states used to refer to ions arriving at a remote detector. The question of whether such measurements could be used to determine the equilibrium charge of ions moving in a solid was the subject of intense discussion. Betz and Grodzins (1970) suggested that an ion emerging from a solid may emit Auger electrons before being recorded. This would imply that the real equilibrium charge during traversal of the material is lower. This suggestion was motivated by the apparent lack at that time of a noticeable gas–solid effect of comparable magnitude on the stopping power.

In measurements by Woods *et al*. (1984) with 36 MeV carbon ions in solid carbon and hydrocarbon gases — where Auger events are negligible — the capture cross section in the solid was found to be 20 % lower than in the equivalent gas and the loss cross section for C^{5+} ions 60 % higher. This confirmed that moving ions were not in their ground states.

An interesting development is the utilization of H^+ emission to study charge states inside the target by Della-Negra *et al*. (1987). Heavy ions penetrating solid foils give rise to emission of H^+ ions from hydrogenated molecules (water, hydrocarbons) adsorbed on the front and exit surfaces. This process was shown to be sensitive to the charge state of the incoming or emerging ion. That dependence was quantitatively established by measurement of emission rates from the front surface of the foils by ions of known charge states. By assuming that this dependence was the same for incident and exiting ions, the emission rate at the exit surface could be used to determine an approximate charge number of an ion emerging from the exit surface. Although this method is indirect and implies mechanisms that are not understood in detail, it is clear that hydrogen ejection precedes post-foil Auger emission and that the so-determined charges states must be close to those inside the target just before ejection.

Charge equilibration could thus be observed by varying the foil thickness. Equilibrium charge states were determined for several ions from sulphur to iodine in carbon and gold foils (Brunelle *et al*., 1989). For 1.16 MeV/u Kr ions incident on 500 Å carbon and 1000 Å gold foils, charge states inside the bulk material were found to be 18.4+ and 16.6+, while those measured after exiting the targets were 20+ and 19.7+, respectively. These measurements showed that the Auger process leads to the emission of 1.6 electrons from C and 3 from Au targets. This small number of Auger electrons and the relatively high charge states inside the bulk material represent another confirmation of the dominance of the model of Bohr and Lindhard (1954) for partially ionized heavy ions.

The surprisingly small absolute number of Auger electrons was also confirmed in experiments by Schramm and Betz (1992). These measurements demonstrated the existence of a post-foil ionization as well as a gas–solid effect on the equilibrium charge state. In the region around the Bragg peak this effect does not lead to an observable gas–solid difference in the stopping powers because the relation between ion charge and stopping power does not just reflect a q_1^2 law (see Sections 3.4.3, 4.9, and 5.2.2, especially Figures 3.10 and 3.11). However, at higher energies, this gas–solid effect is also observed in the stopping powers and will be discussed in Section 4.10.3.

4.5.3 Nonequilibrium

For high-speed highly stripped ions, mean free paths for charge exchange become large enough even in solid materials to allow measurements of electron-capture and -loss cross sections as well as the approach to charge equilibrium. These phenomena have been studied experimentally by Scheidenberger *et al*. (1998) and compared to theoretical predictions. Ionization cross sections of Au and Bi ions, carrying one electron each, in different solid targets are in good agreement with predictions of Eichler and Meyerhof (1995). As far as electron capture is concerned, three distinct processes are involved:

1. Radiative electron capture, in which electron capture is accompanied by photon emission, a process which is theoretically described by Stobbe (1930) and Eichler (1985);
2. Nonradiative capture, described by the relativistic eikonal approximation tabulated by Ichihara *et al*. (1993); and
3. Resonant transfer and excitation resulting in excitation of another projectile electron (Hahn, 1987).

These processes have drastically different dependences on Z_1 and Z_2 and hence can be separated experimentally (Geissel *et al*., 2002).

The charge-state evolution versus target thickness may also be measured and compared to theory. This was done by Scheidenberger *et al*. (1998) for 1000 MeV/u Au ions penetrating through Al and Au. The result of this comparison is shown in Figure 4.3. For both targets the incident charge state is 69^+. Due to the small charge-exchange cross sections at these relativistic energies, charge equilibrium is reached only at about 300 mg/cm^2 in Al and 100 mg/cm^2 in Au. Experimental distributions are well reproduced by predictions based on high-energy approximations (Eichler and Meyerhof, 1995).

The literature on measurements of charge-exchange cross sections in gases is extensive (Lo and Fite, 1969; Hvelplund *et al*., 1992). Pertinent work on gaseous and solid materials at tandem-accelerator energies, *e.g.*, 10 MeV/u, was reported by Cowern *et al*. (1983b), Woods *et al*. (1984), Read (1984) and others. Cross sections for charge exchange and equilibrium charge states may be extracted from codes like ETACHA (Rozet *et al*., 1996) or GLOBAL (Scheidenberger *et al*., 1998).

4.6 METHODS OF ENERGY-LOSS MEASUREMENT

4.6.1 General

Methods to measure energy loss have been reviewed in Chapter 9 of ICRU Report 49 . This section is primarily intended to be an update to that review.

Heavy-ion accelerators provide monoisotopic beams characterized by well-defined energies and charge states. Accelerated swift heavy-ion beams have small longitudinal (momentum spread $\Delta p/p < 10^{-3}$) and transverse (<5π mm mr) emittances. In the relativistic regime, in which nuclear reactions are not negligible, full particle identification with respect to mass and atomic number can become necessary.

Stopping power is determined by the energy loss in a target of known thickness that, according to Eq. (2.11), should be small enough so that the variation of stopping with projectile energy is small. This requirement can be relaxed somewhat by assigning the extracted stopping power to a projectile energy $\overline{E} = (E_{\rm in} + E_{\rm out})/2$, where $E_{\rm in}$ and $E_{\rm out}$ are the incident and mean exit beam energy [cf. Eq. (3.74)]. On the other hand, in measurements of equilibrium stopping powers the target thickness must be much larger than the thickness necessary to ensure charge

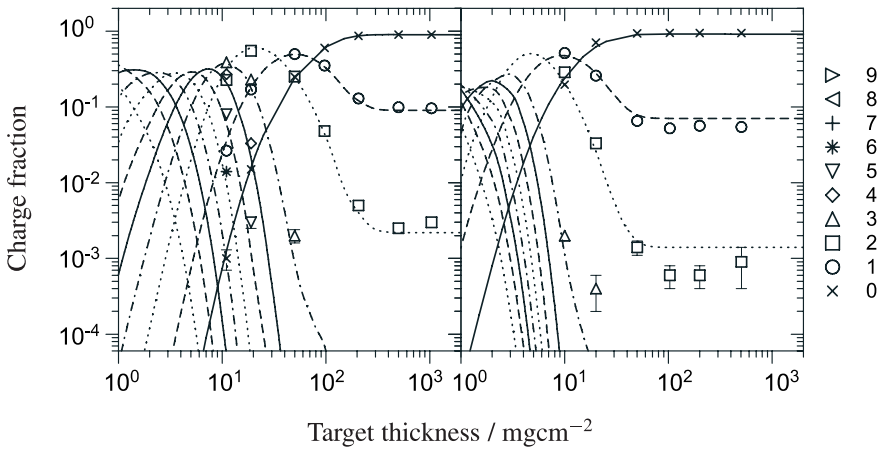


Figure 4.3. Measured and calculated charge-state evolution of 1 GeV/u $^{197}Au^{69+}$ ions penetrating aluminum (left) and gold (right) targets of different thicknesses. Numbers define the number of electrons carried by the ion (Scheidenberger *et al*., 1998).

equilibration of the projectile. This condition can be very stringent for the heaviest ions at high energy. The use of a stripper placed before the target can then be necessary to establish charge equilibration before the projectile enters the target.

The determination of the average energy loss requires energy measurements with and without the target inserted into the projectile beam. In the most common techniques this average is obtained through a precise determination of the energy-loss distribution. Energy-loss measurements can be done in transmission or in Rutherford-backscattering geometry. For protons, both methods have been carefully investigated, and it has been concluded that either method provides reliable results with uncertainties of 2–3 % (Bauer, 1987; Mertens, 1987). The transmission method is the most versatile method for heavy ions and will be described in what follows.

High-resolution devices are needed to accurately measure energy-loss distributions for heavy ions. Semiconductor detectors are successfully used for spectroscopy of photons and light ions. With heavy ions, high ionization density along the particle trajectory, dead layers at the entrance, and energy loss from elastic collisions cause strong nonlinearities in detector response. This makes it difficult to use such detectors for absolute energy measurements without using very specific calibration techniques. Also, the performance of semiconductor detectors is very sensitive to inevitable radiation damage due to implanted heavy ions. Finally it is an experimental problem to reduce the high intensity of the primary beam to manageable rates ($<10^4$/s) for precision particle detectors. However, these difficulties have been overcome by performing the whole experiment with a scattered beam (Bimbot *et al*., 1989a,b), or with recoil ions from elastic scattering (Harikumar *et al*., 1997). This makes it possible to:

- keep the beam intensity in the range of 10^3–10^4 s^{-1}, and
- proceed to frequent energy calibrations of the detectors, with the same beam (*i.e.*, the same detector response), the energy of which can be varied in a known way by changing the scattering angle and/or the nature of the scattering target.

It is thus possible to follow the evolution of the detector characteristics.

Alternative methods are presented in the following sections.

4.6.2 Calorimetric detection

In pioneering stopping measurements with protons and deuterons, Andersen *et al*. (1966) measured the energy by a calorimetric-compensation technique operated at liquid-helium temperature. Projectiles were stopped in a metal block, and the temperature rise was measured in the block and in the penetrated foil. After the beam was switched off, electric power sources P_f and P_b were connected to the foil and stopper block, respectively, until the same temperature rises were observed. The mean energy loss in the foil is then given by

$$\Delta E = E\frac{P_f}{P_f + P_b}, \tag{4.1}$$

where E is the energy at the entrance of the foil. Although the mean energy loss can be reliably determined, this method does not provide information on straggling.

In calorimetric detectors the deposited energy is converted into heat. The temperature rise ΔT due to a deposited energy E is given by (Booth *et al*., 1996)

$$\Delta T = \frac{E}{C(T)}e^{-t/\tau}, \quad \tau = \frac{C(T)}{G(T)}, \tag{4.2}$$

where $C(T)$ and $G(T)$ are the heat capacity of the absorber and the thermal conductance of the link between absorber and reservoir, respectively.

The principle of the calorimetric method was further developed using thermistors that allow the recording of the temperature rise due to a single heavy ion (Kienlin *et al*., 1996; Egelhof, 1999). Here a constant current is applied, and the change in resistance with temperature results in a voltage pulse. Highly doped semiconductors or superconducting materials like thin aluminium layers are used as thermistors (Figure 4.4). Superconducting thermistors are transition-edge thermometers operated near the critical temperature. For a 10 nm aluminium layer, this transition temperature is about 1.49 K (Figure 4.5).

In this way, single heavy ions can be detected at moderate count rates (10^3/s). Relative energy resolutions of a few times 10^{-3} have been achieved for various heavy-ion beams over an energy range

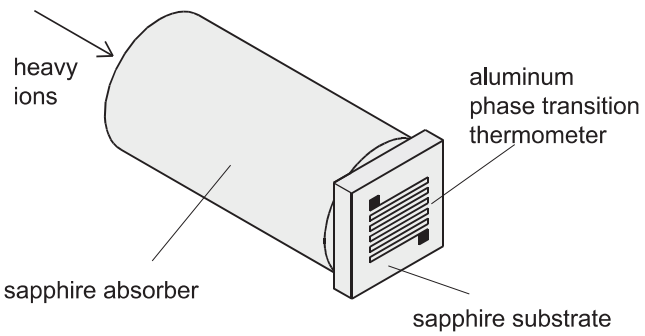


Figure 4.4. Calorimetric detector equipped with a superconducting aluminium thermistor (Egelhof, 1999).

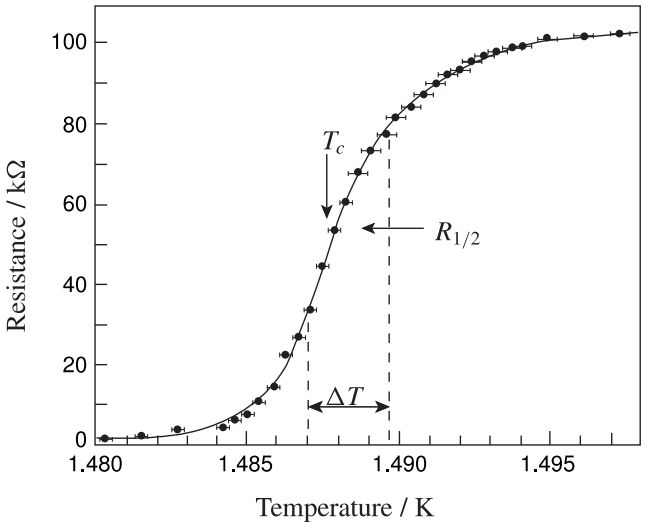


Figure 4.5. Resistance change of a 10 nm superconducting aluminum thermistor near the transition temperature T_c (Egelhof, 1999).

from 0.1 to 300 MeV/u. Systematic errors occur in the absolute energy determination by this method due to photon and particle emission that do not contribute to temperature rise in the stopper block. This is a minor effect at energies near and below the Coulomb barrier.

4.6.3 Secondary-particle detection

Indirect energy measurements can be performed using recoil protons (Bimbot *et al*., 1980) or convoy[30] electrons (Mann *et al*., 1988) generated by the heavy-ion beam. Protons are detected in well-defined directions by using tight collimation. The energy of these secondary particles can easily be connected to that of the primary beam with the help of kinematic relations.

A schematic setup for recoil protons is illustrated in Figure 4.6. A disadvantage of this method is the damage produced in the target by the high beam current ($\geqslant 10^9$/s) needed because of the low cross section for the production of secondary particles.

4.6.4 Time-of-flight spectrometers

A very versatile and accurate method for energy measurements is time-of-flight (TOF) spectrometry, which has been successfully applied at velocities up to $E \lesssim 20$ MeV/u (Geissel *et al*., 1980; Lennard *et al*., 1982) and which avoids most of the drawbacks of other methods.

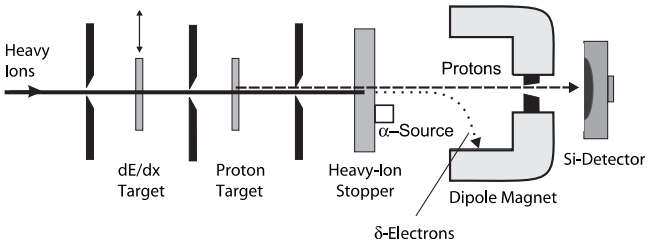


Figure 4.6. Energy-loss measurement via spectroscopy of recoil protons (Bimbot *et al*., 1980). Recoil protons are produced in a plastic foil, acting as a proton target, placed behind the sample. The heavy-ion beam is stopped completely in a thick gold foil that forward-emitted protons can penetrate with only a small energy loss. δ-electrons are deflected by a small dipole magnet.

TOF start signals are commonly derived from the high frequency of an accelerator providing bunched beams or from transmission particle detectors. High-resolution heavy-ion start detectors consist of a thin carbon foil (few μg/cm^2) from which secondary electrons are released and focused isochronously onto a multi-channel plate (MCP), providing a fast timing signal with a rise time below 1 ns. Electron amplification (10^6) in the MCP is efficiently performed without introducing a significant time jitter. With a combination of two such MCP-foil detectors, overall time resolutions of better than 100 ps (FWHM) have been achieved (Geissel, 1982). These times include the energy-loss straggling in the foil of the start detector. Such a time resolution corresponds to relative uncertainties of the order of 10^{-3} on the measured energies, for 5 MeV/u heavy ions and for a flight path of 6 m.[31]

Absolute calibration is performed by changing the path length. A special mechanical, motor-driven device can do this with an accuracy of about 0.1 mm (Geissel, 1982). Another adequate method is to insert a delay line into the stop and start branch of the timing electronics (Lennard *et al*., 1982). The two different TOF spectra with the delay in the two branches yield the absolute flight time.

A TOF system can also be realized by nondestructive detectors. In this case no material from the TOF spectrometer is placed in the beam axis. This can be achieved if the accelerator provides a bunched beam structure (Geissel *et al*., 1983a). TOF signals are induced from the ion bunches and are recorded with capacitive probes placed at well-defined positions along the beamline. At least three probes are required for absolute velocity measurements.

[30]Convoy or cusp electrons are common names for electrons emerging from a solid or gas target with a velocity close to that of the projectile (Groeneveld *et al*., 1984). Distributions in speed and direction of convoy electrons are characterized by sharp peaks (cusps) around the speed and emergence angle of the ion beam.

[31]Since the energy loss is obtained as a difference between two measured energies, a 10^{-3} error on each will yield a 2% uncertainty for $\Delta E/E = 0.1$.

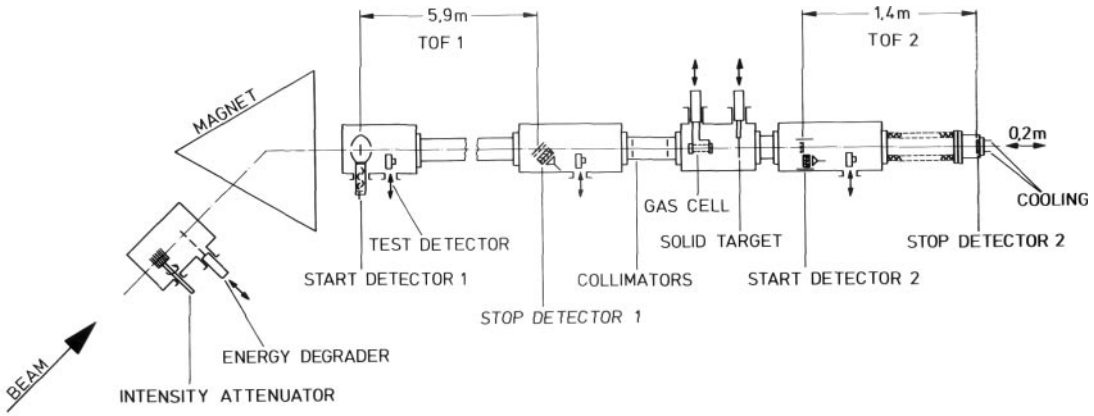


Figure 4.7. Double-time-of-flight spectrometer (Geissel *et al*., 1980) for energy-loss and straggling experiments of heavy ions in the MeV/u domain. Broad incident energy distributions or energy fluctuations of the accelerator can be handled by this setup without deterioration in the quality of the measurement.

Measuring event-by-event avoids errors due to possible fluctuations of the incident beam. This is an advantage in straggling measurements. This idea was utilized in an experiment in which the stopping foil only covered part of the active area of a detector (Sofield *et al*., 1978). A more versatile solution can be obtained by using a double-time-of-flight (DTOF) spectrometer (Geissel *et al*., 1980; Geissel, 1982). Such an arrangement (Figure 4.7) is very efficient for experiments at cyclotrons where any required energy change of the incident projectiles is very time consuming. An experimental solution is to use an energy degrader or a scattering foil to provide a wide energy distribution of the incident beam in front of a DTOF spectrometer. The DTOF system can then select event-by-event the incident energy slice of the projectiles. The energy loss of projectiles can be measured simultaneously by this method over a wider energy range.

The energy resolution of a TOF spectrometer is given by

$$\frac{\Delta E}{E} = \frac{\beta^2\gamma^3}{\gamma - 1}\frac{\Delta v}{v}, \tag{4.3}$$

where γ and β are given by Eqs. (2.2) and (2.3). Clearly, the energy resolution decreases with increasing speed. Usually this cannot be compensated by an increase in the path length between the start and the stop detectors, which would also require a drastic enlargement of the stop detector to preserve the acceptance. Therefore, TOF systems for single-particle counting are practicable only up to about 20 MeV/u. The relative resolution of a TOF spectrometer of 30 m length and a time spread of 100 ps is in the range of a few percent only above 1000 MeV/u.

4.6.5 Doppler-shift attenuation

Doppler-shift attenuation (DSA) has been applied in nuclear physics for lifetime measurements of excited nuclear states decaying via γ-ray emission when the lifetime is of the order of the slowing-down time in the medium and the stopping power is known. The method can be reversed for ions with well-known lifetimes and can thus be utilized to measure the energy loss of heavy ions in bulk targets (Neuwirth *et al*., 1969; Arstila *et al*., 1995; Arstila, 2000). In such inverted DSA (IDSA) experiments, the ion speed is deduced from the Doppler-shifted energy of γ-rays emitted along the complete path of the ion in the material. Although it is not difficult to find suitable excited states in a variety of ions, proper x-ray line analysis is complicated. On the other hand, only the density of the medium must be known while target thickness does not enter. Combination of IDSA and transmission method offers a powerful tool to measure stopping powers of bulk materials for heavy ions (Arstila, 2000).

4.6.6 Electrostatic and magnetic spectrometers

Many energy-loss measurements have been performed with transverse dispersive magnetic and electrostatic spectrometers. At energies near and below the Bragg peak, this experimental method has the disadvantage of a too-small phase-space acceptance. The broad angular and charge-state distributions of such low-energy heavy ions require different solutions. Violent collisions cause scattering of projectiles out of the acceptance of the apparatus, *i.e.,* only restricted-stopping-power or restricted-straggling results are obtained under these conditions. The severeness of the restriction depends on Z_1, Z_2 target thickness and spectrometer acceptance (cf. Section 3.14). Conversely, high-resolution magnetic spectrometers can be successfully used when the energy is sufficient for these phenomena to become negligible, *i.e.*, at a few MeV/u for the

lightest ions (C–Ar), and over 15–20 MeV/u for the heaviest ones (U).

A high-resolution magnetic spectrometer determines the magnetic rigidity $B\rho$ of a particle with charge q and momentum p,

$$B\rho = \frac{p}{q} = \frac{E}{cq}\left(1 + 2\frac{M_1c^2}{E}\right)^{1/2}, \qquad (4.4)$$

from which the kinetic energy E can be extracted if q is known or if it can be deduced from the measurement. This technique has been extensively used for stopping-power measurements (Bimbot *et al*., 1986; Gauvin *et al*., 1987, 1990; Scheidenberger *et al*., 1994). Here the beam profile in the focal plane of the spectrometer is accurately measured. One centers the profile on the optical axis of the spectrometer, which then yields the curvature radius ρ. In addition, the dipole field B needs to be known as well as the rest mass of the projectile in a selected charge state. One can reach a relative precision of $\sim 10^{-4}$ and better on the energy, depending on the ion-optical resolution of the magnetic spectrometer.

The device is even more suitable for precision measurements if the ion-optical system can be operated in the mode of an energy-loss spectrometer (Geissel *et al*., 1992a). Such a spectrometer allows precise momentum measurements independent of the momentum spread of the incident beam. This means that the momentum spread of the incident projectiles is cancelled in the image at the final focal plane (Figure 4.8). This can be achieved by two dispersive spectrometer stages with equal momentum-resolving powers. Such precision measurements have been performed at intermediate energies (Bianchi *et al*., 1989; Schwab *et al*., 1990) and at relativistic velocities up to $v/c = 0.9$ (1.2 GeV/u) (Geissel *et al*., 1992a; Scheidenberger *et al*., 1996). These spectrometers have also been used successfully to measure angular and charge-state distributions (Schwab *et al*., 1990). In this case the angular distribution is deduced from particle tracking.

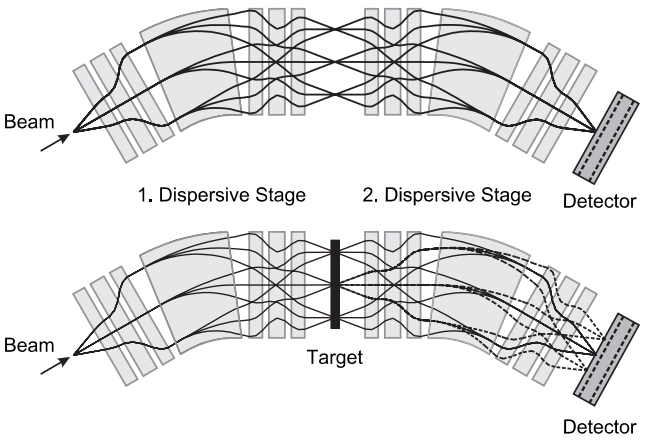


Figure 4.8. Principle of an energy-loss spectrometer. The main optical elements, the dipole and quadrupole fields, and the beam envelopes are shown in the dispersive plane. Upper panel: achromatic characteristics illustrated for three incident momenta and angles. Initial conditions do not contribute to the image size at the final focal plane. Lower panel: only momentum changes due to slowing down in the target will contribute to the image size in the final focal plane (dashed lines).

4.7 ASPECTS OF DATA ANALYSIS AND INTERPRETATION

Numerous data on heavy-ion stopping have been determined in transmission geometry with a limited acceptance by the detector system. The restricted acceptance angle can disturb the interpretation, especially at low energy when nuclear stopping contributes significantly. It is generally assumed that the energy-loss distribution measured within a restricted cone centered around the incident-beam direction reflects almost the full electronic but only a portion of the nuclear stopping power.

Theoretical aspects, in particular the concept of restricted energy loss, have been discussed in Section 3.14. Energy- and angle-dependent energy loss was studied experimentally by Geissel *et al*. (1984) and interpreted by Monte Carlo simulations with a code of Jackson (1980). Figure 4.9 shows measured specific energy losses *versus* target thickness. A recent theoretical study by Glazov and Sigmund (2003) confirmed that the best fit is achieved for those data by adopting an electronic stopping power of 2.72 MeVcm^2/mg, the value extracted in an alternative way by the authors of the experimental paper.

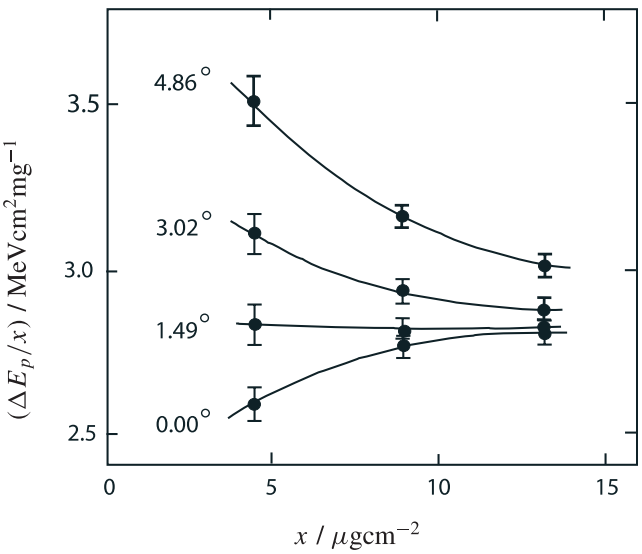


Figure 4.9. Measured specific energy loss for 16 keV/u ^{20}Ne ions in carbon *versus* target thickness for four angles of emergence of the beam. From Geissel *et al*. (1984).

Another problem is the shape of a measured energy-loss distribution. It is difficult experimentally to avoid the contribution of unwanted scattering events in different parts of a setup (apertures, edge zones of detectors) that give rise to a low-energy tail in a recorded spectrum. Therefore, most probable energy loss and half width are more reliable and reproducible experimental quantities than the mean value and variance that are prime quantities in theory (Lennard *et al*., 1986a). In an accurate comparison of experimental results with theory, such considerations have to be taken into account (cf. Section 3.12).

A severe experimental problem is related to the fact that conventional particle detectors work reliably only at moderate count rates. Therefore, some experimental groups, *e.g.*, Mertens and Krist (1982), performed measurements with detector systems positioned at emergent angles different from 0° in order to reduce the rate of detected projectiles. Such geometrical arrangements can severely affect results and interpretation. Systematic energy–angle measurements with heavy ions in the 25 keV/u energy region have demonstrated that the thickness dependence of the specific energy loss varies strongly with the angle of emergence (Geissel *et al*., 1984). With this taken into account, pre-equilibrium stopping could be resolved in agreement with theoretical predictions.

4.8 STOPPING OF STRIPPED IONS

4.8.1 Light ions

Since the appearance of ICRU Report 49 substantial progress has been made in experimental and theoretical work on light-ion, especially antiproton stopping. This includes new measurements (Møller *et al*., 1997, 2002; Møller, 1998) on a number of materials as well as nonperturbative theory (Arista and Lifschitz, 1999; Sigmund and Schinner, 2001a; Arista and Lifschitz, 2002). An example has been shown in Figure 3.6. The importance of these results lies primarily in successful descriptions of the Barkas–Andersen effect over a major portion of the velocity interval where it is important.

It is worth noting that the lower limit of some of the quoted antiproton measurements lies below 2 keV. An adequate expression for shell corrections is a prerequisite for a successful theoretical description by one single theory over a wide energy range down to so low a level. Arista and Lifschitz (1999) employ the Fermi-gas model for the stopping medium. In the binary theory (Sigmund and Schinner, 2001a) the essential ingredient is Eq. (3.14). The traditional theory of shell corrections is computationally intensive (Bichsel, 2002). It has been demonstrated that binary theory in conjunction with Eq. (3.14) is quite efficient and accurate (Sigmund and Schinner, 2002c).

4.8.2 Heavy ions

Until some time ago the Bethe theory in the form of Eq. (3.15) including the Fermi density effect was the accepted standard of reference for stopping measurements involving stripped ions, *i.e.*, for $v \gg Z_1^{2/3} v_0$. Initially, experimental evidence for the need of corrections came from range measurements in emulsion (Tarlé and Solarz 1978; Salamon *et al*., 1981; Ahlen and Tarlé, 1983). Subsequently, energy-loss measurements in transmission geometry by Scheidenberger *et al*. (1994) revealed systematic deviations of up to 10% (Figure 4.10). The graph demonstrates that data are well described by the Bethe formula only for $\kappa/2 = Z_1 v_0/v \leqslant 0.2$.

First attempts to reconcile this discrepancy were based on the second-order Born approximation and/or Mott cross section. The resulting enhancement in the stopping cross section originated in close collisions (Scheidenberger *et al*., 1994). This work stimulated the development of relativistic stopping theory on the basis of the Dirac equation by Lindhard and Sørensen (1996), which was discussed in Section 3.3.3. Figures 4.10 and 4.11 demonstrate improved agreement with experimental data at both high and moderate velocities.

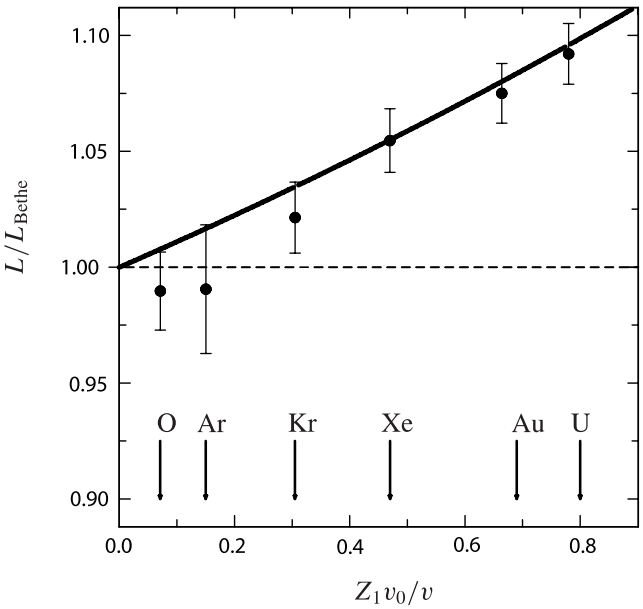


Figure 4.10. Ratio between measured stopping power and prediction from Bethe formula (3.15) for ions with $v/c = 0.84$ in Be *versus* Sommerfeld parameter $Z_1 v_0/v$. Measurements of Scheidenberger *et al*. (1994). Theoretical prediction of Lindhard and Sørensen (1996).

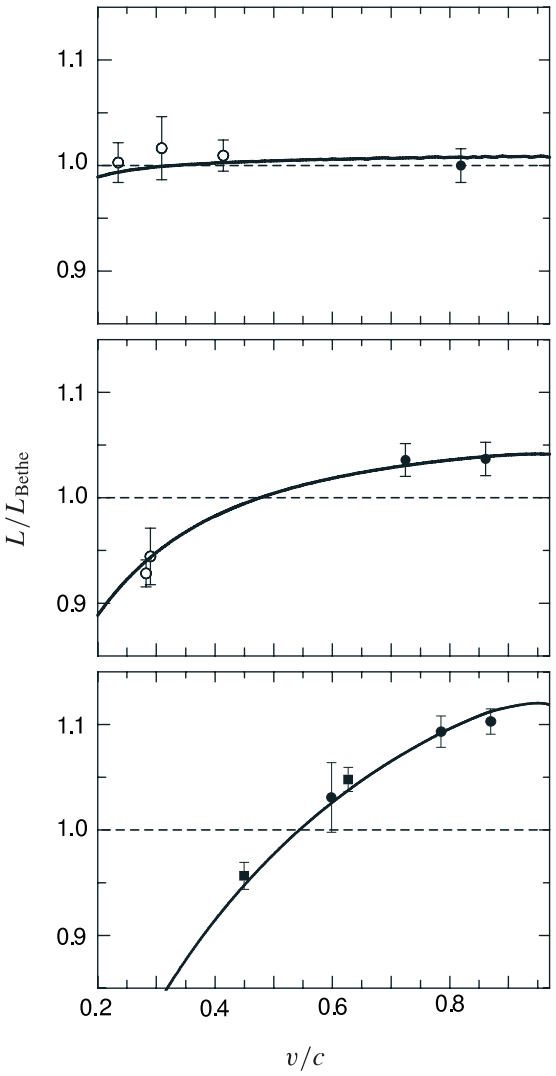


Figure 4.11. Stopping of O in Be (top), Kr in Be (middle) and Au in Cu (bottom): Experimental verification of the correction by Lindhard and Sørensen (1996). Data by Weick *et al*. (2000), Geissel and Scheidenberger (1998) (filled symbols) and Bimbot *et al*. (1989a,b) (open symbols).

While one may conclude that the stopping of bare heavy ions is well described by present theory, it is emphasized that the screening limit $v = Z_1^{2/3} v_0$ in Figure 3.2 marks the onset of *pronounced screening*, whereas the limit of complete stripping lies at a considerably higher speed, *i.e.*, $v \geqslant Z_1 v_0$. As an example, even at 950 MeV/u, *i.e.*, close to the rest energy, 9% of the ions in a Bi beam still carry an electron in charge equilibrium (Weick *et al*., 2000).

4.9 CHARGE-DEPENDENT STOPPING

Charge-dependent stopping is of interest from both a theoretical and an experimental point of view. Comparing theoretical predictions with experimental data taken under well-controlled conditions provides a stringent test. It is crucial here to carefully distinguish between the ion charge $q_1 e$ and the nuclear charge $Z_1 e$. While it has been tempting in the past to assume the stopping power to be proportional to q_1^2 to the lowest order, Barkas terms proportional to q_1^3 and a Bloch term proportional to q_1^4, the discussion in Section 3 makes it clear that none of these assertions can be correct in general:

1. According to Figure 3.2 the velocity regime in which projectiles tend to be screened lies entirely in the classical regime where not even the stopping power for a point charge is proportional to Z_1^2.
2. In the simplest picture, *i.e.,* Bohr theory plus screening, the relation between stopping power and ion charge depends on the ratio Z_1/Z_2 according to Figure 3.10; this dependence originates in the fact that the charge seen by a target electron depends on the impact parameter.
3. For the same reason, the Barkas–Andersen correction cannot be expected to show a straight q_1^3-dependence, even in the velocity regime where it is small.
4. Describing stopping by the Bethe theory requires addition of a Bloch correction. As this is a close-collision correction it is governed by an effective charge closer to[32] Z_1 than to q_1.

Experiments by Allison *et al*. (1962) and by Cuevas *et al*., (1964) with H and He ions in H_2 gas are mentioned here because they initiated this line of research and because they made it clear that energy loss by charge exchange may be significant. Partial stopping powers were measured by trajectory selection in a strong transverse magnetic field. The energy loss due to charge-changing collisions was determined to be 27 % of the total energy loss at 140 keV and 37 % at 400 keV.

In channeling experiments, frozen charges have been observed, *i.e.*, a certain fraction of a penetrating ion beam that has not undergone charge exchange (Datz *et al*., 1972). Distinction from ions having undergone one or more capture-loss cycles can be made by inspection of measured energy-loss spectra. Extraction of frozen-charge energy losses is rather straightforward for best-channeled particles for which the ratio between the cross sections for charge exchange and energy loss is exceptionally low.

Experiments by Datz *et al*. (1977) and Golovchenko *et al*. (1981) with well-channeled

[32]However, arguments supporting a Bloch correction based on the *ion charge* instead of the nuclear charge have been brought forward by Arista (2002).

heavy ions in gold and silicon, respectively, were performed to measure the Barkas–Andersen effect by comparison of frozen-charge stopping powers for a series of charge states of the same ion. The role of close electronic collisions in stopping is reduced in the channeling geometry. Therefore it may be more appropriate to consider an ion with a charge $q_1 e$ as being equivalent to a point charge $q_1 e$.

Since measured energy losses turned out to be strictly proportional to q_1^2 in most reported cases, the conclusion appeared tempting that there was no Barkas–Andersen effect under these conditions. A recent analysis of these experiments by Sigmund and Schinner (2001d) on the basis of binary stopping theory revealed a complex interplay between Barkas–Andersen correction and incomplete screening of the ion charge that can even affect the *sign* of the overall deviation from a strict q_1^2 dependence, in accordance with experiment. Similar conclusions were reached by Grande *et al*. (2002).

Cowern *et al*. (1984b), Read (1984) and Bridwell *et al*. (1986) measured energy losses of 3 MeV/u He^{2+}, Li^{3+}, C^{5+}, C^{6+}, O^{6+}, O^{7+}, and O^{8+} in amorphous carbon. The relative accuracy with He^{2+} as a reference was better than 1 %. Data were analyzed within the statistical scheme of Winterbon (1977). This enabled extraction of frozen-charge stopping powers and energy losses in charge exchange. A most useful result of this analysis is the close agreement between this value and an estimate based upon the sum of the energy losses in a capture-loss cycle [Eq. (3.40)] (Cowern *et al*., 1984a). Another important result is the observation that successful analysis can require inclusion of at least one excited projectile state in addition to the charge states involved (Read, 1984).

The experiments were less informative than anticipated with regard to higher-order Z_1 corrections. Apart from the general problems mentioned above, measurements could be performed only at one single energy. Frozen-charge stopping powers from that work have been shown to agree well with calculations from modified-Bohr and binary theory (Sigmund, 1997; Sigmund and Schinner, 2001c).

Similar work at higher projectile energies, ~10 MeV/u, was performed by Ogawa *et al*. (1992a,b, 1993, 1996a,b 1997) with H, He, Li, C, and O ions in carbon. Stopping powers for ions in selected incident and emergent charge states were measured, and the results used to extract stopping parameters. Independent statistical analysis of some of these data by Glazov and Sigmund (1997, 2000) confirmed the validity and high accuracy of the extracted stopping parameters, which also have been compared to theoretical predictions (Sigmund and Schinner, 2002c; Glazov, 2002a).

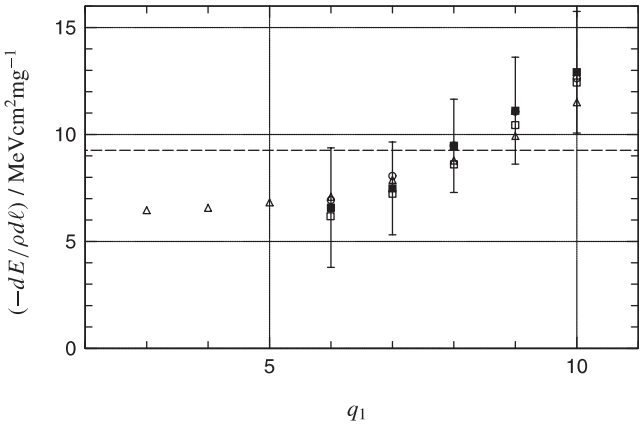


Figure 4.12. Frozen-charge stopping powers for Ne in carbon. Experimental data (filled squares) from Blazevic *et al*. (2002). Calculations from Maynard *et al*. (2002b) (circles), Sigmund and Schinner (2002b) (triangles) and Grande and Schiwietz (2002) (open squares).

Experiments in this category were performed for 2 MeV/u Ne by Blazevic *et al*. (2000). Here, incident and outgoing charge states were independently selected. Previous studies focused on equal entrance and exit charge states to avoid systematic errors due to changes in the magnetic field. Cross sections for charge exchange and energy losses in carbon foils were measured. Figure 4.12 shows that theoretical estimates by Grande and Schiwietz (2002), Maynard *et al*. (2002b) and Sigmund and Schinner (2002b) reproduce these data very well.

Charge-state dependence of the stopping power has been studied with 60 MeV ^{58}Ni projectiles in several incident charge states at a high-resolution Q3D spectrograph — a magnetic spectrograph with a quadrupole lens and three dipole magnets — in carbon (Frey *et al*., 1996) and argon (Schmelmer *et al*., 1998a). Theoretical analysis of these data has so far been less successful (Sigmund and Schinner, 2002c). Obvious complications are the large number of states involved and low beam speed. Energy loss and charge exchange may be tightly correlated (Schmelmer *et al*., 1998a). Surface effects and dynamical screening by target electrons have been invoked as additional complications.

4.10 EQUILIBRIUM STOPPING

4.10.1 General considerations

A survey of available experimental data on stopping of heavy ions will be given in Section 5. Generally one finds a consistent behavior in the trends, but significant scatter between the results of different authors, in particular when different techniques are applied. An example of good agreement within

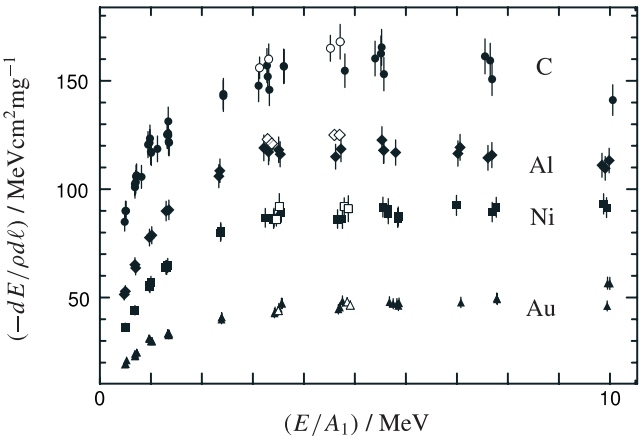


Figure 4.13. Stopping powers for uranium ions in C, Al, Ni and Au (top to bottom), measured by time-of-flight (filled symbols) and recoil-proton method (open symbols) (Geissel, 1982; Bimbot *et al*., 1980).

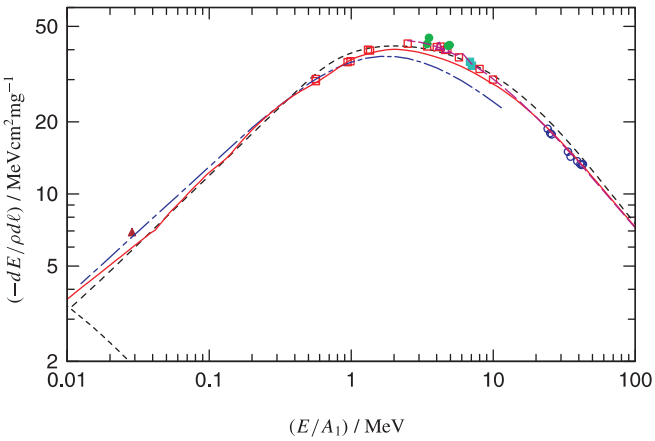


Figure 4.14. Equilibrium electronic stopping power of aluminium for krypton ions: Dashed line: Hubert *et al*. 1990; solid line: Ziegler (2003); dot-dashed line: Northcliffe and Schilling (1970); thick short-dashed line: PASS; thin short-dashed line: unrestricted nuclear stopping. Experimental data from Bimbot *et al*. (1978) (filled circles), Gauvin *et al*. (1990) (open circles), Teplova *et al*. (1962) (filled triangles), Bimbot *et al*. (1980) (open triangles), Geissel and Scheidenberger (1998) (open squares) and Hahn *et al*. (1981) (filled squares).

experimental errors is given in Figure 4.13 in which stopping powers determined by time-of-flight measurements (Geissel, 1982) are compared with data found by the recoil-proton method (Bimbot *et al*., 1980). Similar comparisons are more difficult in the keV/u regime because of uncertainties concerning the nuclear-stopping correction. Often such comparisons yield systematic deviations between 5 and 10 % (Ward *et al*., 1979).

As indicated in Section 4.8, heavy-ion stopping powers can be calculated reliably by the theory of Lindhard and Sørensen (1996) in the energy range from 200 MeV/u up to 160 000 MeV/u, the highest energies for which penetration properties have been measured with heavy ions. The agreement between theory and data is at the best about 2%. For 200–500 MeV/u the charge-state population, partial stopping powers and screening have to be included for the heaviest projectiles to achieve this accuracy (Weick *et al*., 2002; Sørensen, 2002).

For ions heavier than argon, the tabulations by Northcliffe and Schilling (1970), Ziegler (2001), and Hubert *et al*. (1990) have served as standards of reference for many years. Figure 4.14 shows quite good agreement for Kr in Al between experimental data and tabulations by Hubert *et al*. (1990) and Ziegler (2001) and calculations by the PASS code of Sigmund and Schinner (2002b).

Figure 4.15 shows limitations. While pronounced gas–solid differences are found experimentally between Ti and Ar and between Zr and Kr, the tabulation by Ziegler (2001) does not reproduce this feature. Clearly, the adoption of an adequate expression for the equilibrium ion charge — or equilibrium charge fractions — is essential in the prediction of stopping powers for heavier ions.

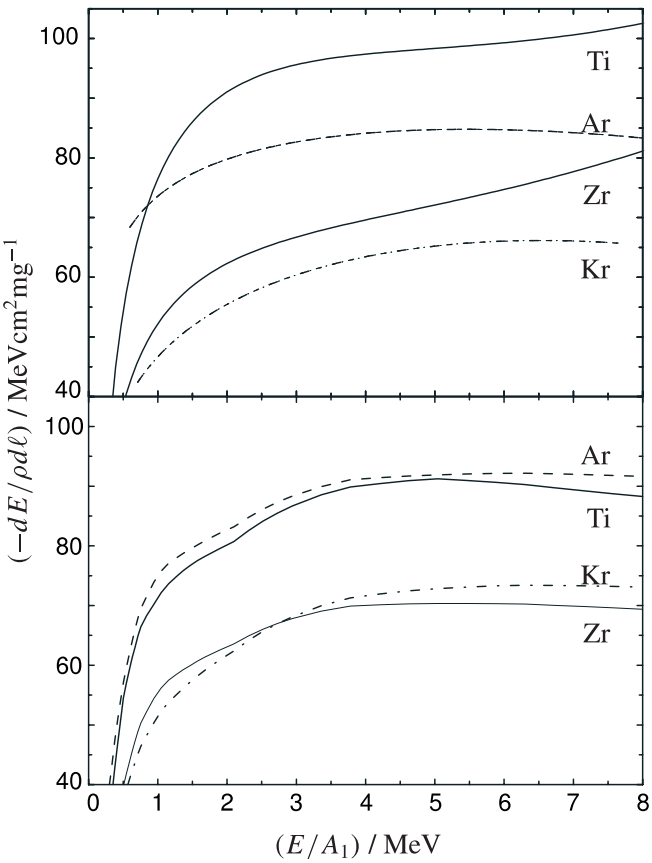


Figure 4.15. Gas–solid differences for uranium ions. Experimental data from Geissel (1982) and Bimbot *et al*. (1980) (upper graph) compared with predictions of Ziegler (2001) (lower graph). Lines represent fits through experimental and calculated data points.

4.10.2 Screening in high-velocity stopping

The case of high-energy heavy ions carrying electrons mainly in the K- and L-shells is characterized by good knowledge of charge-state distributions and charge-exchange cross sections. However, caution is indicated in stopping measurements because the thickness to reach charge equilibrium may be very large, such as 660 and 40 mg/cm^2 for 1000 MeV/u gold in beryllium and lead, respectively. This can represent a significant part of the total target thickness. At the same time the initial charge state of ions can be quite different from equilibrium. Therefore a stripper target is normally placed in front of the sample. Moreover, the target thickness must be chosen large enough to ensure that the measured energy loss is insensitive to the selected emergent charge state for the $B\rho$ analysis with the magnetic spectrometer (cf. Section 4.6.6).

Figure 4.16 shows measured equilibrium stopping powers for Au, Pb, and Bi in seven materials as a function of energy, divided by the theoretical prediction of Lindhard and Sørensen (1996). The good agreement in the upper-left graph down to 500 MeV/u indicates dominance of bare nuclei in the charge-equilibrated beam. Screening causes a decrease below this energy which amounts to up to 9% at 100 MeV/u.

An attempt to improve the theoretical estimate by insertion of an effective charge similar to Eq. (3.33) and applying shell and Barkas–Andersen corrections (Geissel and Scheidenberger, 1998) leads to the upper-right graph. The agreement has improved, but it is also evident that an effective charge independent of Z_2 leads to systematic deviations up to 5%, as was found earlier by Bimbot *et al*. (1978).

As a final step the theoretical estimate was based on Eq. (3.32), partial stopping powers corrected for screening and charge fractions $P(v, q_1)$ defined in connection with Eq. (3.31) from measured equilibrium distributions. The bottom graph shows much improved agreement, almost within experimental error but with a slight (about 1 %) systematic deviation.

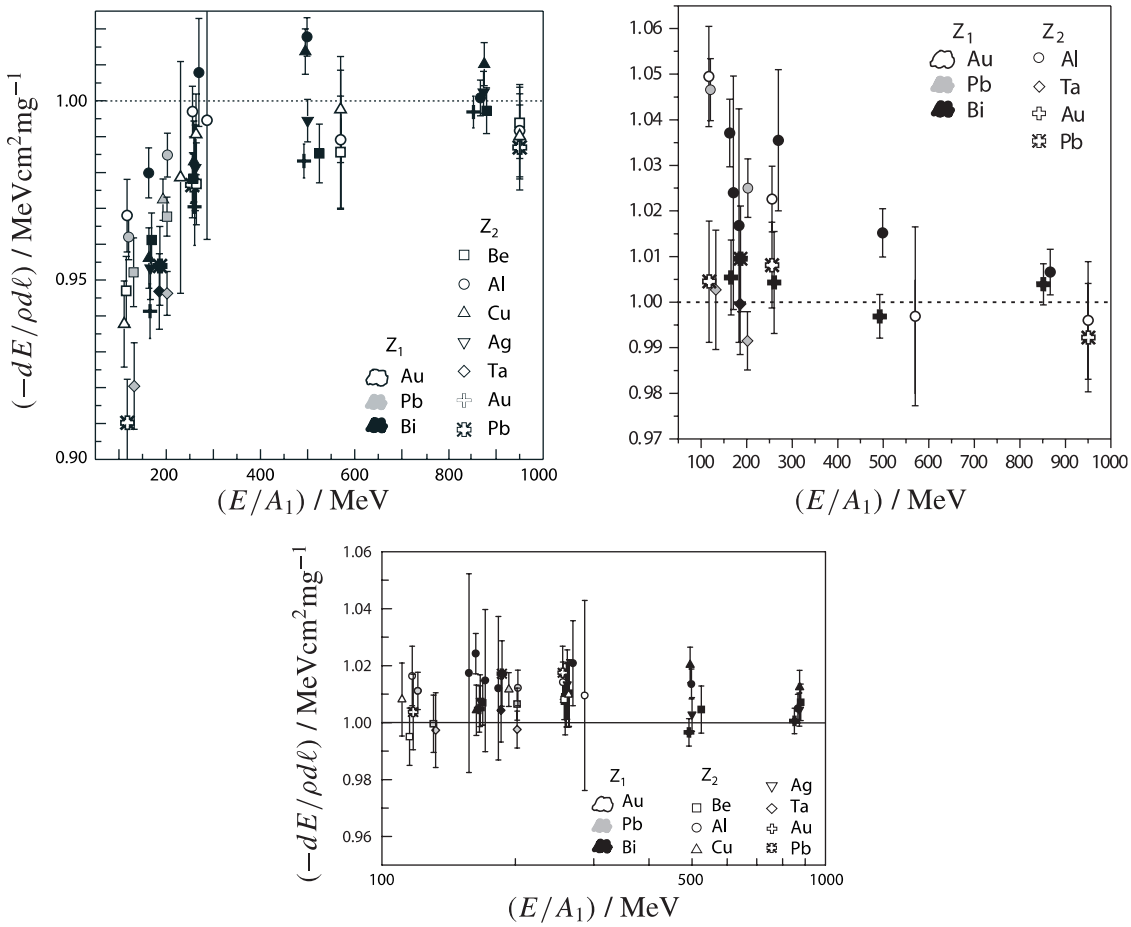


Figure 4.16. Experimental equilibrium stopping powers of Au, Pb and Bi ions projectiles in different solid targets normalized by values calculated according to Lindhard and Sørensen (1996). Upper left: calculation for stripped ions. Upper right: including screening, shell and Barkas–Andersen correction. Bottom: calculated from Eq. (3.32). Open, gray and black symbols denote Au, Pb, and Bi ions, respectively. Figure from Weick *et al*. (2000).

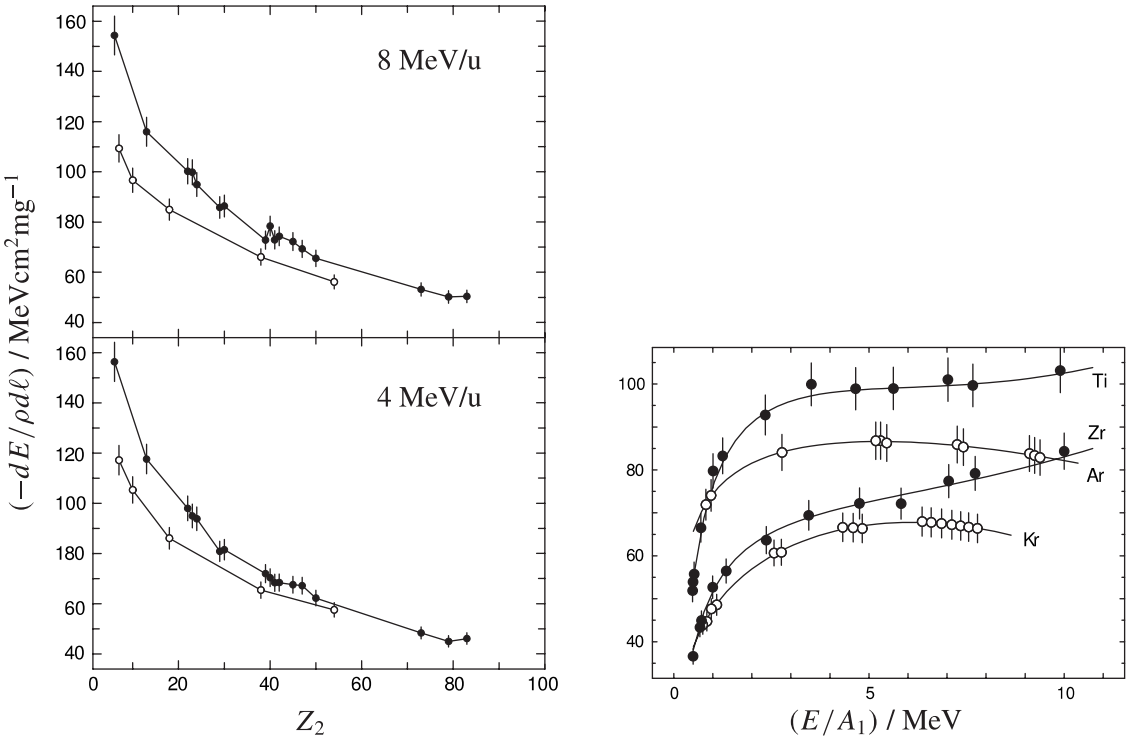


Figure 4.17. Stopping of uranium in different solids (filled circles) and gases (open circles). Left: *versus* Z_2 at 8 MeV/u and 4 MeV/u; right: *versus* energy for Ti, Zr, Kr, and Ar. Lines to guide the eye. Figures from Geissel (1982).

4.10.3 Gas–solid effect in high-velocity stopping

It was noted in Section 4.5 that equilibrium charge states of swift heavy ions are higher in solid than in gaseous targets. The expected accompanying effect in the equilibrium stopping power interferes with Z_2 structure and is hence difficult to verify unambiguously.

Experiments by Geissel *et al*. (1982) with partially stripped heavy ions from Kr to U at several MeV/u showed stopping powers of gases up to 20% below those for solids at neighboring Z_2 (Figure 4.17, left). Figure 4.17 (right) shows that the effect depends on ion energy. Above 1 MeV/u, stopping powers of Ar and Kr are lower than those of Ti and Zr, respectively. In the absence of a gas–solid effect, the higher I-values of Ar and Kr would suggest that the difference should *decrease* with increasing energy.

Systematic studies on 12 gases from H_2 to Xe confirmed the existence of the effect from 2 to 13 MeV/u (Bimbot *et al*., 1989a,b) and later at higher energies (Herault *et al*., 1991; Bimbot *et al*., 1996, 2000) (cf. Figure 4.18, (left). The connection to the charge state is demonstrated by the disappearance of the effect for fully stripped ions, *e.g.*, for 25 MeV/u oxygen in Figure 4.18 (right).

Note that the gas–solid difference in stopping power for a given gas–solid difference in charge state depends on the relation between stopping power and charge state. Figure 3.10 would suggest a pronounced effect for $Z_1 \gg Z_2$ and a negligible effect in the opposite limit. Figure 4.18 (right) appears to provide qualitative evidence supporting such a behavior.

Figure 4.19 shows a comparison of three tabulations with experimental data for uranium ions up to 10 MeV/u. The table by Hubert *et al*. (1990) shows the best agreement for solids, while none of them describes the gas data.

4.10.4 Stopping in plasmas

Stopping in plasmas must differ from stopping in cold matter (Deutsch *et al*., 1983; Arnold and Meyer-Ter-Vehn, 1987) for two main reasons:

1. The plasma state affects the charge-state evolution of the beam because of a drastic reduction of the cross section for electron capture and, consequently, an increased population of high charge states.
2. The excitation spectrum of the medium is governed by free electrons and, hence, becomes density-dependent.

For both reasons, the stopping power of a plasma is expected to be greater than that of a cold gas. Figures 4.20 and 4.21 show supporting experimental evidence.

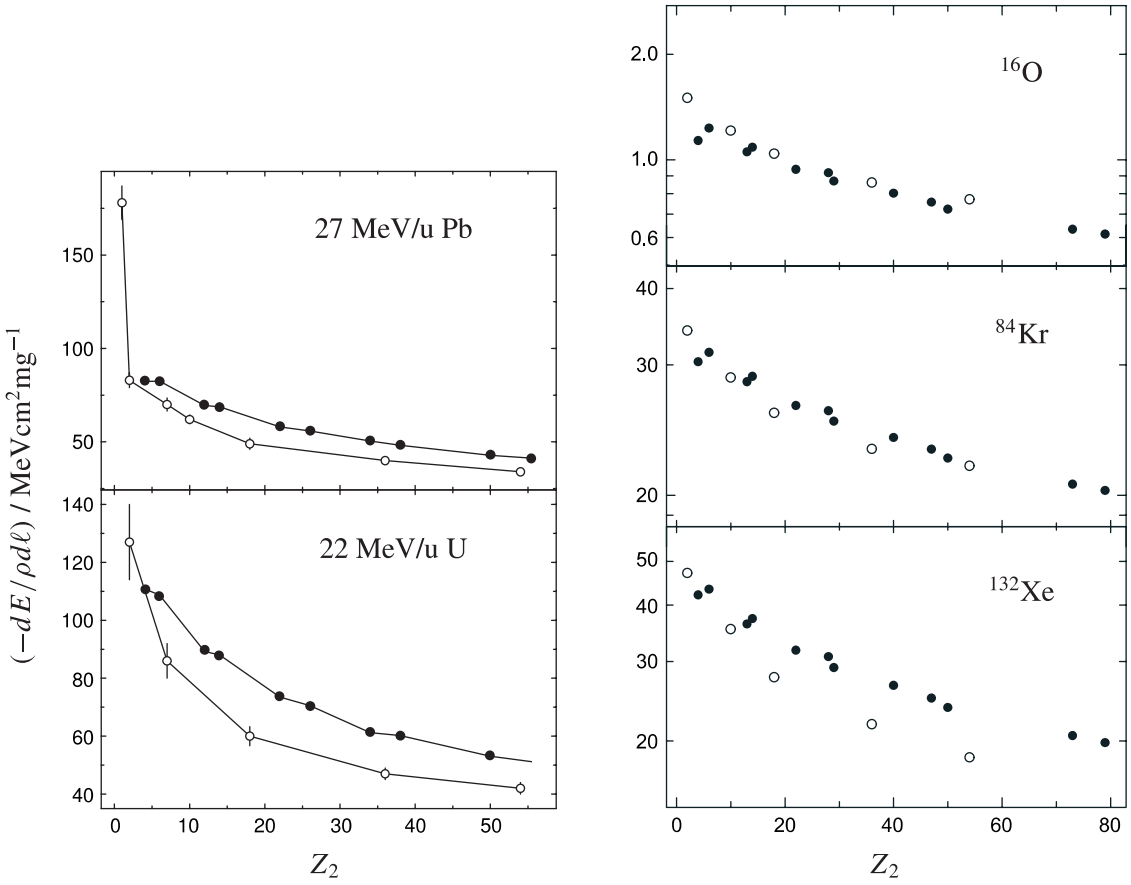


Figure 4.18. Gas–solid effect in equilibrium stopping at high speed. Filled symbols: solids; open symbols: gases. Lines to guide the eye. Left: for 27 MeV/u Pb and 22 MeV/u U ions. Figure from Bimbot *et al*. (1996). Right: for 25 MeV/u O, Kr, and Xe. Oxygen is fully stripped. The vanishing gas–solid difference for this ion demonstrates the relation to the charge state. Figure from Herault *et al*. (1991).

4.11 ENERGY-LOSS STRAGGLING

4.11.1 Stripped and few-electron ions

Figure 4.22 shows a comparison between experimental data on straggling for O, Xe, Au, and U in different materials by Scheidenberger *et al*. (1996) with the prediction of the theory of Lindhard and Sørensen (1996), both normalized to the relativistic Bohr formula. It is seen that deviations of up to a factor of 2.5 from Bohr straggling are well reproduced by the theory. The predicted decrease at much higher energies (cf. Figure 3.25), has not yet been tested experimentally.

For an ion carrying electrons, charge-exchange straggling contributes to the observed width of the energy-loss profile. Eq. (3.84) describes the situation when only three states are involved.

In this connection, Figure 4.23 is of interest, which shows the mean free path λ for charge exchange of H-like ^{209}Bi calculated with the computer code GLOBAL (Scheidenberger *et al*., 1998) in Be, Al, Cu, Ag, and Au. It is seen that λ decreases drastically with increasing Z_2. This observation can be utilized for switching on or off the contribution from charge exchange to straggling.

Figure 4.24 shows energy-loss straggling of ^{209}Bi in different solid materials at 1000 and 200 MeV/u incident energy. The results are compared with predictions of the theory of Lindhard and Sørensen (1996)[33] and with results from a Monte Carlo simulation. The Monte Carlo code operated with calculated mean free paths for capture and loss and mean energy loss according to Lindhard and Sørensen (1996). Agreement with experiment is found at 1000 MeV/u for heavier target materials, irrespective of the screening model. Pronounced deviations are observed for beryllium that are asserted to be due to deficiencies in the description of charge-exchange straggling. At 200 MeV/u some contribution is missing also for the heavy target materials.

[33]In the reported measurements, the mean energy loss was 10–30 % of the incident energy E_0. This was taken into account by means of Eq. (3.76).

4.11.2 Heavily screened ions

At energies near the Bragg peak, energy-loss straggling data for heavy ions are available for gases (Al-Bedri and Harris, 1975; Efken *et al*., 1975; Geissel *et al*., 1983b). Representative results for 1.4 MeV/u Pb, Xe, and Kr ions in xenon gas are shown in Figure 4.25 (Geissel *et al*., 1983b). The experimental data can be well reproduced for up to 30 % energy loss with the Firsov–Hvelplund formula (3.101). Numerous data exist for solid targets (Anthony, 1983; Antolak *et al*., 1991; Brière and Biersack, 1992; Cowern *et al*., 1979, 1983a; Goppelt-Langer *et al*., 1996; Hahn *et al*., 1981; Ouichaoui *et al*., 2000; Ouichaoui and Bouzid, 2002; Schmelmer *et al*., 1998b; Takahashi *et al*., 1979; Wu *et al*., 1994; Yang *et al*., 1993). Thickness non-uniformities of self-supporting solid targets frequently tend to mask the physical contribution. A detailed analysis with recent theory (Sigmund and Schinner, 2002a) might be helpful but has not yet been performed.

Reliable energy-loss straggling data in the energy domain of keV/u are difficult to find. Apart from gas data (Hvelplund, 1971, 1975) there are data on solid films by Andersen *et al*. (1978, 1980), Araujo *et al*. (2002), Geissel *et al*. (1982), Lennard *et al*. (1986b), and Lennard and Geissel (1987). Figure 3.32 shows a comparison between experimental data for lithium and a recent calculation. An interesting projectile dependence and correlation with inner-shell excitation were observed in systematic investigations on amorphous carbon foils at 16 keV/u (Lennard *et al*., 1986b).

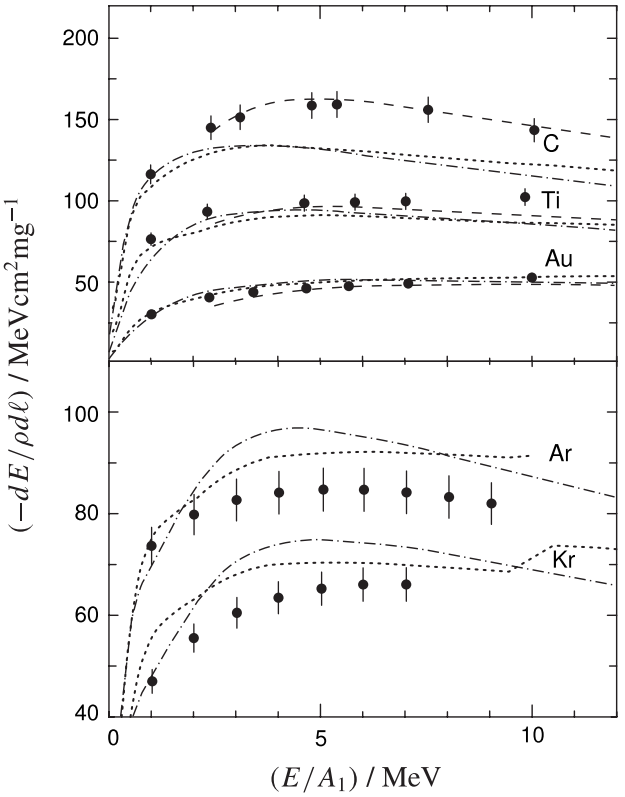


Figure 4.19. Stopping of uranium in solids and gases. Experimental data from Geissel (1982) compared with semiempirical predictions: Hubert *et al*. (1990) (dashed lines); Ziegler (2001) (dotted lines); and Northcliffe and Schilling (1970) (dash-dotted lines).

4.12 ANGULAR DEFLECTION

4.12.1 Experimental techniques

Angular distributions can be measured by a detector system counting the scattered projectiles in a selected solid angle. A detector at a fixed

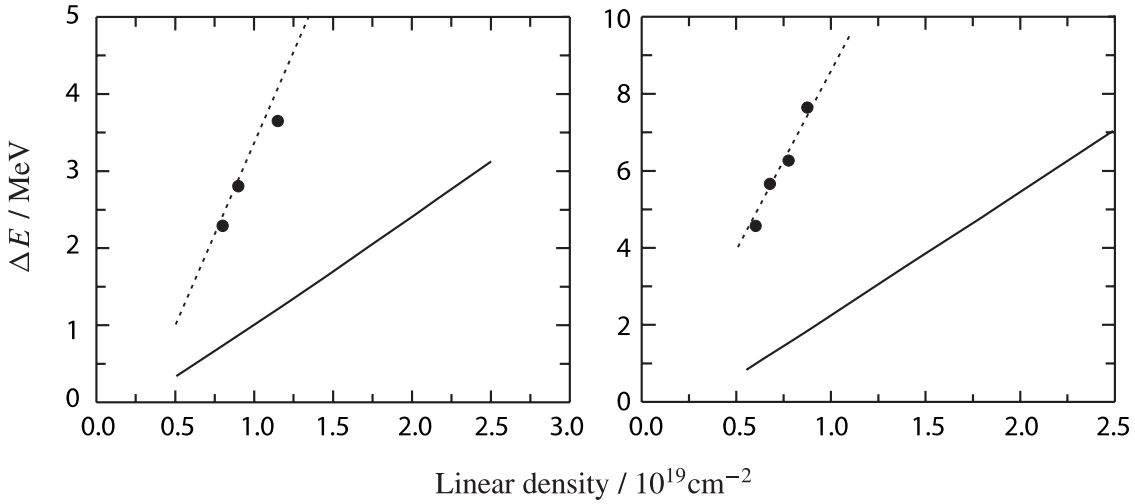


Figure 4.20. Energy loss of 1 MeV/u S^{7+} (left) and 0.9 MeV/u Br^{6+} (right) in hydrogen. Solid circles: measurements for a fully ionized hydrogen plasma. Solid and dotted lines refer to calculations at room temperature and in a fully ionized hydrogen plasma on the basis of a theoretical model by Deutsch *et al*. (1989). From Gardès *et al*. (1992).

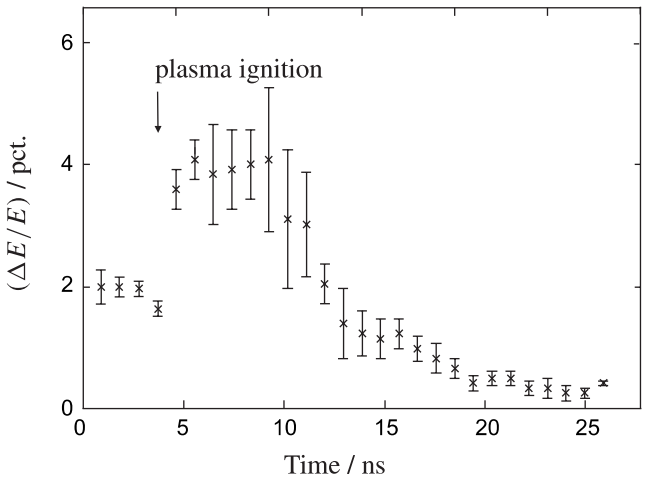


Figure 4.21. Relative energy loss of 5 MeV/u ^{68}Zn ions in laser-produced carbon plasma as a function of time. Enhanced energy loss is observed at the time of ignition. Figure from Roth *et al*. (2000).

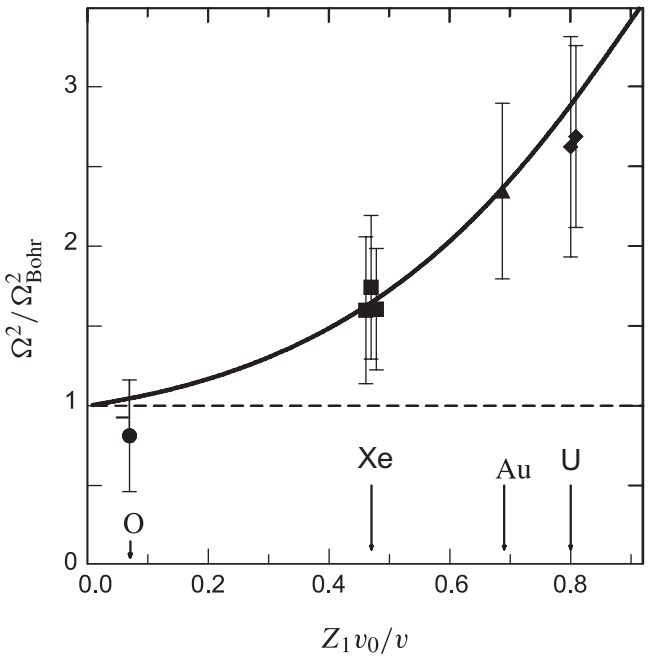


Figure 4.22. Measured energy-loss straggling normalized to relativistic Bohr formula for different projectiles at 785 MeV/u as a function of the Sommerfeld parameter $Z_1 v_0/v$ (Geissel and Scheidenberger, 1998). Theoretical prediction of Lindhard and Sørensen (1996) (solid line). Experimental data taken for $0.81 \leqslant v/c \leqslant 0.87$ were transformed to $v/c = 0.84$ (785 MeV/u).

position can be used for normalization, while a movable counter with a small entrance aperture maps the angular range. This simple setup can be modified by using position-sensitive detectors or by combination with energy or velocity measurements (Geissel *et al*., 1985).

Angular scattering of ions emerging from a target placed at the entrance of an achromatic

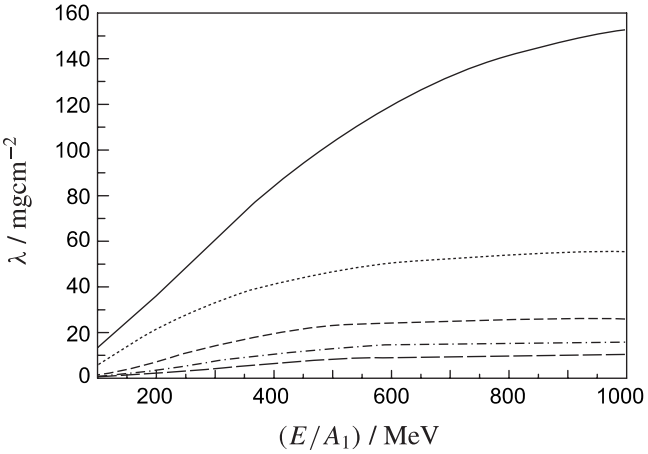


Figure 4.23. Mean free path for charge exchange of $^{209}Bi^{82+}$ in Be, Al, Cu, Ag and Au calculated by Scheidenberger *et al*. (1998).

spectrometer like LISE at GANIL (Anne *et al*., 1988) can be measured by recording the position distribution in the dispersive coordinate x at the final focal plane. This conversion of an angular distribution into a position distribution is achieved by special requirements for the imaging matrix of the ion-optical system: The matrix element for x-position magnification from the target to the final image plane is set to zero, and the elements characterizing an achromatic condition in first-order optics are required in addition. The first-order matrix coefficient has to be determined by calibration. In principle the accuracy of the method is limited by the influence of possible higher-order image aberrations that can be kept small by applying hexapole correction fields. Furthermore, one has to ensure that the spectrometer acceptance does not truncate the angular distribution, a requirement which is easy to fulfill at high energies. The technique has been used by Anne *et al*. (1988) and Schwab *et al*. (1990) at intermediate energies and by Scheidenberger *et al*. (1994) in the relativistic regime.

4.12.2 Multiple scattering

Multiple angular scattering of swift heavy ions is mainly caused by elastic nuclear scattering. Over a very wide energy range and for most heavy-ion-target combinations the classical treatment outlined in Section 3.13 is applicable. Good agreement with the theory of Sigmund and Winterbon (1974) has been established in many heavy-ion experiments in the low-MeV energy range (Andersen and Bøttiger, 1971; Andersen *et al*., 1972, 1974; Besenbacher *et al*., 1978; Geissel *et al*., 1985; Knudsen and Andersen 1976; Sidenius *et al*., 1976). Figure 4.26 indicates that the scaling variables used by Meyer (1971) and

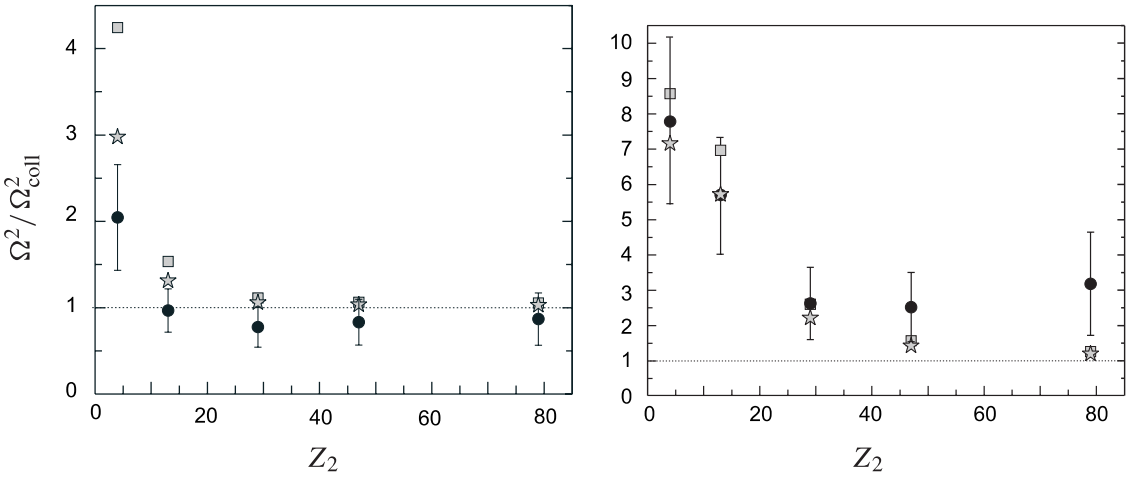


Figure 4.24. Measured energy-loss straggling (full circles) of ^{209}Bi projectiles in different solid target materials compared to Monte Carlo simulation assuming point-like projectiles (squares) and a realistic charge distribution (stars), both normalized to theory by Lindhard and Sørensen (1996). Left: incident energy 1000 MeV/u and mean energy loss 17 %. Right: incident energy 200 MeV/u and mean energy loss 22 %.

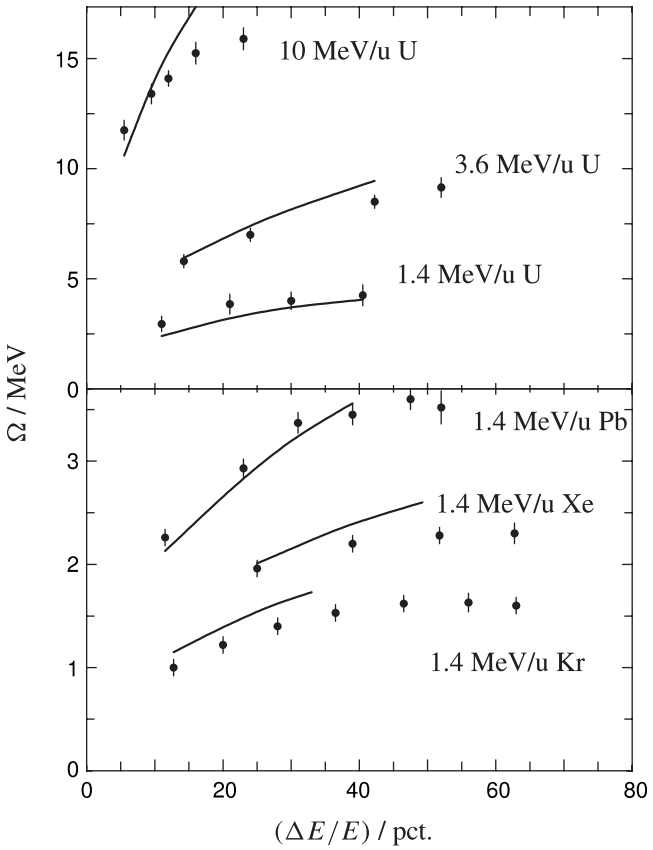


Figure 4.25. Energy-loss straggling for Kr, Xe, Pb and U in Xe: Ω compared with the Firsov–Hvelplund formula (3.01).

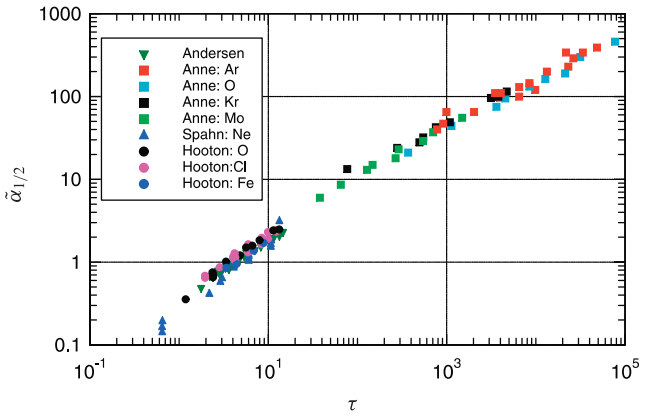


Figure 4.26. Scaled multiple-scattering halfwidth *versus* scaled thickness τ, [Eq. (3.108)], for a wide range of ions (specified in legends), targets and energies. Measurements of Andersen and Bøttiger (1971), Spahn and Groeneveld (1975), Hooton *et al.* (1975) and Anne *et al.* (1988).

Sigmund and Winterbon (1974) accurately describe the behavior beyond the range covered by the original tabulations.

Experiments at 85 MeV/u (Schwab *et al.*, 1990) required the extension of the τ range. For the large target thicknesses used in such high-energy experiments, the short-range portion of the screening will be most important. This is not well described in the Thomas–Fermi atomic model. Therefore, realistic electron densities were calculated for each target atom. The multiple-scattering distribution obtained was then approximated by power-law scattering using the method of Marwick and Sigmund (1975). The agreement of the data with the extended Sigmund–Winterbon theory was within 5 % (Schwab *et al.*, 1990). The result could be summarized by the power law for the diffusion limit, $\tilde{\alpha} = \text{const} \times \tau^{1/2}$ (Figure 4.27). It is important here to use the relativistic relation (3.110) in the determination of the scaling variable from Eq. (3.108).

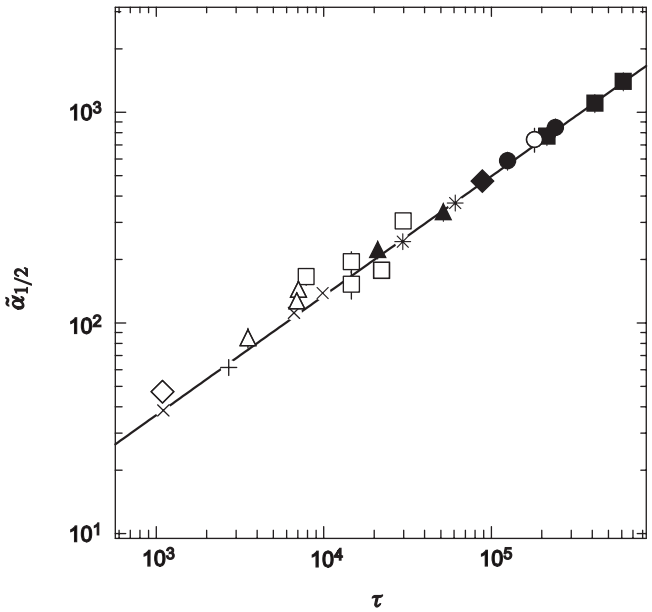


Figure 4.27. Comparison of measured half-widths of projected angular distributions with a power-law formula according to the SW theory (Sigmund and Winterbon, 1974). The results of a linear least-square fit are given in the plot. The data are taken from Anne *et al*. (1988), Schwab *et al*. (1990), (Scheidenberger *et al*. (1998): 85 MeV/u Ar → Al (full circles), Pt (full square), Au (full triangles), 1500 MeV/u C → Pb (asterisk), 940 MeV/u U → Al (open circles), Ti (open squares) and Au (open triangles).

4.13 RANGE AND RANGE STRAGGLING

Basic range quantities have been defined in Section 2.2. Experimental studies require implantation and subsequent analysis of the implanted sample. Numerous experimental methods are available to determine the location of implanted projectiles (Mayer *et al*., 1970; Bird and Williams, 1989).

For very low-energy ions, ranges and range stragglings can be measured by a new method involving the electron recoil detection analysis (ERDA) technique. This method is well adapted to determine very low ranges for keV/u projectiles. For example, in the work of Sillanpää *et al*. (1999), it was used to study the depth distribution of 5–100 keV/u He ions implanted into matrices of several elements (Mo, Cr, Cu and Ni). After the implantation step, the samples were irradiated by a 25 MeV oxygen beam. The energy distribution of the He atoms ejected from the sample by elastic scattering was measured at a precise angle to the incident beam. The profile concentration of the implanted atoms — which led to range and range-straggling determinations — could be deduced from the analysis of this measured energy distribution. Of course such an analysis requires the knowledge of the stopping powers for both the incident oxygen ions and the recoiling helium ions in the matrix. But the energy of these ions is in the MeV region, and their stopping powers are much better known than those of helium in the keV domain, which are the object of the experiment.

Finally the stopping powers can be derived from such range measurements using numerical simulations.

At high energy, ranges can be measured in transmission, where ions penetrate thin foils and are recorded in a detector system. Transmitted ions are recorded as a function of the total penetrated thickness. The primary result is a number–distance curve which, after differentiation, is a good approximation for range distributions at high energies. However, particles are lost also by wide-angle deflection. Moreover, detector systems have thresholds and dead layers. This can limit the registration of low-energy ions.

Measured range distributions represent integral properties. Although they have great practical importance, they contribute less to the understanding of stopping. Nevertheless, stopping parameters have been extracted from ranges measured at different incident energies (cf. Section 3.15.7). Examples will be mentioned in Section 5; this can be utilized to estimate nuclear stopping if electronic stopping is either negligible or assumed to be known (Kalbitzer *et al*., 1976), or vice versa (Ziegler *et al*., 1985).

4.14 SUMMARY

Reliable stopping measurements require good control of beam and target properties as well as the experimental method.

Earlier problems in achieving adequate beam properties have been resolved. High-purity beams of heavy ions of virtually any element can be produced over a very wide range of beam intensities and energies. Moreover, if beams of a particular element in a particular energy range should be difficult or impossible to produce it is unlikely that there will be a need for stopping data.

Control of target properties is much more of a critical issue, and requirements on target purity, uniformity and thickness measurement summarized in this section are far from being fulfilled in numerous experimental studies. It is hoped that this report can contribute to the development of common standards in this important area.

While several independent techniques are available to measure stopping parameters, systematic comparisons of measurements on identical targets invoking different techniques have had a significant impact in light-ion stopping and would be highly desirable also in heavy-ion stopping, in particular at intermediate and low beam energies.

The following list of areas in which further experimental work would be desirable concludes this section:

- Very little experimental information is available in general on stopping in elemental (solid and liquid) insulators.
- Systematic stopping measurements are needed for numerous materials of practical importance such as silicon, compound semiconductors and metal oxides.
- Studies on deviations from the Bragg additivity for ions heavier than helium are almost completely missing. Measurements on alkali halides would be of particular interest in this context.
- Studies of Z_1 structure in low-velocity stopping, in particular for insulators and gas targets, are needed to delimit the range of validity of existing theory.
- Studies of Z_2 structure for gaseous and solid materials are desirable to confirm or reject the existence of a gas-solid effect at low beam velocities.
- Measurements of straggling, especially in gases in the velocity range around the Bragg maximum, are of general interest.
- In particular, systematic measurements involving different ion-target combinations are needed to separate the effects of charge exchange and correlation in straggling.

Journal of the ICRU Vol 5 No 1 (2005) Report 73
Oxford University Press
doi:10.1093/jicru/ndi012

5 DATA COMPILATIONS, TABLES, PROGRAMS AND COMPARISONS WITH EXPERIMENTAL DATA

5.1 INTRODUCTORY SURVEY

Experimental data on heavy-ion stopping prior to 1980 were compiled and presented graphically by Ziegler (1980). These data were employed in the development of a comprehensive scaling procedure for stopping powers of all elements for all ions by Ziegler *et al*. (1985), which forms the experimental basis for the electronic-stopping part of the TRIM (now SRIM) code. The database and the code have been updated regularly. Some citations and many data plots are now available on the Internet (Ziegler, 2003).

A central piece of input to the present report is an extensive compilation of stopping data following up on work by Berger and Paul (1995). More than 1800 data files have been extracted from the literature for projectiles with $Z_1 \geqslant 3$. Targets are about 60 elements (solid and gaseous), about 30 compounds, and air. Only equilibrium stopping powers are considered.

Table 5.1 shows a survey of elemental ion–target combinations up to $Z_1 = 36$. It is seen that materials best covered by experimental data include carbon, aluminium, nickel, silver, and gold, and to some extent copper and silicon, whereas nitrogen, oxygen and argon, and to some extent carbon and neon are dominating ions. Considering that one data set rarely covers more than one order of magnitude in energy, the conclusion is inevitable that only a very small fraction of the total parameter space is covered by experimental data.

Graphical presentations of most of these data (also for heavier ions), references to the original publications, and experimental errors as given in the papers can be found on the Internet (Paul, 2003).

5.2 SCALING PROCEDURES

5.2.1 General

In the absence of absolute theoretical predictions, establishing scaling relations used to be a necessity for interpolation between experimental data as a function of speed v and atomic numbers Z_1 and Z_2. The effective-charge postulate (Northcliffe, 1960, 1963) described in Section 3.4.3 has served this purpose most often. The effective-charge fraction[34] γ is defined empirically *via*

$$\gamma^2 = \frac{S(v, Z_1, Z_2)/Z_1^2}{S(v, Z_{1,\mathrm{ref}}, Z_2)/Z_{1,\mathrm{ref}}^2} = \frac{L(v, Z_1, Z_2)}{L(v, Z_{1,\mathrm{ref}}, Z_2)}, \qquad (5.1)$$

where S and L denote stopping cross sections and stopping numbers, respectively, and $Z_{1,\mathrm{ref}}$ specifies a reference ion, in practice hydrogen or helium.

Definition (5.1) is used in connection with equilibrium stopping powers. According to the underlying reasoning described in Section 3.4.3 the denominators in Eq. (5.1) ought to refer to bare ions. In practice, equilibrium stopping powers are employed also for the reference ion.

Eq. (5.1) defines γ as a function of v, Z_1 and Z_2. A scaling procedure consists in finding a smooth functional dependence of γ on all or part of these variables. This problem is simplified if

- γ is assumed independent of Z_2, and
- the dependence on v and Z_1 is assumed to follow the Thomas–Fermi velocity $v/v_0 Z_1^{2/3}$ or a similar scaling variable.

Two major problems are attached to the effective-charge concept as applied in practice,

- The assumption of smooth variation tends to ignore Z_1 and Z_2 structure if the grid is too wide. This may cause pronounced errors particularly at velocities around and below the stopping maximum.
- The asserted Z_2 independence and the adopted velocity scaling, based on scaling properties of the ion charge, have led to the seeming paradox that the magnitude and scaling behavior of γ as extracted from Eq. (5.1) shows little similarity to the mean fractional charge of ions emerging from a foil (cf. Sections 3.4.3 and 4.5.2).

[34]Concerning γ the reader is reminded of footnote 4 on page 23.

© International Commission on Radiation Units and Measurements 2005

Table 5.1. Elemental ion–target combinations for $3 \leq Z_1 \leq 36$ covered in database (Paul, 2003) by 1 October 2003. First row: Z_1; first column: Z_2. Black-on-white numbers denote 1–5 available data files; white-on-black numbers denote 6 or more.

	3	4	5	6	7	8	9	10	11	12	13	14	15	16	17	18	19	20	21	22	23	24	25	26	27	28	29	32	33	35	36
1	2		1	1	2	2		3						1	1	6											2			1	3
2	3		1	1	5	3	1	3	1	1				1	1	4											1			1	3
4	1			2	1	6	1	1								5		1												1	4
5	3		1	1	1	1	1	1	1																						
6	14	5	6	18	14	21	10	13	7	6	9	7	5	4	9	18	6	5	4	9	1	3	5	6	2	3	9	2		4	9
7	1		1	2	2	3	1	3						2	2	6											1			1	3
8	1		2	1	1	2	1																								
10	2	1	1	1	3	3	1	2	1	1						4											1				4
12																											1				
13	14	3	6	13	17	18	7	10	5	4	6	6	3	3	5	13	2	2		3		1	1	2	1	3	4	2		3	8
14	6		4	7	13	8	4	2		1		4	2		1	4		1											2	1	2
18	3	1	4	4	7	4	1	6	1		1			1	2	6											1			1	5
22	3		1	4	3	5	3			2	1	1		1	1	5		1		1						1	1				5
23	2	1	1		1					1		1																			
24	2	1	1		1															1							1				1
25					1																										
26	2	1	1		1		1			2	1	1		1	1																
27			1	1	1		1			1		1																			
28	8	2	7	15	17	18	6	6	1	3	2	2	2	3	5	8	1	2		1						1	2			2	6
29	7	1	1	4	6	5	3			2	2	2		2	2	5				2				1		3	3	1		2	2
30	1	1	1		1							1																			
32	1			1	1	1				1		1	1		1																
34	2																														
36	1				1	2		1						2		4											1			1	4
39						1									1																
40				1	2							2				2				1							1				3
41			1	1	2	1	1			1		1																			
42				2	1		1			1		1																			1
45					1																										
46	1		1	1		1	1			1																					
47	10	1	4	13	14	15	6	4	2	3	4	4	2	3	7	8	1	2		3				2		4	3	2		4	6
48					1																										
49	1		1	1	1	1																									
50	2		1	2	1	1										2				1							1				1
52	1				1																										
54	1				1	2		1								4											1				4
57	1	1	1		1																										
58					1																										
59					1																										
60	1	1	1		1																										
62					1											2															
64	1		1	1	1	1																									
65	1	1	1		1																										
66	1	1	1		1																										
67					1																										
68					1																										1
69					1																										
70					1											2				1											
71	2	1	2	1	1	1																									
72										1		1																			
73	3	1	1	4	2	5				2	1	1				4				1						1	2				4
74	1			1	1					1		1																			
75	1	1			1					1		1																			
77					1																										1
78	1	1			2					1		1				1															
79	11	2	3	14	17	18	4	5	2	5	5	5	2	6	5	13	1	2		2		1		1		1	3	1		4	7
82				2	1	1										2				1							1				
83	1	1			1											1				1							1				1
90					1																										
92																2															

In the survey of available procedures and tabulations, attention will be paid to the way these aspects have been handled. Here, some empirical and theoretical evidence is summarized briefly.

5.2.2 Effective charge

The effective-charge postulate, already discussed in Section 3.4.3, was introduced originally to account

for screening of the projectile nucleus by bound electrons.

Figure 5.1 shows γ^2 for oxygen and nitrogen ions based on experimental data compiled for over 20 target materials.[35] Equilibrium stopping powers for helium from ICRU Report 49 serve as the reference. Similar graphs have been compiled by Paul (2003) for most ions up to $Z_1 = 22$. For oxygen the postulated scaling behavior is best obeyed above 10 MeV/u with a scatter of less than 5 % around $\gamma^2 = 1$. The scatter increases substantially (>10 %) as soon as γ^2 starts to decrease, and it becomes quite large (>20 %) below 0.1 MeV/u. At energies around and below 0.01 MeV/u, drastic differences are found between the energy dependencies for, *e.g.*, Al, C, and Cu.

There exists a fair amount of experimental data for oxygen ions, and effective-charge scaling is relatively well fulfilled. Nitrogen, despite a comparable amount of data, shows more drastic deviations from effective-charge scaling in Figure 5.1. The scatter at low energies has been partly ascribed to a gas–solid difference and partly to experimental errors (Paul and Schinner, 2002).

Theoretical objections to the effective-charge picture have already been made in Section 3.4.3. Figure 5.2 shows the results of calculations based on binary stopping theory for three ions and ten materials. *I*-values for these materials vary from 19.2 to 790 eV. Labels 'classical limit' and 'screening' relate to Figure 3.2. Bare protons have been employed as the reference ion. This is strictly in the spirit of the effective-charge picture and reduces ambiguities due to the effective charge of the reference ion. Differing reference ions are the main cause of deviations in absolute magnitude between the upper graph in Figure 5.1 and the middle graph of Figure 5.2.

The three graphs in Figure 5.2 show perfect scaling behavior above the classical limit.[36] The decrease below the asymptotic level originates in the transition from the Bethe to the Bohr regime and is unrelated to screening (Sigmund and Schinner, 2001b). Good scaling behavior is observed further down, but deviations are observed at energies below the screening limit. Initially, these deviations are smaller than the scatter found in Figure 5.1, presumably due to experimental scatter, but below 0.1 MeV/u they become large, more than a factor of two. Evidently, these figures do not encourage the use of a Z_2-independent effective charge below about 0.1 MeV/u.

Figure 5.3 shows effective-charge factors for argon, but with screened instead of bare ions taken as the reference. These ions have a smaller stopping number, causing γ to increase, and at the same time the relative deviation from Z_2 independence decreases.

According to the respective bottom graphs of Figures 5.2 and 5.3, the low-energy limit of the stopping number for beryllium ions lies about an order of magnitude below that for bare protons but about an order of magnitude above that for screened argon ions. This would suggest beryllium to be the preferred reference ion for effective-charge scaling of stopping powers for ions from hydrogen to argon. In the absence of a sufficient amount of experimental data, helium ions as a basis are more operational.

5.2.3 Z_1 structure

Z_1 oscillations in the stopping force, discussed in Sections 3.6.4 and 3.6.5, have been measured systematically in amorphous carbon over a broad range of atomic numbers Z_1 and velocities (Ormrod *et al*., 1965; Fastrup *et al*., 1966; Hvelplund, 1968; Lennard *et al*., 1986a) (cf. Figure 3.16). In particular, the decrease in amplitude with increasing speed shown in Figure 3.20 was emerging already from early experiments (Fastrup *et al*., 1966). Z_1 structure is barely visible at $E/A_1 \gtrsim 0.5$ MeV.

Hoffmann *et al*. (1976) reported a noticeable shift in the first stopping maximum when comparing carbon with silicon, whereas Ward *et al*. (1979), comparing Z_1 dependences for $Z_1 \leq 20$ in C, Al, Ni, Ag, and Au, did not find significant variations in the positions of maxima and minima but found a pronounced material dependence in the magnitudes of the variation. Evidently, the empirical basis for incorporating Z_1 structure in a comprehensive tabulation of stopping forces was not available until 1979, and, even at present, considerable caution needs to be exerted toward a tabulation covering the domain of Z_1 oscillations solely on an empirical basis.

Amongst the four theoretical schemes discussed in Section 3.7, only the one of Arista (2002) predicts Z_1 structure.

5.2.4 Z_2 structure

Z_2 structure, well established in light-ion stopping, was discussed in Section 3.3.7. An oscillatory dependence of the *I*-value on Z_2, governed by the shell structure and discussed extensively in ICRU Report 37 and ICRU Report 49, affects proton and helium stopping over a very wide velocity

[35]Most of the graphs in this chapter become clearer when inspected in the Internet version of this report which allows for colors.

[36]Curves for Pt and Ta lie somewhat outside all others, not only in the low-velocity region but also around the classical limit. This is caused by the use of different shell corrections (cf. Section 6.3.3).

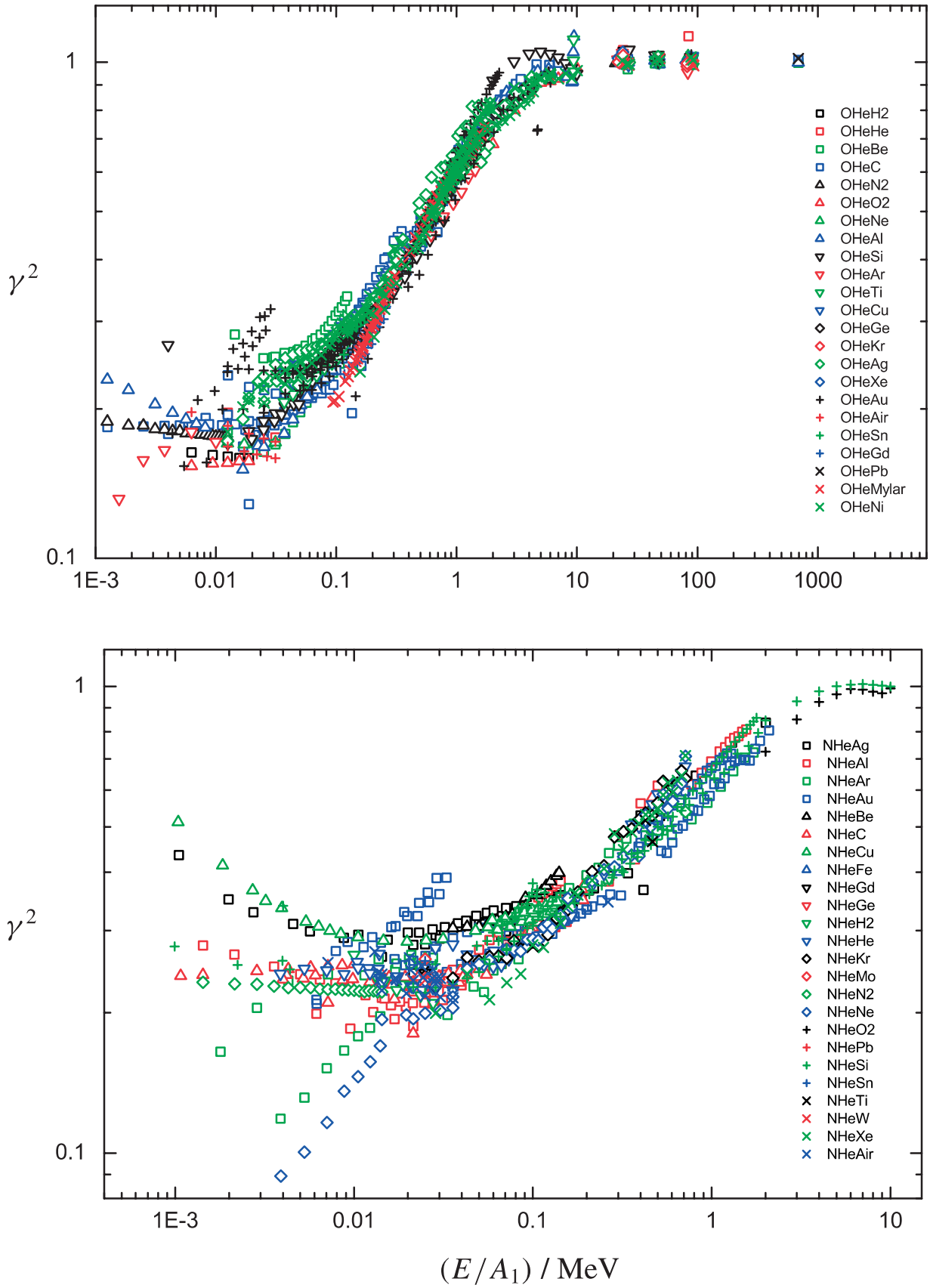


Figure 5.1. Effective-charge factor γ^2, Eq. (5.1), extracted from measured stopping powers for oxygen (upper graph) and nitrogen (lower graph) ions with helium ions as a reference. Data from Paul (2003).

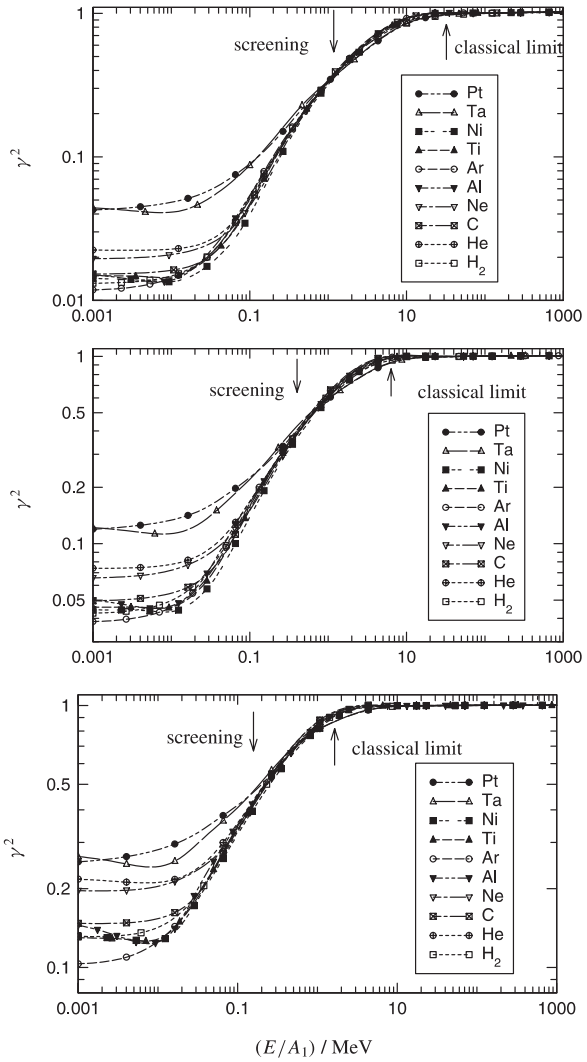


Figure 5.2. Effective-charge factor γ^2, Eq. (5.1), for argon, oxygen and beryllium ions (top to bottom), calculated from PASS with bare protons as the reference ion.

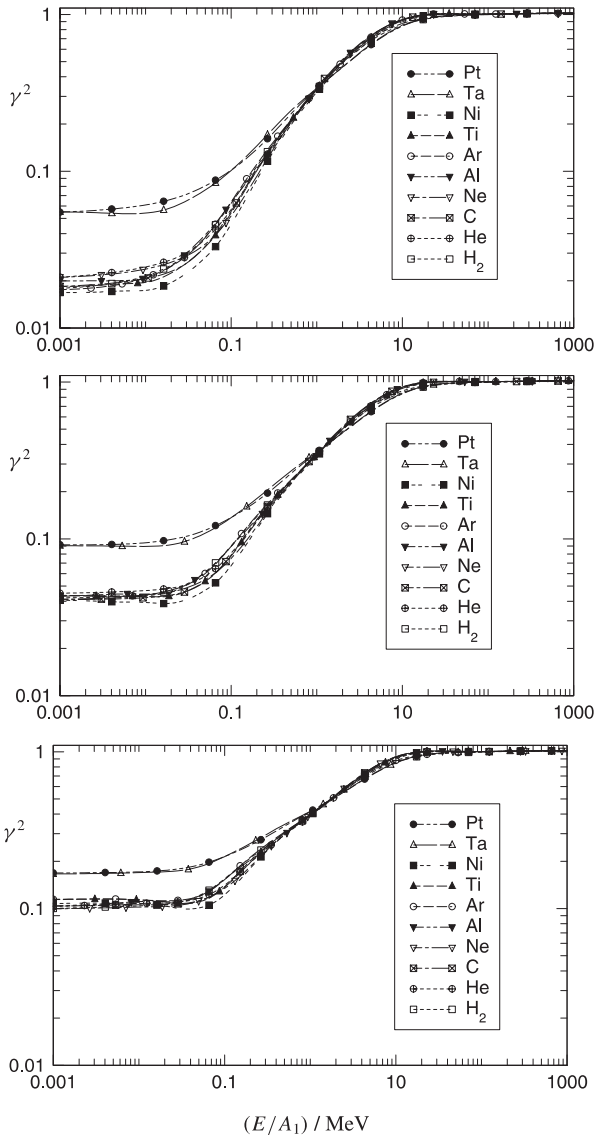


Figure 5.3. Effective-charge factor γ^2, Eq. (5.1), for argon with hydrogen, helium and beryllium in charge equilibrium taken as reference ions (top to bottom), calculated from PASS.

range. The logarithmic dependence on I causes the relative amplitude of the variations to decrease with increasing speed.

In addition to I-values other effects are sensitive to the target shell structure, most noticeably shell corrections. This leads to enhanced Z_2 structure around and below the stopping maximum, found long ago experimentally in proton stopping (Green *et al*., 1955; White and Mueller, 1969).

Z_2 structure in heavy-ion stopping has been studied by Forster *et al*. (1976), Bimbot *et al.* (1978, 1980) and Geissel *et al*. (1980) (cf. Figure 3.7). For $E/A_1 = 0.32$ MeV, pronounced variations were found for Cl ions and $22 \leq Z_2 \leq 40$, which were very similar to those observed for ^{4}He at the same speed. At $E/A_1 = 2.5$ MeV no such structure was visible for either ion.

Only limited experimental information is available about the systematics of Z_2 structure at low velocities (Section 3.6.7). In particular, comparisons between different experiments are difficult because of uncertainties in the nuclear-stopping correction (Glazov and Sigmund, 2003). This is illustrated in Figure 5.4 for neon ions at $v = v_0$. While stopping powers in He, N_2, Ne, Ar, and Kr are clearly lower than those in the other elements, it is not clear whether this is due to Z_2 structure, a gas–solid difference, a conductor–insulator difference or experimental problems.

Theoretical considerations (cf. Sections 3.4.8 and 5.2.2), suggest that Z_2 structure becomes less pronounced with increasing screening. This implies that Z_2 structure decreases with increasing

Z_1 at a given projectile speed. This, in turn implies that Z_2 structure becomes more pronounced in the effective charge than in the stopping power (Sigmund *et al.*, 2003). Direct experimental evidence to support or reject this finding appears unavailable.

5.2.5 Gas–solid difference

Several of the codes to be discussed in the following paragraphs offer different scaling procedures for gaseous and solid target materials. This can include the option of different stopping cross sections for one and the same atom, dependent on its environment. Examples are different mass stopping powers for water vapor and liquid water, or for oxygen in O_2 and in an oxide.

Gas–solid differences in stopping are well documented in the velocity range $v \simeq Z_1^{2/3} v_0$ (Geissel, 1982; Bimbot *et al.*, 1989a,b), as discussed in Section 4.10.3. The effect is primarily due to different charge states and hence vanishes for stripped ions. It leads to *enhanced* stopping in solids. Its dependence on atomic number Z_2 is generally assumed to be smooth.

The existence of gas–solid differences at lower velocities is much less documented because the effect is hard to distinguish from Z_2 structure and chemical effects.

A comparatively large number of stopping measurements has been performed on noble gas targets. These elements have high excitation energies and hence exceptionally low stopping powers, in particular at low velocities, as is evident from Figure 5.4. This does not necessarily imply a gas–solid difference: argon has been found to have the same stopping power in the condensed phase as in the gas phase at least for He over a wide velocity range (Besenbacher *et al.*, 1981).

Gas–solid differences at low velocities must be expected to originate primarily in changes of the configuration of outer-shell electrons. Drastic effects of this type were predicted for protons especially in alkalis (Oddershede *et al.*, 1983). Experimental studies of protons in Zn (Bauer *et al.*, 1992) and Mg (Bergsmann *et al.*, 1998, 2000) confirmed the existence of such effects, but with the stopping force of the gas *exceeding* that of the solid. Charge-state effects were found to be crucial in the interpretation of those experiments. It is not obvious whether similar effects are to be found for heavy ions in the same velocity range.

5.3 TABLES AND COMPUTER CODES

An overview of existing tables and computer programs for determining heavy-ion stopping powers and related quantities is shown in Table 5.8.

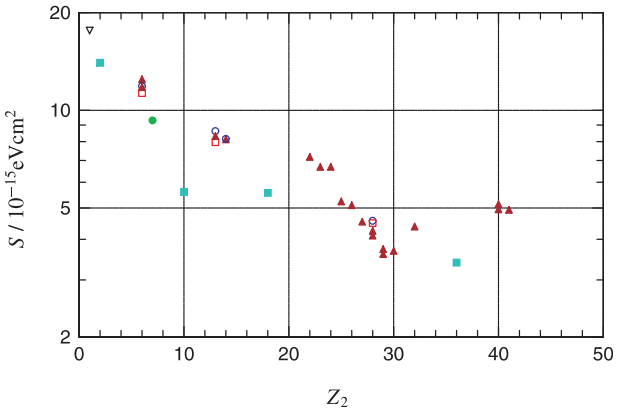


Figure 5.4. Stopping cross sections for nitrogen ions at $v = v_0$, according to Land *et al.* (1985) (filled triangles), Santry and Werner (1991) (open circles), Ward *et al.* (1979) (open squares), Ormrod (1968) (filled circles), Weyl (1953) (open triangles) and Price *et al.* (1993) (filled squares).

5.3.1 Tables of Steward

The code of Steward (1968) is based on interpolation among experimental data and makes use of then available theory. In particular, proper transition to the Bethe limit is ensured, and the Lindhard–Scharff formula is employed for ions with $Z_1 \geqslant 10$ in the appropriate velocity range. The effective charge is assumed to be independent of Z_2. Z_1 and Z_2 structure are ignored. The code was rewritten by Chukreev (1992). Examples are shown in Figures 5.10 and 5.11.

5.3.2 Tables of Northcliffe and Schilling

The widely used tables of Northcliffe and Schilling (1970) rely on the effective-charge concept. γ^2 is assumed to be target-independent and found by interpolation between experimental data for $Z_2 = 6$, 13, 28, 47, and 79, and by extrapolation. Different dependences are adopted for gaseous and solid materials.

The procedure does not recover Z_1 and Z_2 structure, but tabulated stopping cross sections for gases are lower than for solids. Examples have been included in Figures 5.5–5.7 and 5.9–5.11. Good agreement with experimental results is found in numerous cases (Tables 5.2–5.6). However, a detailed comparison with measured stopping cross sections in solids at 4–5 MeV/u by Bimbot *et al.* (1980) revealed systematic differences up to 38 % for xenon in carbon.

Figure 5.10 shows comparisons for nitrogen ions at $v = v_0$ with experimental data by Land *et al.* (1985) for solid targets[37] and by Price *et al.* (1993) for inert gases. Although Z_2-oscillations are ignored,

[37]Data deduced from range measurements.

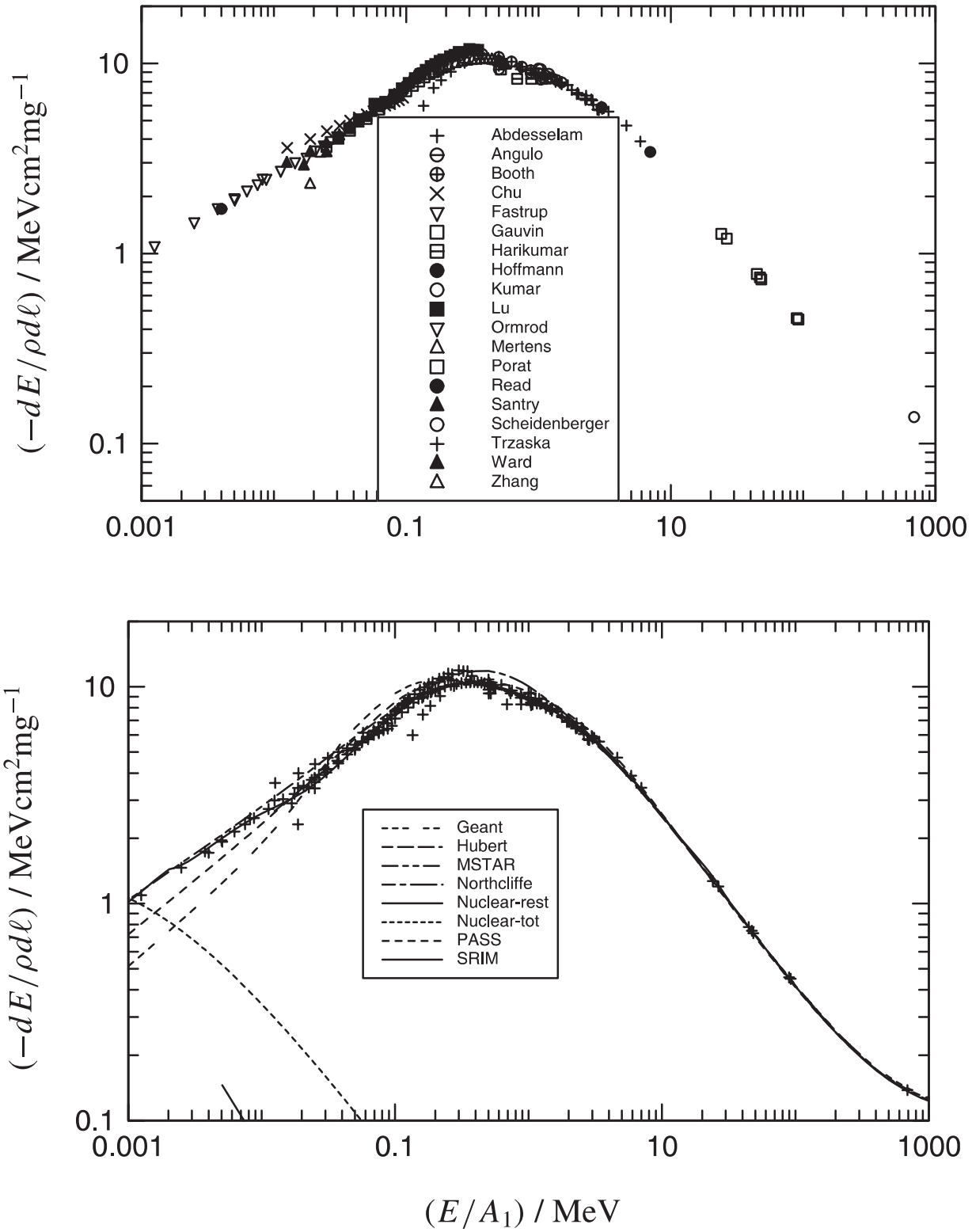


Figure 5.5. Stopping power of carbon for oxygen ions. Upper graph: experimental data from Abdesselam *et al*. (1992), Angulo *et al*. (2000), Booth and Grant (1965), Chu *et al*. (1968), Fastrup *et al*. (1966), Gauvin *et al*. (1987), Harikumar *et al*. (1996), Hoffmann *et al*. (1976), Kumar *et al*. (1996), Lu *et al*. (2000), Mertens (1978), Ormrod and Duckworth (1963), Porat and Ramavataram (1961), Read *et al*. (1987), Santry and Werner (1992), Scheidenberger *et al*. (1994), Trzaska *et al*. (2002), Ward *et al*. (1979), Zhang (2002). Lower graph: curves from Geant4: version 4.4.0 (triple-dotted line), Hubert *et al*. (1990) (dashed lines), MSTAR (double-dot-dashed line), Northcliffe and Schilling (1970) (dot-dashed line), restricted nuclear stopping for 15 μg/cm^2 and forward detection from Fastrup *et al*. (1966) (thin solid line), unrestricted nuclear stopping from SRIM (thin short-dashed line), PASS (thick short-dashed line), and SRIM 2003 (solid line). Crosses denote experimental data specified in the upper graph.

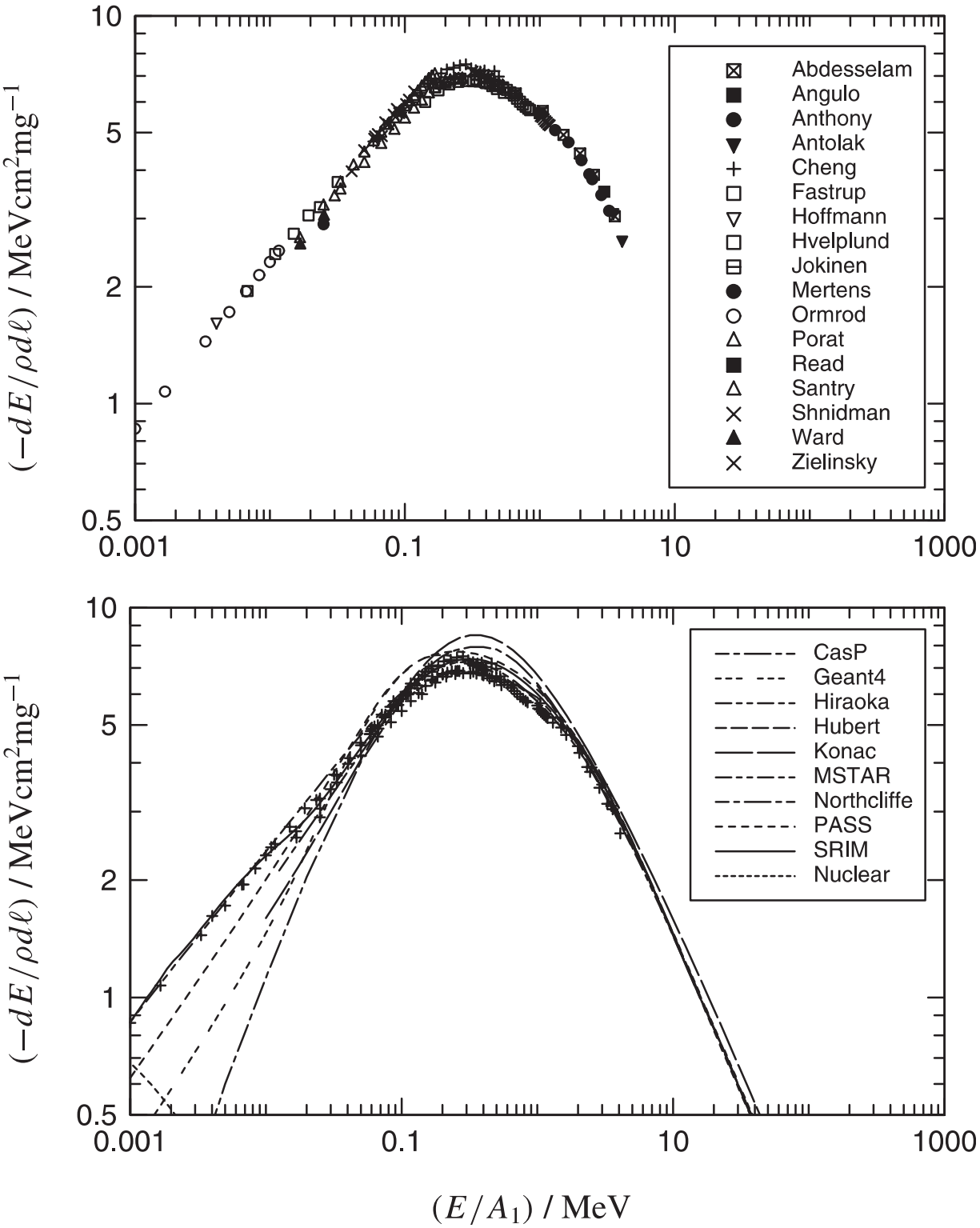


Figure 5.6. Electronic stopping power of amorphous carbon for carbon ions. Experimental data (upper graph) from Santry and Werner (1991), Read *et al*. (1987), Ward *et al*. (1979), Anthony and Lanford (1982), Angulo *et al*. (2000), Porat and Ramavataram (1962), Fastrup *et al*. (1966), Mertens (1978), Abdesselam *et al*. (1991), Antolak *et al*. (1991), Zielinski *et al*. (1988), Shnidman *et al*. (1973), Jokinen (1977), Ormrod and Duckworth (1963), Hvelplund (1968), Hoffmann *et al*. (1976) and Zheng *et al*. (1998). Curves (lower graph) from CasP, Geant4, Hiraoka and Bichsel (2000), Hubert *et al*. (1990), Konac *et al*. (1998b), MSTAR, Northcliffe and Schilling (1970), PASS, SRIM 2003, and unrestricted nuclear stopping power according to SRIM. Crosses denote experimental data identified in the upper graph.

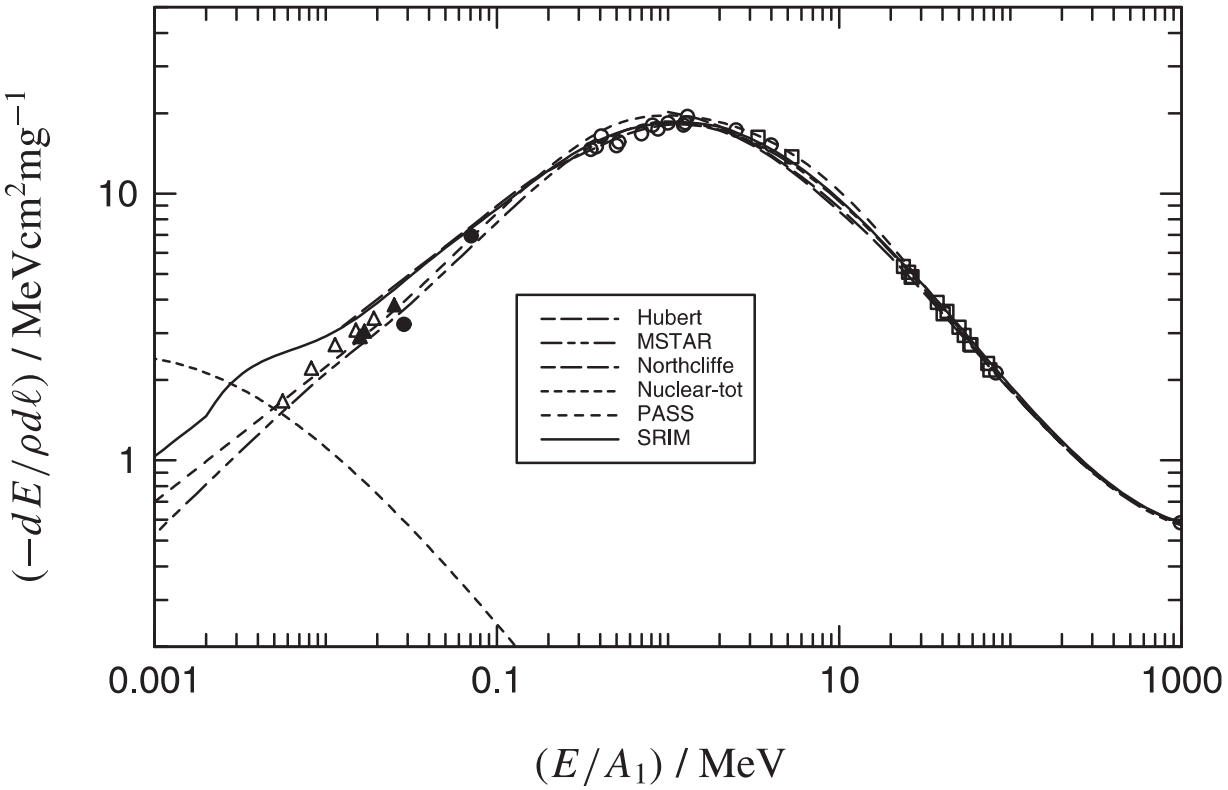


Figure 5.7. Stopping power of aluminium for argon ions. Experimental data from Bimbot *et al*. (1978) and Bimbot *et al*. (1986) (open squares), Geissel *et al*. (1980), Scheidenberger *et al*. (1994), Schwab *et al*. (1990) and Geissel and Scheidenberger (1998) (open circles), Schulz and Brandt (1982) (open triangles), Ward *et al*. (1979) and Lennard and Geissel (1987) (filled triangles), Teplova *et al*. (1962) (filled circles). Curves according to Hubert *et al*. (1990) (dashed line), MSTAR (double-dot-dashed line), Northcliffe and Schilling (1970) (dash-dotted line), unrestricted nuclear stopping (thin short-dashed line), PASS (thick short-dashed line) and SRIM 2001 (solid line).

Table 5.2. Statistical analysis according to Eq. (5.2): oxygen in carbon.

(E/A_1)/MeV Number of points	0.00–0.01 10	0.01–0.1 52	0.1–1 68	1–10 41	10–100 7	100–1000 1	0–1000 180
Hubert *et al*. (1990)				1.4 ± 3.7	0.6 ± 0.7		1.2 ± 3.0
MSTAR	−3.1 ± 1.8	−9.3 ± 9.3	0.9 ± 8.7	2.9 ± 2.8	0.8 ± 0.7	0.0	−1.9 ± 9.0
SRIM 2003	−2.0 ± 2.0	1.6 ± 8.7	−0.4 ± 8.6	0.4 ± 3.0	−0.6 ± 2.0	1.1	0.3 ± 7.3
Geant4	37 ± 5.2	−12 ± 19	−7.9 ± 14	0.6 ± 3.3	−0.6 ± 0.8	−2.3	−4.4 ± 17
Northcliffe (1970)		−0.5 ± 8.8	−8.5 ± 10.8	−6.6 ± 5.7			−5.5 ± 9.7
PASS		−4.5 ± 7.0	−3.0 ± 9.3	−5.4 ± 3.4	2.1 ± 0.7	−0.8	−3.8 ± 7.4

Table 5.3. Statistical analysis according to Eq. (5.2): carbon in carbon.

(E/A_1)/MeV Number of points	0.00–0.01 8	0.01–0.1 40	0.1–1 77	1–10 23	0.00–10 148
Hubert *et al*. (1990)				−0.6 ± 2.8	−0.6 ± 2.8
SRIM (2003)	–2.7 ± 1.5	0.1 ± 3.5	−4.9 ± 4.2	−5.8 ± 2.6	−3.6 ± 4.4
MSTAR	3.7 ± 1.2	−1.3 ± 4.2	−1.0 ± 4.0	−3.6 ± 2.2	−1.2 ± 4.0
Geant4	44 ± 5.1	−1.2 ± 17	−7.4 ± 6.8	−2.5 ± 2.4	−0.6 ± 17
Northcliffe and Schilling (1970)		3.7 ± 4.4	−11.0 ± 6.6	−8.9 ± 4.6	−6.7 ± 8.6
Konac *et al*. (1998b)		9.1 ± 10	−17 ± 8.0	−14.2 ± 5.5	−9.1 ± 14
Hiraoka and Bichsel (2000)				−7.3 ± 5.3	−7.3 ± 5.3
CasP 1.2	68 ± 12	16.6 ± 14	3.1 ± 3.7	−8.4 ± 3.2	10.3 ± 21
PASS		−6.6 ± 3.9	−7.8 ± 3.9	−7.1 ± 2.7	−7.4 ± 3.7

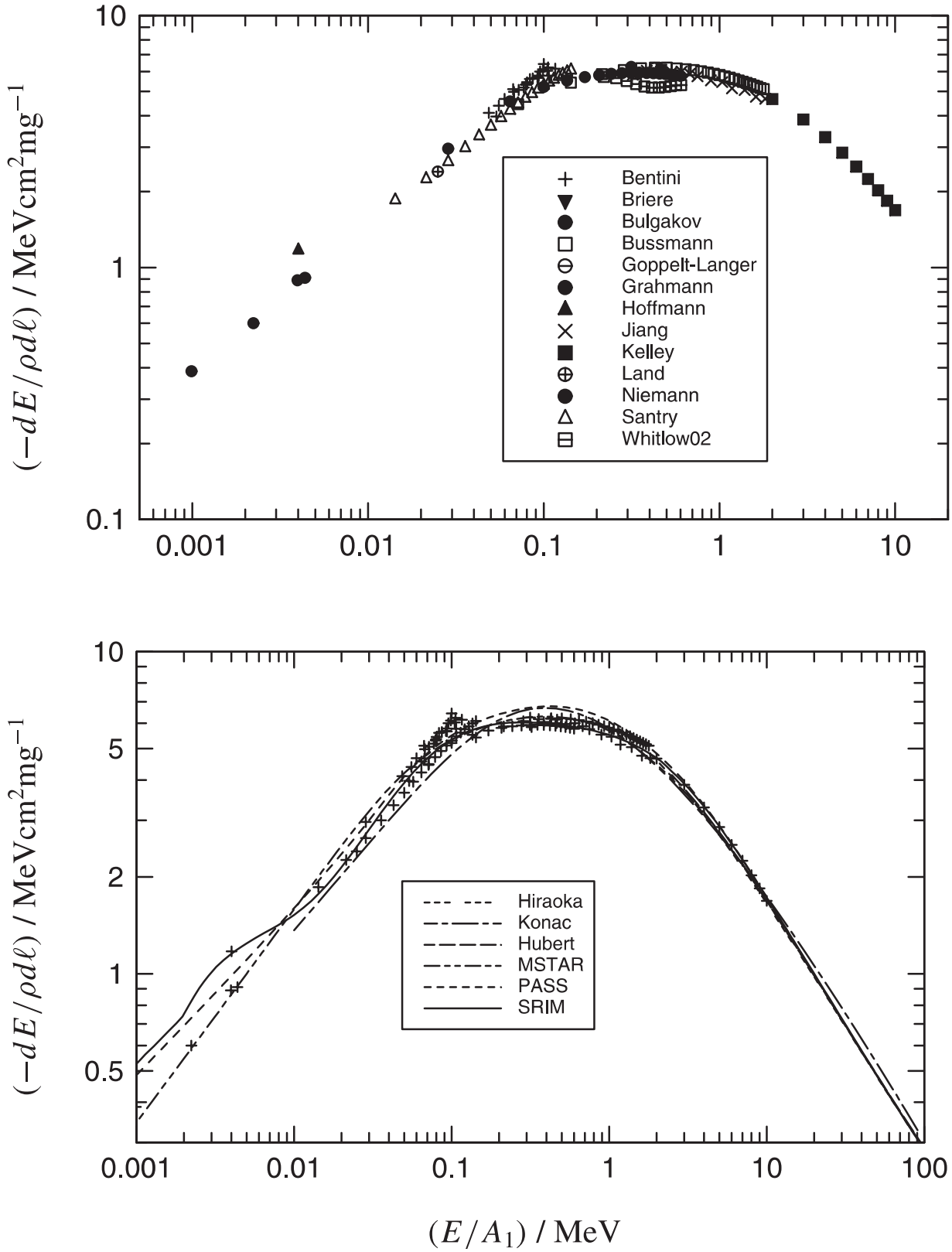


Figure 5.8. Electronic stopping power of silicon for nitrogen ions. Upper graph: experimental data from Bentini *et al*. (1991, 1993), Brière and Biersack (1992), Bulgakov *et al*. (1974), Bussmann *et al*. (1986), Goppelt-Langer *et al*. (1996), Grahmann and Kalbitzer (1976), Hoffmann *et al*. (1976), Jiang *et al*. (1999), Kelley *et al*. (1973), Land *et al*. (1985), Niemann *et al*. (1996), Santry and Werner (1991) and Whitlow *et al*. (2002). Lower graph: curves from SRIM 2003 (solid line), Konac *et al*. (1998b) (dot-dashed line), Hiraoka and Bichsel (2000) (triple-dotted line), PASS (short-dashed line), MSTAR (double-dot-dashed line) and Hubert *et al*. (1990) (dashed line). Crosses denote experimental data from the upper graph.

Table 5.4. Statistical analysis according to Eq. (5.2): all solid elements covered.

		(E/A_1)/MeV	Z_1 range	Number of points
Hubert *et al*. (1990)	0.2 ± 4.3	2.5–1000	3–18	592
Hubert *et al*. (1990)	0.2 ± 4.3	2.5–1000	3–36	919
MSTAR	0.2 ± 5.1	2.5–1000	3–18	579
SRIM 2003	−0.4 ± 5.0	2.5–1000	3–18	577
PASS	−2.9 ± 6.0	2.5–1000	3–18	577

a gas–solid difference is built into the scheme, and on the average, results are in rough agreement with the experimental data.

5.3.3 Brice formula

A three-parameter formula of Brice (1972) was proposed for the electronic stopping cross section at nonrelativistic velocities, based on interpolation between a modified-Firsov and Bethe theory. Parameters for each ion–target combination need to be determined by fitting experimental data. The original

Table 5.5. Statistical analysis according to Eq. (5.2): MSTAR and Hubert *et al.* (1990) for all ions with $3 \leq Z_1 \leq 18$ in all elemental solids covered by the respective program.

(E/A_1)/MeV	0.00–0.01	0.01–0.1	0.1–1	1–10	10–100	100–1000	0–1000
Hubert *et al*. (1990)				0.1 ± 5.1	0.6 ± 2.1	1.1 ± 1.7	0.2 ± 4.3
Number of points				409	187	2	598
SRIM 2003	−16 ± 26	0.4 ± 12	−1.1 ± 7.2	−0.3 ± 5.6	−1.5 ± 2.8	−0.1 ± 1.6	−1.4 ± 11
MSTAR	−1.9 ± 20	1.9 ± 11	−0.1 ± 7.7	0.9 ± 5.5	0.1 ± 2.1	0.7 ± 1.4	0.5 ± 9.4
Number of points	387	1920	3173	1302	188	11	6981
Northcliffe (1970)		−4.0 ± 16	2.0 ± 11	−0.2 ± 6.5	4.0 ± 4.1		−0.2 ± 12
PASS		−12 ± 20	−7.1 ± 12	−3.1 ± 6.6	−0.9 ± 3.0	−0.7 ± 2.1	−7.1 ± 14
Number of points		1363	2948	1238	174	9	5732

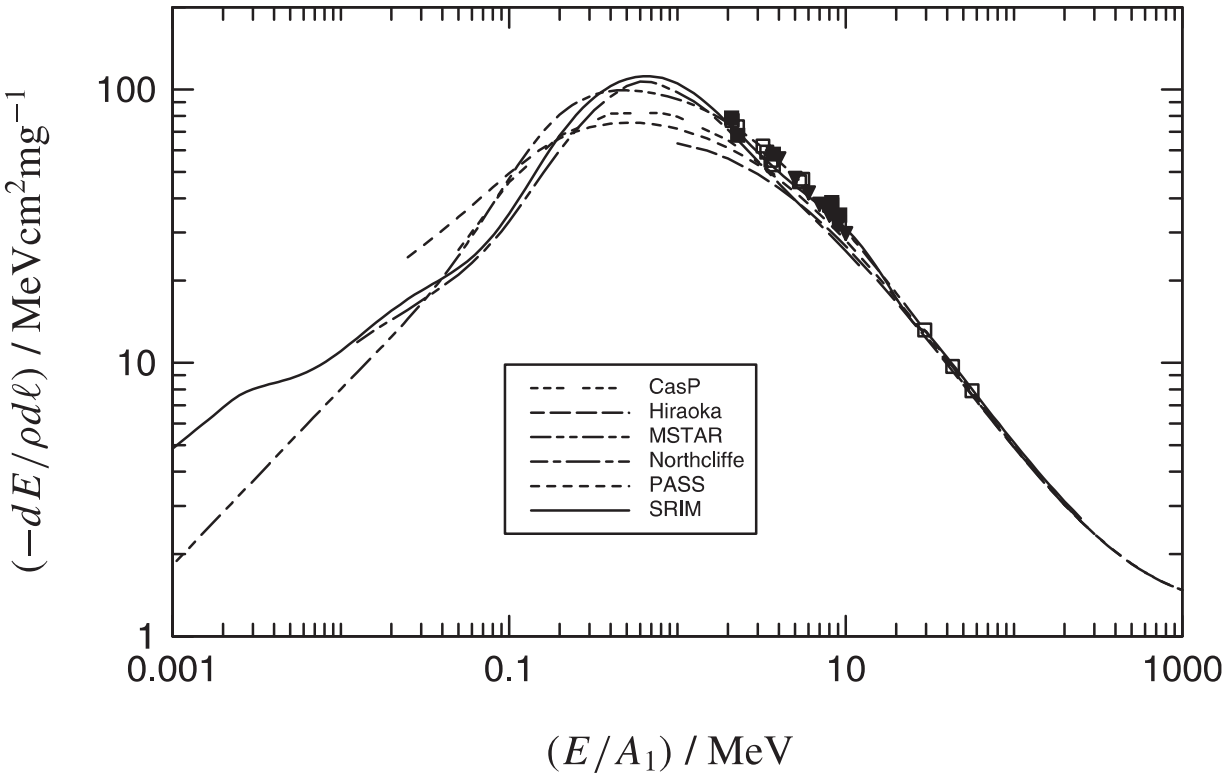


Figure 5.9. Electronic stopping power of hydrogen for argon ions. Experimental data from Martin and Northcliffe (1962) (triangles), Bimbot *et al*. (1989a) and Herault *et al*. (1991) (open squares), and data for D_2 targets from Bimbot *et al*. (1989a) (filled squares). Curves according to Northcliffe and Schilling (1970) (dash-dotted line), Hiraoka and Bichsel (2000) (dashed line), SRIM 2001 (solid line), MSTAR (double-dot-dashed line), CasP (triple-dotted line) and PASS (thick short-dashed line). Mass stopping power of deuterium multiplied by 2.

paper focused on hydrogen and helium ions, but for sulphur ions in various gases, experimental data by Pierce and Blann (1968) were represented with an average accuracy of 1–7 %, dependent on the target.

5.3.4 SRIM (TRIM) program package

The widely used TRIM (now SRIM) package has been described by Ziegler *et al*. (1985). Later versions were provided to interested users and may now be obtained through the Internet (Ziegler, 2003). The main ingredients are:

1. a scheme to estimate electronic stopping powers, which replaced an earlier procedure by Ziegler (1980);
2. a routine based on classical scattering theory and an adopted interatomic potential to evaluate nuclear stopping and scattering (cf. Section 3.8.2); and
3. a Monte Carlo program to describe ion penetration in matter and associated radiation effects (cf. Section 3.11.4).

Electronic stopping powers are deduced from those for protons by means of an effective-charge fraction assumed to be independent of the target. An effort to empirically justify this assumption was limited in practice to the stopping of helium ions. The expression for the effective charge was deduced by reference to Brandt and Kitagawa (1982). Low-velocity stopping was originally assumed to be velocity-proportional with empirical proportionality factors.

The procedure has undergone modifications subsequently. In particular, low-velocity stopping powers are not necessarily assumed to be velocity-

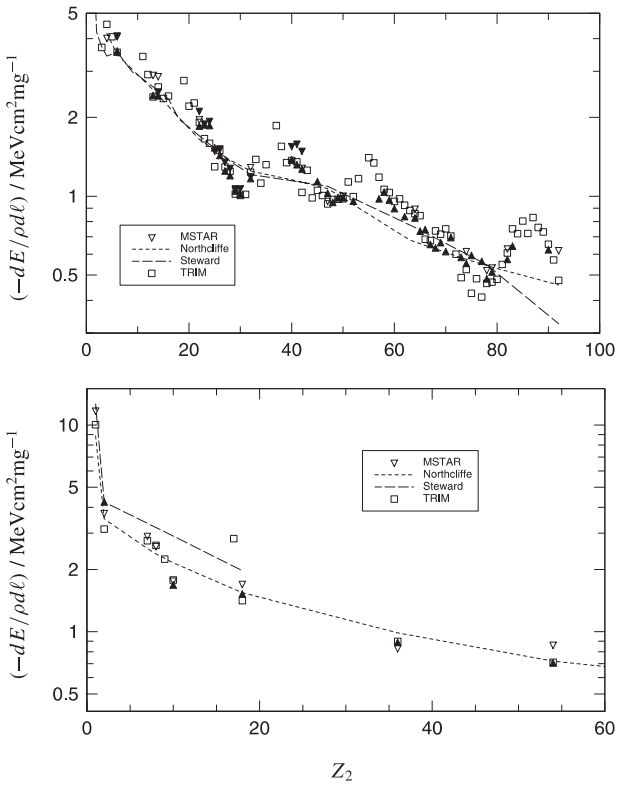


Figure 5.10. Electronic stopping power at $v = v_0$ for nitrogen ions. Experimental data from Land *et al*. (1985) and Land and Brennan (1976) for solids (upper graph, filled symbols) and from Price *et al*. (1993) (lower graph, filled symbols) for inert gases. Tabulated data from MSTAR, Northcliffe and Schilling (1970) and Steward (1968). TRIM data taken from STOP (Ziegler, 1998) for solids and SRIM 2001 for gases.

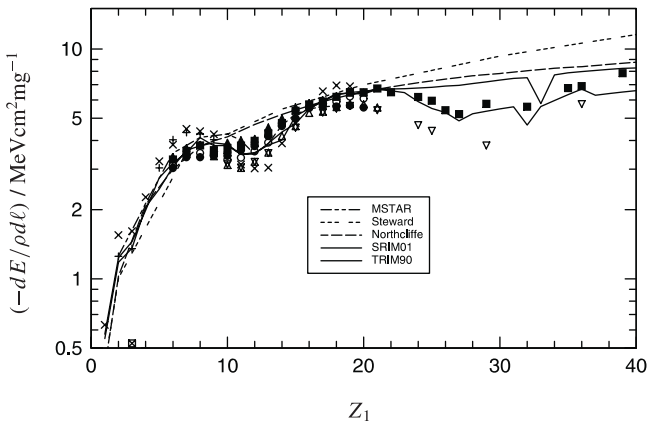


Figure 5.11. Electronic stopping power of carbon at $v = v_0$ for ions from hydrogen to yttrium. Experimental data taken at different velocities were converted to v_0. Data from Fastrup *et al*. (1966) (solid triangles) were interpolated. Data from Ward *et al*. (1979) (solid circles), Hvelplund and Fastrup (1968) (solid squares), Ward *et al*. (1979) (open circles), Lennard *et al*. (1986a), Lennard and Geissel (1987) (open triangles) Hoffmann *et al*. (1976) and Ormrod *et al*. (1965) (crosses) were extrapolated from $v/v_0 = 1.006, 0.91, 0.823, 0.8, 0.411$ and 0.402, respectively. Tabulated values from MSTAR (double-dot-dashed line), Steward (1968) (triple-dotted line), Northcliffe and Schilling (1970) (dashed line), SRIM 2001 (thick solid line) and TRIM 1990 (thin solid line).

Table 5.6. Statistical analysis according to Eq. (5.2): gas targets for all ions with $3 \leq Z_1 \leq 18$.

(E/A_1)/MeV	0.025–0.1	0.1–1	1–10	10–100	0.025–100
Number of points	109	159	504	151	923
SRIM 2003	4.2 ± 11	−8.6 ± 11	−0.2 ± 5.2	−2.2 ± 4.2	−1.8 ± 8.4
MSTAR	−2.5 ± 11	−4.2 ± 11	0.0 ± 3.9	0.8 ± 2.6	−1.0 ± 7.1
Northcliffe (1970)	−12.3 ± 40	−3.7 ± 11	2.9 ± 6.0	3.8 ± 4.4	−2.2 ± 22
PASS	−52 ± 29	−4.7 ± 15	−2.0 ± 11	−0.2 ± 4.2	−9.8 ± 23

proportional, but different power-laws, dependent on Z_1 and Z_2, have been adopted. This has given rise to significant variations in tabulated stopping powers from version to version. It is recommended, therefore, to identify the TRIM or SRIM version used in applications of this program.

Since 1995 separate tables of expansion coefficients were adopted for solid and gaseous targets, including the solid and gaseous phase of the same element.

Stopping powers for compounds are determined on the basis of an extensive study of experimental data for proton, helium and lithium bombardment (Ziegler and Manoyan, 1988). The resulting scaling procedure was found to reproduce available experimental data, but caution was expressed with regard to extrapolation to materials outside the original database (Thwaites, 1992). The conclusions drawn from Figure 3.12 on the dependence of Z_2 structure on Z_1 and v must be expected to apply also to chemical effects.

Figures 5.5–5.9 and Tables 5.2–5.6 show generally good agreement of SRIM with available experimental data. Figure 5.10 shows reasonable agreement with experimental Z_2 structure at $v = v_0$. Somewhat surprisingly, Figure 5.11 indicates that Z_1 structure beyond $Z_1 = 22$ (Ti) is described better by TRIM 1990 than by SRIM 2001.

It is of interest to analyze how Z_1 and Z_2 structure are built into the code. Because the effective charge is assumed to be independent of Z_2, all Z_2 structure is determined by the Z_2 structure in the stopping power of the reference ion at the same projectile speed. Thus, effects of the type discussed in connection with Figure 3.12 are eliminated from the start. Z_1 structure, being a low-speed effect, is built in *via* empirical modification of the formula of Lindhard and Scharff (1961). The procedure applied has been found to lead to unrealistic predictions, in particular for very heavy ions, as pointed out by Sigmund (1998).

Major advantages of SRIM are user-friendliness, high speed, easy conversion from one system of units to another, and a very wide parameter space.

5.3.5 Tables of Hubert and coworkers

The tables of Hubert *et al*. (1990) are an update to an earlier version (Hubert *et al*. 1980) with an energy range expanded from 100 to 500 MeV/u. As in the earlier version, the 1990 tables were based on an effective charge that depends on Z_2, but new data obtained in the energy range 20–100 MeV/u were incorporated into the experimental data base. This resulted in major improvements in the high-energy behavior above 20 MeV/u. Helium stopping powers from Ziegler (1977) and scaled Janni (1982) tables were used as a reference. γ^2 was determined by fitting to a large set of measured stopping powers as a function of E/A_1, Z_1 and Z_2 by suitable empirical functions. Detailed documentation was presented by Bimbot (1992). Z_1 structure has not been incorporated. For that reason the lower energy limit was set to $E/A_1 = 2.5$ MeV.

Figures 5.5–5.9 show very good agreement with available experimental data. This is also seen from Tables 5.2–5.5. Diwan *et al*. (2001b) pointed out that the formula of Hubert *et al*. (1990) can be employed to match stopping powers of solid targets also in an energy range 0.5–2.5 MeV/u if one of the coefficients is modified.

5.3.6 Formula of Xia and Tan

Xia and Tan (1986) have produced a set of four-parameter formulae for the electronic stopping power of solids for ions below 0.2 MeV/u. They calculate γ^2 relative to the proton stopping power of Andersen and Ziegler (1977) by fitting experimental data.

5.3.7 Code of Tai and coworkers

A code for stopping powers and ranges, used at the NASA Langley Research Center for shielding calculations, has been described by Tai *et al*. (1977). These authors have made comparisons to Hubert *et al*. (1990) with which good agreement was found.

5.3.8 Formula of Konac and coworkers

Konac *et al*. (1998b) presented a fitting formula for electronic stopping of all ions in carbon and silicon, based on their own measurements for $E/A_1 < 1$ MeV and on the tables of Hubert *et al*. (1990) for higher energies. The formula depends on a power of E at low energy and approaches the Bethe formula at high energy. Adopted I-values ($= Z_1 \times 10$ eV) cause significant discrepancies at high energy. Examples are shown in Figures 5.6 and 5.8 (cf. also Table 5.3).

5.3.9 Geant4 program package

The RD44 collaboration (Agostinelli *et al*., 2003) has produced the program package Geant4 for the simulation of the passage of particles through matter. It provides a complete set of tools for all domains of detector simulation and can also be used to produce stopping power tables (Ivanchenko *et al*., 1999). Examples are shown in Figures 5.5 and 5.6.

5.3.10 CasP code

The CasP code of Grande and Schiwietz (2000, 2001) is available on the Internet and implements

theoretical work described in Section 3.7.1. The program avoids the effective-charge postulate and, hence, does not make use of input based on stopping experiments.

The target can be represented either by its I-value or by a spectrum of oscillator strengths. Owing to the absence of Barkas–Andersen and shell corrections, reliable predictions around and below the stopping maximum are currently not possible. Moreover, version 1.2, which is available on the Internet, does not incorporate projectile excitation/ionization. On the other hand, the option 'charge state scan' [Eq. (3.32)] has been allowed as an alternative to the mean equilibrium charge to account for projectile screening. Moreover, different equilibrium charge states have been adopted for gases and solids.

Examples of the use of the code are given in Figures 5.6 and 5.9 (cf. also Table 5.3).

5.3.11 Tables of Hiraoka and Bichsel

Hiraoka and Bichsel (2000)[38] have produced stopping-power and range tables for solids and gases using the algorithm of Hubert *et al*. (1989) for the effective charge in conjunction with Bethe theory. Tables for gas targets are not valid, since the tables by Hubert *et al*. (1990) do not refer to gases.

Agreement with measurements of average energy loss (Bichsel *et al*., 2000) of C ions from 90 to 290 MeV/u is stated to be within 0.3 % or better. At lower energies, the error margin is significantly larger (cf. Table 5.3). While Figures 5.6 and 5.8 show agreement comparable with other tabulations, results reported for Ar in hydrogen are 30 % low compared to measurements by Bimbot *et al*. (1989a) at 2 MeV/u (Figure 5.9).

5.3.12 MSTAR code

In the MSTAR code of Paul and Schinner (2001) the effective-charge ratio γ is determined from Eq. (5.1) with the numerator taken from measured equilibrium stopping powers and the denominator from the tabulations in ICRU Report 49 for helium ions. Different parameter sets determine γ for solids and gases, and a slight Z_2-dependence of γ^2 is allowed for. The code has been updated repeatedly and is available on the Internet (Paul and Schinner, 2002; Paul, 2003).

MSTAR produces stopping powers for $3 \leq Z_1 \leq 18$. Target materials are elements and compounds covered in ICRU Report 49 as well as B, Ni, Zr and Ta.

Stopping powers for compounds and mixtures are determined by multiplying tabulated values for helium ions from ICRU Report 49 by the effective-charge fraction adopted for elemental materials. This implies that deviations from Bragg additivity become independent of the bombarding ion. This limits the validity of the scheme to materials with only small deviations from Bragg additivity.

Z_1 and Z_2 structure are included in the code. For Z_2 structure the remarks made in Section 5.3.4 apply. Z_1 structure is governed by the Z_1 dependence of the effective charge. This makes it difficult to arrive at a proper parameterization to reproduce drastic differences in Z_1 oscillations from one material to another. This is illustrated in Figure 5.12, which shows a comparison between measured Z_1 structure for Au and Ni (Ward *et al*., 1979) and calculations by MSTAR and SRIM.

MSTAR has been built upon a very extensive database comprising the most recent data within the chosen limitation on Z_1. Because the code employs simple interpolation formulae, it is very fast and can easily be incorporated into any other program requiring stopping powers. Examples of its use are given in Figures 5.5–5.12 and Tables 5.2–5.6.

5.3.13 PASS code

The PASS code (Sigmund and Schinner, 2002b) implements binary stopping theory described in Section 3.7.2. Like CasP, the program avoids the effective-charge postulate and, hence, does not make use of input based on stopping experiments. The code has undergone considerable development which, together with the default input, will be discussed in detail in Section 6.2.

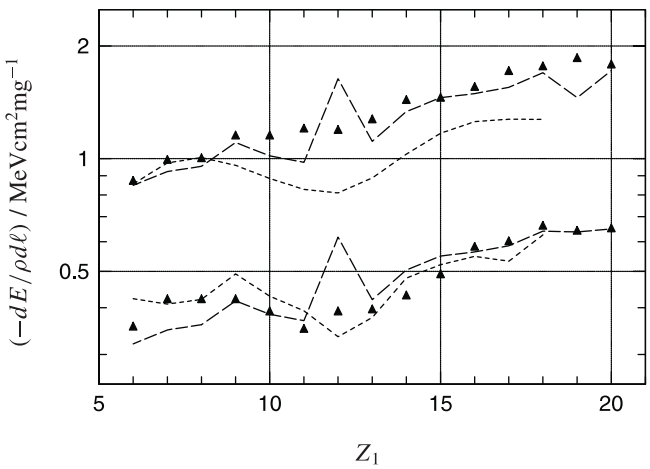


Figure 5.12. Electronic stopping powers at $v/v_0 = 0.82$ in nickel (upper group) and gold (lower group). Experimental data (triangles) from Ward *et al*. (1979). Calculations from MSTAR (short-dashed lines) and SRIM 2003 (long-dashed lines).

[38]The journal quoted in the bibliography is not generally available. Personal communication from H. Bichsel, 22nd Ave. East, Seattle, WA 98112-3534, USA.

In principle, PASS allows the computation of stopping forces for all ions in all elemental materials and compounds. However, the accuracy of the predictions depends on available information on atomic or molecular oscillator strengths. While Z_2 structure is an intrinsic part of the code, Z_1 structure is ignored at the present stage.

So far, mainly that part of the (Z_1, Z_2, E) parameter space has been explored which is covered in the present report. Comparisons with experiments are shown in Figures 5.5–5.9 as well as Figures 5.15 and 5.17 and Tables 5.2–5.7.

5.3.14 Formula of Weijers *et al.*

A semi-empirical scaling formula has been developed by Weijers *et al*. (2004) which does not make use of the effective-charge concept. The scheme starts at Eq. (3.8), and a large number of experimental stopping data is inserted into a plot of stopping number L versus Bohr parameter $\xi = mv^3/Z_1e^2\omega$. This scheme came too late for incorporation into numerical comparisons performed in this report.

5.4 FURTHER COMPARISONS

Figure 5.13 shows comparisons for Pb ions in solids at 1.4 MeV/u (Geissel, 1982) and at 3.25–3.96 MeV/u with SRIM-2000 (Bimbot *et al*., 1980). At 3.25–3.96 MeV/u systematic deviations are observed. The agreement is slightly better at 1.4 MeV/u. Comparisons of the predictions of Ziegler (2001) and Hubert *et al*. (1990) with data for Pb ions up to 200 MeV/u are shown in Figure 5.14.

Comparisons between equilibrium stopping powers calculated by the PASS code and experimental data were reported by Sigmund and Schinner (2002b) for ions from the second and third row of the periodic table in a normal metal (Al), a transition metal (Ni), a noble gas (Ar), a semiconductor (Si), and an insulator (amorphous carbon). Figure 5.16 shows a comparison between predictions of PASS and SRIM for iron ions in target materials for which experimental data have not been found. These ion–target combinations lie in 'white areas'

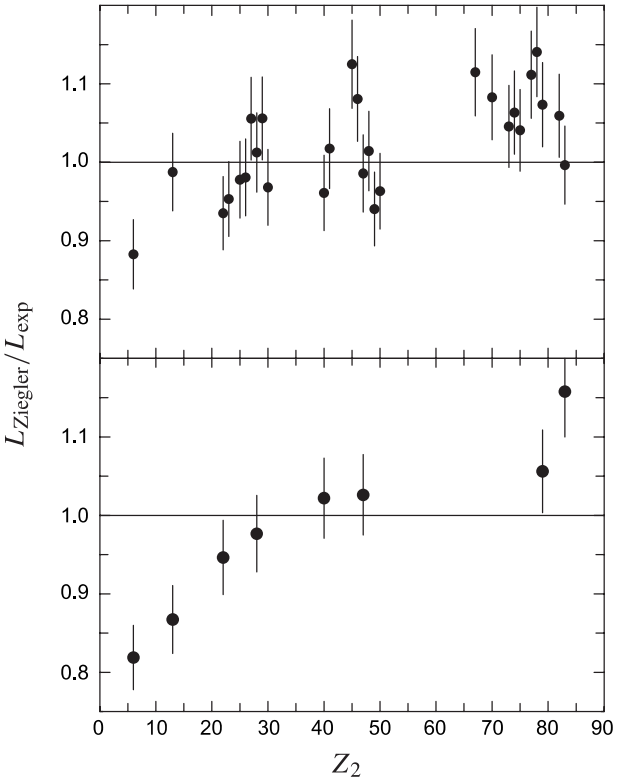


Figure 5.13. Experimental electronic stopping powers for ^{208}Pb ions in solids at 1.4 MeV/u (Geisse, 1982) (upper graph) and at 3.25–3.96 MeV/u (Bimbot *et al*., 1980) (lower graph) compared with predictions of Ziegler (2001).

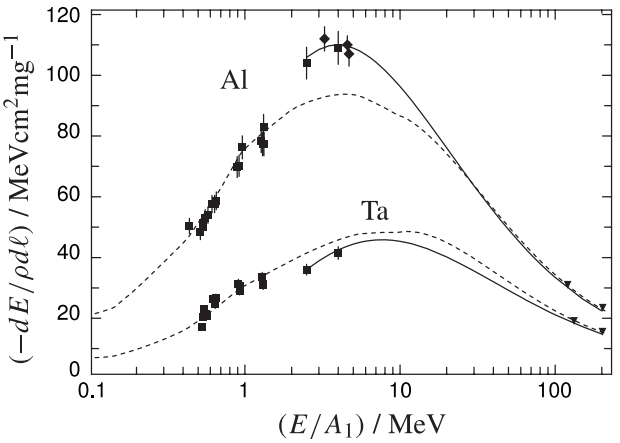


Figure 5.14. Experimental stopping powers for ^{208}Pb ions in aluminium and tantalum compared with the semiempirical predictions of Hubert *et al*. (1990) (solid lines) and SRIM 2001 (dotted lines). Symbols represent experimental data from Geissel (1982), Weick *et al*. (2000) and Bimbot *et al*. (1980).

Table 5.7. Statistical analysis according to Eq. (5.2): ions with 19 $\leq Z_1 \leq$ 92 in C and Al.

(E/A_1)/MeV	0.025–0.1	0.1–1	1–10	10–100	0.025–100
Hubert *et al*. (1990)			0.2 ± 4.7	1.1 ± 4.8	0.4 ± 4.8
Number of points			482	153	635
PASS	−5.9 ± 9.7	2.5 ± 8.5	2.7 ± 6.6	−4.7 ± 4.5	1.8 ± 8.3
Number of points	65	540	309	26	9409

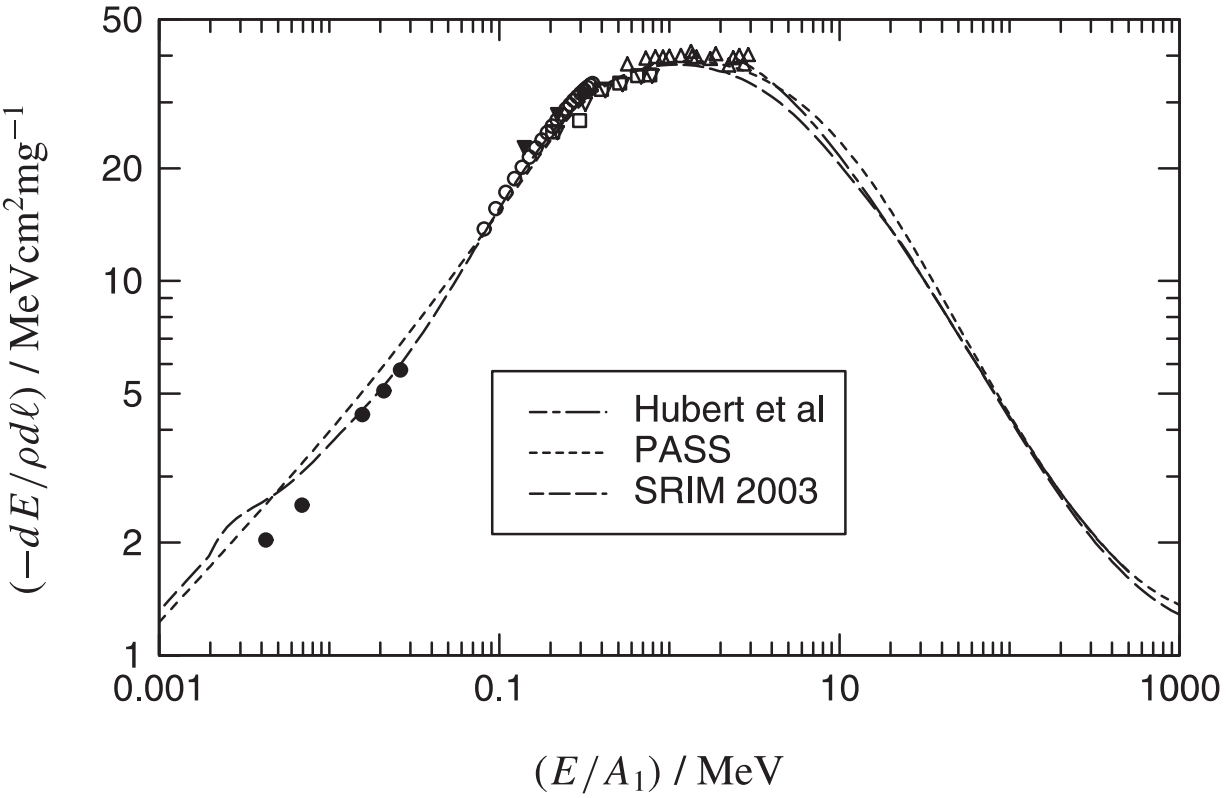


Figure 5.15. Stopping of iron in carbon. Experimental data from Anthony and Lanford (1982) (open upward triangles), Harikumar *et al*. (1996, 1997) (open and filled downward triangles), Hvelplund (1968) (filled circles), Kumar *et al*. (1996) (open squares) Zhang (2002) and Zhang *et al*. (2002) (open circles). Curves from Hubert *et al*. (1990), PASS and SRIM.

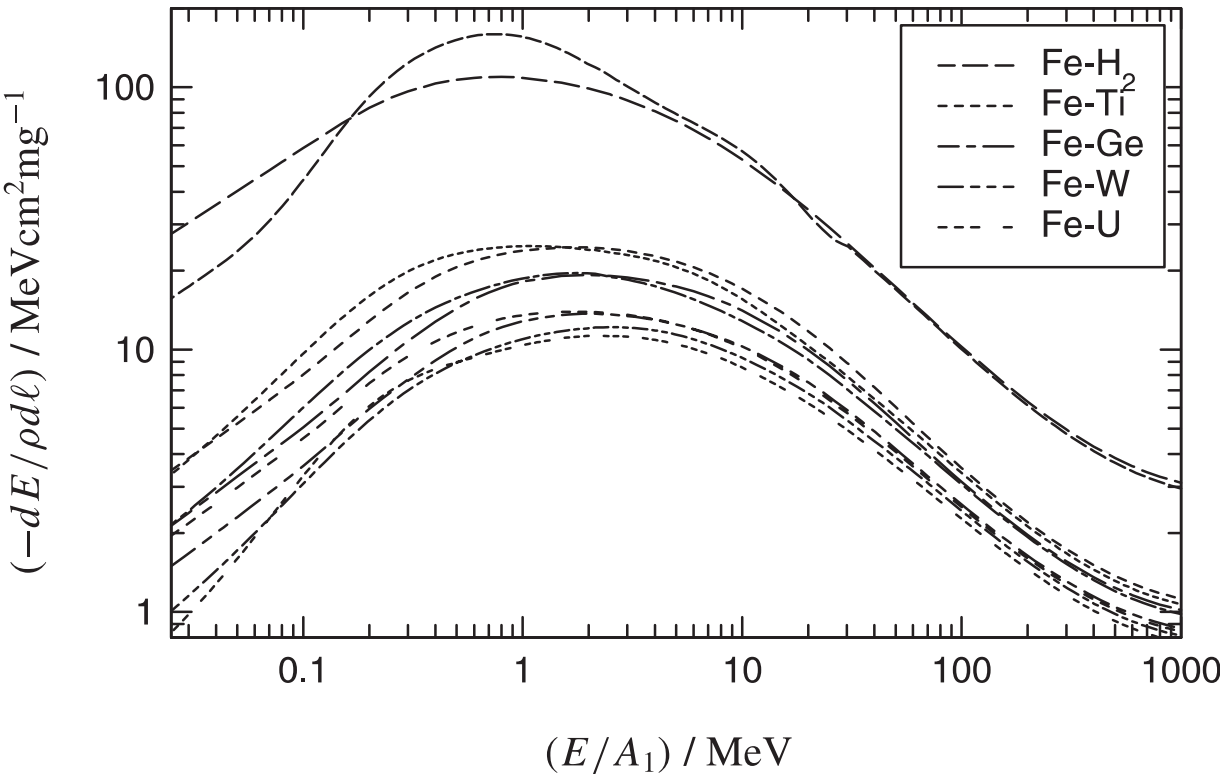


Figure 5.16. Stopping of iron in solids. Predictions from PASS (thick lines) and SRIM (thin lines).

of Table 5.1. Pronounced differences are found for hydrogen and for uranium. Differences in the high-speed regime are caused by the neglect of the correction of Lindhard and Sørensen (1996) in SRIM and, for uranium, by uncertainty in the I-value.

Sharma *et al*. (1995) made systematic comparisons for many different solid targets and found that the formulation by Hubert *et al*. (1989, 1990) best represents experimental data for ions from Li to U and energies above 3 MeV/u. For lower energies (0.5–2.5 MeV/u), numerical comparisons were made with a modified Hubert formulation (Diwan *et al*., 2001b).

Diwan *et al*. (2001a) compared experimental stopping powers of gaseous targets for ions with $Z_1 \geq 8$ with the formulations of Benton and Henke (1969), Northcliffe and Schilling (1970), Mukherji and Nayak (1979), Hubert *et al*. (1989) and SRIM-2000, in an energy range of 1–80 MeV/u. They find that SRIM-2000 provides best agreement for ions with $Z_1 \leq 47$ in all targets except H_2. For the heaviest ions (Xe, Pb, and U), all formulations exceed the experimental data considerably.

Not many experimental data for compound targets are available. Examples are shown for Ar ions in carbon dioxide in Figure 5.17 and for polycarbonate in Figure 5.18. Further comparisons have been performed by Sharma *et al*. (2004b).

5.5 DISCUSSION

5.5.1 General

The accuracy of theoretical predictions tends to deteriorate with decreasing speed, and at the same time the scatter between experimental data from group to group and from run to run tends to increase for all ion–target combinations. Obvious reasons for this have been discussed in Sections 3 and 4.

5.5.2 Nuclear stopping

A topic of particular importance in this connection is nuclear stopping. Theoretical input entering into various schemes mentioned in this section refers solely to electronic stopping. Hence, a meaningful comparison between theoretical predictions and experimental data implies proper extraction of electronic stopping powers from raw experimental data. This problem is less obvious in purely empirical interpolation schemes in which experimental data are fitted without reference to their physical significance. On the other hand, nuclear stopping is clearly one of the factors that complicate scaling behavior in the low-speed regime. Moreover, when stopping data are *applied*, proper identification of electronic versus nuclear stopping can be crucial.

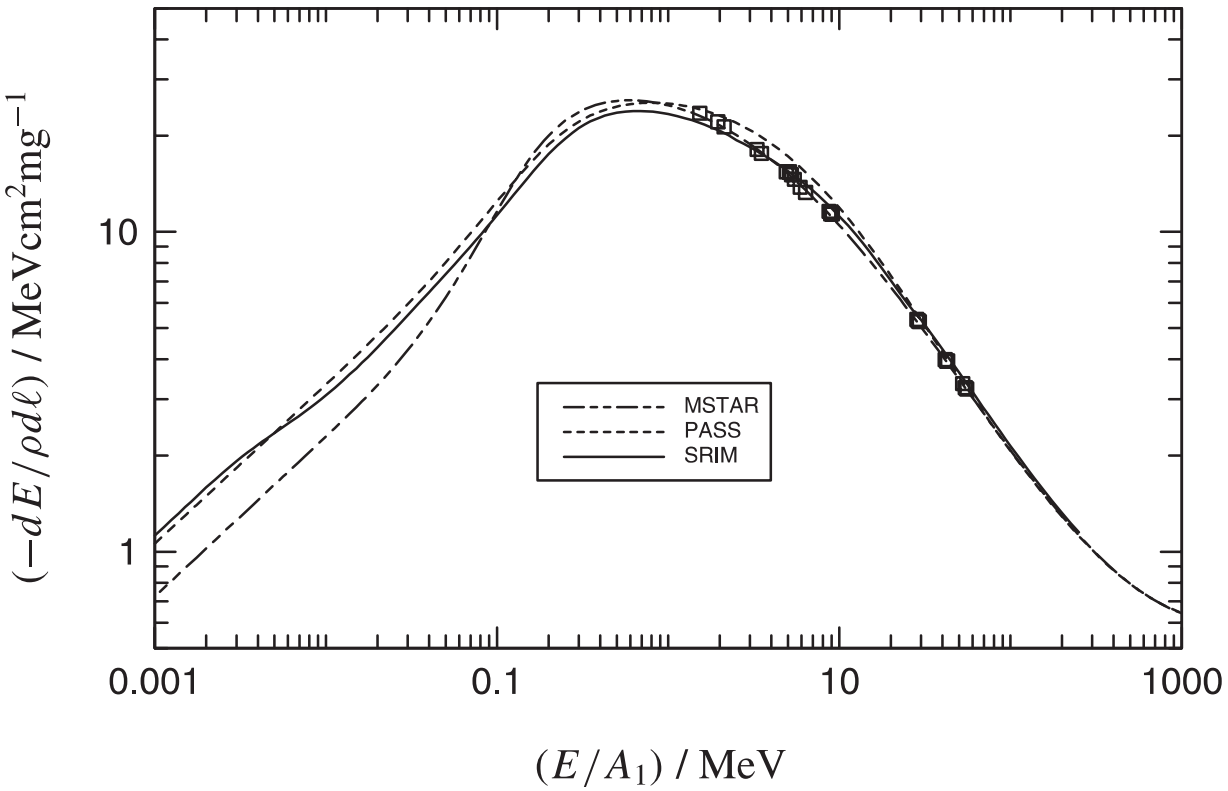


Figure 5.17. Electronic stopping power of carbon dioxide for argon ions. Experimental data from Herault *et al*. (1991) and Bimbot *et al*. (1989a) (squares). Tabulated values from MSTAR (double-dash-dotted line), SRIM 2001 (solid line), and PASS (short-dashed line).

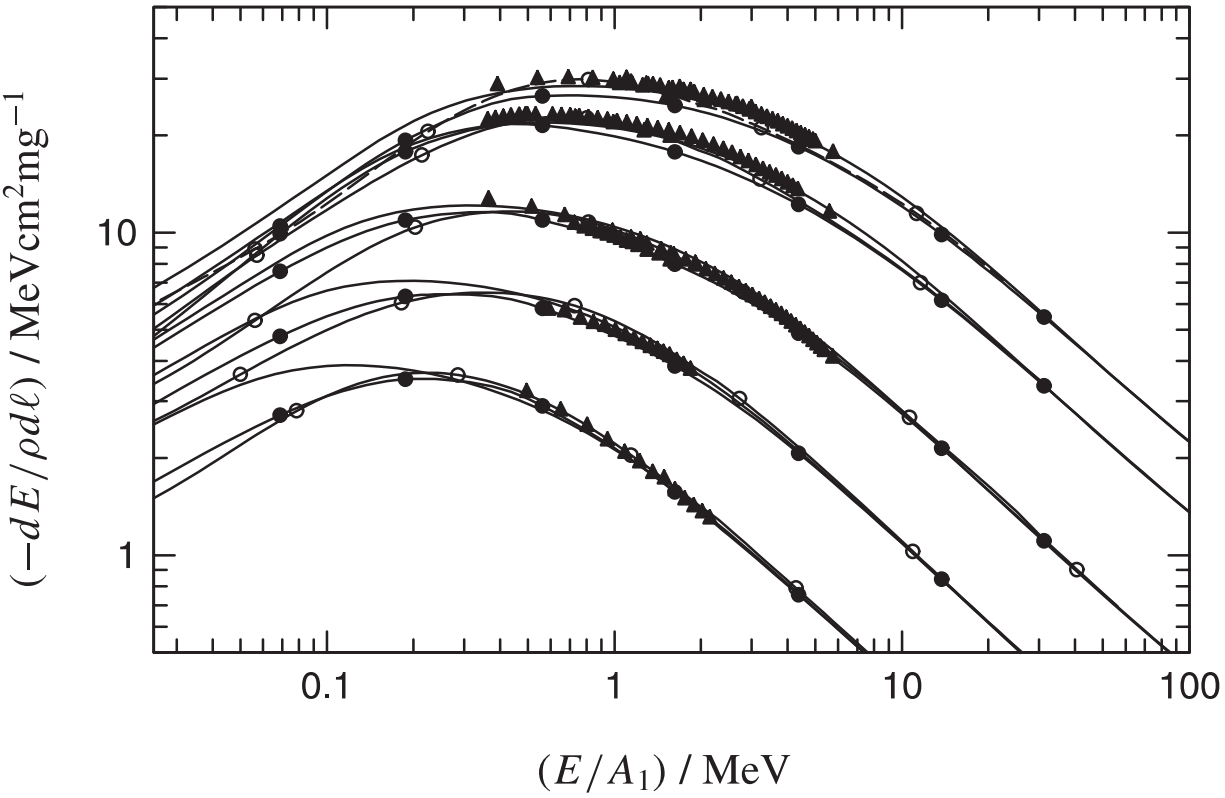


Figure 5.18. Stopping of Ar, Si, O, B and Li in polycarbonate (top to bottom). Filled triangles: Experimental data from Alanko *et al*. (2001, 2002), Rauhala and Räisänen (1990), Sharma *et al*. (2002); lines without symbol: PASS (data from Sharma *et al*. (2004b); lines with filled circles: SRIM; lines with empty circles: MSTAR.

While it is straightforward to identify the energy/velocity range in which nuclear stopping can be neglected (cf. Figures 5.5–5.7), proper data analysis is more complicated when the effect does contribute. There is a significant uncertainty regarding magnitude and functional behavior of the unrestricted nuclear stopping power, to which must be added some ambiguity with regard to the kind of restriction applying to a particular experiment.

The problem has been discussed on theoretical grounds in Section 3.2.7. With the exception of Figure 5.5 which shows estimates of both total and restricted stopping power, curves labelled 'nuclear' refer to unrestricted for the reason that the restricted nuclear stopping power depends sensitively on target thickness (cf. Figure 3.37). Although the angular-restricted stopping power in Figure 5.5 is significantly smaller than the total for the specific target thickness, the correction is not generally negligible in the velocity range below v_0.

Glazov and Sigmund (2003) discussed the validity of nuclear-stopping corrections applied in several widely quoted data sets. It was found that the procedures applied in those studies in which corrections were made were well-founded, but that the Thomas–Fermi interaction potential adopted in most of those studies is likely to overestimate the magnitude of the nuclear-stopping correction. This suggests that extracted electronic stopping powers are likely to be too small. This was found to primarily affect data by Ormrod and Duckworth (1963), Ormrod *et al*. (1965) and Ormrod (1968) with the largest nuclear-stopping corrections. Applying an alternative correction would require detailed documentation on target thickness for every data point.

Other potential sources of error which are usually not mentioned and consequently have not been studied in any detail are:

- skewness of the electronic-energy-loss profile, including inner-shell effects (Lennard *et al*., 1986b); and
- correlations between electronic and nuclear energy loss of the type studied for swift protons (Eckardt *et al*., 1984; Gras-Marti, 1985; Lantschner *et al*., 1987).

Stopping powers deduced from range measurements do not suffer from ambiguities due to restricted nuclear stopping but are more sensitive to the adopted nuclear-stopping model, as ranges are governed by stopping and scattering parameters over the

Table 5.8. Tables and computer programs for stopping power.

Reference	Type[a] name	(E/A_1)/MeV	Z_1	Targets	Ranges?	Remarks
Benton and Henke (1969)	F, P	0.1–1200	Any ion	Any solid	Yes	Stopping power obtained as derivative of range
Brice (1972)	F	0.1–2.8	16	Gases	No	3-parameter formula
CERN (2001)	P Geant4	Wide range	All particles	All targets		See Tables 5.2–5.3
Diwan *et al*. (2001)	F	0.5–2.5	3–35	16 solids	No	Adaptation of Hubert formula to lower energy
Grande and Schiwietz (2000, 2001)	P CasP	0.001–200	≥ 1	$1 \leq Z_2 \leq 92$	No	See Table 5.3
Hiraoka and Bichsel (2000)	T	1–1000	6, 7, 10, 14, 18	72 materials	Yes	See Table 5.3
Hubert *et al*. (1980)	F, T	2.5–100	2–103	18 solid elements	Yes	
Hubert *et al*. (1989, 1990)	F, T	2.5–500	2–103	36 solid elements	Yes	See Tables 5.2–5.7
ICRU 49	T, P PSTAR, ASTAR	0.001–10000, 0.00025–250	1, 2	25 elements, 48 mixtures and compounds	Yes	
Konac *et al*. (1998)	F	0.01–100	1–100	C, Si	No	See Table 5.3
Mukherji and Nayak (1979)	F	≤ 10	6–18	Various		
Northcliffe and Schilling (1970)	T	0.0125–12	1–103	24 materials	Yes	See Tables 5.2–5.6
Paul (2003)	P MSTAR	0.001–250	3–18	Same as ICRU 49 + Ni	No	See Tables 5.2–5.5
Sigmund and Schinner (2002)	P PASS	>0.025 (recommended)	3–92 (recommended)	Potentially all elements and compounds	No	See Tables 5.2–5.7
Steward (1968)	T		6, 10, 18, 92	Al, U, H_2O	Yes	
	C	0.01–500	1, 2, 6, 10, 18, 54, 86	H_2O, Al, Cu, Ag, Pb, U		
	P		all	all	Yes	
Xia and Tan (1986)	F	0.00025–0.2	3–82 (many)	Solids	No	Relative to p stopping by Andersen and Ziegler (1977)
Ziegler (1980)	T	0.2–1000	1–92	All elements	Yes	
Ziegler (2003)	P TRIM, SRIM	Energy = 1 eV–2 GeV	1–92	All elements, many other targets	Yes	See Tables 5.2–5.6

[a]F = formula; T = table; P = program; C = curve.

entire energy range from the initial to zero energy (cf. Section 3.15.7 and the last two paragraphs of Section 5.3.4).

5.5.3 Deviations between tabulations and experimental data

Tables 5.2–5.7 characterize the quality of tabulations and codes as judged by the agreement with available experimental data. The analysis was performed by the program JUDGE (Paul and Schinner, 2002, 2003b). Each entry shows an average relative deviation

$$\Delta = \left(\langle x \rangle \pm \sqrt{\langle x^2 \rangle - \langle x \rangle^2} \right), \tag{5.2}$$

in per cent, where $\langle \ldots \rangle$ denotes an average with constant weights,[39] $x = (d - t)/d$, d being an experimental data point and t the corresponding table value.

Table entries for individual programs have been evaluated for different ranges of specific energy as given in the table heading. The number of points[40] averaged, given in the second header line, gives an

[39]All data points are treated equally, except that some discrepant measurements were omitted and that for some measurements with an exceptionally large number of points, this number was reduced (Paul and Schinner, 2001).

[40]These numbers refer to those covered by SRIM, MSTAR, and Geant4 and may be smaller for other tables.

indication of the statistical significance of a table entry.

Table 5.2 shows results for oxygen in carbon based on the set of data underlying Figure 5.5. Similarly, Table 5.3 shows numerical comparisons for carbon ions in carbon based on the data presented in Figure 5.6.

For oxygen in carbon (Table 5.2), all tabulations and codes reproduce the available data accurately from 10 MeV/u upward, and minor discrepancies for 1–10 MeV/u are barely outside experimental uncertainty. At lower velocities, predictions of the Geant4 code show increasing discrepancies while differences between all other codes appear insignificant.

It is important to note here that for Hubert *et al*. (1990), SRIM, MSTAR, and Geant4, the sample of experimental data serving as input for JUDGE is essentially the same as the one serving as input into the respective program. Therefore, mean deviations $\langle x \rangle$ *must* be small in those cases. However, this is of little help to the user as long as the scatter is much larger than the mean deviation. From this point of view, the quality of the predictions of Northcliffe and Schilling (1970) and PASS is equivalent with that of Hubert *et al*. (1990), SRIM, and MSTAR. This conclusion is strengthened by inspection of the last column, which shows a large scatter compared to the mean deviation for all schemes, and where only Geant4 shows an exceptionally large scatter. [The smaller scatter for Hubert *et al*. (1990) stems from the restricted energy range.]

For carbon in carbon (Table 5.3), similar observations may be made, although quantitative differences are found. Mean deviations $\langle x \rangle$ are found to be noticeably greater than for oxygen in carbon, even for SRIM and MSTAR where this is unexpected. Allowing for experimental uncertainty, significant discrepancies are found mainly for Geant4 below 0.01 MeV/u, for CasP below 0.1 MeV/u, for Northcliffe and Schilling (1970) from 0.1 to 1 MeV, and for all predictions of Konac *et al*. (1998b).

Tables 5.4 and 5.5 show deviations for solid elemental targets and $3 \leq Z_1 \leq 18$ for the tables of Northcliffe and Schilling (1970) and Hubert *et al*. (1990), and the MSTAR and PASS codes. It is seen that both over the entire energy range and in the individual energy intervals, small average deviations are found for Hubert *et al*. (1990) as well as SRIM and MSTAR, as it must be. It is emphasized that mean deviations $\langle x \rangle$ depend on the relative weight of the underlying experimental data (cf. footnote 39). Considering the large scatter found in Figure 5.1, one may assume that another weighting might deliver significantly different mean deviations.

Noticeable average deviations, although still smaller than the scatter at all energies, are found for Northcliffe and Schilling (1970) and PASS. The accompanying scatter is comparable to that of MSTAR and SRIM down to 1 MeV/u, while a scatter between 10 and 20 % is found at lower energies.

Considering the amount of experimental data that has accumulated since 1970, the quality of the predictions of Northcliffe and Schilling (1970) is astonishingly high.

The relatively large scatter (20 %) found from PASS for 0.01–0.1 MeV/u is partly due to the neglect of Z_1 oscillations in the present implementation of binary stopping theory.

Table 5.6 shows comparisons for gas targets. Here, a difference is observed between the three schemes that allow empirically for a gas–solid difference and the PASS code which treats such differences as Z_2 structure. The fact that with the exception of the behavior in the lowest energy interval, mean deviations do not differ significantly from code to code, indicates that observed discrepancies are unrelated to the gas–solid effect in equilibrium charges discussed in Section 4.10.3.

Although predictions of CasP and PASS generally show larger deviations from experimental data in the low-energy range than several empirical codes, predictions on ion–target combinations not covered by experimental data must be expected to have a comparable degree of reliability, while the error of empirical schemes must be expected to increase.

5.6 SUMMARY

With the exception of the CasP and PASS codes (Sections 3.7.1 and 3.7.2), calculational schemes mentioned in this section are fully or partially empirically based. The size of the three-dimensional parameter space (Z_1, Z_2, v) covered reliably by various schemes is limited in all cases, but there are significant differences from scheme to scheme, and the actual regime of validity is frequently neither stated nor known.

A major criterion for quality of an empirical scheme must be the size of the underlying database. Under otherwise equal conditions this sets a strong preference on interpolations based on recent databases. The tables of Northcliffe and Schilling (1970), having served as the standard in the field for several decades, are based on data available until 1969, for which the grid covered by experimental data was much wider than it is now (cf. Figure 5.1). Nevertheless, Tables 5.2–5.6 indicate that over a significant part of the parameter space, the tabulation still can compete with more recent numerical schemes.

The tables of Hubert *et al*. (1990) and the code of Paul and Schinner (2001) are based upon more

extensive data collections but are both limited in scope, Hubert *et al*. (1990) in the velocity range and Paul and Schinner (2001) in the selection of penetrating ions. The joint parameter space covered by these two codes is still less than that covered by SRIM, but in regimes of mutual overlap the three codes appear to deliver data of comparable quality in comparison with existing experiments. The accessible parameter space for PASS is potentially equivalent with the one for SRIM, but input in terms of oscillator strengths, atomic and molecular velocity distributions and charge states is incomplete.

The tables of Hubert *et al*. (1990) were deliberately limited to a velocity range where effective-charge scaling must be well obeyed. This regime is also well covered by CasP, MSTAR, PASS, and SRIM. At lower velocities, on the other hand, the *a priori* accuracy of a prediction of any of these available schemes is rarely better than 10 %. For empirical schemes, such a figure is dictated by the accuracy of most of the underlying experimental data and their analysis, and similar reservations hold for the input into theoretical schemes and their underlying principles.

The question remains to what extent predictions within this error margin can be produced in regions of parameter space that are poorly or not at all covered by data and hence do not significantly affect the determination of fitting parameters. Here, theoretical schemes like CasP and PASS have a considerable potential. For empirical schemes, caution is indicated with regard to low-velocity stopping, in particular to Z_1 and Z_2 structure, and to all compounds with substantial deviations from Bragg additivity.

Journal of the ICRU Vol 5 No 1 (2005) Report 73
Oxford University Press
doi:10.1093/jicru/ndi013

6 TABLES

6.1 INTRODUCTORY SURVEY

This section presents tables of electronic mass stopping forces for selected elemental and compound materials and penetrating ions. Choices had to be made for the procedure to be employed to produce the tables, and for the ion–target combinations and the range of beam energies to be covered. As it was decided to produce tables by the PASS code, some development was found necessary beyond what has been described in Section 3.7.2 and the references quoted there. Moreover, the PASS code offers a variety of options that had to be fixed, and the necessary input in terms of oscillator-strength spectra, electronic velocity spectra and equilibrium charge states had to be specified.

6.1.1 Choice of procedure

The choice between an empirical and a theoretical procedure was made in favor of a theoretical scheme. This would not have been possible at the time when the project was commissioned, but theoretical work within and outside the report committee has provided competitive theoretical schemes over a few years preceding the appearance of this report.

With regard to the ability to reproduce existing experimental data, differences between the best empirical and theoretical schemes seem marginal, as documented in Section 5.5.3. There is, however, little doubt that theoretical schemes have a greater potential for improvement. Indeed, while upcoming sets of high-precision stopping data only very gradually will affect the predictions of existing empirical schemes, an improvement on a single feature of any theoretical code may initiate considerable progress. Moreover, improved database input on a specific target material can produce improved predictions for this material for all penetrating ions without any coupling to other materials.

The choice between the four available theoretical schemes discussed in Section 3.7 was made in favor of the binary theory, *i.e.*, the PASS code. At present, this scheme has the widest range of applicability in terms of beam energy and the electronic structure of the stopping material. A specific shortcoming of the PASS code is its lack of ability to produce Z_1 structure. Therefore, an attempt was made to improve this feature by appropriate incorporation of the code of Arista (2002). This work is in progress, but has not yet proceeded to the point that it would be appropriate to incorporate it in the present tables.

6.1.2 Choice of projectiles and targets

Tables in this section cover medium-mass ions from lithium to argon, *i.e.*, $3 \leqslant Z_1 \leqslant 18$ as well as iron ($Z_1 = 26$). This reflects necessary limitations on the size of a printed table rather than a limitation of the PASS code. Ions covered here are of prime interest in biomedical applications.

The selection of materials to be covered follows primarily that made in ICRU Report 49, with the omission of some compound materials which were assumed either to have less importance or to be sufficiently similar to some included material. Elements covered are listed in Table 6.2, and Table 6.1 lists compound materials numbered by the codes employed in ICRU Report 49; Table 6.1 also documents whether stopping forces for compounds were computed on the basis of optical data or from elemental stopping forces making use of Bragg's additivity rule.

The reliability of predictions by the PASS code — as judged by the agreement with published experimental data — is not uniform across the variety of target materials. However, as mentioned already, specific improvements in particular on available optical data for a specific elemental or compound material may cause substantial improvement of predicted stopping parameters.

6.1.3 Range of beam energies

Stopping forces are needed in practical applications over an energy range from eV to GeV energies. An upper limit of 1 GeV/u has been chosen for the tables, but as the PASS code incorporates the relativistic correction of Lindhard and Sørensen (1996),

© International Commission on Radiation Units and Measurements 2005

Table 6.1. Compound materials for which mass stopping forces have been tabulated in this section. Compositions not quoted in the second column are listed in ICRU Reports 37 and 49. The third column refers to materials for which tables have not been included but for which accurate substitutes exist. The fourth column shows the identification number according to ICRU Report 49. The fifth column identifies the procedure applied; Bragg: Bragg additivity assumed; B02: oscillator strengths of outer shells extracted from Berkowitz (2002); HOC: oscillator strengths of outer shells extracted from Palik (2000).

Material	Composition	Substitute	ID	Procedure
A-150 tissue-equivalent plastic			99	Bragg
Adipose tissue (ICRP)			103	Bragg
Air, dry, sea level			104	Bragg
Aluminium oxide	Al_2O_3		106	HOC
Bone, compact (ICRU)			119	Bragg
Bone, cortical (ICRP)			120	Bragg
C-552 air-equivalent plastic			126	Bragg
Calcium fluoride	CaF_2		130	HOC
Carbon dioxide	CO_2		134	B02
Cesium iodide	CsI	Xenon	141	
Glass, borosilicate (Pyrex)			169	Bragg
Kapton polyimide film	$(C_{22}H_{10}N_2O_5)_n$		179	Bragg
Lithium fluoride	LiF		185	HOC
Lithium tetraborate	$(Li_2B_4O_7)$		189	Bragg
Methane	CH_4		197	B02
Muscle striated (ICRU)			202	Bragg
Nylon, type 6 and type 6/6	$(C_6H_{11}O)_n$		209	Bragg
Photographic emulsion			215	Bragg
Plastic scintillator (vinyltoluene based)			216	Bragg
Polycarbonate (makrolon, lexan)	$(C_{16}H_{14}O_3)_n$		219	Bragg
Polyethylene	$(C_2H_4)_n$		221	Bragg
Polyethylene terephthalate (Mylar)	$(C_{10}H_8O_4)_n$		222	Bragg
Polymethyl methacrylate (Lucite, perspex)	$(C_5H_8O_2)_n$		223	Bragg
Polystyrene	$(C_8H_8)_n$		226	Bragg
Polytetrafluoroethylene (Teflon)	$(C_2F_4)_n$		227	Bragg
Propane	C_3H_8		238	Bragg
Silicon dioxide	SiO_2		245	HOC
Sodium iodide	NaI		252	Modelled as NeXe
Tissue-equivalent gas (methane based)			263	Bragg
Tissue-equivalent gas (propane based)			264	Bragg
Water, liquid	H_2O		276	HOC
Water, vapor	H_2O		277	B02

calculations at considerably higher beam energies would still produce reliable results.

This is different at the low-energy end, where considerable uncertainties prevail in all theoretical schemes, as well as in the experimental data that can be utilized to test the accuracy of predictions, as documented in Section 5. While a lower energy limit of 1 keV/u for electronic stopping was aimed at, none of the available schemes — whether empirical or theoretical — was found to produce sufficiently reliable data to justify this as a general lower limit for all tables to be produced.

Binary stopping theory was developed to describe the stopping of ions at velocities exceeding the Bohr velocity v_0. As it turns out, excellent agreement has been achieved with experimental data for some systems such as C and Al significantly below the equivalent energy, 25 keV/u. On the other hand, noticeable discrepancies are observed above that limit for other stopping materials such as neon and argon. With this in mind, 25 keV/u was chosen as the lower limit. It is expected that this limit will be relaxed in a future update of these tables.

6.2 COMPUTATIONAL PROCEDURE

6.2.1 The basic scheme

The basic quantity calculated by the program PASS, written by Andreas Schinner, is the energy transfer to an electron initially at rest *versus* impact parameter, $T = T(p)$, depending on projectile speed v, atomic number Z_1 and charge number q_1,

Table 6.2. Input data for PASS code specifying target elements. The first row in a block shows atomic Number Z, atomic weight A, I-value/eV according to ICRU Report 49 and mass density/gcm^{-3}. Subsequent rows in a block show principal quantum number n, azimuthal quantum number ℓ, subshell occupation $Z_2 f_j$, subshell I-value $\hbar\omega_j$/eV, and subshell binding energy U_j/eV. $n = 0$ denotes a free-electron shell.

1		1.00794	19.2	0.00008988
1	0	1.000	19.2	15.42
2		4.0026	41.8	0.0001785
1	0	2.000	41.8	24.588
4		9.0122	63.7	1.848
1	0	1.930	209.11	114.3
0	0	2.070	21.68	9.32
6		12.0111	81.0	1.90
1	0	1.992	486.2	288.2
2	0	1.841	60.95	16.59
2	1	2.167	23.43	11.26
7		14.0067	82.0	.001250
1	0	1.741	732.61	403.8
2	0	1.680	100.646	20.33
2	1	3.579	23.550	14.534
8		15.9994	95.0	.001429
1	0	1.802	965.1	538.2
2	0	1.849	129.85	28.7
2	1	4.349	31.60	13.618
10		20.180	137.0	0.0008999
1	0	1.788	1525.9	869.5
2	0	2.028	234.9	47.7
2	1	6.184	56.18	21.564
13		26.9815	166.	2.699
1	0	1.623	2701.	1564.1
2	0	2.147	476.5	121.5
2	1	6.259	150.42	76.75
0	1	2.971	16.89	9.08
14		28.086	173.	2.329
1	0	1.631	3206.1	1844.1
2	0	2.094	586.4	154.04
2	1	6.588	186.8	103.71
3	0	2.041	23.52	13.46
3	1	1.646	14.91	8.1517
18		39.948	188.	.0017837
1	0	1.535	5551.6	3206.2
2	1	8.655	472.43	266.85
3	0	1.706	124.85	29.24
3	1	6.104	22.332	15.937
22		47.88	233.	4.508
1	0	1.581	8554.6	4969.9
2	1	8.358	850.58	487.5
3	1	8.183	93.47	44.37
3	2	2.000	39.19	8.1
0	0	1.878	19.46	6.8282
26		55.847	286.	7.873
1	0	1.516	12254.7	7112.
2	1	8.325	1279.29	750.8
3	1	8.461	200.35	68.85
3	2	6.579	49.19	9.34
0	0	1.119	17.66	7.90

Table 6.2. Continued

28		58.7	311.	8.907
1	0	1.422	14346.9	8337.8
2	1	7.81	1532.28	903.01
3	1	8.385	262.71	84.88
3	2	8.216	74.37	10.213
0	0	2.167	23.03	7.6398
29		63.546	322.	8.933
1	0	1.458	15438.5	8983.9
2	1	8.049	1667.96	984.3
3	1	8.79	294.1	92.0
3	2	9.695	70.69	10.62
0	0	1.008	16.447	7.7264
32		72.59	350.	5.323
1	0	1.442	19022.1	11105.
2	1	7.791	2150.79	1276.7
3	1	7.837	455.79	140.37
3	2	10.122	179.87	31.82
4	0	2.463	57.89	14.3
4	1	2.345	20.95	7.9
36		83.80	352.	.003743
1	0	1.645	24643.	14328.
2	1	7.765	2906.4	1753.2
3	1	19.192	366.85	157.25
4	1	7.398	22.24	17.38
42		95.94	424.	10.22
1	0	1.313	34394.	20003.
2	1	6.409	4365.3	2639.0
3	1	19.229	589.36	321.46
4	1	8.633	129.42	47.98
4	2	5.036	35.59	8.56
0	0	1.380	18.42	7.09
47		107.868	470.	10.500
1	0	1.295	43664.3	25518.
2	1	6.219	5824.91	3513.9
3	1	18.751	909.79	484.5
4	1	8.748	175.47	73.71
4	2	10.184	54.89	10.4
0	0	1.803	19.63	7.576
50		118.69	488.	7.285
1	0	1.277	49948.	29203.
2	1	6.099	6818.2	4123.9
3	1	20.386	1036.1	616.19
4	1	8.011	172.65	104.44
4	2	10.007	70.89	28.12
5	0	2.272	33.87	12.
0	1	1.948	14.54	7.34
54		131.3	482.	.005895
1	0	1.563	58987.	34563.
2	1	6.312	8159.	5032.2
3	1	21.868	1296.6	831.38
4	1	5.762	356.75	168.77
4	2	11.245	101.03	68.15
5	1	7.250	16.52	15.27
74		183.85	727.	19.254
1	0	1.202	115025.9	69525.
2	1	5.582	17827.44	11181.625
3	2	19.527	3214.36	2125.98
4	2	18.741	750.41	354.33
5	1	8.411	305.21	49.6875
4	3	14.387	105.50	32.5
5	2	4.042	38.09	9.0
6	0	2.108	21.25	7.89

Table 6.2. Continued

78		195.09	790.	21.45
1	0	1.159	128342.	78395.
2	1	5.467	20254.	12570.
3	1	18.802	3601.8	2488.
4	2	33.905	608.1	280.9
5	1	8.300	115.0	69.0
5	2	9.342	42.75	9.6
0	0	1.025	17.04	9.
79		196.9665	790.	19.291
1	0	1.124	131872.	80725.
2	1	5.331	20903.	12981.
3	1	18.078	3757.4	2585.7
4	2	34.604	682.1	300.8
5	1	8.127	105.2	74.30
5	2	10.414	44.89	11.66
0	0	1.322	17.575	9.226
82		207.2	823.	11.343
1	0	2.000	154449.	88005.
2	1	8.000	25067.	14283.
3	2	18.000	5105.0	2908.78
4	2	18.000	987.44	562.49
4	3	14.000	247.59	140.59
5	1	8.000	188.1	106.8098
5	2	10.000	40.61	20.904
6	0	2.000	19.2	10.
0	1	2.000	15.17	7.4167
92		238.0289	890.	19.05
1	0	2.000	167282.	115606.
2	1	8.000	27868.	19259.5
3	2	18.000	6022.7	4162.13
4	3	32.000	1020.4	704.71
5	2	18.000	244.81	164.15
6	1	8.000	51.33	33.
7	0	2.000	13.	6.1941
6	2	1.000	11.06	6.1
0	3	3.000	14.43	6.

resonance frequency ω and binding energy U. This calculation (Sigmund and Schinner, 2000) involves the center-of-mass scattering integral as well as the time integral, both being evaluated numerically for a spherically symmetric potential given by

$$V(r) = -\frac{q_1 e^2}{r} e^{-r/a_{\rm ad}} - \frac{(Z_1 - q_1)e^2}{r}\chi(r/a), \qquad (6.1)$$

where $\chi(r/a)$ is a screening function, $a_{\rm ad} = v/\omega$ the adiabatic radius and

$$\frac{1}{a^2} = \frac{1}{a_{\rm ad}^2} + \frac{1}{a_{\rm sc}^2}. \qquad (6.2)$$

The screening radius $a_{\rm sc}$ is given by (Sigmund, 1997)

$$a_{\rm sc} = a_{\rm TF}\left(1 - \frac{q_1}{Z_1}\right)^{\mathbf{r}}, \qquad (6.3)$$

where $a_{\rm TF} = 0.8853 a_0/{Z_1}^{1/3}$ and **r** is a numerical coefficient with the default value 1. Alternative choices for $a_{\rm TF}$ and **r** are allowed for.

For the screening function, the default option underlying all data tabulated below is

$$\chi(r/a) = e^{-r/a}, \qquad (6.4)$$

but the screening function of Molière (1947),

$$\chi(r) = \sum_j A_j e^{-\alpha_j r/a}. \qquad (6.5)$$

with

$$A = (0.35,\ 0.55,\ 0.10), \quad \alpha = (0.3,\ 1.2,\ 6.0) \qquad (6.6)$$

has been implemented as an alternative. The energy transfer is composed of a kinetic and a potential term (Sigmund and Schinner, 2000),

$$T(p,v) = 2mv^2 \sin^2\frac{\theta(p,v)}{2} + W(p,v), \qquad (6.7)$$

where

$$\frac{1}{W(p,v)} = \frac{1}{W_0(p,v)} + \frac{s}{U} + \frac{t}{T}, \qquad (6.8)$$

and $W_0\,(p,v)$ is the potential-energy transfer evaluated from the scattering integrals. Equaion (6.8) ensures that the potential-energy transfer cannot exceed a fraction $1/s$ of the ionization energy U with the default value $s = 2$. The last term ensures that W cannot exceed a fraction $1/t$ of the kinetic-energy transfer T, with the default value $t = 0$.

Since perturbation expansion is avoided, the scheme incorporates an estimate of the Barkas–Andersen effect. For stripped ions the Barkas–Andersen effect can be eliminated by taking the average between the stopping cross sections for atomic numbers Z_1 and the corresponding antiparticle $(-Z_1)$.

6.2.2 Energy loss to target atom

A target atom with atomic number Z_2 contains Z_2 electrons that are grouped into shells or subshells characterized by resonance frequencies ω_j, binding energies U_j, as well as oscillator strengths f_j obeying the sum rule

$$\sum_j f_j = 1 \qquad (6.9)$$

so that each shell or subshell contains $Z_2 f_j$ electrons. $Z_2 f_j$ is generally not an integer.

The stopping cross section S_{0j} per target electron in the jth shell or subshell, excluding shell correction,

is then determined by integration,

$$S_{0j} = \int_0^\infty T_j(p) 2\pi p \, \mathrm{d}p, \tag{6.10}$$

and the stopping cross section per atom, again excluding shell correction, is found from

$$S_0 = \sum_j Z_2 \, f_j \, S_{0j}. \tag{6.11}$$

6.2.3 Shell Correction

Shell corrections account for intrinsic motion of target electrons. For free binary collisions this implies transformation between the laboratory system and a reference frame in which a given target electron is at rest. The transformation between the respective stopping cross sections reads (Sigmund, 1982)

$$S_j(v) = \left\langle \frac{\boldsymbol{v}\cdot(\boldsymbol{v}-\boldsymbol{v}_e)}{v|\boldsymbol{v}-\boldsymbol{v}_e|} S_{0j}(|\boldsymbol{v}-\boldsymbol{v}_e|) \right\rangle_j, \tag{6.12}$$

where $\langle \cdots \rangle_j$ indicates an average over electron velocities $\boldsymbol{v}_e$ in the jth shell or subshell and $\boldsymbol{v}$ denotes the projectile velocity vector.

Velocity distributions used for determining these averages are discussed in Section 6.3.2.

6.2.4 Quantum correction

A smooth transition into the quantum regime is provided by the inverse Bloch correction, (3.20). However, even though this correction goes to zero at low velocity, the approach is so slow that the stopping number (before shell correction) may turn negative over a certain interval. This artifact, discussed by (Sigmund and Schinner 2002b), is related to the failure of the logarithmic approximation underlying Bethe's, Bohr's and Bloch's theory at low projectile speed.

The problem has been avoided (Sigmund and Schinner, 2002b) by

1. replacing the straight Bohr logarithm by

$$ln(C\xi) \to \ln(B + C\xi) - \ln B; \quad B = 0.880, \tag{6.13}$$

   in accordance with the numerical behavior at low velocity (Sigmund, 1996), and
2. replacing the ψ functions with elementary approximations proposed by Lindhard and Sørensen (1996).

As a result one obtains the following expression for the inverse-Bloch correction,

$$\Delta L = \ln \frac{1 + 2\xi \Big/ \left(B\sqrt{C^2 + (\hbar v / Z_1 e^2)^2} \right)}{1 + 2\xi/BC}. \tag{6.14}$$

6.2.5 Relativity

The standard relativity correction (Bethe, 1932; Fano, 1963)

$$\Delta S = \frac{4\pi Z_1^2 Z_2 \, e^4}{m v^2} \left[-\frac{v^2}{c^2} - \ln\left(1 - \frac{v^2}{c^2}\right) \right] \tag{6.15}$$

can be added where appropriate.[41] The code of Lindhard and Sørensen (1996) has been incorporated as a subroutine that can be called by PASS to allows for a smooth transition into the highly relativistic regime.

Neither Eq. (6.15) nor the code of Lindhard and Sørensen (1996) allow for projectile screening. This could give rise to some error for very heavy ions.

6.2.6 Projectile excitation

Projectile excitation can be included. It has been pointed out by Sigmund and Glazov (2003) that it is necessary to distinguish between ionizing and nonionizing processes on the projectile.

Nonionizing collisions can be treated by inverting the roles of target and projectile. However,

- projectile atoms carry charge; hence, their excitation spectra differ from those of neutral atoms
- projectile ions are not necessarily in their ground states; also this feature affects excitation spectra.

Associated uncertainties may be estimated by two options:

1. the number of electrons in every shell is reduced by a common factor q_1/Z_1, or
2. projectile states are filled up from the bottom.

In either case, shifts in excitation frequencies are ignored. This tends to overestimate stopping. The second option must lead to a lower stopping force

[41] It is emphasized that Eq. (6.15) represents the relativity correction following from the Bethe theory, while Bohr (1915) derived a slightly different result. For lighter ions, the correction will typically become significant in the Born regime. For heavier ions, the correction due to Lindhard and Sørensen (1996) needs to be allowed for, and that correction is defined relative to the Bethe expression.

than the first because of a higher weight of high excitation frequencies. The first option is the default.

A technical problem arises from the fact that the interaction potential (6.1) in conjunction with Eq. (6.4) reduces to a simple attractive Yukawa potential between the neutral target atom and a projectile electron. This potential is known to lead to resonant interactions in classical scattering at low velocity. Those resonances also occur in target excitation, but their effect is much less significant there because even a small charge on the projectile is sufficient to wipe them out.

Such resonances are not easily identified after incorporation of shell corrections, but their effect persists *via* an enhanced contribution to the stopping force. This is an artifact inherent in the basic approximation as the real interaction potential is a stochastic quantity.

Resonances can be avoided by evaluating projectile excitation on the basis of Lindhard's 'magic formula' (Lindhard *et al*. 1968) for classical scattering off a screened-Coulomb potential, applied to Eq. (6.1) for $q_1 = 0$. This option, which has been adopted as the default for projectile excitation and which underlies all tabulations given below, ignores the Barkas–Andersen effect in projectile excitation.

6.2.7 Charge exchange

The contribution to energy loss from *projectile-ionizing collisions* has initially been estimated by the same procedure as for nonionizing events. According to the discussion in Section 3.4.7 this tends to overestimate stopping. This has been compensated by allowing for an asymmetry correction given by

$$\Delta T = -\sqrt{T_1(T_1 - U_1)}, \tag{6.16}$$

where T_1 is the uncorrected energy transfer to a projectile electron emerging from the above scheme and U_1 the binding energy in the respective projectile shell.

Energy loss due to electron capture can likewise be included. The cross section for such events is taken to be identical to the electron-loss cross section for equilibrium stopping.[42] The energy loss in a capture event is taken as $mv^2/2$, *i.e.*, the energy spent in accelerating a target electron from zero to the projectile speed. The binding energy to the target atom is not subtracted because that contribution is already taken care of in the main contribution to the stopping cross section, and the binding energy to the projectile is ignored since it is usually small because of capture proceeding into high-angular-momentum states.

6.3 INPUT

6.3.1 Frequency spectra

Frequency spectra are characterized in terms of data pairs (f_j, ω_j). They are the most important piece of numerical input. This input is summarized in a database which is read by PASS during every run of the program.

This database has been compiled from experimental and calculated oscillator-strength spectra in the literature. Main references have been the books of Palik (1985, 1991, 1996) and an electronic version (Palik, 2000), the article by Henke *et al*. (1993) and an electronic version (LBL, 2002), and the books by Berkowitz (1979, 2002).

Considerable differences are found between these compilations as far as elemental materials are concerned. Information on compounds is scarce with a few exceptions such as ionic crystals and other optically important materials. In selecting data for the present use the focus has been on the *f*-sum rule.[43] Major uncertainties mostly concern outer electron shells. Where feasible and necessary, analog behavior of chemically similar elements has been postulated.

Once an oscillator-strength spectrum has been found with less than one electron missing or in excess, oscillator strengths have been bundled into shells or subshells. Inner-shell data are bundled into principal shells, while subshells are limited to one or two outermost shells. This bundling was guided by absorption edges, tabulated subshell binding energies, nominal occupation numbers of shells and/or subshells and the grid of the tabulated data. The angular-momentum quantum number ℓ was chosen to be the nearest integer to the average.

f_j and ω_j were then determined by integration,

$$\begin{aligned} f_j &= \int_j \mathrm{d}(\hbar\omega) f(\hbar\omega), \\ \ln(\hbar\omega_j) &= \frac{\int_j \mathrm{d}(\hbar\omega) f(\hbar\omega) \ln(\hbar\omega)}{\int_j \mathrm{d}(\hbar\omega) f(\hbar\omega)}, \end{aligned} \tag{6.17}$$

[42] This relation is obviously invalid for charge states far from equilibrium. Its use in the current context is justified by the fact that the contribution from charge exchange to stopping is altogether quite small.

[43] Most available data do not strictly satisfy the *f*-sum rule. In case of minor deficiencies (~1 electron for heavier elements), renormalization was performed so that the sum rule was fulfilled, without changing the frequencies.

where $\int_j$ indicates the adopted energy interval specifying the jth shell. Deviations in $Z_2\, f_j$ of up to 0.5 from nominal occupation numbers were taken to be tolerable.

The above procedure is not operative for all elements because of insufficent information on oscillator-strength spectra. Amongst a number of options, the procedure by Sternheimer *et al*. (1982) was chosen in such cases which utilizes nominal occupation numbers for shells and subshells and a simple scaling procedure to relate I values for each shell to the respective shell binding energy U such as to ensure the appropriate I value of the material. This procedure has been applied in this report to lead and uranium with the values from ICRU Report 49 for the I value.

Entries for specific compounds are allowed in the PASS database. In those cases where stopping forces were computed without invoking Bragg additivity, a standard procedure has been followed (Sharma *et al*., 2004a) which utilizes atomic data for the inner shells of the constituent atoms, while outer-shell electrons are collected in one single valence shell. The I-value of the valence shell is determined from available molecular data. Details for individual compounds are listed in Table 6.1. This list contains also a few substances for which stopping data can be computed *via* substitute materials. Replacement of alkali halides by 'compounds' of neighboring noble-gas atoms has been found justifiable by a comparison between LiF and Ne, where complete agreement has been found over the entire energy range.

A complete list of (f_j, ω_j)-pairs entering stopping data presented below may be found in Table 6.2.

6.3.2 Shell correction

Evaluation of shell corrections from Eq. (6.12) requires velocity spectra. For valence and conduction electrons in metals such spectra were evaluated either from atomic wave functions by the procedure described below, or from a Fermi destribution with the Fermi energy given by the number of electrons occupying the respective shell.

Evaluation from atomic wave functions proceeds over Fourier transform according to

$$F_{n\ell}(k) = \frac{1}{2\pi^2}\left|\int_0^\infty \mathrm{d}r\, r^2 R_{n\ell}(r) j_\ell(kr)\right|^2, \tag{6.18}$$

where $R_{n\ell}(r)$ is the radial wave function of the (n,ℓ)th subshell and $j_\ell(x)$ a spherical Bessel function.

Hartree–Fock radial wave functions taken from Clementi and Roetti (1974) were explored extensively in previous applications of binary stopping theory, and with good success (Sigmund and Schinner, 2001a, 2002c). Subsequently it was found that these functions overestimate one-electron kinetic energies needed in the above transformation (6.12). Therefore, hydrogenic wave functions were found to be more appropriate in the present context, with the effective charge $Z_{j,\mathrm{eff}}$ of the jth shell determined by the respective ionization energy,

$$U_j = \frac{Z_{j,\mathrm{eff}}^2}{n^2}\mathsf{R}, \tag{6.19}$$

where n is the principal quantum number and R the Rydberg energy.

Both in the previous and the present procedure, radial wave functions are expressed as sums of Slater functions,

$$R_{n\ell}(r) = \sum_{j'} a_{j'}^{n\ell} N_{j'}^{n\ell} r^{n_{j'}^{n\ell}-1} e^{-\zeta_{j'}^{n\ell} r}; \tag{6.20}$$

$$N_{j'}^{n\ell} = \frac{(2\zeta_{j'}^{n\ell})^{n_{j'}^{n\ell}+\frac{1}{2}}}{\sqrt{(2n_{j'}^{n\ell})!}}. \tag{6.21}$$

For hydrogenic wave functions one finds

$$\zeta_{j'}^{n\ell} = \frac{Z_{j',\mathrm{eff}}}{n}, \tag{6.22}$$

$$n_{j'}^{n\ell} = \ell + j', \tag{6.23}$$

$$a_{j'}^{n\ell} = \frac{(-1)^{j'-1}}{(j'-1)!}\binom{n+\ell}{n-\ell-j'} \times\sqrt{\frac{(n-\ell-1)!(2\ell+2j')!}{2n(n+\ell)!}} \tag{6.24}$$

for the numerical coefficients, where j' runs from 1 to $n-\ell$. All lengths are taken in Bohr radii.

Insertion of Eq. (6.20) into Eq. (6.18) yields

$$F_{n\ell}(k) = \frac{1}{2\pi^2}\left|\sum_{j'}\frac{a_{j'}^{n\ell} N_{j'}^{n\ell}}{k^{n_{j'}^{n\ell}+2}} I_{\ell,n_{j'}^{n\ell}+1}\left(\frac{\zeta_{j'}^{n\ell}}{k}\right)\right|^2, \tag{6.25}$$

where

$$I_{\ell,m}(z) \equiv \int_0^\infty \mathrm{d}x\, e^{-zx} j_\ell'(x) x^m. \tag{6.26}$$

The $I_{\ell,m}$ can be calculated without explicit integration by utilizing recurrence relations

(Talman, 1978),

$$I_{\ell,\ell+1} = \frac{2\ell}{1+z^2} I_{\ell-1,\ell},$$
$$I_{\ell,\ell} = (2\ell-1) I_{\ell-1,\ell-1} - z I_{\ell-1,\ell}, \qquad (6.27)$$
$$I_{\ell,m} = \frac{(1+z^2) I_{\ell,m+2} - 2z(m+1) I_{\ell,m+1}}{(\ell-m)(\ell+m+1)}$$

and

$$I_{0,0} = \arctan\frac{1}{z},\ I_{0,1} = \frac{1}{1+z^2}, \qquad (6.28)$$

where the argument z of I has been omitted for brevity.

Thus, the problem of the Fourier–Bessel transform Eq. (6.18) is reduced to the finite sum (6.25) in combination with fast and numerically stable recurrence relations, leading to a fast and reliable numerical representation of the velocity distribution.

Although these velocity distributions are calculated semi-analytically, evaluation of Eq. (6.12) — which is a double integral in practice — by straight numerical integration is not an available option since the computation of uncorrected stopping numbers is already rather time consuming. This would involve the evaluation of L_k^0 at least at several hundred points for a *single velocity* of L_k, which obviously would result in intolerably high computation times.

To overcome this problem a prescan of $L_k^0(v)$ is made, using an exponential mesh optimally adapted to the problem. The inner integral of Eq. (6.12) between arbitrary boundaries is then calculated using a monotonicity-preserving piecewise cubic Hermite interpolant, whereas the outer (semi-infinite) integral can be easily carried out with the aid of a standard adaptive automatic integrator.

The combination of these methods with the compact representation of the velocity distributions makes the transformation from L_k^0 to L_k very fast and numerically stable.

6.3.3 Options for shell correction

A major motivation for the replacement of Hartree–Fock wave functions by hydrogenic functions was a substantial improvement in the agreement of predictions of the PASS code with proton stopping forces (Sharma *et al*. 2004a) which, in general, have a smaller error margin than heavy-ion data at comparable projectile speeds. At the same time this led to improved predictions on stopping of heavy ions, where projectile excitation is significant.

The opposite tendency, however, was found for heavy target materials. While theoretical understanding of this complex is still far from complete, a decision had to be made on the procedure to be followed. Consequently, the tables below have been produced assuming hydrogenic wave functions for all materials up to silver ($Z_2 = 47$) and assuming Hartree–Fock functions for elements from tin ($Z_2 = 50$) on.

PASS allows incorporation of an effective mass differing from the free-electron mass for d electrons of transition metals. This option has *not* been adopted in the computation of tables quoted below.

Outer shells of *metallic projectile ions* are assigned *atomic* velocity distributions. This is handled in practice by using separate databases for projectile and target, the only difference being the assignment of electron velocities of the outermost shells. It is emphasized that the effect of splitting principal target shells into subshells becomes noticeable only after shell correction.

PASS allows to toggle on or off the shell correction, but it is treated as a global option which is either applied to all contributions from all considered projectile and target shells, or to none.

Shell corrections evaluated from molecular wave functions are currently not available in PASS.

6.3.4 Subshell binding energies

Subshell binding energies also enter into the scheme by limiting the potential-energy transfer in an individual collision event in accordance with Eq. (6.8). Binding energies employed in the computations underlying the stopping tables below have been extracted from Williams (1995), who compiled and interpolated data from Slater (1955), Bearden and Burr (1967), Sevier (1972), Fuggle and Mårtensson (1980), and Craseman *et al*. (1987). Weighted averages were taken when subshells were bundled into principle shells. These values are listed in Table 6.2.

6.3.5 Equilibrium ion charge

Binary theory predicts stopping parameters for ions in a given charge state q_1. Stopping parameters in charge equilibrium are of the greatest interest.

Equation (3.32) has been used occasionally (Sigmund and Schinner, 2002c), but the computations reported below have been performed on the basis of Eq. (3.31). This is less rigorous than Eq. (3.32) but has the advantage that established scaling relations as well as tabulated mean equilibrium charges can be utilized.

The present tabulations were performed with a mean equilibrium charge state approximated by a Thomas–Fermi-type expression

$$q_{\text{equil}} = Z_1\left(1 - e^{-v/Z_1^{2/3}v_0}\right). \tag{6.29}$$

Frozen-charge stopping cross sections have been computed occasionally for orientational purposes. This is of interest mostly for the lightest ions.

The PASS code allows incorporation of tabulated charge fractions according to Shima *et al*. (1992) or Itoh *et al*. (1999). Furthermore, input may be parameterized in the form

$$q_{\text{equil}} = Z_1\left(1 - e^{-Av/Z_1^{0.45}v_0}\right)^C \tag{6.30}$$

with parameters A, C for each individual ion. This feature is useful in the computation of stopping forces on very heavy ions, in particular in connection with gas–solid differences of the kind documented in Section 4. In the present tabulations, this option has neither been applied in the main tables for $Z_1 = 18$ nor for Fe ions nor for any of the plots labeled PASS in Section 5.

6.3.6 Computational aspects

The FORTRAN code PASS evaluates the stopping number L as a function of the Bohr variable $\xi = mv^3/\mathrm{Z}_1\ v_0\ I_{\text{ICRU}}$, where I_{ICRU} is the I-value of the target material recommended in ICRU Report 49. The computationally intensive part is the evaluation of the classical-scattering integrals while an efficient procedure described in Section 6.3.2 economizes the computation of shell corrections. Computation times are governed mainly by the number of target and projectile shells to be treated.

Computation of one column in the stopping tables below requires typically about 70 s of computation time per shell on a PC.

A large number of input checks have been built into the code to prevent wrong input such as charge fractions exceeding unity, projectile velocity exceeding the speed of light, etc.

6.3.7 Sensitivity studies

Extensive sensitivity studies have been performed involving various parameters entering the scheme. The interested reader is referred to a summary by Sigmund and Schinner (2002b).

6.4 TABLES: INPUT DATA

Table 6.2 shows input data for the PASS code specifying elements. The first row in a block shows atomic number Z, atomic weight A, I-value [eV] according to ICRU Report 49[44] and the mass density [g/cm^3]. Subsequent rows in a block show principal quantum number n, azimuthal quantum number ℓ, subshell occupation Zf_j, subshell I-value $\hbar\omega_j$ and subshell binding energy U_j.

Two sets of data may be employed for a given element, dependent on whether it enters as target or projectile. As a general rule for both molecular and solid materials, properties listed in Table 6.2 have been determined from target properties, *i.e.*, properties of the solid or the molecular state, depending on the element. By and large, data so found are also applied when the same element occurs as a projectile.

Two types of exceptions are made to this scheme:

1. For molecular targets such as nitrogen and oxygen gas, where both atomic and molecular parameters are available (Berkowitz, 2002), both sets of parameters are utilized, but only molecular parameters are listed in Table 6.2.
2. For metallic solids, one or two outer shells — depending on the particular element — are combined into one free-electron shell for the computation of shell corrections.

[44]The I-value from ICRU Report 49 is used exclusively for the purpose of connecting the energy per nucleon to the Bohr parameter ξ. This implies that the actual I-value that determines the stopping force as a function of projectile speed or energy differs from the ICRU value [cf. Table 3.1].

6.5. TABLES: ELECTRONIC STOPPING FORCE FOR SIXTEEN IONS IN ELEMENTAL MATERIALS

Material: Hydrogen

Ion	Li	Be	B	C	N	O	F	Ne
(E/A_1) / MeV				$(-\mathrm{d}E/\rho\mathrm{d}\ell)$ / MeV cm^2 mg^{-1}				
0.025	8.310E+00	1.050E+01	1.219E+01	1.342E+01	1.465E+01	1.564E+01	1.624E+01	1.675E+01
0.030	8.919E+00	1.136E+01	1.329E+01	1.475E+01	1.614E+01	1.728E+01	1.800E+01	1.860E+01
0.040	9.838E+00	1.272E+01	1.512E+01	1.700E+01	1.873E+01	2.018E+01	2.115E+01	2.196E+01
0.050	1.046E+01	1.372E+01	1.652E+01	1.881E+01	2.087E+01	2.263E+01	2.388E+01	2.492E+01
0.060	1.087E+01	1.444E+01	1.759E+01	2.025E+01	2.262E+01	2.470E+01	2.622E+01	2.751E+01
0.070	1.114E+01	1.496E+01	1.840E+01	2.138E+01	2.405E+01	2.642E+01	2.823E+01	2.977E+01
0.080	1.130E+01	1.533E+01	1.901E+01	2.227E+01	2.520E+01	2.786E+01	2.992E+01	3.171E+01
0.090	1.140E+01	1.558E+01	1.947E+01	2.296E+01	2.614E+01	2.904E+01	3.135E+01	3.337E+01
0.100	1.143E+01	1.576E+01	1.981E+01	2.350E+01	2.689E+01	3.001E+01	3.254E+01	3.479E+01
0.150	1.121E+01	1.590E+01	2.046E+01	2.479E+01	2.888E+01	3.280E+01	3.614E+01	3.925E+01
0.200	1.073E+01	1.553E+01	2.031E+01	2.494E+01	2.939E+01	3.374E+01	3.755E+01	4.116E+01
0.250	1.021E+01	1.501E+01	1.988E+01	2.464E+01	2.929E+01	3.389E+01	3.797E+01	4.189E+01
0.300	9.696E+00	1.446E+01	1.934E+01	2.417E+01	2.892E+01	3.367E+01	3.791E+01	4.203E+01
0.400	8.773E+00	1.338E+01	1.820E+01	2.304E+01	2.786E+01	3.274E+01	3.716E+01	4.148E+01
0.500	7.989E+00	1.241E+01	1.710E+01	2.188E+01	2.668E+01	3.160E+01	3.608E+01	4.049E+01
0.600	7.326E+00	1.155E+01	1.610E+01	2.078E+01	2.553E+01	3.043E+01	3.491E+01	3.936E+01
0.700	6.761E+00	1.079E+01	1.520E+01	1.977E+01	2.444E+01	2.928E+01	3.375E+01	3.819E+01
0.800	6.275E+00	1.012E+01	1.438E+01	1.884E+01	2.342E+01	2.820E+01	3.263E+01	3.705E+01
0.900	5.853E+00	9.533E+00	1.365E+01	1.798E+01	2.247E+01	2.717E+01	3.155E+01	3.594E+01
1.000	5.485E+00	9.006E+00	1.298E+01	1.720E+01	2.159E+01	2.621E+01	3.054E+01	3.489E+01
1.500	4.175E+00	7.054E+00	1.042E+01	1.410E+01	1.802E+01	2.222E+01	2.625E+01	3.034E+01
2.000	3.377E+00	5.801E+00	8.704E+00	1.195E+01	1.547E+01	1.928E+01	2.301E+01	2.683E+01
2.500	2.843E+00	4.933E+00	7.478E+00	1.037E+01	1.355E+01	1.702E+01	2.048E+01	2.406E+01
3.000	2.460E+00	4.297E+00	6.560E+00	9.165E+00	1.206E+01	1.525E+01	1.846E+01	2.182E+01
4.000	1.948E+00	3.427E+00	5.278E+00	7.449E+00	9.897E+00	1.263E+01	1.544E+01	1.841E+01
5.000	1.620E+00	2.862E+00	4.428E+00	6.286E+00	8.406E+00	1.079E+01	1.329E+01	1.594E+01
6.000	1.393E+00	2.464E+00	3.823E+00	5.448E+00	7.316E+00	9.426E+00	1.167E+01	1.408E+01
7.000	1.225E+00	2.169E+00	3.371E+00	4.815E+00	6.486E+00	8.380E+00	1.042E+01	1.261E+01
8.000	1.095E+00	1.941E+00	3.019E+00	4.321E+00	5.831E+00	7.550E+00	9.415E+00	1.143E+01
9.000	9.921E−01	1.759E+00	2.738E+00	3.923E+00	5.303E+00	6.877E+00	8.595E+00	1.046E+01
10.00	9.082E−01	1.610E+00	2.509E+00	3.597E+00	4.867E+00	6.319E+00	7.913E+00	9.649E+00
15.00	6.458E−01	1.146E+00	1.787E+00	2.567E+00	3.484E+00	4.536E+00	5.709E+00	7.002E+00
20.00	5.070E−01	9.002E−01	1.404E+00	2.019E+00	2.742E+00	3.574E+00	4.508E+00	5.542E+00
25.00	4.205E−01	7.468E−01	1.166E+00	1.676E+00	2.278E+00	2.970E+00	3.750E+00	4.616E+00
30.00	3.611E−01	6.415E−01	1.001E+00	1.440E+00	1.958E+00	2.554E+00	3.226E+00	3.975E+00
40.00	2.845E−01	5.055E−01	7.894E−01	1.136E+00	1.545E+00	2.016E+00	2.548E+00	3.141E+00
50.00	2.369E−01	4.212E−01	6.578E−01	9.468E−01	1.288E+00	1.681E+00	2.126E+00	2.622E+00
60.00	2.045E−01	3.635E−01	5.678E−01	8.174E−01	1.112E+00	1.452E+00	1.836E+00	2.265E+00
70.00	1.808E−01	3.214E−01	5.022E−01	7.230E−01	9.839E−01	1.285E+00	1.625E+00	2.005E+00
80.00	1.628E−01	2.894E−01	4.522E−01	6.511E−01	8.861E−01	1.157E+00	1.464E+00	1.807E+00
90.00	1.485E−01	2.641E−01	4.128E−01	5.944E−01	8.090E−01	1.057E+00	1.337E+00	1.650E+00
100.0	1.370E−01	2.437E−01	3.808E−01	5.485E−01	7.466E−01	9.751E−01	1.234E+00	1.523E+00
150.0	1.018E−01	1.810E−01	2.829E−01	4.076E−01	5.549E−01	7.250E−01	9.177E−01	1.133E+00
200.0	8.366E−02	1.488E−01	2.326E−01	3.351E−01	4.564E−01	5.963E−01	7.550E−01	9.324E−01
250.0	7.265E−02	1.292E−01	2.020E−01	2.911E−01	3.964E−01	5.180E−01	6.559E−01	8.102E−01
300.0	6.526E−02	1.161E−01	1.815E−01	2.615E−01	3.562E−01	4.655E−01	5.895E−01	7.282E−01
400.0	5.605E−02	9.971E−02	1.559E−01	2.247E−01	3.060E−01	3.999E−01	5.065E−01	6.258E−01
500.0	5.059E−02	9.001E−02	1.407E−01	2.028E−01	2.763E−01	3.611E−01	4.574E−01	5.651E−01
600.0	4.704E−02	8.370E−02	1.309E−01	1.886E−01	2.569E−01	3.358E−01	4.254E−01	5.256E−01
700.0	4.459E−02	7.933E−02	1.241E−01	1.788E−01	2.436E−01	3.184E−01	4.033E−01	4.983E−01
800.0	4.282E−02	7.619E−02	1.192E−01	1.717E−01	2.339E−01	3.058E−01	3.873E−01	4.786E−01
900.0	4.151E−02	7.386E−02	1.155E−01	1.665E−01	2.268E−01	2.964E−01	3.755E−01	4.640E−01
1000.	4.051E−02	7.207E−02	1.127E−01	1.624E−01	2.213E−01	2.893E−01	3.664E−01	4.528E−01

Material: Hydrogen

Ion	Na	Mg	Al	Si	P	S	Cl	Ar
(E/A_1) / MeV				$(-\mathrm{d}E/\rho\mathrm{d}\ell)$ / MeV cm^2 mg^{-1}				
0.025	1.723E+01	1.800E+01	1.867E+01	1.933E+01	2.027E+01	2.094E+01	2.189E+01	2.230E+01
0.030	1.915E+01	1.994E+01	2.065E+01	2.135E+01	2.234E+01	2.307E+01	2.405E+01	2.450E+01
0.040	2.267E+01	2.352E+01	2.432E+01	2.510E+01	2.616E+01	2.699E+01	2.800E+01	2.852E+01
0.050	2.581E+01	2.677E+01	2.767E+01	2.853E+01	2.967E+01	3.059E+01	3.164E+01	3.220E+01
0.060	2.863E+01	2.972E+01	3.074E+01	3.169E+01	3.292E+01	3.394E+01	3.503E+01	3.564E+01
0.070	3.111E+01	3.237E+01	3.353E+01	3.460E+01	3.593E+01	3.706E+01	3.821E+01	3.887E+01
0.080	3.329E+01	3.473E+01	3.606E+01	3.726E+01	3.870E+01	3.996E+01	4.118E+01	4.191E+01
0.090	3.519E+01	3.682E+01	3.832E+01	3.967E+01	4.124E+01	4.263E+01	4.394E+01	4.476E+01
0.100	3.684E+01	3.865E+01	4.033E+01	4.183E+01	4.354E+01	4.508E+01	4.649E+01	4.741E+01
0.150	4.223E+01	4.489E+01	4.738E+01	4.962E+01	5.203E+01	5.429E+01	5.631E+01	5.782E+01
0.200	4.476E+01	4.802E+01	5.111E+01	5.393E+01	5.689E+01	5.975E+01	6.231E+01	6.439E+01
0.250	4.589E+01	4.956E+01	5.306E+01	5.629E+01	5.967E+01	6.297E+01	6.595E+01	6.846E+01
0.300	4.629E+01	5.024E+01	5.404E+01	5.756E+01	6.124E+01	6.488E+01	6.816E+01	7.100E+01
0.400	4.605E+01	5.033E+01	5.451E+01	5.840E+01	6.249E+01	6.656E+01	7.025E+01	7.353E+01
0.500	4.520E+01	4.967E+01	5.405E+01	5.815E+01	6.248E+01	6.682E+01	7.076E+01	7.431E+01
0.600	4.414E+01	4.870E+01	5.320E+01	5.743E+01	6.190E+01	6.641E+01	7.052E+01	7.425E+01
0.700	4.300E+01	4.760E+01	5.217E+01	5.647E+01	6.104E+01	6.566E+01	6.987E+01	7.372E+01
0.800	4.185E+01	4.647E+01	5.107E+01	5.541E+01	6.004E+01	6.472E+01	6.901E+01	7.294E+01
0.900	4.073E+01	4.534E+01	4.994E+01	5.431E+01	5.896E+01	6.369E+01	6.802E+01	7.201E+01
1.000	3.964E+01	4.423E+01	4.883E+01	5.320E+01	5.786E+01	6.262E+01	6.697E+01	7.100E+01
1.500	3.485E+01	3.925E+01	4.371E+01	4.799E+01	5.258E+01	5.729E+01	6.164E+01	6.570E+01
2.000	3.106E+01	3.523E+01	3.947E+01	4.359E+01	4.802E+01	5.258E+01	5.683E+01	6.083E+01
2.500	2.802E+01	3.196E+01	3.600E+01	3.993E+01	4.417E+01	4.855E+01	5.267E+01	5.657E+01
3.000	2.553E+01	2.925E+01	3.309E+01	3.685E+01	4.089E+01	4.510E+01	4.908E+01	5.286E+01
4.000	2.170E+01	2.504E+01	2.851E+01	3.195E+01	3.565E+01	3.952E+01	4.322E+01	4.678E+01
5.000	1.889E+01	2.191E+01	2.507E+01	2.823E+01	3.164E+01	3.520E+01	3.865E+01	4.199E+01
6.000	1.674E+01	1.950E+01	2.239E+01	2.532E+01	2.846E+01	3.176E+01	3.498E+01	3.813E+01
7.000	1.504E+01	1.758E+01	2.025E+01	2.296E+01	2.588E+01	2.896E+01	3.198E+01	3.495E+01
8.000	1.366E+01	1.601E+01	1.849E+01	2.102E+01	2.375E+01	2.662E+01	2.946E+01	3.228E+01
9.000	1.253E+01	1.471E+01	1.702E+01	1.939E+01	2.195E+01	2.464E+01	2.733E+01	3.000E+01
10.00	1.157E+01	1.361E+01	1.577E+01	1.801E+01	2.041E+01	2.295E+01	2.549E+01	2.804E+01
15.00	8.430E+00	9.966E+00	1.161E+01	1.334E+01	1.519E+01	1.716E+01	1.917E+01	2.122E+01
20.00	6.685E+00	7.921E+00	9.253E+00	1.066E+01	1.218E+01	1.379E+01	1.545E+01	1.717E+01
25.00	5.572E+00	6.612E+00	7.734E+00	8.929E+00	1.021E+01	1.158E+01	1.300E+01	1.448E+01
30.00	4.800E+00	5.700E+00	6.673E+00	7.713E+00	8.829E+00	1.002E+01	1.126E+01	1.256E+01
40.00	3.796E+00	4.511E+00	5.286E+00	6.117E+00	7.009E+00	7.961E+00	8.965E+00	1.002E+01
50.00	3.169E+00	3.768E+00	4.417E+00	5.115E+00	5.864E+00	6.664E+00	7.509E+00	8.400E+00
60.00	2.739E+00	3.257E+00	3.820E+00	4.425E+00	5.075E+00	5.769E+00	6.504E+00	7.280E+00
70.00	2.425E+00	2.884E+00	3.383E+00	3.920E+00	4.497E+00	5.113E+00	5.766E+00	6.457E+00
80.00	2.185E+00	2.600E+00	3.049E+00	3.535E+00	4.055E+00	4.611E+00	5.202E+00	5.826E+00
90.00	1.996E+00	2.375E+00	2.786E+00	3.230E+00	3.706E+00	4.215E+00	4.755E+00	5.327E+00
100.0	1.843E+00	2.193E+00	2.573E+00	2.983E+00	3.423E+00	3.893E+00	4.393E+00	4.922E+00
150.0	1.371E+00	1.632E+00	1.916E+00	2.222E+00	2.551E+00	2.902E+00	3.277E+00	3.673E+00
200.0	1.129E+00	1.344E+00	1.577E+00	1.830E+00	2.101E+00	2.391E+00	2.700E+00	3.028E+00
250.0	9.808E−01	1.168E+00	1.371E+00	1.591E+00	1.827E+00	2.079E+00	2.348E+00	2.634E+00
300.0	8.816E−01	1.050E+00	1.233E+00	1.430E+00	1.643E+00	1.870E+00	2.112E+00	2.369E+00
400.0	7.577E−01	9.023E−01	1.060E+00	1.230E+00	1.413E+00	1.608E+00	1.817E+00	2.038E+00
500.0	6.843E−01	8.149E−01	9.571E−01	1.111E+00	1.276E+00	1.453E+00	1.641E+00	1.841E+00
600.0	6.365E−01	7.580E−01	8.903E−01	1.033E+00	1.187E+00	1.352E+00	1.527E+00	1.713E+00
700.0	6.034E−01	7.187E−01	8.441E−01	9.798E−01	1.126E+00	1.282E+00	1.448E+00	1.625E+00
800.0	5.796E−01	6.903E−01	8.109E−01	9.412E−01	1.081E+00	1.231E+00	1.391E+00	1.561E+00
900.0	5.619E−01	6.693E−01	7.861E−01	9.125E−01	1.048E+00	1.194E+00	1.349E+00	1.514E+00
1000.	5.483E−01	6.531E−01	7.672E−01	8.905E−01	1.023E+00	1.165E+00	1.317E+00	1.477E+00

Material: Helium

Ion	Li	Be	B	C	N	O	F	Ne
(E/A_1) / MeV				$(-\mathrm{d}E/\rho\mathrm{d}\ell)$ / MeV cm^2 mg^{-1}				
0.025	2.636E+00	3.352E+00	3.917E+00	4.345E+00	4.780E+00	5.133E+00	5.370E+00	5.570E+00
0.030	2.851E+00	3.645E+00	4.284E+00	4.779E+00	5.263E+00	5.662E+00	5.934E+00	6.164E+00
0.040	3.202E+00	4.140E+00	4.921E+00	5.548E+00	6.129E+00	6.619E+00	6.966E+00	7.257E+00
0.050	3.470E+00	4.539E+00	5.452E+00	6.207E+00	6.889E+00	7.473E+00	7.897E+00	8.253E+00
0.060	3.676E+00	4.862E+00	5.897E+00	6.774E+00	7.557E+00	8.238E+00	8.742E+00	9.168E+00
0.070	3.832E+00	5.122E+00	6.268E+00	7.260E+00	8.144E+00	8.921E+00	9.509E+00	1.001E+01
0.080	3.948E+00	5.330E+00	6.577E+00	7.675E+00	8.656E+00	9.528E+00	1.020E+01	1.078E+01
0.090	4.035E+00	5.495E+00	6.832E+00	8.027E+00	9.102E+00	1.007E+01	1.082E+01	1.147E+01
0.100	4.097E+00	5.626E+00	7.043E+00	8.325E+00	9.487E+00	1.054E+01	1.138E+01	1.211E+01
0.150	4.194E+00	5.943E+00	7.634E+00	9.235E+00	1.073E+01	1.215E+01	1.333E+01	1.440E+01
0.200	4.123E+00	5.972E+00	7.806E+00	9.584E+00	1.129E+01	1.293E+01	1.435E+01	1.567E+01
0.250	3.996E+00	5.886E+00	7.794E+00	9.671E+00	1.150E+01	1.329E+01	1.486E+01	1.635E+01
0.300	3.850E+00	5.753E+00	7.697E+00	9.631E+00	1.154E+01	1.342E+01	1.509E+01	1.669E+01
0.400	3.558E+00	5.439E+00	7.402E+00	9.382E+00	1.136E+01	1.336E+01	1.513E+01	1.686E+01
0.500	3.290E+00	5.122E+00	7.067E+00	9.051E+00	1.105E+01	1.310E+01	1.492E+01	1.671E+01
0.600	3.052E+00	4.824E+00	6.735E+00	8.703E+00	1.070E+01	1.276E+01	1.461E+01	1.643E+01
0.700	2.842E+00	4.550E+00	6.419E+00	8.360E+00	1.035E+01	1.240E+01	1.426E+01	1.609E+01
0.800	2.656E+00	4.302E+00	6.123E+00	8.029E+00	9.995E+00	1.204E+01	1.390E+01	1.573E+01
0.900	2.492E+00	4.077E+00	5.848E+00	7.717E+00	9.655E+00	1.168E+01	1.353E+01	1.536E+01
1.000	2.346E+00	3.871E+00	5.592E+00	7.423E+00	9.331E+00	1.134E+01	1.317E+01	1.499E+01
1.500	1.812E+00	3.080E+00	4.569E+00	6.202E+00	7.944E+00	9.814E+00	1.155E+01	1.330E+01
2.000	1.476E+00	2.553E+00	3.850E+00	5.306E+00	6.887E+00	8.610E+00	1.024E+01	1.190E+01
2.500	1.247E+00	2.179E+00	3.323E+00	4.629E+00	6.069E+00	7.654E+00	9.184E+00	1.075E+01
3.000	1.082E+00	1.903E+00	2.923E+00	4.104E+00	5.420E+00	6.882E+00	8.317E+00	9.798E+00
4.000	8.605E−01	1.522E+00	2.358E+00	3.344E+00	4.463E+00	5.721E+00	6.989E+00	8.315E+00
5.000	7.182E−01	1.274E+00	1.981E+00	2.826E+00	3.795E+00	4.894E+00	6.025E+00	7.221E+00
6.000	6.189E−01	1.098E+00	1.712E+00	2.450E+00	3.304E+00	4.278E+00	5.297E+00	6.383E+00
7.000	5.455E−01	9.684E−01	1.511E+00	2.166E+00	2.929E+00	3.802E+00	4.729E+00	5.722E+00
8.000	4.889E−01	8.679E−01	1.354E+00	1.944E+00	2.634E+00	3.425E+00	4.274E+00	5.189E+00
9.000	4.437E−01	7.877E−01	1.229E+00	1.766E+00	2.395E+00	3.119E+00	3.901E+00	4.749E+00
10.00	4.068E−01	7.222E−01	1.127E+00	1.620E+00	2.199E+00	2.865E+00	3.591E+00	4.381E+00
15.00	2.911E−01	5.168E−01	8.064E−01	1.160E+00	1.576E+00	2.057E+00	2.591E+00	3.180E+00
20.00	2.296E−01	4.076E−01	6.360E−01	9.147E−01	1.243E+00	1.623E+00	2.048E+00	2.520E+00
25.00	1.910E−01	3.392E−01	5.293E−01	7.613E−01	1.035E+00	1.351E+00	1.706E+00	2.101E+00
30.00	1.644E−01	2.920E−01	4.558E−01	6.557E−01	8.915E−01	1.163E+00	1.470E+00	1.812E+00
40.00	1.300E−01	2.309E−01	3.606E−01	5.189E−01	7.057E−01	9.210E−01	1.164E+00	1.436E+00
50.00	1.085E−01	1.929E−01	3.013E−01	4.336E−01	5.898E−01	7.699E−01	9.736E−01	1.201E+00
60.00	9.382E−02	1.668E−01	2.606E−01	3.751E−01	5.103E−01	6.662E−01	8.427E−01	1.040E+00
70.00	8.309E−02	1.477E−01	2.308E−01	3.323E−01	4.522E−01	5.904E−01	7.469E−01	9.217E−01
80.00	7.490E−02	1.332E−01	2.081E−01	2.996E−01	4.078E−01	5.325E−01	6.738E−01	8.315E−01
90.00	6.844E−02	1.217E−01	1.902E−01	2.739E−01	3.727E−01	4.868E−01	6.160E−01	7.603E−01
100.0	6.320E−02	1.124E−01	1.756E−01	2.529E−01	3.443E−01	4.497E−01	5.691E−01	7.025E−01
150.0	4.710E−02	8.377E−02	1.309E−01	1.886E−01	2.568E−01	3.355E−01	4.248E−01	5.245E−01
200.0	3.880E−02	6.902E−02	1.079E−01	1.555E−01	2.117E−01	2.766E−01	3.503E−01	4.326E−01
250.0	3.375E−02	6.004E−02	9.386E−02	1.352E−01	1.842E−01	2.407E−01	3.048E−01	3.765E−01
300.0	3.036E−02	5.401E−02	8.444E−02	1.217E−01	1.657E−01	2.166E−01	2.743E−01	3.389E−01
400.0	2.612E−02	4.648E−02	7.268E−02	1.047E−01	1.427E−01	1.865E−01	2.362E−01	2.918E−01
500.0	2.362E−02	4.202E−02	6.571E−02	9.470E−02	1.290E−01	1.686E−01	2.136E−01	2.639E−01
600.0	2.199E−02	3.912E−02	6.118E−02	8.818E−02	1.201E−01	1.570E−01	1.989E−01	2.458E−01
700.0	2.086E−02	3.712E−02	5.806E−02	8.367E−02	1.140E−01	1.490E−01	1.888E−01	2.332E−01
800.0	2.006E−02	3.569E−02	5.581E−02	8.044E−02	1.096E−01	1.433E−01	1.815E−01	2.242E−01
900.0	1.946E−02	3.462E−02	5.415E−02	7.804E−02	1.063E−01	1.390E−01	1.761E−01	2.176E−01
1000.	1.900E−02	3.381E−02	5.288E−02	7.621E−02	1.038E−01	1.357E−01	1.720E−01	2.125E−01

Material: Helium

Ion	Na	Mg	Al	Si	P	S	Cl	Ar
(E/A_1) / MeV				$(-\mathrm{d}E/\rho\mathrm{d}\ell)$ / MeV cm^2 mg^{-1}				
0.025	5.709E+00	5.934E+00	6.134E+00	6.339E+00	6.634E+00	6.833E+00	7.144E+00	7.268E+00
0.030	6.323E+00	6.556E+00	6.771E+00	6.990E+00	7.302E+00	7.524E+00	7.843E+00	7.978E+00
0.040	7.464E+00	7.715E+00	7.956E+00	8.198E+00	8.541E+00	8.803E+00	9.139E+00	9.289E+00
0.050	8.515E+00	8.793E+00	9.062E+00	9.326E+00	9.696E+00	9.993E+00	1.034E+01	1.051E+01
0.060	9.493E+00	9.807E+00	1.011E+01	1.040E+01	1.079E+01	1.112E+01	1.149E+01	1.166E+01
0.070	1.040E+01	1.076E+01	1.110E+01	1.142E+01	1.184E+01	1.221E+01	1.259E+01	1.278E+01
0.080	1.124E+01	1.165E+01	1.204E+01	1.239E+01	1.285E+01	1.325E+01	1.365E+01	1.385E+01
0.090	1.202E+01	1.249E+01	1.292E+01	1.331E+01	1.381E+01	1.424E+01	1.468E+01	1.489E+01
0.100	1.273E+01	1.326E+01	1.374E+01	1.418E+01	1.472E+01	1.520E+01	1.566E+01	1.590E+01
0.150	1.540E+01	1.625E+01	1.703E+01	1.773E+01	1.851E+01	1.923E+01	1.988E+01	2.030E+01
0.200	1.695E+01	1.808E+01	1.913E+01	2.007E+01	2.110E+01	2.207E+01	2.295E+01	2.358E+01
0.250	1.783E+01	1.916E+01	2.042E+01	2.157E+01	2.280E+01	2.399E+01	2.506E+01	2.589E+01
0.300	1.831E+01	1.979E+01	2.121E+01	2.251E+01	2.391E+01	2.527E+01	2.650E+01	2.749E+01
0.400	1.866E+01	2.033E+01	2.195E+01	2.346E+01	2.508E+01	2.669E+01	2.814E+01	2.936E+01
0.500	1.860E+01	2.038E+01	2.213E+01	2.376E+01	2.552E+01	2.728E+01	2.887E+01	3.024E+01
0.600	1.838E+01	2.022E+01	2.204E+01	2.375E+01	2.560E+01	2.746E+01	2.915E+01	3.062E+01
0.700	1.807E+01	1.994E+01	2.182E+01	2.357E+01	2.549E+01	2.742E+01	2.917E+01	3.071E+01
0.800	1.772E+01	1.962E+01	2.152E+01	2.331E+01	2.527E+01	2.725E+01	2.905E+01	3.063E+01
0.900	1.736E+01	1.927E+01	2.119E+01	2.299E+01	2.498E+01	2.700E+01	2.883E+01	3.044E+01
1.000	1.699E+01	1.890E+01	2.083E+01	2.265E+01	2.466E+01	2.670E+01	2.855E+01	3.019E+01
1.500	1.525E+01	1.713E+01	1.904E+01	2.085E+01	2.288E+01	2.496E+01	2.684E+01	2.852E+01
2.000	1.376E+01	1.557E+01	1.743E+01	1.920E+01	2.118E+01	2.323E+01	2.509E+01	2.676E+01
2.500	1.252E+01	1.425E+01	1.603E+01	1.775E+01	1.966E+01	2.166E+01	2.348E+01	2.512E+01
3.000	1.147E+01	1.312E+01	1.483E+01	1.648E+01	1.833E+01	2.026E+01	2.203E+01	2.364E+01
4.000	9.812E+00	1.132E+01	1.289E+01	1.441E+01	1.612E+01	1.791E+01	1.958E+01	2.112E+01
5.000	8.571E+00	9.946E+00	1.138E+01	1.280E+01	1.438E+01	1.605E+01	1.761E+01	1.907E+01
6.000	7.609E+00	8.870E+00	1.020E+01	1.151E+01	1.298E+01	1.453E+01	1.600E+01	1.738E+01
7.000	6.843E+00	8.005E+00	9.233E+00	1.046E+01	1.182E+01	1.327E+01	1.466E+01	1.597E+01
8.000	6.220E+00	7.297E+00	8.438E+00	9.590E+00	1.086E+01	1.222E+01	1.352E+01	1.477E+01
9.000	5.704E+00	6.706E+00	7.771E+00	8.853E+00	1.005E+01	1.132E+01	1.255E+01	1.375E+01
10.00	5.269E+00	6.206E+00	7.205E+00	8.225E+00	9.347E+00	1.054E+01	1.172E+01	1.285E+01
15.00	3.838E+00	4.545E+00	5.304E+00	6.096E+00	6.959E+00	7.885E+00	8.814E+00	9.741E+00
20.00	3.045E+00	3.613E+00	4.226E+00	4.873E+00	5.576E+00	6.329E+00	7.099E+00	7.879E+00
25.00	2.540E+00	3.017E+00	3.533E+00	4.081E+00	4.675E+00	5.311E+00	5.969E+00	6.643E+00
30.00	2.190E+00	2.605E+00	3.050E+00	3.527E+00	4.042E+00	4.595E+00	5.170E+00	5.765E+00
40.00	1.736E+00	2.064E+00	2.419E+00	2.801E+00	3.212E+00	3.652E+00	4.115E+00	4.598E+00
50.00	1.452E+00	1.727E+00	2.025E+00	2.345E+00	2.690E+00	3.059E+00	3.449E+00	3.858E+00
60.00	1.257E+00	1.495E+00	1.754E+00	2.032E+00	2.331E+00	2.651E+00	2.990E+00	3.347E+00
70.00	1.115E+00	1.326E+00	1.555E+00	1.803E+00	2.068E+00	2.352E+00	2.653E+00	2.971E+00
80.00	1.006E+00	1.197E+00	1.404E+00	1.627E+00	1.867E+00	2.124E+00	2.396E+00	2.684E+00
90.00	9.197E−01	1.094E+00	1.284E+00	1.488E+00	1.708E+00	1.943E+00	2.192E+00	2.456E+00
100.0	8.499E−01	1.011E+00	1.187E+00	1.376E+00	1.579E+00	1.796E+00	2.027E+00	2.271E+00
150.0	6.348E−01	7.555E−01	8.868E−01	1.029E+00	1.181E+00	1.344E+00	1.517E+00	1.701E+00
200.0	5.236E−01	6.234E−01	7.318E−01	8.490E−01	9.749E−01	1.110E+00	1.253E+00	1.405E+00
250.0	4.558E−01	5.427E−01	6.372E−01	7.394E−01	8.492E−01	9.666E−01	1.092E+00	1.224E+00
300.0	4.103E−01	4.885E−01	5.737E−01	6.657E−01	7.646E−01	8.704E−01	9.831E−01	1.103E+00
400.0	3.533E−01	4.208E−01	4.942E−01	5.735E−01	6.588E−01	7.501E−01	8.473E−01	9.506E−01
500.0	3.196E−01	3.806E−01	4.471E−01	5.189E−01	5.961E−01	6.788E−01	7.668E−01	8.604E−01
600.0	2.976E−01	3.545E−01	4.164E−01	4.833E−01	5.553E−01	6.323E−01	7.144E−01	8.016E−01
700.0	2.825E−01	3.365E−01	3.952E−01	4.588E−01	5.271E−01	6.003E−01	6.782E−01	7.610E−01
800.0	2.716E−01	3.235E−01	3.800E−01	4.411E−01	5.068E−01	5.772E−01	6.522E−01	7.318E−01
900.0	2.635E−01	3.139E−01	3.687E−01	4.280E−01	4.918E−01	5.601E−01	6.329E−01	7.102E−01
1000.	2.573E−01	3.065E−01	3.601E−01	4.180E−01	4.803E−01	5.470E−01	6.181E−01	6.936E−01

Material: Beryllium

Ion	Li	Be	B	C	N	O	F	Ne
(E/A_1) / MeV				$(-\mathrm{d}E/\rho\mathrm{d}\ell)$ / MeV cm^2 mg^{-1}				
0.025	2.148E+00	2.702E+00	3.141E+00	3.484E+00	3.795E+00	4.050E+00	4.249E+00	4.423E+00
0.030	2.307E+00	2.928E+00	3.432E+00	3.837E+00	4.198E+00	4.499E+00	4.737E+00	4.942E+00
0.040	2.562E+00	3.303E+00	3.925E+00	4.444E+00	4.903E+00	5.294E+00	5.609E+00	5.880E+00
0.050	2.753E+00	3.599E+00	4.326E+00	4.949E+00	5.499E+00	5.978E+00	6.369E+00	6.708E+00
0.060	2.897E+00	3.833E+00	4.654E+00	5.372E+00	6.008E+00	6.570E+00	7.035E+00	7.442E+00
0.070	3.003E+00	4.017E+00	4.922E+00	5.727E+00	6.445E+00	7.085E+00	7.621E+00	8.094E+00
0.080	3.080E+00	4.162E+00	5.141E+00	6.025E+00	6.819E+00	7.534E+00	8.137E+00	8.674E+00
0.090	3.132E+00	4.273E+00	5.320E+00	6.275E+00	7.140E+00	7.924E+00	8.591E+00	9.189E+00
0.100	3.166E+00	4.357E+00	5.463E+00	6.483E+00	7.413E+00	8.263E+00	8.991E+00	9.647E+00
0.150	3.193E+00	4.533E+00	5.831E+00	7.078E+00	8.257E+00	9.368E+00	1.035E+01	1.126E+01
0.200	3.127E+00	4.535E+00	5.930E+00	7.297E+00	8.619E+00	9.890E+00	1.103E+01	1.211E+01
0.250	3.033E+00	4.474E+00	5.924E+00	7.363E+00	8.774E+00	1.015E+01	1.139E+01	1.258E+01
0.300	2.931E+00	4.386E+00	5.868E+00	7.353E+00	8.824E+00	1.027E+01	1.159E+01	1.285E+01
0.400	2.727E+00	4.177E+00	5.687E+00	7.220E+00	8.761E+00	1.030E+01	1.170E+01	1.307E+01
0.500	2.538E+00	3.961E+00	5.471E+00	7.020E+00	8.595E+00	1.018E+01	1.164E+01	1.307E+01
0.600	2.368E+00	3.754E+00	5.247E+00	6.796E+00	8.383E+00	9.998E+00	1.148E+01	1.294E+01
0.700	2.217E+00	3.561E+00	5.029E+00	6.566E+00	8.153E+00	9.780E+00	1.128E+01	1.276E+01
0.800	2.082E+00	3.382E+00	4.820E+00	6.339E+00	7.917E+00	9.546E+00	1.105E+01	1.255E+01
0.900	1.961E+00	3.218E+00	4.624E+00	6.120E+00	7.684E+00	9.308E+00	1.081E+01	1.231E+01
1.000	1.854E+00	3.067E+00	4.440E+00	5.911E+00	7.457E+00	9.071E+00	1.057E+01	1.207E+01
1.500	1.451E+00	2.476E+00	3.682E+00	5.014E+00	6.449E+00	7.978E+00	9.420E+00	1.087E+01
2.000	1.192E+00	2.070E+00	3.131E+00	4.332E+00	5.649E+00	7.075E+00	8.439E+00	9.823E+00
2.500	1.013E+00	1.777E+00	2.720E+00	3.805E+00	5.011E+00	6.336E+00	7.621E+00	8.936E+00
3.000	8.818E−01	1.557E+00	2.402E+00	3.388E+00	4.497E+00	5.727E+00	6.937E+00	8.184E+00
4.000	7.042E−01	1.251E+00	1.947E+00	2.775E+00	3.723E+00	4.791E+00	5.866E+00	6.988E+00
5.000	5.894E−01	1.049E+00	1.639E+00	2.350E+00	3.173E+00	4.109E+00	5.072E+00	6.087E+00
6.000	5.089E−01	9.061E−01	1.418E+00	2.039E+00	2.764E+00	3.597E+00	4.465E+00	5.389E+00
7.000	4.493E−01	7.996E−01	1.252E+00	1.803E+00	2.451E+00	3.197E+00	3.987E+00	4.833E+00
8.000	4.032E−01	7.172E−01	1.123E+00	1.619E+00	2.203E+00	2.879E+00	3.602E+00	4.381E+00
9.000	3.664E−01	6.515E−01	1.020E+00	1.470E+00	2.003E+00	2.620E+00	3.286E+00	4.008E+00
10.00	3.363E−01	5.978E−01	9.352E−01	1.349E+00	1.838E+00	2.406E+00	3.023E+00	3.695E+00
15.00	2.416E−01	4.291E−01	6.703E−01	9.657E−01	1.316E+00	1.722E+00	2.175E+00	2.674E+00
20.00	1.911E−01	3.393E−01	5.297E−01	7.624E−01	1.038E+00	1.357E+00	1.716E+00	2.114E+00
25.00	1.593E−01	2.829E−01	4.416E−01	6.354E−01	8.645E−01	1.130E+00	1.429E+00	1.761E+00
30.00	1.373E−01	2.439E−01	3.808E−01	5.479E−01	7.453E−01	9.734E−01	1.231E+00	1.518E+00
40.00	1.088E−01	1.933E−01	3.019E−01	4.345E−01	5.909E−01	7.715E−01	9.757E−01	1.204E+00
50.00	9.100E−02	1.617E−01	2.526E−01	3.636E−01	4.946E−01	6.457E−01	8.168E−01	1.008E+00
60.00	7.877E−02	1.400E−01	2.188E−01	3.149E−01	4.285E−01	5.594E−01	7.077E−01	8.732E−01
70.00	6.984E−02	1.242E−01	1.940E−01	2.793E−01	3.801E−01	4.963E−01	6.279E−01	7.748E−01
80.00	6.301E−02	1.120E−01	1.751E−01	2.521E−01	3.430E−01	4.480E−01	5.668E−01	6.996E−01
90.00	5.761E−02	1.024E−01	1.601E−01	2.305E−01	3.138E−01	4.098E−01	5.186E−01	6.401E−01
100.0	5.323E−02	9.466E−02	1.479E−01	2.131E−01	2.900E−01	3.788E−01	4.794E−01	5.918E−01
150.0	3.976E−02	7.071E−02	1.105E−01	1.592E−01	2.168E−01	2.833E−01	3.586E−01	4.429E−01
200.0	3.280E−02	5.835E−02	9.122E−02	1.314E−01	1.790E−01	2.339E−01	2.962E−01	3.658E−01
250.0	2.856E−02	5.081E−02	7.944E−02	1.145E−01	1.559E−01	2.037E−01	2.580E−01	3.187E−01
300.0	2.571E−02	4.574E−02	7.153E−02	1.031E−01	1.404E−01	1.835E−01	2.324E−01	2.871E−01
400.0	2.215E−02	3.942E−02	6.164E−02	8.883E−02	1.210E−01	1.582E−01	2.003E−01	2.475E−01
500.0	2.005E−02	3.567E−02	5.579E−02	8.040E−02	1.095E−01	1.432E−01	1.814E−01	2.241E−01
600.0	1.868E−02	3.324E−02	5.198E−02	7.492E−02	1.021E−01	1.334E−01	1.690E−01	2.089E−01
700.0	1.774E−02	3.156E−02	4.936E−02	7.115E−02	9.693E−02	1.267E−01	1.605E−01	1.984E−01
800.0	1.706E−02	3.036E−02	4.748E−02	6.844E−02	9.324E−02	1.219E−01	1.544E−01	1.908E−01
900.0	1.656E−02	2.947E−02	4.609E−02	6.643E−02	9.051E−02	1.183E−01	1.499E−01	1.852E−01
1000.	1.618E−02	2.879E−02	4.503E−02	6.490E−02	8.842E−02	1.156E−01	1.465E−01	1.810E−01

Material: Beryllium

Ion	Na	Mg	Al	Si	P	S	Cl	Ar
(E/A_1) / MeV				$(-\mathrm{d}E/\rho\mathrm{d}\ell)$ / MeV cm^2 mg^{-1}				
0.025	4.542E+00	4.691E+00	4.831E+00	4.976E+00	5.153E+00	5.300E+00	5.500E+00	5.619E+00
0.030	5.085E+00	5.249E+00	5.402E+00	5.558E+00	5.747E+00	5.907E+00	6.113E+00	6.238E+00
0.040	6.080E+00	6.282E+00	6.469E+00	6.651E+00	6.866E+00	7.053E+00	7.275E+00	7.409E+00
0.050	6.967E+00	7.213E+00	7.440E+00	7.655E+00	7.902E+00	8.120E+00	8.362E+00	8.508E+00
0.060	7.763E+00	8.055E+00	8.325E+00	8.577E+00	8.859E+00	9.113E+00	9.379E+00	9.542E+00
0.070	8.478E+00	8.819E+00	9.133E+00	9.423E+00	9.743E+00	1.003E+01	1.033E+01	1.051E+01
0.080	9.120E+00	9.511E+00	9.871E+00	1.020E+01	1.056E+01	1.089E+01	1.121E+01	1.142E+01
0.090	9.697E+00	1.014E+01	1.054E+01	1.092E+01	1.131E+01	1.168E+01	1.204E+01	1.228E+01
0.100	1.022E+01	1.071E+01	1.116E+01	1.157E+01	1.201E+01	1.242E+01	1.281E+01	1.307E+01
0.150	1.209E+01	1.283E+01	1.350E+01	1.412E+01	1.476E+01	1.537E+01	1.593E+01	1.635E+01
0.200	1.314E+01	1.406E+01	1.493E+01	1.573E+01	1.655E+01	1.735E+01	1.808E+01	1.866E+01
0.250	1.375E+01	1.480E+01	1.581E+01	1.674E+01	1.772E+01	1.866E+01	1.953E+01	2.025E+01
0.300	1.411E+01	1.527E+01	1.638E+01	1.742E+01	1.850E+01	1.956E+01	2.055E+01	2.137E+01
0.400	1.446E+01	1.575E+01	1.701E+01	1.819E+01	1.944E+01	2.067E+01	2.182E+01	2.280E+01
0.500	1.453E+01	1.591E+01	1.726E+01	1.854E+01	1.990E+01	2.125E+01	2.251E+01	2.361E+01
0.600	1.446E+01	1.589E+01	1.731E+01	1.866E+01	2.010E+01	2.154E+01	2.289E+01	2.407E+01
0.700	1.431E+01	1.577E+01	1.724E+01	1.863E+01	2.014E+01	2.165E+01	2.305E+01	2.429E+01
0.800	1.411E+01	1.560E+01	1.709E+01	1.852E+01	2.008E+01	2.163E+01	2.308E+01	2.437E+01
0.900	1.389E+01	1.539E+01	1.691E+01	1.835E+01	1.994E+01	2.154E+01	2.302E+01	2.434E+01
1.000	1.365E+01	1.516E+01	1.669E+01	1.815E+01	1.977E+01	2.139E+01	2.290E+01	2.425E+01
1.500	1.243E+01	1.393E+01	1.547E+01	1.695E+01	1.862E+01	2.030E+01	2.187E+01	2.327E+01
2.000	1.133E+01	1.279E+01	1.430E+01	1.575E+01	1.740E+01	1.909E+01	2.065E+01	2.205E+01
2.500	1.038E+01	1.179E+01	1.325E+01	1.466E+01	1.627E+01	1.793E+01	1.947E+01	2.085E+01
3.000	9.559E+00	1.091E+01	1.232E+01	1.369E+01	1.526E+01	1.687E+01	1.838E+01	1.974E+01
4.000	8.236E+00	9.483E+00	1.079E+01	1.207E+01	1.353E+01	1.505E+01	1.649E+01	1.778E+01
5.000	7.222E+00	8.370E+00	9.579E+00	1.077E+01	1.213E+01	1.356E+01	1.492E+01	1.614E+01
6.000	6.425E+00	7.485E+00	8.605E+00	9.722E+00	1.099E+01	1.233E+01	1.360E+01	1.477E+01
7.000	5.784E+00	6.765E+00	7.807E+00	8.852E+00	1.004E+01	1.129E+01	1.250E+01	1.361E+01
8.000	5.259E+00	6.171E+00	7.142E+00	8.123E+00	9.232E+00	1.041E+01	1.155E+01	1.261E+01
9.000	4.822E+00	5.673E+00	6.582E+00	7.505E+00	8.545E+00	9.655E+00	1.073E+01	1.175E+01
10.00	4.452E+00	5.249E+00	6.103E+00	6.974E+00	7.953E+00	9.001E+00	1.002E+01	1.099E+01
15.00	3.234E+00	3.836E+00	4.486E+00	5.162E+00	5.914E+00	6.723E+00	7.533E+00	8.323E+00
20.00	2.560E+00	3.042E+00	3.566E+00	4.117E+00	4.725E+00	5.381E+00	6.049E+00	6.714E+00
25.00	2.133E+00	2.537E+00	2.976E+00	3.442E+00	3.953E+00	4.504E+00	5.071E+00	5.646E+00
30.00	1.838E+00	2.187E+00	2.566E+00	2.970E+00	3.412E+00	3.888E+00	4.382E+00	4.888E+00
40.00	1.456E+00	1.733E+00	2.033E+00	2.356E+00	2.706E+00	3.082E+00	3.477E+00	3.887E+00
50.00	1.219E+00	1.450E+00	1.702E+00	1.972E+00	2.265E+00	2.579E+00	2.910E+00	3.257E+00
60.00	1.056E+00	1.257E+00	1.474E+00	1.709E+00	1.962E+00	2.233E+00	2.521E+00	2.823E+00
70.00	9.373E−01	1.115E+00	1.308E+00	1.517E+00	1.741E+00	1.982E+00	2.237E+00	2.505E+00
80.00	8.463E−01	1.007E+00	1.181E+00	1.370E+00	1.572E+00	1.789E+00	2.020E+00	2.263E+00
90.00	7.744E−01	9.214E−01	1.081E+00	1.254E+00	1.439E+00	1.637E+00	1.848E+00	2.071E+00
100.0	7.160E−01	8.520E−01	9.998E−01	1.159E+00	1.331E+00	1.514E+00	1.709E+00	1.916E+00
150.0	5.360E−01	6.379E−01	7.488E−01	8.686E−01	9.972E−01	1.135E+00	1.281E+00	1.436E+00
200.0	4.428E−01	5.271E−01	6.189E−01	7.180E−01	8.245E−01	9.384E−01	1.060E+00	1.188E+00
250.0	3.858E−01	4.594E−01	5.395E−01	6.260E−01	7.189E−01	8.183E−01	9.242E−01	1.037E+00
300.0	3.476E−01	4.139E−01	4.861E−01	5.640E−01	6.479E−01	7.376E−01	8.331E−01	9.345E−01
400.0	2.997E−01	3.570E−01	4.192E−01	4.866E−01	5.590E−01	6.364E−01	7.190E−01	8.066E−01
500.0	2.714E−01	3.232E−01	3.797E−01	4.407E−01	5.063E−01	5.765E−01	6.513E−01	7.308E−01
600.0	2.529E−01	3.013E−01	3.539E−01	4.108E−01	4.720E−01	5.375E−01	6.073E−01	6.815E−01
700.0	2.402E−01	2.862E−01	3.361E−01	3.902E−01	4.484E−01	5.106E−01	5.769E−01	6.474E−01
800.0	2.311E−01	2.753E−01	3.234E−01	3.754E−01	4.314E−01	4.913E−01	5.551E−01	6.229E−01
900.0	2.244E−01	2.673E−01	3.140E−01	3.645E−01	4.188E−01	4.770E−01	5.390E−01	6.048E−01
1000.	2.192E−01	2.611E−01	3.068E−01	3.561E−01	4.092E−01	4.660E−01	5.266E−01	5.910E−01

Material: Amorphous carbon

Ion	Li	Be	B	C	N	O	F	Ne
(E/A_1) / MeV				$(-\mathrm{d}E/\rho\mathrm{d}\ell)$ / MeV cm^2 mg^{-1}				
0.025	2.043E+00	2.540E+00	2.919E+00	3.206E+00	3.445E+00	3.638E+00	3.792E+00	3.927E+00
0.030	2.200E+00	2.761E+00	3.203E+00	3.548E+00	3.836E+00	4.069E+00	4.257E+00	4.419E+00
0.040	2.457E+00	3.135E+00	3.692E+00	4.148E+00	4.530E+00	4.848E+00	5.106E+00	5.328E+00
0.050	2.658E+00	3.441E+00	4.102E+00	4.659E+00	5.131E+00	5.533E+00	5.864E+00	6.149E+00
0.060	2.815E+00	3.694E+00	4.449E+00	5.099E+00	5.657E+00	6.141E+00	6.544E+00	6.893E+00
0.070	2.939E+00	3.902E+00	4.743E+00	5.479E+00	6.119E+00	6.682E+00	7.156E+00	7.570E+00
0.080	3.035E+00	4.072E+00	4.992E+00	5.809E+00	6.527E+00	7.165E+00	7.707E+00	8.185E+00
0.090	3.109E+00	4.210E+00	5.202E+00	6.094E+00	6.885E+00	7.595E+00	8.203E+00	8.744E+00
0.100	3.162E+00	4.321E+00	5.378E+00	6.340E+00	7.200E+00	7.979E+00	8.650E+00	9.252E+00
0.150	3.238E+00	4.588E+00	5.882E+00	7.113E+00	8.259E+00	9.328E+00	1.028E+01	1.115E+01
0.200	3.178E+00	4.608E+00	6.020E+00	7.401E+00	8.728E+00	9.997E+00	1.115E+01	1.223E+01
0.250	3.082E+00	4.546E+00	6.019E+00	7.482E+00	8.914E+00	1.031E+01	1.159E+01	1.281E+01
0.300	2.978E+00	4.455E+00	5.960E+00	7.471E+00	8.969E+00	1.044E+01	1.180E+01	1.312E+01
0.400	2.774E+00	4.245E+00	5.776E+00	7.335E+00	8.905E+00	1.047E+01	1.193E+01	1.335E+01
0.500	2.587E+00	4.032E+00	5.562E+00	7.139E+00	8.742E+00	1.036E+01	1.187E+01	1.335E+01
0.600	2.419E+00	3.830E+00	5.346E+00	6.923E+00	8.541E+00	1.018E+01	1.172E+01	1.324E+01
0.700	2.270E+00	3.641E+00	5.136E+00	6.703E+00	8.324E+00	9.980E+00	1.154E+01	1.308E+01
0.800	2.137E+00	3.467E+00	4.935E+00	6.487E+00	8.103E+00	9.764E+00	1.133E+01	1.288E+01
0.900	2.018E+00	3.306E+00	4.745E+00	6.278E+00	7.884E+00	9.543E+00	1.111E+01	1.267E+01
1.000	1.911E+00	3.159E+00	4.566E+00	6.077E+00	7.668E+00	9.321E+00	1.089E+01	1.245E+01
1.500	1.508E+00	2.572E+00	3.821E+00	5.205E+00	6.698E+00	8.282E+00	9.800E+00	1.133E+01
2.000	1.246E+00	2.163E+00	3.272E+00	4.529E+00	5.910E+00	7.401E+00	8.848E+00	1.032E+01
2.500	1.063E+00	1.866E+00	2.856E+00	3.998E+00	5.273E+00	6.666E+00	8.037E+00	9.442E+00
3.000	9.292E−01	1.641E+00	2.532E+00	3.574E+00	4.751E+00	6.053E+00	7.348E+00	8.686E+00
4.000	7.457E−01	1.325E+00	2.063E+00	2.944E+00	3.957E+00	5.096E+00	6.254E+00	7.464E+00
5.000	6.261E−01	1.115E+00	1.743E+00	2.502E+00	3.386E+00	4.390E+00	5.431E+00	6.529E+00
6.000	5.418E−01	9.653E−01	1.512E+00	2.177E+00	2.958E+00	3.853E+00	4.794E+00	5.796E+00
7.000	4.792E−01	8.533E−01	1.337E+00	1.929E+00	2.627E+00	3.432E+00	4.289E+00	5.208E+00
8.000	4.306E−01	7.664E−01	1.201E+00	1.734E+00	2.364E+00	3.095E+00	3.880E+00	4.728E+00
9.000	3.918E−01	6.969E−01	1.092E+00	1.576E+00	2.152E+00	2.819E+00	3.543E+00	4.329E+00
10.00	3.599E−01	6.400E−01	1.002E+00	1.447E+00	1.975E+00	2.590E+00	3.261E+00	3.993E+00
15.00	2.595E−01	4.609E−01	7.203E−01	1.038E+00	1.417E+00	1.857E+00	2.348E+00	2.892E+00
20.00	2.056E−01	3.651E−01	5.702E−01	8.211E−01	1.119E+00	1.464E+00	1.853E+00	2.286E+00
25.00	1.716E−01	3.049E−01	4.760E−01	6.851E−01	9.325E−01	1.219E+00	1.543E+00	1.905E+00
30.00	1.481E−01	2.632E−01	4.109E−01	5.913E−01	8.046E−01	1.051E+00	1.330E+00	1.642E+00
40.00	1.176E−01	2.089E−01	3.263E−01	4.696E−01	6.388E−01	8.342E−01	1.055E+00	1.302E+00
50.00	9.846E−02	1.750E−01	2.734E−01	3.935E−01	5.353E−01	6.989E−01	8.841E−01	1.091E+00
60.00	8.531E−02	1.517E−01	2.369E−01	3.411E−01	4.641E−01	6.060E−01	7.666E−01	9.460E−01
70.00	7.569E−02	1.346E−01	2.103E−01	3.027E−01	4.120E−01	5.379E−01	6.806E−01	8.400E−01
80.00	6.833E−02	1.215E−01	1.898E−01	2.734E−01	3.721E−01	4.859E−01	6.148E−01	7.588E−01
90.00	6.251E−02	1.112E−01	1.737E−01	2.501E−01	3.405E−01	4.447E−01	5.627E−01	6.946E−01
100.0	5.778E−02	1.028E−01	1.606E−01	2.313E−01	3.149E−01	4.112E−01	5.205E−01	6.425E−01
150.0	4.323E−02	7.689E−02	1.202E−01	1.731E−01	2.358E−01	3.080E−01	3.900E−01	4.816E−01
200.0	3.570E−02	6.351E−02	9.929E−02	1.431E−01	1.948E−01	2.546E−01	3.224E−01	3.982E−01
250.0	3.111E−02	5.534E−02	8.653E−02	1.247E−01	1.698E−01	2.219E−01	2.811E−01	3.472E−01
300.0	2.802E−02	4.985E−02	7.796E−02	1.123E−01	1.530E−01	2.000E−01	2.533E−01	3.129E−01
400.0	2.417E−02	4.300E−02	6.724E−02	9.690E−02	1.320E−01	1.726E−01	2.186E−01	2.700E−01
500.0	2.188E−02	3.894E−02	6.090E−02	8.777E−02	1.196E−01	1.563E−01	1.980E−01	2.447E−01
600.0	2.040E−02	3.631E−02	5.678E−02	8.184E−02	1.115E−01	1.458E−01	1.846E−01	2.282E−01
700.0	1.938E−02	3.449E−02	5.394E−02	7.775E−02	1.059E−01	1.385E−01	1.754E−01	2.168E−01
800.0	1.865E−02	3.319E−02	5.191E−02	7.482E−02	1.019E−01	1.333E−01	1.688E−01	2.086E−01
900.0	1.811E−02	3.223E−02	5.041E−02	7.266E−02	9.899E−02	1.294E−01	1.640E−01	2.026E−01
1000.	1.770E−02	3.149E−02	4.926E−02	7.100E−02	9.674E−02	1.265E−01	1.602E−01	1.980E−01

Material: Amorphous carbon

Ion	Na	Mg	Al	Si	P	S	Cl	Ar
(E/A_1) / MeV				$(-\mathrm{d}E/\rho\mathrm{d}\ell)$ / MeV cm^2 mg^{-1}				
0.025	4.019E+00	4.132E+00	4.239E+00	4.352E+00	4.480E+00	4.597E+00	4.745E+00	4.847E+00
0.030	4.530E+00	4.653E+00	4.770E+00	4.888E+00	5.022E+00	5.146E+00	5.296E+00	5.401E+00
0.040	5.486E+00	5.638E+00	5.781E+00	5.918E+00	6.068E+00	6.210E+00	6.370E+00	6.479E+00
0.050	6.362E+00	6.555E+00	6.732E+00	6.895E+00	7.070E+00	7.235E+00	7.409E+00	7.526E+00
0.060	7.165E+00	7.407E+00	7.623E+00	7.819E+00	8.023E+00	8.216E+00	8.410E+00	8.540E+00
0.070	7.903E+00	8.194E+00	8.455E+00	8.689E+00	8.927E+00	9.151E+00	9.370E+00	9.518E+00
0.080	8.579E+00	8.922E+00	9.228E+00	9.503E+00	9.779E+00	1.004E+01	1.029E+01	1.046E+01
0.090	9.200E+00	9.593E+00	9.947E+00	1.026E+01	1.058E+01	1.088E+01	1.116E+01	1.135E+01
0.100	9.768E+00	1.021E+01	1.061E+01	1.097E+01	1.133E+01	1.167E+01	1.198E+01	1.221E+01
0.150	1.194E+01	1.264E+01	1.328E+01	1.385E+01	1.443E+01	1.497E+01	1.546E+01	1.585E+01
0.200	1.326E+01	1.418E+01	1.503E+01	1.581E+01	1.659E+01	1.733E+01	1.801E+01	1.857E+01
0.250	1.400E+01	1.508E+01	1.611E+01	1.706E+01	1.801E+01	1.894E+01	1.979E+01	2.052E+01
0.300	1.442E+01	1.562E+01	1.677E+01	1.784E+01	1.894E+01	2.000E+01	2.100E+01	2.186E+01
0.400	1.479E+01	1.613E+01	1.744E+01	1.868E+01	1.996E+01	2.122E+01	2.241E+01	2.347E+01
0.500	1.486E+01	1.629E+01	1.770E+01	1.904E+01	2.044E+01	2.183E+01	2.314E+01	2.432E+01
0.600	1.480E+01	1.628E+01	1.775E+01	1.916E+01	2.064E+01	2.212E+01	2.352E+01	2.478E+01
0.700	1.467E+01	1.618E+01	1.769E+01	1.915E+01	2.069E+01	2.223E+01	2.370E+01	2.502E+01
0.800	1.449E+01	1.603E+01	1.757E+01	1.906E+01	2.065E+01	2.224E+01	2.375E+01	2.512E+01
0.900	1.429E+01	1.584E+01	1.741E+01	1.891E+01	2.054E+01	2.217E+01	2.372E+01	2.512E+01
1.000	1.408E+01	1.564E+01	1.722E+01	1.874E+01	2.039E+01	2.206E+01	2.363E+01	2.506E+01
1.500	1.295E+01	1.451E+01	1.611E+01	1.766E+01	1.937E+01	2.111E+01	2.276E+01	2.425E+01
2.000	1.189E+01	1.342E+01	1.499E+01	1.653E+01	1.824E+01	1.999E+01	2.165E+01	2.316E+01
2.500	1.096E+01	1.243E+01	1.397E+01	1.547E+01	1.716E+01	1.889E+01	2.054E+01	2.202E+01
3.000	1.014E+01	1.156E+01	1.305E+01	1.451E+01	1.616E+01	1.786E+01	1.948E+01	2.094E+01
4.000	8.790E+00	1.011E+01	1.150E+01	1.287E+01	1.443E+01	1.605E+01	1.759E+01	1.900E+01
5.000	7.742E+00	8.965E+00	1.025E+01	1.154E+01	1.300E+01	1.453E+01	1.600E+01	1.734E+01
6.000	6.908E+00	8.041E+00	9.242E+00	1.045E+01	1.182E+01	1.326E+01	1.465E+01	1.592E+01
7.000	6.232E+00	7.285E+00	8.412E+00	9.535E+00	1.082E+01	1.218E+01	1.349E+01	1.471E+01
8.000	5.675E+00	6.656E+00	7.705E+00	8.767E+00	9.972E+00	1.125E+01	1.250E+01	1.366E+01
9.000	5.208E+00	6.126E+00	7.108E+00	8.111E+00	9.246E+00	1.045E+01	1.164E+01	1.275E+01
10.00	4.813E+00	5.674E+00	6.597E+00	7.545E+00	8.616E+00	9.757E+00	1.088E+01	1.195E+01
15.00	3.501E+00	4.154E+00	4.860E+00	5.598E+00	6.424E+00	7.313E+00	8.207E+00	9.076E+00
20.00	2.770E+00	3.295E+00	3.865E+00	4.467E+00	5.135E+00	5.857E+00	6.593E+00	7.325E+00
25.00	2.308E+00	2.747E+00	3.225E+00	3.734E+00	4.294E+00	4.900E+00	5.526E+00	6.157E+00
30.00	1.989E+00	2.368E+00	2.780E+00	3.221E+00	3.705E+00	4.228E+00	4.772E+00	5.326E+00
40.00	1.576E+00	1.876E+00	2.203E+00	2.554E+00	2.937E+00	3.349E+00	3.782E+00	4.230E+00
50.00	1.320E+00	1.571E+00	1.844E+00	2.138E+00	2.457E+00	2.800E+00	3.163E+00	3.541E+00
60.00	1.145E+00	1.362E+00	1.598E+00	1.853E+00	2.129E+00	2.425E+00	2.743E+00	3.068E+00
70.00	1.016E+00	1.209E+00	1.419E+00	1.645E+00	1.889E+00	2.151E+00	2.429E+00	2.722E+00
80.00	9.180E−01	1.092E+00	1.282E+00	1.486E+00	1.707E+00	1.943E+00	2.194E+00	2.459E+00
90.00	8.404E−01	1.000E+00	1.174E+00	1.361E+00	1.562E+00	1.778E+00	2.008E+00	2.250E+00
100.0	7.774E−01	9.251E−01	1.086E+00	1.259E+00	1.445E+00	1.645E+00	1.857E+00	2.082E+00
150.0	5.828E−01	6.937E−01	8.143E−01	9.446E−01	1.085E+00	1.234E+00	1.394E+00	1.563E+00
200.0	4.820E−01	5.738E−01	6.737E−01	7.816E−01	8.976E−01	1.022E+00	1.154E+00	1.294E+00
250.0	4.203E−01	5.005E−01	5.877E−01	6.819E−01	7.832E−01	8.916E−01	1.007E+00	1.129E+00
300.0	3.789E−01	4.512E−01	5.298E−01	6.149E−01	7.063E−01	8.041E−01	9.082E−01	1.019E+00
400.0	3.270E−01	3.895E−01	4.574E−01	5.309E−01	6.099E−01	6.945E−01	7.846E−01	8.802E−01
500.0	2.963E−01	3.529E−01	4.145E−01	4.812E−01	5.528E−01	6.295E−01	7.113E−01	7.980E−01
600.0	2.763E−01	3.292E−01	3.866E−01	4.488E−01	5.157E−01	5.873E−01	6.636E−01	7.446E−01
700.0	2.626E−01	3.128E−01	3.674E−01	4.265E−01	4.901E−01	5.581E−01	6.307E−01	7.077E−01
800.0	2.527E−01	3.010E−01	3.536E−01	4.105E−01	4.717E−01	5.372E−01	6.071E−01	6.813E−01
900.0	2.454E−01	2.923E−01	3.434E−01	3.987E−01	4.581E−01	5.218E−01	5.896E−01	6.617E−01
1000.	2.398E−01	2.857E−01	3.357E−01	3.897E−01	4.478E−01	5.100E−01	5.763E−01	6.468E−01

Material: Nitrogen

Ion	Li	Be	B	C	N	O	F	Ne
(E/A_1) / MeV				$(-\mathrm{d}E/\rho\mathrm{d}\ell)$ / MeV cm^2 mg^{-1}				
0.025	2.130E+00	2.650E+00	3.070E+00	3.409E+00	3.704E+00	3.958E+00	4.177E+00	4.375E+00
0.030	2.311E+00	2.892E+00	3.370E+00	3.764E+00	4.106E+00	4.401E+00	4.656E+00	4.884E+00
0.040	2.613E+00	3.309E+00	3.894E+00	4.389E+00	4.820E+00	5.196E+00	5.522E+00	5.813E+00
0.050	2.849E+00	3.658E+00	4.342E+00	4.930E+00	5.441E+00	5.894E+00	6.288E+00	6.641E+00
0.060	3.030E+00	3.947E+00	4.728E+00	5.404E+00	5.993E+00	6.518E+00	6.976E+00	7.388E+00
0.070	3.166E+00	4.181E+00	5.057E+00	5.821E+00	6.487E+00	7.082E+00	7.602E+00	8.071E+00
0.080	3.264E+00	4.367E+00	5.333E+00	6.183E+00	6.927E+00	7.593E+00	8.173E+00	8.698E+00
0.090	3.333E+00	4.512E+00	5.560E+00	6.494E+00	7.315E+00	8.053E+00	8.695E+00	9.275E+00
0.100	3.381E+00	4.622E+00	5.745E+00	6.756E+00	7.654E+00	8.463E+00	9.168E+00	9.805E+00
0.150	3.429E+00	4.861E+00	6.232E+00	7.532E+00	8.740E+00	9.864E+00	1.087E+01	1.179E+01
0.200	3.351E+00	4.862E+00	6.351E+00	7.805E+00	9.198E+00	1.053E+01	1.175E+01	1.289E+01
0.250	3.239E+00	4.781E+00	6.331E+00	7.868E+00	9.369E+00	1.083E+01	1.218E+01	1.348E+01
0.300	3.120E+00	4.671E+00	6.251E+00	7.836E+00	9.404E+00	1.094E+01	1.239E+01	1.378E+01
0.400	2.891E+00	4.427E+00	6.026E+00	7.656E+00	9.295E+00	1.093E+01	1.247E+01	1.398E+01
0.500	2.685E+00	4.186E+00	5.778E+00	7.418E+00	9.088E+00	1.077E+01	1.236E+01	1.393E+01
0.600	2.503E+00	3.963E+00	5.534E+00	7.168E+00	8.847E+00	1.055E+01	1.217E+01	1.377E+01
0.700	2.343E+00	3.757E+00	5.301E+00	6.920E+00	8.597E+00	1.031E+01	1.194E+01	1.356E+01
0.800	2.201E+00	3.570E+00	5.080E+00	6.681E+00	8.347E+00	1.006E+01	1.169E+01	1.332E+01
0.900	2.075E+00	3.399E+00	4.875E+00	6.452E+00	8.105E+00	9.811E+00	1.144E+01	1.307E+01
1.000	1.963E+00	3.242E+00	4.684E+00	6.235E+00	7.870E+00	9.566E+00	1.119E+01	1.282E+01
1.500	1.544E+00	2.629E+00	3.903E+00	5.315E+00	6.839E+00	8.454E+00	1.002E+01	1.160E+01
2.000	1.274E+00	2.208E+00	3.335E+00	4.615E+00	6.021E+00	7.535E+00	9.022E+00	1.054E+01
2.500	1.086E+00	1.903E+00	2.909E+00	4.070E+00	5.367E+00	6.780E+00	8.185E+00	9.628E+00
3.000	9.483E−01	1.673E+00	2.578E+00	3.637E+00	4.834E+00	6.153E+00	7.479E+00	8.851E+00
4.000	7.603E−01	1.350E+00	2.100E+00	2.995E+00	4.024E+00	5.179E+00	6.362E+00	7.601E+00
5.000	6.380E−01	1.136E+00	1.774E+00	2.545E+00	3.443E+00	4.463E+00	5.524E+00	6.648E+00
6.000	5.519E−01	9.828E−01	1.538E+00	2.215E+00	3.008E+00	3.917E+00	4.877E+00	5.901E+00
7.000	4.879E−01	8.685E−01	1.360E+00	1.962E+00	2.672E+00	3.490E+00	4.363E+00	5.303E+00
8.000	4.382E−01	7.799E−01	1.222E+00	1.763E+00	2.405E+00	3.147E+00	3.947E+00	4.813E+00
9.000	3.986E−01	7.090E−01	1.110E+00	1.603E+00	2.188E+00	2.867E+00	3.605E+00	4.407E+00
10.00	3.661E−01	6.509E−01	1.019E+00	1.471E+00	2.009E+00	2.634E+00	3.318E+00	4.065E+00
15.00	2.637E−01	4.683E−01	7.318E−01	1.055E+00	1.440E+00	1.888E+00	2.388E+00	2.941E+00
20.00	2.087E−01	3.707E−01	5.789E−01	8.338E−01	1.136E+00	1.487E+00	1.883E+00	2.324E+00
25.00	1.742E−01	3.094E−01	4.830E−01	6.953E−01	9.465E−01	1.238E+00	1.567E+00	1.934E+00
30.00	1.503E−01	2.670E−01	4.168E−01	5.999E−01	8.163E−01	1.067E+00	1.350E+00	1.667E+00
40.00	1.192E−01	2.118E−01	3.308E−01	4.761E−01	6.477E−01	8.458E−01	1.070E+00	1.321E+00
50.00	9.978E−02	1.774E−01	2.770E−01	3.988E−01	5.425E−01	7.083E−01	8.961E−01	1.106E+00
60.00	8.643E−02	1.537E−01	2.400E−01	3.456E−01	4.702E−01	6.139E−01	7.767E−01	9.586E−01
70.00	7.666E−02	1.363E−01	2.130E−01	3.066E−01	4.173E−01	5.449E−01	6.894E−01	8.508E−01
80.00	6.919E−02	1.230E−01	1.922E−01	2.768E−01	3.768E−01	4.920E−01	6.226E−01	7.685E−01
90.00	6.329E−02	1.125E−01	1.759E−01	2.533E−01	3.447E−01	4.502E−01	5.698E−01	7.033E−01
100.0	5.850E−02	1.040E−01	1.626E−01	2.341E−01	3.187E−01	4.163E−01	5.269E−01	6.504E−01
150.0	4.374E−02	7.779E−02	1.216E−01	1.752E−01	2.385E−01	3.117E−01	3.946E−01	4.872E−01
200.0	3.611E−02	6.423E−02	1.004E−01	1.447E−01	1.970E−01	2.575E−01	3.260E−01	4.027E−01
250.0	3.146E−02	5.596E−02	8.750E−02	1.261E−01	1.717E−01	2.244E−01	2.842E−01	3.511E−01
300.0	2.833E−02	5.040E−02	7.881E−02	1.136E−01	1.547E−01	2.022E−01	2.561E−01	3.163E−01
400.0	2.442E−02	4.346E−02	6.796E−02	9.794E−02	1.334E−01	1.744E−01	2.209E−01	2.729E−01
500.0	2.211E−02	3.935E−02	6.153E−02	8.869E−02	1.208E−01	1.579E−01	2.001E−01	2.472E−01
600.0	2.061E−02	3.668E−02	5.736E−02	8.268E−02	1.126E−01	1.473E−01	1.865E−01	2.305E−01
700.0	1.958E−02	3.484E−02	5.449E−02	7.854E−02	1.070E−01	1.399E−01	1.772E−01	2.190E−01
800.0	1.884E−02	3.352E−02	5.243E−02	7.556E−02	1.030E−01	1.346E−01	1.705E−01	2.107E−01
900.0	1.829E−02	3.255E−02	5.090E−02	7.337E−02	9.996E−02	1.307E−01	1.656E−01	2.046E−01
1000.	1.787E−02	3.180E−02	4.974E−02	7.169E−02	9.768E−02	1.277E−01	1.618E−01	1.999E−01

Material: Nitrogen

Ion	Na	Mg	Al	Si	P	S	Cl	Ar
(E/A_1) / MeV				$(-\mathrm{d}E/\rho\mathrm{d}\ell)$ / MeV cm^2 mg^{-1}				
0.025	4.532E+00	4.702E+00	4.858E+00	5.011E+00	5.170E+00	5.313E+00	5.481E+00	5.604E+00
0.030	5.065E+00	5.251E+00	5.424E+00	5.590E+00	5.761E+00	5.919E+00	6.098E+00	6.233E+00
0.040	6.047E+00	6.272E+00	6.480E+00	6.676E+00	6.874E+00	7.061E+00	7.262E+00	7.416E+00
0.050	6.932E+00	7.203E+00	7.449E+00	7.680E+00	7.910E+00	8.131E+00	8.355E+00	8.529E+00
0.060	7.735E+00	8.054E+00	8.342E+00	8.611E+00	8.877E+00	9.133E+00	9.386E+00	9.581E+00
0.070	8.470E+00	8.835E+00	9.168E+00	9.475E+00	9.779E+00	1.007E+01	1.035E+01	1.057E+01
0.080	9.150E+00	9.559E+00	9.934E+00	1.028E+01	1.062E+01	1.095E+01	1.126E+01	1.151E+01
0.090	9.780E+00	1.023E+01	1.065E+01	1.103E+01	1.141E+01	1.177E+01	1.212E+01	1.239E+01
0.100	1.036E+01	1.086E+01	1.132E+01	1.174E+01	1.215E+01	1.255E+01	1.292E+01	1.322E+01
0.150	1.263E+01	1.338E+01	1.406E+01	1.467E+01	1.528E+01	1.585E+01	1.638E+01	1.682E+01
0.200	1.397E+01	1.495E+01	1.586E+01	1.669E+01	1.750E+01	1.828E+01	1.900E+01	1.960E+01
0.250	1.472E+01	1.587E+01	1.696E+01	1.797E+01	1.897E+01	1.993E+01	2.083E+01	2.161E+01
0.300	1.514E+01	1.641E+01	1.763E+01	1.877E+01	1.992E+01	2.103E+01	2.208E+01	2.300E+01
0.400	1.548E+01	1.690E+01	1.829E+01	1.961E+01	2.095E+01	2.227E+01	2.352E+01	2.465E+01
0.500	1.551E+01	1.701E+01	1.850E+01	1.992E+01	2.139E+01	2.284E+01	2.422E+01	2.548E+01
0.600	1.540E+01	1.695E+01	1.850E+01	1.999E+01	2.154E+01	2.308E+01	2.455E+01	2.590E+01
0.700	1.521E+01	1.680E+01	1.839E+01	1.992E+01	2.154E+01	2.314E+01	2.467E+01	2.608E+01
0.800	1.499E+01	1.660E+01	1.822E+01	1.978E+01	2.144E+01	2.309E+01	2.467E+01	2.612E+01
0.900	1.475E+01	1.637E+01	1.801E+01	1.959E+01	2.128E+01	2.297E+01	2.458E+01	2.607E+01
1.000	1.451E+01	1.613E+01	1.778E+01	1.937E+01	2.108E+01	2.280E+01	2.444E+01	2.596E+01
1.500	1.327E+01	1.488E+01	1.653E+01	1.814E+01	1.990E+01	2.168E+01	2.338E+01	2.495E+01
2.000	1.215E+01	1.372E+01	1.533E+01	1.692E+01	1.867E+01	2.045E+01	2.216E+01	2.373E+01
2.500	1.117E+01	1.269E+01	1.426E+01	1.580E+01	1.752E+01	1.929E+01	2.098E+01	2.253E+01
3.000	1.033E+01	1.179E+01	1.331E+01	1.480E+01	1.648E+01	1.821E+01	1.987E+01	2.139E+01
4.000	8.950E+00	1.030E+01	1.171E+01	1.311E+01	1.470E+01	1.634E+01	1.792E+01	1.938E+01
5.000	7.880E+00	9.125E+00	1.044E+01	1.175E+01	1.324E+01	1.478E+01	1.629E+01	1.767E+01
6.000	7.031E+00	8.183E+00	9.405E+00	1.064E+01	1.203E+01	1.348E+01	1.491E+01	1.623E+01
7.000	6.342E+00	7.413E+00	8.552E+00	9.706E+00	1.101E+01	1.239E+01	1.373E+01	1.499E+01
8.000	5.775E+00	6.773E+00	7.838E+00	8.923E+00	1.015E+01	1.145E+01	1.272E+01	1.392E+01
9.000	5.300E+00	6.233E+00	7.232E+00	8.255E+00	9.409E+00	1.063E+01	1.184E+01	1.299E+01
10.00	4.898E+00	5.773E+00	6.713E+00	7.679E+00	8.768E+00	9.926E+00	1.108E+01	1.217E+01
15.00	3.561E+00	4.225E+00	4.943E+00	5.695E+00	6.536E+00	7.440E+00	8.353E+00	9.243E+00
20.00	2.816E+00	3.349E+00	3.929E+00	4.542E+00	5.223E+00	5.957E+00	6.709E+00	7.457E+00
25.00	2.344E+00	2.790E+00	3.277E+00	3.794E+00	4.367E+00	4.982E+00	5.620E+00	6.264E+00
30.00	2.019E+00	2.404E+00	2.823E+00	3.272E+00	3.764E+00	4.296E+00	4.851E+00	5.417E+00
40.00	1.599E+00	1.904E+00	2.235E+00	2.592E+00	2.981E+00	3.400E+00	3.841E+00	4.297E+00
50.00	1.338E+00	1.593E+00	1.870E+00	2.168E+00	2.492E+00	2.841E+00	3.209E+00	3.594E+00
60.00	1.160E+00	1.380E+00	1.620E+00	1.879E+00	2.158E+00	2.458E+00	2.777E+00	3.111E+00
70.00	1.029E+00	1.225E+00	1.438E+00	1.667E+00	1.915E+00	2.180E+00	2.462E+00	2.760E+00
80.00	9.297E−01	1.106E+00	1.298E+00	1.506E+00	1.729E+00	1.968E+00	2.223E+00	2.491E+00
90.00	8.509E−01	1.013E+00	1.188E+00	1.378E+00	1.582E+00	1.801E+00	2.034E+00	2.280E+00
100.0	7.870E−01	9.365E−01	1.099E+00	1.275E+00	1.464E+00	1.666E+00	1.881E+00	2.108E+00
150.0	5.897E−01	7.019E−01	8.239E−01	9.557E−01	1.097E+00	1.249E+00	1.410E+00	1.581E+00
200.0	4.875E−01	5.804E−01	6.814E−01	7.905E−01	9.078E−01	1.033E+00	1.167E+00	1.309E+00
250.0	4.250E−01	5.061E−01	5.943E−01	6.895E−01	7.920E−01	9.015E−01	1.018E+00	1.142E+00
300.0	3.830E−01	4.561E−01	5.356E−01	6.216E−01	7.140E−01	8.128E−01	9.182E−01	1.030E+00
400.0	3.305E−01	3.936E−01	4.623E−01	5.365E−01	6.164E−01	7.018E−01	7.929E−01	8.896E−01
500.0	2.994E−01	3.566E−01	4.188E−01	4.862E−01	5.586E−01	6.360E−01	7.186E−01	8.063E−01
600.0	2.792E−01	3.325E−01	3.906E−01	4.534E−01	5.210E−01	5.933E−01	6.703E−01	7.522E−01
700.0	2.652E−01	3.159E−01	3.711E−01	4.308E−01	4.950E−01	5.637E−01	6.370E−01	7.148E−01
800.0	2.552E−01	3.040E−01	3.571E−01	4.146E−01	4.764E−01	5.425E−01	6.131E−01	6.880E−01
900.0	2.478E−01	2.952E−01	3.468E−01	4.026E−01	4.626E−01	5.269E−01	5.954E−01	6.681E−01
1000.	2.422E−01	2.885E−01	3.389E−01	3.934E−01	4.521E−01	5.149E−01	5.819E−01	6.530E−01

Material: Oxygen

Ion	Li	Be	B	C	N	O	F	Ne
(E/A_1) / MeV				$(-\mathrm{d}E/\rho\mathrm{d}\ell)$ / MeV cm^2 mg^{-1}				
0.025	1.865E+00	2.293E+00	2.624E+00	2.883E+00	3.103E+00	3.292E+00	3.458E+00	3.612E+00
0.030	2.032E+00	2.519E+00	2.903E+00	3.210E+00	3.469E+00	3.690E+00	3.881E+00	4.056E+00
0.040	2.312E+00	2.909E+00	3.393E+00	3.792E+00	4.130E+00	4.419E+00	4.667E+00	4.889E+00
0.050	2.534E+00	3.236E+00	3.813E+00	4.300E+00	4.714E+00	5.072E+00	5.381E+00	5.655E+00
0.060	2.709E+00	3.509E+00	4.176E+00	4.747E+00	5.236E+00	5.662E+00	6.030E+00	6.357E+00
0.070	2.843E+00	3.735E+00	4.490E+00	5.143E+00	5.704E+00	6.198E+00	6.623E+00	7.003E+00
0.080	2.944E+00	3.918E+00	4.757E+00	5.490E+00	6.124E+00	6.684E+00	7.168E+00	7.601E+00
0.090	3.019E+00	4.065E+00	4.982E+00	5.792E+00	6.497E+00	7.124E+00	7.666E+00	8.152E+00
0.100	3.072E+00	4.180E+00	5.169E+00	6.051E+00	6.827E+00	7.520E+00	8.121E+00	8.661E+00
0.150	3.153E+00	4.458E+00	5.696E+00	6.861E+00	7.932E+00	8.922E+00	9.803E+00	1.061E+01
0.200	3.100E+00	4.489E+00	5.853E+00	7.178E+00	8.439E+00	9.637E+00	1.073E+01	1.175E+01
0.250	3.007E+00	4.433E+00	5.861E+00	7.275E+00	8.650E+00	9.981E+00	1.121E+01	1.239E+01
0.300	2.904E+00	4.342E+00	5.805E+00	7.270E+00	8.715E+00	1.013E+01	1.146E+01	1.274E+01
0.400	2.702E+00	4.132E+00	5.618E+00	7.133E+00	8.653E+00	1.017E+01	1.160E+01	1.300E+01
0.500	2.517E+00	3.919E+00	5.403E+00	6.932E+00	8.486E+00	1.005E+01	1.154E+01	1.300E+01
0.600	2.353E+00	3.719E+00	5.187E+00	6.714E+00	8.281E+00	9.869E+00	1.138E+01	1.288E+01
0.700	2.207E+00	3.534E+00	4.978E+00	6.495E+00	8.063E+00	9.663E+00	1.119E+01	1.271E+01
0.800	2.077E+00	3.364E+00	4.781E+00	6.282E+00	7.843E+00	9.446E+00	1.098E+01	1.251E+01
0.900	1.962E+00	3.207E+00	4.595E+00	6.076E+00	7.627E+00	9.227E+00	1.076E+01	1.230E+01
1.000	1.858E+00	3.064E+00	4.421E+00	5.880E+00	7.417E+00	9.009E+00	1.054E+01	1.208E+01
1.500	1.468E+00	2.497E+00	3.704E+00	5.040E+00	6.482E+00	8.006E+00	9.490E+00	1.099E+01
2.000	1.215E+00	2.105E+00	3.177E+00	4.392E+00	5.729E+00	7.164E+00	8.580E+00	1.002E+01
2.500	1.038E+00	1.819E+00	2.778E+00	3.885E+00	5.121E+00	6.467E+00	7.808E+00	9.187E+00
3.000	9.083E−01	1.602E+00	2.467E+00	3.479E+00	4.623E+00	5.883E+00	7.152E+00	8.466E+00
4.000	7.302E−01	1.296E+00	2.016E+00	2.874E+00	3.862E+00	4.969E+00	6.106E+00	7.298E+00
5.000	6.139E−01	1.092E+00	1.706E+00	2.448E+00	3.312E+00	4.292E+00	5.316E+00	6.400E+00
6.000	5.318E−01	9.469E−01	1.482E+00	2.134E+00	2.899E+00	3.775E+00	4.702E+00	5.692E+00
7.000	4.706E−01	8.378E−01	1.312E+00	1.893E+00	2.578E+00	3.367E+00	4.213E+00	5.122E+00
8.000	4.232E−01	7.530E−01	1.180E+00	1.703E+00	2.323E+00	3.040E+00	3.815E+00	4.655E+00
9.000	3.852E−01	6.851E−01	1.073E+00	1.550E+00	2.115E+00	2.772E+00	3.487E+00	4.266E+00
10.00	3.540E−01	6.295E−01	9.855E−01	1.423E+00	1.944E+00	2.549E+00	3.212E+00	3.937E+00
15.00	2.556E−01	4.539E−01	7.094E−01	1.023E+00	1.396E+00	1.831E+00	2.317E+00	2.855E+00
20.00	2.026E−01	3.599E−01	5.620E−01	8.094E−01	1.103E+00	1.445E+00	1.829E+00	2.258E+00
25.00	1.692E−01	3.006E−01	4.694E−01	6.756E−01	9.199E−01	1.203E+00	1.524E+00	1.881E+00
30.00	1.461E−01	2.596E−01	4.054E−01	5.834E−01	7.939E−01	1.038E+00	1.314E+00	1.622E+00
40.00	1.161E−01	2.063E−01	3.221E−01	4.635E−01	6.306E−01	8.236E−01	1.042E+00	1.286E+00
50.00	9.723E−02	1.728E−01	2.699E−01	3.886E−01	5.286E−01	6.902E−01	8.733E−01	1.078E+00
60.00	8.427E−02	1.498E−01	2.340E−01	3.369E−01	4.585E−01	5.986E−01	7.574E−01	9.347E−01
70.00	7.478E−02	1.330E−01	2.077E−01	2.991E−01	4.071E−01	5.315E−01	6.725E−01	8.301E−01
80.00	6.752E−02	1.201E−01	1.876E−01	2.702E−01	3.677E−01	4.802E−01	6.076E−01	7.500E−01
90.00	6.178E−02	1.099E−01	1.717E−01	2.473E−01	3.366E−01	4.396E−01	5.563E−01	6.866E−01
100.0	5.712E−02	1.016E−01	1.588E−01	2.287E−01	3.113E−01	4.066E−01	5.146E−01	6.352E−01
150.0	4.276E−02	7.605E−02	1.189E−01	1.713E−01	2.332E−01	3.047E−01	3.857E−01	4.763E−01
200.0	3.532E−02	6.284E−02	9.825E−02	1.416E−01	1.928E−01	2.519E−01	3.190E−01	3.940E−01
250.0	3.079E−02	5.477E−02	8.564E−02	1.234E−01	1.681E−01	2.197E−01	2.782E−01	3.437E−01
300.0	2.774E−02	4.935E−02	7.717E−02	1.112E−01	1.515E−01	1.980E−01	2.508E−01	3.098E−01
400.0	2.393E−02	4.258E−02	6.659E−02	9.596E−02	1.307E−01	1.709E−01	2.164E−01	2.674E−01
500.0	2.168E−02	3.857E−02	6.032E−02	8.694E−02	1.184E−01	1.548E−01	1.961E−01	2.424E−01
600.0	2.021E−02	3.597E−02	5.625E−02	8.108E−02	1.105E−01	1.444E−01	1.829E−01	2.261E−01
700.0	1.921E−02	3.418E−02	5.345E−02	7.704E−02	1.050E−01	1.372E−01	1.738E−01	2.148E−01
800.0	1.848E−02	3.289E−02	5.144E−02	7.415E−02	1.010E−01	1.321E−01	1.673E−01	2.068E−01
900.0	1.795E−02	3.194E−02	4.996E−02	7.201E−02	9.811E−02	1.283E−01	1.625E−01	2.008E−01
1000.	1.754E−02	3.122E−02	4.883E−02	7.038E−02	9.589E−02	1.254E−01	1.588E−01	1.963E−01

Material: Oxygen

Ion	Na	Mg	Al	Si	P	S	Cl	Ar
(E/A_1) / MeV				$(-\mathrm{d}E/\rho\mathrm{d}\ell)$ / MeV cm^2 mg^{-1}				
0.025	3.734E+00	3.869E+00	3.995E+00	4.121E+00	4.248E+00	4.365E+00	4.501E+00	4.604E+00
0.030	4.194E+00	4.340E+00	4.477E+00	4.612E+00	4.749E+00	4.877E+00	5.022E+00	5.133E+00
0.040	5.066E+00	5.238E+00	5.398E+00	5.552E+00	5.704E+00	5.853E+00	6.013E+00	6.139E+00
0.050	5.876E+00	6.083E+00	6.269E+00	6.446E+00	6.618E+00	6.788E+00	6.964E+00	7.102E+00
0.060	6.626E+00	6.872E+00	7.090E+00	7.295E+00	7.493E+00	7.688E+00	7.882E+00	8.034E+00
0.070	7.321E+00	7.608E+00	7.864E+00	8.100E+00	8.327E+00	8.549E+00	8.766E+00	8.934E+00
0.080	7.967E+00	8.296E+00	8.591E+00	8.860E+00	9.118E+00	9.370E+00	9.610E+00	9.799E+00
0.090	8.569E+00	8.939E+00	9.273E+00	9.576E+00	9.867E+00	1.015E+01	1.042E+01	1.063E+01
0.100	9.128E+00	9.541E+00	9.915E+00	1.025E+01	1.058E+01	1.089E+01	1.118E+01	1.142E+01
0.150	1.133E+01	1.198E+01	1.256E+01	1.309E+01	1.359E+01	1.407E+01	1.452E+01	1.488E+01
0.200	1.271E+01	1.357E+01	1.437E+01	1.509E+01	1.579E+01	1.646E+01	1.707E+01	1.759E+01
0.250	1.352E+01	1.455E+01	1.552E+01	1.642E+01	1.730E+01	1.815E+01	1.893E+01	1.961E+01
0.300	1.398E+01	1.514E+01	1.625E+01	1.729E+01	1.831E+01	1.931E+01	2.023E+01	2.106E+01
0.400	1.439E+01	1.571E+01	1.699E+01	1.821E+01	1.944E+01	2.064E+01	2.178E+01	2.282E+01
0.500	1.447E+01	1.588E+01	1.726E+01	1.858E+01	1.994E+01	2.128E+01	2.256E+01	2.373E+01
0.600	1.440E+01	1.586E+01	1.731E+01	1.870E+01	2.015E+01	2.158E+01	2.295E+01	2.421E+01
0.700	1.426E+01	1.575E+01	1.724E+01	1.868E+01	2.019E+01	2.168E+01	2.312E+01	2.444E+01
0.800	1.408E+01	1.559E+01	1.711E+01	1.858E+01	2.013E+01	2.167E+01	2.316E+01	2.453E+01
0.900	1.388E+01	1.540E+01	1.694E+01	1.843E+01	2.001E+01	2.159E+01	2.311E+01	2.452E+01
1.000	1.366E+01	1.519E+01	1.674E+01	1.824E+01	1.985E+01	2.146E+01	2.301E+01	2.444E+01
1.500	1.256E+01	1.409E+01	1.564E+01	1.717E+01	1.883E+01	2.051E+01	2.212E+01	2.361E+01
2.000	1.155E+01	1.304E+01	1.457E+01	1.607E+01	1.773E+01	1.942E+01	2.104E+01	2.254E+01
2.500	1.066E+01	1.210E+01	1.359E+01	1.506E+01	1.670E+01	1.837E+01	1.998E+01	2.146E+01
3.000	9.877E+00	1.127E+01	1.272E+01	1.415E+01	1.575E+01	1.739E+01	1.897E+01	2.043E+01
4.000	8.591E+00	9.882E+00	1.123E+01	1.258E+01	1.410E+01	1.566E+01	1.718E+01	1.858E+01
5.000	7.584E+00	8.780E+00	1.004E+01	1.130E+01	1.273E+01	1.421E+01	1.566E+01	1.700E+01
6.000	6.780E+00	7.890E+00	9.066E+00	1.025E+01	1.159E+01	1.299E+01	1.437E+01	1.564E+01
7.000	6.126E+00	7.158E+00	8.257E+00	9.372E+00	1.063E+01	1.195E+01	1.326E+01	1.447E+01
8.000	5.584E+00	6.548E+00	7.577E+00	8.626E+00	9.812E+00	1.106E+01	1.230E+01	1.346E+01
9.000	5.130E+00	6.032E+00	6.998E+00	7.989E+00	9.106E+00	1.029E+01	1.147E+01	1.258E+01
10.00	4.744E+00	5.591E+00	6.501E+00	7.437E+00	8.493E+00	9.614E+00	1.073E+01	1.180E+01
15.00	3.457E+00	4.102E+00	4.800E+00	5.531E+00	6.350E+00	7.228E+00	8.119E+00	8.987E+00
20.00	2.737E+00	3.256E+00	3.820E+00	4.417E+00	5.081E+00	5.796E+00	6.531E+00	7.262E+00
25.00	2.280E+00	2.715E+00	3.188E+00	3.692E+00	4.250E+00	4.852E+00	5.476E+00	6.105E+00
30.00	1.965E+00	2.340E+00	2.748E+00	3.186E+00	3.667E+00	4.186E+00	4.728E+00	5.281E+00
40.00	1.557E+00	1.854E+00	2.178E+00	2.526E+00	2.905E+00	3.315E+00	3.746E+00	4.192E+00
50.00	1.304E+00	1.553E+00	1.823E+00	2.114E+00	2.430E+00	2.771E+00	3.131E+00	3.507E+00
60.00	1.131E+00	1.346E+00	1.580E+00	1.832E+00	2.105E+00	2.399E+00	2.710E+00	3.037E+00
70.00	1.004E+00	1.197E+00	1.403E+00	1.627E+00	1.868E+00	2.128E+00	2.404E+00	2.694E+00
80.00	9.074E−01	1.080E+00	1.267E+00	1.470E+00	1.688E+00	1.922E+00	2.170E+00	2.433E+00
90.00	8.308E−01	9.886E−01	1.160E+00	1.346E+00	1.545E+00	1.759E+00	1.986E+00	2.227E+00
100.0	7.686E−01	9.146E−01	1.073E+00	1.245E+00	1.429E+00	1.627E+00	1.837E+00	2.060E+00
150.0	5.765E−01	6.862E−01	8.055E−01	9.344E−01	1.073E+00	1.221E+00	1.379E+00	1.546E+00
200.0	4.769E−01	5.678E−01	6.667E−01	7.735E−01	8.883E−01	1.011E+00	1.142E+00	1.281E+00
250.0	4.161E−01	4.954E−01	5.817E−01	6.750E−01	7.753E−01	8.826E−01	9.968E−01	1.118E+00
300.0	3.751E−01	4.467E−01	5.246E−01	6.088E−01	6.993E−01	7.961E−01	8.992E−01	1.009E+00
400.0	3.239E−01	3.857E−01	4.530E−01	5.258E−01	6.041E−01	6.878E−01	7.770E−01	8.718E−01
500.0	2.935E−01	3.496E−01	4.106E−01	4.767E−01	5.476E−01	6.236E−01	7.046E−01	7.906E−01
600.0	2.738E−01	3.261E−01	3.831E−01	4.447E−01	5.110E−01	5.819E−01	6.575E−01	7.378E−01
700.0	2.602E−01	3.100E−01	3.641E−01	4.227E−01	4.857E−01	5.531E−01	6.250E−01	7.014E−01
800.0	2.504E−01	2.983E−01	3.505E−01	4.069E−01	4.675E−01	5.325E−01	6.017E−01	6.752E−01
900.0	2.433E−01	2.898E−01	3.404E−01	3.952E−01	4.541E−01	5.172E−01	5.845E−01	6.559E−01
1000.	2.378E−01	2.832E−01	3.328E−01	3.863E−01	4.439E−01	5.056E−01	5.714E−01	6.412E−01

Material: Neon

Ion	Li	Be	B	C	N	O	F	Ne
(E/A_1) / MeV				$(-\mathrm{d}E/\rho\mathrm{d}\ell)$ / MeV cm^2 mg^{-1}				
0.025	1.497E+00	1.876E+00	2.174E+00	2.414E+00	2.603E+00	2.789E+00	2.946E+00	3.091E+00
0.030	1.622E+00	2.046E+00	2.385E+00	2.661E+00	2.879E+00	3.090E+00	3.267E+00	3.431E+00
0.040	1.831E+00	2.338E+00	2.752E+00	3.100E+00	3.377E+00	3.640E+00	3.860E+00	4.061E+00
0.050	1.999E+00	2.580E+00	3.065E+00	3.480E+00	3.817E+00	4.133E+00	4.399E+00	4.640E+00
0.060	2.136E+00	2.787E+00	3.337E+00	3.815E+00	4.210E+00	4.578E+00	4.892E+00	5.175E+00
0.070	2.250E+00	2.964E+00	3.576E+00	4.113E+00	4.565E+00	4.984E+00	5.344E+00	5.670E+00
0.080	2.343E+00	3.117E+00	3.787E+00	4.382E+00	4.887E+00	5.356E+00	5.762E+00	6.130E+00
0.090	2.420E+00	3.248E+00	3.975E+00	4.624E+00	5.181E+00	5.698E+00	6.148E+00	6.558E+00
0.100	2.481E+00	3.360E+00	4.140E+00	4.841E+00	5.450E+00	6.013E+00	6.507E+00	6.957E+00
0.150	2.631E+00	3.697E+00	4.693E+00	5.622E+00	6.461E+00	7.245E+00	7.945E+00	8.590E+00
0.200	2.638E+00	3.808E+00	4.939E+00	6.026E+00	7.043E+00	8.009E+00	8.888E+00	9.709E+00
0.250	2.589E+00	3.811E+00	5.024E+00	6.212E+00	7.352E+00	8.452E+00	9.470E+00	1.043E+01
0.300	2.519E+00	3.765E+00	5.025E+00	6.277E+00	7.499E+00	8.695E+00	9.813E+00	1.089E+01
0.400	2.364E+00	3.618E+00	4.919E+00	6.237E+00	7.553E+00	8.863E+00	1.011E+01	1.132E+01
0.500	2.215E+00	3.452E+00	4.760E+00	6.104E+00	7.465E+00	8.833E+00	1.014E+01	1.143E+01
0.600	2.079E+00	3.290E+00	4.589E+00	5.939E+00	7.320E+00	8.720E+00	1.006E+01	1.139E+01
0.700	1.957E+00	3.136E+00	4.419E+00	5.765E+00	7.153E+00	8.569E+00	9.933E+00	1.129E+01
0.800	1.848E+00	2.993E+00	4.255E+00	5.591E+00	6.978E+00	8.401E+00	9.775E+00	1.115E+01
0.900	1.749E+00	2.861E+00	4.099E+00	5.420E+00	6.801E+00	8.225E+00	9.604E+00	1.098E+01
1.000	1.660E+00	2.738E+00	3.952E+00	5.256E+00	6.627E+00	8.048E+00	9.426E+00	1.081E+01
1.500	1.322E+00	2.249E+00	3.335E+00	4.538E+00	5.834E+00	7.204E+00	8.547E+00	9.909E+00
2.000	1.100E+00	1.905E+00	2.875E+00	3.975E+00	5.184E+00	6.481E+00	7.768E+00	9.083E+00
2.500	9.434E−01	1.652E+00	2.523E+00	3.529E+00	4.652E+00	5.873E+00	7.097E+00	8.359E+00
3.000	8.276E−01	1.460E+00	2.247E+00	3.170E+00	4.213E+00	5.360E+00	6.523E+00	7.728E+00
4.000	6.681E−01	1.186E+00	1.845E+00	2.631E+00	3.537E+00	4.550E+00	5.597E+00	6.696E+00
5.000	5.634E−01	1.003E+00	1.567E+00	2.249E+00	3.044E+00	3.945E+00	4.891E+00	5.894E+00
6.000	4.893E−01	8.715E−01	1.364E+00	1.965E+00	2.671E+00	3.479E+00	4.338E+00	5.256E+00
7.000	4.339E−01	7.727E−01	1.211E+00	1.747E+00	2.381E+00	3.111E+00	3.895E+00	4.741E+00
8.000	3.908E−01	6.956E−01	1.090E+00	1.574E+00	2.149E+00	2.813E+00	3.534E+00	4.316E+00
9.000	3.562E−01	6.338E−01	9.929E−01	1.434E+00	1.959E+00	2.569E+00	3.234E+00	3.961E+00
10.00	3.278E−01	5.830E−01	9.130E−01	1.319E+00	1.802E+00	2.365E+00	2.983E+00	3.660E+00
15.00	2.377E−01	4.223E−01	6.601E−01	9.521E−01	1.300E+00	1.706E+00	2.160E+00	2.664E+00
20.00	1.890E−01	3.358E−01	5.244E−01	7.554E−01	1.030E+00	1.349E+00	1.710E+00	2.112E+00
25.00	1.582E−01	2.811E−01	4.389E−01	6.318E−01	8.604E−01	1.126E+00	1.426E+00	1.762E+00
30.00	1.368E−01	2.431E−01	3.796E−01	5.464E−01	7.437E−01	9.721E−01	1.231E+00	1.520E+00
40.00	1.089E−01	1.936E−01	3.023E−01	4.351E−01	5.920E−01	7.732E−01	9.786E−01	1.208E+00
50.00	9.140E−02	1.625E−01	2.538E−01	3.653E−01	4.971E−01	6.494E−01	8.212E−01	1.014E+00
60.00	7.932E−02	1.410E−01	2.203E−01	3.172E−01	4.316E−01	5.636E−01	7.131E−01	8.802E−01
70.00	7.047E−02	1.253E−01	1.958E−01	2.819E−01	3.836E−01	5.009E−01	6.339E−01	7.824E−01
80.00	6.368E−02	1.132E−01	1.770E−01	2.548E−01	3.468E−01	4.529E−01	5.732E−01	7.075E−01
90.00	5.831E−02	1.037E−01	1.621E−01	2.334E−01	3.177E−01	4.149E−01	5.251E−01	6.482E−01
100.0	5.395E−02	9.594E−02	1.499E−01	2.160E−01	2.940E−01	3.840E−01	4.860E−01	6.000E−01
150.0	4.047E−02	7.198E−02	1.125E−01	1.621E−01	2.208E−01	2.884E−01	3.652E−01	4.510E−01
200.0	3.348E−02	5.956E−02	9.313E−02	1.342E−01	1.827E−01	2.388E−01	3.024E−01	3.735E−01
250.0	2.921E−02	5.197E−02	8.127E−02	1.171E−01	1.595E−01	2.085E−01	2.640E−01	3.262E−01
300.0	2.634E−02	4.687E−02	7.329E−02	1.056E−01	1.439E−01	1.881E−01	2.382E−01	2.943E−01
400.0	2.275E−02	4.049E−02	6.332E−02	9.125E−02	1.243E−01	1.625E−01	2.058E−01	2.543E−01
500.0	2.063E−02	3.671E−02	5.741E−02	8.275E−02	1.127E−01	1.474E−01	1.867E−01	2.307E−01
600.0	1.925E−02	3.426E−02	5.358E−02	7.724E−02	1.052E−01	1.376E−01	1.743E−01	2.154E−01
700.0	1.830E−02	3.257E−02	5.095E−02	7.344E−02	1.001E−01	1.308E−01	1.657E−01	2.049E−01
800.0	1.763E−02	3.137E−02	4.906E−02	7.072E−02	9.636E−02	1.260E−01	1.596E−01	1.975E−01
900.0	1.713E−02	3.048E−02	4.767E−02	6.872E−02	9.363E−02	1.224E−01	1.551E−01	1.919E−01
1000.	1.674E−02	2.980E−02	4.661E−02	6.719E−02	9.155E−02	1.197E−01	1.517E−01	1.874E−01

Material: Neon

Ion	Na	Mg	Al	Si	P	S	Cl	Ar
(E/A_1) / MeV				$(-\mathrm{d}E/\rho\mathrm{d}\ell)$ / MeV cm^2 mg^{-1}				
0.025	3.201E+00	3.316E+00	3.429E+00	3.539E+00	3.647E+00	3.750E+00	3.861E+00	3.955E+00
0.030	3.555E+00	3.680E+00	3.801E+00	3.919E+00	4.032E+00	4.145E+00	4.261E+00	4.360E+00
0.040	4.218E+00	4.365E+00	4.503E+00	4.635E+00	4.759E+00	4.888E+00	5.013E+00	5.120E+00
0.050	4.832E+00	5.005E+00	5.164E+00	5.311E+00	5.448E+00	5.592E+00	5.725E+00	5.839E+00
0.060	5.406E+00	5.608E+00	5.791E+00	5.957E+00	6.108E+00	6.268E+00	6.413E+00	6.536E+00
0.070	5.941E+00	6.176E+00	6.386E+00	6.574E+00	6.744E+00	6.922E+00	7.081E+00	7.216E+00
0.080	6.442E+00	6.710E+00	6.950E+00	7.164E+00	7.355E+00	7.554E+00	7.730E+00	7.880E+00
0.090	6.910E+00	7.213E+00	7.485E+00	7.725E+00	7.942E+00	8.163E+00	8.359E+00	8.526E+00
0.100	7.349E+00	7.688E+00	7.992E+00	8.261E+00	8.503E+00	8.749E+00	8.965E+00	9.152E+00
0.150	9.177E+00	9.693E+00	1.016E+01	1.058E+01	1.096E+01	1.134E+01	1.167E+01	1.197E+01
0.200	1.048E+01	1.117E+01	1.180E+01	1.236E+01	1.289E+01	1.341E+01	1.388E+01	1.429E+01
0.250	1.136E+01	1.220E+01	1.298E+01	1.369E+01	1.437E+01	1.503E+01	1.562E+01	1.616E+01
0.300	1.193E+01	1.290E+01	1.381E+01	1.465E+01	1.546E+01	1.625E+01	1.697E+01	1.762E+01
0.400	1.252E+01	1.366E+01	1.476E+01	1.579E+01	1.681E+01	1.781E+01	1.875E+01	1.960E+01
0.500	1.272E+01	1.396E+01	1.517E+01	1.633E+01	1.749E+01	1.864E+01	1.973E+01	2.073E+01
0.600	1.274E+01	1.404E+01	1.532E+01	1.656E+01	1.782E+01	1.907E+01	2.026E+01	2.137E+01
0.700	1.267E+01	1.400E+01	1.533E+01	1.662E+01	1.795E+01	1.927E+01	2.053E+01	2.172E+01
0.800	1.255E+01	1.390E+01	1.527E+01	1.658E+01	1.796E+01	1.934E+01	2.065E+01	2.189E+01
0.900	1.240E+01	1.377E+01	1.515E+01	1.649E+01	1.791E+01	1.932E+01	2.068E+01	2.195E+01
1.000	1.223E+01	1.361E+01	1.500E+01	1.636E+01	1.780E+01	1.925E+01	2.063E+01	2.194E+01
1.500	1.133E+01	1.271E+01	1.412E+01	1.551E+01	1.700E+01	1.852E+01	1.998E+01	2.135E+01
2.000	1.047E+01	1.182E+01	1.321E+01	1.458E+01	1.609E+01	1.761E+01	1.909E+01	2.047E+01
2.500	9.695E+00	1.101E+01	1.237E+01	1.372E+01	1.520E+01	1.672E+01	1.819E+01	1.956E+01
3.000	9.015E+00	1.029E+01	1.161E+01	1.292E+01	1.438E+01	1.587E+01	1.732E+01	1.868E+01
4.000	7.882E+00	9.066E+00	1.031E+01	1.155E+01	1.293E+01	1.437E+01	1.577E+01	1.707E+01
5.000	6.985E+00	8.086E+00	9.247E+00	1.042E+01	1.173E+01	1.309E+01	1.443E+01	1.567E+01
6.000	6.262E+00	7.287E+00	8.373E+00	9.473E+00	1.071E+01	1.200E+01	1.327E+01	1.446E+01
7.000	5.670E+00	6.626E+00	7.644E+00	8.679E+00	9.845E+00	1.107E+01	1.228E+01	1.342E+01
8.000	5.179E+00	6.073E+00	7.027E+00	8.004E+00	9.104E+00	1.026E+01	1.142E+01	1.251E+01
9.000	4.764E+00	5.603E+00	6.501E+00	7.423E+00	8.463E+00	9.562E+00	1.066E+01	1.170E+01
10.00	4.412E+00	5.200E+00	6.046E+00	6.920E+00	7.904E+00	8.947E+00	9.997E+00	1.099E+01
15.00	3.227E+00	3.830E+00	4.483E+00	5.169E+00	5.936E+00	6.758E+00	7.597E+00	8.416E+00
20.00	2.561E+00	3.047E+00	3.576E+00	4.137E+00	4.761E+00	5.433E+00	6.127E+00	6.817E+00
25.00	2.136E+00	2.544E+00	2.988E+00	3.463E+00	3.988E+00	4.555E+00	5.145E+00	5.740E+00
30.00	1.843E+00	2.195E+00	2.579E+00	2.991E+00	3.444E+00	3.934E+00	4.447E+00	4.970E+00
40.00	1.463E+00	1.742E+00	2.047E+00	2.375E+00	2.733E+00	3.119E+00	3.527E+00	3.949E+00
50.00	1.227E+00	1.461E+00	1.715E+00	1.990E+00	2.288E+00	2.610E+00	2.951E+00	3.306E+00
60.00	1.065E+00	1.268E+00	1.488E+00	1.726E+00	1.984E+00	2.261E+00	2.556E+00	2.865E+00
70.00	9.466E−01	1.127E+00	1.322E+00	1.534E+00	1.762E+00	2.007E+00	2.268E+00	2.543E+00
80.00	8.560E−01	1.019E+00	1.196E+00	1.387E+00	1.593E+00	1.814E+00	2.049E+00	2.297E+00
90.00	7.843E−01	9.333E−01	1.095E+00	1.270E+00	1.459E+00	1.661E+00	1.876E+00	2.104E+00
100.0	7.260E−01	8.640E−01	1.014E+00	1.176E+00	1.351E+00	1.537E+00	1.736E+00	1.947E+00
150.0	5.458E−01	6.497E−01	7.627E−01	8.847E−01	1.016E+00	1.156E+00	1.306E+00	1.464E+00
200.0	4.522E−01	5.384E−01	6.321E−01	7.334E−01	8.423E−01	9.587E−01	1.083E+00	1.214E+00
250.0	3.949E−01	4.702E−01	5.522E−01	6.407E−01	7.359E−01	8.378E−01	9.463E−01	1.061E+00
300.0	3.563E−01	4.243E−01	4.983E−01	5.783E−01	6.643E−01	7.563E−01	8.544E−01	9.584E−01
400.0	3.080E−01	3.669E−01	4.309E−01	5.001E−01	5.746E−01	6.543E−01	7.392E−01	8.294E−01
500.0	2.794E−01	3.328E−01	3.910E−01	4.538E−01	5.214E−01	5.940E−01	6.710E−01	7.529E−01
600.0	2.609E−01	3.107E−01	3.650E−01	4.238E−01	4.869E−01	5.551E−01	6.266E−01	7.032E−01
700.0	2.481E−01	2.955E−01	3.472E−01	4.030E−01	4.631E−01	5.274E−01	5.961E−01	6.689E−01
800.0	2.389E−01	2.846E−01	3.344E−01	3.882E−01	4.461E−01	5.081E−01	5.741E−01	6.443E−01
900.0	2.322E−01	2.766E−01	3.249E−01	3.772E−01	4.335E−01	4.938E−01	5.580E−01	6.262E−01
1000.	2.270E−01	2.705E−01	3.177E−01	3.689E−01	4.239E−01	4.829E−01	5.457E−01	6.124E−01

Material: Aluminium

Ion	Li	Be	B	C	N	O	F	Ne
(E/A_1) / MeV				$(-\mathrm{d}E/\rho\mathrm{d}\ell)$ / MeV cm^2 mg^{-1}				
0.025	1.388E+00	1.754E+00	2.047E+00	2.284E+00	2.478E+00	2.648E+00	2.795E+00	2.924E+00
0.030	1.496E+00	1.910E+00	2.247E+00	2.525E+00	2.753E+00	2.953E+00	3.126E+00	3.276E+00
0.040	1.670E+00	2.167E+00	2.586E+00	2.940E+00	3.234E+00	3.495E+00	3.719E+00	3.913E+00
0.050	1.800E+00	2.370E+00	2.860E+00	3.284E+00	3.641E+00	3.962E+00	4.238E+00	4.477E+00
0.060	1.898E+00	2.531E+00	3.084E+00	3.571E+00	3.988E+00	4.366E+00	4.693E+00	4.978E+00
0.070	1.971E+00	2.659E+00	3.269E+00	3.813E+00	4.286E+00	4.718E+00	5.094E+00	5.424E+00
0.080	2.024E+00	2.760E+00	3.421E+00	4.016E+00	4.541E+00	5.024E+00	5.448E+00	5.822E+00
0.090	2.063E+00	2.838E+00	3.545E+00	4.188E+00	4.761E+00	5.292E+00	5.762E+00	6.178E+00
0.100	2.093E+00	2.901E+00	3.646E+00	4.332E+00	4.950E+00	5.525E+00	6.039E+00	6.496E+00
0.150	2.164E+00	3.080E+00	3.960E+00	4.800E+00	5.583E+00	6.328E+00	7.017E+00	7.647E+00
0.200	2.172E+00	3.151E+00	4.113E+00	5.049E+00	5.941E+00	6.801E+00	7.606E+00	8.355E+00
0.250	2.150E+00	3.170E+00	4.188E+00	5.192E+00	6.164E+00	7.108E+00	8.001E+00	8.841E+00
0.300	2.111E+00	3.156E+00	4.214E+00	5.269E+00	6.302E+00	7.314E+00	8.275E+00	9.188E+00
0.400	2.010E+00	3.075E+00	4.181E+00	5.301E+00	6.419E+00	7.528E+00	8.590E+00	9.614E+00
0.500	1.901E+00	2.963E+00	4.086E+00	5.241E+00	6.409E+00	7.581E+00	8.709E+00	9.809E+00
0.600	1.797E+00	2.843E+00	3.966E+00	5.136E+00	6.331E+00	7.541E+00	8.712E+00	9.863E+00
0.700	1.701E+00	2.723E+00	3.838E+00	5.010E+00	6.218E+00	7.450E+00	8.648E+00	9.833E+00
0.800	1.612E+00	2.610E+00	3.709E+00	4.876E+00	6.088E+00	7.331E+00	8.544E+00	9.751E+00
0.900	1.532E+00	2.502E+00	3.584E+00	4.741E+00	5.951E+00	7.199E+00	8.418E+00	9.638E+00
1.000	1.459E+00	2.402E+00	3.464E+00	4.608E+00	5.812E+00	7.059E+00	8.281E+00	9.508E+00
1.500	1.176E+00	1.995E+00	2.952E+00	4.013E+00	5.157E+00	6.366E+00	7.563E+00	8.781E+00
2.000	9.856E−01	1.702E+00	2.562E+00	3.537E+00	4.609E+00	5.757E+00	6.906E+00	8.087E+00
2.500	8.498E−01	1.484E+00	2.261E+00	3.157E+00	4.156E+00	5.240E+00	6.336E+00	7.471E+00
3.000	7.483E−01	1.316E+00	2.022E+00	2.847E+00	3.779E+00	4.801E+00	5.843E+00	6.931E+00
4.000	6.073E−01	1.076E+00	1.670E+00	2.378E+00	3.192E+00	4.100E+00	5.044E+00	6.040E+00
5.000	5.140E−01	9.136E−01	1.425E+00	2.042E+00	2.760E+00	3.572E+00	4.428E+00	5.340E+00
6.000	4.476E−01	7.962E−01	1.245E+00	1.791E+00	2.431E+00	3.162E+00	3.942E+00	4.781E+00
7.000	3.977E−01	7.076E−01	1.107E+00	1.596E+00	2.173E+00	2.836E+00	3.551E+00	4.325E+00
8.000	3.588E−01	6.382E−01	9.991E−01	1.442E+00	1.966E+00	2.572E+00	3.230E+00	3.947E+00
9.000	3.275E−01	5.824E−01	9.116E−01	1.316E+00	1.797E+00	2.353E+00	2.963E+00	3.630E+00
10.00	3.018E−01	5.365E−01	8.395E−01	1.212E+00	1.655E+00	2.170E+00	2.737E+00	3.361E+00
15.00	2.198E−01	3.904E−01	6.100E−01	8.796E−01	1.201E+00	1.575E+00	1.994E+00	2.461E+00
20.00	1.752E−01	3.112E−01	4.860E−01	7.000E−01	9.541E−01	1.250E+00	1.584E+00	1.957E+00
25.00	1.469E−01	2.610E−01	4.075E−01	5.866E−01	7.988E−01	1.045E+00	1.324E+00	1.636E+00
30.00	1.273E−01	2.261E−01	3.530E−01	5.080E−01	6.915E−01	9.039E−01	1.145E+00	1.414E+00
40.00	1.015E−01	1.804E−01	2.817E−01	4.055E−01	5.516E−01	7.205E−01	9.119E−01	1.126E+00
50.00	8.530E−02	1.516E−01	2.369E−01	3.409E−01	4.638E−01	6.057E−01	7.664E−01	9.461E−01
60.00	7.411E−02	1.318E−01	2.058E−01	2.963E−01	4.032E−01	5.265E−01	6.662E−01	8.223E−01
70.00	6.589E−02	1.172E−01	1.831E−01	2.636E−01	3.587E−01	4.684E−01	5.927E−01	7.316E−01
80.00	5.958E−02	1.060E−01	1.656E−01	2.384E−01	3.245E−01	4.238E−01	5.363E−01	6.620E−01
90.00	5.459E−02	9.708E−02	1.517E−01	2.185E−01	2.974E−01	3.885E−01	4.916E−01	6.069E−01
100.0	5.053E−02	8.987E−02	1.405E−01	2.023E−01	2.754E−01	3.597E−01	4.553E−01	5.621E−01
150.0	3.797E−02	6.755E−02	1.056E−01	1.521E−01	2.072E−01	2.707E−01	3.427E−01	4.232E−01
200.0	3.146E−02	5.596E−02	8.755E−02	1.261E−01	1.717E−01	2.244E−01	2.842E−01	3.510E−01
250.0	2.747E−02	4.887E−02	7.642E−02	1.101E−01	1.500E−01	1.961E−01	2.483E−01	3.067E−01
300.0	2.479E−02	4.410E−02	6.896E−02	9.939E−02	1.354E−01	1.770E−01	2.241E−01	2.769E−01
400.0	2.143E−02	3.813E−02	5.964E−02	8.596E−02	1.171E−01	1.531E−01	1.939E−01	2.396E−01
500.0	1.945E−02	3.460E−02	5.412E−02	7.801E−02	1.063E−01	1.389E−01	1.760E−01	2.175E−01
600.0	1.816E−02	3.231E−02	5.054E−02	7.285E−02	9.926E−02	1.298E−01	1.644E−01	2.032E−01
700.0	1.727E−02	3.074E−02	4.808E−02	6.931E−02	9.444E−02	1.235E−01	1.564E−01	1.933E−01
800.0	1.664E−02	2.962E−02	4.632E−02	6.677E−02	9.098E−02	1.190E−01	1.507E−01	1.863E−01
900.0	1.618E−02	2.879E−02	4.503E−02	6.491E−02	8.844E−02	1.156E−01	1.465E−01	1.811E−01
1000.	1.582E−02	2.815E−02	4.404E−02	6.348E−02	8.650E−02	1.131E−01	1.433E−01	1.771E−01

Material: Aluminium

Ion	Na	Mg	Al	Si	P	S	Cl	Ar
(E/A_1) / MeV				$(-\mathrm{d}E/\rho\mathrm{d}\ell)$ / MeV cm^2 mg^{-1}				
0.025	3.037E+00	3.156E+00	3.267E+00	3.374E+00	3.473E+00	3.569E+00	3.673E+00	3.756E+00
0.030	3.406E+00	3.539E+00	3.662E+00	3.779E+00	3.887E+00	3.992E+00	4.103E+00	4.193E+00
0.040	4.083E+00	4.245E+00	4.395E+00	4.534E+00	4.662E+00	4.787E+00	4.913E+00	5.016E+00
0.050	4.690E+00	4.883E+00	5.063E+00	5.227E+00	5.378E+00	5.523E+00	5.666E+00	5.782E+00
0.060	5.235E+00	5.462E+00	5.672E+00	5.864E+00	6.039E+00	6.208E+00	6.369E+00	6.499E+00
0.070	5.725E+00	5.987E+00	6.230E+00	6.449E+00	6.650E+00	6.844E+00	7.025E+00	7.171E+00
0.080	6.167E+00	6.463E+00	6.739E+00	6.988E+00	7.216E+00	7.436E+00	7.639E+00	7.803E+00
0.090	6.566E+00	6.895E+00	7.205E+00	7.484E+00	7.740E+00	7.987E+00	8.213E+00	8.397E+00
0.100	6.926E+00	7.288E+00	7.631E+00	7.941E+00	8.226E+00	8.500E+00	8.751E+00	8.956E+00
0.150	8.264E+00	8.778E+00	9.280E+00	9.742E+00	1.017E+01	1.059E+01	1.097E+01	1.129E+01
0.200	9.110E+00	9.738E+00	1.036E+01	1.095E+01	1.151E+01	1.205E+01	1.255E+01	1.299E+01
0.250	9.701E+00	1.041E+01	1.114E+01	1.182E+01	1.247E+01	1.312E+01	1.372E+01	1.425E+01
0.300	1.014E+01	1.092E+01	1.172E+01	1.248E+01	1.322E+01	1.394E+01	1.463E+01	1.524E+01
0.400	1.070E+01	1.159E+01	1.252E+01	1.341E+01	1.428E+01	1.515E+01	1.597E+01	1.670E+01
0.500	1.099E+01	1.196E+01	1.299E+01	1.398E+01	1.496E+01	1.594E+01	1.687E+01	1.770E+01
0.600	1.112E+01	1.214E+01	1.324E+01	1.430E+01	1.538E+01	1.644E+01	1.746E+01	1.838E+01
0.700	1.114E+01	1.220E+01	1.335E+01	1.447E+01	1.561E+01	1.674E+01	1.784E+01	1.882E+01
0.800	1.109E+01	1.217E+01	1.336E+01	1.452E+01	1.572E+01	1.690E+01	1.805E+01	1.909E+01
0.900	1.101E+01	1.210E+01	1.331E+01	1.450E+01	1.574E+01	1.697E+01	1.816E+01	1.924E+01
1.000	1.089E+01	1.199E+01	1.323E+01	1.443E+01	1.570E+01	1.696E+01	1.819E+01	1.930E+01
1.500	1.019E+01	1.128E+01	1.255E+01	1.379E+01	1.512E+01	1.646E+01	1.777E+01	1.896E+01
2.000	9.479E+00	1.054E+01	1.179E+01	1.302E+01	1.436E+01	1.572E+01	1.705E+01	1.826E+01
2.500	8.825E+00	9.851E+00	1.107E+01	1.229E+01	1.361E+01	1.496E+01	1.629E+01	1.749E+01
3.000	8.240E+00	9.231E+00	1.042E+01	1.161E+01	1.291E+01	1.424E+01	1.555E+01	1.674E+01
4.000	7.250E+00	8.178E+00	9.298E+00	1.042E+01	1.166E+01	1.295E+01	1.421E+01	1.537E+01
5.000	6.456E+00	7.325E+00	8.375E+00	9.435E+00	1.062E+01	1.184E+01	1.305E+01	1.416E+01
6.000	5.808E+00	6.625E+00	7.609E+00	8.610E+00	9.727E+00	1.089E+01	1.205E+01	1.312E+01
7.000	5.273E+00	6.042E+00	6.967E+00	7.912E+00	8.969E+00	1.007E+01	1.118E+01	1.220E+01
8.000	4.826E+00	5.551E+00	6.421E+00	7.315E+00	8.314E+00	9.364E+00	1.042E+01	1.140E+01
9.000	4.446E+00	5.132E+00	5.953E+00	6.799E+00	7.745E+00	8.744E+00	9.750E+00	1.069E+01
10.00	4.121E+00	4.772E+00	5.547E+00	6.349E+00	7.248E+00	8.198E+00	9.159E+00	1.007E+01
15.00	3.021E+00	3.537E+00	4.138E+00	4.772E+00	5.479E+00	6.234E+00	7.010E+00	7.762E+00
20.00	2.397E+00	2.823E+00	3.313E+00	3.833E+00	4.411E+00	5.032E+00	5.677E+00	6.314E+00
25.00	1.999E+00	2.363E+00	2.775E+00	3.216E+00	3.704E+00	4.230E+00	4.780E+00	5.331E+00
30.00	1.724E+00	2.042E+00	2.399E+00	2.782E+00	3.204E+00	3.660E+00	4.139E+00	4.625E+00
40.00	1.368E+00	1.624E+00	1.908E+00	2.214E+00	2.548E+00	2.909E+00	3.290E+00	3.684E+00
50.00	1.147E+00	1.363E+00	1.601E+00	1.858E+00	2.136E+00	2.437E+00	2.756E+00	3.088E+00
60.00	9.962E−01	1.184E+00	1.391E+00	1.613E+00	1.854E+00	2.114E+00	2.390E+00	2.679E+00
70.00	8.858E−01	1.053E+00	1.237E+00	1.434E+00	1.648E+00	1.878E+00	2.122E+00	2.379E+00
80.00	8.014E−01	9.532E−01	1.119E+00	1.298E+00	1.491E+00	1.698E+00	1.918E+00	2.151E+00
90.00	7.345E−01	8.739E−01	1.026E+00	1.190E+00	1.366E+00	1.556E+00	1.758E+00	1.971E+00
100.0	6.803E−01	8.094E−01	9.500E−01	1.102E+00	1.265E+00	1.441E+00	1.627E+00	1.825E+00
150.0	5.123E−01	6.098E−01	7.158E−01	8.304E−01	9.536E−01	1.085E+00	1.226E+00	1.375E+00
200.0	4.249E−01	5.059E−01	5.940E−01	6.892E−01	7.915E−01	9.010E−01	1.018E+00	1.141E+00
250.0	3.714E−01	4.422E−01	5.193E−01	6.026E−01	6.922E−01	7.880E−01	8.901E−01	9.984E−01
300.0	3.353E−01	3.993E−01	4.690E−01	5.443E−01	6.253E−01	7.119E−01	8.042E−01	9.022E−01
400.0	2.902E−01	3.456E−01	4.060E−01	4.712E−01	5.414E−01	6.165E−01	6.965E−01	7.815E−01
500.0	2.634E−01	3.138E−01	3.686E−01	4.279E−01	4.917E−01	5.600E−01	6.327E−01	7.100E−01
600.0	2.461E−01	2.932E−01	3.444E−01	3.998E−01	4.594E−01	5.232E−01	5.913E−01	6.635E−01
700.0	2.342E−01	2.790E−01	3.277E−01	3.805E−01	4.374E−01	4.980E−01	5.627E−01	6.315E−01
800.0	2.256E−01	2.688E−01	3.158E−01	3.666E−01	4.217E−01	4.799E−01	5.423E−01	6.086E−01
900.0	2.193E−01	2.613E−01	3.070E−01	3.564E−01	4.099E−01	4.665E−01	5.272E−01	5.917E−01
1000.	2.145E−01	2.556E−01	3.003E−01	3.487E−01	4.007E−01	4.564E−01	5.158E−01	5.789E−01

Material: Silicon

Ion	Li	Be	B	C	N	O	F	Ne
(E/A_1) / MeV				$(-\mathrm{d}E/\rho\mathrm{d}\ell)$ / MeV cm^2 mg^{-1}				
0.025	1.468E+00	1.792E+00	2.047E+00	2.263E+00	2.453E+00	2.634E+00	2.803E+00	2.965E+00
0.030	1.612E+00	1.998E+00	2.299E+00	2.546E+00	2.758E+00	2.956E+00	3.140E+00	3.318E+00
0.040	1.817E+00	2.323E+00	2.729E+00	3.059E+00	3.329E+00	3.568E+00	3.782E+00	3.984E+00
0.050	1.946E+00	2.550E+00	3.055E+00	3.478E+00	3.825E+00	4.125E+00	4.384E+00	4.616E+00
0.060	2.033E+00	2.710E+00	3.297E+00	3.804E+00	4.230E+00	4.603E+00	4.921E+00	5.200E+00
0.070	2.093E+00	2.828E+00	3.480E+00	4.057E+00	4.555E+00	4.997E+00	5.379E+00	5.715E+00
0.080	2.137E+00	2.918E+00	3.623E+00	4.259E+00	4.819E+00	5.323E+00	5.765E+00	6.158E+00
0.090	2.169E+00	2.988E+00	3.738E+00	4.424E+00	5.036E+00	5.595E+00	6.091E+00	6.537E+00
0.100	2.192E+00	3.043E+00	3.831E+00	4.560E+00	5.218E+00	5.825E+00	6.369E+00	6.864E+00
0.150	2.242E+00	3.195E+00	4.113E+00	4.992E+00	5.814E+00	6.596E+00	7.318E+00	7.996E+00
0.200	2.237E+00	3.247E+00	4.241E+00	5.211E+00	6.138E+00	7.031E+00	7.869E+00	8.666E+00
0.250	2.208E+00	3.254E+00	4.300E+00	5.333E+00	6.333E+00	7.307E+00	8.227E+00	9.112E+00
0.300	2.167E+00	3.236E+00	4.318E+00	5.397E+00	6.454E+00	7.490E+00	8.475E+00	9.426E+00
0.400	2.066E+00	3.155E+00	4.283E+00	5.424E+00	6.561E+00	7.688E+00	8.767E+00	9.819E+00
0.500	1.960E+00	3.047E+00	4.193E+00	5.370E+00	6.557E+00	7.746E+00	8.889E+00	1.001E+01
0.600	1.856E+00	2.929E+00	4.079E+00	5.272E+00	6.489E+00	7.719E+00	8.907E+00	1.008E+01
0.700	1.759E+00	2.811E+00	3.954E+00	5.152E+00	6.386E+00	7.640E+00	8.858E+00	1.007E+01
0.800	1.670E+00	2.697E+00	3.827E+00	5.022E+00	6.262E+00	7.531E+00	8.767E+00	1.000E+01
0.900	1.589E+00	2.589E+00	3.702E+00	4.889E+00	6.129E+00	7.404E+00	8.651E+00	9.901E+00
1.000	1.514E+00	2.488E+00	3.581E+00	4.757E+00	5.992E+00	7.268E+00	8.521E+00	9.779E+00
1.500	1.224E+00	2.071E+00	3.060E+00	4.154E+00	5.333E+00	6.575E+00	7.809E+00	9.063E+00
2.000	1.027E+00	1.770E+00	2.660E+00	3.667E+00	4.773E+00	5.955E+00	7.143E+00	8.361E+00
2.500	8.863E−01	1.545E+00	2.350E+00	3.276E+00	4.308E+00	5.425E+00	6.560E+00	7.732E+00
3.000	7.809E−01	1.371E+00	2.103E+00	2.957E+00	3.920E+00	4.974E+00	6.055E+00	7.179E+00
4.000	6.340E−01	1.122E+00	1.739E+00	2.473E+00	3.315E+00	4.254E+00	5.232E+00	6.263E+00
5.000	5.366E−01	9.528E−01	1.484E+00	2.125E+00	2.869E+00	3.709E+00	4.598E+00	5.542E+00
6.000	4.672E−01	8.305E−01	1.297E+00	1.864E+00	2.529E+00	3.285E+00	4.096E+00	4.965E+00
7.000	4.151E−01	7.381E−01	1.154E+00	1.662E+00	2.261E+00	2.949E+00	3.691E+00	4.494E+00
8.000	3.745E−01	6.658E−01	1.042E+00	1.502E+00	2.047E+00	2.675E+00	3.359E+00	4.103E+00
9.000	3.418E−01	6.075E−01	9.505E−01	1.371E+00	1.871E+00	2.448E+00	3.083E+00	3.775E+00
10.00	3.149E−01	5.596E−01	8.753E−01	1.263E+00	1.724E+00	2.259E+00	2.849E+00	3.496E+00
15.00	2.292E−01	4.070E−01	6.359E−01	9.168E−01	1.251E+00	1.640E+00	2.077E+00	2.563E+00
20.00	1.827E−01	3.244E−01	5.065E−01	7.295E−01	9.942E−01	1.302E+00	1.650E+00	2.038E+00
25.00	1.531E−01	2.720E−01	4.247E−01	6.113E−01	8.324E−01	1.089E+00	1.379E+00	1.704E+00
30.00	1.326E−01	2.356E−01	3.678E−01	5.293E−01	7.204E−01	9.416E−01	1.192E+00	1.473E+00
40.00	1.057E−01	1.879E−01	2.934E−01	4.223E−01	5.746E−01	7.504E−01	9.498E−01	1.173E+00
50.00	8.882E−02	1.579E−01	2.466E−01	3.550E−01	4.830E−01	6.307E−01	7.981E−01	9.852E−01
60.00	7.715E−02	1.372E−01	2.143E−01	3.085E−01	4.198E−01	5.482E−01	6.936E−01	8.562E−01
70.00	6.859E−02	1.220E−01	1.906E−01	2.744E−01	3.734E−01	4.876E−01	6.170E−01	7.616E−01
80.00	6.202E−02	1.103E−01	1.724E−01	2.482E−01	3.378E−01	4.412E−01	5.583E−01	6.891E−01
90.00	5.682E−02	1.010E−01	1.579E−01	2.274E−01	3.096E−01	4.043E−01	5.117E−01	6.317E−01
100.0	5.259E−02	9.353E−02	1.462E−01	2.106E−01	2.866E−01	3.744E−01	4.738E−01	5.850E−01
150.0	3.951E−02	7.028E−02	1.099E−01	1.583E−01	2.155E−01	2.816E−01	3.566E−01	4.404E−01
200.0	3.272E−02	5.822E−02	9.102E−02	1.312E−01	1.786E−01	2.334E−01	2.956E−01	3.651E−01
250.0	2.857E−02	5.083E−02	7.948E−02	1.145E−01	1.560E−01	2.039E−01	2.582E−01	3.190E−01
300.0	2.578E−02	4.586E−02	7.172E−02	1.034E−01	1.408E−01	1.840E−01	2.331E−01	2.880E−01
400.0	2.228E−02	3.965E−02	6.201E−02	8.938E−02	1.218E−01	1.592E−01	2.016E−01	2.492E−01
500.0	2.022E−02	3.598E−02	5.627E−02	8.111E−02	1.105E−01	1.445E−01	1.830E−01	2.262E−01
600.0	1.888E−02	3.360E−02	5.254E−02	7.574E−02	1.032E−01	1.349E−01	1.709E−01	2.113E−01
700.0	1.796E−02	3.196E−02	4.998E−02	7.205E−02	9.817E−02	1.284E−01	1.626E−01	2.010E−01
800.0	1.730E−02	3.078E−02	4.815E−02	6.941E−02	9.457E−02	1.237E−01	1.567E−01	1.936E−01
900.0	1.681E−02	2.992E−02	4.680E−02	6.746E−02	9.192E−02	1.202E−01	1.523E−01	1.882E−01
1000.	1.644E−02	2.926E−02	4.577E−02	6.598E−02	8.990E−02	1.175E−01	1.489E−01	1.841E−01

Material: Silicon

Ion	Na	Mg	Al	Si	P	S	Cl	Ar
(E/A_1) / MeV				$(-\mathrm{d}E/\rho\mathrm{d}\ell)$ / MeV cm^2 mg^{-1}				
0.025	3.107E+00	3.257E+00	3.396E+00	3.530E+00	3.652E+00	3.768E+00	3.887E+00	3.994E+00
0.030	3.473E+00	3.639E+00	3.794E+00	3.941E+00	4.078E+00	4.210E+00	4.344E+00	4.465E+00
0.040	4.161E+00	4.347E+00	4.523E+00	4.694E+00	4.853E+00	5.011E+00	5.168E+00	5.314E+00
0.050	4.817E+00	5.018E+00	5.207E+00	5.390E+00	5.562E+00	5.738E+00	5.910E+00	6.074E+00
0.060	5.437E+00	5.665E+00	5.870E+00	6.063E+00	6.244E+00	6.429E+00	6.609E+00	6.781E+00
0.070	6.001E+00	6.268E+00	6.502E+00	6.716E+00	6.910E+00	7.107E+00	7.292E+00	7.469E+00
0.080	6.496E+00	6.809E+00	7.083E+00	7.328E+00	7.547E+00	7.763E+00	7.961E+00	8.146E+00
0.090	6.927E+00	7.287E+00	7.604E+00	7.887E+00	8.139E+00	8.382E+00	8.602E+00	8.803E+00
0.100	7.302E+00	7.707E+00	8.067E+00	8.390E+00	8.678E+00	8.954E+00	9.201E+00	9.426E+00
0.150	8.623E+00	9.209E+00	9.750E+00	1.025E+01	1.071E+01	1.115E+01	1.155E+01	1.192E+01
0.200	9.423E+00	1.013E+01	1.081E+01	1.143E+01	1.203E+01	1.260E+01	1.314E+01	1.363E+01
0.250	9.963E+00	1.077E+01	1.154E+01	1.226E+01	1.296E+01	1.364E+01	1.428E+01	1.487E+01
0.300	1.035E+01	1.123E+01	1.208E+01	1.288E+01	1.366E+01	1.442E+01	1.514E+01	1.582E+01
0.400	1.086E+01	1.185E+01	1.281E+01	1.373E+01	1.464E+01	1.554E+01	1.639E+01	1.720E+01
0.500	1.113E+01	1.221E+01	1.326E+01	1.427E+01	1.529E+01	1.629E+01	1.724E+01	1.815E+01
0.600	1.126E+01	1.240E+01	1.352E+01	1.460E+01	1.570E+01	1.679E+01	1.783E+01	1.882E+01
0.700	1.129E+01	1.247E+01	1.365E+01	1.479E+01	1.595E+01	1.710E+01	1.821E+01	1.927E+01
0.800	1.125E+01	1.247E+01	1.368E+01	1.486E+01	1.608E+01	1.729E+01	1.845E+01	1.956E+01
0.900	1.117E+01	1.241E+01	1.365E+01	1.487E+01	1.612E+01	1.737E+01	1.858E+01	1.974E+01
1.000	1.107E+01	1.232E+01	1.358E+01	1.482E+01	1.610E+01	1.739E+01	1.864E+01	1.983E+01
1.500	1.036E+01	1.164E+01	1.294E+01	1.422E+01	1.558E+01	1.696E+01	1.830E+01	1.957E+01
2.000	9.634E+00	1.089E+01	1.218E+01	1.345E+01	1.483E+01	1.622E+01	1.759E+01	1.889E+01
2.500	8.966E+00	1.019E+01	1.145E+01	1.270E+01	1.407E+01	1.546E+01	1.682E+01	1.812E+01
3.000	8.369E+00	9.554E+00	1.078E+01	1.201E+01	1.335E+01	1.472E+01	1.607E+01	1.735E+01
4.000	7.365E+00	8.473E+00	9.630E+00	1.079E+01	1.208E+01	1.340E+01	1.470E+01	1.594E+01
5.000	6.562E+00	7.595E+00	8.682E+00	9.782E+00	1.100E+01	1.226E+01	1.351E+01	1.470E+01
6.000	5.909E+00	6.874E+00	7.894E+00	8.932E+00	1.008E+01	1.128E+01	1.248E+01	1.362E+01
7.000	5.370E+00	6.273E+00	7.231E+00	8.212E+00	9.303E+00	1.044E+01	1.159E+01	1.268E+01
8.000	4.919E+00	5.765E+00	6.668E+00	7.595E+00	8.628E+00	9.713E+00	1.080E+01	1.185E+01
9.000	4.537E+00	5.333E+00	6.184E+00	7.062E+00	8.042E+00	9.073E+00	1.012E+01	1.112E+01
10.00	4.210E+00	4.960E+00	5.764E+00	6.598E+00	7.527E+00	8.509E+00	9.505E+00	1.047E+01
15.00	3.102E+00	3.680E+00	4.306E+00	4.964E+00	5.697E+00	6.480E+00	7.285E+00	8.078E+00
20.00	2.471E+00	2.939E+00	3.448E+00	3.990E+00	4.590E+00	5.235E+00	5.904E+00	6.575E+00
25.00	2.066E+00	2.460E+00	2.890E+00	3.349E+00	3.856E+00	4.402E+00	4.973E+00	5.553E+00
30.00	1.785E+00	2.126E+00	2.498E+00	2.897E+00	3.336E+00	3.810E+00	4.308E+00	4.818E+00
40.00	1.421E+00	1.691E+00	1.987E+00	2.305E+00	2.653E+00	3.028E+00	3.425E+00	3.837E+00
50.00	1.192E+00	1.420E+00	1.667E+00	1.934E+00	2.225E+00	2.537E+00	2.869E+00	3.217E+00
60.00	1.036E+00	1.233E+00	1.448E+00	1.680E+00	1.931E+00	2.201E+00	2.488E+00	2.790E+00
70.00	9.215E−01	1.097E+00	1.287E+00	1.493E+00	1.716E+00	1.955E+00	2.209E+00	2.477E+00
80.00	8.340E−01	9.923E−01	1.165E+00	1.351E+00	1.552E+00	1.767E+00	1.997E+00	2.239E+00
90.00	7.649E−01	9.096E−01	1.068E+00	1.238E+00	1.422E+00	1.619E+00	1.829E+00	2.051E+00
100.0	7.080E−01	8.424E−01	9.887E−01	1.147E+00	1.317E+00	1.499E+00	1.694E+00	1.899E+00
150.0	5.330E−01	6.344E−01	7.448E−01	8.640E−01	9.921E−01	1.129E+00	1.275E+00	1.430E+00
200.0	4.420E−01	5.263E−01	6.179E−01	7.169E−01	8.234E−01	9.372E−01	1.059E+00	1.187E+00
250.0	3.863E−01	4.600E−01	5.401E−01	6.268E−01	7.199E−01	8.196E−01	9.258E−01	1.038E+00
300.0	3.487E−01	4.153E−01	4.878E−01	5.661E−01	6.503E−01	7.403E−01	8.363E−01	9.382E−01
400.0	3.017E−01	3.594E−01	4.221E−01	4.900E−01	5.629E−01	6.410E−01	7.242E−01	8.126E−01
500.0	2.739E−01	3.263E−01	3.833E−01	4.449E−01	5.112E−01	5.822E−01	6.578E−01	7.381E−01
600.0	2.558E−01	3.048E−01	3.580E−01	4.157E−01	4.776E−01	5.439E−01	6.147E−01	6.898E−01
700.0	2.434E−01	2.900E−01	3.407E−01	3.955E−01	4.545E−01	5.176E−01	5.850E−01	6.565E−01
800.0	2.345E−01	2.794E−01	3.282E−01	3.811E−01	4.379E−01	4.988E−01	5.637E−01	6.326E−01
900.0	2.280E−01	2.716E−01	3.191E−01	3.705E−01	4.257E−01	4.849E−01	5.480E−01	6.150E−01
1000.	2.230E−01	2.656E−01	3.121E−01	3.623E−01	4.164E−01	4.743E−01	5.360E−01	6.016E−01

Material: Argon

Ion	Li	Be	B	C	N	O	F	Ne
(E/A_1) / MeV				$(-\mathrm{d}E/\rho\mathrm{d}\ell)$ / MeV cm^2 mg^{-1}				
0.025	1.288E+00	1.578E+00	1.804E+00	1.988E+00	2.142E+00	2.285E+00	2.419E+00	2.550E+00
0.030	1.410E+00	1.748E+00	2.017E+00	2.236E+00	2.417E+00	2.582E+00	2.731E+00	2.874E+00
0.040	1.603E+00	2.032E+00	2.382E+00	2.672E+00	2.912E+00	3.126E+00	3.314E+00	3.487E+00
0.050	1.742E+00	2.253E+00	2.680E+00	3.040E+00	3.340E+00	3.606E+00	3.838E+00	4.048E+00
0.060	1.838E+00	2.422E+00	2.920E+00	3.347E+00	3.708E+00	4.027E+00	4.306E+00	4.556E+00
0.070	1.904E+00	2.549E+00	3.111E+00	3.601E+00	4.020E+00	4.394E+00	4.721E+00	5.014E+00
0.080	1.949E+00	2.645E+00	3.261E+00	3.808E+00	4.283E+00	4.710E+00	5.085E+00	5.422E+00
0.090	1.979E+00	2.716E+00	3.380E+00	3.978E+00	4.504E+00	4.980E+00	5.402E+00	5.783E+00
0.100	1.998E+00	2.769E+00	3.474E+00	4.116E+00	4.689E+00	5.212E+00	5.678E+00	6.101E+00
0.150	2.017E+00	2.886E+00	3.723E+00	4.520E+00	5.262E+00	5.963E+00	6.609E+00	7.210E+00
0.200	1.985E+00	2.898E+00	3.801E+00	4.682E+00	5.524E+00	6.336E+00	7.100E+00	7.824E+00
0.250	1.936E+00	2.870E+00	3.810E+00	4.742E+00	5.648E+00	6.532E+00	7.374E+00	8.183E+00
0.300	1.882E+00	2.825E+00	3.787E+00	4.752E+00	5.701E+00	6.635E+00	7.533E+00	8.402E+00
0.400	1.773E+00	2.716E+00	3.699E+00	4.700E+00	5.701E+00	6.700E+00	7.667E+00	8.616E+00
0.500	1.672E+00	2.604E+00	3.591E+00	4.609E+00	5.638E+00	6.673E+00	7.682E+00	8.679E+00
0.600	1.580E+00	2.495E+00	3.479E+00	4.502E+00	5.547E+00	6.605E+00	7.640E+00	8.668E+00
0.700	1.498E+00	2.393E+00	3.367E+00	4.390E+00	5.442E+00	6.515E+00	7.567E+00	8.616E+00
0.800	1.423E+00	2.297E+00	3.258E+00	4.276E+00	5.331E+00	6.412E+00	7.475E+00	8.539E+00
0.900	1.355E+00	2.207E+00	3.154E+00	4.164E+00	5.218E+00	6.302E+00	7.372E+00	8.446E+00
1.000	1.293E+00	2.123E+00	3.054E+00	4.054E+00	5.104E+00	6.188E+00	7.261E+00	8.342E+00
1.500	1.053E+00	1.779E+00	2.624E+00	3.559E+00	4.564E+00	5.621E+00	6.682E+00	7.760E+00
2.000	8.894E−01	1.528E+00	2.292E+00	3.155E+00	4.101E+00	5.111E+00	6.134E+00	7.185E+00
2.500	7.709E−01	1.340E+00	2.032E+00	2.828E+00	3.713E+00	4.670E+00	5.649E+00	6.662E+00
3.000	6.814E−01	1.193E+00	1.825E+00	2.561E+00	3.388E+00	4.292E+00	5.226E+00	6.199E+00
4.000	5.556E−01	9.809E−01	1.516E+00	2.151E+00	2.878E+00	3.686E+00	4.534E+00	5.428E+00
5.000	4.714E−01	8.355E−01	1.299E+00	1.855E+00	2.500E+00	3.225E+00	3.996E+00	4.818E+00
6.000	4.111E−01	7.297E−01	1.138E+00	1.632E+00	2.209E+00	2.865E+00	3.570E+00	4.327E+00
7.000	3.656E−01	6.495E−01	1.014E+00	1.458E+00	1.980E+00	2.576E+00	3.224E+00	3.925E+00
8.000	3.301E−01	5.864E−01	9.162E−01	1.319E+00	1.795E+00	2.342E+00	2.940E+00	3.590E+00
9.000	3.014E−01	5.355E−01	8.370E−01	1.206E+00	1.643E+00	2.147E+00	2.702E+00	3.308E+00
10.00	2.778E−01	4.936E−01	7.714E−01	1.112E+00	1.516E+00	1.983E+00	2.501E+00	3.068E+00
15.00	2.026E−01	3.597E−01	5.618E−01	8.096E−01	1.104E+00	1.447E+00	1.831E+00	2.259E+00
20.00	1.616E−01	2.870E−01	4.481E−01	6.453E−01	8.792E−01	1.151E+00	1.458E+00	1.801E+00
25.00	1.356E−01	2.409E−01	3.760E−01	5.412E−01	7.369E−01	9.637E−01	1.221E+00	1.508E+00
30.00	1.175E−01	2.087E−01	3.259E−01	4.690E−01	6.383E−01	8.341E−01	1.056E+00	1.305E+00
40.00	9.376E−02	1.666E−01	2.603E−01	3.746E−01	5.096E−01	6.655E−01	8.423E−01	1.040E+00
50.00	7.882E−02	1.401E−01	2.189E−01	3.151E−01	4.287E−01	5.598E−01	7.083E−01	8.744E−01
60.00	6.850E−02	1.218E−01	1.903E−01	2.740E−01	3.728E−01	4.868E−01	6.160E−01	7.603E−01
70.00	6.092E−02	1.083E−01	1.693E−01	2.438E−01	3.317E−01	4.332E−01	5.482E−01	6.766E−01
80.00	5.511E−02	9.800E−02	1.532E−01	2.206E−01	3.002E−01	3.921E−01	4.961E−01	6.124E−01
90.00	5.050E−02	8.981E−02	1.404E−01	2.022E−01	2.752E−01	3.594E−01	4.549E−01	5.615E−01
100.0	4.675E−02	8.315E−02	1.300E−01	1.872E−01	2.548E−01	3.329E−01	4.213E−01	5.202E−01
150.0	3.515E−02	6.254E−02	9.777E−02	1.409E−01	1.919E−01	2.506E−01	3.173E−01	3.919E−01
200.0	2.913E−02	5.183E−02	8.104E−02	1.168E−01	1.590E−01	2.078E−01	2.632E−01	3.251E−01
250.0	2.545E−02	4.527E−02	7.079E−02	1.020E−01	1.390E−01	1.816E−01	2.300E−01	2.842E−01
300.0	2.297E−02	4.086E−02	6.390E−02	9.209E−02	1.255E−01	1.640E−01	2.077E−01	2.566E−01
400.0	1.986E−02	3.535E−02	5.528E−02	7.967E−02	1.085E−01	1.419E−01	1.798E−01	2.221E−01
500.0	1.803E−02	3.208E−02	5.018E−02	7.233E−02	9.854E−02	1.288E−01	1.632E−01	2.017E−01
600.0	1.684E−02	2.997E−02	4.687E−02	6.756E−02	9.205E−02	1.204E−01	1.525E−01	1.884E−01
700.0	1.602E−02	2.851E−02	4.460E−02	6.429E−02	8.759E−02	1.146E−01	1.451E−01	1.793E−01
800.0	1.544E−02	2.747E−02	4.297E−02	6.194E−02	8.440E−02	1.104E−01	1.398E−01	1.728E−01
900.0	1.501E−02	2.670E−02	4.177E−02	6.022E−02	8.205E−02	1.073E−01	1.359E−01	1.680E−01
1000.	1.468E−02	2.612E−02	4.085E−02	5.889E−02	8.025E−02	1.049E−01	1.330E−01	1.643E−01

Material: Argon

Ion	Na	Mg	Al	Si	P	S	Cl	Ar
(E/A_1) / MeV				$(-\mathrm{d}E/\rho\mathrm{d}\ell)$ / MeV cm^2 mg^{-1}				
0.025	2.671E+00	2.799E+00	2.923E+00	3.044E+00	3.158E+00	3.270E+00	3.382E+00	3.489E+00
0.030	3.004E+00	3.140E+00	3.272E+00	3.402E+00	3.525E+00	3.647E+00	3.770E+00	3.890E+00
0.040	3.641E+00	3.794E+00	3.942E+00	4.085E+00	4.220E+00	4.357E+00	4.494E+00	4.630E+00
0.050	4.233E+00	4.410E+00	4.577E+00	4.736E+00	4.883E+00	5.032E+00	5.178E+00	5.325E+00
0.060	4.776E+00	4.981E+00	5.173E+00	5.351E+00	5.514E+00	5.678E+00	5.835E+00	5.991E+00
0.070	5.271E+00	5.509E+00	5.727E+00	5.928E+00	6.110E+00	6.291E+00	6.462E+00	6.630E+00
0.080	5.718E+00	5.992E+00	6.240E+00	6.467E+00	6.671E+00	6.872E+00	7.059E+00	7.240E+00
0.090	6.120E+00	6.430E+00	6.712E+00	6.967E+00	7.197E+00	7.420E+00	7.625E+00	7.822E+00
0.100	6.478E+00	6.826E+00	7.142E+00	7.428E+00	7.686E+00	7.933E+00	8.160E+00	8.376E+00
0.150	7.764E+00	8.279E+00	8.757E+00	9.196E+00	9.599E+00	9.984E+00	1.034E+01	1.067E+01
0.200	8.509E+00	9.153E+00	9.761E+00	1.033E+01	1.086E+01	1.137E+01	1.184E+01	1.229E+01
0.250	8.961E+00	9.699E+00	1.041E+01	1.107E+01	1.171E+01	1.232E+01	1.290E+01	1.345E+01
0.300	9.249E+00	1.006E+01	1.084E+01	1.158E+01	1.230E+01	1.300E+01	1.366E+01	1.429E+01
0.400	9.555E+00	1.046E+01	1.134E+01	1.219E+01	1.302E+01	1.385E+01	1.463E+01	1.539E+01
0.500	9.674E+00	1.064E+01	1.159E+01	1.251E+01	1.342E+01	1.433E+01	1.520E+01	1.604E+01
0.600	9.701E+00	1.071E+01	1.170E+01	1.267E+01	1.365E+01	1.461E+01	1.555E+01	1.645E+01
0.700	9.676E+00	1.071E+01	1.174E+01	1.274E+01	1.376E+01	1.478E+01	1.576E+01	1.671E+01
0.800	9.617E+00	1.067E+01	1.173E+01	1.276E+01	1.381E+01	1.486E+01	1.588E+01	1.687E+01
0.900	9.537E+00	1.061E+01	1.168E+01	1.273E+01	1.381E+01	1.490E+01	1.595E+01	1.697E+01
1.000	9.443E+00	1.052E+01	1.161E+01	1.268E+01	1.378E+01	1.489E+01	1.596E+01	1.701E+01
1.500	8.874E+00	9.972E+00	1.109E+01	1.220E+01	1.336E+01	1.453E+01	1.568E+01	1.680E+01
2.000	8.280E+00	9.364E+00	1.048E+01	1.158E+01	1.276E+01	1.395E+01	1.513E+01	1.626E+01
2.500	7.726E+00	8.785E+00	9.876E+00	1.097E+01	1.214E+01	1.333E+01	1.451E+01	1.564E+01
3.000	7.227E+00	8.254E+00	9.319E+00	1.039E+01	1.154E+01	1.272E+01	1.389E+01	1.501E+01
4.000	6.381E+00	7.342E+00	8.347E+00	9.361E+00	1.046E+01	1.160E+01	1.273E+01	1.382E+01
5.000	5.700E+00	6.599E+00	7.543E+00	8.502E+00	9.552E+00	1.064E+01	1.172E+01	1.277E+01
6.000	5.145E+00	5.986E+00	6.873E+00	7.779E+00	8.774E+00	9.809E+00	1.085E+01	1.185E+01
7.000	4.686E+00	5.473E+00	6.308E+00	7.165E+00	8.108E+00	9.093E+00	1.009E+01	1.104E+01
8.000	4.300E+00	5.039E+00	5.826E+00	6.637E+00	7.532E+00	8.470E+00	9.419E+00	1.034E+01
9.000	3.973E+00	4.668E+00	5.411E+00	6.181E+00	7.030E+00	7.923E+00	8.830E+00	9.712E+00
10.00	3.692E+00	4.348E+00	5.051E+00	5.782E+00	6.589E+00	7.441E+00	8.309E+00	9.155E+00
15.00	2.733E+00	3.241E+00	3.791E+00	4.370E+00	5.012E+00	5.695E+00	6.401E+00	7.101E+00
20.00	2.183E+00	2.596E+00	3.045E+00	3.522E+00	4.050E+00	4.615E+00	5.205E+00	5.798E+00
25.00	1.828E+00	2.176E+00	2.556E+00	2.962E+00	3.409E+00	3.889E+00	4.394E+00	4.908E+00
30.00	1.581E+00	1.883E+00	2.212E+00	2.566E+00	2.953E+00	3.371E+00	3.811E+00	4.264E+00
40.00	1.260E+00	1.500E+00	1.762E+00	2.044E+00	2.352E+00	2.684E+00	3.037E+00	3.403E+00
50.00	1.058E+00	1.260E+00	1.480E+00	1.717E+00	1.974E+00	2.252E+00	2.547E+00	2.855E+00
60.00	9.201E−01	1.095E+00	1.286E+00	1.492E+00	1.714E+00	1.954E+00	2.209E+00	2.478E+00
70.00	8.187E−01	9.743E−01	1.144E+00	1.327E+00	1.524E+00	1.737E+00	1.963E+00	2.202E+00
80.00	7.410E−01	8.819E−01	1.035E+00	1.201E+00	1.379E+00	1.571E+00	1.775E+00	1.991E+00
90.00	6.794E−01	8.086E−01	9.491E−01	1.101E+00	1.264E+00	1.440E+00	1.626E+00	1.824E+00
100.0	6.294E−01	7.491E−01	8.792E−01	1.020E+00	1.171E+00	1.333E+00	1.506E+00	1.689E+00
150.0	4.743E−01	5.646E−01	6.628E−01	7.689E−01	8.830E−01	1.005E+00	1.135E+00	1.273E+00
200.0	3.936E−01	4.686E−01	5.502E−01	6.384E−01	7.332E−01	8.346E−01	9.427E−01	1.057E+00
250.0	3.441E−01	4.098E−01	4.812E−01	5.584E−01	6.413E−01	7.301E−01	8.247E−01	9.252E−01
300.0	3.107E−01	3.701E−01	4.346E−01	5.044E−01	5.795E−01	6.597E−01	7.453E−01	8.361E−01
400.0	2.690E−01	3.204E−01	3.763E−01	4.368E−01	5.019E−01	5.715E−01	6.457E−01	7.245E−01
500.0	2.443E−01	2.910E−01	3.418E−01	3.968E−01	4.559E−01	5.192E−01	5.867E−01	6.584E−01
600.0	2.282E−01	2.719E−01	3.194E−01	3.708E−01	4.261E−01	4.853E−01	5.484E−01	6.154E−01
700.0	2.172E−01	2.588E−01	3.040E−01	3.529E−01	4.056E−01	4.619E−01	5.220E−01	5.859E−01
800.0	2.093E−01	2.494E−01	2.930E−01	3.401E−01	3.909E−01	4.452E−01	5.031E−01	5.647E−01
900.0	2.035E−01	2.424E−01	2.848E−01	3.307E−01	3.800E−01	4.329E−01	4.892E−01	5.490E−01
1000.	1.990E−01	2.371E−01	2.786E−01	3.235E−01	3.718E−01	4.234E−01	4.786E−01	5.371E−01

Material: Titanium

Ion	Li	Be	B	C	N	O	F	Ne
(E/A_1) / MeV				$(-\mathrm{d}E/\rho\mathrm{d}\ell)$ / MeV cm^2 mg^{-1}				
0.025	1.008E+00	1.218E+00	1.374E+00	1.498E+00	1.600E+00	1.696E+00	1.789E+00	1.883E+00
0.030	1.108E+00	1.356E+00	1.544E+00	1.692E+00	1.812E+00	1.922E+00	2.024E+00	2.125E+00
0.040	1.272E+00	1.594E+00	1.846E+00	2.047E+00	2.207E+00	2.348E+00	2.474E+00	2.593E+00
0.050	1.400E+00	1.789E+00	2.103E+00	2.358E+00	2.563E+00	2.742E+00	2.896E+00	3.037E+00
0.060	1.500E+00	1.949E+00	2.321E+00	2.631E+00	2.883E+00	3.102E+00	3.289E+00	3.457E+00
0.070	1.577E+00	2.081E+00	2.507E+00	2.869E+00	3.168E+00	3.428E+00	3.651E+00	3.849E+00
0.080	1.635E+00	2.187E+00	2.664E+00	3.075E+00	3.420E+00	3.723E+00	3.984E+00	4.214E+00
0.090	1.680E+00	2.274E+00	2.796E+00	3.253E+00	3.643E+00	3.988E+00	4.287E+00	4.551E+00
0.100	1.715E+00	2.345E+00	2.907E+00	3.406E+00	3.839E+00	4.225E+00	4.561E+00	4.860E+00
0.150	1.785E+00	2.538E+00	3.249E+00	3.912E+00	4.516E+00	5.076E+00	5.582E+00	6.044E+00
0.200	1.777E+00	2.587E+00	3.381E+00	4.147E+00	4.869E+00	5.555E+00	6.192E+00	6.786E+00
0.250	1.743E+00	2.579E+00	3.419E+00	4.247E+00	5.044E+00	5.816E+00	6.547E+00	7.241E+00
0.300	1.700E+00	2.548E+00	3.414E+00	4.279E+00	5.125E+00	5.956E+00	6.751E+00	7.517E+00
0.400	1.612E+00	2.464E+00	3.353E+00	4.258E+00	5.160E+00	6.060E+00	6.932E+00	7.788E+00
0.500	1.527E+00	2.372E+00	3.268E+00	4.190E+00	5.122E+00	6.060E+00	6.976E+00	7.882E+00
0.600	1.448E+00	2.281E+00	3.175E+00	4.105E+00	5.053E+00	6.014E+00	6.956E+00	7.894E+00
0.700	1.376E+00	2.193E+00	3.081E+00	4.012E+00	4.968E+00	5.944E+00	6.903E+00	7.862E+00
0.800	1.311E+00	2.110E+00	2.988E+00	3.916E+00	4.876E+00	5.860E+00	6.831E+00	7.804E+00
0.900	1.251E+00	2.032E+00	2.898E+00	3.821E+00	4.781E+00	5.768E+00	6.746E+00	7.730E+00
1.000	1.197E+00	1.959E+00	2.812E+00	3.727E+00	4.685E+00	5.673E+00	6.655E+00	7.645E+00
1.500	9.831E−01	1.656E+00	2.438E+00	3.300E+00	4.224E+00	5.194E+00	6.170E+00	7.164E+00
2.000	8.357E−01	1.433E+00	2.145E+00	2.947E+00	3.823E+00	4.756E+00	5.705E+00	6.679E+00
2.500	7.282E−01	1.263E+00	1.912E+00	2.657E+00	3.481E+00	4.371E+00	5.284E+00	6.230E+00
3.000	6.465E−01	1.130E+00	1.725E+00	2.416E+00	3.191E+00	4.036E+00	4.911E+00	5.824E+00
4.000	5.304E−01	9.349E−01	1.442E+00	2.043E+00	2.730E+00	3.490E+00	4.290E+00	5.134E+00
5.000	4.520E−01	7.999E−01	1.241E+00	1.770E+00	2.382E+00	3.068E+00	3.800E+00	4.580E+00
6.000	3.954E−01	7.010E−01	1.091E+00	1.563E+00	2.113E+00	2.736E+00	3.407E+00	4.129E+00
7.000	3.525E−01	6.255E−01	9.755E−01	1.401E+00	1.900E+00	2.468E+00	3.087E+00	3.756E+00
8.000	3.188E−01	5.659E−01	8.833E−01	1.270E+00	1.727E+00	2.249E+00	2.822E+00	3.445E+00
9.000	2.916E−01	5.177E−01	8.084E−01	1.164E+00	1.583E+00	2.067E+00	2.599E+00	3.181E+00
10.00	2.690E−01	4.777E−01	7.461E−01	1.075E+00	1.464E+00	1.912E+00	2.410E+00	2.955E+00
15.00	1.969E−01	3.497E−01	5.460E−01	7.864E−01	1.072E+00	1.403E+00	1.776E+00	2.190E+00
20.00	1.575E−01	2.797E−01	4.366E−01	6.286E−01	8.562E−01	1.120E+00	1.419E+00	1.752E+00
25.00	1.324E−01	2.351E−01	3.670E−01	5.282E−01	7.190E−01	9.401E−01	1.191E+00	1.471E+00
30.00	1.148E−01	2.040E−01	3.185E−01	4.584E−01	6.237E−01	8.150E−01	1.032E+00	1.275E+00
40.00	9.182E−02	1.632E−01	2.549E−01	3.668E−01	4.990E−01	6.517E−01	8.248E−01	1.018E+00
50.00	7.730E−02	1.374E−01	2.147E−01	3.090E−01	4.204E−01	5.490E−01	6.946E−01	8.575E−01
60.00	6.725E−02	1.196E−01	1.868E−01	2.690E−01	3.660E−01	4.779E−01	6.047E−01	7.464E−01
70.00	5.986E−02	1.064E−01	1.663E−01	2.395E−01	3.260E−01	4.257E−01	5.386E−01	6.648E−01
80.00	5.418E−02	9.636E−02	1.506E−01	2.169E−01	2.952E−01	3.855E−01	4.879E−01	6.022E−01
90.00	4.968E−02	8.836E−02	1.381E−01	1.989E−01	2.708E−01	3.536E−01	4.476E−01	5.525E−01
100.0	4.602E−02	8.185E−02	1.279E−01	1.843E−01	2.509E−01	3.277E−01	4.148E−01	5.121E−01
150.0	3.466E−02	6.167E−02	9.641E−02	1.389E−01	1.892E−01	2.472E−01	3.130E−01	3.865E−01
200.0	2.876E−02	5.117E−02	8.001E−02	1.153E−01	1.570E−01	2.052E−01	2.599E−01	3.210E−01
250.0	2.514E−02	4.473E−02	6.995E−02	1.008E−01	1.373E−01	1.795E−01	2.273E−01	2.808E−01
300.0	2.271E−02	4.040E−02	6.318E−02	9.106E−02	1.241E−01	1.622E−01	2.054E−01	2.538E−01
400.0	1.966E−02	3.498E−02	5.471E−02	7.886E−02	1.074E−01	1.405E−01	1.779E−01	2.199E−01
500.0	1.786E−02	3.178E−02	4.970E−02	7.164E−02	9.761E−02	1.276E−01	1.617E−01	1.998E−01
600.0	1.669E−02	2.970E−02	4.645E−02	6.697E−02	9.124E−02	1.193E−01	1.511E−01	1.868E−01
700.0	1.589E−02	2.827E−02	4.422E−02	6.375E−02	8.687E−02	1.136E−01	1.439E−01	1.779E−01
800.0	1.531E−02	2.725E−02	4.263E−02	6.146E−02	8.374E−02	1.095E−01	1.387E−01	1.715E−01
900.0	1.489E−02	2.650E−02	4.146E−02	5.976E−02	8.143E−02	1.065E−01	1.349E−01	1.668E−01
1000.	1.457E−02	2.593E−02	4.056E−02	5.847E−02	7.967E−02	1.042E−01	1.320E−01	1.632E−01

Material: Titanium

Ion	Na	Mg	Al	Si	P	S	Cl	Ar
(E/A_1) / MeV				$(-\mathrm{d}E/\rho\mathrm{d}\ell)$ / MeV cm^2 mg^{-1}				
0.025	1.969E+00	2.062E+00	2.154E+00	2.246E+00	2.330E+00	2.246E+00	2.500E+00	2.585E+00
0.030	2.218E+00	2.316E+00	2.414E+00	2.512E+00	2.602E+00	2.512E+00	2.786E+00	2.879E+00
0.040	2.700E+00	2.808E+00	2.917E+00	3.023E+00	3.122E+00	3.023E+00	3.327E+00	3.433E+00
0.050	3.162E+00	3.283E+00	3.402E+00	3.518E+00	3.624E+00	3.518E+00	3.844E+00	3.958E+00
0.060	3.603E+00	3.740E+00	3.873E+00	3.998E+00	4.112E+00	3.998E+00	4.346E+00	4.467E+00
0.070	4.020E+00	4.178E+00	4.326E+00	4.465E+00	4.589E+00	4.465E+00	4.838E+00	4.965E+00
0.080	4.413E+00	4.594E+00	4.762E+00	4.915E+00	5.052E+00	4.915E+00	5.320E+00	5.454E+00
0.090	4.780E+00	4.987E+00	5.177E+00	5.348E+00	5.500E+00	5.348E+00	5.792E+00	5.934E+00
0.100	5.121E+00	5.356E+00	5.570E+00	5.762E+00	5.932E+00	5.762E+00	6.250E+00	6.403E+00
0.150	6.462E+00	6.841E+00	7.192E+00	7.509E+00	7.792E+00	7.509E+00	8.302E+00	8.533E+00
0.200	7.338E+00	7.846E+00	8.324E+00	8.763E+00	9.166E+00	8.763E+00	9.896E+00	1.023E+01
0.250	7.900E+00	8.514E+00	9.101E+00	9.648E+00	1.016E+01	9.648E+00	1.110E+01	1.153E+01
0.300	8.255E+00	8.953E+00	9.626E+00	1.026E+01	1.086E+01	1.026E+01	1.199E+01	1.252E+01
0.400	8.629E+00	9.436E+00	1.023E+01	1.098E+01	1.172E+01	1.098E+01	1.313E+01	1.380E+01
0.500	8.784E+00	9.658E+00	1.052E+01	1.135E+01	1.218E+01	1.135E+01	1.377E+01	1.453E+01
0.600	8.835E+00	9.753E+00	1.066E+01	1.155E+01	1.243E+01	1.155E+01	1.416E+01	1.499E+01
0.700	8.830E+00	9.777E+00	1.072E+01	1.164E+01	1.257E+01	1.164E+01	1.439E+01	1.527E+01
0.800	8.790E+00	9.758E+00	1.072E+01	1.167E+01	1.264E+01	1.167E+01	1.453E+01	1.545E+01
0.900	8.728E+00	9.711E+00	1.070E+01	1.166E+01	1.265E+01	1.166E+01	1.461E+01	1.555E+01
1.000	8.653E+00	9.646E+00	1.064E+01	1.163E+01	1.264E+01	1.163E+01	1.464E+01	1.560E+01
1.500	8.186E+00	9.197E+00	1.023E+01	1.125E+01	1.231E+01	1.125E+01	1.445E+01	1.548E+01
2.000	7.690E+00	8.694E+00	9.723E+00	1.075E+01	1.183E+01	1.075E+01	1.401E+01	1.507E+01
2.500	7.218E+00	8.204E+00	9.219E+00	1.024E+01	1.132E+01	1.024E+01	1.351E+01	1.457E+01
3.000	6.783E+00	7.745E+00	8.741E+00	9.740E+00	1.081E+01	9.740E+00	1.299E+01	1.404E+01
4.000	6.031E+00	6.939E+00	7.886E+00	8.842E+00	9.876E+00	8.842E+00	1.200E+01	1.302E+01
5.000	5.415E+00	6.267E+00	7.162E+00	8.071E+00	9.059E+00	8.071E+00	1.110E+01	1.210E+01
6.000	4.906E+00	5.706E+00	6.550E+00	7.413E+00	8.354E+00	7.413E+00	1.032E+01	1.127E+01
7.000	4.482E+00	5.233E+00	6.029E+00	6.848E+00	7.742E+00	6.848E+00	9.620E+00	1.054E+01
8.000	4.124E+00	4.831E+00	5.583E+00	6.359E+00	7.210E+00	6.359E+00	9.006E+00	9.887E+00
9.000	3.818E+00	4.484E+00	5.196E+00	5.934E+00	6.744E+00	5.934E+00	8.461E+00	9.308E+00
10.00	3.554E+00	4.184E+00	4.859E+00	5.561E+00	6.333E+00	5.561E+00	7.976E+00	8.791E+00
15.00	2.648E+00	3.139E+00	3.670E+00	4.231E+00	4.848E+00	4.231E+00	6.186E+00	6.864E+00
20.00	2.123E+00	2.524E+00	2.959E+00	3.423E+00	3.934E+00	3.423E+00	5.051E+00	5.629E+00
25.00	1.782E+00	2.122E+00	2.491E+00	2.886E+00	3.320E+00	2.886E+00	4.277E+00	4.778E+00
30.00	1.544E+00	1.839E+00	2.160E+00	2.505E+00	2.882E+00	2.505E+00	3.718E+00	4.160E+00
40.00	1.233E+00	1.468E+00	1.725E+00	2.002E+00	2.302E+00	2.002E+00	2.971E+00	3.330E+00
50.00	1.038E+00	1.235E+00	1.451E+00	1.683E+00	1.936E+00	1.683E+00	2.496E+00	2.799E+00
60.00	9.032E−01	1.075E+00	1.262E+00	1.464E+00	1.683E+00	1.464E+00	2.169E+00	2.432E+00
70.00	8.044E−01	9.574E−01	1.124E+00	1.304E+00	1.498E+00	1.304E+00	1.929E+00	2.163E+00
80.00	7.286E−01	8.671E−01	1.018E+00	1.181E+00	1.356E+00	1.181E+00	1.745E+00	1.958E+00
90.00	6.685E−01	7.956E−01	9.338E−01	1.083E+00	1.244E+00	1.083E+00	1.600E+00	1.795E+00
100.0	6.196E−01	7.374E−01	8.655E−01	1.004E+00	1.153E+00	1.004E+00	1.483E+00	1.663E+00
150.0	4.678E−01	5.569E−01	6.538E−01	7.584E−01	8.709E−01	7.584E−01	1.120E+00	1.256E+00
200.0	3.886E−01	4.627E−01	5.433E−01	6.304E−01	7.240E−01	6.304E−01	9.309E−01	1.044E+00
250.0	3.400E−01	4.050E−01	4.756E−01	5.519E−01	6.339E−01	5.519E−01	8.152E−01	9.145E−01
300.0	3.076E−01	3.660E−01	4.299E−01	4.989E−01	5.731E−01	4.989E−01	7.372E−01	8.270E−01
400.0	2.663E−01	3.172E−01	3.726E−01	4.325E−01	4.969E−01	4.325E−01	6.393E−01	7.174E−01
500.0	2.420E−01	2.883E−01	3.387E−01	3.932E−01	4.518E−01	3.932E−01	5.814E−01	6.524E−01
600.0	2.263E−01	2.695E−01	3.167E−01	3.676E−01	4.225E−01	3.676E−01	5.437E−01	6.102E−01
700.0	2.154E−01	2.567E−01	3.016E−01	3.501E−01	4.023E−01	3.501E−01	5.179E−01	5.812E−01
800.0	2.077E−01	2.475E−01	2.907E−01	3.376E−01	3.879E−01	3.376E−01	4.994E−01	5.604E−01
900.0	2.020E−01	2.407E−01	2.828E−01	3.283E−01	3.773E−01	3.283E−01	4.857E−01	5.451E−01
1000.	1.976E−01	2.355E−01	2.767E−01	3.212E−01	3.692E−01	3.212E−01	4.753E−01	5.334E−01

Material: Iron

Ion	Li	Be	B	C	N	O	F	Ne
(E/A_1) / MeV				$(-\mathrm{d}E/\rho\mathrm{d}\ell)$ / MeV cm^2 mg^{-1}				
0.025	8.835E−01	1.055E+00	1.178E+00	1.273E+00	1.349E+00	1.422E+00	1.492E+00	1.564E+00
0.030	9.749E−01	1.181E+00	1.330E+00	1.446E+00	1.535E+00	1.617E+00	1.695E+00	1.772E+00
0.040	1.128E+00	1.398E+00	1.603E+00	1.764E+00	1.886E+00	1.994E+00	2.089E+00	2.179E+00
0.050	1.249E+00	1.580E+00	1.839E+00	2.047E+00	2.208E+00	2.347E+00	2.466E+00	2.574E+00
0.060	1.346E+00	1.732E+00	2.044E+00	2.299E+00	2.500E+00	2.674E+00	2.820E+00	2.951E+00
0.070	1.422E+00	1.859E+00	2.221E+00	2.522E+00	2.765E+00	2.974E+00	3.151E+00	3.306E+00
0.080	1.481E+00	1.964E+00	2.373E+00	2.719E+00	3.003E+00	3.249E+00	3.458E+00	3.640E+00
0.090	1.526E+00	2.051E+00	2.502E+00	2.892E+00	3.217E+00	3.500E+00	3.741E+00	3.953E+00
0.100	1.561E+00	2.121E+00	2.612E+00	3.042E+00	3.407E+00	3.727E+00	4.002E+00	4.244E+00
0.150	1.644E+00	2.322E+00	2.956E+00	3.543E+00	4.072E+00	4.558E+00	4.993E+00	5.386E+00
0.200	1.652E+00	2.391E+00	3.108E+00	3.794E+00	4.434E+00	5.037E+00	5.594E+00	6.111E+00
0.250	1.630E+00	2.401E+00	3.170E+00	3.920E+00	4.636E+00	5.324E+00	5.970E+00	6.580E+00
0.300	1.595E+00	2.383E+00	3.182E+00	3.976E+00	4.745E+00	5.495E+00	6.208E+00	6.890E+00
0.400	1.515E+00	2.312E+00	3.140E+00	3.980E+00	4.815E+00	5.643E+00	6.444E+00	7.226E+00
0.500	1.436E+00	2.227E+00	3.064E+00	3.924E+00	4.792E+00	5.663E+00	6.514E+00	7.354E+00
0.600	1.363E+00	2.142E+00	2.978E+00	3.846E+00	4.731E+00	5.627E+00	6.508E+00	7.383E+00
0.700	1.297E+00	2.061E+00	2.891E+00	3.760E+00	4.654E+00	5.564E+00	6.463E+00	7.360E+00
0.800	1.236E+00	1.984E+00	2.805E+00	3.672E+00	4.569E+00	5.487E+00	6.397E+00	7.309E+00
0.900	1.180E+00	1.912E+00	2.722E+00	3.584E+00	4.481E+00	5.403E+00	6.319E+00	7.241E+00
1.000	1.130E+00	1.844E+00	2.642E+00	3.497E+00	4.392E+00	5.315E+00	6.235E+00	7.163E+00
1.500	9.314E−01	1.565E+00	2.298E+00	3.105E+00	3.968E+00	4.875E+00	5.788E+00	6.721E+00
2.000	7.945E−01	1.359E+00	2.029E+00	2.782E+00	3.602E+00	4.475E+00	5.364E+00	6.279E+00
2.500	6.945E−01	1.202E+00	1.815E+00	2.516E+00	3.291E+00	4.126E+00	4.984E+00	5.872E+00
3.000	6.183E−01	1.078E+00	1.642E+00	2.295E+00	3.026E+00	3.821E+00	4.646E+00	5.505E+00
4.000	5.096E−01	8.965E−01	1.380E+00	1.952E+00	2.602E+00	3.321E+00	4.079E+00	4.879E+00
5.000	4.358E−01	7.699E−01	1.193E+00	1.698E+00	2.281E+00	2.933E+00	3.629E+00	4.370E+00
6.000	3.822E−01	6.767E−01	1.052E+00	1.504E+00	2.030E+00	2.624E+00	3.265E+00	3.953E+00
7.000	3.414E−01	6.051E−01	9.424E−01	1.351E+00	1.830E+00	2.374E+00	2.967E+00	3.607E+00
8.000	3.092E−01	5.484E−01	8.551E−01	1.228E+00	1.667E+00	2.168E+00	2.718E+00	3.316E+00
9.000	2.831E−01	5.024E−01	7.837E−01	1.127E+00	1.532E+00	1.996E+00	2.509E+00	3.068E+00
10.00	2.615E−01	4.642E−01	7.243E−01	1.042E+00	1.418E+00	1.850E+00	2.330E+00	2.855E+00
15.00	1.921E−01	3.410E−01	5.322E−01	7.662E−01	1.044E+00	1.365E+00	1.727E+00	2.128E+00
20.00	1.539E−01	2.733E−01	4.266E−01	6.140E−01	8.360E−01	1.093E+00	1.384E+00	1.709E+00
25.00	1.295E−01	2.301E−01	3.591E−01	5.168E−01	7.033E−01	9.193E−01	1.164E+00	1.438E+00
30.00	1.125E−01	1.999E−01	3.120E−01	4.490E−01	6.108E−01	7.980E−01	1.010E+00	1.248E+00
40.00	9.008E−02	1.601E−01	2.501E−01	3.599E−01	4.896E−01	6.393E−01	8.090E−01	9.988E−01
50.00	7.592E−02	1.350E−01	2.109E−01	3.035E−01	4.129E−01	5.391E−01	6.822E−01	8.420E−01
60.00	6.610E−02	1.175E−01	1.837E−01	2.644E−01	3.598E−01	4.698E−01	5.944E−01	7.337E−01
70.00	5.888E−02	1.047E−01	1.636E−01	2.356E−01	3.206E−01	4.187E−01	5.298E−01	6.540E−01
80.00	5.332E−02	9.484E−02	1.482E−01	2.135E−01	2.905E−01	3.794E−01	4.802E−01	5.927E−01
90.00	4.892E−02	8.700E−02	1.360E−01	1.959E−01	2.666E−01	3.482E−01	4.407E−01	5.441E−01
100.0	4.533E−02	8.063E−02	1.260E−01	1.815E−01	2.471E−01	3.228E−01	4.086E−01	5.045E−01
150.0	3.420E−02	6.084E−02	9.512E−02	1.370E−01	1.866E−01	2.439E−01	3.088E−01	3.814E−01
200.0	2.840E−02	5.052E−02	7.901E−02	1.139E−01	1.551E−01	2.027E−01	2.567E−01	3.170E−01
250.0	2.484E−02	4.420E−02	6.912E−02	9.962E−02	1.357E−01	1.774E−01	2.247E−01	2.776E−01
300.0	2.245E−02	3.994E−02	6.247E−02	9.004E−02	1.227E−01	1.603E−01	2.031E−01	2.509E−01
400.0	1.945E−02	3.461E−02	5.414E−02	7.804E−02	1.063E−01	1.390E−01	1.761E−01	2.176E−01
500.0	1.768E−02	3.146E−02	4.921E−02	7.094E−02	9.666E−02	1.264E−01	1.602E−01	1.979E−01
600.0	1.653E−02	2.942E−02	4.602E−02	6.634E−02	9.040E−02	1.182E−01	1.498E−01	1.851E−01
700.0	1.574E−02	2.802E−02	4.383E−02	6.318E−02	8.610E−02	1.126E−01	1.426E−01	1.763E−01
800.0	1.518E−02	2.702E−02	4.226E−02	6.093E−02	8.302E−02	1.086E−01	1.376E−01	1.700E−01
900.0	1.477E−02	2.628E−02	4.111E−02	5.927E−02	8.076E−02	1.056E−01	1.338E−01	1.654E−01
1000.	1.445E−02	2.572E−02	4.023E−02	5.800E−02	7.903E−02	1.033E−01	1.310E−01	1.619E−01

Material: Iron

Ion	Na	Mg	Al	Si	P	S	Cl	Ar
(E/A_1) / MeV				$(-\mathrm{d}E/\rho\mathrm{d}\ell)$ / MeV cm^2 mg^{-1}				
0.025	1.632E+00	1.706E+00	1.778E+00	1.851E+00	1.919E+00	1.987E+00	2.055E+00	2.127E+00
0.030	1.845E+00	1.923E+00	2.000E+00	2.078E+00	2.151E+00	2.225E+00	2.300E+00	2.378E+00
0.040	2.262E+00	2.348E+00	2.432E+00	2.517E+00	2.597E+00	2.681E+00	2.764E+00	2.854E+00
0.050	2.670E+00	2.765E+00	2.857E+00	2.948E+00	3.033E+00	3.122E+00	3.211E+00	3.308E+00
0.060	3.064E+00	3.173E+00	3.274E+00	3.373E+00	3.463E+00	3.559E+00	3.651E+00	3.753E+00
0.070	3.441E+00	3.566E+00	3.681E+00	3.790E+00	3.888E+00	3.991E+00	4.087E+00	4.194E+00
0.080	3.799E+00	3.943E+00	4.074E+00	4.196E+00	4.305E+00	4.416E+00	4.519E+00	4.631E+00
0.090	4.136E+00	4.302E+00	4.451E+00	4.588E+00	4.709E+00	4.831E+00	4.943E+00	5.062E+00
0.100	4.454E+00	4.643E+00	4.811E+00	4.965E+00	5.101E+00	5.235E+00	5.357E+00	5.485E+00
0.150	5.738E+00	6.055E+00	6.343E+00	6.603E+00	6.833E+00	7.050E+00	7.244E+00	7.434E+00
0.200	6.588E+00	7.026E+00	7.433E+00	7.808E+00	8.149E+00	8.470E+00	8.760E+00	9.040E+00
0.250	7.155E+00	7.690E+00	8.196E+00	8.669E+00	9.109E+00	9.527E+00	9.911E+00	1.028E+01
0.300	7.543E+00	8.156E+00	8.742E+00	9.296E+00	9.819E+00	1.032E+01	1.079E+01	1.124E+01
0.400	7.990E+00	8.719E+00	9.426E+00	1.010E+01	1.076E+01	1.140E+01	1.200E+01	1.258E+01
0.500	8.187E+00	8.992E+00	9.779E+00	1.054E+01	1.129E+01	1.203E+01	1.273E+01	1.342E+01
0.600	8.259E+00	9.113E+00	9.955E+00	1.077E+01	1.159E+01	1.240E+01	1.318E+01	1.394E+01
0.700	8.264E+00	9.150E+00	1.003E+01	1.089E+01	1.175E+01	1.261E+01	1.344E+01	1.426E+01
0.800	8.232E+00	9.140E+00	1.005E+01	1.093E+01	1.183E+01	1.273E+01	1.360E+01	1.446E+01
0.900	8.177E+00	9.100E+00	1.002E+01	1.093E+01	1.186E+01	1.278E+01	1.368E+01	1.457E+01
1.000	8.108E+00	9.041E+00	9.979E+00	1.090E+01	1.185E+01	1.280E+01	1.372E+01	1.463E+01
1.500	7.678E+00	8.628E+00	9.594E+00	1.055E+01	1.156E+01	1.256E+01	1.356E+01	1.453E+01
2.000	7.226E+00	8.169E+00	9.135E+00	1.010E+01	1.112E+01	1.214E+01	1.316E+01	1.416E+01
2.500	6.799E+00	7.726E+00	8.681E+00	9.637E+00	1.065E+01	1.168E+01	1.271E+01	1.371E+01
3.000	6.407E+00	7.314E+00	8.250E+00	9.193E+00	1.020E+01	1.122E+01	1.224E+01	1.324E+01
4.000	5.726E+00	6.585E+00	7.479E+00	8.384E+00	9.358E+00	1.036E+01	1.136E+01	1.233E+01
5.000	5.162E+00	5.972E+00	6.820E+00	7.684E+00	8.618E+00	9.581E+00	1.055E+01	1.149E+01
6.000	4.694E+00	5.456E+00	6.259E+00	7.082E+00	7.974E+00	8.898E+00	9.832E+00	1.074E+01
7.000	4.300E+00	5.018E+00	5.778E+00	6.560E+00	7.411E+00	8.296E+00	9.195E+00	1.007E+01
8.000	3.965E+00	4.643E+00	5.363E+00	6.107E+00	6.918E+00	7.765E+00	8.628E+00	9.473E+00
9.000	3.679E+00	4.319E+00	5.002E+00	5.710E+00	6.484E+00	7.294E+00	8.123E+00	8.937E+00
10.00	3.431E+00	4.037E+00	4.685E+00	5.360E+00	6.099E+00	6.875E+00	7.671E+00	8.455E+00
15.00	2.572E+00	3.048E+00	3.561E+00	4.104E+00	4.699E+00	5.331E+00	5.987E+00	6.645E+00
20.00	2.069E+00	2.459E+00	2.882E+00	3.333E+00	3.828E+00	4.356E+00	4.910E+00	5.471E+00
25.00	1.741E+00	2.072E+00	2.432E+00	2.817E+00	3.239E+00	3.692E+00	4.169E+00	4.657E+00
30.00	1.511E+00	1.799E+00	2.112E+00	2.449E+00	2.818E+00	3.213E+00	3.632E+00	4.064E+00
40.00	1.209E+00	1.440E+00	1.691E+00	1.961E+00	2.256E+00	2.573E+00	2.910E+00	3.261E+00
50.00	1.019E+00	1.213E+00	1.424E+00	1.652E+00	1.900E+00	2.166E+00	2.449E+00	2.747E+00
60.00	8.878E−01	1.057E+00	1.240E+00	1.439E+00	1.654E+00	1.884E+00	2.130E+00	2.390E+00
70.00	7.913E−01	9.417E−01	1.105E+00	1.282E+00	1.473E+00	1.678E+00	1.897E+00	2.127E+00
80.00	7.172E−01	8.535E−01	1.002E+00	1.162E+00	1.335E+00	1.520E+00	1.717E+00	1.926E+00
90.00	6.583E−01	7.835E−01	9.195E−01	1.067E+00	1.225E+00	1.395E+00	1.576E+00	1.767E+00
100.0	6.104E−01	7.265E−01	8.527E−01	9.890E−01	1.136E+00	1.293E+00	1.461E+00	1.638E+00
150.0	4.616E−01	5.495E−01	6.451E−01	7.483E−01	8.594E−01	9.782E−01	1.105E+00	1.239E+00
200.0	3.838E−01	4.570E−01	5.366E−01	6.227E−01	7.151E−01	8.141E−01	9.195E−01	1.031E+00
250.0	3.361E−01	4.002E−01	4.700E−01	5.455E−01	6.266E−01	7.133E−01	8.058E−01	9.039E−01
300.0	3.039E−01	3.619E−01	4.251E−01	4.934E−01	5.668E−01	6.453E−01	7.291E−01	8.179E−01
400.0	2.635E−01	3.139E−01	3.688E−01	4.281E−01	4.918E−01	5.601E−01	6.328E−01	7.101E−01
500.0	2.397E−01	2.855E−01	3.354E−01	3.894E−01	4.474E−01	5.096E−01	5.758E−01	6.462E−01
600.0	2.242E−01	2.671E−01	3.138E−01	3.643E−01	4.186E−01	4.768E−01	5.388E−01	6.047E−01
700.0	2.136E−01	2.544E−01	2.989E−01	3.471E−01	3.988E−01	4.543E−01	5.134E−01	5.762E−01
800.0	2.059E−01	2.454E−01	2.883E−01	3.347E−01	3.847E−01	4.382E−01	4.952E−01	5.558E−01
900.0	2.003E−01	2.387E−01	2.805E−01	3.256E−01	3.743E−01	4.263E−01	4.818E−01	5.408E−01
1000.	1.961E−01	2.336E−01	2.745E−01	3.187E−01	3.663E−01	4.173E−01	4.716E−01	5.293E−01

Material: Nickel

Ion	Li	Be	B	C	N	O	F	Ne
(E/A_1) / MeV				$(-\mathrm{d}E/\rho\mathrm{d}\ell)$ / MeV cm^2 mg^{-1}				
0.025	8.314E−01	9.896E−01	1.103E+00	1.191E+00	1.262E+00	1.329E+00	1.395E+00	1.461E+00
0.030	9.198E−01	1.109E+00	1.245E+00	1.350E+00	1.432E+00	1.508E+00	1.581E+00	1.653E+00
0.040	1.070E+00	1.320E+00	1.506E+00	1.649E+00	1.759E+00	1.855E+00	1.942E+00	2.026E+00
0.050	1.193E+00	1.500E+00	1.737E+00	1.923E+00	2.065E+00	2.187E+00	2.293E+00	2.390E+00
0.060	1.294E+00	1.654E+00	1.941E+00	2.170E+00	2.350E+00	2.502E+00	2.631E+00	2.746E+00
0.070	1.376E+00	1.786E+00	2.120E+00	2.393E+00	2.611E+00	2.796E+00	2.952E+00	3.088E+00
0.080	1.443E+00	1.899E+00	2.278E+00	2.594E+00	2.850E+00	3.069E+00	3.254E+00	3.414E+00
0.090	1.495E+00	1.994E+00	2.417E+00	2.774E+00	3.068E+00	3.322E+00	3.536E+00	3.722E+00
0.100	1.536E+00	2.072E+00	2.537E+00	2.934E+00	3.266E+00	3.555E+00	3.800E+00	4.013E+00
0.150	1.634E+00	2.301E+00	2.920E+00	3.485E+00	3.989E+00	4.445E+00	4.848E+00	5.207E+00
0.200	1.649E+00	2.382E+00	3.091E+00	3.763E+00	4.387E+00	4.972E+00	5.506E+00	5.998E+00
0.250	1.632E+00	2.399E+00	3.162E+00	3.904E+00	4.609E+00	5.283E+00	5.914E+00	6.507E+00
0.300	1.601E+00	2.387E+00	3.183E+00	3.971E+00	4.732E+00	5.471E+00	6.173E+00	6.842E+00
0.400	1.525E+00	2.322E+00	3.151E+00	3.991E+00	4.822E+00	5.645E+00	6.440E+00	7.213E+00
0.500	1.447E+00	2.240E+00	3.080E+00	3.942E+00	4.809E+00	5.679E+00	6.529E+00	7.366E+00
0.600	1.375E+00	2.157E+00	2.995E+00	3.867E+00	4.753E+00	5.650E+00	6.533E+00	7.409E+00
0.700	1.308E+00	2.076E+00	2.908E+00	3.781E+00	4.677E+00	5.590E+00	6.492E+00	7.392E+00
0.800	1.247E+00	1.999E+00	2.823E+00	3.693E+00	4.592E+00	5.513E+00	6.427E+00	7.343E+00
0.900	1.192E+00	1.927E+00	2.740E+00	3.605E+00	4.504E+00	5.429E+00	6.350E+00	7.276E+00
1.000	1.141E+00	1.859E+00	2.660E+00	3.518E+00	4.415E+00	5.341E+00	6.265E+00	7.198E+00
1.500	9.420E−01	1.579E+00	2.316E+00	3.125E+00	3.991E+00	4.899E+00	5.816E+00	6.751E+00
2.000	8.042E−01	1.373E+00	2.046E+00	2.802E+00	3.625E+00	4.500E+00	5.392E+00	6.309E+00
2.500	7.035E−01	1.215E+00	1.832E+00	2.537E+00	3.315E+00	4.151E+00	5.012E+00	5.903E+00
3.000	6.266E−01	1.091E+00	1.659E+00	2.316E+00	3.050E+00	3.847E+00	4.675E+00	5.538E+00
4.000	5.169E−01	9.083E−01	1.397E+00	1.972E+00	2.627E+00	3.349E+00	4.111E+00	4.914E+00
5.000	4.423E−01	7.808E−01	1.208E+00	1.718E+00	2.305E+00	2.961E+00	3.662E+00	4.408E+00
6.000	3.881E−01	6.867E−01	1.066E+00	1.523E+00	2.054E+00	2.653E+00	3.299E+00	3.992E+00
7.000	3.468E−01	6.144E−01	9.562E−01	1.370E+00	1.853E+00	2.402E+00	3.000E+00	3.646E+00
8.000	3.142E−01	5.571E−01	8.681E−01	1.246E+00	1.690E+00	2.196E+00	2.751E+00	3.355E+00
9.000	2.878E−01	5.105E−01	7.960E−01	1.144E+00	1.553E+00	2.023E+00	2.541E+00	3.107E+00
10.00	2.660E−01	4.718E−01	7.360E−01	1.058E+00	1.439E+00	1.876E+00	2.361E+00	2.893E+00
15.00	1.954E−01	3.469E−01	5.414E−01	7.792E−01	1.061E+00	1.387E+00	1.754E+00	2.161E+00
20.00	1.567E−01	2.782E−01	4.342E−01	6.248E−01	8.505E−01	1.112E+00	1.407E+00	1.737E+00
25.00	1.319E−01	2.342E−01	3.656E−01	5.261E−01	7.159E−01	9.354E−01	1.184E+00	1.463E+00
30.00	1.145E−01	2.035E−01	3.177E−01	4.571E−01	6.219E−01	8.124E−01	1.028E+00	1.270E+00
40.00	9.175E−02	1.631E−01	2.547E−01	3.665E−01	4.986E−01	6.510E−01	8.238E−01	1.017E+00
50.00	7.734E−02	1.375E−01	2.148E−01	3.092E−01	4.207E−01	5.492E−01	6.949E−01	8.577E−01
60.00	6.735E−02	1.198E−01	1.871E−01	2.694E−01	3.666E−01	4.787E−01	6.056E−01	7.475E−01
70.00	6.000E−02	1.067E−01	1.667E−01	2.401E−01	3.267E−01	4.267E−01	5.399E−01	6.664E−01
80.00	5.434E−02	9.665E−02	1.511E−01	2.175E−01	2.961E−01	3.867E−01	4.893E−01	6.040E−01
90.00	4.986E−02	8.868E−02	1.386E−01	1.996E−01	2.717E−01	3.549E−01	4.492E−01	5.545E−01
100.0	4.620E−02	8.218E−02	1.285E−01	1.850E−01	2.519E−01	3.291E−01	4.165E−01	5.142E−01
150.0	3.487E−02	6.203E−02	9.698E−02	1.397E−01	1.903E−01	2.487E−01	3.148E−01	3.888E−01
200.0	2.896E−02	5.152E−02	8.056E−02	1.161E−01	1.581E−01	2.067E−01	2.617E−01	3.233E−01
250.0	2.534E−02	4.508E−02	7.050E−02	1.016E−01	1.384E−01	1.809E−01	2.291E−01	2.831E−01
300.0	2.290E−02	4.074E−02	6.372E−02	9.184E−02	1.251E−01	1.635E−01	2.072E−01	2.560E−01
400.0	1.984E−02	3.531E−02	5.523E−02	7.961E−02	1.085E−01	1.418E−01	1.796E−01	2.220E−01
500.0	1.804E−02	3.210E−02	5.021E−02	7.238E−02	9.861E−02	1.289E−01	1.634E−01	2.019E−01
600.0	1.687E−02	3.002E−02	4.695E−02	6.769E−02	9.223E−02	1.206E−01	1.528E−01	1.888E−01
700.0	1.606E−02	2.859E−02	4.472E−02	6.447E−02	8.785E−02	1.149E−01	1.456E−01	1.799E−01
800.0	1.549E−02	2.757E−02	4.312E−02	6.218E−02	8.472E−02	1.108E−01	1.404E−01	1.735E−01
900.0	1.507E−02	2.682E−02	4.195E−02	6.048E−02	8.242E−02	1.078E−01	1.366E−01	1.688E−01
1000.	1.475E−02	2.625E−02	4.105E−02	5.919E−02	8.066E−02	1.055E−01	1.336E−01	1.652E−01

Material: Nickel

Ion	Na	Mg	Al	Si	P	S	Cl	Ar
(E/A_1) / MeV				$(-\mathrm{d}E/\rho\mathrm{d}\ell)$ / MeV cm^2 mg^{-1}				
0.025	1.522E+00	1.588E+00	1.652E+00	1.717E+00	1.776E+00	1.837E+00	1.899E+00	1.965E+00
0.030	1.719E+00	1.791E+00	1.860E+00	1.930E+00	1.994E+00	2.061E+00	2.127E+00	2.199E+00
0.040	2.102E+00	2.183E+00	2.261E+00	2.340E+00	2.411E+00	2.488E+00	2.563E+00	2.645E+00
0.050	2.477E+00	2.566E+00	2.651E+00	2.737E+00	2.814E+00	2.899E+00	2.981E+00	3.072E+00
0.060	2.846E+00	2.944E+00	3.037E+00	3.129E+00	3.211E+00	3.302E+00	3.389E+00	3.486E+00
0.070	3.205E+00	3.316E+00	3.418E+00	3.517E+00	3.605E+00	3.701E+00	3.792E+00	3.894E+00
0.080	3.552E+00	3.679E+00	3.793E+00	3.901E+00	3.996E+00	4.098E+00	4.193E+00	4.299E+00
0.090	3.883E+00	4.029E+00	4.158E+00	4.278E+00	4.382E+00	4.492E+00	4.593E+00	4.704E+00
0.100	4.198E+00	4.364E+00	4.511E+00	4.645E+00	4.761E+00	4.881E+00	4.989E+00	5.106E+00
0.150	5.524E+00	5.809E+00	6.061E+00	6.290E+00	6.489E+00	6.679E+00	6.847E+00	7.015E+00
0.200	6.447E+00	6.856E+00	7.229E+00	7.571E+00	7.879E+00	8.166E+00	8.422E+00	8.670E+00
0.250	7.062E+00	7.576E+00	8.057E+00	8.504E+00	8.917E+00	9.307E+00	9.660E+00	1.000E+01
0.300	7.479E+00	8.076E+00	8.643E+00	9.178E+00	9.681E+00	1.016E+01	1.060E+01	1.103E+01
0.400	7.967E+00	8.685E+00	9.378E+00	1.004E+01	1.068E+01	1.130E+01	1.189E+01	1.246E+01
0.500	8.194E+00	8.993E+00	9.772E+00	1.053E+01	1.127E+01	1.199E+01	1.268E+01	1.335E+01
0.600	8.284E+00	9.136E+00	9.974E+00	1.079E+01	1.160E+01	1.240E+01	1.317E+01	1.392E+01
0.700	8.298E+00	9.186E+00	1.006E+01	1.092E+01	1.179E+01	1.264E+01	1.347E+01	1.428E+01
0.800	8.269E+00	9.180E+00	1.009E+01	1.098E+01	1.188E+01	1.277E+01	1.364E+01	1.450E+01
0.900	8.215E+00	9.142E+00	1.007E+01	1.098E+01	1.191E+01	1.284E+01	1.374E+01	1.463E+01
1.000	8.146E+00	9.084E+00	1.003E+01	1.096E+01	1.191E+01	1.286E+01	1.378E+01	1.470E+01
1.500	7.713E+00	8.668E+00	9.640E+00	1.061E+01	1.161E+01	1.262E+01	1.362E+01	1.460E+01
2.000	7.259E+00	8.207E+00	9.177E+00	1.015E+01	1.117E+01	1.220E+01	1.322E+01	1.422E+01
2.500	6.833E+00	7.764E+00	8.722E+00	9.683E+00	1.070E+01	1.173E+01	1.276E+01	1.377E+01
3.000	6.442E+00	7.353E+00	8.293E+00	9.239E+00	1.025E+01	1.127E+01	1.230E+01	1.330E+01
4.000	5.765E+00	6.628E+00	7.525E+00	8.435E+00	9.410E+00	1.041E+01	1.141E+01	1.239E+01
5.000	5.204E+00	6.019E+00	6.871E+00	7.740E+00	8.676E+00	9.641E+00	1.061E+01	1.156E+01
6.000	4.737E+00	5.505E+00	6.313E+00	7.141E+00	8.036E+00	8.963E+00	9.901E+00	1.082E+01
7.000	4.344E+00	5.068E+00	5.833E+00	6.621E+00	7.476E+00	8.365E+00	9.267E+00	1.015E+01
8.000	4.010E+00	4.693E+00	5.419E+00	6.169E+00	6.985E+00	7.836E+00	8.703E+00	9.555E+00
9.000	3.723E+00	4.369E+00	5.058E+00	5.772E+00	6.551E+00	7.366E+00	8.200E+00	9.021E+00
10.00	3.474E+00	4.087E+00	4.741E+00	5.423E+00	6.166E+00	6.947E+00	7.749E+00	8.540E+00
15.00	2.610E+00	3.092E+00	3.612E+00	4.161E+00	4.763E+00	5.401E+00	6.064E+00	6.728E+00
20.00	2.103E+00	2.498E+00	2.927E+00	3.385E+00	3.885E+00	4.420E+00	4.980E+00	5.549E+00
25.00	1.771E+00	2.107E+00	2.472E+00	2.864E+00	3.291E+00	3.750E+00	4.233E+00	4.729E+00
30.00	1.538E+00	1.830E+00	2.149E+00	2.491E+00	2.865E+00	3.266E+00	3.691E+00	4.130E+00
40.00	1.231E+00	1.466E+00	1.721E+00	1.996E+00	2.296E+00	2.618E+00	2.960E+00	3.318E+00
50.00	1.038E+00	1.235E+00	1.450E+00	1.683E+00	1.934E+00	2.205E+00	2.493E+00	2.796E+00
60.00	9.045E−01	1.076E+00	1.264E+00	1.466E+00	1.684E+00	1.919E+00	2.170E+00	2.433E+00
70.00	8.063E−01	9.595E−01	1.126E+00	1.306E+00	1.501E+00	1.709E+00	1.932E+00	2.167E+00
80.00	7.308E−01	8.697E−01	1.021E+00	1.184E+00	1.360E+00	1.549E+00	1.750E+00	1.963E+00
90.00	6.709E−01	7.985E−01	9.371E−01	1.087E+00	1.248E+00	1.421E+00	1.606E+00	1.801E+00
100.0	6.222E−01	7.405E−01	8.691E−01	1.008E+00	1.158E+00	1.318E+00	1.489E+00	1.670E+00
150.0	4.706E−01	5.602E−01	6.577E−01	7.630E−01	8.762E−01	9.973E−01	1.126E+00	1.263E+00
200.0	3.914E−01	4.661E−01	5.472E−01	6.350E−01	7.293E−01	8.302E−01	9.377E−01	1.052E+00
250.0	3.428E−01	4.082E−01	4.794E−01	5.563E−01	6.390E−01	7.275E−01	8.218E−01	9.219E−01
300.0	3.100E−01	3.692E−01	4.336E−01	5.032E−01	5.781E−01	6.582E−01	7.436E−01	8.343E−01
400.0	2.689E−01	3.203E−01	3.762E−01	4.367E−01	5.018E−01	5.714E−01	6.456E−01	7.244E−01
500.0	2.445E−01	2.913E−01	3.422E−01	3.973E−01	4.565E−01	5.199E−01	5.875E−01	6.593E−01
600.0	2.287E−01	2.725E−01	3.202E−01	3.717E−01	4.272E−01	4.865E−01	5.498E−01	6.171E−01
700.0	2.179E−01	2.596E−01	3.050E−01	3.542E−01	4.070E−01	4.636E−01	5.239E−01	5.880E−01
800.0	2.102E−01	2.504E−01	2.942E−01	3.416E−01	3.926E−01	4.472E−01	5.054E−01	5.672E−01
900.0	2.045E−01	2.436E−01	2.862E−01	3.323E−01	3.820E−01	4.351E−01	4.917E−01	5.519E−01
1000.	2.001E−01	2.384E−01	2.802E−01	3.253E−01	3.739E−01	4.259E−01	4.813E−01	5.402E−01

Material: Copper

Ion	Li	Be	B	C	N	O	F	Ne
(E/A_1) / MeV				$(-\mathrm{d}E/\rho\mathrm{d}\ell)$ / MeV cm^2 mg^{-1}				
0.025	7.526E−01	8.906E−01	9.874E−01	1.062E+00	1.121E+00	1.180E+00	1.238E+00	1.298E+00
0.030	8.347E−01	1.001E+00	1.119E+00	1.209E+00	1.277E+00	1.343E+00	1.406E+00	1.470E+00
0.040	9.738E−01	1.197E+00	1.361E+00	1.486E+00	1.579E+00	1.662E+00	1.736E+00	1.808E+00
0.050	1.086E+00	1.363E+00	1.574E+00	1.739E+00	1.862E+00	1.968E+00	2.058E+00	2.141E+00
0.060	1.178E+00	1.504E+00	1.762E+00	1.966E+00	2.124E+00	2.258E+00	2.369E+00	2.468E+00
0.070	1.253E+00	1.624E+00	1.926E+00	2.171E+00	2.364E+00	2.528E+00	2.664E+00	2.783E+00
0.080	1.313E+00	1.727E+00	2.070E+00	2.355E+00	2.584E+00	2.779E+00	2.942E+00	3.083E+00
0.090	1.361E+00	1.814E+00	2.197E+00	2.520E+00	2.784E+00	3.011E+00	3.202E+00	3.366E+00
0.100	1.400E+00	1.887E+00	2.307E+00	2.667E+00	2.965E+00	3.225E+00	3.444E+00	3.634E+00
0.150	1.494E+00	2.102E+00	2.666E+00	3.180E+00	3.636E+00	4.049E+00	4.412E+00	4.735E+00
0.200	1.511E+00	2.181E+00	2.829E+00	3.443E+00	4.011E+00	4.543E+00	5.030E+00	5.475E+00
0.250	1.499E+00	2.201E+00	2.900E+00	3.578E+00	4.222E+00	4.838E+00	5.414E+00	5.954E+00
0.300	1.473E+00	2.193E+00	2.924E+00	3.645E+00	4.341E+00	5.018E+00	5.659E+00	6.270E+00
0.400	1.406E+00	2.140E+00	2.902E+00	3.673E+00	4.436E+00	5.191E+00	5.920E+00	6.629E+00
0.500	1.336E+00	2.068E+00	2.841E+00	3.636E+00	4.434E+00	5.235E+00	6.017E+00	6.786E+00
0.600	1.271E+00	1.993E+00	2.767E+00	3.571E+00	4.389E+00	5.216E+00	6.030E+00	6.837E+00
0.700	1.210E+00	1.919E+00	2.689E+00	3.496E+00	4.323E+00	5.166E+00	5.999E+00	6.830E+00
0.800	1.155E+00	1.850E+00	2.612E+00	3.417E+00	4.248E+00	5.099E+00	5.944E+00	6.791E+00
0.900	1.104E+00	1.784E+00	2.537E+00	3.337E+00	4.169E+00	5.024E+00	5.876E+00	6.733E+00
1.000	1.058E+00	1.723E+00	2.464E+00	3.258E+00	4.089E+00	4.946E+00	5.801E+00	6.665E+00
1.500	8.753E−01	1.467E+00	2.150E+00	2.901E+00	3.704E+00	4.546E+00	5.396E+00	6.264E+00
2.000	7.485E−01	1.277E+00	1.903E+00	2.605E+00	3.369E+00	4.181E+00	5.010E+00	5.862E+00
2.500	6.555E−01	1.132E+00	1.706E+00	2.361E+00	3.085E+00	3.862E+00	4.662E+00	5.491E+00
3.000	5.845E−01	1.017E+00	1.547E+00	2.158E+00	2.842E+00	3.583E+00	4.353E+00	5.156E+00
4.000	4.830E−01	8.484E−01	1.304E+00	1.841E+00	2.452E+00	3.125E+00	3.835E+00	4.584E+00
5.000	4.138E−01	7.303E−01	1.130E+00	1.606E+00	2.154E+00	2.767E+00	3.421E+00	4.117E+00
6.000	3.635E−01	6.430E−01	9.983E−01	1.426E+00	1.922E+00	2.481E+00	3.085E+00	3.733E+00
7.000	3.251E−01	5.758E−01	8.959E−01	1.283E+00	1.736E+00	2.249E+00	2.808E+00	3.413E+00
8.000	2.947E−01	5.225E−01	8.139E−01	1.168E+00	1.583E+00	2.057E+00	2.577E+00	3.142E+00
9.000	2.701E−01	4.790E−01	7.468E−01	1.073E+00	1.457E+00	1.897E+00	2.382E+00	2.912E+00
10.00	2.497E−01	4.430E−01	6.908E−01	9.932E−01	1.350E+00	1.760E+00	2.215E+00	2.713E+00
15.00	1.838E−01	3.262E−01	5.091E−01	7.326E−01	9.974E−01	1.304E+00	1.648E+00	2.031E+00
20.00	1.475E−01	2.619E−01	4.087E−01	5.880E−01	8.004E−01	1.046E+00	1.324E+00	1.634E+00
25.00	1.242E−01	2.206E−01	3.444E−01	4.955E−01	6.742E−01	8.809E−01	1.115E+00	1.377E+00
30.00	1.079E−01	1.918E−01	2.994E−01	4.308E−01	5.860E−01	7.655E−01	9.689E−01	1.196E+00
40.00	8.652E−02	1.538E−01	2.402E−01	3.457E−01	4.702E−01	6.139E−01	7.768E−01	9.590E−01
50.00	7.297E−02	1.297E−01	2.027E−01	2.917E−01	3.969E−01	5.182E−01	6.556E−01	8.092E−01
60.00	6.357E−02	1.130E−01	1.766E−01	2.543E−01	3.460E−01	4.518E−01	5.716E−01	7.056E−01
70.00	5.665E−02	1.007E−01	1.574E−01	2.267E−01	3.085E−01	4.029E−01	5.098E−01	6.292E−01
80.00	5.132E−02	9.128E−02	1.427E−01	2.055E−01	2.796E−01	3.652E−01	4.622E−01	5.705E−01
90.00	4.709E−02	8.377E−02	1.309E−01	1.886E−01	2.567E−01	3.353E−01	4.243E−01	5.238E−01
100.0	4.365E−02	7.765E−02	1.214E−01	1.748E−01	2.380E−01	3.109E−01	3.935E−01	4.858E−01
150.0	3.296E−02	5.864E−02	9.169E−02	1.321E−01	1.799E−01	2.351E−01	2.977E−01	3.676E−01
200.0	2.739E−02	4.873E−02	7.620E−02	1.098E−01	1.496E−01	1.955E−01	2.476E−01	3.058E−01
250.0	2.397E−02	4.265E−02	6.670E−02	9.613E−02	1.310E−01	1.712E−01	2.168E−01	2.679E−01
300.0	2.167E−02	3.856E−02	6.030E−02	8.691E−02	1.184E−01	1.548E−01	1.961E−01	2.423E−01
400.0	1.878E−02	3.343E−02	5.229E−02	7.537E−02	1.027E−01	1.343E−01	1.701E−01	2.102E−01
500.0	1.708E−02	3.040E−02	4.755E−02	6.854E−02	9.339E−02	1.221E−01	1.547E−01	1.912E−01
600.0	1.598E−02	2.843E−02	4.448E−02	6.412E−02	8.737E−02	1.142E−01	1.447E−01	1.789E−01
700.0	1.522E−02	2.709E−02	4.237E−02	6.108E−02	8.324E−02	1.088E−01	1.379E−01	1.704E−01
800.0	1.468E−02	2.612E−02	4.087E−02	5.892E−02	8.028E−02	1.050E−01	1.330E−01	1.644E−01
900.0	1.428E−02	2.542E−02	3.976E−02	5.732E−02	7.811E−02	1.021E−01	1.294E−01	1.600E−01
1000.	1.398E−02	2.488E−02	3.891E−02	5.610E−02	7.645E−02	9.997E−02	1.267E−01	1.566E−01

Material: Copper

Ion	Na	Mg	Al	Si	P	S	Cl	Ar
(E/A_1) / MeV				$(-\mathrm{d}E/\rho\mathrm{d}\ell)$ / MeV cm^2 mg^{-1}				
0.025	1.354E+00	1.416E+00	1.476E+00	1.536E+00	1.592E+00	1.649E+00	1.706E+00	1.766E+00
0.030	1.530E+00	1.596E+00	1.660E+00	1.725E+00	1.785E+00	1.848E+00	1.909E+00	1.975E+00
0.040	1.875E+00	1.947E+00	2.017E+00	2.089E+00	2.156E+00	2.227E+00	2.296E+00	2.372E+00
0.050	2.217E+00	2.294E+00	2.368E+00	2.445E+00	2.516E+00	2.592E+00	2.667E+00	2.750E+00
0.060	2.555E+00	2.639E+00	2.719E+00	2.799E+00	2.873E+00	2.953E+00	3.031E+00	3.119E+00
0.070	2.885E+00	2.980E+00	3.068E+00	3.154E+00	3.231E+00	3.314E+00	3.394E+00	3.485E+00
0.080	3.203E+00	3.314E+00	3.412E+00	3.506E+00	3.589E+00	3.677E+00	3.759E+00	3.853E+00
0.090	3.508E+00	3.636E+00	3.747E+00	3.852E+00	3.944E+00	4.038E+00	4.125E+00	4.222E+00
0.100	3.797E+00	3.944E+00	4.072E+00	4.190E+00	4.292E+00	4.395E+00	4.489E+00	4.591E+00
0.150	5.020E+00	5.275E+00	5.500E+00	5.705E+00	5.883E+00	6.052E+00	6.200E+00	6.350E+00
0.200	5.882E+00	6.252E+00	6.588E+00	6.897E+00	7.173E+00	7.430E+00	7.659E+00	7.882E+00
0.250	6.459E+00	6.927E+00	7.363E+00	7.770E+00	8.144E+00	8.496E+00	8.816E+00	9.125E+00
0.300	6.852E+00	7.397E+00	7.913E+00	8.401E+00	8.859E+00	9.295E+00	9.697E+00	1.009E+01
0.400	7.319E+00	7.976E+00	8.609E+00	9.217E+00	9.801E+00	1.037E+01	1.090E+01	1.142E+01
0.500	7.546E+00	8.279E+00	8.992E+00	9.684E+00	1.036E+01	1.102E+01	1.165E+01	1.227E+01
0.600	7.642E+00	8.427E+00	9.197E+00	9.948E+00	1.069E+01	1.143E+01	1.213E+01	1.282E+01
0.700	7.666E+00	8.485E+00	9.295E+00	1.009E+01	1.088E+01	1.167E+01	1.243E+01	1.318E+01
0.800	7.647E+00	8.489E+00	9.327E+00	1.015E+01	1.098E+01	1.181E+01	1.261E+01	1.340E+01
0.900	7.602E+00	8.460E+00	9.319E+00	1.016E+01	1.102E+01	1.188E+01	1.271E+01	1.353E+01
1.000	7.543E+00	8.411E+00	9.284E+00	1.014E+01	1.102E+01	1.190E+01	1.276E+01	1.361E+01
1.500	7.156E+00	8.042E+00	8.944E+00	9.841E+00	1.077E+01	1.171E+01	1.263E+01	1.355E+01
2.000	6.744E+00	7.625E+00	8.526E+00	9.427E+00	1.037E+01	1.133E+01	1.228E+01	1.321E+01
2.500	6.355E+00	7.221E+00	8.112E+00	9.005E+00	9.950E+00	1.091E+01	1.187E+01	1.280E+01
3.000	5.998E+00	6.845E+00	7.720E+00	8.601E+00	9.537E+00	1.049E+01	1.144E+01	1.238E+01
4.000	5.376E+00	6.181E+00	7.017E+00	7.865E+00	8.772E+00	9.704E+00	1.064E+01	1.155E+01
5.000	4.860E+00	5.620E+00	6.415E+00	7.226E+00	8.099E+00	8.999E+00	9.906E+00	1.079E+01
6.000	4.429E+00	5.146E+00	5.900E+00	6.674E+00	7.509E+00	8.375E+00	9.250E+00	1.011E+01
7.000	4.065E+00	4.742E+00	5.457E+00	6.194E+00	6.993E+00	7.823E+00	8.666E+00	9.493E+00
8.000	3.755E+00	4.395E+00	5.073E+00	5.775E+00	6.538E+00	7.334E+00	8.145E+00	8.942E+00
9.000	3.489E+00	4.094E+00	4.738E+00	5.408E+00	6.136E+00	6.899E+00	7.679E+00	8.448E+00
10.00	3.257E+00	3.831E+00	4.444E+00	5.083E+00	5.779E+00	6.511E+00	7.261E+00	8.002E+00
15.00	2.453E+00	2.905E+00	3.393E+00	3.909E+00	4.473E+00	5.072E+00	5.694E+00	6.318E+00
20.00	1.978E+00	2.350E+00	2.754E+00	3.184E+00	3.654E+00	4.156E+00	4.683E+00	5.217E+00
25.00	1.667E+00	1.984E+00	2.327E+00	2.696E+00	3.098E+00	3.530E+00	3.984E+00	4.451E+00
30.00	1.449E+00	1.724E+00	2.024E+00	2.347E+00	2.699E+00	3.076E+00	3.476E+00	3.889E+00
40.00	1.161E+00	1.382E+00	1.623E+00	1.882E+00	2.165E+00	2.468E+00	2.791E+00	3.128E+00
50.00	9.793E−01	1.166E+00	1.368E+00	1.588E+00	1.825E+00	2.080E+00	2.352E+00	2.638E+00
60.00	8.537E−01	1.016E+00	1.193E+00	1.383E+00	1.590E+00	1.811E+00	2.048E+00	2.297E+00
70.00	7.613E−01	9.059E−01	1.063E+00	1.233E+00	1.417E+00	1.614E+00	1.824E+00	2.046E+00
80.00	6.902E−01	8.214E−01	9.649E−01	1.118E+00	1.284E+00	1.463E+00	1.653E+00	1.854E+00
90.00	6.338E−01	7.543E−01	8.853E−01	1.027E+00	1.179E+00	1.343E+00	1.517E+00	1.701E+00
100.0	5.879E−01	6.996E−01	8.212E−01	9.525E−01	1.094E+00	1.245E+00	1.407E+00	1.578E+00
150.0	4.450E−01	5.297E−01	6.219E−01	7.214E−01	8.284E−01	9.430E−01	1.065E+00	1.194E+00
200.0	3.702E−01	4.409E−01	5.177E−01	6.006E−01	6.899E−01	7.853E−01	8.870E−01	9.949E−01
250.0	3.243E−01	3.862E−01	4.536E−01	5.264E−01	6.047E−01	6.884E−01	7.777E−01	8.724E−01
300.0	2.934E−01	3.494E−01	4.104E−01	4.763E−01	5.472E−01	6.230E−01	7.039E−01	7.897E−01
400.0	2.546E−01	3.032E−01	3.562E−01	4.135E−01	4.751E−01	5.410E−01	6.113E−01	6.860E−01
500.0	2.316E−01	2.759E−01	3.241E−01	3.763E−01	4.324E−01	4.924E−01	5.565E−01	6.245E−01
600.0	2.167E−01	2.582E−01	3.033E−01	3.521E−01	4.047E−01	4.609E−01	5.209E−01	5.846E−01
700.0	2.065E−01	2.460E−01	2.890E−01	3.356E−01	3.856E−01	4.393E−01	4.964E−01	5.572E−01
800.0	1.992E−01	2.373E−01	2.788E−01	3.237E−01	3.720E−01	4.238E−01	4.789E−01	5.376E−01
900.0	1.938E−01	2.309E−01	2.713E−01	3.150E−01	3.620E−01	4.124E−01	4.661E−01	5.231E−01
1000.	1.897E−01	2.260E−01	2.656E−01	3.083E−01	3.544E−01	4.037E−01	4.563E−01	5.121E−01

Material: Germanium

Ion	Li	Be	B	C	N	O	F	Ne
(E/A_1) / MeV				$(-\mathrm{d}E/\rho\mathrm{d}\ell)$ / MeV cm^2 mg^{-1}				
0.025	6.441E−01	7.658E−01	8.579E−01	9.323E−01	9.928E−01	1.053E+00	1.111E+00	1.169E+00
0.030	7.195E−01	8.635E−01	9.711E−01	1.057E+00	1.126E+00	1.192E+00	1.254E+00	1.316E+00
0.040	8.420E−01	1.037E+00	1.182E+00	1.294E+00	1.382E+00	1.462E+00	1.535E+00	1.605E+00
0.050	9.317E−01	1.178E+00	1.367E+00	1.512E+00	1.623E+00	1.720E+00	1.806E+00	1.887E+00
0.060	9.987E−01	1.290E+00	1.522E+00	1.706E+00	1.847E+00	1.966E+00	2.068E+00	2.160E+00
0.070	1.050E+00	1.379E+00	1.651E+00	1.873E+00	2.047E+00	2.194E+00	2.317E+00	2.424E+00
0.080	1.091E+00	1.452E+00	1.759E+00	2.016E+00	2.224E+00	2.401E+00	2.549E+00	2.675E+00
0.090	1.124E+00	1.513E+00	1.850E+00	2.139E+00	2.379E+00	2.586E+00	2.760E+00	2.910E+00
0.100	1.152E+00	1.565E+00	1.929E+00	2.247E+00	2.515E+00	2.751E+00	2.951E+00	3.125E+00
0.150	1.233E+00	1.733E+00	2.198E+00	2.626E+00	3.010E+00	3.362E+00	3.677E+00	3.961E+00
0.200	1.266E+00	1.819E+00	2.352E+00	2.856E+00	3.321E+00	3.758E+00	4.159E+00	4.530E+00
0.250	1.272E+00	1.860E+00	2.441E+00	3.001E+00	3.530E+00	4.034E+00	4.504E+00	4.945E+00
0.300	1.263E+00	1.874E+00	2.488E+00	3.091E+00	3.669E+00	4.227E+00	4.754E+00	5.254E+00
0.400	1.222E+00	1.855E+00	2.510E+00	3.168E+00	3.815E+00	4.451E+00	5.063E+00	5.655E+00
0.500	1.171E+00	1.809E+00	2.482E+00	3.170E+00	3.858E+00	4.545E+00	5.213E+00	5.868E+00
0.600	1.119E+00	1.753E+00	2.432E+00	3.136E+00	3.849E+00	4.568E+00	5.272E+00	5.969E+00
0.700	1.069E+00	1.695E+00	2.373E+00	3.083E+00	3.810E+00	4.549E+00	5.278E+00	6.003E+00
0.800	1.023E+00	1.637E+00	2.311E+00	3.022E+00	3.756E+00	4.507E+00	5.251E+00	5.996E+00
0.900	9.797E−01	1.582E+00	2.249E+00	2.958E+00	3.695E+00	4.452E+00	5.206E+00	5.963E+00
1.000	9.402E−01	1.530E+00	2.188E+00	2.893E+00	3.630E+00	4.390E+00	5.150E+00	5.916E+00
1.500	7.833E−01	1.311E+00	1.920E+00	2.590E+00	3.305E+00	4.057E+00	4.816E+00	5.592E+00
2.000	6.730E−01	1.147E+00	1.707E+00	2.335E+00	3.018E+00	3.744E+00	4.486E+00	5.249E+00
2.500	5.915E−01	1.020E+00	1.536E+00	2.123E+00	2.771E+00	3.468E+00	4.186E+00	4.930E+00
3.000	5.289E−01	9.192E−01	1.396E+00	1.946E+00	2.560E+00	3.226E+00	3.918E+00	4.640E+00
4.000	4.390E−01	7.703E−01	1.183E+00	1.668E+00	2.218E+00	2.825E+00	3.466E+00	4.141E+00
5.000	3.774E−01	6.653E−01	1.028E+00	1.460E+00	1.957E+00	2.511E+00	3.102E+00	3.732E+00
6.000	3.323E−01	5.874E−01	9.111E−01	1.300E+00	1.751E+00	2.258E+00	2.806E+00	3.394E+00
7.000	2.979E−01	5.272E−01	8.196E−01	1.173E+00	1.585E+00	2.052E+00	2.561E+00	3.110E+00
8.000	2.705E−01	4.793E−01	7.460E−01	1.070E+00	1.449E+00	1.881E+00	2.355E+00	2.870E+00
9.000	2.483E−01	4.401E−01	6.857E−01	9.843E−01	1.335E+00	1.737E+00	2.181E+00	2.664E+00
10.00	2.298E−01	4.075E−01	6.352E−01	9.125E−01	1.239E+00	1.615E+00	2.031E+00	2.487E+00
15.00	1.699E−01	3.014E−01	4.703E−01	6.765E−01	9.205E−01	1.203E+00	1.520E+00	1.872E+00
20.00	1.366E−01	2.426E−01	3.785E−01	5.446E−01	7.410E−01	9.683E−01	1.225E+00	1.512E+00
25.00	1.153E−01	2.048E−01	3.196E−01	4.597E−01	6.254E−01	8.171E−01	1.034E+00	1.277E+00
30.00	1.003E−01	1.782E−01	2.782E−01	4.003E−01	5.445E−01	7.110E−01	8.998E−01	1.111E+00
40.00	8.055E−02	1.432E−01	2.236E−01	3.218E−01	4.377E−01	5.715E−01	7.231E−01	8.925E−01
50.00	6.803E−02	1.209E−01	1.889E−01	2.720E−01	3.700E−01	4.831E−01	6.111E−01	7.543E−01
60.00	5.932E−02	1.055E−01	1.648E−01	2.373E−01	3.229E−01	4.216E−01	5.334E−01	6.584E−01
70.00	5.290E−02	9.409E−02	1.470E−01	2.117E−01	2.881E−01	3.763E−01	4.761E−01	5.876E−01
80.00	4.796E−02	8.531E−02	1.333E−01	1.920E−01	2.614E−01	3.413E−01	4.319E−01	5.332E−01
90.00	4.404E−02	7.833E−02	1.225E−01	1.763E−01	2.401E−01	3.135E−01	3.968E−01	4.899E−01
100.0	4.084E−02	7.264E−02	1.136E−01	1.636E−01	2.227E−01	2.909E−01	3.682E−01	4.546E−01
150.0	3.089E−02	5.496E−02	8.593E−02	1.238E−01	1.686E−01	2.203E−01	2.790E−01	3.446E−01
200.0	2.569E−02	4.572E−02	7.150E−02	1.030E−01	1.403E−01	1.834E−01	2.323E−01	2.870E−01
250.0	2.251E−02	4.005E−02	6.263E−02	9.027E−02	1.230E−01	1.607E−01	2.036E−01	2.515E−01
300.0	2.036E−02	3.623E−02	5.666E−02	8.166E−02	1.113E−01	1.454E−01	1.842E−01	2.277E−01
400.0	1.767E−02	3.144E−02	4.917E−02	7.088E−02	9.658E−02	1.263E−01	1.600E−01	1.977E−01
500.0	1.607E−02	2.861E−02	4.475E−02	6.451E−02	8.790E−02	1.149E−01	1.456E−01	1.800E−01
600.0	1.504E−02	2.678E−02	4.188E−02	6.039E−02	8.228E−02	1.076E−01	1.363E−01	1.685E−01
700.0	1.434E−02	2.552E−02	3.992E−02	5.756E−02	7.843E−02	1.026E−01	1.299E−01	1.606E−01
800.0	1.383E−02	2.462E−02	3.852E−02	5.553E−02	7.567E−02	9.896E−02	1.254E−01	1.550E−01
900.0	1.346E−02	2.396E−02	3.749E−02	5.405E−02	7.365E−02	9.631E−02	1.220E−01	1.508E−01
1000.	1.318E−02	2.346E−02	3.670E−02	5.292E−02	7.211E−02	9.430E−02	1.195E−01	1.477E−01

Material: Germanium

Ion	Na	Mg	Al	Si	P	S	Cl	Ar
(E/A_1) / MeV				$(-\mathrm{d}E/\rho\mathrm{d}\ell)$ / MeV cm^2 mg^{-1}				
0.025	1.224E+00	1.281E+00	1.335E+00	1.389E+00	1.437E+00	1.485E+00	1.533E+00	1.585E+00
0.030	1.375E+00	1.438E+00	1.498E+00	1.558E+00	1.612E+00	1.667E+00	1.721E+00	1.779E+00
0.040	1.671E+00	1.739E+00	1.806E+00	1.873E+00	1.936E+00	2.002E+00	2.066E+00	2.137E+00
0.050	1.960E+00	2.035E+00	2.106E+00	2.178E+00	2.244E+00	2.315E+00	2.384E+00	2.463E+00
0.060	2.242E+00	2.325E+00	2.402E+00	2.478E+00	2.548E+00	2.622E+00	2.695E+00	2.778E+00
0.070	2.518E+00	2.608E+00	2.692E+00	2.773E+00	2.848E+00	2.927E+00	3.002E+00	3.088E+00
0.080	2.784E+00	2.885E+00	2.977E+00	3.064E+00	3.143E+00	3.227E+00	3.305E+00	3.395E+00
0.090	3.038E+00	3.154E+00	3.256E+00	3.351E+00	3.435E+00	3.523E+00	3.605E+00	3.698E+00
0.100	3.275E+00	3.409E+00	3.525E+00	3.631E+00	3.723E+00	3.818E+00	3.903E+00	4.000E+00
0.150	4.216E+00	4.448E+00	4.654E+00	4.841E+00	5.006E+00	5.162E+00	5.300E+00	5.439E+00
0.200	4.872E+00	5.187E+00	5.477E+00	5.744E+00	5.988E+00	6.218E+00	6.424E+00	6.629E+00
0.250	5.358E+00	5.742E+00	6.101E+00	6.438E+00	6.750E+00	7.047E+00	7.319E+00	7.587E+00
0.300	5.729E+00	6.174E+00	6.593E+00	6.990E+00	7.363E+00	7.721E+00	8.050E+00	8.375E+00
0.400	6.228E+00	6.772E+00	7.293E+00	7.791E+00	8.270E+00	8.733E+00	9.166E+00	9.592E+00
0.500	6.511E+00	7.129E+00	7.728E+00	8.305E+00	8.868E+00	9.419E+00	9.940E+00	1.045E+01
0.600	6.662E+00	7.334E+00	7.991E+00	8.628E+00	9.258E+00	9.878E+00	1.047E+01	1.105E+01
0.700	6.730E+00	7.440E+00	8.140E+00	8.823E+00	9.504E+00	1.018E+01	1.083E+01	1.147E+01
0.800	6.746E+00	7.484E+00	8.215E+00	8.931E+00	9.652E+00	1.037E+01	1.106E+01	1.174E+01
0.900	6.730E+00	7.486E+00	8.241E+00	8.982E+00	9.733E+00	1.048E+01	1.121E+01	1.193E+01
1.000	6.693E+00	7.463E+00	8.235E+00	8.995E+00	9.768E+00	1.054E+01	1.129E+01	1.204E+01
1.500	6.388E+00	7.181E+00	7.987E+00	8.789E+00	9.621E+00	1.046E+01	1.128E+01	1.210E+01
2.000	6.039E+00	6.829E+00	7.637E+00	8.446E+00	9.294E+00	1.015E+01	1.100E+01	1.184E+01
2.500	5.705E+00	6.482E+00	7.282E+00	8.086E+00	8.935E+00	9.797E+00	1.066E+01	1.150E+01
3.000	5.396E+00	6.158E+00	6.945E+00	7.738E+00	8.580E+00	9.438E+00	1.030E+01	1.114E+01
4.000	4.855E+00	5.580E+00	6.335E+00	7.100E+00	7.918E+00	8.756E+00	9.599E+00	1.042E+01
5.000	4.404E+00	5.091E+00	5.810E+00	6.543E+00	7.331E+00	8.143E+00	8.963E+00	9.764E+00
6.000	4.024E+00	4.674E+00	5.358E+00	6.059E+00	6.815E+00	7.598E+00	8.390E+00	9.167E+00
7.000	3.704E+00	4.318E+00	4.968E+00	5.637E+00	6.361E+00	7.113E+00	7.878E+00	8.629E+00
8.000	3.428E+00	4.010E+00	4.628E+00	5.267E+00	5.959E+00	6.682E+00	7.419E+00	8.145E+00
9.000	3.191E+00	3.743E+00	4.330E+00	4.941E+00	5.603E+00	6.297E+00	7.007E+00	7.708E+00
10.00	2.984E+00	3.508E+00	4.068E+00	4.651E+00	5.286E+00	5.952E+00	6.636E+00	7.313E+00
15.00	2.260E+00	2.676E+00	3.124E+00	3.598E+00	4.116E+00	4.664E+00	5.234E+00	5.808E+00
20.00	1.829E+00	2.172E+00	2.545E+00	2.941E+00	3.374E+00	3.837E+00	4.321E+00	4.815E+00
25.00	1.545E+00	1.838E+00	2.156E+00	2.497E+00	2.869E+00	3.267E+00	3.687E+00	4.118E+00
30.00	1.345E+00	1.601E+00	1.879E+00	2.178E+00	2.503E+00	2.853E+00	3.223E+00	3.606E+00
40.00	1.080E+00	1.286E+00	1.510E+00	1.751E+00	2.013E+00	2.295E+00	2.595E+00	2.908E+00
50.00	9.127E−01	1.086E+00	1.275E+00	1.479E+00	1.700E+00	1.938E+00	2.191E+00	2.457E+00
60.00	7.966E−01	9.479E−01	1.113E+00	1.291E+00	1.483E+00	1.690E+00	1.910E+00	2.142E+00
70.00	7.110E−01	8.460E−01	9.930E−01	1.152E+00	1.323E+00	1.507E+00	1.703E+00	1.910E+00
80.00	6.451E−01	7.676E−01	9.010E−01	1.045E+00	1.200E+00	1.367E+00	1.544E+00	1.732E+00
90.00	5.927E−01	7.053E−01	8.278E−01	9.602E−01	1.103E+00	1.255E+00	1.418E+00	1.591E+00
100.0	5.500E−01	6.546E−01	7.683E−01	8.911E−01	1.023E+00	1.165E+00	1.316E+00	1.476E+00
150.0	4.171E−01	4.965E−01	5.829E−01	6.762E−01	7.765E−01	8.839E−01	9.983E−01	1.120E+00
200.0	3.474E−01	4.137E−01	4.858E−01	5.636E−01	6.474E−01	7.370E−01	8.324E−01	9.337E−01
250.0	3.046E−01	3.627E−01	4.260E−01	4.944E−01	5.679E−01	6.466E−01	7.304E−01	8.194E−01
300.0	2.757E−01	3.284E−01	3.857E−01	4.476E−01	5.143E−01	5.856E−01	6.615E−01	7.422E−01
400.0	2.394E−01	2.852E−01	3.351E−01	3.890E−01	4.469E−01	5.090E−01	5.751E−01	6.454E−01
500.0	2.180E−01	2.597E−01	3.051E−01	3.542E−01	4.070E−01	4.636E−01	5.239E−01	5.879E−01
600.0	2.041E−01	2.432E−01	2.857E−01	3.317E−01	3.812E−01	4.342E−01	4.907E−01	5.507E−01
700.0	1.946E−01	2.318E−01	2.724E−01	3.162E−01	3.634E−01	4.140E−01	4.679E−01	5.252E−01
800.0	1.878E−01	2.237E−01	2.628E−01	3.052E−01	3.508E−01	3.996E−01	4.516E−01	5.069E−01
900.0	1.827E−01	2.177E−01	2.558E−01	2.971E−01	3.414E−01	3.889E−01	4.396E−01	4.934E−01
1000.	1.789E−01	2.132E−01	2.505E−01	2.909E−01	3.343E−01	3.809E−01	4.305E−01	4.832E−01

Material: Krypton

Ion	Li	Be	B	C	N	O	F	Ne
(E/A_1) / MeV				$(-\mathrm{d}E/\rho\mathrm{d}\ell)$ / MeV cm^2 mg^{-1}				
0.025	8.260E−01	9.936E−01	1.119E+00	1.219E+00	1.301E+00	1.380E+00	1.456E+00	1.533E+00
0.030	9.063E−01	1.106E+00	1.256E+00	1.375E+00	1.470E+00	1.559E+00	1.642E+00	1.724E+00
0.040	1.029E+00	1.292E+00	1.495E+00	1.656E+00	1.784E+00	1.897E+00	1.998E+00	2.094E+00
0.050	1.113E+00	1.432E+00	1.689E+00	1.896E+00	2.062E+00	2.204E+00	2.329E+00	2.443E+00
0.060	1.170E+00	1.534E+00	1.840E+00	2.094E+00	2.301E+00	2.479E+00	2.631E+00	2.767E+00
0.070	1.211E+00	1.611E+00	1.958E+00	2.254E+00	2.501E+00	2.716E+00	2.901E+00	3.064E+00
0.080	1.241E+00	1.671E+00	2.052E+00	2.384E+00	2.668E+00	2.918E+00	3.136E+00	3.329E+00
0.090	1.265E+00	1.720E+00	2.128E+00	2.492E+00	2.807E+00	3.091E+00	3.339E+00	3.561E+00
0.100	1.282E+00	1.759E+00	2.192E+00	2.583E+00	2.927E+00	3.239E+00	3.516E+00	3.765E+00
0.150	1.324E+00	1.872E+00	2.393E+00	2.882E+00	3.331E+00	3.753E+00	4.140E+00	4.499E+00
0.200	1.328E+00	1.917E+00	2.492E+00	3.043E+00	3.562E+00	4.057E+00	4.521E+00	4.958E+00
0.250	1.317E+00	1.931E+00	2.543E+00	3.138E+00	3.706E+00	4.256E+00	4.776E+00	5.273E+00
0.300	1.298E+00	1.929E+00	2.567E+00	3.195E+00	3.802E+00	4.394E+00	4.959E+00	5.503E+00
0.400	1.247E+00	1.894E+00	2.565E+00	3.240E+00	3.904E+00	4.559E+00	5.192E+00	5.809E+00
0.500	1.188E+00	1.838E+00	2.525E+00	3.227E+00	3.928E+00	4.628E+00	5.311E+00	5.981E+00
0.600	1.130E+00	1.775E+00	2.466E+00	3.182E+00	3.907E+00	4.637E+00	5.355E+00	6.064E+00
0.700	1.076E+00	1.710E+00	2.399E+00	3.121E+00	3.859E+00	4.608E+00	5.348E+00	6.086E+00
0.800	1.026E+00	1.647E+00	2.330E+00	3.051E+00	3.795E+00	4.556E+00	5.311E+00	6.068E+00
0.900	9.803E−01	1.588E+00	2.262E+00	2.980E+00	3.725E+00	4.491E+00	5.256E+00	6.025E+00
1.000	9.389E−01	1.532E+00	2.197E+00	2.908E+00	3.653E+00	4.421E+00	5.190E+00	5.967E+00
1.500	7.771E−01	1.304E+00	1.913E+00	2.583E+00	3.301E+00	4.054E+00	4.820E+00	5.602E+00
2.000	6.654E−01	1.135E+00	1.692E+00	2.318E+00	2.999E+00	3.723E+00	4.466E+00	5.232E+00
2.500	5.835E−01	1.007E+00	1.518E+00	2.101E+00	2.744E+00	3.435E+00	4.151E+00	4.894E+00
3.000	5.210E−01	9.061E−01	1.377E+00	1.921E+00	2.528E+00	3.186E+00	3.874E+00	4.592E+00
4.000	4.315E−01	7.574E−01	1.163E+00	1.641E+00	2.183E+00	2.780E+00	3.412E+00	4.080E+00
5.000	3.705E−01	6.533E−01	1.010E+00	1.434E+00	1.921E+00	2.465E+00	3.047E+00	3.668E+00
6.000	3.260E−01	5.763E−01	8.939E−01	1.275E+00	1.717E+00	2.214E+00	2.752E+00	3.329E+00
7.000	2.920E−01	5.170E−01	8.036E−01	1.150E+00	1.553E+00	2.010E+00	2.509E+00	3.048E+00
8.000	2.652E−01	4.698E−01	7.312E−01	1.048E+00	1.419E+00	1.842E+00	2.306E+00	2.810E+00
9.000	2.433E−01	4.313E−01	6.718E−01	9.642E−01	1.308E+00	1.700E+00	2.134E+00	2.608E+00
10.00	2.252E−01	3.993E−01	6.223E−01	8.938E−01	1.214E+00	1.580E+00	1.988E+00	2.433E+00
15.00	1.663E−01	2.952E−01	4.605E−01	6.623E−01	9.010E−01	1.177E+00	1.487E+00	1.831E+00
20.00	1.337E−01	2.375E−01	3.706E−01	5.331E−01	7.253E−01	9.475E−01	1.199E+00	1.479E+00
25.00	1.128E−01	2.004E−01	3.128E−01	4.500E−01	6.121E−01	7.995E−01	1.012E+00	1.249E+00
30.00	9.814E−02	1.744E−01	2.723E−01	3.917E−01	5.328E−01	6.957E−01	8.804E−01	1.087E+00
40.00	7.880E−02	1.401E−01	2.188E−01	3.148E−01	4.283E−01	5.591E−01	7.074E−01	8.731E−01
50.00	6.654E−02	1.183E−01	1.848E−01	2.660E−01	3.619E−01	4.725E−01	5.978E−01	7.378E−01
60.00	5.802E−02	1.032E−01	1.612E−01	2.321E−01	3.158E−01	4.124E−01	5.218E−01	6.440E−01
70.00	5.173E−02	9.201E−02	1.438E−01	2.071E−01	2.818E−01	3.680E−01	4.656E−01	5.747E−01
80.00	4.690E−02	8.342E−02	1.304E−01	1.878E−01	2.556E−01	3.338E−01	4.224E−01	5.214E−01
90.00	4.306E−02	7.659E−02	1.197E−01	1.724E−01	2.347E−01	3.066E−01	3.880E−01	4.790E−01
100.0	3.993E−02	7.102E−02	1.110E−01	1.599E−01	2.177E−01	2.844E−01	3.600E−01	4.445E−01
150.0	3.020E−02	5.373E−02	8.401E−02	1.210E−01	1.649E−01	2.154E−01	2.728E−01	3.369E−01
200.0	2.512E−02	4.469E−02	6.989E−02	1.007E−01	1.372E−01	1.793E−01	2.271E−01	2.805E−01
250.0	2.200E−02	3.915E−02	6.122E−02	8.824E−02	1.202E−01	1.571E−01	1.990E−01	2.459E−01
300.0	1.990E−02	3.541E−02	5.538E−02	7.982E−02	1.087E−01	1.422E−01	1.801E−01	2.225E−01
400.0	1.727E−02	3.073E−02	4.806E−02	6.928E−02	9.440E−02	1.234E−01	1.564E−01	1.932E−01
500.0	1.571E−02	2.796E−02	4.374E−02	6.305E−02	8.591E−02	1.123E−01	1.423E−01	1.759E−01
600.0	1.470E−02	2.617E−02	4.093E−02	5.901E−02	8.042E−02	1.052E−01	1.332E−01	1.647E−01
700.0	1.401E−02	2.494E−02	3.901E−02	5.625E−02	7.665E−02	1.002E−01	1.270E−01	1.570E−01
800.0	1.352E−02	2.406E−02	3.764E−02	5.427E−02	7.395E−02	9.670E−02	1.225E−01	1.515E−01
900.0	1.316E−02	2.342E−02	3.663E−02	5.281E−02	7.197E−02	9.411E−02	1.193E−01	1.474E−01
1000.	1.288E−02	2.292E−02	3.586E−02	5.170E−02	7.046E−02	9.213E−02	1.167E−01	1.443E−01

Material: Krypton

Ion	Na	Mg	Al	Si	P	S	Cl	Ar
(E/A_1) / MeV				$(-\mathrm{d}E/\rho\mathrm{d}\ell)$ / MeV cm^2 mg^{-1}				
0.025	1.606E+00	1.684E+00	1.759E+00	1.833E+00	1.901E+00	1.970E+00	2.038E+00	2.110E+00
0.030	1.803E+00	1.886E+00	1.968E+00	2.049E+00	2.126E+00	2.204E+00	2.280E+00	2.362E+00
0.040	2.183E+00	2.275E+00	2.365E+00	2.455E+00	2.541E+00	2.631E+00	2.720E+00	2.817E+00
0.050	2.546E+00	2.649E+00	2.748E+00	2.845E+00	2.936E+00	3.033E+00	3.128E+00	3.234E+00
0.060	2.889E+00	3.005E+00	3.114E+00	3.220E+00	3.318E+00	3.421E+00	3.521E+00	3.633E+00
0.070	3.208E+00	3.341E+00	3.464E+00	3.581E+00	3.687E+00	3.796E+00	3.902E+00	4.019E+00
0.080	3.498E+00	3.653E+00	3.793E+00	3.924E+00	4.041E+00	4.160E+00	4.272E+00	4.394E+00
0.090	3.758E+00	3.937E+00	4.099E+00	4.247E+00	4.378E+00	4.509E+00	4.630E+00	4.759E+00
0.100	3.988E+00	4.193E+00	4.377E+00	4.544E+00	4.693E+00	4.838E+00	4.972E+00	5.111E+00
0.150	4.831E+00	5.141E+00	5.427E+00	5.690E+00	5.932E+00	6.164E+00	6.375E+00	6.587E+00
0.200	5.369E+00	5.757E+00	6.122E+00	6.464E+00	6.783E+00	7.089E+00	7.374E+00	7.656E+00
0.250	5.745E+00	6.193E+00	6.621E+00	7.024E+00	7.407E+00	7.776E+00	8.122E+00	8.465E+00
0.300	6.024E+00	6.522E+00	7.000E+00	7.454E+00	7.889E+00	8.311E+00	8.709E+00	9.104E+00
0.400	6.408E+00	6.984E+00	7.541E+00	8.075E+00	8.594E+00	9.102E+00	9.584E+00	1.006E+01
0.500	6.641E+00	7.278E+00	7.898E+00	8.496E+00	9.083E+00	9.660E+00	1.021E+01	1.076E+01
0.600	6.769E+00	7.454E+00	8.126E+00	8.777E+00	9.422E+00	1.006E+01	1.067E+01	1.127E+01
0.700	6.823E+00	7.546E+00	8.257E+00	8.951E+00	9.643E+00	1.033E+01	1.099E+01	1.164E+01
0.800	6.828E+00	7.577E+00	8.319E+00	9.046E+00	9.775E+00	1.050E+01	1.120E+01	1.190E+01
0.900	6.801E+00	7.569E+00	8.334E+00	9.085E+00	9.844E+00	1.060E+01	1.133E+01	1.206E+01
1.000	6.754E+00	7.535E+00	8.316E+00	9.087E+00	9.867E+00	1.065E+01	1.141E+01	1.216E+01
1.500	6.404E+00	7.205E+00	8.019E+00	8.831E+00	9.667E+00	1.051E+01	1.134E+01	1.217E+01
2.000	6.024E+00	6.818E+00	7.632E+00	8.447E+00	9.297E+00	1.016E+01	1.101E+01	1.186E+01
2.500	5.668E+00	6.447E+00	7.249E+00	8.056E+00	8.903E+00	9.764E+00	1.062E+01	1.147E+01
3.000	5.344E+00	6.104E+00	6.890E+00	7.684E+00	8.522E+00	9.376E+00	1.023E+01	1.107E+01
4.000	4.786E+00	5.506E+00	6.255E+00	7.016E+00	7.825E+00	8.656E+00	9.491E+00	1.031E+01
5.000	4.329E+00	5.008E+00	5.718E+00	6.445E+00	7.221E+00	8.021E+00	8.831E+00	9.628E+00
6.000	3.949E+00	4.589E+00	5.263E+00	5.955E+00	6.698E+00	7.466E+00	8.247E+00	9.016E+00
7.000	3.629E+00	4.233E+00	4.872E+00	5.531E+00	6.241E+00	6.978E+00	7.730E+00	8.472E+00
8.000	3.357E+00	3.928E+00	4.534E+00	5.162E+00	5.841E+00	6.547E+00	7.270E+00	7.987E+00
9.000	3.122E+00	3.664E+00	4.240E+00	4.839E+00	5.487E+00	6.164E+00	6.860E+00	7.551E+00
10.00	2.919E+00	3.433E+00	3.981E+00	4.553E+00	5.173E+00	5.823E+00	6.492E+00	7.158E+00
15.00	2.209E+00	2.616E+00	3.054E+00	3.518E+00	4.022E+00	4.557E+00	5.113E+00	5.675E+00
20.00	1.788E+00	2.124E+00	2.487E+00	2.875E+00	3.297E+00	3.747E+00	4.220E+00	4.702E+00
25.00	1.511E+00	1.797E+00	2.108E+00	2.441E+00	2.803E+00	3.191E+00	3.600E+00	4.022E+00
30.00	1.316E+00	1.565E+00	1.837E+00	2.129E+00	2.447E+00	2.787E+00	3.148E+00	3.522E+00
40.00	1.057E+00	1.258E+00	1.476E+00	1.712E+00	1.968E+00	2.243E+00	2.536E+00	2.841E+00
50.00	8.928E−01	1.062E+00	1.247E+00	1.447E+00	1.663E+00	1.894E+00	2.141E+00	2.401E+00
60.00	7.791E−01	9.271E−01	1.088E+00	1.262E+00	1.450E+00	1.652E+00	1.867E+00	2.094E+00
70.00	6.953E−01	8.274E−01	9.711E−01	1.126E+00	1.294E+00	1.473E+00	1.665E+00	1.868E+00
80.00	6.309E−01	7.507E−01	8.811E−01	1.022E+00	1.174E+00	1.336E+00	1.510E+00	1.693E+00
90.00	5.796E−01	6.898E−01	8.096E−01	9.389E−01	1.078E+00	1.228E+00	1.387E+00	1.555E+00
100.0	5.378E−01	6.401E−01	7.517E−01	8.714E−01	1.001E+00	1.139E+00	1.287E+00	1.443E+00
150.0	4.078E−01	4.854E−01	5.699E−01	6.611E−01	7.592E−01	8.641E−01	9.760E−01	1.095E+00
200.0	3.396E−01	4.044E−01	4.749E−01	5.510E−01	6.329E−01	7.204E−01	8.138E−01	9.128E−01
250.0	2.977E−01	3.546E−01	4.164E−01	4.833E−01	5.552E−01	6.321E−01	7.140E−01	8.010E−01
300.0	2.695E−01	3.210E−01	3.770E−01	4.376E−01	5.027E−01	5.724E−01	6.466E−01	7.255E−01
400.0	2.340E−01	2.788E−01	3.275E−01	3.802E−01	4.368E−01	4.975E−01	5.621E−01	6.308E−01
500.0	2.131E−01	2.538E−01	2.982E−01	3.462E−01	3.978E−01	4.531E−01	5.120E−01	5.753E−01
600.0	1.995E−01	2.377E−01	2.792E−01	3.242E−01	3.726E−01	4.244E−01	4.796E−01	5.383E−01
700.0	1.901E−01	2.266E−01	2.662E−01	3.091E−01	3.552E−01	4.046E−01	4.573E−01	5.132E−01
800.0	1.835E−01	2.186E−01	2.569E−01	2.983E−01	3.428E−01	3.905E−01	4.413E−01	4.953E−01
900.0	1.786E−01	2.128E−01	2.500E−01	2.903E−01	3.336E−01	3.801E−01	4.296E−01	4.822E−01
1000.	1.748E−01	2.083E−01	2.448E−01	2.842E−01	3.267E−01	3.721E−01	4.206E−01	4.721E−01

Material: Molybdenum

Ion	Li	Be	B	C	N	O	F	Ne
(E/A_1) / MeV				$(-\mathrm{d}E/\rho\mathrm{d}\ell)$ / MeV cm^2 mg^{-1}				
0.025	6.534E−01	7.836E−01	8.829E−01	9.635E−01	1.029E+00	1.092E+00	1.150E+00	1.205E+00
0.030	7.272E−01	8.807E−01	9.968E−01	1.089E+00	1.164E+00	1.232E+00	1.296E+00	1.357E+00
0.040	8.512E−01	1.052E+00	1.205E+00	1.326E+00	1.421E+00	1.505E+00	1.581E+00	1.651E+00
0.050	9.467E−01	1.196E+00	1.389E+00	1.541E+00	1.661E+00	1.764E+00	1.854E+00	1.937E+00
0.060	1.019E+00	1.312E+00	1.547E+00	1.735E+00	1.882E+00	2.007E+00	2.115E+00	2.211E+00
0.070	1.073E+00	1.406E+00	1.680E+00	1.905E+00	2.083E+00	2.234E+00	2.361E+00	2.473E+00
0.080	1.114E+00	1.480E+00	1.791E+00	2.050E+00	2.261E+00	2.441E+00	2.592E+00	2.722E+00
0.090	1.147E+00	1.542E+00	1.883E+00	2.175E+00	2.418E+00	2.627E+00	2.804E+00	2.956E+00
0.100	1.173E+00	1.592E+00	1.962E+00	2.283E+00	2.554E+00	2.792E+00	2.995E+00	3.171E+00
0.150	1.235E+00	1.741E+00	2.215E+00	2.649E+00	3.039E+00	3.394E+00	3.712E+00	3.998E+00
0.200	1.244E+00	1.796E+00	2.331E+00	2.840E+00	3.313E+00	3.757E+00	4.166E+00	4.543E+00
0.250	1.236E+00	1.812E+00	2.385E+00	2.942E+00	3.471E+00	3.978E+00	4.455E+00	4.904E+00
0.300	1.220E+00	1.810E+00	2.408E+00	2.997E+00	3.566E+00	4.118E+00	4.645E+00	5.148E+00
0.400	1.177E+00	1.782E+00	2.408E+00	3.038E+00	3.659E+00	4.273E+00	4.867E+00	5.446E+00
0.500	1.130E+00	1.739E+00	2.379E+00	3.034E+00	3.687E+00	4.340E+00	4.979E+00	5.606E+00
0.600	1.083E+00	1.689E+00	2.337E+00	3.006E+00	3.681E+00	4.361E+00	5.030E+00	5.692E+00
0.700	1.037E+00	1.638E+00	2.287E+00	2.964E+00	3.653E+00	4.352E+00	5.043E+00	5.731E+00
0.800	9.929E−01	1.586E+00	2.232E+00	2.913E+00	3.611E+00	4.323E+00	5.031E+00	5.738E+00
0.900	9.519E−01	1.534E+00	2.176E+00	2.857E+00	3.560E+00	4.281E+00	5.000E+00	5.722E+00
1.000	9.138E−01	1.485E+00	2.120E+00	2.798E+00	3.504E+00	4.230E+00	4.957E+00	5.689E+00
1.500	7.605E−01	1.272E+00	1.862E+00	2.509E+00	3.199E+00	3.922E+00	4.656E+00	5.406E+00
2.000	6.532E−01	1.112E+00	1.654E+00	2.262E+00	2.920E+00	3.619E+00	4.337E+00	5.076E+00
2.500	5.743E−01	9.894E−01	1.489E+00	2.056E+00	2.681E+00	3.351E+00	4.045E+00	4.765E+00
3.000	5.137E−01	8.922E−01	1.354E+00	1.885E+00	2.476E+00	3.116E+00	3.785E+00	4.483E+00
4.000	4.269E−01	7.484E−01	1.148E+00	1.616E+00	2.147E+00	2.730E+00	3.348E+00	4.000E+00
5.000	3.673E−01	6.472E−01	9.989E−01	1.417E+00	1.895E+00	2.428E+00	2.999E+00	3.606E+00
6.000	3.238E−01	5.719E−01	8.861E−01	1.262E+00	1.697E+00	2.186E+00	2.714E+00	3.281E+00
7.000	2.904E−01	5.138E−01	7.979E−01	1.140E+00	1.538E+00	1.988E+00	2.479E+00	3.010E+00
8.000	2.640E−01	4.674E−01	7.269E−01	1.041E+00	1.408E+00	1.825E+00	2.283E+00	2.780E+00
9.000	2.424E−01	4.295E−01	6.686E−01	9.587E−01	1.299E+00	1.687E+00	2.115E+00	2.583E+00
10.00	2.245E−01	3.979E−01	6.199E−01	8.896E−01	1.207E+00	1.570E+00	1.972E+00	2.413E+00
15.00	1.663E−01	2.950E−01	4.601E−01	6.614E−01	8.993E−01	1.174E+00	1.482E+00	1.823E+00
20.00	1.339E−01	2.377E−01	3.709E−01	5.334E−01	7.254E−01	9.471E−01	1.198E+00	1.477E+00
25.00	1.130E−01	2.008E−01	3.134E−01	4.507E−01	6.130E−01	8.003E−01	1.012E+00	1.249E+00
30.00	9.840E−02	1.748E−01	2.730E−01	3.927E−01	5.340E−01	6.972E−01	8.820E−01	1.088E+00
40.00	7.908E−02	1.406E−01	2.195E−01	3.159E−01	4.297E−01	5.609E−01	7.096E−01	8.757E−01
50.00	6.681E−02	1.188E−01	1.856E−01	2.671E−01	3.634E−01	4.744E−01	6.002E−01	7.407E−01
60.00	5.828E−02	1.037E−01	1.619E−01	2.332E−01	3.173E−01	4.142E−01	5.241E−01	6.468E−01
70.00	5.199E−02	9.246E−02	1.445E−01	2.081E−01	2.832E−01	3.698E−01	4.679E−01	5.775E−01
80.00	4.714E−02	8.385E−02	1.311E−01	1.887E−01	2.569E−01	3.355E−01	4.246E−01	5.241E−01
90.00	4.329E−02	7.700E−02	1.204E−01	1.734E−01	2.360E−01	3.083E−01	3.901E−01	4.816E−01
100.0	4.015E−02	7.142E−02	1.117E−01	1.608E−01	2.190E−01	2.860E−01	3.620E−01	4.470E−01
150.0	3.039E−02	5.407E−02	8.454E−02	1.218E−01	1.659E−01	2.168E−01	2.745E−01	3.390E−01
200.0	2.529E−02	4.499E−02	7.036E−02	1.014E−01	1.381E−01	1.805E−01	2.286E−01	2.824E−01
250.0	2.215E−02	3.942E−02	6.166E−02	8.887E−02	1.211E−01	1.583E−01	2.004E−01	2.477E−01
300.0	2.004E−02	3.567E−02	5.579E−02	8.042E−02	1.096E−01	1.432E−01	1.814E−01	2.242E−01
400.0	1.740E−02	3.097E−02	4.844E−02	6.982E−02	9.514E−02	1.244E−01	1.576E−01	1.947E−01
500.0	1.584E−02	2.819E−02	4.409E−02	6.356E−02	8.661E−02	1.132E−01	1.435E−01	1.773E−01
600.0	1.483E−02	2.639E−02	4.128E−02	5.951E−02	8.109E−02	1.060E−01	1.344E−01	1.661E−01
700.0	1.413E−02	2.515E−02	3.935E−02	5.673E−02	7.730E−02	1.011E−01	1.281E−01	1.583E−01
800.0	1.364E−02	2.427E−02	3.797E−02	5.474E−02	7.460E−02	9.755E−02	1.236E−01	1.528E−01
900.0	1.327E−02	2.362E−02	3.696E−02	5.328E−02	7.261E−02	9.495E−02	1.203E−01	1.487E−01
1000.	1.299E−02	2.313E−02	3.618E−02	5.217E−02	7.109E−02	9.297E−02	1.178E−01	1.456E−01

Material: Molybdenum

Ion	Na	Mg	Al	Si	P	S	Cl	Ar
(E/A_1) / MeV				$(-\mathrm{d}E/\rho\mathrm{d}\ell)$ / MeV cm^2 mg^{-1}				
0.025	1.256E+00	1.308E+00	1.356E+00	1.403E+00	1.446E+00	1.490E+00	1.533E+00	1.583E+00
0.030	1.414E+00	1.471E+00	1.526E+00	1.580E+00	1.628E+00	1.677E+00	1.726E+00	1.781E+00
0.040	1.717E+00	1.783E+00	1.847E+00	1.910E+00	1.967E+00	2.028E+00	2.086E+00	2.153E+00
0.050	2.012E+00	2.086E+00	2.157E+00	2.226E+00	2.289E+00	2.357E+00	2.422E+00	2.497E+00
0.060	2.297E+00	2.381E+00	2.459E+00	2.534E+00	2.603E+00	2.676E+00	2.746E+00	2.827E+00
0.070	2.572E+00	2.666E+00	2.753E+00	2.835E+00	2.910E+00	2.988E+00	3.063E+00	3.149E+00
0.080	2.836E+00	2.942E+00	3.039E+00	3.129E+00	3.210E+00	3.294E+00	3.374E+00	3.465E+00
0.090	3.088E+00	3.208E+00	3.316E+00	3.415E+00	3.503E+00	3.594E+00	3.679E+00	3.775E+00
0.100	3.324E+00	3.462E+00	3.584E+00	3.694E+00	3.791E+00	3.889E+00	3.979E+00	4.080E+00
0.150	4.256E+00	4.490E+00	4.702E+00	4.892E+00	5.059E+00	5.220E+00	5.362E+00	5.508E+00
0.200	4.890E+00	5.211E+00	5.507E+00	5.777E+00	6.022E+00	6.255E+00	6.465E+00	6.675E+00
0.250	5.325E+00	5.721E+00	6.092E+00	6.436E+00	6.754E+00	7.057E+00	7.335E+00	7.610E+00
0.300	5.628E+00	6.083E+00	6.515E+00	6.922E+00	7.304E+00	7.672E+00	8.013E+00	8.351E+00
0.400	6.008E+00	6.547E+00	7.068E+00	7.567E+00	8.046E+00	8.515E+00	8.957E+00	9.397E+00
0.500	6.224E+00	6.822E+00	7.405E+00	7.967E+00	8.517E+00	9.059E+00	9.575E+00	1.009E+01
0.600	6.350E+00	6.991E+00	7.620E+00	8.231E+00	8.834E+00	9.430E+00	1.000E+01	1.058E+01
0.700	6.418E+00	7.092E+00	7.757E+00	8.405E+00	9.049E+00	9.689E+00	1.031E+01	1.092E+01
0.800	6.448E+00	7.147E+00	7.840E+00	8.517E+00	9.195E+00	9.870E+00	1.053E+01	1.118E+01
0.900	6.449E+00	7.167E+00	7.883E+00	8.585E+00	9.290E+00	9.993E+00	1.068E+01	1.136E+01
1.000	6.429E+00	7.163E+00	7.896E+00	8.618E+00	9.346E+00	1.007E+01	1.078E+01	1.149E+01
1.500	6.173E+00	6.939E+00	7.716E+00	8.491E+00	9.285E+00	1.008E+01	1.087E+01	1.166E+01
2.000	5.839E+00	6.606E+00	7.389E+00	8.174E+00	8.989E+00	9.812E+00	1.063E+01	1.144E+01
2.500	5.514E+00	6.269E+00	7.044E+00	7.825E+00	8.642E+00	9.470E+00	1.030E+01	1.112E+01
3.000	5.213E+00	5.952E+00	6.714E+00	7.485E+00	8.295E+00	9.119E+00	9.946E+00	1.076E+01
4.000	4.688E+00	5.390E+00	6.121E+00	6.863E+00	7.649E+00	8.453E+00	9.264E+00	1.007E+01
5.000	4.253E+00	4.917E+00	5.612E+00	6.323E+00	7.079E+00	7.857E+00	8.645E+00	9.424E+00
6.000	3.888E+00	4.517E+00	5.177E+00	5.855E+00	6.581E+00	7.330E+00	8.091E+00	8.846E+00
7.000	3.580E+00	4.175E+00	4.802E+00	5.449E+00	6.143E+00	6.863E+00	7.598E+00	8.327E+00
8.000	3.317E+00	3.880E+00	4.476E+00	5.094E+00	5.758E+00	6.450E+00	7.157E+00	7.862E+00
9.000	3.090E+00	3.624E+00	4.191E+00	4.782E+00	5.417E+00	6.081E+00	6.763E+00	7.443E+00
10.00	2.892E+00	3.400E+00	3.940E+00	4.505E+00	5.114E+00	5.751E+00	6.408E+00	7.065E+00
15.00	2.199E+00	2.602E+00	3.037E+00	3.496E+00	3.994E+00	4.521E+00	5.070E+00	5.626E+00
20.00	1.785E+00	2.119E+00	2.480E+00	2.866E+00	3.284E+00	3.730E+00	4.198E+00	4.677E+00
25.00	1.511E+00	1.796E+00	2.106E+00	2.438E+00	2.798E+00	3.183E+00	3.590E+00	4.009E+00
30.00	1.317E+00	1.567E+00	1.838E+00	2.129E+00	2.446E+00	2.785E+00	3.144E+00	3.517E+00
40.00	1.060E+00	1.261E+00	1.480E+00	1.716E+00	1.972E+00	2.246E+00	2.538E+00	2.844E+00
50.00	8.961E−01	1.066E+00	1.251E+00	1.451E+00	1.668E+00	1.900E+00	2.147E+00	2.407E+00
60.00	7.825E−01	9.310E−01	1.093E+00	1.267E+00	1.456E+00	1.658E+00	1.874E+00	2.101E+00
70.00	6.986E−01	8.313E−01	9.756E−01	1.131E+00	1.300E+00	1.480E+00	1.672E+00	1.875E+00
80.00	6.341E−01	7.545E−01	8.855E−01	1.027E+00	1.179E+00	1.343E+00	1.517E+00	1.701E+00
90.00	5.827E−01	6.934E−01	8.138E−01	9.439E−01	1.084E+00	1.234E+00	1.394E+00	1.563E+00
100.0	5.408E−01	6.437E−01	7.554E−01	8.762E−01	1.006E+00	1.145E+00	1.293E+00	1.451E+00
150.0	4.103E−01	4.885E−01	5.735E−01	6.653E−01	7.640E−01	8.696E−01	9.821E−01	1.102E+00
200.0	3.420E−01	4.072E−01	4.781E−01	5.548E−01	6.372E−01	7.254E−01	8.193E−01	9.190E−01
250.0	2.999E−01	3.571E−01	4.194E−01	4.868E−01	5.592E−01	6.366E−01	7.192E−01	8.068E−01
300.0	2.715E−01	3.234E−01	3.798E−01	4.408E−01	5.064E−01	5.767E−01	6.515E−01	7.309E−01
400.0	2.359E−01	2.810E−01	3.301E−01	3.832E−01	4.403E−01	5.014E−01	5.666E−01	6.358E−01
500.0	2.148E−01	2.559E−01	3.006E−01	3.490E−01	4.011E−01	4.568E−01	5.163E−01	5.794E−01
600.0	2.012E−01	2.397E−01	2.816E−01	3.269E−01	3.757E−01	4.279E−01	4.836E−01	5.428E−01
700.0	1.918E−01	2.285E−01	2.685E−01	3.117E−01	3.583E−01	4.081E−01	4.612E−01	5.177E−01
800.0	1.851E−01	2.205E−01	2.591E−01	3.009E−01	3.458E−01	3.939E−01	4.452E−01	4.997E−01
900.0	1.802E−01	2.147E−01	2.522E−01	2.929E−01	3.366E−01	3.835E−01	4.334E−01	4.865E−01
1000.	1.764E−01	2.102E−01	2.470E−01	2.868E−01	3.296E−01	3.755E−01	4.244E−01	4.764E−01

Material: Silver

Ion	Li	Be	B	C	N	O	F	Ne
(E/A_1) / MeV				$(-\mathrm{d}E/\rho\mathrm{d}\ell)$ / MeV cm^2 mg^{-1}				
0.025	6.160E−01	7.283E−01	8.167E−01	8.963E−01	9.709E−01	1.047E+00	1.120E+00	1.189E+00
0.030	6.950E−01	8.324E−01	9.362E−01	1.023E+00	1.099E+00	1.177E+00	1.254E+00	1.331E+00
0.040	8.256E−01	1.015E+00	1.158E+00	1.271E+00	1.362E+00	1.447E+00	1.527E+00	1.607E+00
0.050	9.274E−01	1.166E+00	1.352E+00	1.499E+00	1.615E+00	1.716E+00	1.807E+00	1.893E+00
0.060	1.006E+00	1.292E+00	1.520E+00	1.702E+00	1.847E+00	1.972E+00	2.080E+00	2.178E+00
0.070	1.064E+00	1.394E+00	1.664E+00	1.884E+00	2.060E+00	2.210E+00	2.339E+00	2.453E+00
0.080	1.108E+00	1.475E+00	1.785E+00	2.043E+00	2.252E+00	2.431E+00	2.582E+00	2.715E+00
0.090	1.141E+00	1.540E+00	1.886E+00	2.180E+00	2.424E+00	2.632E+00	2.809E+00	2.963E+00
0.100	1.165E+00	1.591E+00	1.969E+00	2.297E+00	2.574E+00	2.814E+00	3.019E+00	3.196E+00
0.150	1.222E+00	1.734E+00	2.219E+00	2.669E+00	3.076E+00	3.450E+00	3.786E+00	4.090E+00
0.200	1.224E+00	1.781E+00	2.326E+00	2.850E+00	3.340E+00	3.804E+00	4.234E+00	4.633E+00
0.250	1.207E+00	1.786E+00	2.367E+00	2.937E+00	3.483E+00	4.010E+00	4.508E+00	4.979E+00
0.300	1.184E+00	1.772E+00	2.374E+00	2.974E+00	3.558E+00	4.129E+00	4.676E+00	5.202E+00
0.400	1.131E+00	1.726E+00	2.348E+00	2.980E+00	3.608E+00	4.233E+00	4.843E+00	5.440E+00
0.500	1.079E+00	1.672E+00	2.300E+00	2.948E+00	3.600E+00	4.256E+00	4.902E+00	5.541E+00
0.600	1.031E+00	1.617E+00	2.246E+00	2.901E+00	3.567E+00	4.241E+00	4.910E+00	5.576E+00
0.700	9.856E−01	1.563E+00	2.190E+00	2.847E+00	3.521E+00	4.207E+00	4.891E+00	5.574E+00
0.800	9.444E−01	1.512E+00	2.133E+00	2.790E+00	3.468E+00	4.161E+00	4.855E+00	5.551E+00
0.900	9.066E−01	1.463E+00	2.079E+00	2.733E+00	3.412E+00	4.109E+00	4.809E+00	5.514E+00
1.000	8.719E−01	1.418E+00	2.026E+00	2.676E+00	3.354E+00	4.054E+00	4.758E+00	5.468E+00
1.500	7.337E−01	1.226E+00	1.792E+00	2.413E+00	3.074E+00	3.767E+00	4.472E+00	5.192E+00
2.000	6.350E−01	1.079E+00	1.602E+00	2.188E+00	2.822E+00	3.495E+00	4.186E+00	4.898E+00
2.500	5.609E−01	9.641E−01	1.448E+00	1.998E+00	2.601E+00	3.248E+00	3.920E+00	4.616E+00
3.000	5.032E−01	8.719E−01	1.320E+00	1.836E+00	2.409E+00	3.029E+00	3.677E+00	4.354E+00
4.000	4.193E−01	7.337E−01	1.123E+00	1.579E+00	2.095E+00	2.661E+00	3.262E+00	3.896E+00
5.000	3.612E−01	6.354E−01	9.791E−01	1.387E+00	1.853E+00	2.370E+00	2.926E+00	3.517E+00
6.000	3.185E−01	5.619E−01	8.694E−01	1.237E+00	1.661E+00	2.136E+00	2.651E+00	3.204E+00
7.000	2.857E−01	5.050E−01	7.834E−01	1.118E+00	1.507E+00	1.945E+00	2.424E+00	2.941E+00
8.000	2.596E−01	4.595E−01	7.140E−01	1.021E+00	1.380E+00	1.786E+00	2.233E+00	2.718E+00
9.000	2.384E−01	4.223E−01	6.570E−01	9.412E−01	1.274E+00	1.653E+00	2.071E+00	2.527E+00
10.00	2.208E−01	3.913E−01	6.092E−01	8.736E−01	1.184E+00	1.538E+00	1.931E+00	2.362E+00
15.00	1.636E−01	2.902E−01	4.525E−01	6.504E−01	8.837E−01	1.153E+00	1.454E+00	1.789E+00
20.00	1.318E−01	2.340E−01	3.650E−01	5.248E−01	7.135E−01	9.313E−01	1.177E+00	1.451E+00
25.00	1.113E−01	1.977E−01	3.085E−01	4.437E−01	6.034E−01	7.876E−01	9.960E−01	1.229E+00
30.00	9.691E−02	1.722E−01	2.688E−01	3.867E−01	5.259E−01	6.864E−01	8.682E−01	1.071E+00
40.00	7.792E−02	1.385E−01	2.163E−01	3.113E−01	4.234E−01	5.527E−01	6.991E−01	8.626E−01
50.00	6.585E−02	1.171E−01	1.829E−01	2.633E−01	3.582E−01	4.676E−01	5.915E−01	7.300E−01
60.00	5.746E−02	1.022E−01	1.597E−01	2.299E−01	3.128E−01	4.084E−01	5.167E−01	6.377E−01
70.00	5.126E−02	9.118E−02	1.425E−01	2.052E−01	2.793E−01	3.647E−01	4.614E−01	5.695E−01
80.00	4.649E−02	8.270E−02	1.293E−01	1.862E−01	2.534E−01	3.310E−01	4.188E−01	5.169E−01
90.00	4.270E−02	7.596E−02	1.187E−01	1.710E−01	2.328E−01	3.041E−01	3.849E−01	4.751E−01
100.0	3.961E−02	7.046E−02	1.102E−01	1.587E−01	2.160E−01	2.822E−01	3.572E−01	4.410E−01
150.0	2.999E−02	5.336E−02	8.344E−02	1.202E−01	1.638E−01	2.140E−01	2.710E−01	3.346E−01
200.0	2.497E−02	4.442E−02	6.947E−02	1.001E−01	1.364E−01	1.783E−01	2.258E−01	2.789E−01
250.0	2.188E−02	3.893E−02	6.089E−02	8.776E−02	1.196E−01	1.563E−01	1.980E−01	2.446E−01
300.0	1.980E−02	3.523E−02	5.511E−02	7.943E−02	1.082E−01	1.415E−01	1.792E−01	2.214E−01
400.0	1.719E−02	3.060E−02	4.786E−02	6.899E−02	9.400E−02	1.229E−01	1.557E−01	1.924E−01
500.0	1.565E−02	2.785E−02	4.357E−02	6.282E−02	8.559E−02	1.119E−01	1.418E−01	1.753E−01
600.0	1.465E−02	2.608E−02	4.080E−02	5.882E−02	8.015E−02	1.048E−01	1.328E−01	1.641E−01
700.0	1.397E−02	2.486E−02	3.890E−02	5.608E−02	7.642E−02	9.994E−02	1.266E−01	1.565E−01
800.0	1.348E−02	2.400E−02	3.754E−02	5.412E−02	7.376E−02	9.645E−02	1.222E−01	1.511E−01
900.0	1.312E−02	2.336E−02	3.654E−02	5.268E−02	7.180E−02	9.389E−02	1.190E−01	1.471E−01
1000.	1.285E−02	2.287E−02	3.578E−02	5.158E−02	7.030E−02	9.193E−02	1.165E−01	1.440E−01

Material: Silver

Ion	Na	Mg	Al	Si	P	S	Cl	Ar
(E/A_1) / MeV				$(-\mathrm{d}E/\rho\mathrm{d}\ell)$ / MeV cm^2 mg^{-1}				
0.025	1.251E+00	1.311E+00	1.366E+00	1.419E+00	1.465E+00	1.511E+00	1.555E+00	1.605E+00
0.030	1.402E+00	1.472E+00	1.537E+00	1.597E+00	1.650E+00	1.703E+00	1.753E+00	1.810E+00
0.040	1.685E+00	1.766E+00	1.845E+00	1.922E+00	1.990E+00	2.059E+00	2.123E+00	2.193E+00
0.050	1.974E+00	2.058E+00	2.140E+00	2.221E+00	2.298E+00	2.377E+00	2.454E+00	2.539E+00
0.060	2.267E+00	2.356E+00	2.441E+00	2.525E+00	2.603E+00	2.685E+00	2.767E+00	2.858E+00
0.070	2.555E+00	2.653E+00	2.744E+00	2.832E+00	2.912E+00	2.997E+00	3.080E+00	3.175E+00
0.080	2.832E+00	2.942E+00	3.043E+00	3.138E+00	3.223E+00	3.312E+00	3.397E+00	3.494E+00
0.090	3.098E+00	3.221E+00	3.334E+00	3.438E+00	3.530E+00	3.625E+00	3.714E+00	3.814E+00
0.100	3.350E+00	3.490E+00	3.615E+00	3.730E+00	3.831E+00	3.933E+00	4.028E+00	4.133E+00
0.150	4.362E+00	4.609E+00	4.830E+00	5.028E+00	5.199E+00	5.361E+00	5.505E+00	5.653E+00
0.200	5.003E+00	5.348E+00	5.666E+00	5.958E+00	6.222E+00	6.471E+00	6.696E+00	6.919E+00
0.250	5.424E+00	5.844E+00	6.240E+00	6.610E+00	6.951E+00	7.277E+00	7.578E+00	7.875E+00
0.300	5.705E+00	6.185E+00	6.644E+00	7.077E+00	7.483E+00	7.875E+00	8.242E+00	8.603E+00
0.400	6.023E+00	6.586E+00	7.133E+00	7.659E+00	8.164E+00	8.659E+00	9.129E+00	9.596E+00
0.500	6.173E+00	6.788E+00	7.392E+00	7.978E+00	8.550E+00	9.115E+00	9.659E+00	1.020E+01
0.600	6.240E+00	6.892E+00	7.535E+00	8.163E+00	8.782E+00	9.397E+00	9.994E+00	1.059E+01
0.700	6.260E+00	6.937E+00	7.608E+00	8.266E+00	8.920E+00	9.572E+00	1.021E+01	1.084E+01
0.800	6.252E+00	6.947E+00	7.638E+00	8.319E+00	8.999E+00	9.678E+00	1.034E+01	1.101E+01
0.900	6.226E+00	6.934E+00	7.641E+00	8.338E+00	9.039E+00	9.740E+00	1.043E+01	1.112E+01
1.000	6.189E+00	6.906E+00	7.624E+00	8.336E+00	9.052E+00	9.771E+00	1.048E+01	1.118E+01
1.500	5.928E+00	6.666E+00	7.413E+00	8.160E+00	8.924E+00	9.692E+00	1.045E+01	1.121E+01
2.000	5.632E+00	6.370E+00	7.124E+00	7.880E+00	8.662E+00	9.452E+00	1.024E+01	1.102E+01
2.500	5.338E+00	6.068E+00	6.817E+00	7.572E+00	8.357E+00	9.154E+00	9.951E+00	1.074E+01
3.000	5.060E+00	5.776E+00	6.515E+00	7.262E+00	8.043E+00	8.839E+00	9.637E+00	1.043E+01
4.000	4.563E+00	5.246E+00	5.956E+00	6.678E+00	7.439E+00	8.218E+00	9.004E+00	9.784E+00
5.000	4.145E+00	4.792E+00	5.468E+00	6.160E+00	6.894E+00	7.648E+00	8.413E+00	9.172E+00
6.000	3.794E+00	4.406E+00	5.048E+00	5.709E+00	6.413E+00	7.140E+00	7.880E+00	8.615E+00
7.000	3.496E+00	4.075E+00	4.685E+00	5.316E+00	5.990E+00	6.689E+00	7.403E+00	8.113E+00
8.000	3.241E+00	3.789E+00	4.370E+00	4.972E+00	5.617E+00	6.289E+00	6.976E+00	7.663E+00
9.000	3.021E+00	3.541E+00	4.094E+00	4.670E+00	5.287E+00	5.932E+00	6.595E+00	7.258E+00
10.00	2.829E+00	3.324E+00	3.851E+00	4.402E+00	4.993E+00	5.613E+00	6.251E+00	6.892E+00
15.00	2.156E+00	2.551E+00	2.975E+00	3.424E+00	3.909E+00	4.422E+00	4.957E+00	5.500E+00
20.00	1.753E+00	2.080E+00	2.434E+00	2.811E+00	3.220E+00	3.655E+00	4.111E+00	4.579E+00
25.00	1.486E+00	1.766E+00	2.069E+00	2.394E+00	2.747E+00	3.123E+00	3.521E+00	3.931E+00
30.00	1.296E+00	1.541E+00	1.807E+00	2.093E+00	2.404E+00	2.736E+00	3.087E+00	3.452E+00
40.00	1.044E+00	1.242E+00	1.457E+00	1.689E+00	1.940E+00	2.210E+00	2.496E+00	2.796E+00
50.00	8.831E−01	1.051E+00	1.233E+00	1.430E+00	1.642E+00	1.870E+00	2.113E+00	2.369E+00
60.00	7.714E−01	9.178E−01	1.077E+00	1.249E+00	1.435E+00	1.634E+00	1.846E+00	2.069E+00
70.00	6.889E−01	8.197E−01	9.620E−01	1.116E+00	1.281E+00	1.459E+00	1.648E+00	1.848E+00
80.00	6.254E−01	7.442E−01	8.733E−01	1.013E+00	1.163E+00	1.324E+00	1.496E+00	1.677E+00
90.00	5.749E−01	6.841E−01	8.028E−01	9.311E−01	1.069E+00	1.217E+00	1.375E+00	1.541E+00
100.0	5.336E−01	6.350E−01	7.453E−01	8.644E−01	9.926E−01	1.130E+00	1.276E+00	1.431E+00
150.0	4.051E−01	4.822E−01	5.661E−01	6.567E−01	7.542E−01	8.584E−01	9.695E−01	1.087E+00
200.0	3.377E−01	4.021E−01	4.721E−01	5.478E−01	6.292E−01	7.163E−01	8.090E−01	9.075E−01
250.0	2.962E−01	3.527E−01	4.143E−01	4.808E−01	5.523E−01	6.288E−01	7.103E−01	7.968E−01
300.0	2.682E−01	3.194E−01	3.752E−01	4.355E−01	5.003E−01	5.697E−01	6.436E−01	7.223E−01
400.0	2.331E−01	2.777E−01	3.262E−01	3.786E−01	4.351E−01	4.955E−01	5.599E−01	6.283E−01
500.0	2.123E−01	2.529E−01	2.971E−01	3.450E−01	3.964E−01	4.515E−01	5.103E−01	5.727E−01
600.0	1.988E−01	2.369E−01	2.784E−01	3.232E−01	3.714E−01	4.231E−01	4.781E−01	5.366E−01
700.0	1.896E−01	2.259E−01	2.655E−01	3.082E−01	3.542E−01	4.035E−01	4.560E−01	5.119E−01
800.0	1.830E−01	2.181E−01	2.562E−01	2.975E−01	3.420E−01	3.895E−01	4.403E−01	4.942E−01
900.0	1.782E−01	2.123E−01	2.494E−01	2.896E−01	3.329E−01	3.792E−01	4.286E−01	4.811E−01
1000.	1.744E−01	2.079E−01	2.443E−01	2.836E−01	3.260E−01	3.714E−01	4.197E−01	4.712E−01

Material: Tin

Ion	Li	Be	B	C	N	O	F	Ne
(E/A_1) / MeV				$(-\mathrm{d}E/\rho\mathrm{d}\ell)$ / MeV cm^2 mg^{-1}				
0.025	5.096E−01	6.712E−01	8.182E−01	9.537E−01	1.078E+00	1.198E+00	1.311E+00	1.420E+00
0.030	5.567E−01	7.388E−01	9.040E−01	1.056E+00	1.194E+00	1.327E+00	1.452E+00	1.571E+00
0.040	6.320E−01	8.518E−01	1.052E+00	1.235E+00	1.401E+00	1.559E+00	1.705E+00	1.845E+00
0.050	6.872E−01	9.402E−01	1.173E+00	1.386E+00	1.579E+00	1.762E+00	1.930E+00	2.089E+00
0.060	7.280E−01	1.009E+00	1.271E+00	1.513E+00	1.733E+00	1.940E+00	2.130E+00	2.309E+00
0.070	7.589E−01	1.063E+00	1.351E+00	1.619E+00	1.864E+00	2.096E+00	2.308E+00	2.507E+00
0.080	7.833E−01	1.107E+00	1.416E+00	1.708E+00	1.976E+00	2.231E+00	2.465E+00	2.684E+00
0.090	8.031E−01	1.143E+00	1.471E+00	1.782E+00	2.072E+00	2.348E+00	2.603E+00	2.842E+00
0.100	8.194E−01	1.173E+00	1.517E+00	1.846E+00	2.155E+00	2.450E+00	2.725E+00	2.983E+00
0.150	8.713E−01	1.273E+00	1.674E+00	2.067E+00	2.445E+00	2.813E+00	3.164E+00	3.499E+00
0.200	8.964E−01	1.328E+00	1.766E+00	2.201E+00	2.624E+00	3.042E+00	3.444E+00	3.833E+00
0.250	9.074E−01	1.360E+00	1.824E+00	2.289E+00	2.747E+00	3.202E+00	3.643E+00	4.073E+00
0.300	9.098E−01	1.376E+00	1.860E+00	2.349E+00	2.835E+00	3.319E+00	3.791E+00	4.254E+00
0.400	8.992E−01	1.382E+00	1.892E+00	2.416E+00	2.941E+00	3.470E+00	3.990E+00	4.504E+00
0.500	8.778E−01	1.368E+00	1.893E+00	2.438E+00	2.990E+00	3.550E+00	4.104E+00	4.655E+00
0.600	8.518E−01	1.343E+00	1.876E+00	2.433E+00	3.004E+00	3.585E+00	4.164E+00	4.742E+00
0.700	8.241E−01	1.313E+00	1.848E+00	2.413E+00	2.995E+00	3.592E+00	4.188E+00	4.786E+00
0.800	7.964E−01	1.281E+00	1.815E+00	2.383E+00	2.973E+00	3.579E+00	4.187E+00	4.800E+00
0.900	7.696E−01	1.247E+00	1.779E+00	2.348E+00	2.941E+00	3.555E+00	4.171E+00	4.795E+00
1.000	7.440E−01	1.214E+00	1.742E+00	2.309E+00	2.905E+00	3.522E+00	4.145E+00	4.776E+00
1.500	6.366E−01	1.066E+00	1.562E+00	2.109E+00	2.696E+00	3.312E+00	3.942E+00	4.587E+00
2.000	5.568E−01	9.472E−01	1.409E+00	1.928E+00	2.492E+00	3.093E+00	3.713E+00	4.353E+00
2.500	4.957E−01	8.523E−01	1.282E+00	1.771E+00	2.310E+00	2.889E+00	3.492E+00	4.120E+00
3.000	4.473E−01	7.751E−01	1.175E+00	1.635E+00	2.148E+00	2.705E+00	3.289E+00	3.900E+00
4.000	3.757E−01	6.573E−01	1.007E+00	1.417E+00	1.881E+00	2.392E+00	2.935E+00	3.509E+00
5.000	3.253E−01	5.722E−01	8.819E−01	1.250E+00	1.671E+00	2.140E+00	2.644E+00	3.181E+00
6.000	2.879E−01	5.080E−01	7.861E−01	1.119E+00	1.504E+00	1.935E+00	2.403E+00	2.906E+00
7.000	2.590E−01	4.579E−01	7.105E−01	1.015E+00	1.368E+00	1.767E+00	2.203E+00	2.675E+00
8.000	2.361E−01	4.179E−01	6.494E−01	9.293E−01	1.256E+00	1.627E+00	2.035E+00	2.478E+00
9.000	2.174E−01	3.851E−01	5.991E−01	8.585E−01	1.162E+00	1.508E+00	1.891E+00	2.309E+00
10.00	2.018E−01	3.577E−01	5.569E−01	7.988E−01	1.083E+00	1.407E+00	1.768E+00	2.162E+00
15.00	1.513E−01	2.683E−01	4.183E−01	6.010E−01	8.166E−01	1.065E+00	1.344E+00	1.653E+00
20.00	1.229E−01	2.182E−01	3.402E−01	4.891E−01	6.647E−01	8.674E−01	1.096E+00	1.351E+00
25.00	1.045E−01	1.855E−01	2.894E−01	4.161E−01	5.656E−01	7.381E−01	9.331E−01	1.151E+00
30.00	9.140E−02	1.624E−01	2.534E−01	3.644E−01	4.953E−01	6.463E−01	8.172E−01	1.008E+00
40.00	7.393E−02	1.314E−01	2.052E−01	2.952E−01	4.013E−01	5.237E−01	6.623E−01	8.170E−01
50.00	6.270E−02	1.115E−01	1.741E−01	2.506E−01	3.409E−01	4.449E−01	5.626E−01	6.942E−01
60.00	5.484E−02	9.752E−02	1.524E−01	2.194E−01	2.984E−01	3.896E−01	4.928E−01	6.080E−01
70.00	4.901E−02	8.716E−02	1.362E−01	1.962E−01	2.669E−01	3.485E−01	4.408E−01	5.440E−01
80.00	4.450E−02	7.915E−02	1.237E−01	1.782E−01	2.425E−01	3.166E−01	4.007E−01	4.945E−01
90.00	4.090E−02	7.276E−02	1.137E−01	1.638E−01	2.230E−01	2.912E−01	3.686E−01	4.550E−01
100.0	3.797E−02	6.754E−02	1.056E−01	1.521E−01	2.071E−01	2.705E−01	3.423E−01	4.227E−01
150.0	2.881E−02	5.126E−02	8.015E−02	1.155E−01	1.573E−01	2.055E−01	2.602E−01	3.214E−01
200.0	2.400E−02	4.271E−02	6.680E−02	9.627E−02	1.311E−01	1.714E−01	2.171E−01	2.681E−01
250.0	2.105E−02	3.746E−02	5.858E−02	8.444E−02	1.150E−01	1.504E−01	1.905E−01	2.353E−01
300.0	1.906E−02	3.391E−02	5.304E−02	7.648E−02	1.042E−01	1.362E−01	1.725E−01	2.131E−01
400.0	1.656E−02	2.947E−02	4.610E−02	6.645E−02	9.054E−02	1.184E−01	1.500E−01	1.854E−01
500.0	1.508E−02	2.684E−02	4.199E−02	6.053E−02	8.251E−02	1.079E−01	1.367E−01	1.689E−01
600.0	1.412E−02	2.514E−02	3.933E−02	5.670E−02	7.729E−02	1.010E−01	1.280E−01	1.582E−01
700.0	1.347E−02	2.397E−02	3.750E−02	5.406E−02	7.369E−02	9.634E−02	1.221E−01	1.509E−01
800.0	1.300E−02	2.313E−02	3.619E−02	5.218E−02	7.111E−02	9.299E−02	1.178E−01	1.456E−01
900.0	1.265E−02	2.251E−02	3.522E−02	5.078E−02	6.921E−02	9.050E−02	1.147E−01	1.418E−01
1000.	1.238E−02	2.204E−02	3.448E−02	4.971E−02	6.774E−02	8.859E−02	1.123E−01	1.388E−01

Material: Tin

Ion	Na	Mg	Al	Si	P	S	Cl	Ar
(E/A_1) / MeV				$(-\mathrm{d}E/\rho\mathrm{d}\ell)$ / MeV cm^2 mg^{-1}				
0.025	1.520E+00	1.612E+00	1.705E+00	1.793E+00	1.874E+00	1.954E+00	2.030E+00	2.114E+00
0.030	1.681E+00	1.782E+00	1.883E+00	1.980E+00	2.070E+00	2.158E+00	2.242E+00	2.334E+00
0.040	1.974E+00	2.091E+00	2.208E+00	2.320E+00	2.424E+00	2.527E+00	2.625E+00	2.732E+00
0.050	2.235E+00	2.368E+00	2.500E+00	2.626E+00	2.742E+00	2.858E+00	2.969E+00	3.089E+00
0.060	2.473E+00	2.621E+00	2.767E+00	2.906E+00	3.035E+00	3.163E+00	3.285E+00	3.417E+00
0.070	2.689E+00	2.853E+00	3.014E+00	3.166E+00	3.307E+00	3.446E+00	3.579E+00	3.722E+00
0.080	2.885E+00	3.065E+00	3.242E+00	3.408E+00	3.561E+00	3.712E+00	3.855E+00	4.009E+00
0.090	3.062E+00	3.260E+00	3.453E+00	3.633E+00	3.799E+00	3.962E+00	4.116E+00	4.280E+00
0.100	3.222E+00	3.437E+00	3.646E+00	3.842E+00	4.021E+00	4.197E+00	4.363E+00	4.538E+00
0.150	3.816E+00	4.108E+00	4.392E+00	4.660E+00	4.909E+00	5.152E+00	5.381E+00	5.618E+00
0.200	4.206E+00	4.554E+00	4.896E+00	5.222E+00	5.529E+00	5.830E+00	6.116E+00	6.409E+00
0.250	4.488E+00	4.879E+00	5.266E+00	5.637E+00	5.991E+00	6.338E+00	6.671E+00	7.012E+00
0.300	4.704E+00	5.130E+00	5.552E+00	5.961E+00	6.353E+00	6.740E+00	7.112E+00	7.493E+00
0.400	5.008E+00	5.488E+00	5.968E+00	6.434E+00	6.889E+00	7.339E+00	7.776E+00	8.220E+00
0.500	5.199E+00	5.722E+00	6.246E+00	6.758E+00	7.260E+00	7.761E+00	8.248E+00	8.742E+00
0.600	5.317E+00	5.874E+00	6.432E+00	6.979E+00	7.521E+00	8.062E+00	8.590E+00	9.124E+00
0.700	5.384E+00	5.967E+00	6.552E+00	7.128E+00	7.702E+00	8.275E+00	8.837E+00	9.404E+00
0.800	5.417E+00	6.019E+00	6.625E+00	7.224E+00	7.823E+00	8.423E+00	9.013E+00	9.607E+00
0.900	5.424E+00	6.042E+00	6.665E+00	7.282E+00	7.902E+00	8.524E+00	9.136E+00	9.752E+00
1.000	5.415E+00	6.045E+00	6.681E+00	7.312E+00	7.949E+00	8.588E+00	9.219E+00	9.853E+00
1.500	5.248E+00	5.906E+00	6.576E+00	7.246E+00	7.931E+00	8.624E+00	9.311E+00	9.998E+00
2.000	5.013E+00	5.675E+00	6.354E+00	7.036E+00	7.742E+00	8.456E+00	9.168E+00	9.878E+00
2.500	4.772E+00	5.429E+00	6.105E+00	6.788E+00	7.499E+00	8.222E+00	8.945E+00	9.664E+00
3.000	4.539E+00	5.186E+00	5.855E+00	6.532E+00	7.241E+00	7.965E+00	8.690E+00	9.411E+00
4.000	4.116E+00	4.735E+00	5.380E+00	6.038E+00	6.732E+00	7.443E+00	8.161E+00	8.874E+00
5.000	3.753E+00	4.342E+00	4.959E+00	5.591E+00	6.262E+00	6.952E+00	7.653E+00	8.349E+00
6.000	3.445E+00	4.004E+00	4.591E+00	5.197E+00	5.841E+00	6.508E+00	7.187E+00	7.863E+00
7.000	3.182E+00	3.712E+00	4.271E+00	4.850E+00	5.468E+00	6.110E+00	6.767E+00	7.421E+00
8.000	2.957E+00	3.459E+00	3.992E+00	4.545E+00	5.138E+00	5.755E+00	6.389E+00	7.022E+00
9.000	2.762E+00	3.239E+00	3.747E+00	4.276E+00	4.844E+00	5.438E+00	6.049E+00	6.661E+00
10.00	2.592E+00	3.047E+00	3.531E+00	4.038E+00	4.583E+00	5.154E+00	5.743E+00	6.335E+00
15.00	1.993E+00	2.358E+00	2.750E+00	3.166E+00	3.615E+00	4.091E+00	4.586E+00	5.090E+00
20.00	1.632E+00	1.936E+00	2.266E+00	2.617E+00	2.997E+00	3.402E+00	3.827E+00	4.264E+00
25.00	1.391E+00	1.653E+00	1.937E+00	2.241E+00	2.571E+00	2.923E+00	3.294E+00	3.679E+00
30.00	1.219E+00	1.449E+00	1.699E+00	1.968E+00	2.259E+00	2.571E+00	2.901E+00	3.244E+00
40.00	9.881E−01	1.175E+00	1.379E+00	1.598E+00	1.835E+00	2.090E+00	2.360E+00	2.643E+00
50.00	8.395E−01	9.986E−01	1.172E+00	1.358E+00	1.560E+00	1.776E+00	2.006E+00	2.249E+00
60.00	7.354E−01	8.748E−01	1.026E+00	1.190E+00	1.367E+00	1.556E+00	1.757E+00	1.970E+00
70.00	6.580E−01	7.828E−01	9.185E−01	1.065E+00	1.223E+00	1.392E+00	1.572E+00	1.763E+00
80.00	5.982E−01	7.117E−01	8.351E−01	9.683E−01	1.112E+00	1.265E+00	1.429E+00	1.603E+00
90.00	5.504E−01	6.549E−01	7.685E−01	8.912E−01	1.023E+00	1.164E+00	1.315E+00	1.475E+00
100.0	5.113E−01	6.085E−01	7.140E−01	8.281E−01	9.507E−01	1.082E+00	1.222E+00	1.370E+00
150.0	3.890E−01	4.631E−01	5.436E−01	6.306E−01	7.241E−01	8.242E−01	9.308E−01	1.044E+00
200.0	3.246E−01	3.865E−01	4.539E−01	5.266E−01	6.049E−01	6.885E−01	7.777E−01	8.723E−01
250.0	2.849E−01	3.393E−01	3.985E−01	4.625E−01	5.313E−01	6.049E−01	6.833E−01	7.665E−01
300.0	2.581E−01	3.074E−01	3.611E−01	4.191E−01	4.815E−01	5.483E−01	6.194E−01	6.950E−01
400.0	2.245E−01	2.674E−01	3.142E−01	3.647E−01	4.191E−01	4.772E−01	5.393E−01	6.051E−01
500.0	2.046E−01	2.437E−01	2.863E−01	3.324E−01	3.820E−01	4.351E−01	4.917E−01	5.518E−01
600.0	1.917E−01	2.284E−01	2.683E−01	3.115E−01	3.580E−01	4.078E−01	4.609E−01	5.172E−01
700.0	1.828E−01	2.178E−01	2.559E−01	2.971E−01	3.415E−01	3.890E−01	4.396E−01	4.934E−01
800.0	1.764E−01	2.102E−01	2.470E−01	2.868E−01	3.297E−01	3.755E−01	4.244E−01	4.764E−01
900.0	1.717E−01	2.046E−01	2.404E−01	2.792E−01	3.209E−01	3.655E−01	4.132E−01	4.638E−01
1000.	1.681E−01	2.003E−01	2.354E−01	2.733E−01	3.142E−01	3.579E−01	4.045E−01	4.541E−01

Material: Xenon

Ion	Li	Be	B	C	N	O	F	Ne
(E/A_1) / MeV				$(-\mathrm{d}E/\rho\mathrm{d}\ell)$ / MeV cm^2 mg^{-1}				
0.025	5.617E−01	7.468E−01	9.138E−01	1.065E+00	1.201E+00	1.329E+00	1.448E+00	1.560E+00
0.030	6.027E−01	8.068E−01	9.925E−01	1.162E+00	1.315E+00	1.459E+00	1.593E+00	1.718E+00
0.040	6.687E−01	9.059E−01	1.125E+00	1.327E+00	1.510E+00	1.685E+00	1.845E+00	1.997E+00
0.050	7.189E−01	9.845E−01	1.233E+00	1.463E+00	1.675E+00	1.875E+00	2.061E+00	2.236E+00
0.060	7.574E−01	1.048E+00	1.321E+00	1.578E+00	1.814E+00	2.040E+00	2.249E+00	2.446E+00
0.070	7.872E−01	1.099E+00	1.395E+00	1.675E+00	1.935E+00	2.183E+00	2.413E+00	2.631E+00
0.080	8.104E−01	1.140E+00	1.457E+00	1.758E+00	2.039E+00	2.307E+00	2.559E+00	2.796E+00
0.090	8.285E−01	1.174E+00	1.509E+00	1.829E+00	2.129E+00	2.417E+00	2.687E+00	2.944E+00
0.100	8.426E−01	1.202E+00	1.552E+00	1.889E+00	2.207E+00	2.513E+00	2.801E+00	3.075E+00
0.150	8.788E−01	1.285E+00	1.691E+00	2.090E+00	2.475E+00	2.851E+00	3.212E+00	3.558E+00
0.200	8.879E−01	1.320E+00	1.759E+00	2.197E+00	2.625E+00	3.048E+00	3.458E+00	3.856E+00
0.250	8.864E−01	1.334E+00	1.795E+00	2.259E+00	2.717E+00	3.174E+00	3.619E+00	4.055E+00
0.300	8.800E−01	1.337E+00	1.813E+00	2.297E+00	2.778E+00	3.260E+00	3.732E+00	4.197E+00
0.400	8.595E−01	1.327E+00	1.822E+00	2.332E+00	2.845E+00	3.364E+00	3.875E+00	4.382E+00
0.500	8.342E−01	1.305E+00	1.810E+00	2.336E+00	2.871E+00	3.414E+00	3.953E+00	4.490E+00
0.600	8.070E−01	1.277E+00	1.787E+00	2.322E+00	2.872E+00	3.432E+00	3.991E+00	4.550E+00
0.700	7.794E−01	1.246E+00	1.757E+00	2.297E+00	2.856E+00	3.429E+00	4.002E+00	4.578E+00
0.800	7.523E−01	1.213E+00	1.722E+00	2.265E+00	2.829E+00	3.411E+00	3.994E+00	4.583E+00
0.900	7.263E−01	1.180E+00	1.686E+00	2.229E+00	2.796E+00	3.382E+00	3.973E+00	4.571E+00
1.000	7.016E−01	1.147E+00	1.649E+00	2.190E+00	2.758E+00	3.347E+00	3.943E+00	4.548E+00
1.500	5.984E−01	1.003E+00	1.473E+00	1.991E+00	2.547E+00	3.133E+00	3.733E+00	4.348E+00
2.000	5.227E−01	8.898E−01	1.325E+00	1.814E+00	2.348E+00	2.916E+00	3.504E+00	4.112E+00
2.500	4.653E−01	8.004E−01	1.204E+00	1.664E+00	2.172E+00	2.719E+00	3.290E+00	3.883E+00
3.000	4.202E−01	7.282E−01	1.104E+00	1.537E+00	2.020E+00	2.544E+00	3.095E+00	3.673E+00
4.000	3.538E−01	6.187E−01	9.474E−01	1.333E+00	1.769E+00	2.250E+00	2.762E+00	3.304E+00
5.000	3.069E−01	5.396E−01	8.314E−01	1.178E+00	1.574E+00	2.015E+00	2.490E+00	2.997E+00
6.000	2.720E−01	4.798E−01	7.421E−01	1.056E+00	1.418E+00	1.825E+00	2.266E+00	2.741E+00
7.000	2.450E−01	4.330E−01	6.715E−01	9.584E−01	1.292E+00	1.668E+00	2.079E+00	2.524E+00
8.000	2.235E−01	3.954E−01	6.143E−01	8.786E−01	1.187E+00	1.537E+00	1.922E+00	2.340E+00
9.000	2.058E−01	3.646E−01	5.670E−01	8.122E−01	1.099E+00	1.426E+00	1.787E+00	2.182E+00
10.00	1.912E−01	3.388E−01	5.273E−01	7.561E−01	1.025E+00	1.331E+00	1.672E+00	2.045E+00
15.00	1.434E−01	2.544E−01	3.966E−01	5.698E−01	7.740E−01	1.009E+00	1.273E+00	1.566E+00
20.00	1.166E−01	2.071E−01	3.229E−01	4.642E−01	6.308E−01	8.231E−01	1.040E+00	1.282E+00
25.00	9.925E−02	1.763E−01	2.750E−01	3.954E−01	5.374E−01	7.012E−01	8.864E−01	1.093E+00
30.00	8.692E−02	1.544E−01	2.410E−01	3.466E−01	4.711E−01	6.147E−01	7.771E−01	9.585E−01
40.00	7.043E−02	1.252E−01	1.955E−01	2.812E−01	3.824E−01	4.990E−01	6.309E−01	7.783E−01
50.00	5.982E−02	1.064E−01	1.661E−01	2.391E−01	3.252E−01	4.244E−01	5.368E−01	6.622E−01
60.00	5.237E−02	9.313E−02	1.455E−01	2.095E−01	2.850E−01	3.720E−01	4.706E−01	5.806E−01
70.00	4.683E−02	8.330E−02	1.302E−01	1.874E−01	2.551E−01	3.331E−01	4.213E−01	5.199E−01
80.00	4.255E−02	7.569E−02	1.183E−01	1.704E−01	2.319E−01	3.028E−01	3.832E−01	4.729E−01
90.00	3.914E−02	6.962E−02	1.088E−01	1.567E−01	2.134E−01	2.787E−01	3.527E−01	4.353E−01
100.0	3.634E−02	6.466E−02	1.011E−01	1.456E−01	1.982E−01	2.589E−01	3.277E−01	4.046E−01
150.0	2.761E−02	4.914E−02	7.683E−02	1.107E−01	1.508E−01	1.970E−01	2.495E−01	3.081E−01
200.0	2.303E−02	4.098E−02	6.409E−02	9.237E−02	1.258E−01	1.645E−01	2.083E−01	2.573E−01
250.0	2.021E−02	3.596E−02	5.624E−02	8.107E−02	1.104E−01	1.444E−01	1.829E−01	2.259E−01
300.0	1.830E−02	3.257E−02	5.095E−02	7.344E−02	1.001E−01	1.308E−01	1.657E−01	2.048E−01
400.0	1.591E−02	2.833E−02	4.431E−02	6.387E−02	8.704E−02	1.138E−01	1.442E−01	1.782E−01
500.0	1.450E−02	2.581E−02	4.038E−02	5.822E−02	7.933E−02	1.037E−01	1.314E−01	1.624E−01
600.0	1.359E−02	2.419E−02	3.784E−02	5.455E−02	7.434E−02	9.721E−02	1.232E−01	1.522E−01
700.0	1.296E−02	2.307E−02	3.609E−02	5.203E−02	7.091E−02	9.272E−02	1.175E−01	1.452E−01
800.0	1.251E−02	2.227E−02	3.484E−02	5.023E−02	6.845E−02	8.951E−02	1.134E−01	1.402E−01
900.0	1.218E−02	2.167E−02	3.391E−02	4.889E−02	6.663E−02	8.713E−02	1.104E−01	1.365E−01
1000.	1.192E−02	2.122E−02	3.320E−02	4.786E−02	6.523E−02	8.530E−02	1.081E−01	1.336E−01

Material: Xenon

Ion	Na	Mg	Al	Si	P	S	Cl	Ar
(E/A_1) / MeV				$(-\mathrm{d}E/\rho\mathrm{d}\ell)$ / MeV cm^2 mg^{-1}				
0.025	1.664E+00	1.759E+00	1.854E+00	1.946E+00	2.032E+00	2.116E+00	2.199E+00	2.288E+00
0.030	1.834E+00	1.940E+00	2.046E+00	2.147E+00	2.241E+00	2.335E+00	2.425E+00	2.523E+00
0.040	2.136E+00	2.263E+00	2.389E+00	2.508E+00	2.619E+00	2.729E+00	2.835E+00	2.948E+00
0.050	2.398E+00	2.545E+00	2.690E+00	2.828E+00	2.955E+00	3.080E+00	3.200E+00	3.329E+00
0.060	2.629E+00	2.795E+00	2.958E+00	3.113E+00	3.257E+00	3.397E+00	3.532E+00	3.675E+00
0.070	2.834E+00	3.019E+00	3.199E+00	3.371E+00	3.530E+00	3.686E+00	3.834E+00	3.991E+00
0.080	3.018E+00	3.220E+00	3.418E+00	3.605E+00	3.779E+00	3.949E+00	4.111E+00	4.282E+00
0.090	3.183E+00	3.402E+00	3.616E+00	3.819E+00	4.008E+00	4.192E+00	4.367E+00	4.551E+00
0.100	3.332E+00	3.567E+00	3.797E+00	4.015E+00	4.218E+00	4.416E+00	4.604E+00	4.801E+00
0.150	3.888E+00	4.195E+00	4.495E+00	4.781E+00	5.049E+00	5.311E+00	5.561E+00	5.818E+00
0.200	4.239E+00	4.600E+00	4.955E+00	5.295E+00	5.619E+00	5.935E+00	6.238E+00	6.548E+00
0.250	4.478E+00	4.879E+00	5.276E+00	5.659E+00	6.026E+00	6.386E+00	6.733E+00	7.088E+00
0.300	4.650E+00	5.082E+00	5.512E+00	5.929E+00	6.331E+00	6.728E+00	7.111E+00	7.503E+00
0.400	4.881E+00	5.359E+00	5.838E+00	6.305E+00	6.762E+00	7.214E+00	7.655E+00	8.104E+00
0.500	5.022E+00	5.535E+00	6.050E+00	6.555E+00	7.052E+00	7.547E+00	8.030E+00	8.522E+00
0.600	5.108E+00	5.649E+00	6.192E+00	6.726E+00	7.256E+00	7.784E+00	8.302E+00	8.826E+00
0.700	5.155E+00	5.718E+00	6.284E+00	6.842E+00	7.398E+00	7.954E+00	8.500E+00	9.052E+00
0.800	5.175E+00	5.755E+00	6.339E+00	6.916E+00	7.495E+00	8.073E+00	8.643E+00	9.217E+00
0.900	5.175E+00	5.768E+00	6.367E+00	6.959E+00	7.557E+00	8.154E+00	8.744E+00	9.337E+00
1.000	5.160E+00	5.764E+00	6.375E+00	6.979E+00	7.592E+00	8.206E+00	8.812E+00	9.421E+00
1.500	4.979E+00	5.607E+00	6.248E+00	6.889E+00	7.545E+00	8.206E+00	8.864E+00	9.521E+00
2.000	4.740E+00	5.370E+00	6.017E+00	6.667E+00	7.339E+00	8.020E+00	8.699E+00	9.377E+00
2.500	4.501E+00	5.125E+00	5.767E+00	6.416E+00	7.091E+00	7.778E+00	8.465E+00	9.150E+00
3.000	4.276E+00	4.889E+00	5.522E+00	6.165E+00	6.837E+00	7.522E+00	8.211E+00	8.896E+00
4.000	3.876E+00	4.461E+00	5.071E+00	5.693E+00	6.348E+00	7.021E+00	7.700E+00	8.375E+00
5.000	3.536E+00	4.093E+00	4.675E+00	5.273E+00	5.905E+00	6.557E+00	7.220E+00	7.879E+00
6.000	3.249E+00	3.776E+00	4.331E+00	4.903E+00	5.511E+00	6.140E+00	6.782E+00	7.422E+00
7.000	3.003E+00	3.503E+00	4.031E+00	4.578E+00	5.161E+00	5.767E+00	6.387E+00	7.007E+00
8.000	2.792E+00	3.267E+00	3.770E+00	4.293E+00	4.852E+00	5.435E+00	6.033E+00	6.632E+00
9.000	2.609E+00	3.061E+00	3.540E+00	4.040E+00	4.577E+00	5.137E+00	5.714E+00	6.293E+00
10.00	2.450E+00	2.880E+00	3.337E+00	3.817E+00	4.331E+00	4.870E+00	5.427E+00	5.987E+00
15.00	1.887E+00	2.233E+00	2.604E+00	2.998E+00	3.422E+00	3.871E+00	4.340E+00	4.817E+00
20.00	1.548E+00	1.836E+00	2.149E+00	2.481E+00	2.842E+00	3.225E+00	3.627E+00	4.041E+00
25.00	1.321E+00	1.570E+00	1.839E+00	2.128E+00	2.440E+00	2.774E+00	3.126E+00	3.491E+00
30.00	1.159E+00	1.378E+00	1.615E+00	1.871E+00	2.147E+00	2.443E+00	2.756E+00	3.082E+00
40.00	9.412E−01	1.119E+00	1.313E+00	1.522E+00	1.748E+00	1.989E+00	2.246E+00	2.516E+00
50.00	8.008E−01	9.525E−01	1.117E+00	1.295E+00	1.488E+00	1.694E+00	1.913E+00	2.144E+00
60.00	7.022E−01	8.353E−01	9.800E−01	1.136E+00	1.305E+00	1.485E+00	1.677E+00	1.880E+00
70.00	6.289E−01	7.481E−01	8.778E−01	1.018E+00	1.168E+00	1.330E+00	1.502E+00	1.684E+00
80.00	5.720E−01	6.806E−01	7.986E−01	9.260E−01	1.063E+00	1.210E+00	1.366E+00	1.532E+00
90.00	5.266E−01	6.266E−01	7.353E−01	8.526E−01	9.789E−01	1.114E+00	1.258E+00	1.411E+00
100.0	4.895E−01	5.825E−01	6.835E−01	7.927E−01	9.100E−01	1.036E+00	1.170E+00	1.311E+00
150.0	3.730E−01	4.440E−01	5.212E−01	6.046E−01	6.943E−01	7.902E−01	8.924E−01	1.001E+00
200.0	3.115E−01	3.709E−01	4.356E−01	5.054E−01	5.804E−01	6.607E−01	7.463E−01	8.371E−01
250.0	2.736E−01	3.258E−01	3.827E−01	4.441E−01	5.102E−01	5.808E−01	6.561E−01	7.361E−01
300.0	2.480E−01	2.954E−01	3.469E−01	4.027E−01	4.626E−01	5.268E−01	5.951E−01	6.677E−01
400.0	2.158E−01	2.571E−01	3.020E−01	3.506E−01	4.029E−01	4.588E−01	5.185E−01	5.818E−01
500.0	1.968E−01	2.344E−01	2.754E−01	3.198E−01	3.675E−01	4.186E−01	4.730E−01	5.308E−01
600.0	1.844E−01	2.197E−01	2.582E−01	2.998E−01	3.445E−01	3.924E−01	4.435E−01	4.978E−01
700.0	1.759E−01	2.096E−01	2.463E−01	2.860E−01	3.287E−01	3.744E−01	4.232E−01	4.750E−01
800.0	1.699E−01	2.024E−01	2.378E−01	2.761E−01	3.174E−01	3.616E−01	4.087E−01	4.587E−01
900.0	1.654E−01	1.970E−01	2.315E−01	2.688E−01	3.090E−01	3.520E−01	3.979E−01	4.466E−01
1000.	1.619E−01	1.929E−01	2.267E−01	2.632E−01	3.025E−01	3.447E−01	3.896E−01	4.373E−01

Material: Tungsten

Ion	Li	Be	B	C	N	O	F	Ne
(E/A_1) / MeV				$(-\mathrm{d}E/\rho\mathrm{d}\ell)$ / MeV cm^2 mg^{-1}				
0.025	2.439E−01	3.226E−01	3.961E−01	4.660E−01	5.322E−01	6.002E−01	6.666E−01	7.327E−01
0.030	2.673E−01	3.566E−01	4.392E−01	5.168E−01	5.896E−01	6.640E−01	7.365E−01	8.086E−01
0.040	3.038E−01	4.129E−01	5.140E−01	6.080E−01	6.950E−01	7.818E−01	8.655E−01	9.483E−01
0.050	3.307E−01	4.564E−01	5.747E−01	6.852E−01	7.871E−01	8.875E−01	9.831E−01	1.076E+00
0.060	3.513E−01	4.909E−01	6.241E−01	7.498E−01	8.664E−01	9.807E−01	1.089E+00	1.194E+00
0.070	3.680E−01	5.191E−01	6.653E−01	8.046E−01	9.347E−01	1.062E+00	1.183E+00	1.300E+00
0.080	3.819E−01	5.430E−01	7.005E−01	8.517E−01	9.941E−01	1.134E+00	1.267E+00	1.395E+00
0.090	3.938E−01	5.637E−01	7.311E−01	8.930E−01	1.047E+00	1.198E+00	1.342E+00	1.481E+00
0.100	4.041E−01	5.818E−01	7.582E−01	9.298E−01	1.093E+00	1.255E+00	1.410E+00	1.559E+00
0.150	4.399E−01	6.480E−01	8.591E−01	1.069E+00	1.273E+00	1.477E+00	1.674E+00	1.867E+00
0.200	4.601E−01	6.891E−01	9.250E−01	1.162E+00	1.396E+00	1.632E+00	1.862E+00	2.088E+00
0.250	4.714E−01	7.156E−01	9.703E−01	1.229E+00	1.487E+00	1.748E+00	2.004E+00	2.258E+00
0.300	4.774E−01	7.327E−01	1.002E+00	1.278E+00	1.556E+00	1.837E+00	2.116E+00	2.392E+00
0.400	4.805E−01	7.499E−01	1.040E+00	1.342E+00	1.650E+00	1.964E+00	2.277E+00	2.590E+00
0.500	4.778E−01	7.556E−01	1.059E+00	1.379E+00	1.708E+00	2.046E+00	2.384E+00	2.724E+00
0.600	4.725E−01	7.553E−01	1.067E+00	1.399E+00	1.743E+00	2.099E+00	2.456E+00	2.817E+00
0.700	4.657E−01	7.512E−01	1.069E+00	1.409E+00	1.764E+00	2.132E+00	2.504E+00	2.881E+00
0.800	4.583E−01	7.447E−01	1.066E+00	1.412E+00	1.775E+00	2.153E+00	2.536E+00	2.926E+00
0.900	4.506E−01	7.368E−01	1.060E+00	1.410E+00	1.779E+00	2.165E+00	2.557E+00	2.956E+00
1.000	4.428E−01	7.281E−01	1.052E+00	1.405E+00	1.779E+00	2.170E+00	2.569E+00	2.977E+00
1.500	4.054E−01	6.801E−01	1.000E+00	1.355E+00	1.738E+00	2.144E+00	2.561E+00	2.992E+00
2.000	3.722E−01	6.322E−01	9.409E−01	1.289E+00	1.669E+00	2.075E+00	2.497E+00	2.936E+00
2.500	3.432E−01	5.883E−01	8.833E−01	1.220E+00	1.592E+00	1.993E+00	2.412E+00	2.850E+00
3.000	3.182E−01	5.491E−01	8.299E−01	1.154E+00	1.514E+00	1.906E+00	2.319E+00	2.753E+00
4.000	2.778E−01	4.837E−01	7.381E−01	1.036E+00	1.372E+00	1.742E+00	2.136E+00	2.554E+00
5.000	2.471E−01	4.326E−01	6.641E−01	9.378E−01	1.250E+00	1.597E+00	1.970E+00	2.369E+00
6.000	2.231E−01	3.920E−01	6.042E−01	8.569E−01	1.147E+00	1.473E+00	1.825E+00	2.205E+00
7.000	2.039E−01	3.592E−01	5.551E−01	7.896E−01	1.061E+00	1.366E+00	1.699E+00	2.060E+00
8.000	1.882E−01	3.320E−01	5.141E−01	7.329E−01	9.871E−01	1.274E+00	1.590E+00	1.932E+00
9.000	1.751E−01	3.093E−01	4.795E−01	6.847E−01	9.237E−01	1.195E+00	1.494E+00	1.820E+00
10.00	1.640E−01	2.899E−01	4.499E−01	6.431E−01	8.687E−01	1.125E+00	1.410E+00	1.721E+00
15.00	1.263E−01	2.237E−01	3.481E−01	4.990E−01	6.763E−01	8.796E−01	1.107E+00	1.359E+00
20.00	1.041E−01	1.847E−01	2.877E−01	4.129E−01	5.602E−01	7.295E−01	9.201E−01	1.132E+00
25.00	8.928E−02	1.585E−01	2.471E−01	3.549E−01	4.818E−01	6.278E−01	7.925E−01	9.758E−01
30.00	7.857E−02	1.396E−01	2.177E−01	3.129E−01	4.250E−01	5.539E−01	6.996E−01	8.619E−01
40.00	6.406E−02	1.139E−01	1.778E−01	2.557E−01	3.475E−01	4.532E−01	5.727E−01	7.060E−01
50.00	5.461E−02	9.710E−02	1.517E−01	2.183E−01	2.968E−01	3.873E−01	4.896E−01	6.037E−01
60.00	4.793E−02	8.525E−02	1.332E−01	1.918E−01	2.609E−01	3.405E−01	4.306E−01	5.311E−01
70.00	4.296E−02	7.641E−02	1.194E−01	1.720E−01	2.340E−01	3.055E−01	3.864E−01	4.768E−01
80.00	3.909E−02	6.955E−02	1.087E−01	1.566E−01	2.131E−01	2.783E−01	3.520E−01	4.344E−01
90.00	3.600E−02	6.405E−02	1.001E−01	1.442E−01	1.963E−01	2.564E−01	3.245E−01	4.005E−01
100.0	3.347E−02	5.956E−02	9.311E−02	1.341E−01	1.826E−01	2.385E−01	3.019E−01	3.727E−01
150.0	2.554E−02	4.544E−02	7.107E−02	1.024E−01	1.395E−01	1.823E−01	2.308E−01	2.851E−01
200.0	2.135E−02	3.800E−02	5.943E−02	8.566E−02	1.167E−01	1.525E−01	1.932E−01	2.386E−01
250.0	1.877E−02	3.340E−02	5.225E−02	7.531E−02	1.026E−01	1.341E−01	1.699E−01	2.100E−01
300.0	1.702E−02	3.030E−02	4.739E−02	6.832E−02	9.309E−02	1.217E−01	1.542E−01	1.905E−01
400.0	1.484E−02	2.641E−02	4.131E−02	5.956E−02	8.116E−02	1.061E−01	1.345E−01	1.662E−01
500.0	1.354E−02	2.411E−02	3.771E−02	5.437E−02	7.410E−02	9.689E−02	1.228E−01	1.518E−01
600.0	1.271E−02	2.262E−02	3.538E−02	5.102E−02	6.953E−02	9.092E−02	1.152E−01	1.424E−01
700.0	1.213E−02	2.159E−02	3.378E−02	4.871E−02	6.639E−02	8.682E−02	1.100E−01	1.360E−01
800.0	1.172E−02	2.086E−02	3.263E−02	4.705E−02	6.413E−02	8.387E−02	1.063E−01	1.314E−01
900.0	1.141E−02	2.031E−02	3.178E−02	4.582E−02	6.245E−02	8.168E−02	1.035E−01	1.280E−01
1000.	1.117E−02	1.989E−02	3.112E−02	4.487E−02	6.115E−02	7.998E−02	1.014E−01	1.253E−01

Material: Tungsten

Ion	Na	Mg	Al	Si	P	S	Cl	Ar
(E/A_1) / MeV				$(-\mathrm{d}E/\rho\mathrm{d}\ell)$ / MeV cm^2 mg^{-1}				
0.025	7.964E−01	8.567E−01	9.191E−01	9.809E−01	1.039E+00	1.098E+00	1.154E+00	1.219E+00
0.030	8.785E−01	9.447E−01	1.013E+00	1.081E+00	1.146E+00	1.211E+00	1.273E+00	1.344E+00
0.040	1.028E+00	1.104E+00	1.183E+00	1.262E+00	1.336E+00	1.412E+00	1.486E+00	1.569E+00
0.050	1.166E+00	1.251E+00	1.338E+00	1.425E+00	1.508E+00	1.592E+00	1.674E+00	1.767E+00
0.060	1.294E+00	1.387E+00	1.483E+00	1.577E+00	1.667E+00	1.759E+00	1.848E+00	1.949E+00
0.070	1.411E+00	1.514E+00	1.618E+00	1.721E+00	1.818E+00	1.917E+00	2.013E+00	2.120E+00
0.080	1.517E+00	1.630E+00	1.744E+00	1.856E+00	1.960E+00	2.067E+00	2.169E+00	2.283E+00
0.090	1.614E+00	1.737E+00	1.860E+00	1.981E+00	2.094E+00	2.208E+00	2.317E+00	2.438E+00
0.100	1.702E+00	1.835E+00	1.968E+00	2.097E+00	2.218E+00	2.340E+00	2.457E+00	2.586E+00
0.150	2.053E+00	2.228E+00	2.402E+00	2.572E+00	2.732E+00	2.893E+00	3.046E+00	3.211E+00
0.200	2.308E+00	2.517E+00	2.725E+00	2.928E+00	3.121E+00	3.314E+00	3.499E+00	3.696E+00
0.250	2.506E+00	2.742E+00	2.979E+00	3.210E+00	3.431E+00	3.653E+00	3.865E+00	4.090E+00
0.300	2.663E+00	2.923E+00	3.184E+00	3.439E+00	3.686E+00	3.932E+00	4.169E+00	4.419E+00
0.400	2.898E+00	3.195E+00	3.496E+00	3.791E+00	4.079E+00	4.368E+00	4.649E+00	4.940E+00
0.500	3.062E+00	3.389E+00	3.721E+00	4.049E+00	4.371E+00	4.695E+00	5.010E+00	5.336E+00
0.600	3.178E+00	3.531E+00	3.888E+00	4.242E+00	4.592E+00	4.945E+00	5.290E+00	5.643E+00
0.700	3.261E+00	3.634E+00	4.012E+00	4.386E+00	4.761E+00	5.137E+00	5.507E+00	5.884E+00
0.800	3.320E+00	3.709E+00	4.103E+00	4.496E+00	4.889E+00	5.286E+00	5.676E+00	6.073E+00
0.900	3.362E+00	3.764E+00	4.172E+00	4.578E+00	4.988E+00	5.401E+00	5.809E+00	6.223E+00
1.000	3.392E+00	3.805E+00	4.224E+00	4.642E+00	5.065E+00	5.492E+00	5.915E+00	6.343E+00
1.500	3.435E+00	3.879E+00	4.333E+00	4.790E+00	5.257E+00	5.731E+00	6.202E+00	6.677E+00
2.000	3.390E+00	3.848E+00	4.318E+00	4.794E+00	5.285E+00	5.783E+00	6.282E+00	6.782E+00
2.500	3.307E+00	3.769E+00	4.247E+00	4.732E+00	5.234E+00	5.747E+00	6.262E+00	6.776E+00
3.000	3.207E+00	3.669E+00	4.148E+00	4.636E+00	5.144E+00	5.663E+00	6.186E+00	6.709E+00
4.000	2.995E+00	3.448E+00	3.920E+00	4.403E+00	4.910E+00	5.430E+00	5.957E+00	6.484E+00
5.000	2.793E+00	3.231E+00	3.689E+00	4.161E+00	4.658E+00	5.171E+00	5.692E+00	6.215E+00
6.000	2.610E+00	3.031E+00	3.474E+00	3.931E+00	4.415E+00	4.916E+00	5.428E+00	5.940E+00
7.000	2.446E+00	2.851E+00	3.277E+00	3.719E+00	4.189E+00	4.676E+00	5.175E+00	5.677E+00
8.000	2.301E+00	2.689E+00	3.100E+00	3.527E+00	3.981E+00	4.454E+00	4.940E+00	5.429E+00
9.000	2.173E+00	2.545E+00	2.940E+00	3.352E+00	3.791E+00	4.250E+00	4.722E+00	5.199E+00
10.00	2.058E+00	2.415E+00	2.795E+00	3.193E+00	3.618E+00	4.062E+00	4.521E+00	4.985E+00
15.00	1.634E+00	1.930E+00	2.247E+00	2.583E+00	2.944E+00	3.325E+00	3.722E+00	4.128E+00
20.00	1.364E+00	1.616E+00	1.888E+00	2.177E+00	2.489E+00	2.819E+00	3.166E+00	3.524E+00
25.00	1.178E+00	1.397E+00	1.635E+00	1.889E+00	2.163E+00	2.454E+00	2.762E+00	3.081E+00
30.00	1.041E+00	1.236E+00	1.447E+00	1.674E+00	1.919E+00	2.180E+00	2.456E+00	2.744E+00
40.00	8.531E−01	1.014E+00	1.188E+00	1.376E+00	1.578E+00	1.795E+00	2.024E+00	2.265E+00
50.00	7.297E−01	8.675E−01	1.017E+00	1.178E+00	1.352E+00	1.538E+00	1.736E+00	1.944E+00
60.00	6.421E−01	7.636E−01	8.955E−01	1.038E+00	1.191E+00	1.355E+00	1.529E+00	1.713E+00
70.00	5.765E−01	6.857E−01	8.043E−01	9.322E−01	1.070E+00	1.217E+00	1.374E+00	1.540E+00
80.00	5.255E−01	6.250E−01	7.332E−01	8.500E−01	9.756E−01	1.110E+00	1.253E+00	1.404E+00
90.00	4.845E−01	5.764E−01	6.763E−01	7.841E−01	8.999E−01	1.024E+00	1.156E+00	1.296E+00
100.0	4.509E−01	5.365E−01	6.295E−01	7.299E−01	8.379E−01	9.533E−01	1.076E+00	1.207E+00
150.0	3.450E−01	4.107E−01	4.822E−01	5.593E−01	6.422E−01	7.309E−01	8.254E−01	9.256E−01
200.0	2.889E−01	3.441E−01	4.040E−01	4.688E−01	5.384E−01	6.129E−01	6.923E−01	7.765E−01
250.0	2.542E−01	3.028E−01	3.556E−01	4.127E−01	4.741E−01	5.398E−01	6.098E−01	6.841E−01
300.0	2.308E−01	2.749E−01	3.229E−01	3.748E−01	4.306E−01	4.903E−01	5.539E−01	6.215E−01
400.0	2.013E−01	2.398E−01	2.817E−01	3.271E−01	3.759E−01	4.280E−01	4.837E−01	5.428E−01
500.0	1.838E−01	2.190E−01	2.574E−01	2.988E−01	3.434E−01	3.911E−01	4.420E−01	4.961E−01
600.0	1.725E−01	2.056E−01	2.416E−01	2.805E−01	3.224E−01	3.672E−01	4.150E−01	4.658E−01
700.0	1.648E−01	1.963E−01	2.307E−01	2.679E−01	3.079E−01	3.508E−01	3.965E−01	4.450E−01
800.0	1.592E−01	1.897E−01	2.229E−01	2.588E−01	2.975E−01	3.389E−01	3.831E−01	4.300E−01
900.0	1.550E−01	1.847E−01	2.171E−01	2.521E−01	2.898E−01	3.301E−01	3.731E−01	4.189E−01
1000.	1.518E−01	1.809E−01	2.126E−01	2.469E−01	2.838E−01	3.233E−01	3.655E−01	4.102E−01

Material: Platinum

Ion	Li	Be	B	C	N	O	F	Ne
(E/A_1) / MeV				$(-\mathrm{d}E/\rho\mathrm{d}\ell)$ / MeV cm^2 mg^{-1}				
0.025	2.992E−01	4.136E−01	5.215E−01	6.218E−01	7.138E−01	8.030E−01	8.862E−01	9.654E−01
0.030	3.235E−01	4.491E−01	5.680E−01	6.790E−01	7.810E−01	8.796E−01	9.718E−01	1.059E+00
0.040	3.633E−01	5.084E−01	6.469E−01	7.771E−01	8.974E−01	1.014E+00	1.122E+00	1.226E+00
0.050	3.948E−01	5.565E−01	7.120E−01	8.591E−01	9.958E−01	1.128E+00	1.252E+00	1.370E+00
0.060	4.203E−01	5.962E−01	7.668E−01	9.292E−01	1.081E+00	1.228E+00	1.366E+00	1.498E+00
0.070	4.415E−01	6.298E−01	8.137E−01	9.899E−01	1.155E+00	1.316E+00	1.468E+00	1.612E+00
0.080	4.596E−01	6.587E−01	8.544E−01	1.043E+00	1.221E+00	1.395E+00	1.559E+00	1.716E+00
0.090	4.752E−01	6.839E−01	8.903E−01	1.090E+00	1.280E+00	1.466E+00	1.641E+00	1.810E+00
0.100	4.888E−01	7.063E−01	9.224E−01	1.132E+00	1.333E+00	1.529E+00	1.716E+00	1.896E+00
0.150	5.363E−01	7.881E−01	1.042E+00	1.294E+00	1.538E+00	1.779E+00	2.012E+00	2.238E+00
0.200	5.617E−01	8.373E−01	1.120E+00	1.402E+00	1.679E+00	1.955E+00	2.223E+00	2.485E+00
0.250	5.743E−01	8.667E−01	1.170E+00	1.475E+00	1.779E+00	2.083E+00	2.380E+00	2.672E+00
0.300	5.791E−01	8.831E−01	1.202E+00	1.526E+00	1.851E+00	2.177E+00	2.499E+00	2.816E+00
0.400	5.764E−01	8.938E−01	1.233E+00	1.584E+00	1.939E+00	2.300E+00	2.658E+00	3.014E+00
0.500	5.666E−01	8.903E−01	1.241E+00	1.608E+00	1.984E+00	2.368E+00	2.751E+00	3.134E+00
0.600	5.541E−01	8.805E−01	1.238E+00	1.615E+00	2.004E+00	2.404E+00	2.804E+00	3.207E+00
0.700	5.405E−01	8.672E−01	1.228E+00	1.611E+00	2.010E+00	2.420E+00	2.834E+00	3.251E+00
0.800	5.270E−01	8.523E−01	1.214E+00	1.601E+00	2.006E+00	2.424E+00	2.847E+00	3.275E+00
0.900	5.137E−01	8.367E−01	1.199E+00	1.588E+00	1.997E+00	2.421E+00	2.851E+00	3.287E+00
1.000	5.011E−01	8.210E−01	1.182E+00	1.572E+00	1.984E+00	2.412E+00	2.847E+00	3.290E+00
1.500	4.460E−01	7.467E−01	1.095E+00	1.480E+00	1.893E+00	2.328E+00	2.775E+00	3.234E+00
2.000	4.022E−01	6.824E−01	1.014E+00	1.385E+00	1.790E+00	2.220E+00	2.666E+00	3.128E+00
2.500	3.663E−01	6.274E−01	9.405E−01	1.296E+00	1.688E+00	2.109E+00	2.549E+00	3.007E+00
3.000	3.365E−01	5.802E−01	8.758E−01	1.215E+00	1.593E+00	2.001E+00	2.431E+00	2.882E+00
4.000	2.897E−01	5.043E−01	7.687E−01	1.077E+00	1.425E+00	1.807E+00	2.214E+00	2.644E+00
5.000	2.551E−01	4.465E−01	6.851E−01	9.665E−01	1.287E+00	1.642E+00	2.025E+00	2.432E+00
6.000	2.285E−01	4.015E−01	6.186E−01	8.768E−01	1.173E+00	1.504E+00	1.863E+00	2.249E+00
7.000	2.074E−01	3.655E−01	5.648E−01	8.032E−01	1.079E+00	1.388E+00	1.726E+00	2.091E+00
8.000	1.904E−01	3.360E−01	5.204E−01	7.419E−01	9.988E−01	1.289E+00	1.608E+00	1.953E+00
9.000	1.763E−01	3.115E−01	4.832E−01	6.901E−01	9.310E−01	1.204E+00	1.505E+00	1.833E+00
10.00	1.644E−01	2.908E−01	4.516E−01	6.458E−01	8.725E−01	1.130E+00	1.416E+00	1.728E+00
15.00	1.249E−01	2.215E−01	3.449E−01	4.948E−01	6.710E−01	8.729E−01	1.099E+00	1.349E+00
20.00	1.023E−01	1.816E−01	2.830E−01	4.065E−01	5.520E−01	7.192E−01	9.075E−01	1.117E+00
25.00	8.743E−02	1.553E−01	2.423E−01	3.482E−01	4.729E−01	6.166E−01	7.787E−01	9.593E−01
30.00	7.685E−02	1.365E−01	2.131E−01	3.064E−01	4.163E−01	5.429E−01	6.860E−01	8.454E−01
40.00	6.264E−02	1.113E−01	1.739E−01	2.501E−01	3.400E−01	4.436E−01	5.608E−01	6.914E−01
50.00	5.344E−02	9.501E−02	1.484E−01	2.136E−01	2.905E−01	3.791E−01	4.793E−01	5.912E−01
60.00	4.695E−02	8.350E−02	1.305E−01	1.878E−01	2.555E−01	3.335E−01	4.218E−01	5.203E−01
70.00	4.211E−02	7.490E−02	1.171E−01	1.686E−01	2.294E−01	2.995E−01	3.788E−01	4.674E−01
80.00	3.835E−02	6.823E−02	1.066E−01	1.536E−01	2.091E−01	2.730E−01	3.453E−01	4.262E−01
90.00	3.535E−02	6.288E−02	9.829E−02	1.416E−01	1.928E−01	2.517E−01	3.185E−01	3.931E−01
100.0	3.288E−02	5.850E−02	9.145E−02	1.317E−01	1.794E−01	2.343E−01	2.965E−01	3.660E−01
150.0	2.513E−02	4.471E−02	6.992E−02	1.008E−01	1.372E−01	1.793E−01	2.271E−01	2.805E−01
200.0	2.103E−02	3.742E−02	5.853E−02	8.438E−02	1.149E−01	1.502E−01	1.902E−01	2.350E−01
250.0	1.849E−02	3.292E−02	5.149E−02	7.422E−02	1.011E−01	1.322E−01	1.674E−01	2.069E−01
300.0	1.678E−02	2.987E−02	4.672E−02	6.735E−02	9.177E−02	1.200E−01	1.520E−01	1.878E−01
400.0	1.463E−02	2.604E−02	4.074E−02	5.873E−02	8.003E−02	1.047E−01	1.326E−01	1.639E−01
500.0	1.336E−02	2.377E−02	3.719E−02	5.363E−02	7.308E−02	9.557E−02	1.211E−01	1.497E−01
600.0	1.253E−02	2.231E−02	3.490E−02	5.032E−02	6.858E−02	8.968E−02	1.136E−01	1.405E−01
700.0	1.197E−02	2.130E−02	3.333E−02	4.805E−02	6.549E−02	8.565E−02	1.085E−01	1.342E−01
800.0	1.156E−02	2.058E−02	3.220E−02	4.643E−02	6.328E−02	8.275E−02	1.049E−01	1.296E−01
900.0	1.126E−02	2.005E−02	3.136E−02	4.522E−02	6.163E−02	8.061E−02	1.022E−01	1.263E−01
1000.	1.103E−02	1.963E−02	3.072E−02	4.429E−02	6.037E−02	7.895E−02	1.001E−01	1.237E−01

Material: Platinum

Ion	Na	Mg	Al	Si	P	S	Cl	Ar
(E/A_1) / MeV				$(-\mathrm{d}E/\rho\mathrm{d}\ell)$ / MeV cm^2 mg^{-1}				
0.025	1.040E+00	1.108E+00	1.176E+00	1.242E+00	1.303E+00	1.363E+00	1.420E+00	1.484E+00
0.030	1.141E+00	1.217E+00	1.292E+00	1.365E+00	1.432E+00	1.498E+00	1.561E+00	1.632E+00
0.040	1.322E+00	1.411E+00	1.499E+00	1.585E+00	1.663E+00	1.741E+00	1.815E+00	1.897E+00
0.050	1.481E+00	1.582E+00	1.683E+00	1.779E+00	1.869E+00	1.957E+00	2.041E+00	2.133E+00
0.060	1.621E+00	1.735E+00	1.847E+00	1.955E+00	2.055E+00	2.154E+00	2.247E+00	2.349E+00
0.070	1.748E+00	1.874E+00	1.997E+00	2.116E+00	2.226E+00	2.334E+00	2.437E+00	2.548E+00
0.080	1.864E+00	2.000E+00	2.135E+00	2.264E+00	2.383E+00	2.501E+00	2.613E+00	2.733E+00
0.090	1.969E+00	2.116E+00	2.262E+00	2.401E+00	2.530E+00	2.657E+00	2.778E+00	2.907E+00
0.100	2.066E+00	2.224E+00	2.379E+00	2.528E+00	2.667E+00	2.804E+00	2.933E+00	3.071E+00
0.150	2.455E+00	2.658E+00	2.860E+00	3.053E+00	3.235E+00	3.414E+00	3.584E+00	3.763E+00
0.200	2.740E+00	2.980E+00	3.218E+00	3.448E+00	3.666E+00	3.882E+00	4.087E+00	4.302E+00
0.250	2.957E+00	3.228E+00	3.498E+00	3.759E+00	4.008E+00	4.255E+00	4.492E+00	4.738E+00
0.300	3.127E+00	3.424E+00	3.720E+00	4.008E+00	4.285E+00	4.560E+00	4.824E+00	5.097E+00
0.400	3.365E+00	3.702E+00	4.042E+00	4.375E+00	4.698E+00	5.019E+00	5.331E+00	5.651E+00
0.500	3.515E+00	3.884E+00	4.255E+00	4.622E+00	4.981E+00	5.340E+00	5.690E+00	6.047E+00
0.600	3.610E+00	4.004E+00	4.400E+00	4.792E+00	5.180E+00	5.568E+00	5.947E+00	6.333E+00
0.700	3.671E+00	4.083E+00	4.498E+00	4.910E+00	5.320E+00	5.731E+00	6.134E+00	6.543E+00
0.800	3.708E+00	4.134E+00	4.564E+00	4.992E+00	5.419E+00	5.849E+00	6.271E+00	6.699E+00
0.900	3.729E+00	4.166E+00	4.608E+00	5.048E+00	5.490E+00	5.935E+00	6.373E+00	6.816E+00
1.000	3.739E+00	4.185E+00	4.637E+00	5.087E+00	5.541E+00	5.998E+00	6.449E+00	6.905E+00
1.500	3.704E+00	4.175E+00	4.655E+00	5.137E+00	5.628E+00	6.124E+00	6.618E+00	7.113E+00
2.000	3.605E+00	4.085E+00	4.577E+00	5.073E+00	5.583E+00	6.100E+00	6.616E+00	7.133E+00
2.500	3.482E+00	3.964E+00	4.460E+00	4.961E+00	5.480E+00	6.008E+00	6.537E+00	7.065E+00
3.000	3.352E+00	3.830E+00	4.325E+00	4.827E+00	5.349E+00	5.880E+00	6.416E+00	6.950E+00
4.000	3.096E+00	3.561E+00	4.044E+00	4.538E+00	5.055E+00	5.584E+00	6.121E+00	6.656E+00
5.000	2.864E+00	3.311E+00	3.778E+00	4.258E+00	4.762E+00	5.281E+00	5.809E+00	6.338E+00
6.000	2.660E+00	3.088E+00	3.537E+00	4.000E+00	4.489E+00	4.994E+00	5.510E+00	6.028E+00
7.000	2.481E+00	2.890E+00	3.321E+00	3.767E+00	4.240E+00	4.730E+00	5.232E+00	5.737E+00
8.000	2.325E+00	2.716E+00	3.129E+00	3.559E+00	4.015E+00	4.489E+00	4.977E+00	5.468E+00
9.000	2.187E+00	2.561E+00	2.958E+00	3.371E+00	3.811E+00	4.270E+00	4.743E+00	5.221E+00
10.00	2.066E+00	2.424E+00	2.804E+00	3.203E+00	3.627E+00	4.071E+00	4.530E+00	4.994E+00
15.00	1.623E+00	1.917E+00	2.232E+00	2.566E+00	2.924E+00	3.302E+00	3.696E+00	4.099E+00
20.00	1.347E+00	1.596E+00	1.864E+00	2.150E+00	2.458E+00	2.785E+00	3.128E+00	3.481E+00
25.00	1.158E+00	1.374E+00	1.608E+00	1.859E+00	2.129E+00	2.416E+00	2.719E+00	3.034E+00
30.00	1.021E+00	1.213E+00	1.421E+00	1.644E+00	1.885E+00	2.141E+00	2.413E+00	2.696E+00
40.00	8.356E−01	9.932E−01	1.164E+00	1.349E+00	1.547E+00	1.760E+00	1.985E+00	2.222E+00
50.00	7.147E−01	8.497E−01	9.964E−01	1.155E+00	1.325E+00	1.507E+00	1.701E+00	1.906E+00
60.00	6.292E−01	7.482E−01	8.775E−01	1.017E+00	1.167E+00	1.328E+00	1.499E+00	1.680E+00
70.00	5.652E−01	6.723E−01	7.886E−01	9.141E−01	1.049E+00	1.194E+00	1.347E+00	1.510E+00
80.00	5.155E−01	6.132E−01	7.193E−01	8.339E−01	9.571E−01	1.089E+00	1.229E+00	1.378E+00
90.00	4.756E−01	5.658E−01	6.638E−01	7.696E−01	8.834E−01	1.005E+00	1.135E+00	1.272E+00
100.0	4.428E−01	5.269E−01	6.182E−01	7.169E−01	8.229E−01	9.362E−01	1.057E+00	1.185E+00
150.0	3.395E−01	4.041E−01	4.744E−01	5.503E−01	6.318E−01	7.191E−01	8.120E−01	9.106E−01
200.0	2.846E−01	3.388E−01	3.979E−01	4.617E−01	5.302E−01	6.036E−01	6.817E−01	7.646E−01
250.0	2.505E−01	2.984E−01	3.504E−01	4.067E−01	4.672E−01	5.319E−01	6.009E−01	6.741E−01
300.0	2.275E−01	2.710E−01	3.183E−01	3.694E−01	4.245E−01	4.833E−01	5.461E−01	6.127E−01
400.0	1.985E−01	2.365E−01	2.778E−01	3.226E−01	3.706E−01	4.221E−01	4.770E−01	5.353E−01
500.0	1.813E−01	2.160E−01	2.538E−01	2.947E−01	3.387E−01	3.858E−01	4.360E−01	4.893E−01
600.0	1.702E−01	2.028E−01	2.383E−01	2.767E−01	3.180E−01	3.622E−01	4.094E−01	4.595E−01
700.0	1.625E−01	1.937E−01	2.276E−01	2.643E−01	3.038E−01	3.460E−01	3.911E−01	4.390E−01
800.0	1.571E−01	1.872E−01	2.199E−01	2.554E−01	2.936E−01	3.344E−01	3.780E−01	4.243E−01
900.0	1.530E−01	1.823E−01	2.142E−01	2.488E−01	2.859E−01	3.258E−01	3.683E−01	4.134E−01
1000.	1.499E−01	1.786E−01	2.099E−01	2.437E−01	2.799E−01	3.192E−01	3.608E−01	4.050E−01

Material: Gold

Ion	Li	Be	B	C	N	O	F	Ne
(E/A_1) / MeV				$(-\mathrm{d}E/\rho\mathrm{d}\ell)$ / MeV cm^2 mg^{-1}				
0.025	3.146E−01	4.344E−01	5.472E−01	6.522E−01	7.484E−01	8.412E−01	9.278E−01	1.010E+00
0.030	3.401E−01	4.717E−01	5.962E−01	7.123E−01	8.189E−01	9.217E−01	1.018E+00	1.109E+00
0.040	3.821E−01	5.341E−01	6.791E−01	8.152E−01	9.409E−01	1.062E+00	1.175E+00	1.283E+00
0.050	4.151E−01	5.845E−01	7.473E−01	9.011E−01	1.044E+00	1.182E+00	1.311E+00	1.433E+00
0.060	4.417E−01	6.261E−01	8.046E−01	9.743E−01	1.133E+00	1.286E+00	1.430E+00	1.567E+00
0.070	4.636E−01	6.609E−01	8.534E−01	1.037E+00	1.210E+00	1.378E+00	1.536E+00	1.686E+00
0.080	4.822E−01	6.907E−01	8.955E−01	1.093E+00	1.279E+00	1.459E+00	1.630E+00	1.793E+00
0.090	4.981E−01	7.167E−01	9.324E−01	1.141E+00	1.339E+00	1.532E+00	1.715E+00	1.890E+00
0.100	5.120E−01	7.395E−01	9.652E−01	1.185E+00	1.394E+00	1.598E+00	1.793E+00	1.979E+00
0.150	5.601E−01	8.225E−01	1.087E+00	1.349E+00	1.602E+00	1.853E+00	2.094E+00	2.329E+00
0.200	5.855E−01	8.719E−01	1.165E+00	1.457E+00	1.744E+00	2.030E+00	2.307E+00	2.579E+00
0.250	5.977E−01	9.009E−01	1.215E+00	1.531E+00	1.844E+00	2.158E+00	2.465E+00	2.767E+00
0.300	6.018E−01	9.167E−01	1.246E+00	1.581E+00	1.916E+00	2.253E+00	2.584E+00	2.911E+00
0.400	5.976E−01	9.255E−01	1.276E+00	1.637E+00	2.003E+00	2.374E+00	2.742E+00	3.108E+00
0.500	5.859E−01	9.198E−01	1.281E+00	1.659E+00	2.045E+00	2.439E+00	2.833E+00	3.227E+00
0.600	5.715E−01	9.076E−01	1.275E+00	1.663E+00	2.062E+00	2.472E+00	2.883E+00	3.297E+00
0.700	5.563E−01	8.921E−01	1.263E+00	1.656E+00	2.064E+00	2.485E+00	2.909E+00	3.337E+00
0.800	5.412E−01	8.750E−01	1.246E+00	1.643E+00	2.057E+00	2.486E+00	2.919E+00	3.357E+00
0.900	5.266E−01	8.575E−01	1.228E+00	1.627E+00	2.045E+00	2.479E+00	2.919E+00	3.365E+00
1.000	5.127E−01	8.400E−01	1.209E+00	1.608E+00	2.029E+00	2.466E+00	2.911E+00	3.364E+00
1.500	4.536E−01	7.597E−01	1.114E+00	1.506E+00	1.926E+00	2.369E+00	2.824E+00	3.291E+00
2.000	4.077E−01	6.921E−01	1.028E+00	1.405E+00	1.816E+00	2.253E+00	2.706E+00	3.175E+00
2.500	3.708E−01	6.352E−01	9.523E−01	1.313E+00	1.710E+00	2.136E+00	2.582E+00	3.046E+00
3.000	3.403E−01	5.868E−01	8.859E−01	1.230E+00	1.611E+00	2.025E+00	2.460E+00	2.916E+00
4.000	2.927E−01	5.095E−01	7.766E−01	1.088E+00	1.440E+00	1.826E+00	2.237E+00	2.671E+00
5.000	2.576E−01	4.509E−01	6.917E−01	9.758E−01	1.299E+00	1.658E+00	2.044E+00	2.456E+00
6.000	2.306E−01	4.052E−01	6.243E−01	8.848E−01	1.184E+00	1.518E+00	1.880E+00	2.269E+00
7.000	2.093E−01	3.687E−01	5.698E−01	8.102E−01	1.088E+00	1.400E+00	1.740E+00	2.108E+00
8.000	1.920E−01	3.389E−01	5.249E−01	7.482E−01	1.007E+00	1.300E+00	1.621E+00	1.969E+00
9.000	1.778E−01	3.142E−01	4.873E−01	6.958E−01	9.385E−01	1.214E+00	1.517E+00	1.848E+00
10.00	1.657E−01	2.932E−01	4.553E−01	6.510E−01	8.794E−01	1.139E+00	1.427E+00	1.741E+00
15.00	1.258E−01	2.231E−01	3.474E−01	4.984E−01	6.759E−01	8.792E−01	1.107E+00	1.359E+00
20.00	1.030E−01	1.828E−01	2.850E−01	4.094E−01	5.558E−01	7.241E−01	9.137E−01	1.124E+00
25.00	8.803E−02	1.563E−01	2.439E−01	3.505E−01	4.761E−01	6.207E−01	7.839E−01	9.656E−01
30.00	7.736E−02	1.374E−01	2.145E−01	3.084E−01	4.191E−01	5.465E−01	6.904E−01	8.509E−01
40.00	6.303E−02	1.120E−01	1.750E−01	2.517E−01	3.422E−01	4.464E−01	5.642E−01	6.957E−01
50.00	5.376E−02	9.559E−02	1.493E−01	2.149E−01	2.923E−01	3.814E−01	4.822E−01	5.947E−01
60.00	4.723E−02	8.399E−02	1.312E−01	1.889E−01	2.570E−01	3.355E−01	4.243E−01	5.234E−01
70.00	4.236E−02	7.534E−02	1.177E−01	1.695E−01	2.307E−01	3.012E−01	3.810E−01	4.701E−01
80.00	3.857E−02	6.862E−02	1.073E−01	1.545E−01	2.102E−01	2.745E−01	3.473E−01	4.286E−01
90.00	3.555E−02	6.324E−02	9.885E−02	1.424E−01	1.938E−01	2.531E−01	3.203E−01	3.954E−01
100.0	3.306E−02	5.883E−02	9.197E−02	1.325E−01	1.804E−01	2.356E−01	2.982E−01	3.681E−01
150.0	2.526E−02	4.496E−02	7.030E−02	1.013E−01	1.380E−01	1.803E−01	2.283E−01	2.820E−01
200.0	2.114E−02	3.762E−02	5.884E−02	8.481E−02	1.155E−01	1.510E−01	1.913E−01	2.363E−01
250.0	1.859E−02	3.309E−02	5.176E−02	7.460E−02	1.016E−01	1.329E−01	1.683E−01	2.080E−01
300.0	1.687E−02	3.002E−02	4.696E−02	6.770E−02	9.224E−02	1.206E−01	1.528E−01	1.888E−01
400.0	1.470E−02	2.617E−02	4.095E−02	5.903E−02	8.044E−02	1.052E−01	1.333E−01	1.647E−01
500.0	1.342E−02	2.389E−02	3.738E−02	5.390E−02	7.345E−02	9.605E−02	1.217E−01	1.504E−01
600.0	1.259E−02	2.242E−02	3.507E−02	5.057E−02	6.892E−02	9.013E−02	1.142E−01	1.412E−01
700.0	1.203E−02	2.141E−02	3.349E−02	4.829E−02	6.581E−02	8.607E−02	1.091E−01	1.348E−01
800.0	1.162E−02	2.068E−02	3.236E−02	4.666E−02	6.359E−02	8.316E−02	1.054E−01	1.303E−01
900.0	1.132E−02	2.014E−02	3.152E−02	4.545E−02	6.193E−02	8.100E−02	1.027E−01	1.269E−01
1000.	1.109E−02	1.973E−02	3.087E−02	4.452E−02	6.066E−02	7.934E−02	1.005E−01	1.243E−01

Material: Gold

Ion	Na	Mg	Al	Si	P	S	Cl	Ar
(E/A_1) / MeV				$(-\mathrm{d}E/\rho\mathrm{d}\ell)$ / MeV cm^2 mg^{-1}				
0.025	1.087E+00	1.158E+00	1.228E+00	1.296E+00	1.358E+00	1.420E+00	1.479E+00	1.543E+00
0.030	1.194E+00	1.272E+00	1.349E+00	1.424E+00	1.493E+00	1.561E+00	1.626E+00	1.697E+00
0.040	1.383E+00	1.475E+00	1.566E+00	1.653E+00	1.734E+00	1.814E+00	1.890E+00	1.973E+00
0.050	1.548E+00	1.653E+00	1.757E+00	1.856E+00	1.949E+00	2.039E+00	2.125E+00	2.219E+00
0.060	1.695E+00	1.813E+00	1.929E+00	2.039E+00	2.142E+00	2.244E+00	2.339E+00	2.443E+00
0.070	1.827E+00	1.957E+00	2.084E+00	2.206E+00	2.320E+00	2.431E+00	2.536E+00	2.650E+00
0.080	1.946E+00	2.088E+00	2.227E+00	2.360E+00	2.483E+00	2.605E+00	2.719E+00	2.842E+00
0.090	2.056E+00	2.208E+00	2.358E+00	2.502E+00	2.635E+00	2.766E+00	2.890E+00	3.022E+00
0.100	2.156E+00	2.319E+00	2.480E+00	2.633E+00	2.776E+00	2.917E+00	3.050E+00	3.191E+00
0.150	2.553E+00	2.764E+00	2.972E+00	3.171E+00	3.359E+00	3.544E+00	3.719E+00	3.903E+00
0.200	2.842E+00	3.090E+00	3.336E+00	3.573E+00	3.798E+00	4.021E+00	4.232E+00	4.453E+00
0.250	3.061E+00	3.341E+00	3.618E+00	3.887E+00	4.145E+00	4.399E+00	4.642E+00	4.895E+00
0.300	3.231E+00	3.537E+00	3.842E+00	4.139E+00	4.424E+00	4.706E+00	4.978E+00	5.259E+00
0.400	3.469E+00	3.816E+00	4.165E+00	4.506E+00	4.838E+00	5.168E+00	5.489E+00	5.817E+00
0.500	3.617E+00	3.996E+00	4.377E+00	4.753E+00	5.122E+00	5.489E+00	5.848E+00	6.213E+00
0.600	3.710E+00	4.113E+00	4.519E+00	4.921E+00	5.318E+00	5.715E+00	6.104E+00	6.499E+00
0.700	3.766E+00	4.188E+00	4.614E+00	5.035E+00	5.455E+00	5.875E+00	6.288E+00	6.706E+00
0.800	3.799E+00	4.236E+00	4.676E+00	5.113E+00	5.551E+00	5.989E+00	6.422E+00	6.859E+00
0.900	3.817E+00	4.264E+00	4.716E+00	5.165E+00	5.617E+00	6.071E+00	6.519E+00	6.971E+00
1.000	3.823E+00	4.279E+00	4.740E+00	5.200E+00	5.663E+00	6.130E+00	6.591E+00	7.056E+00
1.500	3.770E+00	4.250E+00	4.739E+00	5.229E+00	5.729E+00	6.234E+00	6.737E+00	7.241E+00
2.000	3.659E+00	4.147E+00	4.646E+00	5.150E+00	5.668E+00	6.192E+00	6.717E+00	7.241E+00
2.500	3.528E+00	4.016E+00	4.519E+00	5.028E+00	5.554E+00	6.088E+00	6.624E+00	7.160E+00
3.000	3.392E+00	3.877E+00	4.377E+00	4.886E+00	5.414E+00	5.952E+00	6.494E+00	7.036E+00
4.000	3.129E+00	3.599E+00	4.087E+00	4.587E+00	5.109E+00	5.645E+00	6.187E+00	6.729E+00
5.000	2.892E+00	3.343E+00	3.815E+00	4.299E+00	4.809E+00	5.333E+00	5.867E+00	6.401E+00
6.000	2.684E+00	3.116E+00	3.568E+00	4.036E+00	4.530E+00	5.040E+00	5.561E+00	6.083E+00
7.000	2.502E+00	2.915E+00	3.349E+00	3.800E+00	4.276E+00	4.771E+00	5.277E+00	5.787E+00
8.000	2.344E+00	2.738E+00	3.154E+00	3.588E+00	4.047E+00	4.526E+00	5.017E+00	5.513E+00
9.000	2.204E+00	2.581E+00	2.981E+00	3.398E+00	3.841E+00	4.303E+00	4.780E+00	5.261E+00
10.00	2.081E+00	2.442E+00	2.825E+00	3.227E+00	3.654E+00	4.101E+00	4.563E+00	5.031E+00
15.00	1.634E+00	1.930E+00	2.248E+00	2.584E+00	2.944E+00	3.324E+00	3.720E+00	4.126E+00
20.00	1.356E+00	1.606E+00	1.876E+00	2.164E+00	2.474E+00	2.802E+00	3.147E+00	3.503E+00
25.00	1.166E+00	1.383E+00	1.619E+00	1.871E+00	2.142E+00	2.431E+00	2.736E+00	3.052E+00
30.00	1.028E+00	1.221E+00	1.430E+00	1.654E+00	1.896E+00	2.154E+00	2.427E+00	2.712E+00
40.00	8.408E−01	9.994E−01	1.172E+00	1.357E+00	1.557E+00	1.770E+00	1.997E+00	2.235E+00
50.00	7.192E−01	8.549E−01	1.002E+00	1.162E+00	1.333E+00	1.516E+00	1.711E+00	1.917E+00
60.00	6.329E−01	7.526E−01	8.827E−01	1.023E+00	1.174E+00	1.336E+00	1.508E+00	1.689E+00
70.00	5.685E−01	6.762E−01	7.931E−01	9.194E−01	1.055E+00	1.200E+00	1.355E+00	1.519E+00
80.00	5.184E−01	6.167E−01	7.234E−01	8.387E−01	9.626E−01	1.095E+00	1.237E+00	1.386E+00
90.00	4.783E−01	5.690E−01	6.676E−01	7.740E−01	8.884E−01	1.011E+00	1.141E+00	1.279E+00
100.0	4.453E−01	5.298E−01	6.217E−01	7.209E−01	8.275E−01	9.415E−01	1.063E+00	1.192E+00
150.0	3.413E−01	4.063E−01	4.769E−01	5.533E−01	6.353E−01	7.230E−01	8.164E−01	9.155E−01
200.0	2.861E−01	3.406E−01	4.000E−01	4.641E−01	5.330E−01	6.068E−01	6.853E−01	7.687E−01
250.0	2.518E−01	2.999E−01	3.523E−01	4.088E−01	4.696E−01	5.347E−01	6.040E−01	6.776E−01
300.0	2.287E−01	2.724E−01	3.199E−01	3.714E−01	4.266E−01	4.858E−01	5.489E−01	6.158E−01
400.0	1.995E−01	2.377E−01	2.792E−01	3.242E−01	3.725E−01	4.243E−01	4.794E−01	5.380E−01
500.0	1.822E−01	2.171E−01	2.551E−01	2.962E−01	3.404E−01	3.877E−01	4.382E−01	4.918E−01
600.0	1.710E−01	2.038E−01	2.395E−01	2.780E−01	3.196E−01	3.640E−01	4.114E−01	4.618E−01
700.0	1.633E−01	1.946E−01	2.287E−01	2.656E−01	3.053E−01	3.477E−01	3.930E−01	4.412E−01
800.0	1.578E−01	1.881E−01	2.210E−01	2.566E−01	2.950E−01	3.361E−01	3.799E−01	4.264E−01
900.0	1.537E−01	1.832E−01	2.153E−01	2.500E−01	2.874E−01	3.274E−01	3.701E−01	4.154E−01
1000.	1.506E−01	1.795E−01	2.109E−01	2.449E−01	2.815E−01	3.207E−01	3.625E−01	4.070E−01

Material: Lead

Ion	Li	Be	B	C	N	O	F	Ne
(E/A_1) / MeV				$(-\mathrm{d}E/\rho\mathrm{d}\ell)$ / MeV cm^2 mg^{-1}				
0.025	3.483E−01	4.635E−01	5.692E−01	6.665E−01	7.558E−01	8.429E−01	9.254E−01	1.005E+00
0.030	3.786E−01	5.078E−01	6.265E−01	7.355E−01	8.351E−01	9.317E−01	1.023E+00	1.110E+00
0.040	4.260E−01	5.801E−01	7.228E−01	8.541E−01	9.739E−01	1.089E+00	1.197E+00	1.299E+00
0.050	4.605E−01	6.356E−01	7.996E−01	9.515E−01	1.091E+00	1.223E+00	1.348E+00	1.465E+00
0.060	4.861E−01	6.786E−01	8.612E−01	1.032E+00	1.189E+00	1.339E+00	1.479E+00	1.612E+00
0.070	5.059E−01	7.126E−01	9.110E−01	1.098E+00	1.272E+00	1.439E+00	1.594E+00	1.742E+00
0.080	5.217E−01	7.402E−01	9.521E−01	1.154E+00	1.343E+00	1.524E+00	1.695E+00	1.856E+00
0.090	5.346E−01	7.631E−01	9.866E−01	1.201E+00	1.403E+00	1.599E+00	1.783E+00	1.958E+00
0.100	5.454E−01	7.826E−01	1.016E+00	1.242E+00	1.456E+00	1.664E+00	1.860E+00	2.048E+00
0.150	5.801E−01	8.488E−01	1.119E+00	1.386E+00	1.645E+00	1.900E+00	2.146E+00	2.384E+00
0.200	5.962E−01	8.853E−01	1.180E+00	1.475E+00	1.765E+00	2.053E+00	2.334E+00	2.609E+00
0.250	6.020E−01	9.051E−01	1.218E+00	1.534E+00	1.848E+00	2.161E+00	2.469E+00	2.772E+00
0.300	6.016E−01	9.142E−01	1.241E+00	1.573E+00	1.906E+00	2.240E+00	2.570E+00	2.896E+00
0.400	5.907E−01	9.137E−01	1.258E+00	1.614E+00	1.974E+00	2.340E+00	2.703E+00	3.065E+00
0.500	5.742E−01	9.012E−01	1.255E+00	1.626E+00	2.005E+00	2.391E+00	2.778E+00	3.166E+00
0.600	5.559E−01	8.835E−01	1.242E+00	1.621E+00	2.012E+00	2.414E+00	2.817E+00	3.224E+00
0.700	5.375E−01	8.633E−01	1.224E+00	1.607E+00	2.006E+00	2.418E+00	2.833E+00	3.253E+00
0.800	5.197E−01	8.423E−01	1.202E+00	1.588E+00	1.992E+00	2.411E+00	2.835E+00	3.265E+00
0.900	5.029E−01	8.215E−01	1.180E+00	1.566E+00	1.973E+00	2.396E+00	2.827E+00	3.264E+00
1.000	4.873E−01	8.013E−01	1.157E+00	1.543E+00	1.952E+00	2.378E+00	2.812E+00	3.255E+00
1.500	4.243E−01	7.140E−01	1.052E+00	1.427E+00	1.831E+00	2.259E+00	2.700E+00	3.154E+00
2.000	3.787E−01	6.460E−01	9.641E−01	1.323E+00	1.715E+00	2.135E+00	2.571E+00	3.024E+00
2.500	3.436E−01	5.913E−01	8.904E−01	1.232E+00	1.610E+00	2.018E+00	2.445E+00	2.892E+00
3.000	3.154E−01	5.461E−01	8.276E−01	1.153E+00	1.515E+00	1.910E+00	2.327E+00	2.765E+00
4.000	2.722E−01	4.751E−01	7.265E−01	1.021E+00	1.354E+00	1.722E+00	2.114E+00	2.531E+00
5.000	2.406E−01	4.219E−01	6.487E−01	9.172E−01	1.224E+00	1.565E+00	1.934E+00	2.327E+00
6.000	2.163E−01	3.805E−01	5.871E−01	8.336E−01	1.117E+00	1.435E+00	1.781E+00	2.153E+00
7.000	1.971E−01	3.473E−01	5.373E−01	7.650E−01	1.029E+00	1.325E+00	1.651E+00	2.002E+00
8.000	1.814E−01	3.202E−01	4.962E−01	7.079E−01	9.540E−01	1.232E+00	1.539E+00	1.872E+00
9.000	1.684E−01	2.976E−01	4.617E−01	6.597E−01	8.905E−01	1.153E+00	1.442E+00	1.758E+00
10.00	1.574E−01	2.784E−01	4.323E−01	6.184E−01	8.358E−01	1.083E+00	1.358E+00	1.658E+00
15.00	1.206E−01	2.138E−01	3.327E−01	4.771E−01	6.468E−01	8.414E−01	1.060E+00	1.301E+00
20.00	9.928E−02	1.762E−01	2.745E−01	3.940E−01	5.346E−01	6.963E−01	8.784E−01	1.081E+00
25.00	8.515E−02	1.512E−01	2.357E−01	3.385E−01	4.596E−01	5.989E−01	7.561E−01	9.311E−01
30.00	7.497E−02	1.331E−01	2.077E−01	2.985E−01	4.054E−01	5.285E−01	6.675E−01	8.224E−01
40.00	6.118E−02	1.087E−01	1.698E−01	2.442E−01	3.318E−01	4.328E−01	5.469E−01	6.741E−01
50.00	5.221E−02	9.284E−02	1.450E−01	2.087E−01	2.837E−01	3.702E−01	4.680E−01	5.771E−01
60.00	4.587E−02	8.159E−02	1.275E−01	1.835E−01	2.496E−01	3.258E−01	4.120E−01	5.082E−01
70.00	4.114E−02	7.318E−02	1.144E−01	1.647E−01	2.241E−01	2.926E−01	3.700E−01	4.565E−01
80.00	3.746E−02	6.665E−02	1.042E−01	1.500E−01	2.042E−01	2.667E−01	3.374E−01	4.163E−01
90.00	3.452E−02	6.142E−02	9.602E−02	1.383E−01	1.883E−01	2.459E−01	3.112E−01	3.840E−01
100.0	3.211E−02	5.714E−02	8.933E−02	1.287E−01	1.752E−01	2.289E−01	2.896E−01	3.575E−01
150.0	2.454E−02	4.367E−02	6.829E−02	9.842E−02	1.341E−01	1.752E−01	2.218E−01	2.740E−01
200.0	2.054E−02	3.655E−02	5.717E−02	8.241E−02	1.123E−01	1.468E−01	1.859E−01	2.296E−01
250.0	1.807E−02	3.216E−02	5.031E−02	7.252E−02	9.881E−02	1.292E−01	1.636E−01	2.022E−01
300.0	1.640E−02	2.919E−02	4.566E−02	6.583E−02	8.970E−02	1.173E−01	1.486E−01	1.836E−01
400.0	1.431E−02	2.547E−02	3.984E−02	5.744E−02	7.828E−02	1.024E−01	1.297E−01	1.603E−01
500.0	1.307E−02	2.326E−02	3.640E−02	5.248E−02	7.152E−02	9.353E−02	1.185E−01	1.465E−01
600.0	1.227E−02	2.184E−02	3.416E−02	4.926E−02	6.714E−02	8.780E−02	1.113E−01	1.375E−01
700.0	1.171E−02	2.085E−02	3.263E−02	4.705E−02	6.412E−02	8.387E−02	1.063E−01	1.314E−01
800.0	1.132E−02	2.015E−02	3.152E−02	4.546E−02	6.196E−02	8.103E−02	1.027E−01	1.270E−01
900.0	1.102E−02	1.962E−02	3.070E−02	4.427E−02	6.034E−02	7.892E−02	1.000E−01	1.236E−01
1000.	1.079E−02	1.922E−02	3.007E−02	4.336E−02	5.909E−02	7.729E−02	9.795E−02	1.211E−01

Material: Lead

Ion	Na	Mg	Al	Si	P	S	Cl	Ar
(E/A_1) / MeV				$(-\mathrm{d}E/\rho\mathrm{d}\ell)$ / MeV cm^2 mg^{-1}				
0.025	1.081E+00	1.152E+00	1.223E+00	1.293E+00	1.358E+00	1.423E+00	1.485E+00	1.554E+00
0.030	1.193E+00	1.271E+00	1.349E+00	1.426E+00	1.497E+00	1.569E+00	1.637E+00	1.713E+00
0.040	1.396E+00	1.487E+00	1.577E+00	1.666E+00	1.748E+00	1.831E+00	1.910E+00	1.998E+00
0.050	1.576E+00	1.679E+00	1.781E+00	1.880E+00	1.973E+00	2.065E+00	2.154E+00	2.252E+00
0.060	1.736E+00	1.851E+00	1.965E+00	2.075E+00	2.178E+00	2.280E+00	2.377E+00	2.485E+00
0.070	1.880E+00	2.007E+00	2.133E+00	2.253E+00	2.366E+00	2.477E+00	2.584E+00	2.700E+00
0.080	2.008E+00	2.148E+00	2.285E+00	2.417E+00	2.540E+00	2.661E+00	2.776E+00	2.901E+00
0.090	2.123E+00	2.275E+00	2.424E+00	2.567E+00	2.700E+00	2.831E+00	2.955E+00	3.089E+00
0.100	2.226E+00	2.390E+00	2.551E+00	2.705E+00	2.848E+00	2.989E+00	3.122E+00	3.265E+00
0.150	2.613E+00	2.828E+00	3.040E+00	3.243E+00	3.435E+00	3.624E+00	3.802E+00	3.990E+00
0.200	2.875E+00	3.128E+00	3.378E+00	3.621E+00	3.851E+00	4.078E+00	4.296E+00	4.522E+00
0.250	3.068E+00	3.351E+00	3.632E+00	3.905E+00	4.167E+00	4.426E+00	4.675E+00	4.934E+00
0.300	3.216E+00	3.523E+00	3.830E+00	4.129E+00	4.417E+00	4.703E+00	4.980E+00	5.266E+00
0.400	3.422E+00	3.767E+00	4.114E+00	4.455E+00	4.787E+00	5.118E+00	5.440E+00	5.771E+00
0.500	3.551E+00	3.925E+00	4.303E+00	4.675E+00	5.042E+00	5.408E+00	5.765E+00	6.132E+00
0.600	3.630E+00	4.028E+00	4.429E+00	4.827E+00	5.220E+00	5.614E+00	6.000E+00	6.394E+00
0.700	3.676E+00	4.092E+00	4.512E+00	4.928E+00	5.344E+00	5.760E+00	6.170E+00	6.586E+00
0.800	3.699E+00	4.129E+00	4.563E+00	4.995E+00	5.428E+00	5.863E+00	6.291E+00	6.726E+00
0.900	3.708E+00	4.148E+00	4.593E+00	5.038E+00	5.484E+00	5.934E+00	6.378E+00	6.827E+00
1.000	3.706E+00	4.154E+00	4.608E+00	5.062E+00	5.520E+00	5.982E+00	6.439E+00	6.901E+00
1.500	3.621E+00	4.090E+00	4.569E+00	5.051E+00	5.543E+00	6.040E+00	6.536E+00	7.035E+00
2.000	3.493E+00	3.968E+00	4.455E+00	4.947E+00	5.454E+00	5.968E+00	6.483E+00	6.999E+00
2.500	3.358E+00	3.831E+00	4.318E+00	4.813E+00	5.326E+00	5.847E+00	6.371E+00	6.897E+00
3.000	3.223E+00	3.691E+00	4.175E+00	4.669E+00	5.181E+00	5.705E+00	6.233E+00	6.762E+00
4.000	2.970E+00	3.422E+00	3.894E+00	4.376E+00	4.882E+00	5.401E+00	5.927E+00	6.454E+00
5.000	2.746E+00	3.180E+00	3.634E+00	4.101E+00	4.594E+00	5.101E+00	5.617E+00	6.136E+00
6.000	2.550E+00	2.965E+00	3.401E+00	3.851E+00	4.328E+00	4.820E+00	5.324E+00	5.831E+00
7.000	2.380E+00	2.776E+00	3.193E+00	3.627E+00	4.087E+00	4.564E+00	5.053E+00	5.547E+00
8.000	2.231E+00	2.609E+00	3.009E+00	3.426E+00	3.869E+00	4.330E+00	4.805E+00	5.285E+00
9.000	2.100E+00	2.461E+00	2.845E+00	3.246E+00	3.673E+00	4.119E+00	4.579E+00	5.044E+00
10.00	1.984E+00	2.330E+00	2.698E+00	3.084E+00	3.496E+00	3.927E+00	4.372E+00	4.824E+00
15.00	1.565E+00	1.849E+00	2.154E+00	2.477E+00	2.823E+00	3.189E+00	3.571E+00	3.962E+00
20.00	1.303E+00	1.544E+00	1.804E+00	2.081E+00	2.379E+00	2.695E+00	3.028E+00	3.371E+00
25.00	1.124E+00	1.333E+00	1.560E+00	1.803E+00	2.065E+00	2.343E+00	2.637E+00	2.942E+00
30.00	9.932E−01	1.179E+00	1.381E+00	1.598E+00	1.831E+00	2.080E+00	2.344E+00	2.619E+00
40.00	8.146E−01	9.679E−01	1.134E+00	1.314E+00	1.507E+00	1.713E+00	1.932E+00	2.163E+00
50.00	6.975E−01	8.291E−01	9.720E−01	1.126E+00	1.292E+00	1.469E+00	1.658E+00	1.857E+00
60.00	6.143E−01	7.304E−01	8.566E−01	9.926E−01	1.139E+00	1.296E+00	1.462E+00	1.638E+00
70.00	5.520E−01	6.565E−01	7.700E−01	8.924E−01	1.024E+00	1.165E+00	1.315E+00	1.474E+00
80.00	5.035E−01	5.989E−01	7.025E−01	8.143E−01	9.345E−01	1.063E+00	1.200E+00	1.345E+00
90.00	4.645E−01	5.526E−01	6.483E−01	7.516E−01	8.627E−01	9.814E−01	1.108E+00	1.242E+00
100.0	4.325E−01	5.146E−01	6.038E−01	7.001E−01	8.036E−01	9.143E−01	1.032E+00	1.157E+00
150.0	3.316E−01	3.948E−01	4.634E−01	5.376E−01	6.172E−01	7.024E−01	7.932E−01	8.895E−01
200.0	2.780E−01	3.311E−01	3.888E−01	4.511E−01	5.181E−01	5.898E−01	6.661E−01	7.472E−01
250.0	2.449E−01	2.916E−01	3.425E−01	3.975E−01	4.567E−01	5.199E−01	5.873E−01	6.589E−01
300.0	2.224E−01	2.649E−01	3.112E−01	3.612E−01	4.150E−01	4.726E−01	5.339E−01	5.990E−01
400.0	1.942E−01	2.313E−01	2.718E−01	3.156E−01	3.626E−01	4.130E−01	4.667E−01	5.238E−01
500.0	1.775E−01	2.115E−01	2.485E−01	2.885E−01	3.315E−01	3.776E−01	4.268E−01	4.790E−01
600.0	1.666E−01	1.986E−01	2.333E−01	2.709E−01	3.114E−01	3.547E−01	4.009E−01	4.500E−01
700.0	1.592E−01	1.897E−01	2.229E−01	2.588E−01	2.975E−01	3.389E−01	3.831E−01	4.300E−01
800.0	1.538E−01	1.833E−01	2.154E−01	2.501E−01	2.875E−01	3.275E−01	3.702E−01	4.156E−01
900.0	1.498E−01	1.785E−01	2.098E−01	2.436E−01	2.801E−01	3.191E−01	3.607E−01	4.049E−01
1000.	1.467E−01	1.748E−01	2.055E−01	2.386E−01	2.743E−01	3.125E−01	3.533E−01	3.966E−01

Material: Uranium

Ion	Li	Be	B	C	N	O	F	Ne
(E/A_1) / MeV				$(-\mathrm{d}E/\rho\mathrm{d}\ell)$ / MeV cm^2 mg^{-1}				
0.025	4.158E−01	5.309E−01	6.283E−01	7.126E−01	7.860E−01	8.561E−01	9.213E−01	9.839E−01
0.030	4.488E−01	5.804E−01	6.928E−01	7.900E−01	8.741E−01	9.532E−01	1.026E+00	1.096E+00
0.040	4.987E−01	6.584E−01	7.987E−01	9.217E−01	1.029E+00	1.127E+00	1.217E+00	1.300E+00
0.050	5.342E−01	7.166E−01	8.807E−01	1.027E+00	1.156E+00	1.275E+00	1.383E+00	1.483E+00
0.060	5.603E−01	7.614E−01	9.455E−01	1.112E+00	1.261E+00	1.400E+00	1.526E+00	1.642E+00
0.070	5.798E−01	7.965E−01	9.979E−01	1.183E+00	1.350E+00	1.506E+00	1.649E+00	1.782E+00
0.080	5.944E−01	8.243E−01	1.041E+00	1.241E+00	1.425E+00	1.597E+00	1.756E+00	1.904E+00
0.090	6.054E−01	8.465E−01	1.076E+00	1.291E+00	1.489E+00	1.676E+00	1.849E+00	2.012E+00
0.100	6.139E−01	8.645E−01	1.105E+00	1.332E+00	1.543E+00	1.744E+00	1.932E+00	2.107E+00
0.150	6.323E−01	9.152E−01	1.196E+00	1.468E+00	1.728E+00	1.982E+00	2.223E+00	2.453E+00
0.200	6.313E−01	9.314E−01	1.235E+00	1.535E+00	1.828E+00	2.116E+00	2.394E+00	2.664E+00
0.250	6.230E−01	9.324E−01	1.250E+00	1.569E+00	1.883E+00	2.196E+00	2.501E+00	2.800E+00
0.300	6.119E−01	9.264E−01	1.253E+00	1.585E+00	1.914E+00	2.245E+00	2.570E+00	2.891E+00
0.400	5.877E−01	9.057E−01	1.243E+00	1.590E+00	1.941E+00	2.296E+00	2.648E+00	2.999E+00
0.500	5.640E−01	8.816E−01	1.224E+00	1.580E+00	1.944E+00	2.314E+00	2.684E+00	3.055E+00
0.600	5.413E−01	8.569E−01	1.201E+00	1.563E+00	1.935E+00	2.316E+00	2.698E+00	3.083E+00
0.700	5.196E−01	8.318E−01	1.175E+00	1.540E+00	1.917E+00	2.306E+00	2.698E+00	3.094E+00
0.800	4.992E−01	8.068E−01	1.149E+00	1.514E+00	1.895E+00	2.289E+00	2.688E+00	3.092E+00
0.900	4.801E−01	7.824E−01	1.122E+00	1.486E+00	1.869E+00	2.267E+00	2.670E+00	3.080E+00
1.000	4.623E−01	7.591E−01	1.095E+00	1.458E+00	1.841E+00	2.241E+00	2.648E+00	3.063E+00
1.500	3.915E−01	6.601E−01	9.736E−01	1.322E+00	1.697E+00	2.094E+00	2.504E+00	2.927E+00
2.000	3.427E−01	5.867E−01	8.778E−01	1.207E+00	1.567E+00	1.953E+00	2.355E+00	2.773E+00
2.500	3.074E−01	5.313E−01	8.024E−01	1.113E+00	1.457E+00	1.829E+00	2.220E+00	2.629E+00
3.000	2.806E−01	4.878E−01	7.416E−01	1.036E+00	1.364E+00	1.722E+00	2.101E+00	2.500E+00
4.000	2.419E−01	4.235E−01	6.491E−01	9.142E−01	1.215E+00	1.546E+00	1.902E+00	2.279E+00
5.000	2.148E−01	3.773E−01	5.810E−01	8.227E−01	1.099E+00	1.407E+00	1.740E+00	2.097E+00
6.000	1.943E−01	3.421E−01	5.283E−01	7.506E−01	1.007E+00	1.294E+00	1.607E+00	1.944E+00
7.000	1.781E−01	3.140E−01	4.859E−01	6.920E−01	9.307E−01	1.200E+00	1.495E+00	1.814E+00
8.000	1.649E−01	2.910E−01	4.508E−01	6.431E−01	8.667E−01	1.120E+00	1.398E+00	1.701E+00
9.000	1.538E−01	2.716E−01	4.212E−01	6.017E−01	8.120E−01	1.051E+00	1.315E+00	1.603E+00
10.00	1.443E−01	2.551E−01	3.959E−01	5.660E−01	7.647E−01	9.908E−01	1.242E+00	1.516E+00
15.00	1.119E−01	1.982E−01	3.084E−01	4.421E−01	5.990E−01	7.787E−01	9.802E−01	1.203E+00
20.00	9.264E−02	1.643E−01	2.560E−01	3.673E−01	4.983E−01	6.487E−01	8.180E−01	1.006E+00
25.00	7.970E−02	1.415E−01	2.206E−01	3.168E−01	4.300E−01	5.602E−01	7.070E−01	8.703E−01
30.00	7.033E−02	1.249E−01	1.949E−01	2.801E−01	3.803E−01	4.957E−01	6.259E−01	7.709E−01
40.00	5.758E−02	1.023E−01	1.598E−01	2.298E−01	3.124E−01	4.073E−01	5.147E−01	6.343E−01
50.00	4.924E−02	8.757E−02	1.368E−01	1.968E−01	2.677E−01	3.492E−01	4.414E−01	5.443E−01
60.00	4.334E−02	7.708E−02	1.204E−01	1.734E−01	2.359E−01	3.078E−01	3.893E−01	4.801E−01
70.00	3.891E−02	6.923E−02	1.082E−01	1.558E−01	2.120E−01	2.768E−01	3.501E−01	4.319E−01
80.00	3.547E−02	6.311E−02	9.866E−02	1.421E−01	1.934E−01	2.526E−01	3.195E−01	3.943E−01
90.00	3.272E−02	5.821E−02	9.101E−02	1.311E−01	1.785E−01	2.331E−01	2.950E−01	3.641E−01
100.0	3.045E−02	5.419E−02	8.473E−02	1.221E−01	1.662E−01	2.171E−01	2.748E−01	3.392E−01
150.0	2.333E−02	4.152E−02	6.494E−02	9.359E−02	1.275E−01	1.666E−01	2.110E−01	2.606E−01
200.0	1.956E−02	3.481E−02	5.445E−02	7.849E−02	1.069E−01	1.398E−01	1.770E−01	2.187E−01
250.0	1.722E−02	3.066E−02	4.796E−02	6.914E−02	9.421E−02	1.232E−01	1.560E−01	1.928E−01
300.0	1.565E−02	2.785E−02	4.357E−02	6.281E−02	8.559E−02	1.119E−01	1.418E−01	1.752E−01
400.0	1.366E−02	2.433E−02	3.806E−02	5.487E−02	7.478E−02	9.779E−02	1.239E−01	1.532E−01
500.0	1.249E−02	2.224E−02	3.480E−02	5.017E−02	6.838E−02	8.943E−02	1.133E−01	1.401E−01
600.0	1.173E−02	2.089E−02	3.269E−02	4.713E−02	6.424E−02	8.401E−02	1.065E−01	1.316E−01
700.0	1.121E−02	1.996E−02	3.123E−02	4.504E−02	6.138E−02	8.028E−02	1.017E−01	1.258E−01
800.0	1.084E−02	1.929E−02	3.018E−02	4.353E−02	5.933E−02	7.759E−02	9.834E−02	1.216E−01
900.0	1.056E−02	1.879E−02	2.940E−02	4.240E−02	5.779E−02	7.559E−02	9.580E−02	1.184E−01
1000.	1.034E−02	1.841E−02	2.880E−02	4.153E−02	5.661E−02	7.404E−02	9.384E−02	1.160E−01

Material: Uranium

Ion	Na	Mg	Al	Si	P	S	Cl	Ar
(E/A_1) / MeV				$(-\mathrm{d}E/\rho\mathrm{d}\ell)$ / MeV cm^2 mg^{-1}				
0.025	1.043E+00	1.098E+00	1.155E+00	1.209E+00	1.261E+00	1.313E+00	1.363E+00	1.419E+00
0.030	1.161E+00	1.222E+00	1.284E+00	1.345E+00	1.402E+00	1.459E+00	1.514E+00	1.577E+00
0.040	1.378E+00	1.450E+00	1.522E+00	1.592E+00	1.658E+00	1.725E+00	1.789E+00	1.861E+00
0.050	1.574E+00	1.657E+00	1.740E+00	1.819E+00	1.893E+00	1.967E+00	2.038E+00	2.118E+00
0.060	1.749E+00	1.845E+00	1.939E+00	2.029E+00	2.111E+00	2.193E+00	2.271E+00	2.358E+00
0.070	1.903E+00	2.013E+00	2.120E+00	2.221E+00	2.313E+00	2.404E+00	2.490E+00	2.585E+00
0.080	2.040E+00	2.164E+00	2.283E+00	2.396E+00	2.499E+00	2.599E+00	2.694E+00	2.797E+00
0.090	2.162E+00	2.298E+00	2.431E+00	2.555E+00	2.669E+00	2.780E+00	2.884E+00	2.996E+00
0.100	2.271E+00	2.420E+00	2.564E+00	2.700E+00	2.825E+00	2.946E+00	3.060E+00	3.181E+00
0.150	2.672E+00	2.875E+00	3.074E+00	3.262E+00	3.437E+00	3.607E+00	3.767E+00	3.935E+00
0.200	2.924E+00	3.168E+00	3.408E+00	3.638E+00	3.854E+00	4.065E+00	4.266E+00	4.474E+00
0.250	3.090E+00	3.365E+00	3.637E+00	3.900E+00	4.150E+00	4.396E+00	4.630E+00	4.872E+00
0.300	3.204E+00	3.503E+00	3.801E+00	4.090E+00	4.367E+00	4.641E+00	4.904E+00	5.175E+00
0.400	3.344E+00	3.677E+00	4.011E+00	4.340E+00	4.658E+00	4.975E+00	5.283E+00	5.599E+00
0.500	3.422E+00	3.780E+00	4.140E+00	4.495E+00	4.844E+00	5.192E+00	5.532E+00	5.879E+00
0.600	3.468E+00	3.844E+00	4.224E+00	4.599E+00	4.971E+00	5.342E+00	5.707E+00	6.078E+00
0.700	3.491E+00	3.883E+00	4.277E+00	4.669E+00	5.058E+00	5.449E+00	5.833E+00	6.223E+00
0.800	3.499E+00	3.902E+00	4.309E+00	4.713E+00	5.118E+00	5.524E+00	5.924E+00	6.330E+00
0.900	3.496E+00	3.908E+00	4.324E+00	4.739E+00	5.156E+00	5.575E+00	5.989E+00	6.408E+00
1.000	3.484E+00	3.903E+00	4.328E+00	4.751E+00	5.178E+00	5.608E+00	6.033E+00	6.463E+00
1.500	3.361E+00	3.798E+00	4.244E+00	4.692E+00	5.149E+00	5.611E+00	6.073E+00	6.537E+00
2.000	3.206E+00	3.645E+00	4.096E+00	4.551E+00	5.020E+00	5.495E+00	5.972E+00	6.451E+00
2.500	3.056E+00	3.490E+00	3.939E+00	4.394E+00	4.865E+00	5.345E+00	5.828E+00	6.313E+00
3.000	2.918E+00	3.345E+00	3.788E+00	4.240E+00	4.709E+00	5.189E+00	5.673E+00	6.159E+00
4.000	2.677E+00	3.088E+00	3.517E+00	3.956E+00	4.416E+00	4.888E+00	5.368E+00	5.849E+00
5.000	2.476E+00	2.870E+00	3.282E+00	3.707E+00	4.153E+00	4.614E+00	5.084E+00	5.556E+00
6.000	2.304E+00	2.681E+00	3.077E+00	3.486E+00	3.919E+00	4.367E+00	4.825E+00	5.286E+00
7.000	2.157E+00	2.517E+00	2.896E+00	3.291E+00	3.709E+00	4.143E+00	4.589E+00	5.038E+00
8.000	2.028E+00	2.372E+00	2.737E+00	3.117E+00	3.521E+00	3.941E+00	4.373E+00	4.811E+00
9.000	1.915E+00	2.244E+00	2.595E+00	2.961E+00	3.351E+00	3.757E+00	4.177E+00	4.603E+00
10.00	1.814E+00	2.131E+00	2.467E+00	2.820E+00	3.197E+00	3.590E+00	3.998E+00	4.412E+00
15.00	1.446E+00	1.708E+00	1.989E+00	2.287E+00	2.606E+00	2.943E+00	3.295E+00	3.655E+00
20.00	1.212E+00	1.436E+00	1.677E+00	1.934E+00	2.210E+00	2.503E+00	2.810E+00	3.128E+00
25.00	1.050E+00	1.245E+00	1.457E+00	1.683E+00	1.926E+00	2.185E+00	2.458E+00	2.743E+00
30.00	9.308E−01	1.105E+00	1.293E+00	1.496E+00	1.714E+00	1.946E+00	2.192E+00	2.449E+00
40.00	7.663E−01	9.105E−01	1.067E+00	1.235E+00	1.416E+00	1.610E+00	1.815E+00	2.031E+00
50.00	6.578E−01	7.818E−01	9.165E−01	1.062E+00	1.218E+00	1.385E+00	1.562E+00	1.749E+00
60.00	5.804E−01	6.901E−01	8.091E−01	9.376E−01	1.076E+00	1.223E+00	1.381E+00	1.547E+00
70.00	5.223E−01	6.211E−01	7.284E−01	8.443E−01	9.686E−01	1.102E+00	1.243E+00	1.393E+00
80.00	4.768E−01	5.672E−01	6.653E−01	7.711E−01	8.849E−01	1.007E+00	1.136E+00	1.273E+00
90.00	4.403E−01	5.238E−01	6.145E−01	7.124E−01	8.176E−01	9.301E−01	1.050E+00	1.177E+00
100.0	4.103E−01	4.882E−01	5.728E−01	6.642E−01	7.623E−01	8.672E−01	9.790E−01	1.097E+00
150.0	3.154E−01	3.755E−01	4.407E−01	5.113E−01	5.870E−01	6.681E−01	7.544E−01	8.459E−01
200.0	2.648E−01	3.154E−01	3.703E−01	4.297E−01	4.935E−01	5.618E−01	6.345E−01	7.117E−01
250.0	2.335E−01	2.781E−01	3.266E−01	3.791E−01	4.356E−01	4.958E−01	5.601E−01	6.283E−01
300.0	2.122E−01	2.528E−01	2.970E−01	3.447E−01	3.961E−01	4.510E−01	5.096E−01	5.717E−01
400.0	1.855E−01	2.210E−01	2.597E−01	3.015E−01	3.465E−01	3.946E−01	4.459E−01	5.005E−01
500.0	1.697E−01	2.022E−01	2.376E−01	2.759E−01	3.171E−01	3.612E−01	4.082E−01	4.581E−01
600.0	1.595E−01	1.900E−01	2.233E−01	2.593E−01	2.980E−01	3.395E−01	3.837E−01	4.307E−01
700.0	1.524E−01	1.816E−01	2.134E−01	2.478E−01	2.848E−01	3.245E−01	3.668E−01	4.117E−01
800.0	1.473E−01	1.755E−01	2.063E−01	2.396E−01	2.754E−01	3.137E−01	3.546E−01	3.981E−01
900.0	1.435E−01	1.710E−01	2.010E−01	2.334E−01	2.683E−01	3.057E−01	3.455E−01	3.879E−01
1000.	1.406E−01	1.675E−01	1.969E−01	2.286E−01	2.628E−01	2.994E−01	3.385E−01	3.800E−01

6.6. TABLES: ELECTRONIC STOPPING FORCE FOR IRON IONS IN SIXTEEN ELEMENTAL MATERIALS

				Ion: Iron				
Material	H_2	He	Be	C	N_2	O_2	Ne	Al
(E/A_1) / MeV				$(-dE/\rho d\ell)$ / MeV cm^2 mg^{-1}				
0.025	2.760E+01	9.071E+00	7.231E+00	6.513E+00	7.196E+00	5.927E+00	4.522E+00	5.170E+00
0.030	3.046E+01	9.992E+00	8.001E+00	7.256E+00	7.991E+00	6.602E+00	5.012E+00	5.727E+00
0.040	3.563E+01	1.168E+01	9.429E+00	8.631E+00	9.457E+00	7.858E+00	5.923E+00	6.746E+00
0.050	4.023E+01	1.322E+01	1.074E+01	9.900E+00	1.080E+01	9.021E+00	6.771E+00	7.678E+00
0.060	4.441E+01	1.465E+01	1.198E+01	1.109E+01	1.207E+01	1.012E+01	7.576E+00	8.549E+00
0.070	4.828E+01	1.601E+01	1.315E+01	1.222E+01	1.328E+01	1.118E+01	8.354E+00	9.369E+00
0.080	5.191E+01	1.731E+01	1.426E+01	1.329E+01	1.443E+01	1.220E+01	9.113E+00	1.015E+01
0.090	5.535E+01	1.856E+01	1.532E+01	1.431E+01	1.552E+01	1.319E+01	9.858E+00	1.089E+01
0.100	5.862E+01	1.977E+01	1.632E+01	1.528E+01	1.657E+01	1.415E+01	1.059E+01	1.160E+01
0.150	7.281E+01	2.534E+01	2.070E+01	1.972E+01	2.116E+01	1.850E+01	1.406E+01	1.473E+01
0.200	8.345E+01	3.009E+01	2.417E+01	2.371E+01	2.497E+01	2.219E+01	1.714E+01	1.729E+01
0.250	9.110E+01	3.392E+01	2.687E+01	2.695E+01	2.817E+01	2.529E+01	1.983E+01	1.934E+01
0.300	9.654E+01	3.691E+01	2.894E+01	2.943E+01	3.072E+01	2.784E+01	2.214E+01	2.100E+01
0.400	1.032E+02	4.096E+01	3.186E+01	3.276E+01	3.422E+01	3.147E+01	2.574E+01	2.358E+01
0.500	1.068E+02	4.337E+01	3.377E+01	3.481E+01	3.634E+01	3.372E+01	2.821E+01	2.550E+01
0.600	1.085E+02	4.482E+01	3.507E+01	3.617E+01	3.768E+01	3.515E+01	2.989E+01	2.697E+01
0.700	1.093E+02	4.569E+01	3.597E+01	3.708E+01	3.855E+01	3.609E+01	3.102E+01	2.809E+01
0.800	1.095E+02	4.620E+01	3.657E+01	3.770E+01	3.912E+01	3.671E+01	3.180E+01	2.892E+01
0.900	1.092E+02	4.645E+01	3.697E+01	3.813E+01	3.948E+01	3.712E+01	3.233E+01	2.953E+01
1.000	1.086E+02	4.653E+01	3.722E+01	3.842E+01	3.969E+01	3.738E+01	3.270E+01	2.997E+01
1.500	1.041E+02	4.569E+01	3.722E+01	3.865E+01	3.965E+01	3.753E+01	3.324E+01	3.072E+01
2.000	9.890E+01	4.406E+01	3.633E+01	3.799E+01	3.883E+01	3.687E+01	3.287E+01	3.045E+01
2.500	9.387E+01	4.229E+01	3.519E+01	3.701E+01	3.774E+01	3.594E+01	3.221E+01	2.984E+01
3.000	8.923E+01	4.053E+01	3.398E+01	3.592E+01	3.657E+01	3.491E+01	3.141E+01	2.912E+01
4.000	8.115E+01	3.730E+01	3.163E+01	3.370E+01	3.426E+01	3.283E+01	2.975E+01	2.760E+01
5.000	7.443E+01	3.447E+01	2.948E+01	3.160E+01	3.212E+01	3.087E+01	2.812E+01	2.611E+01
6.000	6.878E+01	3.202E+01	2.756E+01	2.969E+01	3.017E+01	2.906E+01	2.659E+01	2.472E+01
7.000	6.397E+01	2.988E+01	2.585E+01	2.795E+01	2.840E+01	2.742E+01	2.518E+01	2.344E+01
8.000	5.981E+01	2.801E+01	2.431E+01	2.638E+01	2.682E+01	2.593E+01	2.389E+01	2.227E+01
9.000	5.619E+01	2.635E+01	2.294E+01	2.496E+01	2.538E+01	2.457E+01	2.270E+01	2.120E+01
10.00	5.300E+01	2.489E+01	2.171E+01	2.368E+01	2.407E+01	2.333E+01	2.161E+01	2.020E+01
15.00	4.143E+01	1.948E+01	1.705E+01	1.874E+01	1.907E+01	1.856E+01	1.733E+01	1.629E+01
20.00	3.416E+01	1.603E+01	1.402E+01	1.545E+01	1.573E+01	1.535E+01	1.440E+01	1.359E+01
25.00	2.915E+01	1.365E+01	1.190E+01	1.313E+01	1.337E+01	1.306E+01	1.229E+01	1.163E+01
30.00	2.550E+01	1.192E+01	1.035E+01	1.142E+01	1.163E+01	1.137E+01	1.072E+01	1.017E+01
40.00	2.053E+01	9.560E+00	8.254E+00	9.087E+00	9.250E+00	9.051E+00	8.553E+00	8.131E+00
50.00	1.731E+01	8.040E+00	6.906E+00	7.588E+00	7.718E+00	7.553E+00	7.146E+00	6.803E+00
60.00	1.505E+01	6.981E+00	5.972E+00	6.550E+00	6.657E+00	6.516E+00	6.167E+00	5.876E+00
70.00	1.338E+01	6.200E+00	5.289E+00	5.792E+00	5.883E+00	5.757E+00	5.451E+00	5.196E+00
80.00	1.209E+01	5.601E+00	4.768E+00	5.215E+00	5.293E+00	5.180E+00	4.906E+00	4.677E+00
90.00	1.107E+01	5.126E+00	4.357E+00	4.761E+00	4.831E+00	4.727E+00	4.478E+00	4.270E+00
100.0	1.024E+01	4.741E+00	4.025E+00	4.396E+00	4.458E+00	4.362E+00	4.133E+00	3.941E+00
150.0	7.662E+00	3.553E+00	3.010E+00	3.282E+00	3.323E+00	3.253E+00	3.084E+00	2.942E+00
200.0	6.326E+00	2.939E+00	2.489E+00	2.714E+00	2.746E+00	2.688E+00	2.552E+00	2.434E+00
250.0	5.510E+00	2.563E+00	2.172E+00	2.369E+00	2.396E+00	2.346E+00	2.229E+00	2.127E+00
300.0	4.960E+00	2.310E+00	1.960E+00	2.137E+00	2.161E+00	2.117E+00	2.012E+00	1.921E+00
400.0	4.272E+00	1.994E+00	1.693E+00	1.848E+00	1.868E+00	1.831E+00	1.742E+00	1.664E+00
500.0	3.864E+00	1.806E+00	1.535E+00	1.677E+00	1.694E+00	1.661E+00	1.582E+00	1.512E+00
600.0	3.597E+00	1.684E+00	1.432E+00	1.565E+00	1.581E+00	1.551E+00	1.479E+00	1.413E+00
700.0	3.412E+00	1.599E+00	1.361E+00	1.488E+00	1.503E+00	1.475E+00	1.407E+00	1.345E+00
800.0	3.279E+00	1.538E+00	1.310E+00	1.433E+00	1.447E+00	1.420E+00	1.356E+00	1.296E+00
900.0	3.180E+00	1.493E+00	1.272E+00	1.392E+00	1.405E+00	1.380E+00	1.318E+00	1.260E+00
1000.	3.104E+00	1.458E+00	1.243E+00	1.361E+00	1.374E+00	1.349E+00	1.289E+00	1.233E+00

Ion: Iron								
Material	Si	Ar	Ti	Fe	Ni	Cu	Ge	Kr
(E/A_1) / MeV	$(-\mathrm{d}E/\rho\mathrm{d}\ell)$ / MeV cm^2 mg^{-1}							
0.025	5.179E+00	4.640E+00	3.463E+00	2.849E+00	2.634E+00	2.375E+00	2.136E+00	2.888E+00
0.030	5.792E+00	5.184E+00	3.857E+00	3.182E+00	2.937E+00	2.651E+00	2.387E+00	3.222E+00
0.040	6.906E+00	6.169E+00	4.576E+00	3.799E+00	3.504E+00	3.165E+00	2.854E+00	3.838E+00
0.050	7.894E+00	7.042E+00	5.231E+00	4.367E+00	4.033E+00	3.642E+00	3.284E+00	4.386E+00
0.060	8.779E+00	7.836E+00	5.840E+00	4.900E+00	4.536E+00	4.090E+00	3.678E+00	4.875E+00
0.070	9.583E+00	8.580E+00	6.417E+00	5.406E+00	5.017E+00	4.517E+00	4.043E+00	5.326E+00
0.080	1.033E+01	9.290E+00	6.971E+00	5.896E+00	5.480E+00	4.929E+00	4.391E+00	5.754E+00
0.090	1.105E+01	9.972E+00	7.510E+00	6.375E+00	5.930E+00	5.331E+00	4.730E+00	6.164E+00
0.100	1.176E+01	1.063E+01	8.037E+00	6.847E+00	6.372E+00	5.729E+00	5.064E+00	6.563E+00
0.150	1.509E+01	1.362E+01	1.056E+01	9.117E+00	8.530E+00	7.707E+00	6.677E+00	8.427E+00
0.200	1.774E+01	1.604E+01	1.286E+01	1.120E+01	1.058E+01	9.605E+00	8.224E+00	9.958E+00
0.250	1.979E+01	1.796E+01	1.484E+01	1.305E+01	1.247E+01	1.135E+01	9.597E+00	1.119E+01
0.300	2.143E+01	1.949E+01	1.650E+01	1.461E+01	1.412E+01	1.289E+01	1.079E+01	1.221E+01
0.400	2.390E+01	2.168E+01	1.899E+01	1.702E+01	1.669E+01	1.528E+01	1.278E+01	1.383E+01
0.500	2.572E+01	2.315E+01	2.064E+01	1.875E+01	1.851E+01	1.699E+01	1.434E+01	1.508E+01
0.600	2.711E+01	2.417E+01	2.176E+01	2.000E+01	1.983E+01	1.823E+01	1.557E+01	1.608E+01
0.700	2.818E+01	2.491E+01	2.255E+01	2.088E+01	2.078E+01	1.915E+01	1.651E+01	1.689E+01
0.800	2.901E+01	2.545E+01	2.312E+01	2.151E+01	2.147E+01	1.982E+01	1.723E+01	1.753E+01
0.900	2.964E+01	2.586E+01	2.353E+01	2.197E+01	2.197E+01	2.031E+01	1.777E+01	1.802E+01
1.000	3.011E+01	2.617E+01	2.385E+01	2.230E+01	2.234E+01	2.066E+01	1.819E+01	1.840E+01
1.500	3.100E+01	2.681E+01	2.452E+01	2.301E+01	2.310E+01	2.143E+01	1.913E+01	1.922E+01
2.000	3.079E+01	2.669E+01	2.450E+01	2.302E+01	2.311E+01	2.148E+01	1.925E+01	1.926E+01
2.500	3.022E+01	2.625E+01	2.420E+01	2.277E+01	2.285E+01	2.125E+01	1.910E+01	1.903E+01
3.000	2.950E+01	2.567E+01	2.377E+01	2.239E+01	2.247E+01	2.092E+01	1.883E+01	1.870E+01
4.000	2.798E+01	2.438E+01	2.273E+01	2.148E+01	2.156E+01	2.010E+01	1.814E+01	1.792E+01
5.000	2.650E+01	2.311E+01	2.165E+01	2.052E+01	2.061E+01	1.924E+01	1.740E+01	1.712E+01
6.000	2.511E+01	2.191E+01	2.060E+01	1.959E+01	1.969E+01	1.839E+01	1.667E+01	1.635E+01
7.000	2.382E+01	2.081E+01	1.962E+01	1.870E+01	1.881E+01	1.759E+01	1.597E+01	1.563E+01
8.000	2.264E+01	1.979E+01	1.870E+01	1.786E+01	1.798E+01	1.683E+01	1.531E+01	1.496E+01
9.000	2.155E+01	1.886E+01	1.786E+01	1.709E+01	1.721E+01	1.612E+01	1.469E+01	1.433E+01
10.00	2.056E+01	1.801E+01	1.708E+01	1.637E+01	1.650E+01	1.545E+01	1.410E+01	1.375E+01
15.00	1.661E+01	1.461E+01	1.396E+01	1.345E+01	1.359E+01	1.276E+01	1.171E+01	1.139E+01
20.00	1.387E+01	1.225E+01	1.175E+01	1.138E+01	1.151E+01	1.082E+01	9.967E+00	9.689E+00
25.00	1.189E+01	1.052E+01	1.014E+01	9.844E+00	9.971E+00	9.381E+00	8.666E+00	8.425E+00
30.00	1.039E+01	9.221E+00	8.910E+00	8.673E+00	8.793E+00	8.279E+00	7.664E+00	7.454E+00
40.00	8.322E+00	7.405E+00	7.185E+00	7.018E+00	7.127E+00	6.716E+00	6.237E+00	6.071E+00
50.00	6.967E+00	6.211E+00	6.043E+00	5.918E+00	6.015E+00	5.673E+00	5.279E+00	5.143E+00
60.00	6.020E+00	5.374E+00	5.239E+00	5.139E+00	5.227E+00	4.933E+00	4.597E+00	4.482E+00
70.00	5.324E+00	4.757E+00	4.644E+00	4.562E+00	4.643E+00	4.383E+00	4.090E+00	3.990E+00
80.00	4.794E+00	4.286E+00	4.189E+00	4.119E+00	4.193E+00	3.963E+00	3.699E+00	3.610E+00
90.00	4.377E+00	3.914E+00	3.829E+00	3.768E+00	3.838E+00	3.625E+00	3.389E+00	3.309E+00
100.0	4.040E+00	3.615E+00	3.538E+00	3.484E+00	3.550E+00	3.354E+00	3.137E+00	3.064E+00
150.0	3.017E+00	2.701E+00	2.651E+00	2.615E+00	2.666E+00	2.521E+00	2.363E+00	2.309E+00
200.0	2.497E+00	2.236E+00	2.198E+00	2.171E+00	2.214E+00	2.094E+00	1.966E+00	1.921E+00
250.0	2.182E+00	1.955E+00	1.923E+00	1.901E+00	1.939E+00	1.835E+00	1.723E+00	1.685E+00
300.0	1.971E+00	1.766E+00	1.738E+00	1.720E+00	1.754E+00	1.660E+00	1.561E+00	1.526E+00
400.0	1.708E+00	1.530E+00	1.508E+00	1.493E+00	1.524E+00	1.443E+00	1.358E+00	1.327E+00
500.0	1.552E+00	1.391E+00	1.372E+00	1.360E+00	1.387E+00	1.314E+00	1.237E+00	1.209E+00
600.0	1.451E+00	1.301E+00	1.284E+00	1.273E+00	1.299E+00	1.231E+00	1.160E+00	1.133E+00
700.0	1.381E+00	1.239E+00	1.223E+00	1.213E+00	1.238E+00	1.173E+00	1.106E+00	1.081E+00
800.0	1.331E+00	1.194E+00	1.180E+00	1.171E+00	1.195E+00	1.132E+00	1.068E+00	1.044E+00
900.0	1.295E+00	1.161E+00	1.148E+00	1.139E+00	1.163E+00	1.102E+00	1.040E+00	1.016E+00
1000.	1.266E+00	1.136E+00	1.123E+00	1.115E+00	1.138E+00	1.079E+00	1.018E+00	9.949E−01

6.7. TABLES: ELECTRONIC STOPPING FORCE FOR SIXTEEN IONS IN COMPOUND MATERIALS

Material: A-150 tissue-equivalent plastic

Ion	Li	Be	B	C	N	O	F	Ne
(E/A_1) / MeV				$(-\mathrm{d}E/\rho\mathrm{d}\ell)$ / MeV cm^2 mg^{-1}				
0.025	2.748E+00	3.391E+00	3.899E+00	4.300E+00	4.670E+00	4.999E+00	5.251E+00	5.481E+00
0.030	2.992E+00	3.718E+00	4.300E+00	4.767E+00	5.188E+00	5.564E+00	5.856E+00	6.119E+00
0.040	3.386E+00	4.275E+00	5.003E+00	5.598E+00	6.120E+00	6.589E+00	6.959E+00	7.290E+00
0.050	3.674E+00	4.722E+00	5.593E+00	6.316E+00	6.941E+00	7.500E+00	7.948E+00	8.347E+00
0.060	3.877E+00	5.070E+00	6.081E+00	6.933E+00	7.664E+00	8.319E+00	8.846E+00	9.312E+00
0.070	4.016E+00	5.333E+00	6.474E+00	7.453E+00	8.295E+00	9.049E+00	9.660E+00	1.019E+01
0.080	4.108E+00	5.527E+00	6.784E+00	7.883E+00	8.836E+00	9.693E+00	1.039E+01	1.100E+01
0.090	4.166E+00	5.668E+00	7.025E+00	8.233E+00	9.293E+00	1.025E+01	1.104E+01	1.174E+01
0.100	4.200E+00	5.769E+00	7.210E+00	8.514E+00	9.673E+00	1.073E+01	1.161E+01	1.239E+01
0.150	4.186E+00	5.944E+00	7.643E+00	9.262E+00	1.077E+01	1.220E+01	1.346E+01	1.462E+01
0.200	4.059E+00	5.889E+00	7.704E+00	9.476E+00	1.117E+01	1.282E+01	1.431E+01	1.571E+01
0.250	3.906E+00	5.762E+00	7.633E+00	9.487E+00	1.129E+01	1.307E+01	1.469E+01	1.625E+01
0.300	3.751E+00	5.610E+00	7.509E+00	9.409E+00	1.128E+01	1.314E+01	1.485E+01	1.650E+01
0.400	3.458E+00	5.291E+00	7.202E+00	9.143E+00	1.108E+01	1.304E+01	1.485E+01	1.661E+01
0.500	3.200E+00	4.986E+00	6.881E+00	8.827E+00	1.079E+01	1.279E+01	1.465E+01	1.648E+01
0.600	2.974E+00	4.706E+00	6.570E+00	8.504E+00	1.048E+01	1.250E+01	1.438E+01	1.624E+01
0.700	2.777E+00	4.450E+00	6.277E+00	8.189E+00	1.015E+01	1.218E+01	1.407E+01	1.595E+01
0.800	2.603E+00	4.219E+00	6.004E+00	7.888E+00	9.843E+00	1.186E+01	1.375E+01	1.564E+01
0.900	2.449E+00	4.008E+00	5.750E+00	7.603E+00	9.537E+00	1.154E+01	1.343E+01	1.532E+01
1.000	2.313E+00	3.817E+00	5.515E+00	7.333E+00	9.243E+00	1.123E+01	1.311E+01	1.500E+01
1.500	1.807E+00	3.075E+00	4.562E+00	6.205E+00	7.973E+00	9.852E+00	1.165E+01	1.347E+01
2.000	1.485E+00	2.571E+00	3.881E+00	5.361E+00	6.983E+00	8.734E+00	1.044E+01	1.217E+01
2.500	1.263E+00	2.210E+00	3.373E+00	4.712E+00	6.200E+00	7.828E+00	9.434E+00	1.108E+01
3.000	1.100E+00	1.938E+00	2.982E+00	4.200E+00	5.569E+00	7.082E+00	8.594E+00	1.015E+01
4.000	8.801E−01	1.560E+00	2.423E+00	3.448E+00	4.621E+00	5.938E+00	7.282E+00	8.689E+00
5.000	7.372E−01	1.310E+00	2.043E+00	2.925E+00	3.946E+00	5.105E+00	6.309E+00	7.581E+00
6.000	6.368E−01	1.132E+00	1.769E+00	2.542E+00	3.444E+00	4.475E+00	5.562E+00	6.721E+00
7.000	5.623E−01	1.000E+00	1.564E+00	2.251E+00	3.057E+00	3.984E+00	4.973E+00	6.034E+00
8.000	5.046E−01	8.972E−01	1.403E+00	2.022E+00	2.751E+00	3.591E+00	4.497E+00	5.475E+00
9.000	4.586E−01	8.151E−01	1.275E+00	1.837E+00	2.502E+00	3.271E+00	4.106E+00	5.012E+00
10.00	4.209E−01	7.480E−01	1.169E+00	1.686E+00	2.297E+00	3.005E+00	3.779E+00	4.623E+00
15.00	3.023E−01	5.369E−01	8.387E−01	1.208E+00	1.646E+00	2.154E+00	2.721E+00	3.348E+00
20.00	2.390E−01	4.244E−01	6.626E−01	9.538E−01	1.298E+00	1.698E+00	2.147E+00	2.647E+00
25.00	1.991E−01	3.537E−01	5.522E−01	7.947E−01	1.081E+00	1.413E+00	1.787E+00	2.204E+00
30.00	1.716E−01	3.050E−01	4.761E−01	6.851E−01	9.321E−01	1.217E+00	1.540E+00	1.899E+00
40.00	1.360E−01	2.417E−01	3.774E−01	5.431E−01	7.388E−01	9.646E−01	1.220E+00	1.505E+00
50.00	1.137E−01	2.021E−01	3.157E−01	4.545E−01	6.183E−01	8.072E−01	1.021E+00	1.259E+00
60.00	9.844E−02	1.750E−01	2.734E−01	3.935E−01	5.355E−01	6.992E−01	8.845E−01	1.091E+00
70.00	8.726E−02	1.551E−01	2.424E−01	3.490E−01	4.749E−01	6.201E−01	7.846E−01	9.683E−01
80.00	7.872E−02	1.399E−01	2.187E−01	3.149E−01	4.286E−01	5.597E−01	7.083E−01	8.742E−01
90.00	7.197E−02	1.279E−01	2.000E−01	2.880E−01	3.920E−01	5.120E−01	6.479E−01	7.997E−01
100.0	6.650E−02	1.182E−01	1.848E−01	2.661E−01	3.623E−01	4.732E−01	5.989E−01	7.393E−01
150.0	4.965E−02	8.832E−02	1.380E−01	1.988E−01	2.708E−01	3.538E−01	4.479E−01	5.531E−01
200.0	4.096E−02	7.286E−02	1.139E−01	1.641E−01	2.235E−01	2.920E−01	3.698E−01	4.567E−01
250.0	3.566E−02	6.344E−02	9.919E−02	1.429E−01	1.946E−01	2.544E−01	3.221E−01	3.979E−01
300.0	3.210E−02	5.711E−02	8.930E−02	1.286E−01	1.752E−01	2.290E−01	2.901E−01	3.584E−01
400.0	2.765E−02	4.920E−02	7.695E−02	1.108E−01	1.510E−01	1.974E−01	2.500E−01	3.089E−01
500.0	2.502E−02	4.452E−02	6.963E−02	1.003E−01	1.367E−01	1.787E−01	2.263E−01	2.797E−01
600.0	2.331E−02	4.148E−02	6.488E−02	9.351E−02	1.274E−01	1.665E−01	2.109E−01	2.606E−01
700.0	2.213E−02	3.939E−02	6.160E−02	8.879E−02	1.209E−01	1.581E−01	2.003E−01	2.475E−01
800.0	2.129E−02	3.788E−02	5.925E−02	8.540E−02	1.163E−01	1.521E−01	1.927E−01	2.381E−01
900.0	2.066E−02	3.677E−02	5.751E−02	8.290E−02	1.129E−01	1.476E−01	1.870E−01	2.311E−01
1000.	2.018E−02	3.592E−02	5.618E−02	8.098E−02	1.103E−01	1.442E−01	1.827E−01	2.258E−01

Material: A-150 tissue-equivalent plastic

Ion	Na	Mg	Al	Si	P	S	Cl	Ar
(E/A_1) / MeV				$(-\mathrm{d}E/\rho\mathrm{d}\ell)$ / MeV cm^2 mg^{-1}				
0.025	5.684E+00	5.906E+00	6.121E+00	6.335E+00	6.589E+00	6.793E+00	7.055E+00	7.196E+00
0.030	6.355E+00	6.584E+00	6.817E+00	7.047E+00	7.318E+00	7.544E+00	7.821E+00	7.978E+00
0.040	7.597E+00	7.845E+00	8.116E+00	8.378E+00	8.682E+00	8.947E+00	9.248E+00	9.430E+00
0.050	8.728E+00	9.005E+00	9.314E+00	9.610E+00	9.948E+00	1.025E+01	1.057E+01	1.077E+01
0.060	9.768E+00	1.007E+01	1.042E+01	1.075E+01	1.113E+01	1.147E+01	1.182E+01	1.204E+01
0.070	1.073E+01	1.107E+01	1.146E+01	1.183E+01	1.224E+01	1.261E+01	1.299E+01	1.324E+01
0.080	1.162E+01	1.200E+01	1.244E+01	1.284E+01	1.328E+01	1.369E+01	1.410E+01	1.437E+01
0.090	1.244E+01	1.287E+01	1.335E+01	1.380E+01	1.427E+01	1.472E+01	1.515E+01	1.544E+01
0.100	1.319E+01	1.366E+01	1.420E+01	1.469E+01	1.521E+01	1.570E+01	1.616E+01	1.647E+01
0.150	1.586E+01	1.663E+01	1.749E+01	1.827E+01	1.905E+01	1.979E+01	2.046E+01	2.095E+01
0.200	1.728E+01	1.827E+01	1.941E+01	2.045E+01	2.150E+01	2.250E+01	2.342E+01	2.414E+01
0.250	1.804E+01	1.918E+01	2.051E+01	2.174E+01	2.300E+01	2.422E+01	2.534E+01	2.626E+01
0.300	1.846E+01	1.969E+01	2.116E+01	2.253E+01	2.394E+01	2.531E+01	2.659E+01	2.767E+01
0.400	1.878E+01	2.011E+01	2.176E+01	2.331E+01	2.493E+01	2.652E+01	2.801E+01	2.929E+01
0.500	1.878E+01	2.015E+01	2.190E+01	2.357E+01	2.531E+01	2.705E+01	2.867E+01	3.009E+01
0.600	1.863E+01	2.001E+01	2.184E+01	2.357E+01	2.541E+01	2.724E+01	2.895E+01	3.046E+01
0.700	1.841E+01	1.979E+01	2.165E+01	2.344E+01	2.534E+01	2.724E+01	2.902E+01	3.059E+01
0.800	1.813E+01	1.951E+01	2.141E+01	2.323E+01	2.517E+01	2.712E+01	2.895E+01	3.057E+01
0.900	1.784E+01	1.921E+01	2.112E+01	2.296E+01	2.494E+01	2.693E+01	2.880E+01	3.045E+01
1.000	1.754E+01	1.890E+01	2.082E+01	2.267E+01	2.468E+01	2.669E+01	2.859E+01	3.027E+01
1.500	1.601E+01	1.731E+01	1.923E+01	2.109E+01	2.314E+01	2.522E+01	2.718E+01	2.891E+01
2.000	1.462E+01	1.588E+01	1.775E+01	1.958E+01	2.160E+01	2.367E+01	2.563E+01	2.736E+01
2.500	1.342E+01	1.463E+01	1.644E+01	1.822E+01	2.019E+01	2.223E+01	2.415E+01	2.587E+01
3.000	1.238E+01	1.355E+01	1.529E+01	1.701E+01	1.893E+01	2.092E+01	2.280E+01	2.448E+01
4.000	1.069E+01	1.178E+01	1.340E+01	1.500E+01	1.680E+01	1.867E+01	2.046E+01	2.207E+01
5.000	9.381E+00	1.041E+01	1.191E+01	1.340E+01	1.508E+01	1.684E+01	1.853E+01	2.006E+01
6.000	8.343E+00	9.323E+00	1.071E+01	1.210E+01	1.367E+01	1.532E+01	1.692E+01	1.838E+01
7.000	7.504E+00	8.435E+00	9.726E+00	1.103E+01	1.250E+01	1.404E+01	1.555E+01	1.694E+01
8.000	6.815E+00	7.700E+00	8.906E+00	1.013E+01	1.150E+01	1.296E+01	1.439E+01	1.572E+01
9.000	6.239E+00	7.083E+00	8.212E+00	9.368E+00	1.066E+01	1.203E+01	1.338E+01	1.465E+01
10.00	5.753E+00	6.558E+00	7.619E+00	8.711E+00	9.930E+00	1.122E+01	1.251E+01	1.372E+01
15.00	4.145E+00	4.800E+00	5.610E+00	6.458E+00	7.399E+00	8.408E+00	9.426E+00	1.041E+01
20.00	3.258E+00	3.808E+00	4.462E+00	5.154E+00	5.916E+00	6.737E+00	7.577E+00	8.411E+00
25.00	2.701E+00	3.175E+00	3.724E+00	4.309E+00	4.950E+00	5.640E+00	6.354E+00	7.075E+00
30.00	2.319E+00	2.736E+00	3.211E+00	3.718E+00	4.272E+00	4.869E+00	5.491E+00	6.125E+00
40.00	1.829E+00	2.167E+00	2.543E+00	2.948E+00	3.386E+00	3.858E+00	4.354E+00	4.868E+00
50.00	1.528E+00	1.813E+00	2.128E+00	2.466E+00	2.833E+00	3.226E+00	3.642E+00	4.076E+00
60.00	1.322E+00	1.570E+00	1.843E+00	2.136E+00	2.453E+00	2.793E+00	3.153E+00	3.531E+00
70.00	1.172E+00	1.393E+00	1.635E+00	1.896E+00	2.176E+00	2.477E+00	2.797E+00	3.133E+00
80.00	1.058E+00	1.258E+00	1.476E+00	1.711E+00	1.965E+00	2.236E+00	2.525E+00	2.829E+00
90.00	9.679E−01	1.151E+00	1.350E+00	1.566E+00	1.798E+00	2.046E+00	2.310E+00	2.589E+00
100.0	8.948E−01	1.064E+00	1.249E+00	1.448E+00	1.662E+00	1.892E+00	2.136E+00	2.394E+00
150.0	6.694E−01	7.968E−01	9.353E−01	1.084E+00	1.245E+00	1.417E+00	1.600E+00	1.794E+00
200.0	5.529E−01	6.582E−01	7.728E−01	8.966E−01	1.029E+00	1.171E+00	1.323E+00	1.484E+00
250.0	4.817E−01	5.736E−01	6.736E−01	7.816E−01	8.976E−01	1.021E+00	1.154E+00	1.294E+00
300.0	4.339E−01	5.167E−01	6.068E−01	7.042E−01	8.088E−01	9.208E−01	1.040E+00	1.166E+00
400.0	3.741E−01	4.456E−01	5.233E−01	6.074E−01	6.977E−01	7.945E−01	8.975E−01	1.006E+00
500.0	3.387E−01	4.034E−01	4.738E−01	5.500E−01	6.319E−01	7.196E−01	8.130E−01	9.122E−01
600.0	3.157E−01	3.760E−01	4.417E−01	5.127E−01	5.891E−01	6.708E−01	7.580E−01	8.505E−01
700.0	2.998E−01	3.571E−01	4.195E−01	4.870E−01	5.595E−01	6.372E−01	7.200E−01	8.079E−01
800.0	2.884E−01	3.435E−01	4.035E−01	4.684E−01	5.383E−01	6.130E−01	6.927E−01	7.773E−01
900.0	2.799E−01	3.335E−01	3.917E−01	4.548E−01	5.226E−01	5.951E−01	6.725E−01	7.547E−01
1000.	2.735E−01	3.258E−01	3.827E−01	4.443E−01	5.106E−01	5.815E−01	6.571E−01	7.374E−01

Material: Adipose tissue (ICRP)

Ion	Li	Be	B	C	N	O	F	Ne
(E/A_1) / MeV				$(-\mathrm{d}E/\rho\mathrm{d}\ell)$ / MeV cm^2 mg^{-1}				
0.025	2.852E+00	3.530E+00	4.062E+00	4.476E+00	4.857E+00	5.192E+00	5.447E+00	5.677E+00
0.030	3.097E+00	3.861E+00	4.473E+00	4.958E+00	5.394E+00	5.778E+00	6.073E+00	6.338E+00
0.040	3.490E+00	4.421E+00	5.185E+00	5.807E+00	6.352E+00	6.836E+00	7.214E+00	7.550E+00
0.050	3.778E+00	4.867E+00	5.776E+00	6.532E+00	7.185E+00	7.768E+00	8.232E+00	8.641E+00
0.060	3.983E+00	5.214E+00	6.262E+00	7.149E+00	7.913E+00	8.596E+00	9.145E+00	9.630E+00
0.070	4.125E+00	5.479E+00	6.655E+00	7.668E+00	8.544E+00	9.330E+00	9.967E+00	1.052E+01
0.080	4.221E+00	5.677E+00	6.968E+00	8.099E+00	9.085E+00	9.974E+00	1.070E+01	1.134E+01
0.090	4.283E+00	5.823E+00	7.213E+00	8.452E+00	9.543E+00	1.053E+01	1.135E+01	1.207E+01
0.100	4.321E+00	5.929E+00	7.405E+00	8.739E+00	9.927E+00	1.101E+01	1.192E+01	1.273E+01
0.150	4.313E+00	6.119E+00	7.862E+00	9.519E+00	1.106E+01	1.252E+01	1.381E+01	1.499E+01
0.200	4.182E+00	6.064E+00	7.928E+00	9.746E+00	1.148E+01	1.317E+01	1.469E+01	1.612E+01
0.250	4.022E+00	5.930E+00	7.854E+00	9.757E+00	1.161E+01	1.343E+01	1.509E+01	1.668E+01
0.300	3.859E+00	5.769E+00	7.721E+00	9.672E+00	1.159E+01	1.350E+01	1.525E+01	1.695E+01
0.400	3.553E+00	5.434E+00	7.396E+00	9.386E+00	1.138E+01	1.338E+01	1.524E+01	1.705E+01
0.500	3.284E+00	5.115E+00	7.057E+00	9.051E+00	1.107E+01	1.311E+01	1.502E+01	1.690E+01
0.600	3.050E+00	4.822E+00	6.731E+00	8.710E+00	1.073E+01	1.279E+01	1.473E+01	1.664E+01
0.700	2.845E+00	4.557E+00	6.426E+00	8.381E+00	1.039E+01	1.246E+01	1.440E+01	1.633E+01
0.800	2.665E+00	4.317E+00	6.142E+00	8.067E+00	1.006E+01	1.212E+01	1.406E+01	1.600E+01
0.900	2.507E+00	4.100E+00	5.879E+00	7.770E+00	9.744E+00	1.179E+01	1.373E+01	1.566E+01
1.000	2.366E+00	3.902E+00	5.635E+00	7.491E+00	9.439E+00	1.147E+01	1.339E+01	1.532E+01
1.500	1.846E+00	3.139E+00	4.655E+00	6.329E+00	8.128E+00	1.004E+01	1.188E+01	1.374E+01
2.000	1.516E+00	2.623E+00	3.957E+00	5.464E+00	7.114E+00	8.895E+00	1.063E+01	1.240E+01
2.500	1.289E+00	2.254E+00	3.438E+00	4.801E+00	6.314E+00	7.969E+00	9.606E+00	1.128E+01
3.000	1.123E+00	1.977E+00	3.040E+00	4.279E+00	5.672E+00	7.209E+00	8.750E+00	1.034E+01
4.000	8.980E−01	1.591E+00	2.469E+00	3.512E+00	4.706E+00	6.044E+00	7.413E+00	8.848E+00
5.000	7.521E−01	1.336E+00	2.082E+00	2.980E+00	4.019E+00	5.197E+00	6.423E+00	7.721E+00
6.000	6.496E−01	1.155E+00	1.804E+00	2.590E+00	3.508E+00	4.557E+00	5.664E+00	6.845E+00
7.000	5.735E−01	1.019E+00	1.594E+00	2.294E+00	3.115E+00	4.057E+00	5.064E+00	6.146E+00
8.000	5.147E−01	9.150E−01	1.431E+00	2.061E+00	2.803E+00	3.658E+00	4.581E+00	5.578E+00
9.000	4.677E−01	8.313E−01	1.300E+00	1.873E+00	2.550E+00	3.332E+00	4.183E+00	5.107E+00
10.00	4.292E−01	7.627E−01	1.192E+00	1.718E+00	2.341E+00	3.062E+00	3.850E+00	4.711E+00
15.00	3.082E−01	5.474E−01	8.550E−01	1.231E+00	1.678E+00	2.196E+00	2.774E+00	3.412E+00
20.00	2.436E−01	4.326E−01	6.754E−01	9.723E−01	1.323E+00	1.731E+00	2.189E+00	2.698E+00
25.00	2.030E−01	3.606E−01	5.629E−01	8.100E−01	1.102E+00	1.440E+00	1.822E+00	2.247E+00
30.00	1.749E−01	3.108E−01	4.853E−01	6.983E−01	9.500E−01	1.240E+00	1.569E+00	1.936E+00
40.00	1.385E−01	2.463E−01	3.846E−01	5.535E−01	7.529E−01	9.830E−01	1.243E+00	1.534E+00
50.00	1.158E−01	2.059E−01	3.217E−01	4.631E−01	6.300E−01	8.225E−01	1.040E+00	1.283E+00
60.00	1.002E−01	1.783E−01	2.785E−01	4.010E−01	5.456E−01	7.123E−01	9.012E−01	1.112E+00
70.00	8.890E−02	1.580E−01	2.469E−01	3.555E−01	4.838E−01	6.318E−01	7.994E−01	9.865E−01
80.00	8.019E−02	1.425E−01	2.228E−01	3.208E−01	4.366E−01	5.702E−01	7.215E−01	8.905E−01
90.00	7.331E−02	1.303E−01	2.037E−01	2.934E−01	3.993E−01	5.215E−01	6.600E−01	8.147E−01
100.0	6.774E−02	1.204E−01	1.882E−01	2.711E−01	3.690E−01	4.820E−01	6.101E−01	7.531E−01
150.0	5.057E−02	8.995E−02	1.406E−01	2.025E−01	2.758E−01	3.603E−01	4.562E−01	5.633E−01
200.0	4.171E−02	7.420E−02	1.160E−01	1.671E−01	2.276E−01	2.974E−01	3.766E−01	4.651E−01
250.0	3.631E−02	6.460E−02	1.010E−01	1.455E−01	1.982E−01	2.590E−01	3.280E−01	4.052E−01
300.0	3.269E−02	5.815E−02	9.093E−02	1.310E−01	1.784E−01	2.332E−01	2.954E−01	3.649E−01
400.0	2.816E−02	5.010E−02	7.834E−02	1.129E−01	1.538E−01	2.010E−01	2.546E−01	3.146E−01
500.0	2.547E−02	4.533E−02	7.089E−02	1.021E−01	1.391E−01	1.819E−01	2.304E−01	2.847E−01
600.0	2.373E−02	4.223E−02	6.605E−02	9.520E−02	1.297E−01	1.695E−01	2.147E−01	2.653E−01
700.0	2.253E−02	4.010E−02	6.271E−02	9.039E−02	1.231E−01	1.609E−01	2.039E−01	2.520E−01
800.0	2.167E−02	3.857E−02	6.032E−02	8.694E−02	1.184E−01	1.548E−01	1.961E−01	2.424E−01
900.0	2.103E−02	3.743E−02	5.854E−02	8.438E−02	1.149E−01	1.503E−01	1.904E−01	2.353E−01
1000.	2.055E−02	3.656E−02	5.719E−02	8.243E−02	1.123E−01	1.468E−01	1.860E−01	2.298E−01

Material: Adipose tissue (ICRP)

Ion	Na	Mg	Al	Si	P	S	Cl	Ar
(E/A_1) / MeV				$(-\mathrm{d}E/\rho\mathrm{d}\ell)$ / MeV cm^2 mg^{-1}				
0.025	5.885E+00	6.112E+00	6.332E+00	6.551E+00	6.812E+00	7.022E+00	7.291E+00	7.435E+00
0.030	6.579E+00	6.813E+00	7.050E+00	7.286E+00	7.564E+00	7.795E+00	8.078E+00	8.239E+00
0.040	7.866E+00	8.118E+00	8.393E+00	8.660E+00	8.970E+00	9.240E+00	9.546E+00	9.732E+00
0.050	9.036E+00	9.318E+00	9.633E+00	9.935E+00	1.027E+01	1.058E+01	1.091E+01	1.111E+01
0.060	1.010E+01	1.042E+01	1.078E+01	1.112E+01	1.150E+01	1.184E+01	1.220E+01	1.242E+01
0.070	1.108E+01	1.144E+01	1.185E+01	1.223E+01	1.264E+01	1.302E+01	1.341E+01	1.366E+01
0.080	1.199E+01	1.239E+01	1.284E+01	1.326E+01	1.372E+01	1.414E+01	1.455E+01	1.483E+01
0.090	1.281E+01	1.326E+01	1.377E+01	1.423E+01	1.473E+01	1.519E+01	1.564E+01	1.594E+01
0.100	1.356E+01	1.406E+01	1.463E+01	1.514E+01	1.568E+01	1.619E+01	1.667E+01	1.699E+01
0.150	1.627E+01	1.705E+01	1.794E+01	1.874E+01	1.954E+01	2.031E+01	2.100E+01	2.152E+01
0.200	1.773E+01	1.874E+01	1.990E+01	2.097E+01	2.204E+01	2.306E+01	2.400E+01	2.474E+01
0.250	1.853E+01	1.968E+01	2.105E+01	2.231E+01	2.359E+01	2.483E+01	2.598E+01	2.692E+01
0.300	1.896E+01	2.021E+01	2.172E+01	2.313E+01	2.457E+01	2.598E+01	2.728E+01	2.838E+01
0.400	1.928E+01	2.064E+01	2.233E+01	2.393E+01	2.559E+01	2.722E+01	2.874E+01	3.007E+01
0.500	1.927E+01	2.067E+01	2.247E+01	2.418E+01	2.597E+01	2.775E+01	2.941E+01	3.087E+01
0.600	1.910E+01	2.051E+01	2.238E+01	2.417E+01	2.605E+01	2.792E+01	2.968E+01	3.124E+01
0.700	1.885E+01	2.027E+01	2.218E+01	2.402E+01	2.596E+01	2.790E+01	2.973E+01	3.135E+01
0.800	1.855E+01	1.997E+01	2.191E+01	2.378E+01	2.577E+01	2.777E+01	2.964E+01	3.131E+01
0.900	1.824E+01	1.965E+01	2.161E+01	2.350E+01	2.552E+01	2.755E+01	2.947E+01	3.117E+01
1.000	1.792E+01	1.931E+01	2.129E+01	2.319E+01	2.523E+01	2.730E+01	2.924E+01	3.097E+01
1.500	1.633E+01	1.766E+01	1.963E+01	2.153E+01	2.362E+01	2.573E+01	2.774E+01	2.952E+01
2.000	1.490E+01	1.618E+01	1.810E+01	1.996E+01	2.202E+01	2.413E+01	2.613E+01	2.791E+01
2.500	1.367E+01	1.490E+01	1.675E+01	1.857E+01	2.058E+01	2.264E+01	2.461E+01	2.637E+01
3.000	1.260E+01	1.380E+01	1.558E+01	1.733E+01	1.929E+01	2.130E+01	2.322E+01	2.495E+01
4.000	1.087E+01	1.200E+01	1.364E+01	1.528E+01	1.711E+01	1.901E+01	2.083E+01	2.248E+01
5.000	9.542E+00	1.060E+01	1.212E+01	1.365E+01	1.535E+01	1.714E+01	1.886E+01	2.043E+01
6.000	8.487E+00	9.493E+00	1.090E+01	1.233E+01	1.392E+01	1.559E+01	1.722E+01	1.871E+01
7.000	7.634E+00	8.590E+00	9.904E+00	1.123E+01	1.272E+01	1.429E+01	1.583E+01	1.725E+01
8.000	6.934E+00	7.842E+00	9.069E+00	1.032E+01	1.171E+01	1.319E+01	1.465E+01	1.600E+01
9.000	6.349E+00	7.215E+00	8.364E+00	9.542E+00	1.085E+01	1.225E+01	1.362E+01	1.492E+01
10.00	5.854E+00	6.681E+00	7.761E+00	8.873E+00	1.011E+01	1.143E+01	1.273E+01	1.397E+01
15.00	4.221E+00	4.891E+00	5.716E+00	6.581E+00	7.538E+00	8.564E+00	9.602E+00	1.061E+01
20.00	3.319E+00	3.881E+00	4.547E+00	5.252E+00	6.029E+00	6.863E+00	7.720E+00	8.571E+00
25.00	2.751E+00	3.236E+00	3.795E+00	4.391E+00	5.044E+00	5.747E+00	6.475E+00	7.210E+00
30.00	2.363E+00	2.788E+00	3.272E+00	3.789E+00	4.354E+00	4.962E+00	5.595E+00	6.242E+00
40.00	1.864E+00	2.208E+00	2.592E+00	3.004E+00	3.451E+00	3.932E+00	4.438E+00	4.961E+00
50.00	1.556E+00	1.847E+00	2.168E+00	2.513E+00	2.886E+00	3.287E+00	3.711E+00	4.154E+00
60.00	1.347E+00	1.600E+00	1.878E+00	2.177E+00	2.500E+00	2.846E+00	3.213E+00	3.598E+00
70.00	1.194E+00	1.420E+00	1.666E+00	1.931E+00	2.217E+00	2.524E+00	2.849E+00	3.192E+00
80.00	1.077E+00	1.281E+00	1.504E+00	1.744E+00	2.002E+00	2.278E+00	2.572E+00	2.882E+00
90.00	9.859E−01	1.172E+00	1.376E+00	1.595E+00	1.831E+00	2.084E+00	2.353E+00	2.637E+00
100.0	9.114E−01	1.084E+00	1.272E+00	1.475E+00	1.693E+00	1.927E+00	2.176E+00	2.439E+00
150.0	6.818E−01	8.115E−01	9.525E−01	1.104E+00	1.268E+00	1.443E+00	1.630E+00	1.827E+00
200.0	5.631E−01	6.703E−01	7.870E−01	9.131E−01	1.048E+00	1.193E+00	1.347E+00	1.511E+00
250.0	4.906E−01	5.841E−01	6.859E−01	7.958E−01	9.140E−01	1.040E+00	1.175E+00	1.318E+00
300.0	4.418E−01	5.262E−01	6.179E−01	7.170E−01	8.236E−01	9.376E−01	1.059E+00	1.188E+00
400.0	3.809E−01	4.537E−01	5.328E−01	6.184E−01	7.104E−01	8.089E−01	9.138E−01	1.025E+00
500.0	3.448E−01	4.107E−01	4.824E−01	5.600E−01	6.433E−01	7.326E−01	8.277E−01	9.286E−01
600.0	3.214E−01	3.828E−01	4.496E−01	5.219E−01	5.997E−01	6.829E−01	7.716E−01	8.658E−01
700.0	3.052E−01	3.635E−01	4.270E−01	4.957E−01	5.696E−01	6.487E−01	7.329E−01	8.225E−01
800.0	2.935E−01	3.497E−01	4.108E−01	4.769E−01	5.479E−01	6.240E−01	7.051E−01	7.913E−01
900.0	2.849E−01	3.394E−01	3.988E−01	4.629E−01	5.319E−01	6.058E−01	6.846E−01	7.682E−01
1000.	2.784E−01	3.316E−01	3.896E−01	4.523E−01	5.197E−01	5.919E−01	6.688E−01	7.506E−01

Material: Air, dry, sea level

Ion	Li	Be	B	C	N	O	F	Ne
(E/A_1) / MeV				$(-\mathrm{d}E/\rho\mathrm{d}\ell)$ / MeV cm^2 mg^{-1}				
0.025	2.062E+00	2.560E+00	2.959E+00	3.280E+00	3.554E+00	3.796E+00	4.002E+00	4.190E+00
0.030	2.238E+00	2.797E+00	3.253E+00	3.628E+00	3.946E+00	4.228E+00	4.467E+00	4.683E+00
0.040	2.532E+00	3.205E+00	3.766E+00	4.240E+00	4.645E+00	5.005E+00	5.312E+00	5.587E+00
0.050	2.764E+00	3.546E+00	4.204E+00	4.769E+00	5.254E+00	5.690E+00	6.064E+00	6.399E+00
0.060	2.943E+00	3.829E+00	4.582E+00	5.234E+00	5.796E+00	6.302E+00	6.739E+00	7.133E+00
0.070	3.077E+00	4.060E+00	4.905E+00	5.642E+00	6.280E+00	6.856E+00	7.354E+00	7.803E+00
0.080	3.176E+00	4.245E+00	5.178E+00	5.998E+00	6.712E+00	7.357E+00	7.915E+00	8.418E+00
0.090	3.247E+00	4.390E+00	5.404E+00	6.305E+00	7.094E+00	7.808E+00	8.427E+00	8.986E+00
0.100	3.296E+00	4.502E+00	5.588E+00	6.566E+00	7.428E+00	8.212E+00	8.892E+00	9.507E+00
0.150	3.354E+00	4.751E+00	6.086E+00	7.350E+00	8.517E+00	9.609E+00	1.058E+01	1.147E+01
0.200	3.282E+00	4.760E+00	6.216E+00	7.635E+00	8.989E+00	1.028E+01	1.147E+01	1.258E+01
0.250	3.176E+00	4.686E+00	6.203E+00	7.707E+00	9.172E+00	1.059E+01	1.191E+01	1.318E+01
0.300	3.061E+00	4.581E+00	6.130E+00	7.683E+00	9.216E+00	1.072E+01	1.213E+01	1.349E+01
0.400	2.839E+00	4.346E+00	5.915E+00	7.514E+00	9.119E+00	1.072E+01	1.223E+01	1.371E+01
0.500	2.639E+00	4.113E+00	5.676E+00	7.286E+00	8.923E+00	1.057E+01	1.213E+01	1.367E+01
0.600	2.461E+00	3.896E+00	5.439E+00	7.045E+00	8.692E+00	1.036E+01	1.195E+01	1.352E+01
0.700	2.305E+00	3.696E+00	5.212E+00	6.805E+00	8.451E+00	1.013E+01	1.173E+01	1.332E+01
0.800	2.167E+00	3.513E+00	4.998E+00	6.572E+00	8.210E+00	9.893E+00	1.150E+01	1.310E+01
0.900	2.044E+00	3.346E+00	4.799E+00	6.350E+00	7.974E+00	9.653E+00	1.125E+01	1.286E+01
1.000	1.933E+00	3.193E+00	4.612E+00	6.138E+00	7.746E+00	9.415E+00	1.101E+01	1.261E+01
1.500	1.523E+00	2.592E+00	3.848E+00	5.239E+00	6.741E+00	8.332E+00	9.875E+00	1.143E+01
2.000	1.257E+00	2.179E+00	3.292E+00	4.553E+00	5.941E+00	7.434E+00	8.901E+00	1.039E+01
2.500	1.072E+00	1.879E+00	2.872E+00	4.019E+00	5.298E+00	6.695E+00	8.082E+00	9.506E+00
3.000	9.372E−01	1.653E+00	2.547E+00	3.593E+00	4.775E+00	6.079E+00	7.389E+00	8.744E+00
4.000	7.520E−01	1.335E+00	2.076E+00	2.962E+00	3.979E+00	5.121E+00	6.291E+00	7.517E+00
5.000	6.313E−01	1.123E+00	1.755E+00	2.518E+00	3.407E+00	4.415E+00	5.466E+00	6.578E+00
6.000	5.463E−01	9.729E−01	1.522E+00	2.192E+00	2.978E+00	3.877E+00	4.828E+00	5.842E+00
7.000	4.831E−01	8.601E−01	1.347E+00	1.943E+00	2.646E+00	3.456E+00	4.321E+00	5.252E+00
8.000	4.341E−01	7.724E−01	1.210E+00	1.746E+00	2.382E+00	3.117E+00	3.910E+00	4.768E+00
9.000	3.949E−01	7.024E−01	1.100E+00	1.588E+00	2.168E+00	2.840E+00	3.572E+00	4.367E+00
10.00	3.627E−01	6.450E−01	1.009E+00	1.458E+00	1.990E+00	2.610E+00	3.288E+00	4.029E+00
15.00	2.614E−01	4.643E−01	7.256E−01	1.046E+00	1.427E+00	1.871E+00	2.368E+00	2.917E+00
20.00	2.070E−01	3.677E−01	5.742E−01	8.270E−01	1.126E+00	1.475E+00	1.868E+00	2.305E+00
25.00	1.728E−01	3.069E−01	4.792E−01	6.898E−01	9.392E−01	1.228E+00	1.555E+00	1.919E+00
30.00	1.491E−01	2.649E−01	4.136E−01	5.953E−01	8.101E−01	1.058E+00	1.340E+00	1.654E+00
40.00	1.183E−01	2.102E−01	3.284E−01	4.726E−01	6.429E−01	8.396E−01	1.062E+00	1.311E+00
50.00	9.907E−02	1.761E−01	2.750E−01	3.959E−01	5.386E−01	7.033E−01	8.898E−01	1.098E+00
60.00	8.583E−02	1.525E−01	2.383E−01	3.431E−01	4.669E−01	6.097E−01	7.713E−01	9.519E−01
70.00	7.614E−02	1.353E−01	2.115E−01	3.045E−01	4.144E−01	5.411E−01	6.847E−01	8.451E−01
80.00	6.873E−02	1.222E−01	1.910E−01	2.749E−01	3.742E−01	4.887E−01	6.184E−01	7.633E−01
90.00	6.287E−02	1.117E−01	1.747E−01	2.516E−01	3.424E−01	4.472E−01	5.660E−01	6.987E−01
100.0	5.811E−02	1.033E−01	1.615E−01	2.326E−01	3.166E−01	4.136E−01	5.234E−01	6.462E−01
150.0	4.346E−02	7.731E−02	1.208E−01	1.741E−01	2.370E−01	3.097E−01	3.921E−01	4.842E−01
200.0	3.589E−02	6.384E−02	9.982E−02	1.438E−01	1.958E−01	2.559E−01	3.240E−01	4.003E−01
250.0	3.127E−02	5.563E−02	8.698E−02	1.253E−01	1.707E−01	2.231E−01	2.827E−01	3.490E−01
300.0	2.816E−02	5.011E−02	7.835E−02	1.129E−01	1.538E−01	2.010E−01	2.545E−01	3.145E−01
400.0	2.428E−02	4.321E−02	6.757E−02	9.739E−02	1.326E−01	1.734E−01	2.196E−01	2.714E−01
500.0	2.199E−02	3.913E−02	6.119E−02	8.820E−02	1.201E−01	1.570E−01	1.989E−01	2.458E−01
600.0	2.050E−02	3.648E−02	5.705E−02	8.223E−02	1.120E−01	1.464E−01	1.855E−01	2.292E−01
700.0	1.947E−02	3.465E−02	5.420E−02	7.812E−02	1.064E−01	1.391E−01	1.762E−01	2.178E−01
800.0	1.873E−02	3.334E−02	5.215E−02	7.517E−02	1.024E−01	1.339E−01	1.696E−01	2.096E−01
900.0	1.819E−02	3.237E−02	5.064E−02	7.299E−02	9.945E−02	1.300E−01	1.647E−01	2.035E−01
1000.	1.778E−02	3.163E−02	4.948E−02	7.133E−02	9.718E−02	1.270E−01	1.609E−01	1.989E−01

Material: Air, dry, sea level

Ion	Na	Mg	Al	Si	P	S	Cl	Ar
(E/A_1) / MeV				$(-\mathrm{d}E/\rho\mathrm{d}\ell)$ / MeV cm^2 mg^{-1}				
0.025	4.337E+00	4.499E+00	4.647E+00	4.794E+00	4.946E+00	5.082E+00	5.242E+00	5.351E+00
0.030	4.854E+00	5.029E+00	5.193E+00	5.352E+00	5.515E+00	5.665E+00	5.836E+00	5.954E+00
0.040	5.813E+00	6.020E+00	6.215E+00	6.401E+00	6.588E+00	6.766E+00	6.957E+00	7.092E+00
0.050	6.684E+00	6.929E+00	7.160E+00	7.378E+00	7.595E+00	7.802E+00	8.015E+00	8.167E+00
0.060	7.477E+00	7.763E+00	8.035E+00	8.289E+00	8.539E+00	8.779E+00	9.017E+00	9.189E+00
0.070	8.206E+00	8.531E+00	8.846E+00	9.137E+00	9.422E+00	9.697E+00	9.963E+00	1.015E+01
0.080	8.878E+00	9.243E+00	9.599E+00	9.928E+00	1.024E+01	1.055E+01	1.085E+01	1.107E+01
0.090	9.502E+00	9.905E+00	1.030E+01	1.066E+01	1.102E+01	1.136E+01	1.169E+01	1.193E+01
0.100	1.008E+01	1.052E+01	1.096E+01	1.136E+01	1.175E+01	1.213E+01	1.248E+01	1.275E+01
0.150	1.234E+01	1.300E+01	1.365E+01	1.425E+01	1.483E+01	1.538E+01	1.589E+01	1.629E+01
0.200	1.371E+01	1.457E+01	1.545E+01	1.625E+01	1.704E+01	1.779E+01	1.848E+01	1.903E+01
0.250	1.450E+01	1.551E+01	1.657E+01	1.755E+01	1.851E+01	1.945E+01	2.031E+01	2.103E+01
0.300	1.494E+01	1.607E+01	1.725E+01	1.837E+01	1.948E+01	2.056E+01	2.157E+01	2.244E+01
0.400	1.533E+01	1.658E+01	1.793E+01	1.922E+01	2.053E+01	2.182E+01	2.304E+01	2.411E+01
0.500	1.540E+01	1.670E+01	1.816E+01	1.955E+01	2.099E+01	2.241E+01	2.377E+01	2.496E+01
0.600	1.533E+01	1.666E+01	1.817E+01	1.964E+01	2.116E+01	2.267E+01	2.411E+01	2.539E+01
0.700	1.518E+01	1.652E+01	1.808E+01	1.958E+01	2.117E+01	2.274E+01	2.425E+01	2.559E+01
0.800	1.498E+01	1.633E+01	1.791E+01	1.945E+01	2.108E+01	2.270E+01	2.425E+01	2.564E+01
0.900	1.477E+01	1.611E+01	1.771E+01	1.927E+01	2.093E+01	2.259E+01	2.418E+01	2.559E+01
1.000	1.454E+01	1.587E+01	1.749E+01	1.906E+01	2.075E+01	2.243E+01	2.405E+01	2.549E+01
1.500	1.338E+01	1.466E+01	1.628E+01	1.787E+01	1.960E+01	2.136E+01	2.304E+01	2.453E+01
2.000	1.230E+01	1.353E+01	1.512E+01	1.668E+01	1.841E+01	2.017E+01	2.186E+01	2.335E+01
2.500	1.134E+01	1.252E+01	1.407E+01	1.560E+01	1.729E+01	1.903E+01	2.070E+01	2.218E+01
3.000	1.051E+01	1.164E+01	1.314E+01	1.462E+01	1.628E+01	1.798E+01	1.962E+01	2.108E+01
4.000	9.131E+00	1.018E+01	1.157E+01	1.296E+01	1.453E+01	1.615E+01	1.771E+01	1.911E+01
5.000	8.049E+00	9.031E+00	1.032E+01	1.162E+01	1.309E+01	1.462E+01	1.611E+01	1.745E+01
6.000	7.183E+00	8.103E+00	9.310E+00	1.052E+01	1.190E+01	1.334E+01	1.475E+01	1.603E+01
7.000	6.477E+00	7.343E+00	8.470E+00	9.613E+00	1.090E+01	1.226E+01	1.360E+01	1.481E+01
8.000	5.894E+00	6.711E+00	7.765E+00	8.840E+00	1.005E+01	1.133E+01	1.260E+01	1.376E+01
9.000	5.404E+00	6.178E+00	7.166E+00	8.180E+00	9.324E+00	1.053E+01	1.173E+01	1.285E+01
10.00	4.988E+00	5.723E+00	6.653E+00	7.611E+00	8.690E+00	9.839E+00	1.098E+01	1.204E+01
15.00	3.605E+00	4.190E+00	4.903E+00	5.649E+00	6.484E+00	7.380E+00	8.287E+00	9.160E+00
20.00	2.836E+00	3.323E+00	3.898E+00	4.507E+00	5.182E+00	5.911E+00	6.658E+00	7.394E+00
25.00	2.352E+00	2.769E+00	3.251E+00	3.765E+00	4.332E+00	4.945E+00	5.579E+00	6.214E+00
30.00	2.020E+00	2.386E+00	2.802E+00	3.247E+00	3.737E+00	4.265E+00	4.816E+00	5.375E+00
40.00	1.594E+00	1.889E+00	2.219E+00	2.573E+00	2.959E+00	3.376E+00	3.814E+00	4.266E+00
50.00	1.332E+00	1.581E+00	1.856E+00	2.153E+00	2.474E+00	2.821E+00	3.187E+00	3.568E+00
60.00	1.153E+00	1.370E+00	1.608E+00	1.865E+00	2.143E+00	2.441E+00	2.758E+00	3.089E+00
70.00	1.023E+00	1.216E+00	1.427E+00	1.655E+00	1.901E+00	2.165E+00	2.446E+00	2.741E+00
80.00	9.240E−01	1.098E+00	1.289E+00	1.495E+00	1.717E+00	1.955E+00	2.208E+00	2.474E+00
90.00	8.456E−01	1.005E+00	1.180E+00	1.369E+00	1.571E+00	1.789E+00	2.020E+00	2.264E+00
100.0	7.821E−01	9.304E−01	1.092E+00	1.266E+00	1.454E+00	1.654E+00	1.868E+00	2.094E+00
150.0	5.860E−01	6.975E−01	8.188E−01	9.498E−01	1.090E+00	1.241E+00	1.401E+00	1.571E+00
200.0	4.845E−01	5.769E−01	6.773E−01	7.858E−01	9.024E−01	1.027E+00	1.159E+00	1.300E+00
250.0	4.225E−01	5.031E−01	5.908E−01	6.855E−01	7.873E−01	8.962E−01	1.012E+00	1.135E+00
300.0	3.808E−01	4.535E−01	5.325E−01	6.180E−01	7.099E−01	8.082E−01	9.129E−01	1.024E+00
400.0	3.286E−01	3.914E−01	4.597E−01	5.335E−01	6.129E−01	6.979E−01	7.885E−01	8.846E−01
500.0	2.977E−01	3.546E−01	4.165E−01	4.835E−01	5.555E−01	6.326E−01	7.147E−01	8.019E−01
600.0	2.776E−01	3.307E−01	3.885E−01	4.510E−01	5.181E−01	5.901E−01	6.667E−01	7.482E−01
700.0	2.638E−01	3.142E−01	3.691E−01	4.285E−01	4.924E−01	5.608E−01	6.336E−01	7.111E−01
800.0	2.538E−01	3.024E−01	3.552E−01	4.124E−01	4.739E−01	5.397E−01	6.099E−01	6.844E−01
900.0	2.465E−01	2.937E−01	3.450E−01	4.005E−01	4.602E−01	5.242E−01	5.923E−01	6.647E−01
1000.	2.409E−01	2.870E−01	3.372E−01	3.914E−01	4.498E−01	5.123E−01	5.789E−01	6.497E−01

Material: Aluminium oxide

Ion	Li	Be	B	C	N	O	F	Ne
(E/A_1) / MeV				$(-\mathrm{d}E/\rho\mathrm{d}\ell)$ / MeV cm^2 mg^{-1}				
0.025	1.355E+00	1.730E+00	2.040E+00	2.295E+00	2.515E+00	2.707E+00	2.876E+00	3.029E+00
0.030	1.466E+00	1.882E+00	2.230E+00	2.523E+00	2.773E+00	2.993E+00	3.185E+00	3.359E+00
0.040	1.653E+00	2.144E+00	2.562E+00	2.922E+00	3.232E+00	3.506E+00	3.746E+00	3.961E+00
0.050	1.806E+00	2.364E+00	2.845E+00	3.267E+00	3.633E+00	3.959E+00	4.245E+00	4.502E+00
0.060	1.931E+00	2.553E+00	3.093E+00	3.572E+00	3.990E+00	4.366E+00	4.696E+00	4.994E+00
0.070	2.032E+00	2.714E+00	3.311E+00	3.844E+00	4.312E+00	4.735E+00	5.108E+00	5.446E+00
0.080	2.115E+00	2.851E+00	3.503E+00	4.087E+00	4.604E+00	5.073E+00	5.487E+00	5.863E+00
0.090	2.181E+00	2.967E+00	3.671E+00	4.306E+00	4.869E+00	5.383E+00	5.838E+00	6.251E+00
0.100	2.234E+00	3.065E+00	3.816E+00	4.500E+00	5.109E+00	5.667E+00	6.162E+00	6.613E+00
0.150	2.369E+00	3.355E+00	4.292E+00	5.177E+00	5.992E+00	6.753E+00	7.438E+00	8.069E+00
0.200	2.391E+00	3.462E+00	4.511E+00	5.527E+00	6.491E+00	7.409E+00	8.249E+00	9.037E+00
0.250	2.366E+00	3.485E+00	4.603E+00	5.704E+00	6.769E+00	7.800E+00	8.755E+00	9.665E+00
0.300	2.320E+00	3.466E+00	4.627E+00	5.786E+00	6.923E+00	8.035E+00	9.075E+00	1.007E+01
0.400	2.204E+00	3.368E+00	4.576E+00	5.803E+00	7.029E+00	8.247E+00	9.399E+00	1.052E+01
0.500	2.082E+00	3.240E+00	4.464E+00	5.722E+00	6.998E+00	8.278E+00	9.497E+00	1.069E+01
0.600	1.966E+00	3.105E+00	4.328E+00	5.599E+00	6.901E+00	8.218E+00	9.478E+00	1.072E+01
0.700	1.859E+00	2.973E+00	4.185E+00	5.458E+00	6.771E+00	8.110E+00	9.395E+00	1.067E+01
0.800	1.760E+00	2.847E+00	4.043E+00	5.310E+00	6.626E+00	7.976E+00	9.276E+00	1.057E+01
0.900	1.671E+00	2.728E+00	3.905E+00	5.161E+00	6.475E+00	7.829E+00	9.136E+00	1.044E+01
1.000	1.590E+00	2.617E+00	3.773E+00	5.015E+00	6.322E+00	7.675E+00	8.985E+00	1.030E+01
1.500	1.276E+00	2.166E+00	3.207E+00	4.360E+00	5.603E+00	6.915E+00	8.201E+00	9.503E+00
2.000	1.066E+00	1.843E+00	2.777E+00	3.835E+00	4.998E+00	6.244E+00	7.480E+00	8.742E+00
2.500	9.168E−01	1.603E+00	2.444E+00	3.415E+00	4.497E+00	5.673E+00	6.852E+00	8.065E+00
3.000	8.057E−01	1.419E+00	2.182E+00	3.074E+00	4.081E+00	5.188E+00	6.309E+00	7.471E+00
4.000	6.519E−01	1.156E+00	1.796E+00	2.559E+00	3.436E+00	4.416E+00	5.429E+00	6.491E+00
5.000	5.505E−01	9.790E−01	1.528E+00	2.191E+00	2.963E+00	3.836E+00	4.753E+00	5.724E+00
6.000	4.785E−01	8.516E−01	1.332E+00	1.917E+00	2.603E+00	3.388E+00	4.222E+00	5.113E+00
7.000	4.246E−01	7.556E−01	1.183E+00	1.706E+00	2.323E+00	3.033E+00	3.795E+00	4.617E+00
8.000	3.826E−01	6.807E−01	1.066E+00	1.538E+00	2.098E+00	2.745E+00	3.447E+00	4.207E+00
9.000	3.489E−01	6.205E−01	9.714E−01	1.403E+00	1.915E+00	2.509E+00	3.157E+00	3.864E+00
10.00	3.212E−01	5.712E−01	8.937E−01	1.290E+00	1.762E+00	2.311E+00	2.914E+00	3.574E+00
15.00	2.332E−01	4.141E−01	6.471E−01	9.331E−01	1.274E+00	1.670E+00	2.115E+00	2.608E+00
20.00	1.855E−01	3.295E−01	5.145E−01	7.410E−01	1.010E+00	1.323E+00	1.676E+00	2.069E+00
25.00	1.553E−01	2.759E−01	4.308E−01	6.201E−01	8.443E−01	1.104E+00	1.399E+00	1.728E+00
30.00	1.344E−01	2.387E−01	3.727E−01	5.364E−01	7.300E−01	9.542E−01	1.208E+00	1.492E+00
40.00	1.070E−01	1.902E−01	2.970E−01	4.274E−01	5.815E−01	7.594E−01	9.610E−01	1.186E+00
50.00	8.981E−02	1.597E−01	2.494E−01	3.590E−01	4.884E−01	6.377E−01	8.068E−01	9.959E−01
60.00	7.796E−02	1.386E−01	2.165E−01	3.117E−01	4.242E−01	5.539E−01	7.008E−01	8.649E−01
70.00	6.927E−02	1.232E−01	1.924E−01	2.771E−01	3.771E−01	4.924E−01	6.230E−01	7.690E−01
80.00	6.260E−02	1.113E−01	1.740E−01	2.505E−01	3.409E−01	4.453E−01	5.634E−01	6.955E−01
90.00	5.733E−02	1.019E−01	1.593E−01	2.295E−01	3.123E−01	4.079E−01	5.162E−01	6.372E−01
100.0	5.304E−02	9.433E−02	1.474E−01	2.124E−01	2.891E−01	3.776E−01	4.779E−01	5.899E−01
150.0	3.980E−02	7.080E−02	1.107E−01	1.595E−01	2.171E−01	2.837E−01	3.592E−01	4.435E−01
200.0	3.294E−02	5.860E−02	9.162E−02	1.320E−01	1.798E−01	2.350E−01	2.975E−01	3.675E−01
250.0	2.874E−02	5.114E−02	7.996E−02	1.152E−01	1.569E−01	2.051E−01	2.598E−01	3.209E−01
300.0	2.592E−02	4.612E−02	7.212E−02	1.039E−01	1.416E−01	1.851E−01	2.344E−01	2.896E−01
400.0	2.239E−02	3.985E−02	6.232E−02	8.981E−02	1.224E−01	1.599E−01	2.026E−01	2.503E−01
500.0	2.031E−02	3.614E−02	5.651E−02	8.146E−02	1.110E−01	1.451E−01	1.838E−01	2.271E−01
600.0	1.895E−02	3.373E−02	5.275E−02	7.604E−02	1.036E−01	1.354E−01	1.716E−01	2.120E−01
700.0	1.802E−02	3.207E−02	5.016E−02	7.230E−02	9.851E−02	1.288E−01	1.632E−01	2.017E−01
800.0	1.736E−02	3.089E−02	4.831E−02	6.963E−02	9.488E−02	1.240E−01	1.572E−01	1.942E−01
900.0	1.686E−02	3.001E−02	4.694E−02	6.766E−02	9.219E−02	1.205E−01	1.527E−01	1.887E−01
1000.	1.649E−02	2.934E−02	4.590E−02	6.616E−02	9.015E−02	1.179E−01	1.493E−01	1.846E−01

Material: Aluminium oxide

Ion	Na	Mg	Al	Si	P	S	Cl	Ar
(E/A_1) / MeV				$(-\mathrm{d}E/\rho\mathrm{d}\ell)$ / MeV cm^2 mg^{-1}				
0.025	3.151E+00	3.282E+00	3.400E+00	3.513E+00	3.621E+00	3.720E+00	3.832E+00	3.921E+00
0.030	3.498E+00	3.642E+00	3.772E+00	3.896E+00	4.013E+00	4.122E+00	4.242E+00	4.338E+00
0.040	4.137E+00	4.308E+00	4.463E+00	4.608E+00	4.743E+00	4.874E+00	5.008E+00	5.118E+00
0.050	4.716E+00	4.919E+00	5.100E+00	5.268E+00	5.423E+00	5.575E+00	5.726E+00	5.849E+00
0.060	5.247E+00	5.482E+00	5.691E+00	5.884E+00	6.063E+00	6.238E+00	6.406E+00	6.544E+00
0.070	5.736E+00	6.005E+00	6.244E+00	6.463E+00	6.666E+00	6.865E+00	7.054E+00	7.208E+00
0.080	6.191E+00	6.491E+00	6.762E+00	7.008E+00	7.237E+00	7.460E+00	7.669E+00	7.842E+00
0.090	6.615E+00	6.947E+00	7.248E+00	7.521E+00	7.776E+00	8.024E+00	8.255E+00	8.448E+00
0.100	7.012E+00	7.375E+00	7.705E+00	8.006E+00	8.287E+00	8.561E+00	8.814E+00	9.026E+00
0.150	8.647E+00	9.168E+00	9.646E+00	1.008E+01	1.049E+01	1.089E+01	1.126E+01	1.158E+01
0.200	9.778E+00	1.045E+01	1.108E+01	1.165E+01	1.220E+01	1.273E+01	1.322E+01	1.365E+01
0.250	1.054E+01	1.134E+01	1.210E+01	1.280E+01	1.348E+01	1.414E+01	1.475E+01	1.529E+01
0.300	1.105E+01	1.195E+01	1.281E+01	1.362E+01	1.441E+01	1.519E+01	1.591E+01	1.655E+01
0.400	1.163E+01	1.268E+01	1.370E+01	1.466E+01	1.563E+01	1.658E+01	1.747E+01	1.829E+01
0.500	1.189E+01	1.304E+01	1.416E+01	1.523E+01	1.632E+01	1.739E+01	1.841E+01	1.935E+01
0.600	1.198E+01	1.319E+01	1.438E+01	1.553E+01	1.671E+01	1.787E+01	1.899E+01	2.002E+01
0.700	1.197E+01	1.322E+01	1.446E+01	1.566E+01	1.691E+01	1.815E+01	1.933E+01	2.043E+01
0.800	1.190E+01	1.317E+01	1.445E+01	1.569E+01	1.699E+01	1.828E+01	1.952E+01	2.067E+01
0.900	1.178E+01	1.308E+01	1.438E+01	1.565E+01	1.698E+01	1.832E+01	1.960E+01	2.080E+01
1.000	1.165E+01	1.296E+01	1.428E+01	1.557E+01	1.693E+01	1.829E+01	1.961E+01	2.084E+01
1.500	1.086E+01	1.218E+01	1.353E+01	1.485E+01	1.629E+01	1.773E+01	1.913E+01	2.043E+01
2.000	1.007E+01	1.137E+01	1.271E+01	1.402E+01	1.547E+01	1.693E+01	1.835E+01	1.967E+01
2.500	9.354E+00	1.062E+01	1.193E+01	1.322E+01	1.465E+01	1.611E+01	1.752E+01	1.884E+01
3.000	8.713E+00	9.939E+00	1.121E+01	1.248E+01	1.388E+01	1.532E+01	1.672E+01	1.802E+01
4.000	7.637E+00	8.782E+00	9.982E+00	1.118E+01	1.252E+01	1.390E+01	1.525E+01	1.651E+01
5.000	6.781E+00	7.848E+00	8.972E+00	1.010E+01	1.137E+01	1.269E+01	1.398E+01	1.518E+01
6.000	6.089E+00	7.083E+00	8.136E+00	9.201E+00	1.040E+01	1.165E+01	1.288E+01	1.403E+01
7.000	5.520E+00	6.449E+00	7.436E+00	8.441E+00	9.571E+00	1.076E+01	1.193E+01	1.304E+01
8.000	5.046E+00	5.916E+00	6.844E+00	7.792E+00	8.860E+00	9.984E+00	1.110E+01	1.216E+01
9.000	4.647E+00	5.463E+00	6.336E+00	7.234E+00	8.243E+00	9.311E+00	1.038E+01	1.139E+01
10.00	4.306E+00	5.073E+00	5.898E+00	6.748E+00	7.705E+00	8.719E+00	9.736E+00	1.071E+01
15.00	3.157E+00	3.746E+00	4.384E+00	5.053E+00	5.801E+00	6.602E+00	7.420E+00	8.219E+00
20.00	2.509E+00	2.984E+00	3.502E+00	4.050E+00	4.660E+00	5.316E+00	5.994E+00	6.669E+00
25.00	2.095E+00	2.494E+00	2.929E+00	3.394E+00	3.908E+00	4.462E+00	5.039E+00	5.621E+00
30.00	1.808E+00	2.153E+00	2.530E+00	2.933E+00	3.377E+00	3.857E+00	4.359E+00	4.871E+00
40.00	1.437E+00	1.711E+00	2.009E+00	2.331E+00	2.682E+00	3.061E+00	3.461E+00	3.875E+00
50.00	1.205E+00	1.435E+00	1.685E+00	1.954E+00	2.247E+00	2.563E+00	2.897E+00	3.246E+00
60.00	1.047E+00	1.246E+00	1.462E+00	1.696E+00	1.949E+00	2.221E+00	2.511E+00	2.814E+00
70.00	9.304E−01	1.107E+00	1.300E+00	1.507E+00	1.732E+00	1.973E+00	2.229E+00	2.499E+00
80.00	8.414E−01	1.001E+00	1.175E+00	1.363E+00	1.565E+00	1.783E+00	2.014E+00	2.258E+00
90.00	7.710E−01	9.175E−01	1.077E+00	1.249E+00	1.434E+00	1.633E+00	1.844E+00	2.068E+00
100.0	7.138E−01	8.495E−01	9.970E−01	1.156E+00	1.328E+00	1.512E+00	1.707E+00	1.914E+00
150.0	5.368E−01	6.390E−01	7.501E−01	8.702E−01	9.992E−01	1.137E+00	1.284E+00	1.440E+00
200.0	4.449E−01	5.297E−01	6.219E−01	7.215E−01	8.286E−01	9.432E−01	1.065E+00	1.195E+00
250.0	3.885E−01	4.627E−01	5.433E−01	6.304E−01	7.241E−01	8.243E−01	9.311E−01	1.044E+00
300.0	3.506E−01	4.176E−01	4.904E−01	5.691E−01	6.537E−01	7.443E−01	8.408E−01	9.432E−01
400.0	3.032E−01	3.611E−01	4.241E−01	4.923E−01	5.656E−01	6.440E−01	7.276E−01	8.163E−01
500.0	2.751E−01	3.276E−01	3.849E−01	4.468E−01	5.133E−01	5.846E−01	6.605E−01	7.411E−01
600.0	2.568E−01	3.059E−01	3.594E−01	4.172E−01	4.794E−01	5.459E−01	6.169E−01	6.923E−01
700.0	2.442E−01	2.910E−01	3.418E−01	3.968E−01	4.561E−01	5.193E−01	5.869E−01	6.586E−01
800.0	2.353E−01	2.803E−01	3.292E−01	3.822E−01	4.395E−01	5.003E−01	5.654E−01	6.345E−01
900.0	2.286E−01	2.724E−01	3.200E−01	3.715E−01	4.271E−01	4.862E−01	5.495E−01	6.167E−01
1000.	2.236E−01	2.663E−01	3.129E−01	3.633E−01	4.175E−01	4.755E−01	5.374E−01	6.031E−01

Material: Bone, compact (ICRU)

Ion	Li	Be	B	C	N	O	F	Ne
(E/A_1) / MeV				$(-\mathrm{d}E/\rho\mathrm{d}\ell)$ / MeV cm^2 mg^{-1}				
0.025	2.204E+00	2.712E+00	3.108E+00	3.419E+00	3.699E+00	3.948E+00	4.148E+00	4.332E+00
0.030	2.403E+00	2.981E+00	3.438E+00	3.802E+00	4.122E+00	4.407E+00	4.637E+00	4.847E+00
0.040	2.723E+00	3.438E+00	4.018E+00	4.489E+00	4.892E+00	5.250E+00	5.539E+00	5.801E+00
0.050	2.962E+00	3.805E+00	4.502E+00	5.081E+00	5.573E+00	6.009E+00	6.363E+00	6.677E+00
0.060	3.137E+00	4.096E+00	4.904E+00	5.589E+00	6.171E+00	6.688E+00	7.111E+00	7.485E+00
0.070	3.265E+00	4.324E+00	5.236E+00	6.020E+00	6.693E+00	7.293E+00	7.788E+00	8.224E+00
0.080	3.355E+00	4.500E+00	5.506E+00	6.385E+00	7.146E+00	7.829E+00	8.396E+00	8.897E+00
0.090	3.418E+00	4.636E+00	5.725E+00	6.691E+00	7.536E+00	8.300E+00	8.940E+00	9.508E+00
0.100	3.459E+00	4.738E+00	5.900E+00	6.946E+00	7.870E+00	8.711E+00	9.423E+00	1.006E+01
0.150	3.491E+00	4.953E+00	6.355E+00	7.683E+00	8.913E+00	1.007E+01	1.109E+01	1.203E+01
0.200	3.406E+00	4.942E+00	6.459E+00	7.935E+00	9.345E+00	1.070E+01	1.194E+01	1.309E+01
0.250	3.291E+00	4.856E+00	6.430E+00	7.988E+00	9.503E+00	1.099E+01	1.235E+01	1.365E+01
0.300	3.171E+00	4.742E+00	6.345E+00	7.949E+00	9.529E+00	1.109E+01	1.254E+01	1.394E+01
0.400	2.939E+00	4.494E+00	6.115E+00	7.761E+00	9.410E+00	1.106E+01	1.261E+01	1.413E+01
0.500	2.731E+00	4.252E+00	5.863E+00	7.520E+00	9.198E+00	1.090E+01	1.250E+01	1.407E+01
0.600	2.548E+00	4.026E+00	5.616E+00	7.267E+00	8.955E+00	1.067E+01	1.230E+01	1.391E+01
0.700	2.387E+00	3.820E+00	5.381E+00	7.017E+00	8.703E+00	1.043E+01	1.207E+01	1.370E+01
0.800	2.244E+00	3.631E+00	5.160E+00	6.776E+00	8.452E+00	1.018E+01	1.182E+01	1.346E+01
0.900	2.117E+00	3.459E+00	4.954E+00	6.546E+00	8.208E+00	9.928E+00	1.157E+01	1.322E+01
1.000	2.004E+00	3.301E+00	4.762E+00	6.328E+00	7.972E+00	9.682E+00	1.132E+01	1.296E+01
1.500	1.581E+00	2.684E+00	3.975E+00	5.402E+00	6.937E+00	8.563E+00	1.015E+01	1.175E+01
2.000	1.307E+00	2.259E+00	3.404E+00	4.698E+00	6.116E+00	7.642E+00	9.147E+00	1.068E+01
2.500	1.117E+00	1.951E+00	2.974E+00	4.151E+00	5.460E+00	6.886E+00	8.308E+00	9.773E+00
3.000	9.771E−01	1.719E+00	2.640E+00	3.715E+00	4.925E+00	6.257E+00	7.602E+00	8.995E+00
4.000	7.854E−01	1.391E+00	2.158E+00	3.069E+00	4.113E+00	5.281E+00	6.483E+00	7.745E+00
5.000	6.601E−01	1.172E+00	1.827E+00	2.615E+00	3.528E+00	4.562E+00	5.644E+00	6.790E+00
6.000	5.718E−01	1.016E+00	1.588E+00	2.280E+00	3.090E+00	4.014E+00	4.994E+00	6.041E+00
7.000	5.059E−01	8.994E−01	1.406E+00	2.024E+00	2.750E+00	3.583E+00	4.477E+00	5.439E+00
8.000	4.547E−01	8.084E−01	1.264E+00	1.822E+00	2.479E+00	3.237E+00	4.058E+00	4.946E+00
9.000	4.138E−01	7.355E−01	1.150E+00	1.658E+00	2.259E+00	2.954E+00	3.711E+00	4.535E+00
10.00	3.803E−01	6.757E−01	1.057E+00	1.524E+00	2.077E+00	2.718E+00	3.421E+00	4.189E+00
15.00	2.743E−01	4.871E−01	7.609E−01	1.096E+00	1.494E+00	1.957E+00	2.474E+00	3.046E+00
20.00	2.174E−01	3.860E−01	6.027E−01	8.677E−01	1.182E+00	1.546E+00	1.957E+00	2.414E+00
25.00	1.815E−01	3.224E−01	5.033E−01	7.243E−01	9.858E−01	1.289E+00	1.631E+00	2.013E+00
30.00	1.567E−01	2.783E−01	4.346E−01	6.253E−01	8.508E−01	1.112E+00	1.407E+00	1.736E+00
40.00	1.244E−01	2.210E−01	3.452E−01	4.967E−01	6.757E−01	8.824E−01	1.116E+00	1.378E+00
50.00	1.042E−01	1.852E−01	2.892E−01	4.163E−01	5.663E−01	7.394E−01	9.354E−01	1.154E+00
60.00	9.026E−02	1.605E−01	2.507E−01	3.609E−01	4.911E−01	6.412E−01	8.112E−01	1.001E+00
70.00	8.009E−02	1.424E−01	2.225E−01	3.203E−01	4.359E−01	5.692E−01	7.202E−01	8.889E−01
80.00	7.230E−02	1.286E−01	2.009E−01	2.893E−01	3.937E−01	5.142E−01	6.506E−01	8.031E−01
90.00	6.615E−02	1.176E−01	1.838E−01	2.647E−01	3.603E−01	4.706E−01	5.956E−01	7.352E−01
100.0	6.115E−02	1.088E−01	1.700E−01	2.448E−01	3.332E−01	4.353E−01	5.509E−01	6.800E−01
150.0	4.575E−02	8.138E−02	1.272E−01	1.833E−01	2.496E−01	3.261E−01	4.128E−01	5.098E−01
200.0	3.779E−02	6.723E−02	1.051E−01	1.514E−01	2.063E−01	2.695E−01	3.413E−01	4.215E−01
250.0	3.293E−02	5.859E−02	9.161E−02	1.320E−01	1.798E−01	2.350E−01	2.976E−01	3.676E−01
300.0	2.967E−02	5.279E−02	8.254E−02	1.189E−01	1.620E−01	2.118E−01	2.682E−01	3.313E−01
400.0	2.559E−02	4.553E−02	7.120E−02	1.026E−01	1.398E−01	1.827E−01	2.315E−01	2.860E−01
500.0	2.318E−02	4.124E−02	6.449E−02	9.295E−02	1.266E−01	1.655E−01	2.097E−01	2.591E−01
600.0	2.161E−02	3.845E−02	6.014E−02	8.668E−02	1.181E−01	1.544E−01	1.956E−01	2.417E−01
700.0	2.053E−02	3.653E−02	5.713E−02	8.235E−02	1.122E−01	1.467E−01	1.858E−01	2.296E−01
800.0	1.976E−02	3.515E−02	5.498E−02	7.925E−02	1.080E−01	1.412E−01	1.788E−01	2.210E−01
900.0	1.918E−02	3.414E−02	5.339E−02	7.696E−02	1.049E−01	1.371E−01	1.737E−01	2.146E−01
1000.	1.875E−02	3.336E−02	5.218E−02	7.521E−02	1.025E−01	1.340E−01	1.697E−01	2.098E−01

Material: Bone, compact (ICRU)

Ion	Na	Mg	Al	Si	P	S	Cl	Ar
(E/A_1) / MeV				$(-\mathrm{d}E/\rho\mathrm{d}\ell)$ / MeV cm^2 mg^{-1}				
0.025	4.494E+00	4.672E+00	4.842E+00	5.012E+00	5.200E+00	5.360E+00	5.554E+00	5.672E+00
0.030	5.033E+00	5.218E+00	5.403E+00	5.585E+00	5.786E+00	5.962E+00	6.169E+00	6.299E+00
0.040	6.040E+00	6.244E+00	6.458E+00	6.664E+00	6.889E+00	7.094E+00	7.319E+00	7.469E+00
0.050	6.970E+00	7.198E+00	7.440E+00	7.673E+00	7.923E+00	8.155E+00	8.400E+00	8.566E+00
0.060	7.838E+00	8.094E+00	8.367E+00	8.626E+00	8.900E+00	9.159E+00	9.423E+00	9.605E+00
0.070	8.642E+00	8.932E+00	9.243E+00	9.531E+00	9.832E+00	1.012E+01	1.040E+01	1.060E+01
0.080	9.383E+00	9.712E+00	1.006E+01	1.039E+01	1.072E+01	1.103E+01	1.134E+01	1.155E+01
0.090	1.006E+01	1.043E+01	1.083E+01	1.119E+01	1.156E+01	1.191E+01	1.224E+01	1.247E+01
0.100	1.069E+01	1.110E+01	1.155E+01	1.195E+01	1.235E+01	1.273E+01	1.309E+01	1.335E+01
0.150	1.300E+01	1.366E+01	1.436E+01	1.499E+01	1.561E+01	1.620E+01	1.674E+01	1.715E+01
0.200	1.434E+01	1.520E+01	1.613E+01	1.698E+01	1.782E+01	1.862E+01	1.936E+01	1.995E+01
0.250	1.510E+01	1.610E+01	1.720E+01	1.823E+01	1.926E+01	2.024E+01	2.116E+01	2.192E+01
0.300	1.553E+01	1.662E+01	1.786E+01	1.902E+01	2.019E+01	2.132E+01	2.238E+01	2.328E+01
0.400	1.590E+01	1.710E+01	1.851E+01	1.984E+01	2.120E+01	2.254E+01	2.380E+01	2.491E+01
0.500	1.595E+01	1.721E+01	1.872E+01	2.016E+01	2.164E+01	2.311E+01	2.450E+01	2.573E+01
0.600	1.587E+01	1.715E+01	1.872E+01	2.023E+01	2.180E+01	2.336E+01	2.483E+01	2.616E+01
0.700	1.571E+01	1.700E+01	1.862E+01	2.017E+01	2.179E+01	2.342E+01	2.496E+01	2.634E+01
0.800	1.550E+01	1.680E+01	1.844E+01	2.003E+01	2.170E+01	2.337E+01	2.496E+01	2.639E+01
0.900	1.528E+01	1.658E+01	1.824E+01	1.984E+01	2.154E+01	2.325E+01	2.488E+01	2.634E+01
1.000	1.504E+01	1.634E+01	1.801E+01	1.963E+01	2.135E+01	2.309E+01	2.474E+01	2.622E+01
1.500	1.383E+01	1.509E+01	1.676E+01	1.840E+01	2.017E+01	2.197E+01	2.369E+01	2.523E+01
2.000	1.271E+01	1.392E+01	1.557E+01	1.718E+01	1.894E+01	2.074E+01	2.247E+01	2.402E+01
2.500	1.172E+01	1.289E+01	1.449E+01	1.606E+01	1.780E+01	1.957E+01	2.128E+01	2.282E+01
3.000	1.086E+01	1.199E+01	1.353E+01	1.506E+01	1.675E+01	1.849E+01	2.017E+01	2.168E+01
4.000	9.432E+00	1.050E+01	1.193E+01	1.337E+01	1.496E+01	1.661E+01	1.822E+01	1.967E+01
5.000	8.319E+00	9.319E+00	1.066E+01	1.200E+01	1.350E+01	1.506E+01	1.658E+01	1.797E+01
6.000	7.429E+00	8.373E+00	9.617E+00	1.088E+01	1.228E+01	1.375E+01	1.519E+01	1.652E+01
7.000	6.705E+00	7.597E+00	8.759E+00	9.941E+00	1.126E+01	1.265E+01	1.402E+01	1.528E+01
8.000	6.106E+00	6.952E+00	8.039E+00	9.152E+00	1.039E+01	1.170E+01	1.300E+01	1.421E+01
9.000	5.604E+00	6.407E+00	7.428E+00	8.477E+00	9.648E+00	1.089E+01	1.212E+01	1.328E+01
10.00	5.177E+00	5.942E+00	6.903E+00	7.895E+00	9.002E+00	1.018E+01	1.135E+01	1.246E+01
15.00	3.756E+00	4.370E+00	5.109E+00	5.884E+00	6.744E+00	7.665E+00	8.603E+00	9.514E+00
20.00	2.963E+00	3.475E+00	4.073E+00	4.708E+00	5.408E+00	6.160E+00	6.935E+00	7.705E+00
25.00	2.462E+00	2.901E+00	3.404E+00	3.941E+00	4.531E+00	5.165E+00	5.825E+00	6.491E+00
30.00	2.117E+00	2.502E+00	2.938E+00	3.404E+00	3.914E+00	4.463E+00	5.038E+00	5.624E+00
40.00	1.674E+00	1.985E+00	2.330E+00	2.701E+00	3.105E+00	3.540E+00	3.999E+00	4.473E+00
50.00	1.400E+00	1.662E+00	1.951E+00	2.262E+00	2.600E+00	2.962E+00	3.346E+00	3.747E+00
60.00	1.213E+00	1.441E+00	1.691E+00	1.961E+00	2.253E+00	2.566E+00	2.898E+00	3.247E+00
70.00	1.076E+00	1.280E+00	1.502E+00	1.741E+00	2.000E+00	2.277E+00	2.572E+00	2.882E+00
80.00	9.720E−01	1.156E+00	1.357E+00	1.573E+00	1.806E+00	2.056E+00	2.322E+00	2.603E+00
90.00	8.897E−01	1.058E+00	1.242E+00	1.440E+00	1.654E+00	1.882E+00	2.126E+00	2.383E+00
100.0	8.230E−01	9.791E−01	1.149E+00	1.333E+00	1.530E+00	1.741E+00	1.966E+00	2.204E+00
150.0	6.170E−01	7.344E−01	8.620E−01	9.999E−01	1.148E+00	1.307E+00	1.475E+00	1.654E+00
200.0	5.103E−01	6.075E−01	7.133E−01	8.275E−01	9.503E−01	1.082E+00	1.222E+00	1.370E+00
250.0	4.451E−01	5.299E−01	6.223E−01	7.221E−01	8.293E−01	9.440E−01	1.066E+00	1.196E+00
300.0	4.012E−01	4.777E−01	5.610E−01	6.511E−01	7.479E−01	8.514E−01	9.618E−01	1.079E+00
400.0	3.463E−01	4.124E−01	4.844E−01	5.622E−01	6.459E−01	7.355E−01	8.309E−01	9.322E−01
500.0	3.138E−01	3.738E−01	4.390E−01	5.096E−01	5.855E−01	6.667E−01	7.533E−01	8.452E−01
600.0	2.927E−01	3.486E−01	4.095E−01	4.754E−01	5.462E−01	6.220E−01	7.029E−01	7.887E−01
700.0	2.781E−01	3.313E−01	3.892E−01	4.518E−01	5.191E−01	5.912E−01	6.681E−01	7.497E−01
800.0	2.677E−01	3.189E−01	3.746E−01	4.349E−01	4.997E−01	5.691E−01	6.431E−01	7.217E−01
900.0	2.600E−01	3.097E−01	3.638E−01	4.223E−01	4.853E−01	5.527E−01	6.246E−01	7.010E−01
1000.	2.541E−01	3.027E−01	3.556E−01	4.128E−01	4.743E−01	5.402E−01	6.105E−01	6.851E−01

Material: Bone, cortical (ICRP)

Ion	Li	Be	B	C	N	O	F	Ne
(E/A_1) / MeV				$(-\mathrm{d}E/\rho\mathrm{d}\ell)$ / MeV cm^2 mg^{-1}				
0.025	2.041E+00	2.507E+00	2.869E+00	3.155E+00	3.408E+00	3.634E+00	3.820E+00	3.991E+00
0.030	2.227E+00	2.760E+00	3.179E+00	3.512E+00	3.802E+00	4.062E+00	4.275E+00	4.470E+00
0.040	2.528E+00	3.189E+00	3.723E+00	4.157E+00	4.524E+00	4.850E+00	5.117E+00	5.359E+00
0.050	2.754E+00	3.535E+00	4.178E+00	4.714E+00	5.165E+00	5.564E+00	5.891E+00	6.182E+00
0.060	2.923E+00	3.811E+00	4.559E+00	5.192E+00	5.729E+00	6.204E+00	6.596E+00	6.943E+00
0.070	3.048E+00	4.031E+00	4.875E+00	5.601E+00	6.222E+00	6.775E+00	7.235E+00	7.640E+00
0.080	3.138E+00	4.203E+00	5.135E+00	5.950E+00	6.653E+00	7.283E+00	7.810E+00	8.277E+00
0.090	3.201E+00	4.337E+00	5.349E+00	6.245E+00	7.026E+00	7.731E+00	8.326E+00	8.855E+00
0.100	3.244E+00	4.440E+00	5.521E+00	6.492E+00	7.348E+00	8.126E+00	8.787E+00	9.378E+00
0.150	3.289E+00	4.665E+00	5.982E+00	7.226E+00	8.376E+00	9.455E+00	1.041E+01	1.129E+01
0.200	3.217E+00	4.667E+00	6.098E+00	7.489E+00	8.816E+00	1.009E+01	1.125E+01	1.234E+01
0.250	3.113E+00	4.593E+00	6.081E+00	7.554E+00	8.984E+00	1.038E+01	1.167E+01	1.291E+01
0.300	3.003E+00	4.491E+00	6.009E+00	7.528E+00	9.023E+00	1.050E+01	1.188E+01	1.321E+01
0.400	2.789E+00	4.264E+00	5.801E+00	7.364E+00	8.928E+00	1.050E+01	1.197E+01	1.341E+01
0.500	2.596E+00	4.041E+00	5.571E+00	7.145E+00	8.740E+00	1.035E+01	1.188E+01	1.338E+01
0.600	2.425E+00	3.831E+00	5.343E+00	6.914E+00	8.519E+00	1.015E+01	1.171E+01	1.324E+01
0.700	2.275E+00	3.639E+00	5.125E+00	6.683E+00	8.288E+00	9.932E+00	1.150E+01	1.306E+01
0.800	2.141E+00	3.463E+00	4.920E+00	6.460E+00	8.057E+00	9.702E+00	1.127E+01	1.284E+01
0.900	2.021E+00	3.301E+00	4.727E+00	6.246E+00	7.831E+00	9.471E+00	1.104E+01	1.262E+01
1.000	1.915E+00	3.153E+00	4.547E+00	6.042E+00	7.612E+00	9.243E+00	1.081E+01	1.238E+01
1.500	1.515E+00	2.572E+00	3.808E+00	5.174E+00	6.644E+00	8.200E+00	9.719E+00	1.126E+01
2.000	1.256E+00	2.169E+00	3.268E+00	4.510E+00	5.871E+00	7.334E+00	8.781E+00	1.026E+01
2.500	1.074E+00	1.876E+00	2.859E+00	3.991E+00	5.249E+00	6.619E+00	7.990E+00	9.400E+00
3.000	9.407E−01	1.654E+00	2.541E+00	3.576E+00	4.741E+00	6.023E+00	7.319E+00	8.663E+00
4.000	7.572E−01	1.341E+00	2.080E+00	2.959E+00	3.966E+00	5.092E+00	6.254E+00	7.473E+00
5.000	6.371E−01	1.132E+00	1.764E+00	2.524E+00	3.407E+00	4.405E+00	5.451E+00	6.560E+00
6.000	5.522E−01	9.817E−01	1.534E+00	2.203E+00	2.986E+00	3.879E+00	4.828E+00	5.842E+00
7.000	4.889E−01	8.693E−01	1.359E+00	1.957E+00	2.659E+00	3.465E+00	4.331E+00	5.263E+00
8.000	4.397E−01	7.817E−01	1.223E+00	1.762E+00	2.399E+00	3.133E+00	3.928E+00	4.789E+00
9.000	4.003E−01	7.114E−01	1.113E+00	1.605E+00	2.186E+00	2.859E+00	3.594E+00	4.393E+00
10.00	3.679E−01	6.538E−01	1.023E+00	1.475E+00	2.011E+00	2.632E+00	3.314E+00	4.059E+00
15.00	2.657E−01	4.719E−01	7.371E−01	1.062E+00	1.448E+00	1.897E+00	2.399E+00	2.955E+00
20.00	2.107E−01	3.743E−01	5.843E−01	8.413E−01	1.146E+00	1.500E+00	1.898E+00	2.342E+00
25.00	1.760E−01	3.127E−01	4.882E−01	7.026E−01	9.564E−01	1.250E+00	1.583E+00	1.954E+00
30.00	1.520E−01	2.701E−01	4.217E−01	6.068E−01	8.257E−01	1.079E+00	1.365E+00	1.685E+00
40.00	1.208E−01	2.146E−01	3.352E−01	4.823E−01	6.562E−01	8.568E−01	1.084E+00	1.338E+00
50.00	1.012E−01	1.799E−01	2.809E−01	4.044E−01	5.502E−01	7.183E−01	9.088E−01	1.122E+00
60.00	8.771E−02	1.559E−01	2.436E−01	3.507E−01	4.772E−01	6.231E−01	7.883E−01	9.729E−01
70.00	7.784E−02	1.384E−01	2.163E−01	3.114E−01	4.237E−01	5.533E−01	7.001E−01	8.641E−01
80.00	7.029E−02	1.250E−01	1.953E−01	2.813E−01	3.828E−01	4.999E−01	6.326E−01	7.808E−01
90.00	6.432E−02	1.144E−01	1.788E−01	2.574E−01	3.504E−01	4.576E−01	5.791E−01	7.149E−01
100.0	5.947E−02	1.058E−01	1.653E−01	2.381E−01	3.241E−01	4.233E−01	5.358E−01	6.614E−01
150.0	4.452E−02	7.920E−02	1.238E−01	1.784E−01	2.429E−01	3.173E−01	4.017E−01	4.961E−01
200.0	3.679E−02	6.545E−02	1.023E−01	1.474E−01	2.008E−01	2.624E−01	3.323E−01	4.104E−01
250.0	3.207E−02	5.705E−02	8.921E−02	1.285E−01	1.751E−01	2.288E−01	2.898E−01	3.580E−01
300.0	2.890E−02	5.141E−02	8.039E−02	1.159E−01	1.578E−01	2.063E−01	2.612E−01	3.227E−01
400.0	2.493E−02	4.436E−02	6.937E−02	9.998E−02	1.362E−01	1.780E−01	2.255E−01	2.786E−01
500.0	2.259E−02	4.019E−02	6.285E−02	9.059E−02	1.234E−01	1.613E−01	2.044E−01	2.525E−01
600.0	2.106E−02	3.748E−02	5.862E−02	8.449E−02	1.151E−01	1.505E−01	1.906E−01	2.356E−01
700.0	2.001E−02	3.561E−02	5.570E−02	8.029E−02	1.094E−01	1.430E−01	1.812E−01	2.239E−01
800.0	1.926E−02	3.428E−02	5.361E−02	7.727E−02	1.053E−01	1.376E−01	1.744E−01	2.155E−01
900.0	1.871E−02	3.329E−02	5.207E−02	7.505E−02	1.023E−01	1.337E−01	1.694E−01	2.093E−01
1000.	1.828E−02	3.253E−02	5.089E−02	7.335E−02	9.994E−02	1.307E−01	1.655E−01	2.046E−01

Material: Bone, cortical (ICRP)

Ion	Na	Mg	Al	Si	P	S	Cl	Ar
(E/A_1) / MeV				$(-\mathrm{d}E/\rho\mathrm{d}\ell)$ / MeV cm^2 mg^{-1}				
0.025	4.141E+00	4.304E+00	4.461E+00	4.617E+00	4.786E+00	4.931E+00	5.106E+00	5.216E+00
0.030	4.641E+00	4.812E+00	4.982E+00	5.149E+00	5.330E+00	5.490E+00	5.676E+00	5.797E+00
0.040	5.578E+00	5.769E+00	5.965E+00	6.155E+00	6.357E+00	6.543E+00	6.746E+00	6.886E+00
0.050	6.448E+00	6.662E+00	6.884E+00	7.098E+00	7.322E+00	7.534E+00	7.755E+00	7.910E+00
0.060	7.264E+00	7.505E+00	7.756E+00	7.993E+00	8.239E+00	8.475E+00	8.714E+00	8.884E+00
0.070	8.022E+00	8.297E+00	8.583E+00	8.848E+00	9.119E+00	9.379E+00	9.635E+00	9.818E+00
0.080	8.721E+00	9.034E+00	9.360E+00	9.658E+00	9.959E+00	1.025E+01	1.052E+01	1.072E+01
0.090	9.364E+00	9.718E+00	1.009E+01	1.042E+01	1.075E+01	1.107E+01	1.137E+01	1.159E+01
0.100	9.953E+00	1.035E+01	1.076E+01	1.114E+01	1.151E+01	1.186E+01	1.219E+01	1.243E+01
0.150	1.218E+01	1.280E+01	1.345E+01	1.404E+01	1.461E+01	1.516E+01	1.565E+01	1.604E+01
0.200	1.349E+01	1.431E+01	1.518E+01	1.598E+01	1.676E+01	1.750E+01	1.818E+01	1.874E+01
0.250	1.424E+01	1.521E+01	1.625E+01	1.722E+01	1.817E+01	1.910E+01	1.995E+01	2.067E+01
0.300	1.468E+01	1.574E+01	1.691E+01	1.801E+01	1.910E+01	2.017E+01	2.116E+01	2.202E+01
0.400	1.506E+01	1.624E+01	1.757E+01	1.884E+01	2.013E+01	2.139E+01	2.259E+01	2.364E+01
0.500	1.514E+01	1.637E+01	1.780E+01	1.917E+01	2.058E+01	2.198E+01	2.330E+01	2.447E+01
0.600	1.507E+01	1.633E+01	1.783E+01	1.926E+01	2.076E+01	2.224E+01	2.365E+01	2.491E+01
0.700	1.493E+01	1.620E+01	1.774E+01	1.923E+01	2.077E+01	2.232E+01	2.379E+01	2.512E+01
0.800	1.475E+01	1.603E+01	1.759E+01	1.911E+01	2.070E+01	2.229E+01	2.381E+01	2.518E+01
0.900	1.455E+01	1.583E+01	1.741E+01	1.894E+01	2.057E+01	2.220E+01	2.375E+01	2.515E+01
1.000	1.433E+01	1.561E+01	1.720E+01	1.875E+01	2.040E+01	2.205E+01	2.363E+01	2.506E+01
1.500	1.321E+01	1.445E+01	1.606E+01	1.763E+01	1.933E+01	2.104E+01	2.269E+01	2.418E+01
2.000	1.217E+01	1.337E+01	1.494E+01	1.649E+01	1.819E+01	1.991E+01	2.157E+01	2.306E+01
2.500	1.124E+01	1.240E+01	1.393E+01	1.545E+01	1.711E+01	1.882E+01	2.046E+01	2.194E+01
3.000	1.042E+01	1.154E+01	1.303E+01	1.450E+01	1.613E+01	1.780E+01	1.942E+01	2.088E+01
4.000	9.075E+00	1.013E+01	1.151E+01	1.289E+01	1.443E+01	1.603E+01	1.757E+01	1.898E+01
5.000	8.016E+00	9.002E+00	1.029E+01	1.159E+01	1.304E+01	1.454E+01	1.602E+01	1.736E+01
6.000	7.167E+00	8.096E+00	9.299E+00	1.052E+01	1.188E+01	1.330E+01	1.470E+01	1.598E+01
7.000	6.475E+00	7.352E+00	8.476E+00	9.621E+00	1.090E+01	1.224E+01	1.357E+01	1.480E+01
8.000	5.901E+00	6.731E+00	7.784E+00	8.862E+00	1.007E+01	1.134E+01	1.260E+01	1.377E+01
9.000	5.419E+00	6.207E+00	7.196E+00	8.214E+00	9.349E+00	1.055E+01	1.175E+01	1.287E+01
10.00	5.009E+00	5.758E+00	6.690E+00	7.653E+00	8.727E+00	9.865E+00	1.101E+01	1.209E+01
15.00	3.640E+00	4.239E+00	4.957E+00	5.710E+00	6.547E+00	7.442E+00	8.354E+00	9.241E+00
20.00	2.874E+00	3.373E+00	3.954E+00	4.571E+00	5.252E+00	5.984E+00	6.739E+00	7.489E+00
25.00	2.389E+00	2.816E+00	3.306E+00	3.828E+00	4.401E+00	5.019E+00	5.662E+00	6.310E+00
30.00	2.055E+00	2.430E+00	2.853E+00	3.306E+00	3.803E+00	4.337E+00	4.897E+00	5.468E+00
40.00	1.626E+00	1.928E+00	2.264E+00	2.625E+00	3.018E+00	3.441E+00	3.888E+00	4.350E+00
50.00	1.360E+00	1.615E+00	1.896E+00	2.199E+00	2.527E+00	2.880E+00	3.254E+00	3.644E+00
60.00	1.179E+00	1.401E+00	1.644E+00	1.906E+00	2.190E+00	2.495E+00	2.818E+00	3.158E+00
70.00	1.046E+00	1.245E+00	1.460E+00	1.693E+00	1.944E+00	2.214E+00	2.501E+00	2.803E+00
80.00	9.451E−01	1.124E+00	1.319E+00	1.530E+00	1.757E+00	2.000E+00	2.259E+00	2.532E+00
90.00	8.652E−01	1.029E+00	1.208E+00	1.401E+00	1.608E+00	1.831E+00	2.068E+00	2.318E+00
100.0	8.004E−01	9.523E−01	1.118E+00	1.296E+00	1.488E+00	1.694E+00	1.913E+00	2.144E+00
150.0	6.004E−01	7.147E−01	8.389E−01	9.731E−01	1.117E+00	1.272E+00	1.436E+00	1.610E+00
200.0	4.968E−01	5.914E−01	6.944E−01	8.057E−01	9.252E−01	1.053E+00	1.189E+00	1.334E+00
250.0	4.334E−01	5.161E−01	6.060E−01	7.032E−01	8.076E−01	9.194E−01	1.038E+00	1.165E+00
300.0	3.908E−01	4.653E−01	5.465E−01	6.342E−01	7.285E−01	8.293E−01	9.368E−01	1.051E+00
400.0	3.374E−01	4.019E−01	4.720E−01	5.478E−01	6.294E−01	7.166E−01	8.096E−01	9.083E−01
500.0	3.058E−01	3.643E−01	4.279E−01	4.967E−01	5.706E−01	6.498E−01	7.342E−01	8.238E−01
600.0	2.853E−01	3.398E−01	3.992E−01	4.634E−01	5.325E−01	6.064E−01	6.852E−01	7.689E−01
700.0	2.712E−01	3.230E−01	3.795E−01	4.405E−01	5.062E−01	5.764E−01	6.514E−01	7.310E−01
800.0	2.610E−01	3.109E−01	3.653E−01	4.241E−01	4.873E−01	5.550E−01	6.271E−01	7.038E−01
900.0	2.535E−01	3.020E−01	3.548E−01	4.119E−01	4.733E−01	5.391E−01	6.092E−01	6.836E−01
1000.	2.478E−01	2.952E−01	3.468E−01	4.026E−01	4.627E−01	5.269E−01	5.955E−01	6.683E−01

Material: C-552 air-equivalent plastic

Ion	Li	Be	B	C	N	O	F	Ne
(E/A_1) / MeV				$(-\mathrm{d}E/\rho\mathrm{d}\ell)$ / MeV cm^2 mg^{-1}				
0.025	1.926E+00	2.371E+00	2.721E+00	2.999E+00	3.243E+00	3.463E+00	3.645E+00	3.812E+00
0.030	2.103E+00	2.606E+00	3.009E+00	3.334E+00	3.614E+00	3.867E+00	4.075E+00	4.265E+00
0.040	2.397E+00	3.017E+00	3.521E+00	3.936E+00	4.290E+00	4.607E+00	4.870E+00	5.107E+00
0.050	2.623E+00	3.357E+00	3.961E+00	4.466E+00	4.894E+00	5.277E+00	5.595E+00	5.881E+00
0.060	2.794E+00	3.634E+00	4.337E+00	4.933E+00	5.437E+00	5.887E+00	6.263E+00	6.597E+00
0.070	2.920E+00	3.855E+00	4.653E+00	5.339E+00	5.922E+00	6.443E+00	6.877E+00	7.263E+00
0.080	3.013E+00	4.029E+00	4.915E+00	5.687E+00	6.350E+00	6.944E+00	7.441E+00	7.881E+00
0.090	3.079E+00	4.165E+00	5.129E+00	5.983E+00	6.724E+00	7.391E+00	7.953E+00	8.450E+00
0.100	3.126E+00	4.271E+00	5.304E+00	6.233E+00	7.048E+00	7.787E+00	8.413E+00	8.970E+00
0.150	3.192E+00	4.519E+00	5.787E+00	6.986E+00	8.093E+00	9.131E+00	1.005E+01	1.088E+01
0.200	3.136E+00	4.545E+00	5.931E+00	7.280E+00	8.565E+00	9.799E+00	1.091E+01	1.196E+01
0.250	3.044E+00	4.488E+00	5.937E+00	7.372E+00	8.766E+00	1.013E+01	1.137E+01	1.256E+01
0.300	2.941E+00	4.397E+00	5.881E+00	7.366E+00	8.830E+00	1.027E+01	1.161E+01	1.290E+01
0.400	2.737E+00	4.186E+00	5.695E+00	7.230E+00	8.769E+00	1.031E+01	1.175E+01	1.315E+01
0.500	2.551E+00	3.972E+00	5.478E+00	7.029E+00	8.602E+00	1.019E+01	1.168E+01	1.315E+01
0.600	2.384E+00	3.770E+00	5.260E+00	6.809E+00	8.395E+00	1.001E+01	1.153E+01	1.304E+01
0.700	2.236E+00	3.582E+00	5.048E+00	6.587E+00	8.174E+00	9.799E+00	1.134E+01	1.286E+01
0.800	2.105E+00	3.409E+00	4.848E+00	6.370E+00	7.951E+00	9.579E+00	1.112E+01	1.266E+01
0.900	1.987E+00	3.251E+00	4.659E+00	6.161E+00	7.731E+00	9.355E+00	1.090E+01	1.244E+01
1.000	1.882E+00	3.105E+00	4.482E+00	5.961E+00	7.516E+00	9.133E+00	1.068E+01	1.222E+01
1.500	1.486E+00	2.528E+00	3.751E+00	5.103E+00	6.560E+00	8.105E+00	9.598E+00	1.111E+01
2.000	1.229E+00	2.129E+00	3.214E+00	4.443E+00	5.791E+00	7.245E+00	8.667E+00	1.011E+01
2.500	1.050E+00	1.838E+00	2.808E+00	3.926E+00	5.171E+00	6.531E+00	7.878E+00	9.261E+00
3.000	9.178E−01	1.618E+00	2.492E+00	3.513E+00	4.665E+00	5.936E+00	7.210E+00	8.527E+00
4.000	7.373E−01	1.309E+00	2.034E+00	2.899E+00	3.893E+00	5.007E+00	6.147E+00	7.341E+00
5.000	6.196E−01	1.102E+00	1.721E+00	2.468E+00	3.336E+00	4.322E+00	5.347E+00	6.432E+00
6.000	5.365E−01	9.550E−01	1.494E+00	2.150E+00	2.919E+00	3.798E+00	4.727E+00	5.718E+00
7.000	4.747E−01	8.448E−01	1.323E+00	1.907E+00	2.595E+00	3.388E+00	4.234E+00	5.144E+00
8.000	4.267E−01	7.592E−01	1.189E+00	1.715E+00	2.338E+00	3.058E+00	3.834E+00	4.674E+00
9.000	3.883E−01	6.906E−01	1.081E+00	1.561E+00	2.129E+00	2.788E+00	3.504E+00	4.283E+00
10.00	3.569E−01	6.344E−01	9.929E−01	1.433E+00	1.956E+00	2.563E+00	3.228E+00	3.953E+00
15.00	2.575E−01	4.573E−01	7.145E−01	1.030E+00	1.405E+00	1.841E+00	2.329E+00	2.868E+00
20.00	2.041E−01	3.624E−01	5.659E−01	8.149E−01	1.110E+00	1.453E+00	1.840E+00	2.269E+00
25.00	1.704E−01	3.027E−01	4.725E−01	6.801E−01	9.258E−01	1.211E+00	1.532E+00	1.891E+00
30.00	1.471E−01	2.613E−01	4.080E−01	5.872E−01	7.990E−01	1.044E+00	1.321E+00	1.631E+00
40.00	1.168E−01	2.076E−01	3.241E−01	4.664E−01	6.345E−01	8.286E−01	1.048E+00	1.294E+00
50.00	9.782E−02	1.739E−01	2.716E−01	3.909E−01	5.318E−01	6.944E−01	8.785E−01	1.084E+00
60.00	8.477E−02	1.507E−01	2.354E−01	3.389E−01	4.612E−01	6.021E−01	7.618E−01	9.401E−01
70.00	7.522E−02	1.337E−01	2.090E−01	3.009E−01	4.094E−01	5.346E−01	6.764E−01	8.348E−01
80.00	6.791E−02	1.208E−01	1.887E−01	2.717E−01	3.698E−01	4.829E−01	6.111E−01	7.542E−01
90.00	6.213E−02	1.105E−01	1.727E−01	2.486E−01	3.384E−01	4.420E−01	5.594E−01	6.905E−01
100.0	5.744E−02	1.021E−01	1.596E−01	2.299E−01	3.130E−01	4.088E−01	5.174E−01	6.387E−01
150.0	4.298E−02	7.645E−02	1.195E−01	1.722E−01	2.344E−01	3.063E−01	3.878E−01	4.788E−01
200.0	3.550E−02	6.316E−02	9.875E−02	1.423E−01	1.938E−01	2.532E−01	3.206E−01	3.960E−01
250.0	3.094E−02	5.504E−02	8.607E−02	1.240E−01	1.689E−01	2.208E−01	2.796E−01	3.453E−01
300.0	2.787E−02	4.959E−02	7.755E−02	1.117E−01	1.522E−01	1.990E−01	2.520E−01	3.113E−01
400.0	2.404E−02	4.278E−02	6.690E−02	9.641E−02	1.313E−01	1.717E−01	2.175E−01	2.687E−01
500.0	2.178E−02	3.875E−02	6.060E−02	8.734E−02	1.190E−01	1.555E−01	1.970E−01	2.435E−01
600.0	2.030E−02	3.613E−02	5.650E−02	8.144E−02	1.110E−01	1.451E−01	1.838E−01	2.271E−01
700.0	1.929E−02	3.433E−02	5.368E−02	7.738E−02	1.054E−01	1.378E−01	1.746E−01	2.158E−01
800.0	1.856E−02	3.303E−02	5.166E−02	7.447E−02	1.015E−01	1.326E−01	1.680E−01	2.077E−01
900.0	1.803E−02	3.208E−02	5.017E−02	7.232E−02	9.853E−02	1.288E−01	1.632E−01	2.017E−01
1000.	1.762E−02	3.135E−02	4.903E−02	7.068E−02	9.629E−02	1.259E−01	1.595E−01	1.971E−01

Material: C-552 air-equivalent plastic

Ion	Na	Mg	Al	Si	P	S	Cl	Ar
(E/A_1) / MeV				$(-\mathrm{d}E/\rho\mathrm{d}\ell)$ / MeV cm^2 mg^{-1}				
0.025	3.948E+00	4.100E+00	4.243E+00	4.384E+00	4.538E+00	4.670E+00	4.832E+00	4.931E+00
0.030	4.421E+00	4.581E+00	4.737E+00	4.889E+00	5.054E+00	5.200E+00	5.372E+00	5.481E+00
0.040	5.310E+00	5.489E+00	5.669E+00	5.844E+00	6.030E+00	6.202E+00	6.391E+00	6.515E+00
0.050	6.132E+00	6.337E+00	6.544E+00	6.742E+00	6.951E+00	7.148E+00	7.353E+00	7.491E+00
0.060	6.899E+00	7.131E+00	7.369E+00	7.591E+00	7.825E+00	8.047E+00	8.271E+00	8.423E+00
0.070	7.618E+00	7.879E+00	8.148E+00	8.397E+00	8.656E+00	8.904E+00	9.148E+00	9.316E+00
0.080	8.292E+00	8.584E+00	8.886E+00	9.164E+00	9.450E+00	9.723E+00	9.989E+00	1.017E+01
0.090	8.921E+00	9.248E+00	9.587E+00	9.895E+00	1.021E+01	1.051E+01	1.080E+01	1.100E+01
0.100	9.504E+00	9.869E+00	1.025E+01	1.059E+01	1.093E+01	1.126E+01	1.157E+01	1.179E+01
0.150	1.173E+01	1.232E+01	1.293E+01	1.347E+01	1.401E+01	1.452E+01	1.498E+01	1.533E+01
0.200	1.306E+01	1.384E+01	1.466E+01	1.541E+01	1.615E+01	1.686E+01	1.751E+01	1.802E+01
0.250	1.385E+01	1.477E+01	1.576E+01	1.668E+01	1.759E+01	1.847E+01	1.929E+01	1.996E+01
0.300	1.432E+01	1.534E+01	1.646E+01	1.750E+01	1.856E+01	1.958E+01	2.053E+01	2.133E+01
0.400	1.476E+01	1.589E+01	1.718E+01	1.840E+01	1.965E+01	2.088E+01	2.203E+01	2.303E+01
0.500	1.487E+01	1.606E+01	1.745E+01	1.878E+01	2.016E+01	2.152E+01	2.280E+01	2.393E+01
0.600	1.483E+01	1.605E+01	1.751E+01	1.890E+01	2.036E+01	2.182E+01	2.319E+01	2.441E+01
0.700	1.471E+01	1.594E+01	1.744E+01	1.888E+01	2.041E+01	2.193E+01	2.337E+01	2.464E+01
0.800	1.454E+01	1.578E+01	1.731E+01	1.878E+01	2.035E+01	2.192E+01	2.341E+01	2.473E+01
0.900	1.435E+01	1.558E+01	1.713E+01	1.863E+01	2.023E+01	2.184E+01	2.336E+01	2.471E+01
1.000	1.414E+01	1.537E+01	1.693E+01	1.845E+01	2.007E+01	2.171E+01	2.326E+01	2.464E+01
1.500	1.305E+01	1.424E+01	1.581E+01	1.735E+01	1.903E+01	2.073E+01	2.235E+01	2.379E+01
2.000	1.202E+01	1.317E+01	1.471E+01	1.622E+01	1.790E+01	1.961E+01	2.124E+01	2.268E+01
2.500	1.110E+01	1.220E+01	1.371E+01	1.519E+01	1.684E+01	1.853E+01	2.014E+01	2.158E+01
3.000	1.029E+01	1.136E+01	1.281E+01	1.425E+01	1.586E+01	1.752E+01	1.911E+01	2.052E+01
4.000	8.949E+00	9.946E+00	1.131E+01	1.266E+01	1.418E+01	1.576E+01	1.728E+01	1.864E+01
5.000	7.893E+00	8.829E+00	1.009E+01	1.136E+01	1.279E+01	1.429E+01	1.573E+01	1.703E+01
6.000	7.048E+00	7.929E+00	9.109E+00	1.030E+01	1.164E+01	1.305E+01	1.442E+01	1.566E+01
7.000	6.358E+00	7.191E+00	8.292E+00	9.409E+00	1.067E+01	1.200E+01	1.330E+01	1.449E+01
8.000	5.787E+00	6.576E+00	7.606E+00	8.658E+00	9.844E+00	1.110E+01	1.233E+01	1.347E+01
9.000	5.308E+00	6.057E+00	7.024E+00	8.016E+00	9.133E+00	1.032E+01	1.149E+01	1.258E+01
10.00	4.901E+00	5.613E+00	6.524E+00	7.462E+00	8.517E+00	9.639E+00	1.075E+01	1.180E+01
15.00	3.546E+00	4.118E+00	4.817E+00	5.549E+00	6.367E+00	7.244E+00	8.131E+00	8.987E+00
20.00	2.793E+00	3.270E+00	3.835E+00	4.433E+00	5.096E+00	5.810E+00	6.543E+00	7.265E+00
25.00	2.317E+00	2.728E+00	3.202E+00	3.707E+00	4.264E+00	4.866E+00	5.488E+00	6.113E+00
30.00	1.992E+00	2.352E+00	2.762E+00	3.200E+00	3.681E+00	4.200E+00	4.742E+00	5.291E+00
40.00	1.573E+00	1.864E+00	2.189E+00	2.538E+00	2.918E+00	3.329E+00	3.760E+00	4.205E+00
50.00	1.315E+00	1.561E+00	1.833E+00	2.125E+00	2.442E+00	2.783E+00	3.144E+00	3.520E+00
60.00	1.139E+00	1.353E+00	1.589E+00	1.842E+00	2.116E+00	2.411E+00	2.723E+00	3.050E+00
70.00	1.011E+00	1.202E+00	1.410E+00	1.635E+00	1.878E+00	2.139E+00	2.415E+00	2.707E+00
80.00	9.130E−01	1.086E+00	1.274E+00	1.478E+00	1.697E+00	1.932E+00	2.181E+00	2.444E+00
90.00	8.357E−01	9.941E−01	1.167E+00	1.353E+00	1.553E+00	1.768E+00	1.996E+00	2.238E+00
100.0	7.730E−01	9.196E−01	1.079E+00	1.252E+00	1.437E+00	1.636E+00	1.847E+00	2.070E+00
150.0	5.796E−01	6.898E−01	8.097E−01	9.393E−01	1.078E+00	1.227E+00	1.386E+00	1.554E+00
200.0	4.794E−01	5.707E−01	6.700E−01	7.774E−01	8.927E−01	1.016E+00	1.148E+00	1.287E+00
250.0	4.181E−01	4.978E−01	5.846E−01	6.783E−01	7.791E−01	8.869E−01	1.002E+00	1.124E+00
300.0	3.769E−01	4.488E−01	5.271E−01	6.117E−01	7.026E−01	7.999E−01	9.035E−01	1.014E+00
400.0	3.254E−01	3.875E−01	4.551E−01	5.282E−01	6.069E−01	6.910E−01	7.806E−01	8.758E−01
500.0	2.948E−01	3.512E−01	4.125E−01	4.788E−01	5.501E−01	6.264E−01	7.078E−01	7.942E−01
600.0	2.750E−01	3.276E−01	3.848E−01	4.467E−01	5.132E−01	5.845E−01	6.604E−01	7.410E−01
700.0	2.613E−01	3.113E−01	3.657E−01	4.245E−01	4.878E−01	5.555E−01	6.277E−01	7.044E−01
800.0	2.515E−01	2.996E−01	3.520E−01	4.086E−01	4.695E−01	5.347E−01	6.043E−01	6.781E−01
900.0	2.443E−01	2.910E−01	3.419E−01	3.969E−01	4.560E−01	5.194E−01	5.869E−01	6.587E−01
1000.	2.387E−01	2.844E−01	3.341E−01	3.879E−01	4.458E−01	5.077E−01	5.737E−01	6.438E−01

Material: Calcium fluoride

Ion	Li	Be	B	C	N	O	F	Ne
(E/A_1) / MeV				$(-\mathrm{d}E/\rho\mathrm{d}\ell)$ / MeV cm^2 mg^{-1}				
0.025	1.514E+00	1.913E+00	2.238E+00	2.506E+00	2.732E+00	2.934E+00	3.114E+00	3.280E+00
0.030	1.638E+00	2.085E+00	2.453E+00	2.761E+00	3.021E+00	3.251E+00	3.456E+00	3.643E+00
0.040	1.842E+00	2.375E+00	2.825E+00	3.209E+00	3.534E+00	3.824E+00	4.078E+00	4.309E+00
0.050	2.004E+00	2.615E+00	3.138E+00	3.592E+00	3.981E+00	4.329E+00	4.635E+00	4.911E+00
0.060	2.133E+00	2.815E+00	3.406E+00	3.925E+00	4.375E+00	4.779E+00	5.135E+00	5.457E+00
0.070	2.236E+00	2.982E+00	3.637E+00	4.217E+00	4.724E+00	5.183E+00	5.589E+00	5.956E+00
0.080	2.317E+00	3.122E+00	3.836E+00	4.474E+00	5.036E+00	5.547E+00	6.001E+00	6.412E+00
0.090	2.379E+00	3.237E+00	4.007E+00	4.700E+00	5.315E+00	5.876E+00	6.376E+00	6.831E+00
0.100	2.427E+00	3.331E+00	4.152E+00	4.898E+00	5.563E+00	6.173E+00	6.718E+00	7.216E+00
0.150	2.520E+00	3.582E+00	4.594E+00	5.549E+00	6.432E+00	7.259E+00	8.011E+00	8.707E+00
0.200	2.500E+00	3.636E+00	4.753E+00	5.838E+00	6.870E+00	7.855E+00	8.770E+00	9.630E+00
0.250	2.443E+00	3.612E+00	4.786E+00	5.948E+00	7.074E+00	8.168E+00	9.196E+00	1.018E+01
0.300	2.372E+00	3.556E+00	4.762E+00	5.970E+00	7.158E+00	8.324E+00	9.431E+00	1.050E+01
0.400	2.226E+00	3.409E+00	4.642E+00	5.897E+00	7.154E+00	8.406E+00	9.608E+00	1.078E+01
0.500	2.088E+00	3.253E+00	4.488E+00	5.761E+00	7.051E+00	8.348E+00	9.602E+00	1.084E+01
0.600	1.963E+00	3.102E+00	4.327E+00	5.603E+00	6.909E+00	8.231E+00	9.514E+00	1.079E+01
0.700	1.851E+00	2.960E+00	4.169E+00	5.440E+00	6.750E+00	8.086E+00	9.386E+00	1.068E+01
0.800	1.750E+00	2.829E+00	4.018E+00	5.278E+00	6.586E+00	7.927E+00	9.236E+00	1.054E+01
0.900	1.659E+00	2.707E+00	3.874E+00	5.120E+00	6.422E+00	7.764E+00	9.076E+00	1.039E+01
1.000	1.577E+00	2.594E+00	3.738E+00	4.968E+00	6.261E+00	7.599E+00	8.911E+00	1.023E+01
1.500	1.265E+00	2.143E+00	3.169E+00	4.304E+00	5.528E+00	6.818E+00	8.097E+00	9.397E+00
2.000	1.057E+00	1.824E+00	2.743E+00	3.783E+00	4.925E+00	6.147E+00	7.374E+00	8.630E+00
2.500	9.105E−01	1.587E+00	2.415E+00	3.369E+00	4.431E+00	5.582E+00	6.750E+00	7.956E+00
3.000	8.010E−01	1.406E+00	2.158E+00	3.034E+00	4.022E+00	5.105E+00	6.214E+00	7.367E+00
4.000	6.489E−01	1.148E+00	1.779E+00	2.529E+00	3.390E+00	4.349E+00	5.349E+00	6.401E+00
5.000	5.484E−01	9.733E−01	1.516E+00	2.169E+00	2.927E+00	3.783E+00	4.687E+00	5.649E+00
6.000	4.768E−01	8.473E−01	1.323E+00	1.900E+00	2.576E+00	3.345E+00	4.168E+00	5.050E+00
7.000	4.231E−01	7.521E−01	1.176E+00	1.692E+00	2.301E+00	2.998E+00	3.751E+00	4.565E+00
8.000	3.813E−01	6.777E−01	1.060E+00	1.527E+00	2.080E+00	2.717E+00	3.410E+00	4.163E+00
9.000	3.477E−01	6.179E−01	9.664E−01	1.394E+00	1.900E+00	2.485E+00	3.127E+00	3.827E+00
10.00	3.200E−01	5.687E−01	8.893E−01	1.283E+00	1.750E+00	2.291E+00	2.888E+00	3.542E+00
15.00	2.322E−01	4.125E−01	6.443E−01	9.286E−01	1.267E+00	1.660E+00	2.101E+00	2.591E+00
20.00	1.847E−01	3.281E−01	5.122E−01	7.376E−01	1.005E+00	1.316E+00	1.667E+00	2.058E+00
25.00	1.546E−01	2.747E−01	4.289E−01	6.173E−01	8.405E−01	1.099E+00	1.392E+00	1.720E+00
30.00	1.338E−01	2.377E−01	3.711E−01	5.340E−01	7.267E−01	9.498E−01	1.203E+00	1.485E+00
40.00	1.065E−01	1.893E−01	2.956E−01	4.255E−01	5.788E−01	7.560E−01	9.567E−01	1.181E+00
50.00	8.939E−02	1.589E−01	2.482E−01	3.573E−01	4.861E−01	6.348E−01	8.032E−01	9.914E−01
60.00	7.759E−02	1.380E−01	2.155E−01	3.103E−01	4.223E−01	5.513E−01	6.975E−01	8.610E−01
70.00	6.894E−02	1.226E−01	1.915E−01	2.758E−01	3.753E−01	4.901E−01	6.201E−01	7.654E−01
80.00	6.230E−02	1.108E−01	1.731E−01	2.493E−01	3.393E−01	4.432E−01	5.608E−01	6.922E−01
90.00	5.705E−02	1.015E−01	1.586E−01	2.284E−01	3.108E−01	4.060E−01	5.138E−01	6.343E−01
100.0	5.279E−02	9.388E−02	1.467E−01	2.113E−01	2.877E−01	3.758E−01	4.756E−01	5.872E−01
150.0	3.961E−02	7.045E−02	1.101E−01	1.587E−01	2.161E−01	2.823E−01	3.574E−01	4.414E−01
200.0	3.277E−02	5.830E−02	9.116E−02	1.314E−01	1.789E−01	2.338E−01	2.960E−01	3.657E−01
250.0	2.860E−02	5.088E−02	7.956E−02	1.146E−01	1.562E−01	2.041E−01	2.585E−01	3.193E−01
300.0	2.579E−02	4.589E−02	7.176E−02	1.034E−01	1.409E−01	1.841E−01	2.332E−01	2.881E−01
400.0	2.228E−02	3.964E−02	6.200E−02	8.935E−02	1.217E−01	1.591E−01	2.016E−01	2.491E−01
500.0	2.020E−02	3.595E−02	5.622E−02	8.104E−02	1.104E−01	1.444E−01	1.828E−01	2.259E−01
600.0	1.886E−02	3.355E−02	5.248E−02	7.564E−02	1.031E−01	1.348E−01	1.707E−01	2.109E−01
700.0	1.793E−02	3.190E−02	4.990E−02	7.193E−02	9.801E−02	1.281E−01	1.623E−01	2.006E−01
800.0	1.726E−02	3.072E−02	4.806E−02	6.927E−02	9.438E−02	1.234E−01	1.563E−01	1.932E−01
900.0	1.677E−02	2.985E−02	4.669E−02	6.731E−02	9.171E−02	1.199E−01	1.519E−01	1.877E−01
1000.	1.640E−02	2.919E−02	4.565E−02	6.581E−02	8.967E−02	1.172E−01	1.485E−01	1.836E−01

Material: Calcium fluoride

Ion	Na	Mg	Al	Si	P	S	Cl	Ar
(E/A_1) / MeV				$(-\mathrm{d}E/\rho\mathrm{d}\ell)$ / MeV cm^2 mg^{-1}				
0.025	3.422E+00	3.568E+00	3.704E+00	3.835E+00	3.959E+00	4.077E+00	4.203E+00	4.313E+00
0.030	3.803E+00	3.963E+00	4.112E+00	4.255E+00	4.391E+00	4.521E+00	4.656E+00	4.776E+00
0.040	4.507E+00	4.697E+00	4.873E+00	5.039E+00	5.195E+00	5.348E+00	5.500E+00	5.638E+00
0.050	5.148E+00	5.371E+00	5.576E+00	5.767E+00	5.945E+00	6.120E+00	6.289E+00	6.443E+00
0.060	5.736E+00	5.994E+00	6.230E+00	6.447E+00	6.650E+00	6.848E+00	7.036E+00	7.208E+00
0.070	6.277E+00	6.572E+00	6.840E+00	7.086E+00	7.315E+00	7.538E+00	7.747E+00	7.938E+00
0.080	6.775E+00	7.107E+00	7.410E+00	7.686E+00	7.943E+00	8.193E+00	8.424E+00	8.635E+00
0.090	7.236E+00	7.604E+00	7.942E+00	8.250E+00	8.535E+00	8.812E+00	9.068E+00	9.299E+00
0.100	7.661E+00	8.067E+00	8.439E+00	8.779E+00	9.094E+00	9.398E+00	9.679E+00	9.933E+00
0.150	9.347E+00	9.931E+00	1.047E+01	1.097E+01	1.144E+01	1.188E+01	1.230E+01	1.267E+01
0.200	1.044E+01	1.119E+01	1.189E+01	1.254E+01	1.315E+01	1.374E+01	1.429E+01	1.479E+01
0.250	1.112E+01	1.200E+01	1.283E+01	1.362E+01	1.437E+01	1.509E+01	1.577E+01	1.639E+01
0.300	1.154E+01	1.252E+01	1.346E+01	1.435E+01	1.521E+01	1.605E+01	1.684E+01	1.758E+01
0.400	1.195E+01	1.306E+01	1.415E+01	1.518E+01	1.621E+01	1.723E+01	1.819E+01	1.909E+01
0.500	1.208E+01	1.327E+01	1.444E+01	1.557E+01	1.671E+01	1.783E+01	1.891E+01	1.993E+01
0.600	1.207E+01	1.331E+01	1.454E+01	1.573E+01	1.695E+01	1.815E+01	1.931E+01	2.041E+01
0.700	1.199E+01	1.327E+01	1.454E+01	1.577E+01	1.704E+01	1.830E+01	1.952E+01	2.067E+01
0.800	1.187E+01	1.317E+01	1.447E+01	1.573E+01	1.704E+01	1.834E+01	1.960E+01	2.081E+01
0.900	1.173E+01	1.304E+01	1.436E+01	1.564E+01	1.698E+01	1.832E+01	1.961E+01	2.085E+01
1.000	1.158E+01	1.290E+01	1.423E+01	1.553E+01	1.689E+01	1.825E+01	1.957E+01	2.083E+01
1.500	1.075E+01	1.207E+01	1.342E+01	1.475E+01	1.616E+01	1.759E+01	1.898E+01	2.031E+01
2.000	9.946E+00	1.124E+01	1.257E+01	1.389E+01	1.532E+01	1.676E+01	1.817E+01	1.951E+01
2.500	9.227E+00	1.049E+01	1.179E+01	1.308E+01	1.449E+01	1.592E+01	1.733E+01	1.866E+01
3.000	8.591E+00	9.811E+00	1.108E+01	1.234E+01	1.372E+01	1.513E+01	1.652E+01	1.783E+01
4.000	7.530E+00	8.666E+00	9.853E+00	1.105E+01	1.236E+01	1.371E+01	1.505E+01	1.631E+01
5.000	6.689E+00	7.745E+00	8.856E+00	9.980E+00	1.122E+01	1.251E+01	1.379E+01	1.500E+01
6.000	6.011E+00	6.994E+00	8.034E+00	9.092E+00	1.027E+01	1.149E+01	1.271E+01	1.386E+01
7.000	5.454E+00	6.372E+00	7.347E+00	8.344E+00	9.452E+00	1.061E+01	1.177E+01	1.288E+01
8.000	4.990E+00	5.849E+00	6.765E+00	7.707E+00	8.753E+00	9.853E+00	1.096E+01	1.202E+01
9.000	4.598E+00	5.405E+00	6.268E+00	7.158E+00	8.148E+00	9.192E+00	1.025E+01	1.126E+01
10.00	4.264E+00	5.023E+00	5.837E+00	6.681E+00	7.620E+00	8.613E+00	9.617E+00	1.059E+01
15.00	3.135E+00	3.718E+00	4.350E+00	5.014E+00	5.752E+00	6.539E+00	7.349E+00	8.146E+00
20.00	2.494E+00	2.966E+00	3.479E+00	4.025E+00	4.628E+00	5.275E+00	5.947E+00	6.621E+00
25.00	2.084E+00	2.481E+00	2.913E+00	3.376E+00	3.885E+00	4.433E+00	5.006E+00	5.588E+00
30.00	1.800E+00	2.143E+00	2.517E+00	2.919E+00	3.360E+00	3.835E+00	4.334E+00	4.846E+00
40.00	1.430E+00	1.703E+00	2.000E+00	2.320E+00	2.670E+00	3.047E+00	3.444E+00	3.858E+00
50.00	1.200E+00	1.428E+00	1.677E+00	1.946E+00	2.237E+00	2.551E+00	2.884E+00	3.233E+00
60.00	1.042E+00	1.240E+00	1.456E+00	1.688E+00	1.940E+00	2.211E+00	2.500E+00	2.802E+00
70.00	9.261E−01	1.102E+00	1.294E+00	1.500E+00	1.724E+00	1.964E+00	2.219E+00	2.488E+00
80.00	8.375E−01	9.967E−01	1.170E+00	1.357E+00	1.558E+00	1.775E+00	2.005E+00	2.248E+00
90.00	7.674E−01	9.133E−01	1.072E+00	1.243E+00	1.428E+00	1.625E+00	1.836E+00	2.059E+00
100.0	7.105E−01	8.455E−01	9.923E−01	1.151E+00	1.322E+00	1.505E+00	1.699E+00	1.906E+00
150.0	5.342E−01	6.359E−01	7.465E−01	8.660E−01	9.944E−01	1.132E+00	1.278E+00	1.433E+00
200.0	4.427E−01	5.270E−01	6.188E−01	7.180E−01	8.245E−01	9.386E−01	1.060E+00	1.189E+00
250.0	3.866E−01	4.604E−01	5.406E−01	6.273E−01	7.205E−01	8.202E−01	9.265E−01	1.039E+00
300.0	3.489E−01	4.155E−01	4.879E−01	5.662E−01	6.504E−01	7.405E−01	8.365E−01	9.385E−01
400.0	3.016E−01	3.592E−01	4.220E−01	4.898E−01	5.627E−01	6.407E−01	7.239E−01	8.122E−01
500.0	2.736E−01	3.260E−01	3.829E−01	4.445E−01	5.107E−01	5.816E−01	6.571E−01	7.373E−01
600.0	2.555E−01	3.043E−01	3.575E−01	4.150E−01	4.769E−01	5.431E−01	6.137E−01	6.887E−01
700.0	2.430E−01	2.895E−01	3.401E−01	3.948E−01	4.536E−01	5.167E−01	5.838E−01	6.552E−01
800.0	2.340E−01	2.788E−01	3.275E−01	3.803E−01	4.370E−01	4.977E−01	5.624E−01	6.312E−01
900.0	2.274E−01	2.709E−01	3.183E−01	3.695E−01	4.247E−01	4.837E−01	5.466E−01	6.134E−01
1000.	2.224E−01	2.649E−01	3.112E−01	3.613E−01	4.152E−01	4.730E−01	5.345E−01	5.999E−01

Material: Carbon dioxide

Ion	Li	Be	B	C	N	O	F	Ne
(E/A_1) / MeV				$(-\mathrm{d}E/\rho\mathrm{d}\ell)$ / MeV cm^2 mg^{-1}				
0.025	1.909E+00	2.350E+00	2.696E+00	2.972E+00	3.208E+00	3.419E+00	3.605E+00	3.767E+00
0.030	2.083E+00	2.582E+00	2.981E+00	3.304E+00	3.579E+00	3.823E+00	4.037E+00	4.221E+00
0.040	2.374E+00	2.986E+00	3.484E+00	3.899E+00	4.250E+00	4.562E+00	4.835E+00	5.068E+00
0.050	2.602E+00	3.325E+00	3.919E+00	4.422E+00	4.848E+00	5.228E+00	5.560E+00	5.843E+00
0.060	2.778E+00	3.605E+00	4.295E+00	4.885E+00	5.386E+00	5.833E+00	6.223E+00	6.556E+00
0.070	2.910E+00	3.832E+00	4.615E+00	5.292E+00	5.869E+00	6.384E+00	6.833E+00	7.218E+00
0.080	3.008E+00	4.014E+00	4.885E+00	5.645E+00	6.300E+00	6.885E+00	7.395E+00	7.831E+00
0.090	3.079E+00	4.157E+00	5.108E+00	5.949E+00	6.679E+00	7.336E+00	7.907E+00	8.399E+00
0.100	3.128E+00	4.267E+00	5.290E+00	6.207E+00	7.011E+00	7.737E+00	8.372E+00	8.920E+00
0.150	3.196E+00	4.525E+00	5.791E+00	6.988E+00	8.091E+00	9.121E+00	1.005E+01	1.087E+01
0.200	3.137E+00	4.547E+00	5.935E+00	7.286E+00	8.573E+00	9.806E+00	1.094E+01	1.198E+01
0.250	3.042E+00	4.487E+00	5.937E+00	7.374E+00	8.771E+00	1.013E+01	1.140E+01	1.259E+01
0.300	2.938E+00	4.395E+00	5.878E+00	7.365E+00	8.831E+00	1.027E+01	1.163E+01	1.292E+01
0.400	2.733E+00	4.182E+00	5.689E+00	7.224E+00	8.765E+00	1.030E+01	1.176E+01	1.317E+01
0.500	2.547E+00	3.967E+00	5.472E+00	7.022E+00	8.596E+00	1.018E+01	1.169E+01	1.316E+01
0.600	2.380E+00	3.765E+00	5.253E+00	6.802E+00	8.389E+00	1.000E+01	1.154E+01	1.305E+01
0.700	2.232E+00	3.577E+00	5.042E+00	6.580E+00	8.169E+00	9.794E+00	1.134E+01	1.287E+01
0.800	2.101E+00	3.404E+00	4.842E+00	6.364E+00	7.947E+00	9.574E+00	1.113E+01	1.267E+01
0.900	1.984E+00	3.246E+00	4.653E+00	6.155E+00	7.727E+00	9.351E+00	1.090E+01	1.245E+01
1.000	1.878E+00	3.100E+00	4.477E+00	5.956E+00	7.514E+00	9.130E+00	1.068E+01	1.223E+01
1.500	1.484E+00	2.525E+00	3.747E+00	5.101E+00	6.562E+00	8.108E+00	9.605E+00	1.112E+01
2.000	1.227E+00	2.127E+00	3.212E+00	4.443E+00	5.795E+00	7.251E+00	8.676E+00	1.014E+01
2.500	1.048E+00	1.837E+00	2.807E+00	3.927E+00	5.177E+00	6.540E+00	7.889E+00	9.283E+00
3.000	9.166E−01	1.617E+00	2.492E+00	3.515E+00	4.671E+00	5.945E+00	7.221E+00	8.549E+00
4.000	7.364E−01	1.308E+00	2.034E+00	2.901E+00	3.898E+00	5.016E+00	6.158E+00	7.362E+00
5.000	6.188E−01	1.101E+00	1.721E+00	2.469E+00	3.340E+00	4.330E+00	5.357E+00	6.451E+00
6.000	5.359E−01	9.543E−01	1.494E+00	2.151E+00	2.922E+00	3.805E+00	4.735E+00	5.733E+00
7.000	4.741E−01	8.441E−01	1.322E+00	1.907E+00	2.598E+00	3.393E+00	4.241E+00	5.157E+00
8.000	4.262E−01	7.585E−01	1.188E+00	1.715E+00	2.340E+00	3.062E+00	3.840E+00	4.685E+00
9.000	3.879E−01	6.900E−01	1.081E+00	1.560E+00	2.130E+00	2.791E+00	3.509E+00	4.292E+00
10.00	3.565E−01	6.338E−01	9.923E−01	1.433E+00	1.957E+00	2.566E+00	3.231E+00	3.961E+00
15.00	2.572E−01	4.568E−01	7.139E−01	1.029E+00	1.405E+00	1.842E+00	2.330E+00	2.871E+00
20.00	2.039E−01	3.621E−01	5.654E−01	8.143E−01	1.110E+00	1.453E+00	1.839E+00	2.270E+00
25.00	1.702E−01	3.024E−01	4.721E−01	6.796E−01	9.252E−01	1.210E+00	1.532E+00	1.891E+00
30.00	1.470E−01	2.611E−01	4.077E−01	5.867E−01	7.984E−01	1.043E+00	1.321E+00	1.630E+00
40.00	1.167E−01	2.074E−01	3.238E−01	4.661E−01	6.341E−01	8.280E−01	1.048E+00	1.293E+00
50.00	9.774E−02	1.737E−01	2.714E−01	3.906E−01	5.314E−01	6.939E−01	8.778E−01	1.083E+00
60.00	8.470E−02	1.506E−01	2.353E−01	3.387E−01	4.608E−01	6.017E−01	7.612E−01	9.395E−01
70.00	7.516E−02	1.336E−01	2.088E−01	3.006E−01	4.091E−01	5.342E−01	6.759E−01	8.342E−01
80.00	6.786E−02	1.207E−01	1.885E−01	2.715E−01	3.695E−01	4.826E−01	6.106E−01	7.537E−01
90.00	6.208E−02	1.104E−01	1.725E−01	2.485E−01	3.382E−01	4.417E−01	5.590E−01	6.900E−01
100.0	5.740E−02	1.021E−01	1.595E−01	2.298E−01	3.128E−01	4.085E−01	5.170E−01	6.383E−01
150.0	4.295E−02	7.640E−02	1.194E−01	1.721E−01	2.343E−01	3.061E−01	3.875E−01	4.785E−01
200.0	3.548E−02	6.312E−02	9.868E−02	1.422E−01	1.936E−01	2.530E−01	3.204E−01	3.957E−01
250.0	3.092E−02	5.504E−02	8.601E−02	1.239E−01	1.688E−01	2.206E−01	2.794E−01	3.451E−01
300.0	2.786E−02	4.957E−02	7.750E−02	1.117E−01	1.521E−01	1.988E−01	2.518E−01	3.111E−01
400.0	2.403E−02	4.276E−02	6.686E−02	9.636E−02	1.313E−01	1.716E−01	2.173E−01	2.685E−01
500.0	2.176E−02	3.873E−02	6.056E−02	8.729E−02	1.189E−01	1.555E−01	1.969E−01	2.433E−01
600.0	2.029E−02	3.611E−02	5.647E−02	8.140E−02	1.109E−01	1.450E−01	1.837E−01	2.269E−01
700.0	1.928E−02	3.431E−02	5.366E−02	7.734E−02	1.054E−01	1.378E−01	1.745E−01	2.157E−01
800.0	1.855E−02	3.302E−02	5.164E−02	7.443E−02	1.014E−01	1.326E−01	1.680E−01	2.076E−01
900.0	1.802E−02	3.206E−02	5.015E−02	7.228E−02	9.848E−02	1.288E−01	1.631E−01	2.016E−01
1000.	1.761E−02	3.133E−02	4.901E−02	7.064E−02	9.625E−02	1.258E−01	1.594E−01	1.970E−01

Material: Carbon dioxide

Ion	Na	Mg	Al	Si	P	S	Cl	Ar
(E/A_1) / MeV				$(-\mathrm{d}E/\rho\mathrm{d}\ell)$ / MeV cm^2 mg^{-1}				
0.025	3.897E+00	4.043E+00	4.179E+00	4.312E+00	4.450E+00	4.574E+00	4.722E+00	4.820E+00
0.030	4.371E+00	4.528E+00	4.676E+00	4.820E+00	4.968E+00	5.105E+00	5.263E+00	5.370E+00
0.040	5.263E+00	5.444E+00	5.618E+00	5.785E+00	5.953E+00	6.114E+00	6.289E+00	6.411E+00
0.050	6.088E+00	6.300E+00	6.503E+00	6.695E+00	6.887E+00	7.072E+00	7.266E+00	7.401E+00
0.060	6.854E+00	7.098E+00	7.334E+00	7.555E+00	7.774E+00	7.987E+00	8.201E+00	8.352E+00
0.070	7.567E+00	7.845E+00	8.116E+00	8.368E+00	8.615E+00	8.857E+00	9.094E+00	9.262E+00
0.080	8.235E+00	8.547E+00	8.855E+00	9.137E+00	9.415E+00	9.685E+00	9.946E+00	1.013E+01
0.090	8.858E+00	9.207E+00	9.552E+00	9.867E+00	1.018E+01	1.047E+01	1.076E+01	1.097E+01
0.100	9.438E+00	9.826E+00	1.021E+01	1.056E+01	1.090E+01	1.123E+01	1.154E+01	1.177E+01
0.150	1.169E+01	1.229E+01	1.290E+01	1.345E+01	1.398E+01	1.448E+01	1.494E+01	1.530E+01
0.200	1.305E+01	1.386E+01	1.468E+01	1.543E+01	1.616E+01	1.686E+01	1.750E+01	1.802E+01
0.250	1.384E+01	1.480E+01	1.580E+01	1.672E+01	1.764E+01	1.851E+01	1.933E+01	2.000E+01
0.300	1.431E+01	1.537E+01	1.650E+01	1.756E+01	1.861E+01	1.964E+01	2.059E+01	2.140E+01
0.400	1.473E+01	1.592E+01	1.721E+01	1.845E+01	1.970E+01	2.093E+01	2.209E+01	2.310E+01
0.500	1.483E+01	1.608E+01	1.748E+01	1.881E+01	2.019E+01	2.155E+01	2.285E+01	2.399E+01
0.600	1.479E+01	1.606E+01	1.752E+01	1.893E+01	2.039E+01	2.184E+01	2.323E+01	2.446E+01
0.700	1.466E+01	1.595E+01	1.745E+01	1.890E+01	2.043E+01	2.195E+01	2.340E+01	2.468E+01
0.800	1.450E+01	1.579E+01	1.732E+01	1.880E+01	2.037E+01	2.194E+01	2.344E+01	2.477E+01
0.900	1.430E+01	1.559E+01	1.715E+01	1.865E+01	2.025E+01	2.186E+01	2.339E+01	2.475E+01
1.000	1.410E+01	1.538E+01	1.695E+01	1.846E+01	2.009E+01	2.173E+01	2.329E+01	2.467E+01
1.500	1.301E+01	1.426E+01	1.583E+01	1.737E+01	1.905E+01	2.076E+01	2.239E+01	2.383E+01
2.000	1.199E+01	1.319E+01	1.474E+01	1.625E+01	1.794E+01	1.965E+01	2.129E+01	2.274E+01
2.500	1.108E+01	1.223E+01	1.374E+01	1.522E+01	1.688E+01	1.857E+01	2.020E+01	2.164E+01
3.000	1.028E+01	1.138E+01	1.284E+01	1.429E+01	1.591E+01	1.757E+01	1.917E+01	2.059E+01
4.000	8.943E+00	9.973E+00	1.134E+01	1.269E+01	1.423E+01	1.581E+01	1.734E+01	1.871E+01
5.000	7.892E+00	8.854E+00	1.012E+01	1.140E+01	1.284E+01	1.434E+01	1.579E+01	1.710E+01
6.000	7.049E+00	7.952E+00	9.136E+00	1.033E+01	1.168E+01	1.310E+01	1.448E+01	1.573E+01
7.000	6.360E+00	7.211E+00	8.316E+00	9.439E+00	1.071E+01	1.204E+01	1.335E+01	1.455E+01
8.000	5.790E+00	6.593E+00	7.628E+00	8.685E+00	9.878E+00	1.114E+01	1.238E+01	1.352E+01
9.000	5.311E+00	6.072E+00	7.044E+00	8.040E+00	9.164E+00	1.036E+01	1.154E+01	1.263E+01
10.00	4.904E+00	5.627E+00	6.541E+00	7.483E+00	8.545E+00	9.674E+00	1.080E+01	1.184E+01
15.00	3.548E+00	4.125E+00	4.826E+00	5.561E+00	6.383E+00	7.266E+00	8.160E+00	9.019E+00
20.00	2.793E+00	3.273E+00	3.840E+00	4.439E+00	5.106E+00	5.824E+00	6.561E+00	7.286E+00
25.00	2.318E+00	2.729E+00	3.204E+00	3.711E+00	4.270E+00	4.874E+00	5.500E+00	6.126E+00
30.00	1.991E+00	2.352E+00	2.762E+00	3.202E+00	3.684E+00	4.206E+00	4.749E+00	5.300E+00
40.00	1.573E+00	1.864E+00	2.189E+00	2.538E+00	2.919E+00	3.330E+00	3.762E+00	4.208E+00
50.00	1.314E+00	1.560E+00	1.832E+00	2.125E+00	2.442E+00	2.784E+00	3.145E+00	3.522E+00
60.00	1.138E+00	1.353E+00	1.588E+00	1.841E+00	2.115E+00	2.410E+00	2.723E+00	3.050E+00
70.00	1.010E+00	1.201E+00	1.410E+00	1.635E+00	1.877E+00	2.138E+00	2.415E+00	2.706E+00
80.00	9.124E−01	1.085E+00	1.273E+00	1.477E+00	1.696E+00	1.931E+00	2.180E+00	2.444E+00
90.00	8.351E−01	9.934E−01	1.166E+00	1.352E+00	1.552E+00	1.767E+00	1.996E+00	2.237E+00
100.0	7.725E−01	9.190E−01	1.079E+00	1.251E+00	1.436E+00	1.635E+00	1.846E+00	2.069E+00
150.0	5.792E−01	6.894E−01	8.092E−01	9.387E−01	1.078E+00	1.227E+00	1.385E+00	1.553E+00
200.0	4.791E−01	5.703E−01	6.696E−01	7.769E−01	8.922E−01	1.015E+00	1.147E+00	1.286E+00
250.0	4.179E−01	4.975E−01	5.842E−01	6.779E−01	7.786E−01	8.863E−01	1.001E+00	1.123E+00
300.0	3.767E−01	4.486E−01	5.268E−01	6.113E−01	7.022E−01	7.994E−01	9.030E−01	1.013E+00
400.0	3.252E−01	3.873E−01	4.549E−01	5.279E−01	6.065E−01	6.906E−01	7.802E−01	8.753E−01
500.0	2.947E−01	3.510E−01	4.123E−01	4.786E−01	5.498E−01	6.261E−01	7.074E−01	7.937E−01
600.0	2.749E−01	3.274E−01	3.846E−01	4.464E−01	5.130E−01	5.842E−01	6.601E−01	7.407E−01
700.0	2.612E−01	3.111E−01	3.655E−01	4.243E−01	4.875E−01	5.552E−01	6.274E−01	7.041E−01
800.0	2.514E−01	2.995E−01	3.518E−01	4.084E−01	4.693E−01	5.345E−01	6.040E−01	6.778E−01
900.0	2.442E−01	2.909E−01	3.417E−01	3.967E−01	4.558E−01	5.192E−01	5.867E−01	6.584E−01
1000.	2.386E−01	2.843E−01	3.340E−01	3.877E−01	4.455E−01	5.074E−01	5.734E−01	6.436E−01

Material: Glass, borosilicate (Pyrex)

Ion	Li	Be	B	C	N	O	F	Ne
(E/A_1) / MeV				$(-dE/\rho d\ell)$ / MeV cm^2 mg^{-1}				
0.025	1.707E+00	2.090E+00	2.389E+00	2.629E+00	2.835E+00	3.025E+00	3.194E+00	3.352E+00
0.030	1.866E+00	2.310E+00	2.659E+00	2.940E+00	3.177E+00	3.392E+00	3.582E+00	3.759E+00
0.040	2.117E+00	2.678E+00	3.130E+00	3.500E+00	3.806E+00	4.077E+00	4.312E+00	4.526E+00
0.050	2.301E+00	2.965E+00	3.515E+00	3.976E+00	4.359E+00	4.696E+00	4.983E+00	5.240E+00
0.060	2.438E+00	3.192E+00	3.829E+00	4.376E+00	4.837E+00	5.245E+00	5.591E+00	5.899E+00
0.070	2.539E+00	3.371E+00	4.088E+00	4.714E+00	5.249E+00	5.726E+00	6.134E+00	6.496E+00
0.080	2.615E+00	3.514E+00	4.302E+00	5.000E+00	5.604E+00	6.147E+00	6.615E+00	7.032E+00
0.090	2.670E+00	3.626E+00	4.479E+00	5.243E+00	5.911E+00	6.517E+00	7.043E+00	7.515E+00
0.100	2.710E+00	3.715E+00	4.625E+00	5.449E+00	6.178E+00	6.843E+00	7.425E+00	7.948E+00
0.150	2.774E+00	3.934E+00	5.041E+00	6.090E+00	7.059E+00	7.970E+00	8.789E+00	9.545E+00
0.200	2.740E+00	3.972E+00	5.183E+00	6.361E+00	7.483E+00	8.559E+00	9.548E+00	1.048E+01
0.250	2.674E+00	3.941E+00	5.211E+00	6.466E+00	7.684E+00	8.870E+00	9.974E+00	1.103E+01
0.300	2.597E+00	3.881E+00	5.185E+00	6.489E+00	7.771E+00	9.032E+00	1.022E+01	1.136E+01
0.400	2.437E+00	3.724E+00	5.061E+00	6.420E+00	7.780E+00	9.134E+00	1.042E+01	1.167E+01
0.500	2.284E+00	3.555E+00	4.899E+00	6.281E+00	7.681E+00	9.089E+00	1.043E+01	1.175E+01
0.600	2.145E+00	3.389E+00	4.725E+00	6.113E+00	7.533E+00	8.973E+00	1.035E+01	1.171E+01
0.700	2.020E+00	3.232E+00	4.551E+00	5.936E+00	7.363E+00	8.820E+00	1.022E+01	1.161E+01
0.800	1.907E+00	3.085E+00	4.383E+00	5.757E+00	7.184E+00	8.648E+00	1.006E+01	1.146E+01
0.900	1.805E+00	2.949E+00	4.223E+00	5.581E+00	7.002E+00	8.467E+00	9.882E+00	1.130E+01
1.000	1.714E+00	2.823E+00	4.071E+00	5.412E+00	6.822E+00	8.284E+00	9.698E+00	1.112E+01
1.500	1.366E+00	2.319E+00	3.434E+00	4.669E+00	6.001E+00	7.408E+00	8.787E+00	1.018E+01
2.000	1.136E+00	1.964E+00	2.960E+00	4.088E+00	5.327E+00	6.658E+00	7.977E+00	9.324E+00
2.500	9.741E−01	1.703E+00	2.597E+00	3.629E+00	4.779E+00	6.029E+00	7.283E+00	8.573E+00
3.000	8.543E−01	1.504E+00	2.313E+00	3.259E+00	4.327E+00	5.500E+00	6.689E+00	7.922E+00
4.000	6.893E−01	1.222E+00	1.898E+00	2.704E+00	3.630E+00	4.666E+00	5.736E+00	6.858E+00
5.000	5.809E−01	1.033E+00	1.612E+00	2.311E+00	3.124E+00	4.044E+00	5.010E+00	6.034E+00
6.000	5.042E−01	8.972E−01	1.403E+00	2.019E+00	2.741E+00	3.566E+00	4.443E+00	5.380E+00
7.000	4.469E−01	7.952E−01	1.245E+00	1.794E+00	2.443E+00	3.188E+00	3.989E+00	4.852E+00
8.000	4.023E−01	7.156E−01	1.120E+00	1.617E+00	2.204E+00	2.883E+00	3.619E+00	4.417E+00
9.000	3.666E−01	6.518E−01	1.020E+00	1.473E+00	2.010E+00	2.633E+00	3.313E+00	4.054E+00
10.00	3.372E−01	5.994E−01	9.381E−01	1.354E+00	1.849E+00	2.424E+00	3.055E+00	3.746E+00
15.00	2.442E−01	4.337E−01	6.776E−01	9.771E−01	1.333E+00	1.748E+00	2.213E+00	2.728E+00
20.00	1.940E−01	3.445E−01	5.380E−01	7.748E−01	1.056E+00	1.383E+00	1.751E+00	2.162E+00
25.00	1.622E−01	2.882E−01	4.499E−01	6.477E−01	8.819E−01	1.153E+00	1.461E+00	1.804E+00
30.00	1.402E−01	2.492E−01	3.890E−01	5.598E−01	7.619E−01	9.958E−01	1.261E+00	1.557E+00
40.00	1.115E−01	1.982E−01	3.096E−01	4.455E−01	6.061E−01	7.916E−01	1.002E+00	1.237E+00
50.00	9.355E−02	1.663E−01	2.597E−01	3.739E−01	5.087E−01	6.642E−01	8.403E−01	1.037E+00
60.00	8.115E−02	1.443E−01	2.254E−01	3.245E−01	4.415E−01	5.765E−01	7.294E−01	9.002E−01
70.00	7.206E−02	1.281E−01	2.002E−01	2.883E−01	3.923E−01	5.122E−01	6.481E−01	8.000E−01
80.00	6.510E−02	1.158E−01	1.809E−01	2.605E−01	3.545E−01	4.630E−01	5.859E−01	7.232E−01
90.00	5.959E−02	1.060E−01	1.656E−01	2.385E−01	3.247E−01	4.240E−01	5.366E−01	6.624E−01
100.0	5.512E−02	9.803E−02	1.532E−01	2.207E−01	3.004E−01	3.924E−01	4.966E−01	6.131E−01
150.0	4.132E−02	7.350E−02	1.149E−01	1.655E−01	2.254E−01	2.945E−01	3.728E−01	4.604E−01
200.0	3.417E−02	6.079E−02	9.504E−02	1.369E−01	1.865E−01	2.437E−01	3.086E−01	3.812E−01
250.0	2.980E−02	5.302E−02	8.290E−02	1.195E−01	1.627E−01	2.127E−01	2.693E−01	3.327E−01
300.0	2.687E−02	4.780E−02	7.474E−02	1.077E−01	1.467E−01	1.918E−01	2.429E−01	3.001E−01
400.0	2.319E−02	4.127E−02	6.454E−02	9.302E−02	1.267E−01	1.657E−01	2.098E−01	2.593E−01
500.0	2.102E−02	3.741E−02	5.851E−02	8.433E−02	1.149E−01	1.502E−01	1.903E−01	2.351E−01
600.0	1.961E−02	3.490E−02	5.459E−02	7.868E−02	1.072E−01	1.402E−01	1.775E−01	2.194E−01
700.0	1.864E−02	3.318E−02	5.189E−02	7.480E−02	1.019E−01	1.332E−01	1.688E−01	2.086E−01
800.0	1.795E−02	3.194E−02	4.996E−02	7.202E−02	9.812E−02	1.283E−01	1.625E−01	2.009E−01
900.0	1.744E−02	3.103E−02	4.854E−02	6.996E−02	9.532E−02	1.246E−01	1.579E−01	1.951E−01
1000.	1.705E−02	3.034E−02	4.745E−02	6.839E−02	9.319E−02	1.218E−01	1.544E−01	1.908E−01

Material: Glass, borosilicate (Pyrex)

Ion	Na	Mg	Al	Si	P	S	Cl	Ar
(E/A_1) / MeV				$(-\mathrm{d}E/\rho\mathrm{d}\ell)$ / MeV cm^2 mg^{-1}				
0.025	3.483E+00	3.626E+00	3.759E+00	3.889E+00	4.017E+00	4.134E+00	4.266E+00	4.361E+00
0.030	3.906E+00	4.061E+00	4.208E+00	4.350E+00	4.488E+00	4.620E+00	4.762E+00	4.869E+00
0.040	4.707E+00	4.882E+00	5.051E+00	5.213E+00	5.371E+00	5.527E+00	5.689E+00	5.813E+00
0.050	5.459E+00	5.657E+00	5.846E+00	6.027E+00	6.202E+00	6.377E+00	6.554E+00	6.692E+00
0.060	6.163E+00	6.391E+00	6.605E+00	6.805E+00	6.998E+00	7.191E+00	7.382E+00	7.531E+00
0.070	6.813E+00	7.076E+00	7.323E+00	7.550E+00	7.765E+00	7.978E+00	8.184E+00	8.343E+00
0.080	7.405E+00	7.708E+00	7.994E+00	8.253E+00	8.496E+00	8.733E+00	8.958E+00	9.130E+00
0.090	7.942E+00	8.287E+00	8.614E+00	8.908E+00	9.184E+00	9.450E+00	9.698E+00	9.889E+00
0.100	8.430E+00	8.816E+00	9.185E+00	9.516E+00	9.827E+00	1.013E+01	1.040E+01	1.061E+01
0.150	1.028E+01	1.086E+01	1.143E+01	1.194E+01	1.243E+01	1.290E+01	1.333E+01	1.368E+01
0.200	1.141E+01	1.216E+01	1.291E+01	1.359E+01	1.425E+01	1.489E+01	1.547E+01	1.596E+01
0.250	1.212E+01	1.298E+01	1.387E+01	1.470E+01	1.551E+01	1.629E+01	1.701E+01	1.763E+01
0.300	1.256E+01	1.352E+01	1.451E+01	1.545E+01	1.638E+01	1.728E+01	1.812E+01	1.886E+01
0.400	1.303E+01	1.410E+01	1.525E+01	1.634E+01	1.744E+01	1.851E+01	1.954E+01	2.044E+01
0.500	1.321E+01	1.435E+01	1.559E+01	1.678E+01	1.800E+01	1.920E+01	2.034E+01	2.136E+01
0.600	1.324E+01	1.442E+01	1.573E+01	1.699E+01	1.829E+01	1.957E+01	2.081E+01	2.191E+01
0.700	1.318E+01	1.438E+01	1.574E+01	1.705E+01	1.841E+01	1.977E+01	2.107E+01	2.223E+01
0.800	1.307E+01	1.429E+01	1.568E+01	1.702E+01	1.843E+01	1.984E+01	2.119E+01	2.240E+01
0.900	1.293E+01	1.415E+01	1.556E+01	1.694E+01	1.838E+01	1.983E+01	2.121E+01	2.247E+01
1.000	1.277E+01	1.399E+01	1.542E+01	1.681E+01	1.828E+01	1.976E+01	2.118E+01	2.246E+01
1.500	1.186E+01	1.306E+01	1.451E+01	1.593E+01	1.747E+01	1.902E+01	2.052E+01	2.186E+01
2.000	1.098E+01	1.214E+01	1.356E+01	1.497E+01	1.651E+01	1.808E+01	1.959E+01	2.095E+01
2.500	1.018E+01	1.130E+01	1.269E+01	1.407E+01	1.559E+01	1.714E+01	1.865E+01	2.000E+01
3.000	9.467E+00	1.055E+01	1.190E+01	1.324E+01	1.473E+01	1.626E+01	1.775E+01	1.908E+01
4.000	8.279E+00	9.285E+00	1.055E+01	1.182E+01	1.324E+01	1.470E+01	1.613E+01	1.742E+01
5.000	7.335E+00	8.277E+00	9.462E+00	1.066E+01	1.199E+01	1.338E+01	1.475E+01	1.598E+01
6.000	6.573E+00	7.457E+00	8.565E+00	9.687E+00	1.095E+01	1.226E+01	1.356E+01	1.475E+01
7.000	5.948E+00	6.779E+00	7.817E+00	8.874E+00	1.006E+01	1.131E+01	1.254E+01	1.368E+01
8.000	5.428E+00	6.212E+00	7.186E+00	8.183E+00	9.303E+00	1.048E+01	1.166E+01	1.274E+01
9.000	4.989E+00	5.732E+00	6.647E+00	7.589E+00	8.647E+00	9.766E+00	1.088E+01	1.192E+01
10.00	4.615E+00	5.319E+00	6.183E+00	7.075E+00	8.076E+00	9.137E+00	1.020E+01	1.120E+01
15.00	3.359E+00	3.919E+00	4.585E+00	5.285E+00	6.066E+00	6.902E+00	7.755E+00	8.579E+00
20.00	2.654E+00	3.118E+00	3.658E+00	4.230E+00	4.866E+00	5.550E+00	6.256E+00	6.953E+00
25.00	2.207E+00	2.604E+00	3.058E+00	3.542E+00	4.077E+00	4.654E+00	5.255E+00	5.857E+00
30.00	1.899E+00	2.247E+00	2.639E+00	3.060E+00	3.522E+00	4.021E+00	4.543E+00	5.074E+00
40.00	1.503E+00	1.783E+00	2.094E+00	2.429E+00	2.794E+00	3.189E+00	3.605E+00	4.034E+00
50.00	1.258E+00	1.494E+00	1.754E+00	2.035E+00	2.340E+00	2.668E+00	3.016E+00	3.378E+00
60.00	1.091E+00	1.296E+00	1.522E+00	1.765E+00	2.028E+00	2.311E+00	2.612E+00	2.927E+00
70.00	9.687E−01	1.153E+00	1.352E+00	1.568E+00	1.801E+00	2.052E+00	2.318E+00	2.598E+00
80.00	8.755E−01	1.041E+00	1.222E+00	1.417E+00	1.628E+00	1.854E+00	2.094E+00	2.347E+00
90.00	8.020E−01	9.538E−01	1.119E+00	1.298E+00	1.491E+00	1.697E+00	1.917E+00	2.149E+00
100.0	7.420E−01	8.828E−01	1.036E+00	1.202E+00	1.380E+00	1.571E+00	1.774E+00	1.989E+00
150.0	5.573E−01	6.633E−01	7.786E−01	9.032E−01	1.037E+00	1.180E+00	1.333E+00	1.495E+00
200.0	4.614E−01	5.494E−01	6.450E−01	7.484E−01	8.594E−01	9.782E−01	1.105E+00	1.239E+00
250.0	4.028E−01	4.796E−01	5.632E−01	6.535E−01	7.506E−01	8.545E−01	9.652E−01	1.083E+00
300.0	3.633E−01	4.327E−01	5.081E−01	5.897E−01	6.774E−01	7.712E−01	8.712E−01	9.773E−01
400.0	3.140E−01	3.739E−01	4.392E−01	5.098E−01	5.857E−01	6.669E−01	7.534E−01	8.453E−01
500.0	2.847E−01	3.391E−01	3.984E−01	4.624E−01	5.313E−01	6.050E−01	6.836E−01	7.671E−01
600.0	2.657E−01	3.165E−01	3.718E−01	4.317E−01	4.960E−01	5.648E−01	6.383E−01	7.162E−01
700.0	2.527E−01	3.010E−01	3.536E−01	4.105E−01	4.717E−01	5.372E−01	6.070E−01	6.812E−01
800.0	2.433E−01	2.898E−01	3.405E−01	3.953E−01	4.542E−01	5.173E−01	5.846E−01	6.560E−01
900.0	2.364E−01	2.816E−01	3.308E−01	3.840E−01	4.413E−01	5.026E−01	5.680E−01	6.375E−01
1000.	2.311E−01	2.753E−01	3.234E−01	3.755E−01	4.315E−01	4.915E−01	5.554E−01	6.233E−01

Material: Kapton polyimide film

Ion	Li	Be	B	C	N	O	F	Ne
(E/A_1) / MeV				$(-\mathrm{d}E/\rho\mathrm{d}\ell)$ / MeV cm^2 mg^{-1}				
0.025	2.149E+00	2.637E+00	3.024E+00	3.334E+00	3.611E+00	3.860E+00	4.066E+00	4.255E+00
0.030	2.349E+00	2.902E+00	3.346E+00	3.707E+00	4.025E+00	4.310E+00	4.547E+00	4.762E+00
0.040	2.681E+00	3.364E+00	3.920E+00	4.380E+00	4.777E+00	5.135E+00	5.433E+00	5.702E+00
0.050	2.933E+00	3.746E+00	4.415E+00	4.974E+00	5.451E+00	5.880E+00	6.238E+00	6.560E+00
0.060	3.118E+00	4.054E+00	4.836E+00	5.497E+00	6.058E+00	6.560E+00	6.978E+00	7.353E+00
0.070	3.250E+00	4.294E+00	5.185E+00	5.949E+00	6.599E+00	7.179E+00	7.662E+00	8.091E+00
0.080	3.342E+00	4.477E+00	5.468E+00	6.332E+00	7.073E+00	7.735E+00	8.287E+00	8.776E+00
0.090	3.405E+00	4.616E+00	5.695E+00	6.651E+00	7.482E+00	8.228E+00	8.853E+00	9.406E+00
0.100	3.445E+00	4.718E+00	5.874E+00	6.914E+00	7.829E+00	8.658E+00	9.357E+00	9.978E+00
0.150	3.476E+00	4.931E+00	6.329E+00	7.658E+00	8.893E+00	1.005E+01	1.107E+01	1.201E+01
0.200	3.393E+00	4.923E+00	6.435E+00	7.912E+00	9.326E+00	1.068E+01	1.192E+01	1.308E+01
0.250	3.281E+00	4.841E+00	6.411E+00	7.969E+00	9.489E+00	1.097E+01	1.234E+01	1.364E+01
0.300	3.163E+00	4.733E+00	6.333E+00	7.939E+00	9.524E+00	1.109E+01	1.254E+01	1.394E+01
0.400	2.935E+00	4.492E+00	6.113E+00	7.764E+00	9.421E+00	1.108E+01	1.262E+01	1.414E+01
0.500	2.729E+00	4.254E+00	5.870E+00	7.533E+00	9.222E+00	1.092E+01	1.252E+01	1.410E+01
0.600	2.547E+00	4.031E+00	5.627E+00	7.287E+00	8.987E+00	1.071E+01	1.234E+01	1.395E+01
0.700	2.386E+00	3.825E+00	5.395E+00	7.041E+00	8.741E+00	1.048E+01	1.212E+01	1.375E+01
0.800	2.243E+00	3.637E+00	5.175E+00	6.803E+00	8.495E+00	1.023E+01	1.188E+01	1.352E+01
0.900	2.116E+00	3.464E+00	4.969E+00	6.574E+00	8.252E+00	9.990E+00	1.163E+01	1.327E+01
1.000	2.002E+00	3.306E+00	4.777E+00	6.356E+00	8.017E+00	9.746E+00	1.138E+01	1.302E+01
1.500	1.576E+00	2.684E+00	3.984E+00	5.424E+00	6.976E+00	8.623E+00	1.020E+01	1.180E+01
2.000	1.300E+00	2.255E+00	3.406E+00	4.711E+00	6.144E+00	7.689E+00	9.196E+00	1.072E+01
2.500	1.109E+00	1.944E+00	2.971E+00	4.156E+00	5.476E+00	6.919E+00	8.344E+00	9.805E+00
3.000	9.689E−01	1.709E+00	2.633E+00	3.713E+00	4.932E+00	6.278E+00	7.624E+00	9.014E+00
4.000	7.770E−01	1.379E+00	2.145E+00	3.058E+00	4.106E+00	5.283E+00	6.485E+00	7.741E+00
5.000	6.521E−01	1.160E+00	1.812E+00	2.599E+00	3.513E+00	4.552E+00	5.631E+00	6.771E+00
6.000	5.641E−01	1.004E+00	1.571E+00	2.261E+00	3.070E+00	3.996E+00	4.971E+00	6.011E+00
7.000	4.987E−01	8.878E−01	1.390E+00	2.004E+00	2.727E+00	3.560E+00	4.448E+00	5.402E+00
8.000	4.480E−01	7.972E−01	1.248E+00	1.801E+00	2.455E+00	3.211E+00	4.025E+00	4.904E+00
9.000	4.075E−01	7.248E−01	1.134E+00	1.638E+00	2.234E+00	2.925E+00	3.676E+00	4.491E+00
10.00	3.743E−01	6.655E−01	1.041E+00	1.503E+00	2.051E+00	2.688E+00	3.384E+00	4.143E+00
15.00	2.696E−01	4.789E−01	7.484E−01	1.078E+00	1.471E+00	1.928E+00	2.437E+00	3.001E+00
20.00	2.135E−01	3.792E−01	5.921E−01	8.527E−01	1.161E+00	1.520E+00	1.924E+00	2.373E+00
25.00	1.782E−01	3.165E−01	4.941E−01	7.112E−01	9.681E−01	1.265E+00	1.602E+00	1.976E+00
30.00	1.537E−01	2.731E−01	4.264E−01	6.137E−01	8.350E−01	1.091E+00	1.380E+00	1.703E+00
40.00	1.219E−01	2.167E−01	3.385E−01	4.871E−01	6.627E−01	8.654E−01	1.094E+00	1.351E+00
50.00	1.021E−01	1.815E−01	2.835E−01	4.080E−01	5.551E−01	7.248E−01	9.169E−01	1.131E+00
60.00	8.845E−02	1.572E−01	2.456E−01	3.536E−01	4.812E−01	6.283E−01	7.948E−01	9.809E−01
70.00	7.846E−02	1.395E−01	2.179E−01	3.138E−01	4.270E−01	5.576E−01	7.055E−01	8.707E−01
80.00	7.082E−02	1.259E−01	1.967E−01	2.833E−01	3.856E−01	5.036E−01	6.372E−01	7.865E−01
90.00	6.477E−02	1.151E−01	1.800E−01	2.592E−01	3.528E−01	4.608E−01	5.831E−01	7.198E−01
100.0	5.987E−02	1.064E−01	1.664E−01	2.396E−01	3.262E−01	4.261E−01	5.393E−01	6.657E−01
150.0	4.477E−02	7.963E−02	1.244E−01	1.793E−01	2.441E−01	3.190E−01	4.039E−01	4.987E−01
200.0	3.696E−02	6.576E−02	1.028E−01	1.481E−01	2.017E−01	2.636E−01	3.338E−01	4.122E−01
250.0	3.220E−02	5.729E−02	8.958E−02	1.290E−01	1.758E−01	2.297E−01	2.909E−01	3.594E−01
300.0	2.900E−02	5.160E−02	8.069E−02	1.162E−01	1.583E−01	2.070E−01	2.621E−01	3.238E−01
400.0	2.500E−02	4.449E−02	6.958E−02	1.002E−01	1.366E−01	1.785E−01	2.261E−01	2.794E−01
500.0	2.264E−02	4.029E−02	6.300E−02	9.081E−02	1.237E−01	1.617E−01	2.048E−01	2.531E−01
600.0	2.110E−02	3.755E−02	5.873E−02	8.466E−02	1.153E−01	1.507E−01	1.910E−01	2.360E−01
700.0	2.004E−02	3.567E−02	5.579E−02	8.042E−02	1.095E−01	1.432E−01	1.814E−01	2.242E−01
800.0	1.929E−02	3.432E−02	5.368E−02	7.738E−02	1.054E−01	1.378E−01	1.746E−01	2.157E−01
900.0	1.872E−02	3.332E−02	5.212E−02	7.513E−02	1.023E−01	1.338E−01	1.695E−01	2.095E−01
1000.	1.830E−02	3.256E−02	5.093E−02	7.341E−02	1.000E−01	1.307E−01	1.656E−01	2.047E−01

Material: Kapton polyimide film

Ion	Na	Mg	Al	Si	P	S	Cl	Ar
(E/A_1) / MeV				$(-\mathrm{d}E/\rho\mathrm{d}\ell)$ / MeV cm^2 mg^{-1}				
0.025	4.408E+00	4.579E+00	4.741E+00	4.901E+00	5.077E+00	5.227E+00	5.413E+00	5.524E+00
0.030	4.939E+00	5.119E+00	5.295E+00	5.468E+00	5.658E+00	5.824E+00	6.021E+00	6.145E+00
0.040	5.931E+00	6.133E+00	6.339E+00	6.538E+00	6.753E+00	6.950E+00	7.168E+00	7.310E+00
0.050	6.845E+00	7.075E+00	7.313E+00	7.539E+00	7.782E+00	8.008E+00	8.248E+00	8.406E+00
0.060	7.693E+00	7.954E+00	8.224E+00	8.480E+00	8.752E+00	9.008E+00	9.270E+00	9.446E+00
0.070	8.488E+00	8.779E+00	9.083E+00	9.369E+00	9.669E+00	9.954E+00	1.024E+01	1.043E+01
0.080	9.234E+00	9.557E+00	9.897E+00	1.021E+01	1.054E+01	1.085E+01	1.116E+01	1.137E+01
0.090	9.930E+00	1.029E+01	1.066E+01	1.101E+01	1.137E+01	1.171E+01	1.204E+01	1.227E+01
0.100	1.057E+01	1.097E+01	1.139E+01	1.177E+01	1.216E+01	1.254E+01	1.289E+01	1.314E+01
0.150	1.296E+01	1.362E+01	1.430E+01	1.491E+01	1.552E+01	1.609E+01	1.661E+01	1.699E+01
0.200	1.431E+01	1.517E+01	1.610E+01	1.694E+01	1.777E+01	1.857E+01	1.930E+01	1.988E+01
0.250	1.506E+01	1.607E+01	1.717E+01	1.819E+01	1.921E+01	2.020E+01	2.112E+01	2.186E+01
0.300	1.550E+01	1.660E+01	1.783E+01	1.898E+01	2.014E+01	2.128E+01	2.234E+01	2.323E+01
0.400	1.588E+01	1.709E+01	1.849E+01	1.981E+01	2.117E+01	2.251E+01	2.377E+01	2.485E+01
0.500	1.595E+01	1.722E+01	1.871E+01	2.014E+01	2.162E+01	2.309E+01	2.448E+01	2.569E+01
0.600	1.588E+01	1.717E+01	1.873E+01	2.022E+01	2.179E+01	2.335E+01	2.483E+01	2.613E+01
0.700	1.574E+01	1.703E+01	1.863E+01	2.017E+01	2.181E+01	2.343E+01	2.498E+01	2.633E+01
0.800	1.555E+01	1.684E+01	1.847E+01	2.004E+01	2.172E+01	2.340E+01	2.499E+01	2.639E+01
0.900	1.533E+01	1.662E+01	1.827E+01	1.987E+01	2.158E+01	2.329E+01	2.492E+01	2.635E+01
1.000	1.510E+01	1.639E+01	1.805E+01	1.966E+01	2.139E+01	2.314E+01	2.479E+01	2.625E+01
1.500	1.390E+01	1.514E+01	1.681E+01	1.844E+01	2.023E+01	2.204E+01	2.376E+01	2.528E+01
2.000	1.277E+01	1.396E+01	1.560E+01	1.721E+01	1.899E+01	2.081E+01	2.254E+01	2.407E+01
2.500	1.178E+01	1.292E+01	1.452E+01	1.608E+01	1.783E+01	1.963E+01	2.134E+01	2.285E+01
3.000	1.090E+01	1.200E+01	1.355E+01	1.507E+01	1.678E+01	1.854E+01	2.022E+01	2.170E+01
4.000	9.461E+00	1.049E+01	1.192E+01	1.335E+01	1.496E+01	1.663E+01	1.823E+01	1.966E+01
5.000	8.331E+00	9.297E+00	1.063E+01	1.196E+01	1.347E+01	1.505E+01	1.657E+01	1.793E+01
6.000	7.427E+00	8.338E+00	9.580E+00	1.083E+01	1.224E+01	1.372E+01	1.516E+01	1.647E+01
7.000	6.693E+00	7.554E+00	8.712E+00	9.885E+00	1.121E+01	1.260E+01	1.397E+01	1.521E+01
8.000	6.086E+00	6.902E+00	7.985E+00	9.087E+00	1.033E+01	1.165E+01	1.294E+01	1.413E+01
9.000	5.578E+00	6.353E+00	7.368E+00	8.408E+00	9.580E+00	1.082E+01	1.205E+01	1.318E+01
10.00	5.147E+00	5.884E+00	6.839E+00	7.822E+00	8.927E+00	1.010E+01	1.127E+01	1.235E+01
15.00	3.715E+00	4.309E+00	5.040E+00	5.805E+00	6.659E+00	7.577E+00	8.502E+00	9.395E+00
20.00	2.922E+00	3.419E+00	4.009E+00	4.633E+00	5.325E+00	6.070E+00	6.834E+00	7.586E+00
25.00	2.423E+00	2.850E+00	3.345E+00	3.873E+00	4.453E+00	5.080E+00	5.729E+00	6.379E+00
30.00	2.081E+00	2.456E+00	2.884E+00	3.341E+00	3.843E+00	4.384E+00	4.948E+00	5.520E+00
40.00	1.643E+00	1.946E+00	2.285E+00	2.649E+00	3.045E+00	3.472E+00	3.921E+00	4.385E+00
50.00	1.372E+00	1.629E+00	1.912E+00	2.217E+00	2.548E+00	2.903E+00	3.279E+00	3.670E+00
60.00	1.188E+00	1.412E+00	1.657E+00	1.921E+00	2.207E+00	2.514E+00	2.839E+00	3.179E+00
70.00	1.054E+00	1.253E+00	1.470E+00	1.705E+00	1.958E+00	2.230E+00	2.518E+00	2.821E+00
80.00	9.520E−01	1.132E+00	1.328E+00	1.540E+00	1.768E+00	2.013E+00	2.273E+00	2.548E+00
90.00	8.712E−01	1.036E+00	1.216E+00	1.410E+00	1.619E+00	1.842E+00	2.080E+00	2.332E+00
100.0	8.057E−01	9.585E−01	1.124E+00	1.304E+00	1.497E+00	1.704E+00	1.924E+00	2.157E+00
150.0	6.036E−01	7.185E−01	8.434E−01	9.783E−01	1.123E+00	1.278E+00	1.443E+00	1.618E+00
200.0	4.990E−01	5.941E−01	6.975E−01	8.093E−01	9.294E−01	1.057E+00	1.194E+00	1.339E+00
250.0	4.351E−01	5.181E−01	6.084E−01	7.059E−01	8.108E−01	9.229E−01	1.042E+00	1.169E+00
300.0	3.921E−01	4.670E−01	5.484E−01	6.364E−01	7.310E−01	8.322E−01	9.400E−01	1.054E+00
400.0	3.383E−01	4.030E−01	4.733E−01	5.493E−01	6.311E−01	7.186E−01	8.118E−01	9.108E−01
500.0	3.065E−01	3.651E−01	4.288E−01	4.978E−01	5.719E−01	6.512E−01	7.358E−01	8.256E−01
600.0	2.858E−01	3.404E−01	3.999E−01	4.642E−01	5.334E−01	6.074E−01	6.864E−01	7.702E−01
700.0	2.715E−01	3.235E−01	3.800E−01	4.411E−01	5.069E−01	5.772E−01	6.523E−01	7.319E−01
800.0	2.613E−01	3.113E−01	3.657E−01	4.245E−01	4.878E−01	5.555E−01	6.278E−01	7.045E−01
900.0	2.537E−01	3.023E−01	3.551E−01	4.122E−01	4.737E−01	5.395E−01	6.097E−01	6.842E−01
1000.	2.479E−01	2.954E−01	3.470E−01	4.029E−01	4.630E−01	5.273E−01	5.958E−01	6.687E−01

Material: Lithium fluoride

Ion	Li	Be	B	C	N	O	F	Ne
(E/A_1) / MeV				$(-\mathrm{d}E/\rho\mathrm{d}\ell)$ / MeV cm^2 mg^{-1}				
0.025	1.622E+00	2.038E+00	2.368E+00	2.629E+00	2.856E+00	3.056E+00	3.218E+00	3.364E+00
0.030	1.757E+00	2.224E+00	2.601E+00	2.905E+00	3.166E+00	3.396E+00	3.582E+00	3.749E+00
0.040	1.984E+00	2.541E+00	3.005E+00	3.391E+00	3.721E+00	4.013E+00	4.251E+00	4.461E+00
0.050	2.165E+00	2.806E+00	3.348E+00	3.810E+00	4.207E+00	4.561E+00	4.853E+00	5.110E+00
0.060	2.312E+00	3.029E+00	3.645E+00	4.178E+00	4.639E+00	5.053E+00	5.398E+00	5.702E+00
0.070	2.429E+00	3.218E+00	3.903E+00	4.503E+00	5.025E+00	5.498E+00	5.894E+00	6.246E+00
0.080	2.522E+00	3.376E+00	4.127E+00	4.791E+00	5.373E+00	5.902E+00	6.349E+00	6.747E+00
0.090	2.595E+00	3.507E+00	4.320E+00	5.046E+00	5.686E+00	6.269E+00	6.765E+00	7.210E+00
0.100	2.652E+00	3.616E+00	4.486E+00	5.270E+00	5.966E+00	6.603E+00	7.148E+00	7.637E+00
0.150	2.774E+00	3.918E+00	5.003E+00	6.024E+00	6.963E+00	7.841E+00	8.610E+00	9.314E+00
0.200	2.762E+00	3.997E+00	5.207E+00	6.377E+00	7.487E+00	8.547E+00	9.495E+00	1.038E+01
0.250	2.702E+00	3.981E+00	5.260E+00	6.522E+00	7.744E+00	8.930E+00	1.001E+01	1.103E+01
0.300	2.624E+00	3.922E+00	5.241E+00	6.559E+00	7.854E+00	9.126E+00	1.030E+01	1.142E+01
0.400	2.457E+00	3.757E+00	5.109E+00	6.483E+00	7.860E+00	9.234E+00	1.051E+01	1.176E+01
0.500	2.297E+00	3.577E+00	4.932E+00	6.326E+00	7.740E+00	9.166E+00	1.050E+01	1.181E+01
0.600	2.152E+00	3.402E+00	4.746E+00	6.142E+00	7.571E+00	9.024E+00	1.039E+01	1.174E+01
0.700	2.022E+00	3.237E+00	4.561E+00	5.950E+00	7.382E+00	8.849E+00	1.023E+01	1.160E+01
0.800	1.905E+00	3.084E+00	4.384E+00	5.760E+00	7.187E+00	8.658E+00	1.005E+01	1.143E+01
0.900	1.800E+00	2.943E+00	4.217E+00	5.575E+00	6.993E+00	8.462E+00	9.855E+00	1.124E+01
1.000	1.705E+00	2.813E+00	4.059E+00	5.397E+00	6.803E+00	8.265E+00	9.656E+00	1.104E+01
1.500	1.349E+00	2.294E+00	3.403E+00	4.628E+00	5.947E+00	7.346E+00	8.694E+00	1.005E+01
2.000	1.116E+00	1.933E+00	2.918E+00	4.032E+00	5.254E+00	6.572E+00	7.857E+00	9.166E+00
2.500	9.538E−01	1.670E+00	2.551E+00	3.565E+00	4.695E+00	5.928E+00	7.147E+00	8.398E+00
3.000	8.343E−01	1.471E+00	2.264E+00	3.192E+00	4.237E+00	5.390E+00	6.544E+00	7.737E+00
4.000	6.707E−01	1.190E+00	1.850E+00	2.636E+00	3.538E+00	4.550E+00	5.584E+00	6.667E+00
5.000	5.639E−01	1.003E+00	1.566E+00	2.245E+00	3.034E+00	3.929E+00	4.861E+00	5.846E+00
6.000	4.886E−01	8.695E−01	1.360E+00	1.957E+00	2.655E+00	3.455E+00	4.299E+00	5.199E+00
7.000	4.325E−01	7.696E−01	1.205E+00	1.736E+00	2.362E+00	3.083E+00	3.853E+00	4.680E+00
8.000	3.889E−01	6.918E−01	1.083E+00	1.562E+00	2.129E+00	2.784E+00	3.491E+00	4.254E+00
9.000	3.540E−01	6.295E−01	9.854E−01	1.422E+00	1.939E+00	2.539E+00	3.191E+00	3.900E+00
10.00	3.255E−01	5.785E−01	9.052E−01	1.306E+00	1.782E+00	2.335E+00	2.941E+00	3.602E+00
15.00	2.350E−01	4.175E−01	6.522E−01	9.401E−01	1.282E+00	1.680E+00	2.125E+00	2.617E+00
20.00	1.864E−01	3.311E−01	5.169E−01	7.443E−01	1.014E+00	1.327E+00	1.680E+00	2.072E+00
25.00	1.557E−01	2.766E−01	4.319E−01	6.215E−01	8.461E−01	1.106E+00	1.400E+00	1.728E+00
30.00	1.345E−01	2.389E−01	3.730E−01	5.368E−01	7.304E−01	9.544E−01	1.208E+00	1.491E+00
40.00	1.068E−01	1.899E−01	2.965E−01	4.267E−01	5.804E−01	7.579E−01	9.589E−01	1.183E+00
50.00	8.951E−02	1.591E−01	2.485E−01	3.577E−01	4.867E−01	6.354E−01	8.038E−01	9.920E−01
60.00	7.759E−02	1.379E−01	2.155E−01	3.102E−01	4.222E−01	5.511E−01	6.973E−01	8.605E−01
70.00	6.886E−02	1.224E−01	1.913E−01	2.754E−01	3.748E−01	4.894E−01	6.193E−01	7.643E−01
80.00	6.218E−02	1.106E−01	1.728E−01	2.488E−01	3.386E−01	4.422E−01	5.596E−01	6.906E−01
90.00	5.690E−02	1.012E−01	1.581E−01	2.277E−01	3.100E−01	4.048E−01	5.123E−01	6.324E−01
100.0	5.261E−02	9.357E−02	1.462E−01	2.106E−01	2.867E−01	3.745E−01	4.739E−01	5.850E−01
150.0	3.939E−02	7.006E−02	1.095E−01	1.578E−01	2.148E−01	2.807E−01	3.554E−01	4.388E−01
200.0	3.255E−02	5.790E−02	9.052E−02	1.304E−01	1.776E−01	2.321E−01	2.939E−01	3.630E−01
250.0	2.837E−02	5.047E−02	7.892E−02	1.137E−01	1.549E−01	2.024E−01	2.563E−01	3.167E−01
300.0	2.556E−02	4.548E−02	7.112E−02	1.025E−01	1.396E−01	1.825E−01	2.311E−01	2.855E−01
400.0	2.205E−02	3.924E−02	6.137E−02	8.844E−02	1.205E−01	1.575E−01	1.995E−01	2.465E−01
500.0	1.998E−02	3.555E−02	5.560E−02	8.013E−02	1.092E−01	1.427E−01	1.808E−01	2.234E−01
600.0	1.863E−02	3.315E−02	5.185E−02	7.474E−02	1.018E−01	1.331E−01	1.686E−01	2.084E−01
700.0	1.770E−02	3.150E−02	4.927E−02	7.102E−02	9.676E−02	1.265E−01	1.603E−01	1.980E−01
800.0	1.704E−02	3.032E−02	4.742E−02	6.836E−02	9.313E−02	1.218E−01	1.543E−01	1.906E−01
900.0	1.655E−02	2.945E−02	4.606E−02	6.639E−02	9.045E−02	1.183E−01	1.498E−01	1.852E−01
1000.	1.617E−02	2.878E−02	4.502E−02	6.489E−02	8.841E−02	1.156E−01	1.464E−01	1.810E−01

Material: Lithium fluoride

Ion	Na	Mg	Al	Si	P	S	Cl	Ar
(E/A_1) / MeV				$(-\mathrm{d}E/\rho\mathrm{d}\ell)$ / MeV cm^2 mg^{-1}				
0.025	3.476E+00	3.604E+00	3.723E+00	3.840E+00	3.971E+00	4.080E+00	4.220E+00	4.299E+00
0.030	3.878E+00	4.015E+00	4.144E+00	4.270E+00	4.409E+00	4.530E+00	4.677E+00	4.762E+00
0.040	4.632E+00	4.786E+00	4.937E+00	5.081E+00	5.238E+00	5.379E+00	5.538E+00	5.633E+00
0.050	5.327E+00	5.505E+00	5.679E+00	5.844E+00	6.020E+00	6.182E+00	6.353E+00	6.458E+00
0.060	5.970E+00	6.174E+00	6.378E+00	6.566E+00	6.764E+00	6.950E+00	7.136E+00	7.252E+00
0.070	6.565E+00	6.798E+00	7.034E+00	7.248E+00	7.472E+00	7.683E+00	7.889E+00	8.018E+00
0.080	7.116E+00	7.380E+00	7.649E+00	7.893E+00	8.144E+00	8.382E+00	8.609E+00	8.755E+00
0.090	7.629E+00	7.924E+00	8.228E+00	8.502E+00	8.782E+00	9.047E+00	9.298E+00	9.463E+00
0.100	8.107E+00	8.434E+00	8.772E+00	9.077E+00	9.387E+00	9.680E+00	9.956E+00	1.014E+01
0.150	1.003E+01	1.052E+01	1.103E+01	1.150E+01	1.196E+01	1.241E+01	1.281E+01	1.311E+01
0.200	1.131E+01	1.196E+01	1.264E+01	1.327E+01	1.389E+01	1.449E+01	1.504E+01	1.546E+01
0.250	1.214E+01	1.291E+01	1.375E+01	1.452E+01	1.529E+01	1.604E+01	1.672E+01	1.727E+01
0.300	1.266E+01	1.353E+01	1.449E+01	1.539E+01	1.629E+01	1.716E+01	1.797E+01	1.864E+01
0.400	1.318E+01	1.418E+01	1.531E+01	1.638E+01	1.748E+01	1.855E+01	1.955E+01	2.041E+01
0.500	1.335E+01	1.441E+01	1.565E+01	1.683E+01	1.805E+01	1.926E+01	2.040E+01	2.138E+01
0.600	1.335E+01	1.444E+01	1.575E+01	1.700E+01	1.831E+01	1.961E+01	2.084E+01	2.191E+01
0.700	1.327E+01	1.437E+01	1.572E+01	1.702E+01	1.839E+01	1.976E+01	2.105E+01	2.218E+01
0.800	1.313E+01	1.424E+01	1.562E+01	1.695E+01	1.836E+01	1.978E+01	2.112E+01	2.230E+01
0.900	1.297E+01	1.408E+01	1.548E+01	1.683E+01	1.827E+01	1.973E+01	2.110E+01	2.231E+01
1.000	1.279E+01	1.390E+01	1.531E+01	1.667E+01	1.814E+01	1.962E+01	2.102E+01	2.226E+01
1.500	1.183E+01	1.289E+01	1.432E+01	1.570E+01	1.722E+01	1.877E+01	2.023E+01	2.152E+01
2.000	1.090E+01	1.193E+01	1.333E+01	1.470E+01	1.622E+01	1.777E+01	1.924E+01	2.055E+01
2.500	1.008E+01	1.107E+01	1.243E+01	1.377E+01	1.527E+01	1.680E+01	1.826E+01	1.955E+01
3.000	9.351E+00	1.031E+01	1.163E+01	1.293E+01	1.439E+01	1.590E+01	1.734E+01	1.861E+01
4.000	8.140E+00	9.035E+00	1.027E+01	1.150E+01	1.288E+01	1.431E+01	1.569E+01	1.692E+01
5.000	7.185E+00	8.027E+00	9.178E+00	1.033E+01	1.163E+01	1.298E+01	1.429E+01	1.547E+01
6.000	6.419E+00	7.213E+00	8.286E+00	9.367E+00	1.059E+01	1.187E+01	1.311E+01	1.424E+01
7.000	5.793E+00	6.544E+00	7.547E+00	8.563E+00	9.708E+00	1.091E+01	1.210E+01	1.318E+01
8.000	5.275E+00	5.987E+00	6.926E+00	7.883E+00	8.960E+00	1.010E+01	1.122E+01	1.225E+01
9.000	4.840E+00	5.517E+00	6.398E+00	7.301E+00	8.316E+00	9.394E+00	1.046E+01	1.145E+01
10.00	4.470E+00	5.115E+00	5.945E+00	6.798E+00	7.758E+00	8.779E+00	9.792E+00	1.074E+01
15.00	3.237E+00	3.757E+00	4.395E+00	5.062E+00	5.807E+00	6.606E+00	7.415E+00	8.196E+00
20.00	2.551E+00	2.986E+00	3.502E+00	4.048E+00	4.652E+00	5.304E+00	5.972E+00	6.632E+00
25.00	2.118E+00	2.492E+00	2.926E+00	3.387E+00	3.896E+00	4.444E+00	5.013E+00	5.584E+00
30.00	1.821E+00	2.150E+00	2.524E+00	2.925E+00	3.364E+00	3.839E+00	4.334E+00	4.836E+00
40.00	1.439E+00	1.705E+00	2.002E+00	2.322E+00	2.669E+00	3.045E+00	3.438E+00	3.846E+00
50.00	1.203E+00	1.429E+00	1.677E+00	1.945E+00	2.235E+00	2.547E+00	2.877E+00	3.221E+00
60.00	1.043E+00	1.239E+00	1.454E+00	1.686E+00	1.937E+00	2.206E+00	2.492E+00	2.792E+00
70.00	9.255E−01	1.100E+00	1.291E+00	1.497E+00	1.720E+00	1.958E+00	2.211E+00	2.478E+00
80.00	8.360E−01	9.942E−01	1.167E+00	1.353E+00	1.554E+00	1.769E+00	1.997E+00	2.239E+00
90.00	7.654E−01	9.104E−01	1.068E+00	1.239E+00	1.423E+00	1.619E+00	1.828E+00	2.049E+00
100.0	7.080E−01	8.424E−01	9.886E−01	1.146E+00	1.316E+00	1.498E+00	1.692E+00	1.896E+00
150.0	5.311E−01	6.322E−01	7.421E−01	8.608E−01	9.884E−01	1.125E+00	1.270E+00	1.424E+00
200.0	4.394E−01	5.232E−01	6.143E−01	7.127E−01	8.184E−01	9.315E−01	1.052E+00	1.180E+00
250.0	3.834E−01	4.565E−01	5.360E−01	6.220E−01	7.144E−01	8.132E−01	9.185E−01	1.030E+00
300.0	3.457E−01	4.116E−01	4.834E−01	5.610E−01	6.444E−01	7.336E−01	8.287E−01	9.296E−01
400.0	2.985E−01	3.555E−01	4.175E−01	4.846E−01	5.567E−01	6.339E−01	7.162E−01	8.035E−01
500.0	2.705E−01	3.222E−01	3.785E−01	4.393E−01	5.048E−01	5.748E−01	6.495E−01	7.287E−01
600.0	2.524E−01	3.006E−01	3.531E−01	4.099E−01	4.710E−01	5.364E−01	6.061E−01	6.801E−01
700.0	2.399E−01	2.857E−01	3.357E−01	3.897E−01	4.477E−01	5.099E−01	5.762E−01	6.466E−01
800.0	2.309E−01	2.750E−01	3.231E−01	3.751E−01	4.310E−01	4.909E−01	5.547E−01	6.225E−01
900.0	2.243E−01	2.672E−01	3.139E−01	3.644E−01	4.187E−01	4.769E−01	5.389E−01	6.047E−01
1000.	2.192E−01	2.611E−01	3.068E−01	3.562E−01	4.093E−01	4.661E−01	5.268E−01	5.912E−01

Material: Lithium tetraborate

Ion	Li	Be	B	C	N	O	F	Ne
(E/A_1) / MeV				$(-\mathrm{d}E/\rho\mathrm{d}\ell)$ / MeV cm^2 mg^{-1}				
0.025	1.968E+00	2.403E+00	2.739E+00	3.003E+00	3.237E+00	3.448E+00	3.630E+00	3.799E+00
0.030	2.150E+00	2.652E+00	3.045E+00	3.358E+00	3.628E+00	3.869E+00	4.073E+00	4.263E+00
0.040	2.444E+00	3.075E+00	3.580E+00	3.992E+00	4.341E+00	4.647E+00	4.905E+00	5.137E+00
0.050	2.663E+00	3.412E+00	4.026E+00	4.538E+00	4.970E+00	5.349E+00	5.665E+00	5.946E+00
0.060	2.824E+00	3.679E+00	4.396E+00	5.005E+00	5.522E+00	5.977E+00	6.357E+00	6.692E+00
0.070	2.943E+00	3.890E+00	4.701E+00	5.403E+00	6.003E+00	6.536E+00	6.982E+00	7.375E+00
0.080	3.029E+00	4.055E+00	4.952E+00	5.740E+00	6.421E+00	7.030E+00	7.543E+00	7.996E+00
0.090	3.091E+00	4.184E+00	5.157E+00	6.024E+00	6.781E+00	7.464E+00	8.043E+00	8.558E+00
0.100	3.133E+00	4.283E+00	5.324E+00	6.262E+00	7.092E+00	7.845E+00	8.489E+00	9.064E+00
0.150	3.185E+00	4.511E+00	5.779E+00	6.980E+00	8.093E+00	9.135E+00	1.006E+01	1.091E+01
0.200	3.123E+00	4.526E+00	5.908E+00	7.255E+00	8.541E+00	9.774E+00	1.089E+01	1.194E+01
0.250	3.027E+00	4.464E+00	5.906E+00	7.335E+00	8.726E+00	1.008E+01	1.133E+01	1.252E+01
0.300	2.922E+00	4.371E+00	5.846E+00	7.324E+00	8.781E+00	1.022E+01	1.155E+01	1.283E+01
0.400	2.717E+00	4.157E+00	5.656E+00	7.181E+00	8.712E+00	1.024E+01	1.167E+01	1.307E+01
0.500	2.530E+00	3.942E+00	5.438E+00	6.978E+00	8.541E+00	1.012E+01	1.160E+01	1.306E+01
0.600	2.363E+00	3.739E+00	5.218E+00	6.756E+00	8.332E+00	9.934E+00	1.145E+01	1.294E+01
0.700	2.215E+00	3.550E+00	5.006E+00	6.533E+00	8.109E+00	9.723E+00	1.125E+01	1.276E+01
0.800	2.083E+00	3.377E+00	4.804E+00	6.314E+00	7.884E+00	9.500E+00	1.103E+01	1.255E+01
0.900	1.966E+00	3.218E+00	4.615E+00	6.104E+00	7.662E+00	9.274E+00	1.081E+01	1.233E+01
1.000	1.861E+00	3.072E+00	4.437E+00	5.904E+00	7.447E+00	9.051E+00	1.058E+01	1.210E+01
1.500	1.466E+00	2.497E+00	3.706E+00	5.045E+00	6.488E+00	8.019E+00	9.495E+00	1.098E+01
2.000	1.211E+00	2.100E+00	3.171E+00	4.386E+00	5.720E+00	7.157E+00	8.562E+00	9.992E+00
2.500	1.033E+00	1.811E+00	2.768E+00	3.872E+00	5.102E+00	6.446E+00	7.775E+00	9.139E+00
3.000	9.028E−01	1.593E+00	2.454E+00	3.462E+00	4.599E+00	5.853E+00	7.109E+00	8.407E+00
4.000	7.245E−01	1.286E+00	2.001E+00	2.853E+00	3.832E+00	4.931E+00	6.053E+00	7.228E+00
5.000	6.083E−01	1.083E+00	1.691E+00	2.426E+00	3.280E+00	4.251E+00	5.260E+00	6.326E+00
6.000	5.265E−01	9.375E−01	1.467E+00	2.112E+00	2.868E+00	3.733E+00	4.646E+00	5.619E+00
7.000	4.656E−01	8.289E−01	1.298E+00	1.872E+00	2.548E+00	3.327E+00	4.158E+00	5.051E+00
8.000	4.184E−01	7.446E−01	1.166E+00	1.683E+00	2.294E+00	3.002E+00	3.764E+00	4.587E+00
9.000	3.807E−01	6.771E−01	1.060E+00	1.531E+00	2.088E+00	2.735E+00	3.438E+00	4.202E+00
10.00	3.498E−01	6.219E−01	9.734E−01	1.405E+00	1.918E+00	2.514E+00	3.166E+00	3.877E+00
15.00	2.522E−01	4.479E−01	6.998E−01	1.009E+00	1.376E+00	1.804E+00	2.282E+00	2.810E+00
20.00	1.998E−01	3.548E−01	5.540E−01	7.978E−01	1.087E+00	1.423E+00	1.801E+00	2.222E+00
25.00	1.668E−01	2.962E−01	4.625E−01	6.656E−01	9.061E−01	1.185E+00	1.500E+00	1.851E+00
30.00	1.439E−01	2.557E−01	3.992E−01	5.745E−01	7.818E−01	1.022E+00	1.293E+00	1.596E+00
40.00	1.142E−01	2.030E−01	3.170E−01	4.562E−01	6.207E−01	8.105E−01	1.025E+00	1.266E+00
50.00	9.566E−02	1.700E−01	2.656E−01	3.823E−01	5.201E−01	6.790E−01	8.590E−01	1.060E+00
60.00	8.288E−02	1.473E−01	2.302E−01	3.314E−01	4.509E−01	5.887E−01	7.448E−01	9.192E−01
70.00	7.353E−02	1.307E−01	2.043E−01	2.941E−01	4.002E−01	5.226E−01	6.612E−01	8.161E−01
80.00	6.638E−02	1.180E−01	1.844E−01	2.656E−01	3.614E−01	4.720E−01	5.973E−01	7.372E−01
90.00	6.072E−02	1.080E−01	1.687E−01	2.430E−01	3.308E−01	4.320E−01	5.467E−01	6.748E−01
100.0	5.613E−02	9.983E−02	1.560E−01	2.247E−01	3.059E−01	3.995E−01	5.056E−01	6.242E−01
150.0	4.199E−02	7.469E−02	1.168E−01	1.682E−01	2.290E−01	2.992E−01	3.788E−01	4.678E−01
200.0	3.468E−02	6.169E−02	9.645E−02	1.390E−01	1.892E−01	2.473E−01	3.131E−01	3.868E−01
250.0	3.022E−02	5.376E−02	8.405E−02	1.211E−01	1.650E−01	2.156E−01	2.730E−01	3.372E−01
300.0	2.722E−02	4.843E−02	7.572E−02	1.091E−01	1.486E−01	1.943E−01	2.460E−01	3.040E−01
400.0	2.347E−02	4.176E−02	6.531E−02	9.413E−02	1.282E−01	1.676E−01	2.123E−01	2.623E−01
500.0	2.126E−02	3.782E−02	5.915E−02	8.525E−02	1.161E−01	1.518E−01	1.923E−01	2.376E−01
600.0	1.982E−02	3.526E−02	5.515E−02	7.949E−02	1.083E−01	1.416E−01	1.793E−01	2.216E−01
700.0	1.883E−02	3.350E−02	5.239E−02	7.552E−02	1.029E−01	1.345E−01	1.704E−01	2.106E−01
800.0	1.812E−02	3.224E−02	5.042E−02	7.267E−02	9.901E−02	1.294E−01	1.640E−01	2.026E−01
900.0	1.759E−02	3.130E−02	4.896E−02	7.057E−02	9.614E−02	1.257E−01	1.592E−01	1.968E−01
1000.	1.719E−02	3.059E−02	4.784E−02	6.896E−02	9.396E−02	1.228E−01	1.556E−01	1.923E−01

Material: Lithium tetraborate

Ion	Na	Mg	Al	Si	P	S	Cl	Ar
(E/A_1) / MeV				$(-\mathrm{d}E/\rho\mathrm{d}\ell)$ / MeV cm^2 mg^{-1}				
0.025	3.933E+00	4.086E+00	4.230E+00	4.374E+00	4.527E+00	4.659E+00	4.821E+00	4.923E+00
0.030	4.415E+00	4.576E+00	4.732E+00	4.887E+00	5.052E+00	5.201E+00	5.374E+00	5.487E+00
0.040	5.328E+00	5.507E+00	5.684E+00	5.858E+00	6.042E+00	6.216E+00	6.409E+00	6.539E+00
0.050	6.184E+00	6.386E+00	6.586E+00	6.779E+00	6.982E+00	7.177E+00	7.386E+00	7.527E+00
0.060	6.983E+00	7.213E+00	7.441E+00	7.658E+00	7.882E+00	8.100E+00	8.323E+00	8.475E+00
0.070	7.724E+00	7.988E+00	8.250E+00	8.495E+00	8.744E+00	8.985E+00	9.227E+00	9.391E+00
0.080	8.407E+00	8.709E+00	9.011E+00	9.287E+00	9.566E+00	9.833E+00	1.010E+01	1.027E+01
0.090	9.032E+00	9.376E+00	9.721E+00	1.003E+01	1.034E+01	1.064E+01	1.093E+01	1.112E+01
0.100	9.603E+00	9.991E+00	1.038E+01	1.073E+01	1.108E+01	1.141E+01	1.172E+01	1.194E+01
0.150	1.175E+01	1.235E+01	1.297E+01	1.353E+01	1.408E+01	1.461E+01	1.509E+01	1.545E+01
0.200	1.303E+01	1.382E+01	1.465E+01	1.541E+01	1.615E+01	1.687E+01	1.752E+01	1.804E+01
0.250	1.378E+01	1.472E+01	1.571E+01	1.663E+01	1.755E+01	1.843E+01	1.925E+01	1.992E+01
0.300	1.423E+01	1.526E+01	1.638E+01	1.742E+01	1.848E+01	1.950E+01	2.046E+01	2.126E+01
0.400	1.464E+01	1.579E+01	1.707E+01	1.828E+01	1.953E+01	2.075E+01	2.190E+01	2.289E+01
0.500	1.474E+01	1.594E+01	1.732E+01	1.864E+01	2.001E+01	2.136E+01	2.264E+01	2.375E+01
0.600	1.469E+01	1.592E+01	1.736E+01	1.875E+01	2.020E+01	2.164E+01	2.301E+01	2.421E+01
0.700	1.457E+01	1.581E+01	1.729E+01	1.872E+01	2.023E+01	2.174E+01	2.317E+01	2.443E+01
0.800	1.440E+01	1.564E+01	1.715E+01	1.861E+01	2.017E+01	2.172E+01	2.320E+01	2.451E+01
0.900	1.420E+01	1.544E+01	1.697E+01	1.846E+01	2.004E+01	2.164E+01	2.315E+01	2.449E+01
1.000	1.399E+01	1.523E+01	1.677E+01	1.827E+01	1.988E+01	2.150E+01	2.304E+01	2.440E+01
1.500	1.289E+01	1.408E+01	1.564E+01	1.715E+01	1.882E+01	2.050E+01	2.211E+01	2.352E+01
2.000	1.186E+01	1.300E+01	1.453E+01	1.603E+01	1.769E+01	1.938E+01	2.099E+01	2.241E+01
2.500	1.095E+01	1.204E+01	1.353E+01	1.499E+01	1.662E+01	1.829E+01	1.989E+01	2.130E+01
3.000	1.015E+01	1.120E+01	1.264E+01	1.406E+01	1.565E+01	1.729E+01	1.886E+01	2.024E+01
4.000	8.813E+00	9.795E+00	1.114E+01	1.247E+01	1.397E+01	1.553E+01	1.703E+01	1.836E+01
5.000	7.768E+00	8.687E+00	9.934E+00	1.118E+01	1.259E+01	1.406E+01	1.549E+01	1.677E+01
6.000	6.931E+00	7.795E+00	8.956E+00	1.013E+01	1.145E+01	1.284E+01	1.419E+01	1.540E+01
7.000	6.250E+00	7.065E+00	8.148E+00	9.246E+00	1.049E+01	1.179E+01	1.307E+01	1.424E+01
8.000	5.686E+00	6.457E+00	7.471E+00	8.504E+00	9.670E+00	1.090E+01	1.212E+01	1.323E+01
9.000	5.213E+00	5.945E+00	6.896E+00	7.870E+00	8.968E+00	1.013E+01	1.128E+01	1.235E+01
10.00	4.812E+00	5.508E+00	6.402E+00	7.323E+00	8.359E+00	9.462E+00	1.056E+01	1.158E+01
15.00	3.477E+00	4.036E+00	4.721E+00	5.438E+00	6.240E+00	7.101E+00	7.970E+00	8.808E+00
20.00	2.736E+00	3.202E+00	3.756E+00	4.341E+00	4.991E+00	5.691E+00	6.408E+00	7.115E+00
25.00	2.269E+00	2.670E+00	3.134E+00	3.629E+00	4.174E+00	4.763E+00	5.372E+00	5.983E+00
30.00	1.949E+00	2.301E+00	2.702E+00	3.131E+00	3.602E+00	4.110E+00	4.640E+00	5.178E+00
40.00	1.539E+00	1.824E+00	2.141E+00	2.483E+00	2.855E+00	3.255E+00	3.677E+00	4.112E+00
50.00	1.286E+00	1.527E+00	1.792E+00	2.078E+00	2.388E+00	2.722E+00	3.075E+00	3.442E+00
60.00	1.114E+00	1.323E+00	1.553E+00	1.801E+00	2.069E+00	2.357E+00	2.662E+00	2.982E+00
70.00	9.882E−01	1.176E+00	1.379E+00	1.599E+00	1.836E+00	2.091E+00	2.361E+00	2.646E+00
80.00	8.924E−01	1.061E+00	1.245E+00	1.444E+00	1.658E+00	1.888E+00	2.132E+00	2.389E+00
90.00	8.167E−01	9.715E−01	1.140E+00	1.322E+00	1.518E+00	1.728E+00	1.951E+00	2.187E+00
100.0	7.554E−01	8.987E−01	1.055E+00	1.223E+00	1.404E+00	1.598E+00	1.805E+00	2.023E+00
150.0	5.662E−01	6.739E−01	7.910E−01	9.176E−01	1.054E+00	1.199E+00	1.354E+00	1.518E+00
200.0	4.682E−01	5.574E−01	6.544E−01	7.593E−01	8.719E−01	9.924E−01	1.121E+00	1.257E+00
250.0	4.083E−01	4.862E−01	5.709E−01	6.624E−01	7.608E−01	8.661E−01	9.782E−01	1.097E+00
300.0	3.680E−01	4.383E−01	5.147E−01	5.973E−01	6.860E−01	7.810E−01	8.822E−01	9.896E−01
400.0	3.176E−01	3.783E−01	4.443E−01	5.157E−01	5.924E−01	6.746E−01	7.621E−01	8.550E−01
500.0	2.878E−01	3.428E−01	4.026E−01	4.674E−01	5.370E−01	6.115E−01	6.908E−01	7.752E−01
600.0	2.684E−01	3.197E−01	3.756E−01	4.359E−01	5.009E−01	5.704E−01	6.445E−01	7.232E−01
700.0	2.550E−01	3.038E−01	3.569E−01	4.143E−01	4.760E−01	5.421E−01	6.126E−01	6.874E−01
800.0	2.454E−01	2.924E−01	3.435E−01	3.987E−01	4.582E−01	5.218E−01	5.896E−01	6.617E−01
900.0	2.384E−01	2.839E−01	3.336E−01	3.872E−01	4.450E−01	5.068E−01	5.727E−01	6.427E−01
1000.	2.329E−01	2.775E−01	3.260E−01	3.785E−01	4.349E−01	4.953E−01	5.598E−01	6.282E−01

Material: Methane

Ion	Li	Be	B	C	N	O	F	Ne
(E/A_1) / MeV				$(-\mathrm{d}E/\rho\mathrm{d}\ell)$ / MeV cm^2 mg^{-1}				
0.025	3.507E+00	4.480E+00	5.276E+00	5.909E+00	6.512E+00	7.020E+00	7.390E+00	7.713E+00
0.030	3.775E+00	4.839E+00	5.728E+00	6.449E+00	7.125E+00	7.704E+00	8.136E+00	8.512E+00
0.040	4.211E+00	5.448E+00	6.503E+00	7.385E+00	8.193E+00	8.902E+00	9.451E+00	9.933E+00
0.050	4.539E+00	5.940E+00	7.151E+00	8.181E+00	9.111E+00	9.939E+00	1.059E+01	1.117E+01
0.060	4.780E+00	6.331E+00	7.691E+00	8.863E+00	9.914E+00	1.085E+01	1.161E+01	1.228E+01
0.070	4.952E+00	6.635E+00	8.133E+00	9.444E+00	1.061E+01	1.167E+01	1.253E+01	1.329E+01
0.080	5.072E+00	6.866E+00	8.489E+00	9.930E+00	1.122E+01	1.239E+01	1.335E+01	1.420E+01
0.090	5.152E+00	7.040E+00	8.772E+00	1.033E+01	1.174E+01	1.302E+01	1.408E+01	1.503E+01
0.100	5.203E+00	7.169E+00	8.995E+00	1.066E+01	1.217E+01	1.356E+01	1.472E+01	1.576E+01
0.150	5.217E+00	7.410E+00	9.539E+00	1.157E+01	1.347E+01	1.528E+01	1.686E+01	1.832E+01
0.200	5.066E+00	7.349E+00	9.619E+00	1.183E+01	1.396E+01	1.602E+01	1.786E+01	1.961E+01
0.250	4.872E+00	7.185E+00	9.522E+00	1.183E+01	1.409E+01	1.630E+01	1.830E+01	2.023E+01
0.300	4.671E+00	6.985E+00	9.352E+00	1.171E+01	1.405E+01	1.636E+01	1.847E+01	2.051E+01
0.400	4.291E+00	6.562E+00	8.935E+00	1.134E+01	1.374E+01	1.616E+01	1.839E+01	2.056E+01
0.500	3.955E+00	6.159E+00	8.501E+00	1.090E+01	1.333E+01	1.579E+01	1.807E+01	2.032E+01
0.600	3.664E+00	5.791E+00	8.087E+00	1.046E+01	1.289E+01	1.537E+01	1.767E+01	1.995E+01
0.700	3.410E+00	5.459E+00	7.700E+00	1.004E+01	1.244E+01	1.492E+01	1.723E+01	1.953E+01
0.800	3.188E+00	5.160E+00	7.342E+00	9.640E+00	1.202E+01	1.448E+01	1.679E+01	1.909E+01
0.900	2.992E+00	4.891E+00	7.013E+00	9.265E+00	1.161E+01	1.405E+01	1.635E+01	1.864E+01
1.000	2.819E+00	4.647E+00	6.710E+00	8.915E+00	1.123E+01	1.364E+01	1.592E+01	1.820E+01
1.500	2.187E+00	3.713E+00	5.503E+00	7.474E+00	9.590E+00	1.184E+01	1.401E+01	1.620E+01
2.000	1.790E+00	3.091E+00	4.657E+00	6.421E+00	8.349E+00	1.043E+01	1.247E+01	1.454E+01
2.500	1.517E+00	2.648E+00	4.034E+00	5.624E+00	7.384E+00	9.310E+00	1.122E+01	1.318E+01
3.000	1.320E+00	2.319E+00	3.559E+00	5.000E+00	6.615E+00	8.399E+00	1.019E+01	1.204E+01
4.000	1.052E+00	1.862E+00	2.884E+00	4.094E+00	5.473E+00	7.017E+00	8.599E+00	1.026E+01
5.000	8.799E−01	1.561E+00	2.428E+00	3.468E+00	4.667E+00	6.023E+00	7.436E+00	8.933E+00
6.000	7.590E−01	1.348E+00	2.102E+00	3.012E+00	4.070E+00	5.275E+00	6.549E+00	7.909E+00
7.000	6.694E−01	1.189E+00	1.856E+00	2.666E+00	3.612E+00	4.695E+00	5.853E+00	7.098E+00
8.000	6.001E−01	1.066E+00	1.665E+00	2.394E+00	3.249E+00	4.232E+00	5.292E+00	6.439E+00
9.000	5.449E−01	9.678E−01	1.512E+00	2.175E+00	2.956E+00	3.855E+00	4.832E+00	5.894E+00
10.00	4.998E−01	8.876E−01	1.386E+00	1.995E+00	2.713E+00	3.542E+00	4.448E+00	5.436E+00
15.00	3.580E−01	6.356E−01	9.923E−01	1.428E+00	1.944E+00	2.540E+00	3.205E+00	3.940E+00
20.00	2.824E−01	5.015E−01	7.828E−01	1.126E+00	1.532E+00	2.002E+00	2.530E+00	3.116E+00
25.00	2.350E−01	4.175E−01	6.517E−01	9.376E−01	1.275E+00	1.665E+00	2.106E+00	2.596E+00
30.00	2.024E−01	3.596E−01	5.613E−01	8.076E−01	1.098E+00	1.434E+00	1.813E+00	2.236E+00
40.00	1.601E−01	2.845E−01	4.442E−01	6.393E−01	8.695E−01	1.135E+00	1.435E+00	1.771E+00
50.00	1.337E−01	2.377E−01	3.712E−01	5.343E−01	7.269E−01	9.489E−01	1.200E+00	1.481E+00
60.00	1.156E−01	2.056E−01	3.212E−01	4.623E−01	6.291E−01	8.213E−01	1.039E+00	1.282E+00
70.00	1.024E−01	1.821E−01	2.846E−01	4.097E−01	5.575E−01	7.280E−01	9.210E−01	1.137E+00
80.00	9.236E−02	1.642E−01	2.566E−01	3.695E−01	5.029E−01	6.567E−01	8.309E−01	1.026E+00
90.00	8.440E−02	1.501E−01	2.345E−01	3.377E−01	4.597E−01	6.004E−01	7.597E−01	9.378E−01
100.0	7.795E−02	1.386E−01	2.166E−01	3.120E−01	4.247E−01	5.547E−01	7.020E−01	8.666E−01
150.0	5.812E−02	1.034E−01	1.616E−01	2.328E−01	3.169E−01	4.141E−01	5.242E−01	6.473E−01
200.0	4.790E−02	8.520E−02	1.332E−01	1.919E−01	2.613E−01	3.415E−01	4.324E−01	5.340E−01
250.0	4.167E−02	7.413E−02	1.159E−01	1.670E−01	2.274E−01	2.972E−01	3.764E−01	4.649E−01
300.0	3.749E−02	6.669E−02	1.043E−01	1.503E−01	2.047E−01	2.675E−01	3.388E−01	4.185E−01
400.0	3.227E−02	5.741E−02	8.977E−02	1.294E−01	1.762E−01	2.303E−01	2.917E−01	3.604E−01
500.0	2.918E−02	5.192E−02	8.119E−02	1.170E−01	1.594E−01	2.084E−01	2.639E−01	3.261E−01
600.0	2.717E−02	4.835E−02	7.561E−02	1.090E−01	1.484E−01	1.941E−01	2.458E−01	3.037E−01
700.0	2.579E−02	4.588E−02	7.176E−02	1.034E−01	1.409E−01	1.842E−01	2.333E−01	2.883E−01
800.0	2.479E−02	4.411E−02	6.899E−02	9.943E−02	1.355E−01	1.771E−01	2.243E−01	2.772E−01
900.0	2.405E−02	4.280E−02	6.694E−02	9.648E−02	1.314E−01	1.718E−01	2.177E−01	2.690E−01
1000.	2.349E−02	4.180E−02	6.537E−02	9.422E−02	1.284E−01	1.678E−01	2.126E−01	2.627E−01

Material: Methane

Ion	Na	Mg	Al	Si	P	S	Cl	Ar
(E/A_1) / MeV				$(-\mathrm{d}E/\rho\mathrm{d}\ell)$ / MeV cm^2 mg^{-1}				
0.025	7.985E+00	8.334E+00	8.640E+00	8.940E+00	9.314E+00	9.598E+00	9.983E+00	1.018E+01
0.030	8.827E+00	9.200E+00	9.535E+00	9.859E+00	1.026E+01	1.057E+01	1.097E+01	1.119E+01
0.040	1.034E+01	1.077E+01	1.116E+01	1.154E+01	1.199E+01	1.237E+01	1.280E+01	1.305E+01
0.050	1.167E+01	1.216E+01	1.262E+01	1.306E+01	1.356E+01	1.400E+01	1.446E+01	1.475E+01
0.060	1.287E+01	1.342E+01	1.395E+01	1.444E+01	1.500E+01	1.549E+01	1.600E+01	1.632E+01
0.070	1.395E+01	1.458E+01	1.516E+01	1.570E+01	1.632E+01	1.687E+01	1.742E+01	1.778E+01
0.080	1.495E+01	1.564E+01	1.628E+01	1.688E+01	1.754E+01	1.815E+01	1.874E+01	1.914E+01
0.090	1.587E+01	1.662E+01	1.733E+01	1.797E+01	1.869E+01	1.934E+01	1.998E+01	2.042E+01
0.100	1.670E+01	1.753E+01	1.830E+01	1.900E+01	1.976E+01	2.047E+01	2.115E+01	2.163E+01
0.150	1.970E+01	2.092E+01	2.205E+01	2.307E+01	2.414E+01	2.514E+01	2.606E+01	2.677E+01
0.200	2.130E+01	2.284E+01	2.428E+01	2.560E+01	2.697E+01	2.827E+01	2.946E+01	3.043E+01
0.250	2.214E+01	2.390E+01	2.557E+01	2.712E+01	2.871E+01	3.026E+01	3.168E+01	3.288E+01
0.300	2.257E+01	2.448E+01	2.632E+01	2.803E+01	2.980E+01	3.154E+01	3.313E+01	3.452E+01
0.400	2.280E+01	2.491E+01	2.696E+01	2.889E+01	3.090E+01	3.289E+01	3.473E+01	3.637E+01
0.500	2.265E+01	2.487E+01	2.705E+01	2.911E+01	3.127E+01	3.342E+01	3.542E+01	3.721E+01
0.600	2.234E+01	2.462E+01	2.687E+01	2.902E+01	3.127E+01	3.354E+01	3.564E+01	3.755E+01
0.700	2.195E+01	2.426E+01	2.657E+01	2.876E+01	3.109E+01	3.343E+01	3.561E+01	3.759E+01
0.800	2.152E+01	2.386E+01	2.619E+01	2.842E+01	3.080E+01	3.319E+01	3.543E+01	3.746E+01
0.900	2.108E+01	2.342E+01	2.578E+01	2.803E+01	3.044E+01	3.288E+01	3.515E+01	3.722E+01
1.000	2.064E+01	2.298E+01	2.535E+01	2.761E+01	3.005E+01	3.251E+01	3.481E+01	3.691E+01
1.500	1.856E+01	2.086E+01	2.319E+01	2.545E+01	2.791E+01	3.042E+01	3.277E+01	3.493E+01
2.000	1.680E+01	1.900E+01	2.127E+01	2.347E+01	2.588E+01	2.836E+01	3.069E+01	3.284E+01
2.500	1.532E+01	1.743E+01	1.961E+01	2.173E+01	2.408E+01	2.649E+01	2.878E+01	3.089E+01
3.000	1.407E+01	1.608E+01	1.817E+01	2.022E+01	2.249E+01	2.484E+01	2.706E+01	2.912E+01
4.000	1.209E+01	1.393E+01	1.584E+01	1.775E+01	1.985E+01	2.205E+01	2.415E+01	2.611E+01
5.000	1.059E+01	1.227E+01	1.404E+01	1.580E+01	1.776E+01	1.981E+01	2.179E+01	2.364E+01
6.000	9.417E+00	1.097E+01	1.260E+01	1.424E+01	1.607E+01	1.798E+01	1.984E+01	2.160E+01
7.000	8.480E+00	9.911E+00	1.143E+01	1.296E+01	1.466E+01	1.646E+01	1.821E+01	1.988E+01
8.000	7.713E+00	9.042E+00	1.046E+01	1.189E+01	1.349E+01	1.517E+01	1.683E+01	1.842E+01
9.000	7.076E+00	8.315E+00	9.637E+00	1.099E+01	1.249E+01	1.407E+01	1.564E+01	1.715E+01
10.00	6.537E+00	7.698E+00	8.938E+00	1.021E+01	1.163E+01	1.312E+01	1.461E+01	1.605E+01
15.00	4.758E+00	5.636E+00	6.582E+00	7.573E+00	8.661E+00	9.825E+00	1.100E+01	1.217E+01
20.00	3.769E+00	4.474E+00	5.239E+00	6.047E+00	6.931E+00	7.879E+00	8.852E+00	9.834E+00
25.00	3.140E+00	3.732E+00	4.374E+00	5.058E+00	5.803E+00	6.603E+00	7.432E+00	8.278E+00
30.00	2.705E+00	3.217E+00	3.772E+00	4.366E+00	5.011E+00	5.704E+00	6.426E+00	7.171E+00
40.00	2.142E+00	2.547E+00	2.988E+00	3.462E+00	3.974E+00	4.524E+00	5.102E+00	5.705E+00
50.00	1.791E+00	2.130E+00	2.499E+00	2.896E+00	3.325E+00	3.784E+00	4.270E+00	4.778E+00
60.00	1.551E+00	1.844E+00	2.164E+00	2.508E+00	2.879E+00	3.276E+00	3.697E+00	4.140E+00
70.00	1.375E+00	1.636E+00	1.919E+00	2.224E+00	2.553E+00	2.905E+00	3.279E+00	3.673E+00
80.00	1.241E+00	1.476E+00	1.732E+00	2.008E+00	2.304E+00	2.622E+00	2.959E+00	3.316E+00
90.00	1.134E+00	1.350E+00	1.584E+00	1.836E+00	2.108E+00	2.398E+00	2.707E+00	3.033E+00
100.0	1.048E+00	1.248E+00	1.464E+00	1.698E+00	1.949E+00	2.217E+00	2.502E+00	2.805E+00
150.0	7.834E−01	9.324E−01	1.094E+00	1.269E+00	1.458E+00	1.659E+00	1.873E+00	2.099E+00
200.0	6.464E−01	7.696E−01	9.035E−01	1.048E+00	1.204E+00	1.370E+00	1.547E+00	1.735E+00
250.0	5.628E−01	6.702E−01	7.869E−01	9.130E−01	1.049E+00	1.194E+00	1.348E+00	1.512E+00
300.0	5.067E−01	6.033E−01	7.085E−01	8.222E−01	9.443E−01	1.075E+00	1.214E+00	1.362E+00
400.0	4.365E−01	5.198E−01	6.105E−01	7.085E−01	8.139E−01	9.267E−01	1.047E+00	1.174E+00
500.0	3.949E−01	4.703E−01	5.524E−01	6.412E−01	7.366E−01	8.387E−01	9.476E−01	1.063E+00
600.0	3.678E−01	4.381E−01	5.146E−01	5.973E−01	6.863E−01	7.815E−01	8.830E−01	9.908E−01
700.0	3.492E−01	4.159E−01	4.885E−01	5.671E−01	6.516E−01	7.420E−01	8.384E−01	9.407E−01
800.0	3.357E−01	3.999E−01	4.698E−01	5.453E−01	6.266E−01	7.136E−01	8.063E−01	9.047E−01
900.0	3.258E−01	3.881E−01	4.559E−01	5.292E−01	6.081E−01	6.925E−01	7.825E−01	8.781E−01
1000.	3.182E−01	3.790E−01	4.453E−01	5.169E−01	5.939E−01	6.764E−01	7.643E−01	8.577E−01

Material: Muscle striated (ICRU)

Ion	Li	Be	B	C	N	O	F	Ne
(E/A_1) / MeV				$(-\mathrm{d}E/\rho\mathrm{d}\ell)$ / MeV cm^2 mg^{-1}				
0.025	2.654E+00	3.290E+00	3.785E+00	4.166E+00	4.507E+00	4.804E+00	5.032E+00	5.239E+00
0.030	2.875E+00	3.594E+00	4.166E+00	4.615E+00	5.009E+00	5.352E+00	5.618E+00	5.856E+00
0.040	3.232E+00	4.103E+00	4.817E+00	5.399E+00	5.902E+00	6.342E+00	6.689E+00	6.994E+00
0.050	3.499E+00	4.510E+00	5.355E+00	6.062E+00	6.671E+00	7.210E+00	7.641E+00	8.019E+00
0.060	3.697E+00	4.833E+00	5.801E+00	6.626E+00	7.339E+00	7.973E+00	8.489E+00	8.942E+00
0.070	3.840E+00	5.088E+00	6.169E+00	7.106E+00	7.919E+00	8.648E+00	9.247E+00	9.776E+00
0.080	3.942E+00	5.286E+00	6.471E+00	7.512E+00	8.421E+00	9.242E+00	9.924E+00	1.053E+01
0.090	4.013E+00	5.438E+00	6.715E+00	7.852E+00	8.854E+00	9.765E+00	1.053E+01	1.121E+01
0.100	4.059E+00	5.552E+00	6.912E+00	8.137E+00	9.225E+00	1.022E+01	1.106E+01	1.182E+01
0.150	4.086E+00	5.786E+00	7.417E+00	8.959E+00	1.039E+01	1.174E+01	1.292E+01	1.401E+01
0.200	3.975E+00	5.758E+00	7.519E+00	9.230E+00	1.086E+01	1.244E+01	1.386E+01	1.519E+01
0.250	3.828E+00	5.641E+00	7.465E+00	9.267E+00	1.102E+01	1.273E+01	1.430E+01	1.580E+01
0.300	3.676E+00	5.493E+00	7.347E+00	9.200E+00	1.102E+01	1.283E+01	1.449E+01	1.610E+01
0.400	3.388E+00	5.179E+00	7.046E+00	8.940E+00	1.084E+01	1.274E+01	1.451E+01	1.625E+01
0.500	3.134E+00	4.878E+00	6.727E+00	8.626E+00	1.055E+01	1.250E+01	1.433E+01	1.612E+01
0.600	2.912E+00	4.602E+00	6.420E+00	8.306E+00	1.023E+01	1.220E+01	1.405E+01	1.589E+01
0.700	2.719E+00	4.351E+00	6.131E+00	7.995E+00	9.915E+00	1.189E+01	1.375E+01	1.560E+01
0.800	2.548E+00	4.124E+00	5.863E+00	7.699E+00	9.603E+00	1.157E+01	1.343E+01	1.529E+01
0.900	2.398E+00	3.918E+00	5.614E+00	7.419E+00	9.302E+00	1.126E+01	1.311E+01	1.497E+01
1.000	2.264E+00	3.731E+00	5.384E+00	7.155E+00	9.015E+00	1.095E+01	1.280E+01	1.465E+01
1.500	1.770E+00	3.007E+00	4.456E+00	6.057E+00	7.779E+00	9.606E+00	1.138E+01	1.317E+01
2.000	1.455E+00	2.517E+00	3.794E+00	5.238E+00	6.820E+00	8.524E+00	1.020E+01	1.191E+01
2.500	1.238E+00	2.165E+00	3.301E+00	4.609E+00	6.063E+00	7.649E+00	9.227E+00	1.085E+01
3.000	1.080E+00	1.901E+00	2.922E+00	4.112E+00	5.452E+00	6.928E+00	8.415E+00	9.956E+00
4.000	8.645E−01	1.532E+00	2.377E+00	3.382E+00	4.532E+00	5.820E+00	7.144E+00	8.532E+00
5.000	7.247E−01	1.287E+00	2.007E+00	2.873E+00	3.876E+00	5.012E+00	6.199E+00	7.456E+00
6.000	6.264E−01	1.114E+00	1.740E+00	2.499E+00	3.386E+00	4.399E+00	5.471E+00	6.616E+00
7.000	5.534E−01	9.840E−01	1.539E+00	2.214E+00	3.008E+00	3.920E+00	4.896E+00	5.946E+00
8.000	4.968E−01	8.833E−01	1.381E+00	1.990E+00	2.708E+00	3.536E+00	4.431E+00	5.399E+00
9.000	4.516E−01	8.027E−01	1.255E+00	1.810E+00	2.465E+00	3.223E+00	4.048E+00	4.945E+00
10.00	4.146E−01	7.368E−01	1.152E+00	1.661E+00	2.264E+00	2.962E+00	3.727E+00	4.562E+00
15.00	2.981E−01	5.294E−01	8.269E−01	1.191E+00	1.624E+00	2.126E+00	2.687E+00	3.307E+00
20.00	2.358E−01	4.187E−01	6.537E−01	9.410E−01	1.281E+00	1.676E+00	2.121E+00	2.615E+00
25.00	1.965E−01	3.491E−01	5.450E−01	7.843E−01	1.067E+00	1.395E+00	1.765E+00	2.178E+00
30.00	1.695E−01	3.011E−01	4.700E−01	6.764E−01	9.202E−01	1.202E+00	1.521E+00	1.877E+00
40.00	1.343E−01	2.387E−01	3.727E−01	5.364E−01	7.296E−01	9.527E−01	1.205E+00	1.487E+00
50.00	1.123E−01	1.997E−01	3.119E−01	4.489E−01	6.108E−01	7.974E−01	1.009E+00	1.245E+00
60.00	9.726E−02	1.729E−01	2.701E−01	3.889E−01	5.291E−01	6.908E−01	8.740E−01	1.079E+00
70.00	8.623E−02	1.533E−01	2.395E−01	3.449E−01	4.693E−01	6.129E−01	7.754E−01	9.570E−01
80.00	7.780E−02	1.383E−01	2.162E−01	3.113E−01	4.236E−01	5.532E−01	7.000E−01	8.640E−01
90.00	7.114E−02	1.265E−01	1.977E−01	2.847E−01	3.875E−01	5.061E−01	6.404E−01	7.905E−01
100.0	6.574E−02	1.169E−01	1.827E−01	2.631E−01	3.582E−01	4.678E−01	5.921E−01	7.309E−01
150.0	4.911E−02	8.734E−02	1.365E−01	1.967E−01	2.678E−01	3.499E−01	4.430E−01	5.470E−01
200.0	4.052E−02	7.208E−02	1.127E−01	1.624E−01	2.211E−01	2.889E−01	3.658E−01	4.519E−01
250.0	3.528E−02	6.277E−02	9.814E−02	1.414E−01	1.926E−01	2.517E−01	3.187E−01	3.937E−01
300.0	3.177E−02	5.651E−02	8.837E−02	1.273E−01	1.734E−01	2.267E−01	2.871E−01	3.547E−01
400.0	2.737E−02	4.870E−02	7.616E−02	1.098E−01	1.495E−01	1.954E−01	2.475E−01	3.058E−01
500.0	2.477E−02	4.408E−02	6.893E−02	9.935E−02	1.353E−01	1.769E−01	2.241E−01	2.769E−01
600.0	2.308E−02	4.108E−02	6.424E−02	9.259E−02	1.261E−01	1.649E−01	2.089E−01	2.581E−01
700.0	2.192E−02	3.901E−02	6.100E−02	8.792E−02	1.198E−01	1.566E−01	1.984E−01	2.451E−01
800.0	2.109E−02	3.752E−02	5.868E−02	8.458E−02	1.152E−01	1.506E−01	1.908E−01	2.358E−01
900.0	2.047E−02	3.642E−02	5.696E−02	8.210E−02	1.119E−01	1.462E−01	1.853E−01	2.289E−01
1000.	2.000E−02	3.558E−02	5.565E−02	8.021E−02	1.093E−01	1.429E−01	1.810E−01	2.237E−01

Material: Muscle striated (ICRU)

Ion	Na	Mg	Al	Si	P	S	Cl	Ar
(E/A_1) / MeV				$(-\mathrm{d}E/\rho\mathrm{d}\ell)$ / MeV cm^2 mg^{-1}				
0.025	5.425E+00	5.628E+00	5.824E+00	6.020E+00	6.246E+00	6.433E+00	6.668E+00	6.799E+00
0.030	6.072E+00	6.282E+00	6.493E+00	6.703E+00	6.943E+00	7.148E+00	7.395E+00	7.541E+00
0.040	7.277E+00	7.507E+00	7.751E+00	7.987E+00	8.254E+00	8.491E+00	8.757E+00	8.924E+00
0.050	8.376E+00	8.639E+00	8.919E+00	9.187E+00	9.482E+00	9.751E+00	1.004E+01	1.022E+01
0.060	9.379E+00	9.680E+00	1.000E+01	1.031E+01	1.064E+01	1.094E+01	1.125E+01	1.145E+01
0.070	1.029E+01	1.064E+01	1.101E+01	1.136E+01	1.172E+01	1.207E+01	1.240E+01	1.262E+01
0.080	1.113E+01	1.152E+01	1.194E+01	1.234E+01	1.274E+01	1.312E+01	1.349E+01	1.374E+01
0.090	1.189E+01	1.233E+01	1.281E+01	1.325E+01	1.370E+01	1.412E+01	1.452E+01	1.480E+01
0.100	1.258E+01	1.307E+01	1.361E+01	1.409E+01	1.459E+01	1.505E+01	1.549E+01	1.580E+01
0.150	1.517E+01	1.591E+01	1.673E+01	1.747E+01	1.821E+01	1.891E+01	1.955E+01	2.004E+01
0.200	1.666E+01	1.762E+01	1.870E+01	1.968E+01	2.066E+01	2.159E+01	2.245E+01	2.314E+01
0.250	1.751E+01	1.862E+01	1.989E+01	2.107E+01	2.225E+01	2.340E+01	2.445E+01	2.533E+01
0.300	1.797E+01	1.919E+01	2.061E+01	2.194E+01	2.328E+01	2.459E+01	2.581E+01	2.684E+01
0.400	1.833E+01	1.967E+01	2.128E+01	2.281E+01	2.437E+01	2.591E+01	2.735E+01	2.861E+01
0.500	1.833E+01	1.972E+01	2.145E+01	2.309E+01	2.479E+01	2.647E+01	2.806E+01	2.946E+01
0.600	1.818E+01	1.959E+01	2.138E+01	2.310E+01	2.489E+01	2.667E+01	2.836E+01	2.986E+01
0.700	1.795E+01	1.936E+01	2.120E+01	2.296E+01	2.482E+01	2.667E+01	2.842E+01	2.999E+01
0.800	1.767E+01	1.909E+01	2.095E+01	2.275E+01	2.464E+01	2.655E+01	2.835E+01	2.996E+01
0.900	1.738E+01	1.879E+01	2.067E+01	2.248E+01	2.441E+01	2.635E+01	2.819E+01	2.984E+01
1.000	1.707E+01	1.847E+01	2.036E+01	2.219E+01	2.415E+01	2.611E+01	2.798E+01	2.965E+01
1.500	1.558E+01	1.692E+01	1.880E+01	2.064E+01	2.263E+01	2.465E+01	2.657E+01	2.830E+01
2.000	1.424E+01	1.553E+01	1.737E+01	1.916E+01	2.113E+01	2.315E+01	2.507E+01	2.679E+01
2.500	1.308E+01	1.432E+01	1.610E+01	1.785E+01	1.977E+01	2.175E+01	2.364E+01	2.535E+01
3.000	1.207E+01	1.328E+01	1.499E+01	1.668E+01	1.856E+01	2.049E+01	2.234E+01	2.401E+01
4.000	1.044E+01	1.157E+01	1.315E+01	1.473E+01	1.650E+01	1.832E+01	2.008E+01	2.168E+01
5.000	9.172E+00	1.024E+01	1.171E+01	1.318E+01	1.483E+01	1.655E+01	1.821E+01	1.974E+01
6.000	8.168E+00	9.174E+00	1.054E+01	1.192E+01	1.346E+01	1.507E+01	1.665E+01	1.810E+01
7.000	7.356E+00	8.308E+00	9.579E+00	1.087E+01	1.231E+01	1.383E+01	1.532E+01	1.671E+01
8.000	6.687E+00	7.589E+00	8.777E+00	9.990E+00	1.135E+01	1.278E+01	1.419E+01	1.551E+01
9.000	6.127E+00	6.985E+00	8.098E+00	9.241E+00	1.052E+01	1.187E+01	1.321E+01	1.447E+01
10.00	5.653E+00	6.471E+00	7.517E+00	8.596E+00	9.800E+00	1.108E+01	1.235E+01	1.356E+01
15.00	4.083E+00	4.742E+00	5.543E+00	6.383E+00	7.314E+00	8.312E+00	9.325E+00	1.031E+01
20.00	3.213E+00	3.763E+00	4.411E+00	5.096E+00	5.852E+00	6.665E+00	7.501E+00	8.331E+00
25.00	2.666E+00	3.138E+00	3.681E+00	4.261E+00	4.897E+00	5.581E+00	6.292E+00	7.008E+00
30.00	2.290E+00	2.704E+00	3.174E+00	3.677E+00	4.226E+00	4.818E+00	5.436E+00	6.067E+00
40.00	1.807E+00	2.142E+00	2.514E+00	2.914E+00	3.349E+00	3.817E+00	4.310E+00	4.820E+00
50.00	1.510E+00	1.792E+00	2.103E+00	2.439E+00	2.801E+00	3.191E+00	3.604E+00	4.034E+00
60.00	1.307E+00	1.552E+00	1.822E+00	2.112E+00	2.426E+00	2.763E+00	3.120E+00	3.494E+00
70.00	1.159E+00	1.379E+00	1.616E+00	1.874E+00	2.152E+00	2.450E+00	2.767E+00	3.100E+00
80.00	1.046E+00	1.244E+00	1.459E+00	1.692E+00	1.943E+00	2.212E+00	2.497E+00	2.798E+00
90.00	9.568E−01	1.138E+00	1.336E+00	1.549E+00	1.778E+00	2.024E+00	2.285E+00	2.561E+00
100.0	8.846E−01	1.052E+00	1.235E+00	1.432E+00	1.644E+00	1.871E+00	2.113E+00	2.368E+00
150.0	6.621E−01	7.880E−01	9.250E−01	1.073E+00	1.232E+00	1.402E+00	1.583E+00	1.775E+00
200.0	5.470E−01	6.512E−01	7.645E−01	8.870E−01	1.019E+00	1.159E+00	1.309E+00	1.468E+00
250.0	4.767E−01	5.676E−01	6.665E−01	7.733E−01	8.882E−01	1.011E+00	1.142E+00	1.281E+00
300.0	4.294E−01	5.114E−01	6.005E−01	6.969E−01	8.005E−01	9.113E−01	1.029E+00	1.155E+00
400.0	3.703E−01	4.411E−01	5.180E−01	6.012E−01	6.907E−01	7.864E−01	8.884E−01	9.967E−01
500.0	3.353E−01	3.994E−01	4.691E−01	5.445E−01	6.256E−01	7.124E−01	8.049E−01	9.031E−01
600.0	3.126E−01	3.723E−01	4.374E−01	5.077E−01	5.833E−01	6.642E−01	7.505E−01	8.422E−01
700.0	2.969E−01	3.537E−01	4.154E−01	4.822E−01	5.541E−01	6.310E−01	7.130E−01	8.001E−01
800.0	2.856E−01	3.402E−01	3.997E−01	4.640E−01	5.331E−01	6.071E−01	6.861E−01	7.699E−01
900.0	2.773E−01	3.303E−01	3.880E−01	4.505E−01	5.176E−01	5.895E−01	6.661E−01	7.475E−01
1000.	2.709E−01	3.227E−01	3.791E−01	4.401E−01	5.058E−01	5.760E−01	6.509E−01	7.304E−01

Material: Nylon, type 6 and type 6/6

Ion	Li	Be	B	C	N	O	F	Ne
(E/A_1) / MeV				$(-\mathrm{d}E/\rho\mathrm{d}\ell)$ / MeV cm^2 mg^{-1}				
0.025	2.784E+00	3.441E+00	3.957E+00	4.362E+00	4.740E+00	5.063E+00	7.121E+00	5.543E+00
0.030	3.026E+00	3.767E+00	4.361E+00	4.834E+00	5.265E+00	5.635E+00	7.892E+00	6.188E+00
0.040	3.417E+00	4.322E+00	5.063E+00	5.668E+00	6.205E+00	6.671E+00	9.331E+00	7.373E+00
0.050	3.703E+00	4.765E+00	5.649E+00	6.385E+00	7.026E+00	7.587E+00	1.067E+01	8.442E+00
0.060	3.906E+00	5.110E+00	6.133E+00	6.997E+00	7.747E+00	8.405E+00	1.193E+01	9.413E+00
0.070	4.047E+00	5.374E+00	6.524E+00	7.514E+00	8.374E+00	9.133E+00	1.312E+01	1.030E+01
0.080	4.141E+00	5.570E+00	6.834E+00	7.942E+00	8.912E+00	9.773E+00	1.424E+01	1.111E+01
0.090	4.202E+00	5.714E+00	7.078E+00	8.292E+00	9.367E+00	1.033E+01	1.531E+01	1.184E+01
0.100	4.238E+00	5.818E+00	7.266E+00	8.576E+00	9.748E+00	1.081E+01	1.632E+01	1.249E+01
0.150	4.231E+00	6.004E+00	7.715E+00	9.344E+00	1.087E+01	1.230E+01	2.061E+01	1.473E+01
0.200	4.103E+00	5.951E+00	7.782E+00	9.568E+00	1.129E+01	1.294E+01	2.359E+01	1.584E+01
0.250	3.948E+00	5.822E+00	7.711E+00	9.581E+00	1.141E+01	1.320E+01	2.553E+01	1.640E+01
0.300	3.790E+00	5.666E+00	7.583E+00	9.501E+00	1.140E+01	1.327E+01	2.682E+01	1.666E+01
0.400	3.492E+00	5.341E+00	7.270E+00	9.227E+00	1.119E+01	1.316E+01	2.826E+01	1.677E+01
0.500	3.230E+00	5.031E+00	6.941E+00	8.903E+00	1.089E+01	1.291E+01	2.893E+01	1.663E+01
0.600	3.001E+00	4.746E+00	6.625E+00	8.573E+00	1.057E+01	1.260E+01	2.921E+01	1.638E+01
0.700	2.801E+00	4.487E+00	6.327E+00	8.253E+00	1.024E+01	1.227E+01	2.927E+01	1.608E+01
0.800	2.625E+00	4.252E+00	6.050E+00	7.947E+00	9.915E+00	1.195E+01	2.919E+01	1.576E+01
0.900	2.469E+00	4.039E+00	5.792E+00	7.657E+00	9.604E+00	1.162E+01	2.903E+01	1.544E+01
1.000	2.331E+00	3.845E+00	5.554E+00	7.384E+00	9.307E+00	1.131E+01	2.881E+01	1.511E+01
1.500	1.821E+00	3.096E+00	4.592E+00	6.245E+00	8.022E+00	9.911E+00	2.736E+01	1.356E+01
2.000	1.496E+00	2.589E+00	3.905E+00	5.394E+00	7.024E+00	8.784E+00	2.579E+01	1.225E+01
2.500	1.272E+00	2.225E+00	3.395E+00	4.741E+00	6.237E+00	7.871E+00	2.430E+01	1.115E+01
3.000	1.108E+00	1.952E+00	3.001E+00	4.226E+00	5.602E+00	7.122E+00	2.294E+01	1.022E+01
4.000	8.863E−01	1.571E+00	2.438E+00	3.470E+00	4.650E+00	5.972E+00	2.059E+01	8.743E+00
5.000	7.423E−01	1.319E+00	2.057E+00	2.944E+00	3.971E+00	5.136E+00	1.864E+01	7.630E+00
6.000	6.413E−01	1.140E+00	1.782E+00	2.559E+00	3.466E+00	4.503E+00	1.702E+01	6.764E+00
7.000	5.662E−01	1.007E+00	1.575E+00	2.266E+00	3.077E+00	4.009E+00	1.565E+01	6.074E+00
8.000	5.082E−01	9.035E−01	1.413E+00	2.036E+00	2.769E+00	3.615E+00	1.448E+01	5.512E+00
9.000	4.618E−01	8.208E−01	1.284E+00	1.850E+00	2.519E+00	3.293E+00	1.347E+01	5.046E+00
10.00	4.239E−01	7.532E−01	1.178E+00	1.698E+00	2.313E+00	3.025E+00	1.259E+01	4.655E+00
15.00	3.045E−01	5.407E−01	8.445E−01	1.217E+00	1.657E+00	2.169E+00	9.491E+00	3.372E+00
20.00	2.406E−01	4.274E−01	6.672E−01	9.604E−01	1.308E+00	1.710E+00	7.630E+00	2.666E+00
25.00	2.005E−01	3.562E−01	5.561E−01	8.002E−01	1.089E+00	1.423E+00	6.400E+00	2.220E+00
30.00	1.729E−01	3.071E−01	4.795E−01	6.899E−01	9.385E−01	1.226E+00	5.530E+00	1.913E+00
40.00	1.369E−01	2.434E−01	3.800E−01	5.469E−01	7.439E−01	9.713E−01	4.386E+00	1.516E+00
50.00	1.145E−01	2.035E−01	3.179E−01	4.576E−01	6.225E−01	8.127E−01	3.668E+00	1.269E+00
60.00	9.911E−02	1.762E−01	2.753E−01	3.963E−01	5.392E−01	7.039E−01	3.176E+00	1.099E+00
70.00	8.786E−02	1.562E−01	2.441E−01	3.514E−01	4.782E−01	6.244E−01	2.816E+00	9.749E−01
80.00	7.926E−02	1.409E−01	2.202E−01	3.171E−01	4.316E−01	5.636E−01	2.542E+00	8.801E−01
90.00	7.246E−02	1.289E−01	2.014E−01	2.900E−01	3.947E−01	5.155E−01	2.326E+00	8.052E−01
100.0	6.695E−02	1.191E−01	1.861E−01	2.680E−01	3.648E−01	4.765E−01	2.151E+00	7.444E−01
150.0	4.999E−02	8.892E−02	1.390E−01	2.002E−01	2.726E−01	3.562E−01	1.611E+00	5.568E−01
200.0	4.124E−02	7.336E−02	1.147E−01	1.652E−01	2.250E−01	2.940E−01	1.332E+00	4.599E−01
250.0	3.590E−02	6.387E−02	9.986E−02	1.439E−01	1.960E−01	2.561E−01	1.162E+00	4.006E−01
300.0	3.232E−02	5.750E−02	8.990E−02	1.295E−01	1.765E−01	2.306E−01	1.047E+00	3.608E−01
400.0	2.784E−02	4.954E−02	7.746E−02	1.116E−01	1.521E−01	1.988E−01	9.035E−01	3.111E−01
500.0	2.519E−02	4.483E−02	7.010E−02	1.010E−01	1.376E−01	1.799E−01	8.184E−01	2.816E−01
600.0	2.347E−02	4.176E−02	6.532E−02	9.414E−02	1.282E−01	1.677E−01	7.630E−01	2.624E−01
700.0	2.229E−02	3.965E−02	6.202E−02	8.939E−02	1.218E−01	1.592E−01	7.248E−01	2.492E−01
800.0	2.143E−02	3.814E−02	5.965E−02	8.597E−02	1.171E−01	1.531E−01	6.973E−01	2.397E−01
900.0	2.080E−02	3.702E−02	5.790E−02	8.345E−02	1.137E−01	1.486E−01	6.770E−01	2.327E−01
1000.	2.032E−02	3.616E−02	5.656E−02	8.152E−02	1.111E−01	1.452E−01	6.615E−01	2.273E−01

Material: Nylon, type 6 and type 6/6

Ion	Na	Mg	Al	Si	P	S	Cl	Ar
(E/A_1) / MeV				$(-\mathrm{d}E/\rho\mathrm{d}\ell)$ / MeV cm^2 mg^{-1}				
0.025	5.732E+00	5.969E+00	6.184E+00	6.399E+00	6.653E+00	6.858E+00	7.121E+00	7.278E+00
0.030	6.403E+00	6.654E+00	6.887E+00	7.118E+00	7.389E+00	7.616E+00	7.892E+00	8.066E+00
0.040	7.645E+00	7.930E+00	8.201E+00	8.463E+00	8.766E+00	9.031E+00	9.331E+00	9.530E+00
0.050	8.776E+00	9.104E+00	9.414E+00	9.710E+00	1.005E+01	1.035E+01	1.067E+01	1.089E+01
0.060	9.811E+00	1.019E+01	1.054E+01	1.087E+01	1.124E+01	1.158E+01	1.193E+01	1.217E+01
0.070	1.076E+01	1.119E+01	1.159E+01	1.196E+01	1.237E+01	1.274E+01	1.312E+01	1.338E+01
0.080	1.164E+01	1.212E+01	1.257E+01	1.298E+01	1.342E+01	1.384E+01	1.424E+01	1.453E+01
0.090	1.245E+01	1.299E+01	1.348E+01	1.394E+01	1.442E+01	1.487E+01	1.531E+01	1.562E+01
0.100	1.318E+01	1.378E+01	1.433E+01	1.483E+01	1.536E+01	1.585E+01	1.632E+01	1.666E+01
0.150	1.580E+01	1.675E+01	1.762E+01	1.840E+01	1.919E+01	1.993E+01	2.061E+01	2.114E+01
0.200	1.720E+01	1.842E+01	1.956E+01	2.060E+01	2.166E+01	2.266E+01	2.359E+01	2.434E+01
0.250	1.793E+01	1.934E+01	2.069E+01	2.193E+01	2.319E+01	2.441E+01	2.553E+01	2.649E+01
0.300	1.832E+01	1.987E+01	2.135E+01	2.273E+01	2.415E+01	2.553E+01	2.682E+01	2.793E+01
0.400	1.859E+01	2.029E+01	2.196E+01	2.353E+01	2.516E+01	2.676E+01	2.826E+01	2.960E+01
0.500	1.853E+01	2.033E+01	2.210E+01	2.379E+01	2.555E+01	2.729E+01	2.893E+01	3.041E+01
0.600	1.833E+01	2.019E+01	2.203E+01	2.379E+01	2.563E+01	2.748E+01	2.921E+01	3.078E+01
0.700	1.806E+01	1.995E+01	2.184E+01	2.364E+01	2.556E+01	2.747E+01	2.927E+01	3.091E+01
0.800	1.776E+01	1.967E+01	2.158E+01	2.342E+01	2.538E+01	2.734E+01	2.919E+01	3.088E+01
0.900	1.744E+01	1.936E+01	2.129E+01	2.315E+01	2.514E+01	2.715E+01	2.903E+01	3.076E+01
1.000	1.711E+01	1.904E+01	2.098E+01	2.285E+01	2.487E+01	2.690E+01	2.881E+01	3.057E+01
1.500	1.553E+01	1.742E+01	1.936E+01	2.124E+01	2.330E+01	2.539E+01	2.736E+01	2.917E+01
2.000	1.414E+01	1.598E+01	1.787E+01	1.971E+01	2.174E+01	2.382E+01	2.579E+01	2.760E+01
2.500	1.295E+01	1.472E+01	1.655E+01	1.833E+01	2.032E+01	2.236E+01	2.430E+01	2.609E+01
3.000	1.193E+01	1.363E+01	1.539E+01	1.712E+01	1.905E+01	2.105E+01	2.294E+01	2.469E+01
4.000	1.030E+01	1.186E+01	1.348E+01	1.510E+01	1.691E+01	1.879E+01	2.059E+01	2.225E+01
5.000	9.044E+00	1.048E+01	1.198E+01	1.349E+01	1.518E+01	1.694E+01	1.864E+01	2.022E+01
6.000	8.057E+00	9.379E+00	1.078E+01	1.218E+01	1.376E+01	1.542E+01	1.702E+01	1.852E+01
7.000	7.261E+00	8.487E+00	9.788E+00	1.110E+01	1.258E+01	1.414E+01	1.565E+01	1.708E+01
8.000	6.609E+00	7.749E+00	8.963E+00	1.020E+01	1.158E+01	1.305E+01	1.448E+01	1.584E+01
9.000	6.064E+00	7.129E+00	8.266E+00	9.430E+00	1.073E+01	1.211E+01	1.347E+01	1.477E+01
10.00	5.603E+00	6.601E+00	7.670E+00	8.769E+00	9.995E+00	1.130E+01	1.259E+01	1.383E+01
15.00	4.077E+00	4.833E+00	5.649E+00	6.503E+00	7.450E+00	8.465E+00	9.491E+00	1.050E+01
20.00	3.227E+00	3.835E+00	4.494E+00	5.190E+00	5.958E+00	6.784E+00	7.630E+00	8.478E+00
25.00	2.688E+00	3.197E+00	3.750E+00	4.339E+00	4.985E+00	5.680E+00	6.400E+00	7.130E+00
30.00	2.316E+00	2.755E+00	3.233E+00	3.745E+00	4.302E+00	4.903E+00	5.530E+00	6.172E+00
40.00	1.834E+00	2.182E+00	2.561E+00	2.969E+00	3.410E+00	3.886E+00	4.386E+00	4.905E+00
50.00	1.535E+00	1.826E+00	2.143E+00	2.484E+00	2.853E+00	3.249E+00	3.668E+00	4.106E+00
60.00	1.329E+00	1.582E+00	1.856E+00	2.152E+00	2.471E+00	2.813E+00	3.176E+00	3.557E+00
70.00	1.179E+00	1.403E+00	1.646E+00	1.909E+00	2.192E+00	2.495E+00	2.816E+00	3.155E+00
80.00	1.065E+00	1.267E+00	1.487E+00	1.724E+00	1.979E+00	2.252E+00	2.542E+00	2.849E+00
90.00	9.741E−01	1.159E+00	1.360E+00	1.577E+00	1.811E+00	2.060E+00	2.326E+00	2.607E+00
100.0	9.006E−01	1.072E+00	1.258E+00	1.458E+00	1.674E+00	1.905E+00	2.151E+00	2.411E+00
150.0	6.739E−01	8.022E−01	9.416E−01	1.092E+00	1.254E+00	1.427E+00	1.611E+00	1.807E+00
200.0	5.566E−01	6.627E−01	7.780E−01	9.026E−01	1.037E+00	1.180E+00	1.332E+00	1.494E+00
250.0	4.850E−01	5.775E−01	6.781E−01	7.868E−01	9.037E−01	1.029E+00	1.162E+00	1.303E+00
300.0	4.369E−01	5.202E−01	6.109E−01	7.089E−01	8.143E−01	9.270E−01	1.047E+00	1.175E+00
400.0	3.767E−01	4.486E−01	5.268E−01	6.115E−01	7.024E−01	7.998E−01	9.035E−01	1.014E+00
500.0	3.410E−01	4.061E−01	4.770E−01	5.537E−01	6.362E−01	7.244E−01	8.184E−01	9.183E−01
600.0	3.178E−01	3.786E−01	4.447E−01	5.161E−01	5.930E−01	6.753E−01	7.630E−01	8.562E−01
700.0	3.018E−01	3.595E−01	4.223E−01	4.902E−01	5.633E−01	6.415E−01	7.248E−01	8.133E−01
800.0	2.903E−01	3.458E−01	4.063E−01	4.716E−01	5.419E−01	6.171E−01	6.973E−01	7.825E−01
900.0	2.818E−01	3.357E−01	3.944E−01	4.578E−01	5.261E−01	5.991E−01	6.770E−01	7.597E−01
1000.	2.753E−01	3.280E−01	3.853E−01	4.473E−01	5.140E−01	5.854E−01	6.615E−01	7.423E−01

Material: Photographic emulsion

Ion	Li	Be	B	C	N	O	F	Ne
(E/A_1) / MeV				$(-\mathrm{d}E/\rho\mathrm{d}\ell)$ / MeV cm^2 mg^{-1}				
0.025	1.023E+00	1.245E+00	1.418E+00	1.557E+00	1.678E+00	1.791E+00	1.889E+00	1.981E+00
0.030	1.127E+00	1.386E+00	1.587E+00	1.747E+00	1.883E+00	2.007E+00	2.115E+00	2.217E+00
0.040	1.298E+00	1.628E+00	1.888E+00	2.097E+00	2.268E+00	2.419E+00	2.548E+00	2.667E+00
0.050	1.427E+00	1.825E+00	2.146E+00	2.406E+00	2.618E+00	2.803E+00	2.958E+00	3.097E+00
0.060	1.522E+00	1.983E+00	2.363E+00	2.676E+00	2.933E+00	3.155E+00	3.340E+00	3.504E+00
0.070	1.591E+00	2.106E+00	2.543E+00	2.910E+00	3.213E+00	3.476E+00	3.694E+00	3.885E+00
0.080	1.641E+00	2.202E+00	2.689E+00	3.107E+00	3.458E+00	3.764E+00	4.020E+00	4.241E+00
0.090	1.677E+00	2.276E+00	2.808E+00	3.273E+00	3.669E+00	4.019E+00	4.313E+00	4.569E+00
0.100	1.704E+00	2.335E+00	2.904E+00	3.411E+00	3.850E+00	4.242E+00	4.575E+00	4.867E+00
0.150	1.755E+00	2.487E+00	3.184E+00	3.837E+00	4.436E+00	4.994E+00	5.493E+00	5.948E+00
0.200	1.743E+00	2.524E+00	3.290E+00	4.029E+00	4.726E+00	5.393E+00	6.004E+00	6.577E+00
0.250	1.711E+00	2.517E+00	3.323E+00	4.114E+00	4.876E+00	5.614E+00	6.304E+00	6.960E+00
0.300	1.671E+00	2.489E+00	3.320E+00	4.146E+00	4.951E+00	5.740E+00	6.485E+00	7.202E+00
0.400	1.585E+00	2.410E+00	3.266E+00	4.132E+00	4.991E+00	5.845E+00	6.663E+00	7.460E+00
0.500	1.500E+00	2.319E+00	3.184E+00	4.070E+00	4.960E+00	5.854E+00	6.716E+00	7.564E+00
0.600	1.420E+00	2.227E+00	3.091E+00	3.986E+00	4.894E+00	5.813E+00	6.704E+00	7.585E+00
0.700	1.346E+00	2.138E+00	2.996E+00	3.892E+00	4.809E+00	5.744E+00	6.654E+00	7.559E+00
0.800	1.279E+00	2.053E+00	2.900E+00	3.794E+00	4.715E+00	5.658E+00	6.580E+00	7.501E+00
0.900	1.218E+00	1.972E+00	2.808E+00	3.695E+00	4.616E+00	5.563E+00	6.493E+00	7.424E+00
1.000	1.162E+00	1.897E+00	2.719E+00	3.598E+00	4.515E+00	5.463E+00	6.397E+00	7.335E+00
1.500	9.451E−01	1.589E+00	2.336E+00	3.158E+00	4.036E+00	4.961E+00	5.885E+00	6.824E+00
2.000	7.987E−01	1.367E+00	2.043E+00	2.803E+00	3.630E+00	4.512E+00	5.404E+00	6.321E+00
2.500	6.937E−01	1.201E+00	1.816E+00	2.517E+00	3.292E+00	4.129E+00	4.984E+00	5.868E+00
3.000	6.149E−01	1.073E+00	1.635E+00	2.285E+00	3.011E+00	3.802E+00	4.620E+00	5.470E+00
4.000	5.043E−01	8.873E−01	1.366E+00	1.930E+00	2.572E+00	3.281E+00	4.026E+00	4.811E+00
5.000	4.302E−01	7.599E−01	1.177E+00	1.674E+00	2.246E+00	2.886E+00	3.567E+00	4.290E+00
6.000	3.768E−01	6.670E−01	1.036E+00	1.480E+00	1.995E+00	2.576E+00	3.201E+00	3.871E+00
7.000	3.364E−01	5.960E−01	9.275E−01	1.328E+00	1.796E+00	2.328E+00	2.905E+00	3.527E+00
8.000	3.046E−01	5.400E−01	8.412E−01	1.207E+00	1.635E+00	2.125E+00	2.659E+00	3.239E+00
9.000	2.788E−01	4.945E−01	7.709E−01	1.107E+00	1.502E+00	1.955E+00	2.453E+00	2.996E+00
10.00	2.575E−01	4.569E−01	7.124E−01	1.024E+00	1.391E+00	1.812E+00	2.278E+00	2.788E+00
15.00	1.891E−01	3.356E−01	5.236E−01	7.531E−01	1.025E+00	1.338E+00	1.691E+00	2.080E+00
20.00	1.514E−01	2.689E−01	4.196E−01	6.037E−01	8.213E−01	1.073E+00	1.357E+00	1.673E+00
25.00	1.274E−01	2.263E−01	3.532E−01	5.081E−01	6.912E−01	9.027E−01	1.142E+00	1.409E+00
30.00	1.106E−01	1.965E−01	3.068E−01	4.414E−01	6.004E−01	7.839E−01	9.917E−01	1.224E+00
40.00	8.854E−02	1.574E−01	2.458E−01	3.537E−01	4.811E−01	6.281E−01	7.945E−01	9.805E−01
50.00	7.459E−02	1.326E−01	2.072E−01	2.982E−01	4.057E−01	5.296E−01	6.700E−01	8.269E−01
60.00	6.493E−02	1.155E−01	1.804E−01	2.597E−01	3.534E−01	4.615E−01	5.838E−01	7.206E−01
70.00	5.782E−02	1.028E−01	1.607E−01	2.314E−01	3.149E−01	4.112E−01	5.203E−01	6.422E−01
80.00	5.236E−02	9.313E−02	1.455E−01	2.096E−01	2.853E−01	3.726E−01	4.715E−01	5.820E−01
90.00	4.803E−02	8.542E−02	1.335E−01	1.923E−01	2.618E−01	3.419E−01	4.327E−01	5.342E−01
100.0	4.450E−02	7.915E−02	1.237E−01	1.782E−01	2.426E−01	3.169E−01	4.012E−01	4.952E−01
150.0	3.356E−02	5.970E−02	9.335E−02	1.345E−01	1.832E−01	2.393E−01	3.030E−01	3.743E−01
200.0	2.786E−02	4.957E−02	7.752E−02	1.117E−01	1.522E−01	1.989E−01	2.518E−01	3.111E−01
250.0	2.437E−02	4.337E−02	6.782E−02	9.774E−02	1.331E−01	1.740E−01	2.204E−01	2.723E−01
300.0	2.202E−02	3.918E−02	6.128E−02	8.833E−02	1.203E−01	1.573E−01	1.992E−01	2.462E−01
400.0	1.908E−02	3.395E−02	5.310E−02	7.654E−02	1.043E−01	1.363E−01	1.727E−01	2.134E−01
500.0	1.734E−02	3.086E−02	4.827E−02	6.958E−02	9.480E−02	1.239E−01	1.570E−01	1.941E−01
600.0	1.621E−02	2.885E−02	4.513E−02	6.506E−02	8.866E−02	1.159E−01	1.469E−01	1.815E−01
700.0	1.544E−02	2.748E−02	4.298E−02	6.196E−02	8.445E−02	1.104E−01	1.399E−01	1.729E−01
800.0	1.488E−02	2.649E−02	4.144E−02	5.974E−02	8.141E−02	1.064E−01	1.349E−01	1.667E−01
900.0	1.448E−02	2.577E−02	4.030E−02	5.810E−02	7.918E−02	1.035E−01	1.312E−01	1.621E−01
1000.	1.417E−02	2.521E−02	3.944E−02	5.686E−02	7.748E−02	1.013E−01	1.284E−01	1.587E−01

Material: Photographic emulsion

Ion	Na	Mg	Al	Si	P	S	Cl	Ar
(E/A_1) / MeV				$(-\mathrm{d}E/\rho\mathrm{d}\ell)$ / MeV cm^2 mg^{-1}				
0.025	2.062E+00	2.147E+00	2.227E+00	2.303E+00	2.379E+00	1.791E+00	2.525E+00	2.583E+00
0.030	2.309E+00	2.400E+00	2.489E+00	2.574E+00	2.659E+00	2.007E+00	2.820E+00	2.886E+00
0.040	2.776E+00	2.877E+00	2.980E+00	3.079E+00	3.178E+00	2.419E+00	3.370E+00	3.449E+00
0.050	3.225E+00	3.336E+00	3.448E+00	3.557E+00	3.665E+00	2.803E+00	3.879E+00	3.970E+00
0.060	3.654E+00	3.778E+00	3.903E+00	4.021E+00	4.137E+00	3.155E+00	4.368E+00	4.466E+00
0.070	4.061E+00	4.201E+00	4.341E+00	4.470E+00	4.597E+00	3.476E+00	4.844E+00	4.948E+00
0.080	4.446E+00	4.604E+00	4.761E+00	4.905E+00	5.043E+00	3.764E+00	5.308E+00	5.419E+00
0.090	4.806E+00	4.986E+00	5.163E+00	5.322E+00	5.474E+00	4.019E+00	5.761E+00	5.879E+00
0.100	5.138E+00	5.344E+00	5.544E+00	5.722E+00	5.890E+00	4.242E+00	6.202E+00	6.328E+00
0.150	6.389E+00	6.735E+00	7.074E+00	7.378E+00	7.660E+00	4.994E+00	8.163E+00	8.364E+00
0.200	7.150E+00	7.608E+00	8.069E+00	8.491E+00	8.890E+00	5.393E+00	9.615E+00	9.915E+00
0.250	7.631E+00	8.174E+00	8.729E+00	9.246E+00	9.743E+00	5.614E+00	1.066E+01	1.105E+01
0.300	7.948E+00	8.553E+00	9.181E+00	9.773E+00	1.035E+01	5.740E+00	1.142E+01	1.189E+01
0.400	8.310E+00	9.000E+00	9.730E+00	1.043E+01	1.112E+01	5.845E+00	1.243E+01	1.302E+01
0.500	8.483E+00	9.226E+00	1.002E+01	1.079E+01	1.156E+01	5.854E+00	1.304E+01	1.371E+01
0.600	8.553E+00	9.334E+00	1.018E+01	1.100E+01	1.183E+01	5.813E+00	1.343E+01	1.416E+01
0.700	8.561E+00	9.368E+00	1.025E+01	1.111E+01	1.198E+01	5.744E+00	1.368E+01	1.446E+01
0.800	8.529E+00	9.354E+00	1.026E+01	1.115E+01	1.206E+01	5.658E+00	1.383E+01	1.465E+01
0.900	8.471E+00	9.308E+00	1.024E+01	1.115E+01	1.208E+01	5.563E+00	1.392E+01	1.476E+01
1.000	8.395E+00	9.241E+00	1.019E+01	1.111E+01	1.207E+01	5.463E+00	1.395E+01	1.482E+01
1.500	7.906E+00	8.762E+00	9.739E+00	1.071E+01	1.172E+01	4.961E+00	1.374E+01	1.467E+01
2.000	7.387E+00	8.231E+00	9.205E+00	1.017E+01	1.120E+01	4.512E+00	1.326E+01	1.422E+01
2.500	6.906E+00	7.730E+00	8.686E+00	9.643E+00	1.066E+01	4.129E+00	1.272E+01	1.368E+01
3.000	6.472E+00	7.275E+00	8.209E+00	9.147E+00	1.015E+01	3.802E+00	1.219E+01	1.315E+01
4.000	5.739E+00	6.498E+00	7.381E+00	8.275E+00	9.236E+00	3.281E+00	1.121E+01	1.214E+01
5.000	5.149E+00	5.865E+00	6.698E+00	7.546E+00	8.462E+00	2.886E+00	1.035E+01	1.126E+01
6.000	4.665E+00	5.342E+00	6.128E+00	6.931E+00	7.802E+00	2.576E+00	9.614E+00	1.048E+01
7.000	4.264E+00	4.905E+00	5.645E+00	6.407E+00	7.235E+00	2.328E+00	8.967E+00	9.805E+00
8.000	3.925E+00	4.532E+00	5.233E+00	5.957E+00	6.743E+00	2.125E+00	8.400E+00	9.206E+00
9.000	3.637E+00	4.213E+00	4.877E+00	5.565E+00	6.314E+00	1.955E+00	7.898E+00	8.674E+00
10.00	3.388E+00	3.937E+00	4.566E+00	5.222E+00	5.935E+00	1.812E+00	7.452E+00	8.200E+00
15.00	2.534E+00	2.974E+00	3.472E+00	3.997E+00	4.571E+00	1.338E+00	5.811E+00	6.438E+00
20.00	2.037E+00	2.403E+00	2.814E+00	3.251E+00	3.729E+00	1.073E+00	4.769E+00	5.306E+00
25.00	1.713E+00	2.027E+00	2.378E+00	2.752E+00	3.160E+00	9.027E−01	4.056E+00	4.524E+00
30.00	1.486E+00	1.762E+00	2.068E+00	2.395E+00	2.752E+00	7.839E−01	3.538E+00	3.954E+00
40.00	1.189E+00	1.412E+00	1.657E+00	1.921E+00	2.208E+00	6.281E−01	2.842E+00	3.182E+00
50.00	1.001E+00	1.190E+00	1.397E+00	1.620E+00	1.861E+00	5.296E−01	2.396E+00	2.685E+00
60.00	8.722E−01	1.037E+00	1.217E+00	1.412E+00	1.621E+00	4.615E−01	2.086E+00	2.339E+00
70.00	7.772E−01	9.246E−01	1.085E+00	1.258E+00	1.445E+00	4.112E−01	1.859E+00	2.084E+00
80.00	7.043E−01	8.378E−01	9.832E−01	1.140E+00	1.309E+00	3.726E−01	1.684E+00	1.888E+00
90.00	6.464E−01	7.691E−01	9.026E−01	1.047E+00	1.202E+00	3.419E−01	1.545E+00	1.733E+00
100.0	5.993E−01	7.131E−01	8.370E−01	9.707E−01	1.115E+00	3.169E−01	1.433E+00	1.607E+00
150.0	4.530E−01	5.393E−01	6.330E−01	7.344E−01	8.433E−01	2.393E−01	1.084E+00	1.216E+00
200.0	3.766E−01	4.484E−01	5.266E−01	6.110E−01	7.017E−01	1.989E−01	9.021E−01	1.012E+00
250.0	3.297E−01	3.927E−01	4.611E−01	5.351E−01	6.147E−01	1.740E−01	7.905E−01	8.868E−01
300.0	2.981E−01	3.551E−01	4.170E−01	4.840E−01	5.560E−01	1.573E−01	7.152E−01	8.024E−01
400.0	2.585E−01	3.079E−01	3.617E−01	4.199E−01	4.824E−01	1.363E−01	6.207E−01	6.965E−01
500.0	2.351E−01	2.800E−01	3.290E−01	3.819E−01	4.388E−01	1.239E−01	5.647E−01	6.337E−01
600.0	2.199E−01	2.619E−01	3.077E−01	3.573E−01	4.105E−01	1.159E−01	5.284E−01	5.930E−01
700.0	2.094E−01	2.495E−01	2.931E−01	3.403E−01	3.911E−01	1.104E−01	5.034E−01	5.650E−01
800.0	2.019E−01	2.406E−01	2.827E−01	3.282E−01	3.772E−01	1.064E−01	4.855E−01	5.450E−01
900.0	1.964E−01	2.340E−01	2.750E−01	3.193E−01	3.669E−01	1.035E−01	4.724E−01	5.302E−01
1000.	1.922E−01	2.290E−01	2.691E−01	3.124E−01	3.591E−01	1.013E−01	4.623E−01	5.189E−01

Material: Plastic scintillator (vinyltoluene based)

Ion	Li	Be	B	C	N	O	F	Ne
(E/A_1) / MeV				$(-\mathrm{d}E/\rho\mathrm{d}\ell)$ / MeV cm^2 mg^{-1}				
0.025	2.597E+00	3.198E+00	3.674E+00	4.051E+00	4.399E+00	4.708E+00	4.950E+00	5.171E+00
0.030	2.831E+00	3.511E+00	4.056E+00	4.495E+00	4.891E+00	5.245E+00	5.523E+00	5.776E+00
0.040	3.212E+00	4.048E+00	4.730E+00	5.289E+00	5.779E+00	6.219E+00	6.572E+00	6.888E+00
0.050	3.493E+00	4.481E+00	5.300E+00	5.980E+00	6.565E+00	7.091E+00	7.516E+00	7.895E+00
0.060	3.691E+00	4.821E+00	5.774E+00	6.577E+00	7.264E+00	7.878E+00	8.376E+00	8.819E+00
0.070	3.828E+00	5.078E+00	6.157E+00	7.083E+00	7.876E+00	8.585E+00	9.161E+00	9.670E+00
0.080	3.919E+00	5.269E+00	6.461E+00	7.502E+00	8.403E+00	9.210E+00	9.871E+00	1.045E+01
0.090	3.977E+00	5.409E+00	6.698E+00	7.845E+00	8.849E+00	9.755E+00	1.050E+01	1.116E+01
0.100	4.012E+00	5.509E+00	6.881E+00	8.121E+00	9.221E+00	1.022E+01	1.106E+01	1.180E+01
0.150	4.006E+00	5.688E+00	7.313E+00	8.862E+00	1.031E+01	1.168E+01	1.288E+01	1.398E+01
0.200	3.890E+00	5.643E+00	7.382E+00	9.081E+00	1.071E+01	1.229E+01	1.372E+01	1.506E+01
0.250	3.747E+00	5.528E+00	7.323E+00	9.103E+00	1.084E+01	1.255E+01	1.410E+01	1.560E+01
0.300	3.601E+00	5.387E+00	7.210E+00	9.036E+00	1.084E+01	1.263E+01	1.427E+01	1.586E+01
0.400	3.326E+00	5.088E+00	6.926E+00	8.794E+00	1.067E+01	1.255E+01	1.429E+01	1.599E+01
0.500	3.081E+00	4.801E+00	6.626E+00	8.500E+00	1.040E+01	1.233E+01	1.412E+01	1.588E+01
0.600	2.867E+00	4.536E+00	6.333E+00	8.198E+00	1.011E+01	1.205E+01	1.387E+01	1.567E+01
0.700	2.679E+00	4.294E+00	6.056E+00	7.901E+00	9.804E+00	1.176E+01	1.359E+01	1.540E+01
0.800	2.513E+00	4.073E+00	5.797E+00	7.617E+00	9.506E+00	1.146E+01	1.329E+01	1.511E+01
0.900	2.366E+00	3.872E+00	5.555E+00	7.346E+00	9.216E+00	1.116E+01	1.299E+01	1.481E+01
1.000	2.235E+00	3.689E+00	5.331E+00	7.090E+00	8.938E+00	1.087E+01	1.269E+01	1.451E+01
1.500	1.750E+00	2.977E+00	4.419E+00	6.012E+00	7.725E+00	9.548E+00	1.130E+01	1.306E+01
2.000	1.439E+00	2.493E+00	3.763E+00	5.200E+00	6.775E+00	8.476E+00	1.013E+01	1.182E+01
2.500	1.224E+00	2.144E+00	3.273E+00	4.574E+00	6.021E+00	7.603E+00	9.163E+00	1.076E+01
3.000	1.068E+00	1.881E+00	2.896E+00	4.079E+00	5.411E+00	6.883E+00	8.353E+00	9.872E+00
4.000	8.543E−01	1.515E+00	2.354E+00	3.351E+00	4.493E+00	5.775E+00	7.083E+00	8.452E+00
5.000	7.158E−01	1.273E+00	1.985E+00	2.844E+00	3.838E+00	4.967E+00	6.139E+00	7.378E+00
6.000	6.185E−01	1.100E+00	1.720E+00	2.472E+00	3.351E+00	4.355E+00	5.414E+00	6.542E+00
7.000	5.463E−01	9.718E−01	1.520E+00	2.189E+00	2.975E+00	3.878E+00	4.841E+00	5.875E+00
8.000	4.904E−01	8.721E−01	1.365E+00	1.967E+00	2.677E+00	3.496E+00	4.378E+00	5.331E+00
9.000	4.457E−01	7.924E−01	1.240E+00	1.787E+00	2.435E+00	3.184E+00	3.998E+00	4.881E+00
10.00	4.092E−01	7.272E−01	1.137E+00	1.640E+00	2.235E+00	2.926E+00	3.680E+00	4.502E+00
15.00	2.941E−01	5.223E−01	8.159E−01	1.176E+00	1.602E+00	2.097E+00	2.650E+00	3.260E+00
20.00	2.326E−01	4.130E−01	6.448E−01	9.283E−01	1.264E+00	1.653E+00	2.091E+00	2.578E+00
25.00	1.939E−01	3.444E−01	5.376E−01	7.736E−01	1.053E+00	1.376E+00	1.741E+00	2.147E+00
30.00	1.672E−01	2.970E−01	4.636E−01	6.671E−01	9.076E−01	1.185E+00	1.500E+00	1.850E+00
40.00	1.325E−01	2.354E−01	3.676E−01	5.290E−01	7.196E−01	9.395E−01	1.188E+00	1.466E+00
50.00	1.108E−01	1.969E−01	3.076E−01	4.428E−01	6.023E−01	7.864E−01	9.947E−01	1.227E+00
60.00	9.592E−02	1.705E−01	2.664E−01	3.835E−01	5.218E−01	6.812E−01	8.618E−01	1.063E+00
70.00	8.504E−02	1.512E−01	2.362E−01	3.401E−01	4.628E−01	6.043E−01	7.646E−01	9.436E−01
80.00	7.672E−02	1.364E−01	2.132E−01	3.070E−01	4.177E−01	5.455E−01	6.903E−01	8.520E−01
90.00	7.015E−02	1.247E−01	1.949E−01	2.807E−01	3.821E−01	4.990E−01	6.315E−01	7.795E−01
100.0	6.482E−02	1.153E−01	1.802E−01	2.595E−01	3.532E−01	4.613E−01	5.838E−01	7.207E−01
150.0	4.842E−02	8.612E−02	1.346E−01	1.939E−01	2.641E−01	3.450E−01	4.368E−01	5.393E−01
200.0	3.995E−02	7.107E−02	1.111E−01	1.601E−01	2.180E−01	2.849E−01	3.607E−01	4.455E−01
250.0	3.479E−02	6.188E−02	9.676E−02	1.394E−01	1.899E−01	2.482E−01	3.143E−01	3.882E−01
300.0	3.132E−02	5.572E−02	8.712E−02	1.255E−01	1.710E−01	2.235E−01	2.830E−01	3.497E−01
400.0	2.698E−02	4.801E−02	7.508E−02	1.082E−01	1.474E−01	1.927E−01	2.440E−01	3.015E−01
500.0	2.442E−02	4.345E−02	6.795E−02	9.794E−02	1.334E−01	1.744E−01	2.209E−01	2.730E−01
600.0	2.276E−02	4.049E−02	6.332E−02	9.127E−02	1.243E−01	1.625E−01	2.059E−01	2.544E−01
700.0	2.161E−02	3.845E−02	6.013E−02	8.667E−02	1.181E−01	1.544E−01	1.955E−01	2.416E−01
800.0	2.078E−02	3.698E−02	5.784E−02	8.337E−02	1.136E−01	1.485E−01	1.881E−01	2.325E−01
900.0	2.017E−02	3.590E−02	5.615E−02	8.093E−02	1.103E−01	1.441E−01	1.826E−01	2.257E−01
1000.	1.971E−02	3.507E−02	5.485E−02	7.906E−02	1.077E−01	1.408E−01	1.784E−01	2.205E−01

Material: Plastic scintillator (vinyltoluene based)

Ion	Na	Mg	Al	Si	P	S	Cl	Ar
(E/A_1) / MeV				$(-\mathrm{d}E/\rho\mathrm{d}\ell)$ / MeV cm^2 mg^{-1}				
0.025	5.362E+00	5.572E+00	5.774E+00	5.976E+00	6.211E+00	6.402E+00	6.647E+00	6.781E+00
0.030	5.997E+00	6.215E+00	6.434E+00	6.651E+00	6.903E+00	7.115E+00	7.373E+00	7.522E+00
0.040	7.176E+00	7.413E+00	7.668E+00	7.915E+00	8.199E+00	8.448E+00	8.730E+00	8.903E+00
0.050	8.252E+00	8.517E+00	8.809E+00	9.089E+00	9.405E+00	9.690E+00	9.996E+00	1.019E+01
0.060	9.245E+00	9.541E+00	9.871E+00	1.018E+01	1.053E+01	1.085E+01	1.118E+01	1.140E+01
0.070	1.017E+01	1.050E+01	1.087E+01	1.121E+01	1.159E+01	1.195E+01	1.230E+01	1.254E+01
0.080	1.103E+01	1.139E+01	1.180E+01	1.218E+01	1.260E+01	1.298E+01	1.337E+01	1.362E+01
0.090	1.182E+01	1.223E+01	1.268E+01	1.310E+01	1.355E+01	1.397E+01	1.438E+01	1.465E+01
0.100	1.254E+01	1.300E+01	1.351E+01	1.397E+01	1.445E+01	1.491E+01	1.535E+01	1.564E+01
0.150	1.516E+01	1.590E+01	1.671E+01	1.745E+01	1.819E+01	1.888E+01	1.951E+01	1.998E+01
0.200	1.655E+01	1.751E+01	1.859E+01	1.959E+01	2.058E+01	2.154E+01	2.241E+01	2.310E+01
0.250	1.730E+01	1.840E+01	1.968E+01	2.086E+01	2.206E+01	2.322E+01	2.429E+01	2.517E+01
0.300	1.772E+01	1.891E+01	2.032E+01	2.164E+01	2.299E+01	2.431E+01	2.553E+01	2.656E+01
0.400	1.806E+01	1.935E+01	2.093E+01	2.243E+01	2.398E+01	2.551E+01	2.694E+01	2.817E+01
0.500	1.808E+01	1.941E+01	2.110E+01	2.270E+01	2.438E+01	2.605E+01	2.761E+01	2.898E+01
0.600	1.795E+01	1.930E+01	2.105E+01	2.273E+01	2.449E+01	2.626E+01	2.791E+01	2.937E+01
0.700	1.774E+01	1.910E+01	2.090E+01	2.262E+01	2.445E+01	2.628E+01	2.800E+01	2.952E+01
0.800	1.749E+01	1.885E+01	2.067E+01	2.243E+01	2.430E+01	2.619E+01	2.796E+01	2.952E+01
0.900	1.722E+01	1.857E+01	2.041E+01	2.219E+01	2.410E+01	2.602E+01	2.783E+01	2.942E+01
1.000	1.693E+01	1.827E+01	2.013E+01	2.192E+01	2.386E+01	2.580E+01	2.764E+01	2.926E+01
1.500	1.549E+01	1.677E+01	1.863E+01	2.043E+01	2.242E+01	2.443E+01	2.633E+01	2.801E+01
2.000	1.417E+01	1.540E+01	1.722E+01	1.899E+01	2.095E+01	2.296E+01	2.486E+01	2.654E+01
2.500	1.302E+01	1.421E+01	1.596E+01	1.769E+01	1.961E+01	2.158E+01	2.346E+01	2.512E+01
3.000	1.202E+01	1.317E+01	1.486E+01	1.653E+01	1.840E+01	2.033E+01	2.216E+01	2.379E+01
4.000	1.039E+01	1.146E+01	1.303E+01	1.459E+01	1.634E+01	1.817E+01	1.991E+01	2.147E+01
5.000	9.122E+00	1.013E+01	1.159E+01	1.305E+01	1.468E+01	1.639E+01	1.804E+01	1.953E+01
6.000	8.117E+00	9.076E+00	1.043E+01	1.179E+01	1.332E+01	1.492E+01	1.648E+01	1.790E+01
7.000	7.303E+00	8.213E+00	9.471E+00	1.074E+01	1.218E+01	1.369E+01	1.516E+01	1.651E+01
8.000	6.634E+00	7.499E+00	8.674E+00	9.870E+00	1.121E+01	1.263E+01	1.403E+01	1.532E+01
9.000	6.075E+00	6.899E+00	7.999E+00	9.126E+00	1.039E+01	1.173E+01	1.305E+01	1.428E+01
10.00	5.602E+00	6.388E+00	7.422E+00	8.486E+00	9.676E+00	1.094E+01	1.220E+01	1.338E+01
15.00	4.038E+00	4.676E+00	5.466E+00	6.293E+00	7.211E+00	8.197E+00	9.191E+00	1.016E+01
20.00	3.174E+00	3.710E+00	4.348E+00	5.022E+00	5.766E+00	6.567E+00	7.388E+00	8.201E+00
25.00	2.631E+00	3.093E+00	3.628E+00	4.198E+00	4.824E+00	5.498E+00	6.195E+00	6.897E+00
30.00	2.259E+00	2.665E+00	3.128E+00	3.623E+00	4.163E+00	4.746E+00	5.352E+00	5.971E+00
40.00	1.783E+00	2.112E+00	2.478E+00	2.872E+00	3.300E+00	3.760E+00	4.244E+00	4.745E+00
50.00	1.489E+00	1.767E+00	2.073E+00	2.404E+00	2.761E+00	3.145E+00	3.550E+00	3.973E+00
60.00	1.288E+00	1.531E+00	1.796E+00	2.082E+00	2.391E+00	2.723E+00	3.074E+00	3.442E+00
70.00	1.143E+00	1.358E+00	1.594E+00	1.848E+00	2.121E+00	2.415E+00	2.726E+00	3.054E+00
80.00	1.031E+00	1.226E+00	1.439E+00	1.668E+00	1.915E+00	2.180E+00	2.461E+00	2.758E+00
90.00	9.434E−01	1.122E+00	1.317E+00	1.527E+00	1.753E+00	1.995E+00	2.252E+00	2.524E+00
100.0	8.722E−01	1.038E+00	1.218E+00	1.412E+00	1.621E+00	1.845E+00	2.083E+00	2.334E+00
150.0	6.528E−01	7.770E−01	9.120E−01	1.058E+00	1.215E+00	1.382E+00	1.561E+00	1.750E+00
200.0	5.393E−01	6.420E−01	7.538E−01	8.745E−01	1.004E+00	1.143E+00	1.291E+00	1.447E+00
250.0	4.700E−01	5.596E−01	6.571E−01	7.624E−01	8.756E−01	9.967E−01	1.126E+00	1.263E+00
300.0	4.234E−01	5.041E−01	5.920E−01	6.870E−01	7.891E−01	8.984E−01	1.015E+00	1.138E+00
400.0	3.651E−01	4.348E−01	5.107E−01	5.927E−01	6.809E−01	7.752E−01	8.758E−01	9.825E−01
500.0	3.306E−01	3.937E−01	4.625E−01	5.368E−01	6.167E−01	7.022E−01	7.934E−01	8.902E−01
600.0	3.081E−01	3.670E−01	4.311E−01	5.004E−01	5.750E−01	6.548E−01	7.398E−01	8.301E−01
700.0	2.927E−01	3.486E−01	4.095E−01	4.754E−01	5.462E−01	6.220E−01	7.028E−01	7.887E−01
800.0	2.815E−01	3.354E−01	3.940E−01	4.573E−01	5.255E−01	5.985E−01	6.762E−01	7.589E−01
900.0	2.733E−01	3.256E−01	3.825E−01	4.440E−01	5.102E−01	5.810E−01	6.566E−01	7.368E−01
1000.	2.670E−01	3.181E−01	3.737E−01	4.338E−01	4.985E−01	5.677E−01	6.416E−01	7.200E−01

Material: Polycarbonate (makrolon, lexan)

Ion	Li	Be	B	C	N	O	F	Ne
(E/A_1) / MeV				$(-\mathrm{d}E/\rho\mathrm{d}\ell)$ / MeV cm^2 mg^{-1}				
0.025	2.358E+00	2.899E+00	3.326E+00	3.666E+00	3.974E+00	4.249E+00	4.469E+00	4.672E+00
0.030	2.573E+00	3.186E+00	3.677E+00	4.073E+00	4.425E+00	4.740E+00	4.993E+00	5.224E+00
0.040	2.927E+00	3.682E+00	4.296E+00	4.802E+00	5.241E+00	5.635E+00	5.956E+00	6.244E+00
0.050	3.191E+00	4.086E+00	4.825E+00	5.440E+00	5.967E+00	6.439E+00	6.826E+00	7.173E+00
0.060	3.383E+00	4.408E+00	5.269E+00	5.996E+00	6.615E+00	7.168E+00	7.623E+00	8.027E+00
0.070	3.517E+00	4.656E+00	5.633E+00	6.471E+00	7.188E+00	7.827E+00	8.352E+00	8.818E+00
0.080	3.609E+00	4.843E+00	5.926E+00	6.871E+00	7.685E+00	8.414E+00	9.016E+00	9.547E+00
0.090	3.671E+00	4.983E+00	6.158E+00	7.201E+00	8.110E+00	8.930E+00	9.611E+00	1.021E+01
0.100	3.709E+00	5.085E+00	6.340E+00	7.471E+00	8.470E+00	9.377E+00	1.013E+01	1.081E+01
0.150	3.726E+00	5.286E+00	6.789E+00	8.219E+00	9.550E+00	1.080E+01	1.190E+01	1.292E+01
0.200	3.628E+00	5.263E+00	6.880E+00	8.460E+00	9.975E+00	1.143E+01	1.275E+01	1.400E+01
0.250	3.501E+00	5.166E+00	6.841E+00	8.503E+00	1.012E+01	1.171E+01	1.316E+01	1.455E+01
0.300	3.370E+00	5.041E+00	6.747E+00	8.456E+00	1.014E+01	1.181E+01	1.335E+01	1.484E+01
0.400	3.119E+00	4.773E+00	6.497E+00	8.249E+00	1.000E+01	1.177E+01	1.340E+01	1.501E+01
0.500	2.895E+00	4.512E+00	6.226E+00	7.988E+00	9.776E+00	1.158E+01	1.327E+01	1.493E+01
0.600	2.698E+00	4.269E+00	5.959E+00	7.715E+00	9.513E+00	1.134E+01	1.306E+01	1.475E+01
0.700	2.524E+00	4.046E+00	5.706E+00	7.445E+00	9.240E+00	1.108E+01	1.281E+01	1.452E+01
0.800	2.370E+00	3.842E+00	5.467E+00	7.185E+00	8.969E+00	1.080E+01	1.254E+01	1.426E+01
0.900	2.234E+00	3.656E+00	5.245E+00	6.936E+00	8.704E+00	1.053E+01	1.226E+01	1.399E+01
1.000	2.112E+00	3.486E+00	5.037E+00	6.700E+00	8.448E+00	1.026E+01	1.199E+01	1.372E+01
1.500	1.658E+00	2.822E+00	4.188E+00	5.699E+00	7.327E+00	9.055E+00	1.071E+01	1.239E+01
2.000	1.366E+00	2.367E+00	3.574E+00	4.940E+00	6.439E+00	8.057E+00	9.634E+00	1.123E+01
2.500	1.163E+00	2.038E+00	3.113E+00	4.352E+00	5.732E+00	7.239E+00	8.728E+00	1.025E+01
3.000	1.015E+00	1.790E+00	2.757E+00	3.886E+00	5.158E+00	6.562E+00	7.967E+00	9.418E+00
4.000	8.137E−01	1.443E+00	2.243E+00	3.196E+00	4.289E+00	5.515E+00	6.767E+00	8.077E+00
5.000	6.824E−01	1.213E+00	1.894E+00	2.715E+00	3.667E+00	4.748E+00	5.871E+00	7.058E+00
6.000	5.900E−01	1.050E+00	1.642E+00	2.361E+00	3.203E+00	4.166E+00	5.181E+00	6.263E+00
7.000	5.214E−01	9.278E−01	1.452E+00	2.092E+00	2.844E+00	3.711E+00	4.635E+00	5.627E+00
8.000	4.682E−01	8.329E−01	1.303E+00	1.880E+00	2.560E+00	3.346E+00	4.193E+00	5.108E+00
9.000	4.258E−01	7.571E−01	1.184E+00	1.709E+00	2.329E+00	3.048E+00	3.829E+00	4.677E+00
10.00	3.910E−01	6.950E−01	1.087E+00	1.568E+00	2.139E+00	2.801E+00	3.525E+00	4.314E+00
15.00	2.813E−01	4.997E−01	7.807E−01	1.125E+00	1.533E+00	2.009E+00	2.539E+00	3.125E+00
20.00	2.226E−01	3.954E−01	6.174E−01	8.889E−01	1.210E+00	1.584E+00	2.004E+00	2.471E+00
25.00	1.857E−01	3.298E−01	5.150E−01	7.411E−01	1.008E+00	1.318E+00	1.668E+00	2.058E+00
30.00	1.601E−01	2.845E−01	4.443E−01	6.393E−01	8.698E−01	1.136E+00	1.437E+00	1.774E+00
40.00	1.270E−01	2.257E−01	3.525E−01	5.072E−01	6.900E−01	9.010E−01	1.139E+00	1.406E+00
50.00	1.062E−01	1.889E−01	2.951E−01	4.247E−01	5.778E−01	7.544E−01	9.543E−01	1.177E+00
60.00	9.204E−02	1.636E−01	2.556E−01	3.680E−01	5.007E−01	6.537E−01	8.271E−01	1.020E+00
70.00	8.162E−02	1.451E−01	2.267E−01	3.264E−01	4.442E−01	5.801E−01	7.340E−01	9.058E−01
80.00	7.366E−02	1.309E−01	2.046E−01	2.947E−01	4.011E−01	5.238E−01	6.627E−01	8.180E−01
90.00	6.736E−02	1.197E−01	1.872E−01	2.695E−01	3.669E−01	4.792E−01	6.064E−01	7.486E−01
100.0	6.226E−02	1.107E−01	1.730E−01	2.492E−01	3.392E−01	4.431E−01	5.607E−01	6.922E−01
150.0	4.653E−02	8.276E−02	1.293E−01	1.863E−01	2.537E−01	3.315E−01	4.197E−01	5.183E−01
200.0	3.840E−02	6.832E−02	1.068E−01	1.539E−01	2.095E−01	2.738E−01	3.467E−01	4.283E−01
250.0	3.345E−02	5.951E−02	9.304E−02	1.340E−01	1.826E−01	2.386E−01	3.022E−01	3.733E−01
300.0	3.012E−02	5.359E−02	8.379E−02	1.207E−01	1.644E−01	2.149E−01	2.722E−01	3.363E−01
400.0	2.596E−02	4.619E−02	7.224E−02	1.041E−01	1.418E−01	1.853E−01	2.348E−01	2.901E−01
500.0	2.350E−02	4.182E−02	6.540E−02	9.425E−02	1.284E−01	1.678E−01	2.126E−01	2.627E−01
600.0	2.190E−02	3.897E−02	6.095E−02	8.785E−02	1.196E−01	1.564E−01	1.982E−01	2.449E−01
700.0	2.080E−02	3.701E−02	5.789E−02	8.344E−02	1.136E−01	1.486E−01	1.882E−01	2.326E−01
800.0	2.001E−02	3.561E−02	5.569E−02	8.028E−02	1.093E−01	1.429E−01	1.811E−01	2.238E−01
900.0	1.942E−02	3.457E−02	5.407E−02	7.794E−02	1.061E−01	1.388E−01	1.758E−01	2.173E−01
1000.	1.898E−02	3.378E−02	5.283E−02	7.615E−02	1.037E−01	1.356E−01	1.718E−01	2.123E−01

Material: Polycarbonate (makrolon, lexan)

Ion	Na	Mg	Al	Si	P	S	Cl	Ar
(E/A_1) / MeV				$(-\mathrm{d}E/\rho\mathrm{d}\ell)$ / MeV cm^2 mg^{-1}				
0.025	4.841E+00	5.029E+00	5.209E+00	5.387E+00	5.591E+00	5.759E+00	5.972E+00	6.093E+00
0.030	5.420E+00	5.617E+00	5.812E+00	6.004E+00	6.222E+00	6.409E+00	6.633E+00	6.768E+00
0.040	6.500E+00	6.716E+00	6.943E+00	7.163E+00	7.409E+00	7.629E+00	7.875E+00	8.031E+00
0.050	7.490E+00	7.735E+00	7.995E+00	8.245E+00	8.520E+00	8.771E+00	9.040E+00	9.213E+00
0.060	8.406E+00	8.682E+00	8.978E+00	9.259E+00	9.564E+00	9.848E+00	1.014E+01	1.033E+01
0.070	9.261E+00	9.568E+00	9.901E+00	1.021E+01	1.054E+01	1.086E+01	1.118E+01	1.139E+01
0.080	1.006E+01	1.040E+01	1.077E+01	1.111E+01	1.148E+01	1.182E+01	1.217E+01	1.239E+01
0.090	1.080E+01	1.118E+01	1.159E+01	1.197E+01	1.237E+01	1.274E+01	1.311E+01	1.336E+01
0.100	1.147E+01	1.190E+01	1.236E+01	1.278E+01	1.321E+01	1.362E+01	1.402E+01	1.428E+01
0.150	1.397E+01	1.466E+01	1.541E+01	1.607E+01	1.674E+01	1.737E+01	1.794E+01	1.836E+01
0.200	1.535E+01	1.625E+01	1.725E+01	1.816E+01	1.907E+01	1.993E+01	2.073E+01	2.135E+01
0.250	1.611E+01	1.716E+01	1.834E+01	1.943E+01	2.053E+01	2.160E+01	2.258E+01	2.339E+01
0.300	1.654E+01	1.768E+01	1.899E+01	2.022E+01	2.147E+01	2.269E+01	2.382E+01	2.478E+01
0.400	1.690E+01	1.815E+01	1.964E+01	2.104E+01	2.249E+01	2.391E+01	2.525E+01	2.641E+01
0.500	1.695E+01	1.825E+01	1.983E+01	2.134E+01	2.292E+01	2.448E+01	2.595E+01	2.724E+01
0.600	1.685E+01	1.817E+01	1.982E+01	2.140E+01	2.306E+01	2.472E+01	2.628E+01	2.765E+01
0.700	1.668E+01	1.800E+01	1.970E+01	2.132E+01	2.305E+01	2.477E+01	2.640E+01	2.783E+01
0.800	1.646E+01	1.778E+01	1.951E+01	2.116E+01	2.294E+01	2.471E+01	2.638E+01	2.786E+01
0.900	1.621E+01	1.753E+01	1.928E+01	2.096E+01	2.276E+01	2.457E+01	2.628E+01	2.780E+01
1.000	1.596E+01	1.727E+01	1.902E+01	2.072E+01	2.255E+01	2.439E+01	2.613E+01	2.767E+01
1.500	1.464E+01	1.590E+01	1.766E+01	1.937E+01	2.125E+01	2.316E+01	2.497E+01	2.656E+01
2.000	1.343E+01	1.464E+01	1.636E+01	1.804E+01	1.991E+01	2.182E+01	2.363E+01	2.523E+01
2.500	1.236E+01	1.352E+01	1.519E+01	1.683E+01	1.867E+01	2.055E+01	2.233E+01	2.392E+01
3.000	1.142E+01	1.255E+01	1.416E+01	1.576E+01	1.754E+01	1.938E+01	2.113E+01	2.268E+01
4.000	9.896E+00	1.095E+01	1.245E+01	1.393E+01	1.561E+01	1.735E+01	1.902E+01	2.052E+01
5.000	8.702E+00	9.694E+00	1.108E+01	1.247E+01	1.404E+01	1.568E+01	1.726E+01	1.869E+01
6.000	7.752E+00	8.688E+00	9.982E+00	1.128E+01	1.275E+01	1.429E+01	1.579E+01	1.714E+01
7.000	6.981E+00	7.867E+00	9.073E+00	1.029E+01	1.166E+01	1.312E+01	1.453E+01	1.583E+01
8.000	6.345E+00	7.186E+00	8.313E+00	9.460E+00	1.075E+01	1.211E+01	1.345E+01	1.469E+01
9.000	5.813E+00	6.613E+00	7.669E+00	8.750E+00	9.965E+00	1.125E+01	1.252E+01	1.371E+01
10.00	5.362E+00	6.125E+00	7.118E+00	8.139E+00	9.285E+00	1.050E+01	1.171E+01	1.284E+01
15.00	3.869E+00	4.485E+00	5.244E+00	6.039E+00	6.924E+00	7.874E+00	8.833E+00	9.761E+00
20.00	3.043E+00	3.558E+00	4.171E+00	4.820E+00	5.537E+00	6.309E+00	7.100E+00	7.882E+00
25.00	2.523E+00	2.967E+00	3.481E+00	4.029E+00	4.632E+00	5.281E+00	5.953E+00	6.629E+00
30.00	2.166E+00	2.557E+00	3.001E+00	3.477E+00	3.997E+00	4.558E+00	5.143E+00	5.737E+00
40.00	1.710E+00	2.025E+00	2.378E+00	2.756E+00	3.168E+00	3.611E+00	4.077E+00	4.559E+00
50.00	1.428E+00	1.695E+00	1.990E+00	2.307E+00	2.650E+00	3.019E+00	3.409E+00	3.816E+00
60.00	1.236E+00	1.469E+00	1.724E+00	1.999E+00	2.295E+00	2.614E+00	2.952E+00	3.306E+00
70.00	1.096E+00	1.304E+00	1.530E+00	1.774E+00	2.037E+00	2.319E+00	2.618E+00	2.933E+00
80.00	9.902E−01	1.177E+00	1.381E+00	1.602E+00	1.839E+00	2.093E+00	2.364E+00	2.649E+00
90.00	9.060E−01	1.077E+00	1.264E+00	1.466E+00	1.683E+00	1.916E+00	2.163E+00	2.424E+00
100.0	8.377E−01	9.967E−01	1.169E+00	1.356E+00	1.557E+00	1.772E+00	2.000E+00	2.242E+00
150.0	6.273E−01	7.467E−01	8.765E−01	1.016E+00	1.167E+00	1.328E+00	1.500E+00	1.681E+00
200.0	5.184E−01	6.172E−01	7.247E−01	8.407E−01	9.655E−01	1.098E+00	1.241E+00	1.391E+00
250.0	4.519E−01	5.381E−01	6.319E−01	7.332E−01	8.421E−01	9.586E−01	1.082E+00	1.214E+00
300.0	4.072E−01	4.849E−01	5.695E−01	6.608E−01	7.591E−01	8.642E−01	9.761E−01	1.095E+00
400.0	3.513E−01	4.183E−01	4.914E−01	5.703E−01	6.551E−01	7.460E−01	8.427E−01	9.455E−01
500.0	3.181E−01	3.789E−01	4.451E−01	5.166E−01	5.936E−01	6.759E−01	7.637E−01	8.568E−01
600.0	2.966E−01	3.533E−01	4.150E−01	4.817E−01	5.535E−01	6.303E−01	7.122E−01	7.992E−01
700.0	2.817E−01	3.356E−01	3.943E−01	4.577E−01	5.259E−01	5.989E−01	6.767E−01	7.594E−01
800.0	2.711E−01	3.229E−01	3.794E−01	4.404E−01	5.060E−01	5.763E−01	6.512E−01	7.308E−01
900.0	2.632E−01	3.135E−01	3.683E−01	4.276E−01	4.914E−01	5.596E−01	6.324E−01	7.097E−01
1000.	2.572E−01	3.064E−01	3.599E−01	4.179E−01	4.802E−01	5.469E−01	6.180E−01	6.935E−01

Material: Polyethylene

Ion	Li	Be	B	C	N	O	F	Ne
(E/A_1) / MeV				$(-\mathrm{d}E/\rho\mathrm{d}\ell)$ / MeV cm^2 mg^{-1}				
0.025	3.038E+00	3.761E+00	4.329E+00	4.774E+00	5.194E+00	5.553E+00	5.826E+00	6.073E+00
0.030	3.300E+00	4.114E+00	4.766E+00	5.286E+00	5.763E+00	6.174E+00	6.490E+00	6.774E+00
0.040	3.719E+00	4.711E+00	5.525E+00	6.188E+00	6.779E+00	7.294E+00	7.698E+00	8.058E+00
0.050	4.021E+00	5.183E+00	6.153E+00	6.959E+00	7.664E+00	8.281E+00	8.774E+00	9.210E+00
0.060	4.232E+00	5.547E+00	6.667E+00	7.613E+00	8.436E+00	9.159E+00	9.741E+00	1.025E+01
0.070	4.375E+00	5.820E+00	7.077E+00	8.160E+00	9.103E+00	9.936E+00	1.061E+01	1.121E+01
0.080	4.469E+00	6.020E+00	7.399E+00	8.609E+00	9.671E+00	1.061E+01	1.139E+01	1.207E+01
0.090	4.527E+00	6.164E+00	7.648E+00	8.972E+00	1.015E+01	1.120E+01	1.207E+01	1.284E+01
0.100	4.560E+00	6.267E+00	7.839E+00	9.264E+00	1.054E+01	1.170E+01	1.267E+01	1.353E+01
0.150	4.531E+00	6.432E+00	8.273E+00	1.003E+01	1.167E+01	1.323E+01	1.459E+01	1.585E+01
0.200	4.384E+00	6.358E+00	8.318E+00	1.023E+01	1.207E+01	1.385E+01	1.545E+01	1.696E+01
0.250	4.211E+00	6.209E+00	8.226E+00	1.022E+01	1.217E+01	1.409E+01	1.583E+01	1.750E+01
0.300	4.037E+00	6.036E+00	8.079E+00	1.012E+01	1.214E+01	1.414E+01	1.597E+01	1.775E+01
0.400	3.712E+00	5.678E+00	7.729E+00	9.809E+00	1.190E+01	1.399E+01	1.592E+01	1.782E+01
0.500	3.428E+00	5.340E+00	7.368E+00	9.450E+00	1.156E+01	1.370E+01	1.568E+01	1.764E+01
0.600	3.181E+00	5.030E+00	7.023E+00	9.088E+00	1.120E+01	1.335E+01	1.536E+01	1.735E+01
0.700	2.966E+00	4.751E+00	6.700E+00	8.738E+00	1.084E+01	1.300E+01	1.501E+01	1.702E+01
0.800	2.777E+00	4.498E+00	6.400E+00	8.406E+00	1.049E+01	1.264E+01	1.465E+01	1.666E+01
0.900	2.610E+00	4.269E+00	6.123E+00	8.093E+00	1.015E+01	1.228E+01	1.430E+01	1.630E+01
1.000	2.462E+00	4.062E+00	5.866E+00	7.799E+00	9.827E+00	1.194E+01	1.394E+01	1.594E+01
1.500	1.918E+00	3.261E+00	4.837E+00	6.576E+00	8.445E+00	1.043E+01	1.234E+01	1.427E+01
2.000	1.574E+00	2.722E+00	4.106E+00	5.669E+00	7.380E+00	9.228E+00	1.103E+01	1.287E+01
2.500	1.337E+00	2.337E+00	3.565E+00	4.976E+00	6.543E+00	8.257E+00	9.950E+00	1.169E+01
3.000	1.164E+00	2.048E+00	3.149E+00	4.431E+00	5.872E+00	7.463E+00	9.055E+00	1.070E+01
4.000	9.296E−01	1.647E+00	2.555E+00	3.634E+00	4.867E+00	6.249E+00	7.662E+00	9.143E+00
5.000	7.780E−01	1.382E+00	2.154E+00	3.081E+00	4.154E+00	5.369E+00	6.633E+00	7.971E+00
6.000	6.717E−01	1.194E+00	1.865E+00	2.677E+00	3.624E+00	4.705E+00	5.845E+00	7.062E+00
7.000	5.928E−01	1.054E+00	1.647E+00	2.369E+00	3.216E+00	4.188E+00	5.225E+00	6.339E+00
8.000	5.318E−01	9.453E−01	1.478E+00	2.128E+00	2.893E+00	3.775E+00	4.725E+00	5.751E+00
9.000	4.832E−01	8.586E−01	1.342E+00	1.934E+00	2.632E+00	3.438E+00	4.313E+00	5.264E+00
10.00	4.433E−01	7.877E−01	1.231E+00	1.774E+00	2.416E+00	3.158E+00	3.970E+00	4.855E+00
15.00	3.181E−01	5.649E−01	8.822E−01	1.271E+00	1.730E+00	2.264E+00	2.859E+00	3.516E+00
20.00	2.513E−01	4.462E−01	6.966E−01	1.003E+00	1.365E+00	1.784E+00	2.256E+00	2.780E+00
25.00	2.093E−01	3.717E−01	5.803E−01	8.350E−01	1.136E+00	1.484E+00	1.877E+00	2.315E+00
30.00	1.803E−01	3.204E−01	5.002E−01	7.197E−01	9.790E−01	1.279E+00	1.617E+00	1.995E+00
40.00	1.428E−01	2.537E−01	3.962E−01	5.702E−01	7.756E−01	1.013E+00	1.281E+00	1.580E+00
50.00	1.193E−01	2.121E−01	3.313E−01	4.769E−01	6.488E−01	8.470E−01	1.071E+00	1.322E+00
60.00	1.033E−01	1.836E−01	2.868E−01	4.129E−01	5.617E−01	7.334E−01	9.278E−01	1.145E+00
70.00	9.152E−02	1.627E−01	2.542E−01	3.660E−01	4.981E−01	6.504E−01	8.229E−01	1.015E+00
80.00	8.254E−02	1.468E−01	2.293E−01	3.302E−01	4.494E−01	5.869E−01	7.426E−01	9.166E−01
90.00	7.545E−02	1.342E−01	2.097E−01	3.019E−01	4.110E−01	5.367E−01	6.792E−01	8.384E−01
100.0	6.970E−02	1.240E−01	1.937E−01	2.790E−01	3.798E−01	4.960E−01	6.278E−01	7.750E−01
150.0	5.202E−02	9.252E−02	1.446E−01	2.083E−01	2.837E−01	3.706E−01	4.692E−01	5.794E−01
200.0	4.290E−02	7.630E−02	1.193E−01	1.719E−01	2.341E−01	3.059E−01	3.873E−01	4.783E−01
250.0	3.734E−02	6.642E−02	1.038E−01	1.496E−01	2.038E−01	2.663E−01	3.373E−01	4.166E−01
300.0	3.360E−02	5.978E−02	9.347E−02	1.347E−01	1.835E−01	2.398E−01	3.037E−01	3.751E−01
400.0	2.894E−02	5.149E−02	8.051E−02	1.160E−01	1.581E−01	2.066E−01	2.617E−01	3.233E−01
500.0	2.618E−02	4.658E−02	7.284E−02	1.050E−01	1.430E−01	1.869E−01	2.368E−01	2.926E−01
600.0	2.439E−02	4.339E−02	6.786E−02	9.780E−02	1.332E−01	1.742E−01	2.206E−01	2.726E−01
700.0	2.315E−02	4.119E−02	6.442E−02	9.285E−02	1.265E−01	1.654E−01	2.095E−01	2.589E−01
800.0	2.226E−02	3.961E−02	6.195E−02	8.929E−02	1.217E−01	1.590E−01	2.015E−01	2.490E−01
900.0	2.161E−02	3.844E−02	6.013E−02	8.666E−02	1.181E−01	1.544E−01	1.955E−01	2.416E−01
1000.	2.110E−02	3.755E−02	5.873E−02	8.465E−02	1.153E−01	1.508E−01	1.910E−01	2.360E−01

Material: Polyethylene

Ion	Na	Mg	Al	Si	P	S	Cl	Ar
(E/A_1) / MeV				$(-\mathrm{d}E/\rho\mathrm{d}\ell)$ / MeV cm^2 mg^{-1}				
0.025	6.280E+00	6.544E+00	6.783E+00	7.021E+00	7.309E+00	7.538E+00	7.835E+00	8.007E+00
0.030	7.010E+00	7.288E+00	7.547E+00	7.803E+00	8.110E+00	8.363E+00	8.674E+00	8.865E+00
0.040	8.355E+00	8.670E+00	8.969E+00	9.260E+00	9.602E+00	9.898E+00	1.023E+01	1.045E+01
0.050	9.574E+00	9.936E+00	1.028E+01	1.061E+01	1.098E+01	1.132E+01	1.168E+01	1.192E+01
0.060	1.069E+01	1.110E+01	1.149E+01	1.186E+01	1.227E+01	1.265E+01	1.304E+01	1.330E+01
0.070	1.171E+01	1.218E+01	1.261E+01	1.302E+01	1.347E+01	1.389E+01	1.431E+01	1.460E+01
0.080	1.265E+01	1.317E+01	1.366E+01	1.411E+01	1.460E+01	1.506E+01	1.551E+01	1.582E+01
0.090	1.351E+01	1.410E+01	1.464E+01	1.513E+01	1.567E+01	1.617E+01	1.665E+01	1.699E+01
0.100	1.428E+01	1.494E+01	1.554E+01	1.609E+01	1.667E+01	1.721E+01	1.773E+01	1.810E+01
0.150	1.702E+01	1.804E+01	1.899E+01	1.985E+01	2.071E+01	2.153E+01	2.227E+01	2.284E+01
0.200	1.842E+01	1.974E+01	2.098E+01	2.211E+01	2.326E+01	2.436E+01	2.536E+01	2.618E+01
0.250	1.915E+01	2.067E+01	2.211E+01	2.344E+01	2.480E+01	2.612E+01	2.734E+01	2.837E+01
0.300	1.952E+01	2.117E+01	2.276E+01	2.424E+01	2.576E+01	2.725E+01	2.863E+01	2.983E+01
0.400	1.975E+01	2.157E+01	2.334E+01	2.501E+01	2.675E+01	2.846E+01	3.006E+01	3.148E+01
0.500	1.966E+01	2.157E+01	2.345E+01	2.524E+01	2.711E+01	2.896E+01	3.070E+01	3.227E+01
0.600	1.942E+01	2.139E+01	2.334E+01	2.520E+01	2.716E+01	2.912E+01	3.095E+01	3.261E+01
0.700	1.911E+01	2.112E+01	2.311E+01	2.502E+01	2.705E+01	2.908E+01	3.098E+01	3.271E+01
0.800	1.877E+01	2.080E+01	2.282E+01	2.476E+01	2.684E+01	2.892E+01	3.087E+01	3.265E+01
0.900	1.842E+01	2.045E+01	2.250E+01	2.446E+01	2.657E+01	2.868E+01	3.067E+01	3.249E+01
1.000	1.806E+01	2.010E+01	2.215E+01	2.413E+01	2.626E+01	2.840E+01	3.042E+01	3.226E+01
1.500	1.634E+01	1.835E+01	2.039E+01	2.237E+01	2.453E+01	2.674E+01	2.881E+01	3.071E+01
2.000	1.485E+01	1.678E+01	1.877E+01	2.071E+01	2.285E+01	2.503E+01	2.710E+01	2.899E+01
2.500	1.358E+01	1.544E+01	1.736E+01	1.924E+01	2.132E+01	2.347E+01	2.550E+01	2.736E+01
3.000	1.250E+01	1.428E+01	1.613E+01	1.794E+01	1.997E+01	2.205E+01	2.404E+01	2.586E+01
4.000	1.077E+01	1.240E+01	1.411E+01	1.580E+01	1.768E+01	1.965E+01	2.153E+01	2.327E+01
5.000	9.448E+00	1.095E+01	1.252E+01	1.410E+01	1.586E+01	1.770E+01	1.947E+01	2.112E+01
6.000	8.411E+00	9.793E+00	1.125E+01	1.272E+01	1.436E+01	1.609E+01	1.776E+01	1.933E+01
7.000	7.577E+00	8.857E+00	1.021E+01	1.159E+01	1.312E+01	1.474E+01	1.632E+01	1.781E+01
8.000	6.894E+00	8.083E+00	9.349E+00	1.064E+01	1.208E+01	1.360E+01	1.509E+01	1.651E+01
9.000	6.324E+00	7.434E+00	8.619E+00	9.832E+00	1.118E+01	1.262E+01	1.403E+01	1.538E+01
10.00	5.843E+00	6.883E+00	7.996E+00	9.140E+00	1.041E+01	1.177E+01	1.311E+01	1.440E+01
15.00	4.250E+00	5.037E+00	5.887E+00	6.775E+00	7.758E+00	8.811E+00	9.875E+00	1.092E+01
20.00	3.364E+00	3.997E+00	4.682E+00	5.407E+00	6.204E+00	7.061E+00	7.939E+00	8.820E+00
25.00	2.802E+00	3.332E+00	3.908E+00	4.521E+00	5.191E+00	5.913E+00	6.659E+00	7.418E+00
30.00	2.414E+00	2.872E+00	3.369E+00	3.901E+00	4.481E+00	5.105E+00	5.755E+00	6.422E+00
40.00	1.912E+00	2.274E+00	2.669E+00	3.093E+00	3.552E+00	4.046E+00	4.565E+00	5.105E+00
50.00	1.599E+00	1.902E+00	2.232E+00	2.588E+00	2.971E+00	3.383E+00	3.819E+00	4.274E+00
60.00	1.385E+00	1.648E+00	1.933E+00	2.241E+00	2.573E+00	2.929E+00	3.306E+00	3.703E+00
70.00	1.228E+00	1.461E+00	1.715E+00	1.988E+00	2.282E+00	2.597E+00	2.932E+00	3.285E+00
80.00	1.109E+00	1.319E+00	1.548E+00	1.795E+00	2.060E+00	2.345E+00	2.647E+00	2.966E+00
90.00	1.014E+00	1.207E+00	1.416E+00	1.642E+00	1.885E+00	2.145E+00	2.421E+00	2.713E+00
100.0	9.376E−01	1.116E+00	1.309E+00	1.518E+00	1.743E+00	1.983E+00	2.239E+00	2.509E+00
150.0	7.012E−01	8.347E−01	9.797E−01	1.136E+00	1.305E+00	1.485E+00	1.676E+00	1.880E+00
200.0	5.790E−01	6.893E−01	8.093E−01	9.389E−01	1.078E+00	1.227E+00	1.386E+00	1.554E+00
250.0	5.043E−01	6.005E−01	7.051E−01	8.182E−01	9.397E−01	1.070E+00	1.208E+00	1.355E+00
300.0	4.542E−01	5.409E−01	6.351E−01	7.370E−01	8.466E−01	9.637E−01	1.089E+00	1.221E+00
400.0	3.915E−01	4.662E−01	5.476E−01	6.355E−01	7.300E−01	8.312E−01	9.390E−01	1.053E+00
500.0	3.543E−01	4.220E−01	4.957E−01	5.753E−01	6.610E−01	7.527E−01	8.504E−01	9.541E−01
600.0	3.302E−01	3.933E−01	4.619E−01	5.362E−01	6.161E−01	7.016E−01	7.927E−01	8.894E−01
700.0	3.135E−01	3.734E−01	4.387E−01	5.092E−01	5.851E−01	6.663E−01	7.528E−01	8.448E−01
800.0	3.015E−01	3.592E−01	4.219E−01	4.898E−01	5.628E−01	6.409E−01	7.242E−01	8.126E−01
900.0	2.927E−01	3.486E−01	4.095E−01	4.754E−01	5.463E−01	6.221E−01	7.030E−01	7.889E−01
1000.	2.859E−01	3.406E−01	4.001E−01	4.644E−01	5.337E−01	6.078E−01	6.868E−01	7.707E−01

Material: Polyethylene terephthalate (Mylar)

Ion	Li	Be	B	C	N	O	F	Ne
(E/A_1) / MeV				$(-dE/\rho d\ell)$ / MeV cm^2 mg^{-1}				
0.025	2.242E+00	2.756E+00	3.161E+00	3.482E+00	3.769E+00	4.026E+00	4.235E+00	4.427E+00
0.030	2.448E+00	3.030E+00	3.495E+00	3.870E+00	4.200E+00	4.495E+00	4.735E+00	4.954E+00
0.040	2.786E+00	3.503E+00	4.086E+00	4.566E+00	4.981E+00	5.352E+00	5.656E+00	5.930E+00
0.050	3.041E+00	3.891E+00	4.592E+00	5.176E+00	5.675E+00	6.122E+00	6.491E+00	6.821E+00
0.060	3.229E+00	4.203E+00	5.019E+00	5.709E+00	6.296E+00	6.821E+00	7.254E+00	7.641E+00
0.070	3.363E+00	4.446E+00	5.372E+00	6.168E+00	6.847E+00	7.453E+00	7.955E+00	8.400E+00
0.080	3.457E+00	4.632E+00	5.660E+00	6.556E+00	7.328E+00	8.019E+00	8.593E+00	9.100E+00
0.090	3.520E+00	4.772E+00	5.889E+00	6.880E+00	7.742E+00	8.519E+00	9.168E+00	9.742E+00
0.100	3.562E+00	4.877E+00	6.072E+00	7.147E+00	8.095E+00	8.955E+00	9.679E+00	1.032E+01
0.150	3.591E+00	5.093E+00	6.535E+00	7.905E+00	9.177E+00	1.037E+01	1.142E+01	1.239E+01
0.200	3.503E+00	5.081E+00	6.639E+00	8.161E+00	9.617E+00	1.102E+01	1.228E+01	1.348E+01
0.250	3.385E+00	4.993E+00	6.611E+00	8.215E+00	9.778E+00	1.130E+01	1.271E+01	1.405E+01
0.300	3.260E+00	4.877E+00	6.525E+00	8.177E+00	9.808E+00	1.141E+01	1.290E+01	1.434E+01
0.400	3.021E+00	4.622E+00	6.291E+00	7.987E+00	9.690E+00	1.139E+01	1.298E+01	1.453E+01
0.500	2.806E+00	4.373E+00	6.033E+00	7.741E+00	9.475E+00	1.122E+01	1.286E+01	1.448E+01
0.600	2.617E+00	4.140E+00	5.779E+00	7.482E+00	9.225E+00	1.100E+01	1.267E+01	1.432E+01
0.700	2.450E+00	3.926E+00	5.536E+00	7.224E+00	8.966E+00	1.075E+01	1.243E+01	1.410E+01
0.800	2.302E+00	3.730E+00	5.308E+00	6.975E+00	8.707E+00	1.049E+01	1.218E+01	1.385E+01
0.900	2.170E+00	3.552E+00	5.094E+00	6.737E+00	8.454E+00	1.023E+01	1.191E+01	1.360E+01
1.000	2.052E+00	3.388E+00	4.894E+00	6.510E+00	8.209E+00	9.978E+00	1.165E+01	1.333E+01
1.500	1.613E+00	2.746E+00	4.076E+00	5.547E+00	7.131E+00	8.813E+00	1.043E+01	1.207E+01
2.000	1.331E+00	2.306E+00	3.482E+00	4.814E+00	6.275E+00	7.851E+00	9.391E+00	1.095E+01
2.500	1.134E+00	1.987E+00	3.035E+00	4.244E+00	5.590E+00	7.061E+00	8.515E+00	1.000E+01
3.000	9.906E−01	1.746E+00	2.689E+00	3.791E+00	5.034E+00	6.405E+00	7.778E+00	9.197E+00
4.000	7.941E−01	1.409E+00	2.190E+00	3.121E+00	4.190E+00	5.388E+00	6.613E+00	7.895E+00
5.000	6.663E−01	1.185E+00	1.850E+00	2.653E+00	3.584E+00	4.642E+00	5.742E+00	6.904E+00
6.000	5.764E−01	1.025E+00	1.604E+00	2.308E+00	3.132E+00	4.074E+00	5.069E+00	6.129E+00
7.000	5.095E−01	9.067E−01	1.419E+00	2.045E+00	2.782E+00	3.630E+00	4.536E+00	5.508E+00
8.000	4.576E−01	8.141E−01	1.274E+00	1.838E+00	2.504E+00	3.274E+00	4.104E+00	5.001E+00
9.000	4.162E−01	7.401E−01	1.158E+00	1.671E+00	2.279E+00	2.983E+00	3.749E+00	4.580E+00
10.00	3.823E−01	6.796E−01	1.063E+00	1.534E+00	2.093E+00	2.742E+00	3.451E+00	4.225E+00
15.00	2.753E−01	4.889E−01	7.639E−01	1.101E+00	1.501E+00	1.967E+00	2.486E+00	3.061E+00
20.00	2.179E−01	3.870E−01	6.043E−01	8.701E−01	1.185E+00	1.551E+00	1.962E+00	2.420E+00
25.00	1.818E−01	3.229E−01	5.042E−01	7.257E−01	9.877E−01	1.291E+00	1.634E+00	2.016E+00
30.00	1.568E−01	2.786E−01	4.351E−01	6.261E−01	8.519E−01	1.113E+00	1.408E+00	1.738E+00
40.00	1.244E−01	2.211E−01	3.453E−01	4.969E−01	6.760E−01	8.827E−01	1.116E+00	1.378E+00
50.00	1.041E−01	1.851E−01	2.891E−01	4.161E−01	5.662E−01	7.392E−01	9.351E−01	1.154E+00
60.00	9.020E−02	1.603E−01	2.505E−01	3.606E−01	4.907E−01	6.407E−01	8.105E−01	1.000E+00
70.00	8.000E−02	1.422E−01	2.222E−01	3.200E−01	4.354E−01	5.686E−01	7.194E−01	8.879E−01
80.00	7.220E−02	1.283E−01	2.006E−01	2.889E−01	3.931E−01	5.134E−01	6.497E−01	8.019E−01
90.00	6.604E−02	1.174E−01	1.835E−01	2.643E−01	3.597E−01	4.698E−01	5.945E−01	7.339E−01
100.0	6.104E−02	1.085E−01	1.696E−01	2.443E−01	3.326E−01	4.344E−01	5.498E−01	6.787E−01
150.0	4.563E−02	8.117E−02	1.268E−01	1.827E−01	2.488E−01	3.251E−01	4.116E−01	5.083E−01
200.0	3.767E−02	6.702E−02	1.047E−01	1.509E−01	2.055E−01	2.686E−01	3.401E−01	4.201E−01
250.0	3.281E−02	5.838E−02	9.128E−02	1.315E−01	1.791E−01	2.341E−01	2.965E−01	3.662E−01
300.0	2.955E−02	5.258E−02	8.222E−02	1.184E−01	1.613E−01	2.109E−01	2.671E−01	3.300E−01
400.0	2.548E−02	4.533E−02	7.089E−02	1.021E−01	1.391E−01	1.819E−01	2.304E−01	2.847E−01
500.0	2.306E−02	4.104E−02	6.419E−02	9.251E−02	1.260E−01	1.647E−01	2.087E−01	2.578E−01
600.0	2.150E−02	3.826E−02	5.983E−02	8.624E−02	1.174E−01	1.536E−01	1.945E−01	2.404E−01
700.0	2.042E−02	3.634E−02	5.683E−02	8.192E−02	1.116E−01	1.459E−01	1.848E−01	2.284E−01
800.0	1.964E−02	3.496E−02	5.468E−02	7.882E−02	1.073E−01	1.403E−01	1.778E−01	2.197E−01
900.0	1.907E−02	3.394E−02	5.309E−02	7.653E−02	1.042E−01	1.363E−01	1.726E−01	2.134E−01
1000.	1.864E−02	3.317E−02	5.187E−02	7.477E−02	1.018E−01	1.332E−01	1.687E−01	2.085E−01

Material: Polyethylene terephthalate (Mylar)

Ion	Na	Mg	Al	Si	P	S	Cl	Ar
(E/A_1) / MeV				$(-\mathrm{d}E/\rho\mathrm{d}\ell)$ / MeV cm^2 mg^{-1}				
0.025	4.585E+00	4.762E+00	4.930E+00	5.097E+00	5.283E+00	5.440E+00	5.636E+00	5.751E+00
0.030	5.138E+00	5.323E+00	5.505E+00	5.685E+00	5.884E+00	6.058E+00	6.266E+00	6.393E+00
0.040	6.169E+00	6.375E+00	6.587E+00	6.793E+00	7.018E+00	7.223E+00	7.450E+00	7.597E+00
0.050	7.118E+00	7.352E+00	7.597E+00	7.830E+00	8.083E+00	8.317E+00	8.566E+00	8.728E+00
0.060	7.997E+00	8.263E+00	8.542E+00	8.806E+00	9.087E+00	9.352E+00	9.623E+00	9.803E+00
0.070	8.817E+00	9.115E+00	9.430E+00	9.725E+00	1.003E+01	1.033E+01	1.062E+01	1.082E+01
0.080	9.583E+00	9.915E+00	1.026E+01	1.059E+01	1.093E+01	1.126E+01	1.158E+01	1.179E+01
0.090	1.029E+01	1.066E+01	1.106E+01	1.142E+01	1.179E+01	1.215E+01	1.249E+01	1.273E+01
0.100	1.094E+01	1.136E+01	1.180E+01	1.220E+01	1.261E+01	1.299E+01	1.336E+01	1.362E+01
0.150	1.338E+01	1.405E+01	1.476E+01	1.539E+01	1.602E+01	1.662E+01	1.716E+01	1.756E+01
0.200	1.475E+01	1.564E+01	1.659E+01	1.745E+01	1.832E+01	1.914E+01	1.989E+01	2.049E+01
0.250	1.553E+01	1.655E+01	1.768E+01	1.873E+01	1.979E+01	2.080E+01	2.174E+01	2.252E+01
0.300	1.597E+01	1.709E+01	1.835E+01	1.954E+01	2.074E+01	2.190E+01	2.299E+01	2.391E+01
0.400	1.635E+01	1.758E+01	1.901E+01	2.037E+01	2.177E+01	2.315E+01	2.444E+01	2.556E+01
0.500	1.641E+01	1.769E+01	1.923E+01	2.069E+01	2.222E+01	2.373E+01	2.516E+01	2.640E+01
0.600	1.632E+01	1.763E+01	1.923E+01	2.077E+01	2.238E+01	2.398E+01	2.550E+01	2.683E+01
0.700	1.616E+01	1.748E+01	1.912E+01	2.070E+01	2.238E+01	2.405E+01	2.563E+01	2.702E+01
0.800	1.595E+01	1.727E+01	1.894E+01	2.056E+01	2.228E+01	2.400E+01	2.563E+01	2.707E+01
0.900	1.572E+01	1.704E+01	1.873E+01	2.036E+01	2.212E+01	2.388E+01	2.554E+01	2.702E+01
1.000	1.548E+01	1.679E+01	1.849E+01	2.014E+01	2.192E+01	2.371E+01	2.540E+01	2.690E+01
1.500	1.422E+01	1.548E+01	1.719E+01	1.886E+01	2.069E+01	2.254E+01	2.430E+01	2.586E+01
2.000	1.306E+01	1.427E+01	1.594E+01	1.759E+01	1.941E+01	2.126E+01	2.303E+01	2.459E+01
2.500	1.203E+01	1.319E+01	1.482E+01	1.642E+01	1.821E+01	2.004E+01	2.179E+01	2.333E+01
3.000	1.113E+01	1.225E+01	1.383E+01	1.538E+01	1.712E+01	1.891E+01	2.063E+01	2.215E+01
4.000	9.654E+00	1.070E+01	1.216E+01	1.362E+01	1.526E+01	1.696E+01	1.859E+01	2.005E+01
5.000	8.497E+00	9.481E+00	1.084E+01	1.220E+01	1.374E+01	1.534E+01	1.689E+01	1.828E+01
6.000	7.574E+00	8.502E+00	9.767E+00	1.104E+01	1.248E+01	1.399E+01	1.545E+01	1.678E+01
7.000	6.824E+00	7.701E+00	8.881E+00	1.007E+01	1.142E+01	1.284E+01	1.423E+01	1.550E+01
8.000	6.205E+00	7.036E+00	8.140E+00	9.264E+00	1.053E+01	1.187E+01	1.318E+01	1.440E+01
9.000	5.686E+00	6.476E+00	7.511E+00	8.571E+00	9.763E+00	1.102E+01	1.227E+01	1.343E+01
10.00	5.247E+00	5.999E+00	6.972E+00	7.973E+00	9.098E+00	1.029E+01	1.148E+01	1.259E+01
15.00	3.788E+00	4.394E+00	5.139E+00	5.919E+00	6.788E+00	7.721E+00	8.663E+00	9.574E+00
20.00	2.980E+00	3.486E+00	4.088E+00	4.724E+00	5.428E+00	6.187E+00	6.964E+00	7.732E+00
25.00	2.471E+00	2.907E+00	3.411E+00	3.949E+00	4.541E+00	5.179E+00	5.839E+00	6.503E+00
30.00	2.122E+00	2.505E+00	2.941E+00	3.408E+00	3.918E+00	4.469E+00	5.044E+00	5.628E+00
40.00	1.675E+00	1.985E+00	2.330E+00	2.701E+00	3.105E+00	3.540E+00	3.998E+00	4.471E+00
50.00	1.399E+00	1.661E+00	1.950E+00	2.261E+00	2.598E+00	2.960E+00	3.343E+00	3.742E+00
60.00	1.212E+00	1.439E+00	1.689E+00	1.959E+00	2.250E+00	2.563E+00	2.894E+00	3.242E+00
70.00	1.075E+00	1.278E+00	1.499E+00	1.739E+00	1.997E+00	2.273E+00	2.567E+00	2.876E+00
80.00	9.707E−01	1.154E+00	1.354E+00	1.570E+00	1.803E+00	2.053E+00	2.318E+00	2.597E+00
90.00	8.882E−01	1.056E+00	1.239E+00	1.437E+00	1.650E+00	1.878E+00	2.121E+00	2.377E+00
100.0	8.214E−01	9.772E−01	1.146E+00	1.329E+00	1.526E+00	1.737E+00	1.961E+00	2.199E+00
150.0	6.153E−01	7.323E−01	8.596E−01	9.971E−01	1.144E+00	1.303E+00	1.471E+00	1.649E+00
200.0	5.086E−01	6.055E−01	7.109E−01	8.248E−01	9.471E−01	1.078E+00	1.217E+00	1.365E+00
250.0	4.434E−01	5.280E−01	6.200E−01	7.194E−01	8.262E−01	9.405E−01	1.062E+00	1.191E+00
300.0	3.996E−01	4.758E−01	5.588E−01	6.484E−01	7.448E−01	8.480E−01	9.578E−01	1.074E+00
400.0	3.447E−01	4.106E−01	4.822E−01	5.597E−01	6.430E−01	7.321E−01	8.271E−01	9.279E−01
500.0	3.123E−01	3.719E−01	4.369E−01	5.071E−01	5.826E−01	6.635E−01	7.496E−01	8.411E−01
600.0	2.912E−01	3.468E−01	4.074E−01	4.729E−01	5.434E−01	6.188E−01	6.992E−01	7.846E−01
700.0	2.766E−01	3.295E−01	3.871E−01	4.493E−01	5.163E−01	5.880E−01	6.644E−01	7.456E−01
800.0	2.662E−01	3.171E−01	3.725E−01	4.324E−01	4.969E−01	5.659E−01	6.394E−01	7.176E−01
900.0	2.584E−01	3.079E−01	3.617E−01	4.199E−01	4.825E−01	5.495E−01	6.210E−01	6.969E−01
1000.	2.525E−01	3.009E−01	3.534E−01	4.103E−01	4.715E−01	5.370E−01	6.069E−01	6.811E−01

Material: Polymethyl methacrylate (lucite, perspex)

Ion	Li	Be	B	C	N	O	F	Ne
(E/A_1) / MeV				$(-\mathrm{d}E/\rho\mathrm{d}\ell)$ / MeV cm^2 mg^{-1}				
0.025	2.534E+00	3.127E+00	3.592E+00	3.958E+00	4.294E+00	4.583E+00	4.813E+00	5.022E+00
0.030	2.757E+00	3.427E+00	3.963E+00	4.390E+00	4.776E+00	5.108E+00	5.373E+00	5.613E+00
0.040	3.121E+00	3.941E+00	4.610E+00	5.159E+00	5.641E+00	6.060E+00	6.399E+00	6.702E+00
0.050	3.391E+00	4.355E+00	5.155E+00	5.822E+00	6.401E+00	6.907E+00	7.321E+00	7.688E+00
0.060	3.587E+00	4.683E+00	5.609E+00	6.393E+00	7.071E+00	7.666E+00	8.155E+00	8.588E+00
0.070	3.725E+00	4.936E+00	5.981E+00	6.880E+00	7.659E+00	8.345E+00	8.912E+00	9.413E+00
0.080	3.820E+00	5.128E+00	6.280E+00	7.288E+00	8.167E+00	8.947E+00	9.594E+00	1.017E+01
0.090	3.884E+00	5.272E+00	6.518E+00	7.625E+00	8.602E+00	9.474E+00	1.020E+01	1.085E+01
0.100	3.924E+00	5.378E+00	6.705E+00	7.902E+00	8.969E+00	9.931E+00	1.074E+01	1.147E+01
0.150	3.937E+00	5.583E+00	7.168E+00	8.673E+00	1.008E+01	1.140E+01	1.256E+01	1.363E+01
0.200	3.829E+00	5.551E+00	7.256E+00	8.918E+00	1.051E+01	1.205E+01	1.343E+01	1.474E+01
0.250	3.690E+00	5.442E+00	7.206E+00	8.952E+00	1.066E+01	1.232E+01	1.385E+01	1.531E+01
0.300	3.547E+00	5.304E+00	7.097E+00	8.892E+00	1.067E+01	1.241E+01	1.403E+01	1.559E+01
0.400	3.276E+00	5.011E+00	6.819E+00	8.656E+00	1.050E+01	1.234E+01	1.406E+01	1.574E+01
0.500	3.035E+00	4.728E+00	6.523E+00	8.367E+00	1.024E+01	1.213E+01	1.390E+01	1.564E+01
0.600	2.824E+00	4.466E+00	6.234E+00	8.068E+00	9.947E+00	1.186E+01	1.365E+01	1.543E+01
0.700	2.639E+00	4.228E+00	5.961E+00	7.776E+00	9.649E+00	1.157E+01	1.337E+01	1.517E+01
0.800	2.476E+00	4.011E+00	5.706E+00	7.496E+00	9.355E+00	1.127E+01	1.308E+01	1.488E+01
0.900	2.331E+00	3.814E+00	5.468E+00	7.230E+00	9.070E+00	1.098E+01	1.278E+01	1.459E+01
1.000	2.202E+00	3.634E+00	5.248E+00	6.978E+00	8.796E+00	1.069E+01	1.249E+01	1.429E+01
1.500	1.725E+00	2.934E+00	4.352E+00	5.920E+00	7.607E+00	9.398E+00	1.112E+01	1.287E+01
2.000	1.420E+00	2.458E+00	3.709E+00	5.124E+00	6.675E+00	8.348E+00	9.983E+00	1.165E+01
2.500	1.208E+00	2.114E+00	3.228E+00	4.510E+00	5.936E+00	7.493E+00	9.035E+00	1.062E+01
3.000	1.054E+00	1.857E+00	2.857E+00	4.024E+00	5.338E+00	6.788E+00	8.241E+00	9.745E+00
4.000	8.438E−01	1.496E+00	2.324E+00	3.308E+00	4.436E+00	5.701E+00	6.995E+00	8.351E+00
5.000	7.073E−01	1.257E+00	1.961E+00	2.809E+00	3.792E+00	4.907E+00	6.067E+00	7.295E+00
6.000	6.114E−01	1.088E+00	1.700E+00	2.443E+00	3.312E+00	4.305E+00	5.353E+00	6.472E+00
7.000	5.401E−01	9.608E−01	1.503E+00	2.164E+00	2.941E+00	3.835E+00	4.789E+00	5.814E+00
8.000	4.850E−01	8.624E−01	1.349E+00	1.945E+00	2.647E+00	3.458E+00	4.333E+00	5.278E+00
9.000	4.409E−01	7.838E−01	1.226E+00	1.768E+00	2.409E+00	3.151E+00	3.957E+00	4.833E+00
10.00	4.048E−01	7.194E−01	1.125E+00	1.623E+00	2.212E+00	2.895E+00	3.643E+00	4.458E+00
15.00	2.911E−01	5.169E−01	8.075E−01	1.164E+00	1.586E+00	2.077E+00	2.624E+00	3.230E+00
20.00	2.302E−01	4.089E−01	6.384E−01	9.191E−01	1.252E+00	1.637E+00	2.071E+00	2.554E+00
25.00	1.920E−01	3.410E−01	5.323E−01	7.661E−01	1.043E+00	1.363E+00	1.724E+00	2.127E+00
30.00	1.655E−01	2.941E−01	4.592E−01	6.607E−01	8.989E−01	1.174E+00	1.486E+00	1.833E+00
40.00	1.312E−01	2.332E−01	3.641E−01	5.240E−01	7.128E−01	9.308E−01	1.177E+00	1.453E+00
50.00	1.098E−01	1.951E−01	3.048E−01	4.387E−01	5.968E−01	7.791E−01	9.856E−01	1.216E+00
60.00	9.504E−02	1.690E−01	2.640E−01	3.800E−01	5.170E−01	6.750E−01	8.540E−01	1.054E+00
70.00	8.427E−02	1.498E−01	2.341E−01	3.371E−01	4.587E−01	5.989E−01	7.578E−01	9.352E−01
80.00	7.604E−02	1.352E−01	2.113E−01	3.042E−01	4.140E−01	5.407E−01	6.841E−01	8.444E−01
90.00	6.953E−02	1.236E−01	1.932E−01	2.782E−01	3.787E−01	4.946E−01	6.259E−01	7.726E−01
100.0	6.425E−02	1.143E−01	1.786E−01	2.572E−01	3.501E−01	4.573E−01	5.787E−01	7.144E−01
150.0	4.800E−02	8.538E−02	1.335E−01	1.923E−01	2.618E−01	3.420E−01	4.330E−01	5.347E−01
200.0	3.961E−02	7.047E−02	1.102E−01	1.587E−01	2.162E−01	2.825E−01	3.577E−01	4.417E−01
250.0	3.450E−02	6.137E−02	9.595E−02	1.383E−01	1.883E−01	2.461E−01	3.116E−01	3.850E−01
300.0	3.106E−02	5.526E−02	8.640E−02	1.245E−01	1.696E−01	2.217E−01	2.807E−01	3.468E−01
400.0	2.677E−02	4.762E−02	7.447E−02	1.073E−01	1.462E−01	1.911E−01	2.420E−01	2.990E−01
500.0	2.422E−02	4.310E−02	6.741E−02	9.715E−02	1.323E−01	1.730E−01	2.191E−01	2.708E−01
600.0	2.257E−02	4.017E−02	6.282E−02	9.054E−02	1.233E−01	1.613E−01	2.043E−01	2.524E−01
700.0	2.144E−02	3.815E−02	5.966E−02	8.599E−02	1.171E−01	1.531E−01	1.940E−01	2.397E−01
800.0	2.062E−02	3.669E−02	5.739E−02	8.272E−02	1.127E−01	1.473E−01	1.866E−01	2.306E−01
900.0	2.002E−02	3.562E−02	5.571E−02	8.030E−02	1.094E−01	1.430E−01	1.812E−01	2.239E−01
1000.	1.956E−02	3.480E−02	5.443E−02	7.845E−02	1.069E−01	1.397E−01	1.770E−01	2.188E−01

Material: Polymethyl methacrylate (lucite, perspex)

Ion	Na	Mg	Al	Si	P	S	Cl	Ar
(E/A_1) / MeV				$(-\mathrm{d}E/\rho\mathrm{d}\ell)$ / MeV cm^2 mg^{-1}				
0.025	5.194E+00	5.404E+00	5.596E+00	5.788E+00	6.009E+00	6.191E+00	6.421E+00	6.564E+00
0.030	5.808E+00	6.031E+00	6.240E+00	6.446E+00	6.682E+00	6.883E+00	7.126E+00	7.283E+00
0.040	6.949E+00	7.205E+00	7.447E+00	7.681E+00	7.945E+00	8.180E+00	8.445E+00	8.624E+00
0.050	7.992E+00	8.289E+00	8.566E+00	8.832E+00	9.126E+00	9.394E+00	9.680E+00	9.878E+00
0.060	8.951E+00	9.292E+00	9.609E+00	9.908E+00	1.023E+01	1.054E+01	1.085E+01	1.106E+01
0.070	9.836E+00	1.022E+01	1.058E+01	1.092E+01	1.128E+01	1.161E+01	1.195E+01	1.219E+01
0.080	1.065E+01	1.109E+01	1.150E+01	1.187E+01	1.226E+01	1.263E+01	1.300E+01	1.326E+01
0.090	1.141E+01	1.190E+01	1.235E+01	1.276E+01	1.319E+01	1.360E+01	1.399E+01	1.428E+01
0.100	1.210E+01	1.265E+01	1.315E+01	1.360E+01	1.407E+01	1.452E+01	1.494E+01	1.525E+01
0.150	1.461E+01	1.548E+01	1.627E+01	1.698E+01	1.770E+01	1.837E+01	1.898E+01	1.947E+01
0.200	1.599E+01	1.711E+01	1.817E+01	1.913E+01	2.009E+01	2.101E+01	2.185E+01	2.254E+01
0.250	1.674E+01	1.805E+01	1.929E+01	2.044E+01	2.160E+01	2.272E+01	2.376E+01	2.464E+01
0.300	1.714E+01	1.858E+01	1.997E+01	2.126E+01	2.257E+01	2.385E+01	2.504E+01	2.608E+01
0.400	1.744E+01	1.905E+01	2.061E+01	2.208E+01	2.360E+01	2.510E+01	2.650E+01	2.775E+01
0.500	1.742E+01	1.912E+01	2.078E+01	2.237E+01	2.402E+01	2.565E+01	2.719E+01	2.859E+01
0.600	1.726E+01	1.901E+01	2.074E+01	2.240E+01	2.414E+01	2.587E+01	2.750E+01	2.899E+01
0.700	1.703E+01	1.881E+01	2.059E+01	2.229E+01	2.409E+01	2.589E+01	2.759E+01	2.915E+01
0.800	1.676E+01	1.856E+01	2.037E+01	2.210E+01	2.395E+01	2.580E+01	2.755E+01	2.915E+01
0.900	1.647E+01	1.828E+01	2.011E+01	2.187E+01	2.375E+01	2.564E+01	2.742E+01	2.906E+01
1.000	1.618E+01	1.799E+01	1.983E+01	2.160E+01	2.351E+01	2.542E+01	2.724E+01	2.890E+01
1.500	1.473E+01	1.652E+01	1.836E+01	2.014E+01	2.209E+01	2.407E+01	2.594E+01	2.766E+01
2.000	1.344E+01	1.518E+01	1.697E+01	1.872E+01	2.066E+01	2.263E+01	2.451E+01	2.623E+01
2.500	1.233E+01	1.401E+01	1.575E+01	1.745E+01	1.934E+01	2.128E+01	2.314E+01	2.483E+01
3.000	1.138E+01	1.299E+01	1.467E+01	1.632E+01	1.816E+01	2.006E+01	2.187E+01	2.353E+01
4.000	9.835E+00	1.132E+01	1.287E+01	1.442E+01	1.614E+01	1.794E+01	1.966E+01	2.125E+01
5.000	8.647E+00	1.002E+01	1.146E+01	1.290E+01	1.451E+01	1.620E+01	1.783E+01	1.935E+01
6.000	7.709E+00	8.974E+00	1.031E+01	1.166E+01	1.317E+01	1.476E+01	1.630E+01	1.774E+01
7.000	6.952E+00	8.125E+00	9.371E+00	1.063E+01	1.205E+01	1.354E+01	1.500E+01	1.637E+01
8.000	6.329E+00	7.421E+00	8.585E+00	9.770E+00	1.110E+01	1.251E+01	1.389E+01	1.519E+01
9.000	5.808E+00	6.829E+00	7.920E+00	9.036E+00	1.029E+01	1.161E+01	1.292E+01	1.417E+01
10.00	5.368E+00	6.325E+00	7.350E+00	8.404E+00	9.584E+00	1.084E+01	1.208E+01	1.327E+01
15.00	3.907E+00	4.632E+00	5.416E+00	6.236E+00	7.148E+00	8.125E+00	9.114E+00	1.008E+01
20.00	3.092E+00	3.676E+00	4.309E+00	4.978E+00	5.717E+00	6.512E+00	7.327E+00	8.142E+00
25.00	2.576E+00	3.065E+00	3.596E+00	4.162E+00	4.783E+00	5.452E+00	6.145E+00	6.847E+00
30.00	2.220E+00	2.641E+00	3.100E+00	3.591E+00	4.128E+00	4.706E+00	5.309E+00	5.926E+00
40.00	1.758E+00	2.092E+00	2.456E+00	2.847E+00	3.271E+00	3.728E+00	4.209E+00	4.708E+00
50.00	1.471E+00	1.751E+00	2.055E+00	2.382E+00	2.737E+00	3.118E+00	3.520E+00	3.941E+00
60.00	1.275E+00	1.517E+00	1.780E+00	2.064E+00	2.370E+00	2.699E+00	3.048E+00	3.414E+00
70.00	1.131E+00	1.347E+00	1.580E+00	1.831E+00	2.103E+00	2.394E+00	2.703E+00	3.029E+00
80.00	1.022E+00	1.215E+00	1.426E+00	1.654E+00	1.899E+00	2.161E+00	2.440E+00	2.734E+00
90.00	9.348E−01	1.112E+00	1.305E+00	1.514E+00	1.738E+00	1.978E+00	2.233E+00	2.502E+00
100.0	8.644E−01	1.029E+00	1.207E+00	1.400E+00	1.607E+00	1.829E+00	2.065E+00	2.314E+00
150.0	6.472E−01	7.703E−01	9.042E−01	1.049E+00	1.204E+00	1.370E+00	1.547E+00	1.735E+00
200.0	5.347E−01	6.366E−01	7.474E−01	8.671E−01	9.958E−01	1.133E+00	1.280E+00	1.435E+00
250.0	4.661E−01	5.549E−01	6.516E−01	7.561E−01	8.684E−01	9.885E−01	1.116E+00	1.252E+00
300.0	4.199E−01	5.000E−01	5.872E−01	6.814E−01	7.826E−01	8.910E−01	1.006E+00	1.129E+00
400.0	3.621E−01	4.313E−01	5.065E−01	5.879E−01	6.754E−01	7.690E−01	8.687E−01	9.746E−01
500.0	3.279E−01	3.906E−01	4.588E−01	5.325E−01	6.118E−01	6.966E−01	7.871E−01	8.831E−01
600.0	3.057E−01	3.641E−01	4.277E−01	4.965E−01	5.704E−01	6.496E−01	7.340E−01	8.236E−01
700.0	2.904E−01	3.459E−01	4.063E−01	4.716E−01	5.419E−01	6.171E−01	6.973E−01	7.825E−01
800.0	2.793E−01	3.328E−01	3.909E−01	4.538E−01	5.214E−01	5.938E−01	6.710E−01	7.530E−01
900.0	2.712E−01	3.231E−01	3.795E−01	4.406E−01	5.063E−01	5.766E−01	6.515E−01	7.311E−01
1000.	2.650E−01	3.157E−01	3.708E−01	4.305E−01	4.947E−01	5.634E−01	6.366E−01	7.144E−01

Material: Polystyrene

Ion	Li	Be	B	C	N	O	F	Ne
(E/A_1) / MeV				$(-\mathrm{d}E/\rho\mathrm{d}\ell)$ / MeV cm^2 mg^{-1}				
0.025	2.541E+00	3.127E+00	3.591E+00	3.960E+00	4.304E+00	4.602E+00	4.840E+00	5.057E+00
0.030	2.772E+00	3.434E+00	3.966E+00	4.395E+00	4.787E+00	5.127E+00	5.401E+00	5.649E+00
0.040	3.148E+00	3.963E+00	4.629E+00	5.175E+00	5.659E+00	6.083E+00	6.429E+00	6.739E+00
0.050	3.426E+00	4.392E+00	5.192E+00	5.856E+00	6.433E+00	6.940E+00	7.356E+00	7.728E+00
0.060	3.623E+00	4.729E+00	5.661E+00	6.445E+00	7.122E+00	7.716E+00	8.203E+00	8.637E+00
0.070	3.759E+00	4.984E+00	6.041E+00	6.946E+00	7.727E+00	8.414E+00	8.977E+00	9.476E+00
0.080	3.849E+00	5.174E+00	6.342E+00	7.362E+00	8.249E+00	9.032E+00	9.679E+00	1.025E+01
0.090	3.907E+00	5.313E+00	6.577E+00	7.702E+00	8.691E+00	9.572E+00	1.030E+01	1.095E+01
0.100	3.942E+00	5.413E+00	6.759E+00	7.977E+00	9.061E+00	1.004E+01	1.085E+01	1.158E+01
0.150	3.940E+00	5.594E+00	7.191E+00	8.714E+00	1.014E+01	1.148E+01	1.266E+01	1.375E+01
0.200	3.827E+00	5.553E+00	7.263E+00	8.935E+00	1.055E+01	1.209E+01	1.350E+01	1.482E+01
0.250	3.688E+00	5.441E+00	7.208E+00	8.961E+00	1.068E+01	1.235E+01	1.388E+01	1.535E+01
0.300	3.546E+00	5.304E+00	7.100E+00	8.899E+00	1.068E+01	1.244E+01	1.405E+01	1.562E+01
0.400	3.276E+00	5.014E+00	6.825E+00	8.665E+00	1.051E+01	1.236E+01	1.408E+01	1.576E+01
0.500	3.037E+00	4.733E+00	6.532E+00	8.380E+00	1.026E+01	1.215E+01	1.392E+01	1.566E+01
0.600	2.827E+00	4.473E+00	6.246E+00	8.085E+00	9.969E+00	1.189E+01	1.368E+01	1.546E+01
0.700	2.642E+00	4.236E+00	5.974E+00	7.795E+00	9.674E+00	1.160E+01	1.341E+01	1.520E+01
0.800	2.479E+00	4.019E+00	5.720E+00	7.517E+00	9.383E+00	1.131E+01	1.312E+01	1.492E+01
0.900	2.335E+00	3.822E+00	5.483E+00	7.251E+00	9.099E+00	1.101E+01	1.282E+01	1.462E+01
1.000	2.206E+00	3.642E+00	5.263E+00	7.000E+00	8.826E+00	1.073E+01	1.253E+01	1.433E+01
1.500	1.728E+00	2.941E+00	4.366E+00	5.940E+00	7.635E+00	9.436E+00	1.116E+01	1.291E+01
2.000	1.422E+00	2.463E+00	3.719E+00	5.140E+00	6.699E+00	8.381E+00	1.002E+01	1.168E+01
2.500	1.210E+00	2.119E+00	3.236E+00	4.523E+00	5.955E+00	7.520E+00	9.063E+00	1.065E+01
3.000	1.055E+00	1.860E+00	2.863E+00	4.035E+00	5.353E+00	6.810E+00	8.264E+00	9.768E+00
4.000	8.447E−01	1.498E+00	2.328E+00	3.315E+00	4.446E+00	5.715E+00	7.010E+00	8.365E+00
5.000	7.079E−01	1.259E+00	1.964E+00	2.814E+00	3.799E+00	4.916E+00	6.077E+00	7.304E+00
6.000	6.118E−01	1.088E+00	1.702E+00	2.446E+00	3.316E+00	4.311E+00	5.359E+00	6.477E+00
7.000	5.404E−01	9.614E−01	1.504E+00	2.166E+00	2.944E+00	3.839E+00	4.792E+00	5.817E+00
8.000	4.851E−01	8.628E−01	1.350E+00	1.946E+00	2.649E+00	3.461E+00	4.334E+00	5.278E+00
9.000	4.410E−01	7.840E−01	1.227E+00	1.769E+00	2.410E+00	3.152E+00	3.958E+00	4.832E+00
10.00	4.049E−01	7.195E−01	1.126E+00	1.623E+00	2.213E+00	2.896E+00	3.643E+00	4.457E+00
15.00	2.911E−01	5.169E−01	8.075E−01	1.163E+00	1.586E+00	2.076E+00	2.623E+00	3.228E+00
20.00	2.302E−01	4.088E−01	6.383E−01	9.189E−01	1.251E+00	1.637E+00	2.070E+00	2.552E+00
25.00	1.919E−01	3.409E−01	5.322E−01	7.658E−01	1.042E+00	1.362E+00	1.723E+00	2.126E+00
30.00	1.655E−01	2.940E−01	4.590E−01	6.604E−01	8.985E−01	1.174E+00	1.485E+00	1.832E+00
40.00	1.312E−01	2.331E−01	3.640E−01	5.238E−01	7.125E−01	9.303E−01	1.177E+00	1.452E+00
50.00	1.097E−01	1.950E−01	3.046E−01	4.384E−01	5.964E−01	7.787E−01	9.850E−01	1.215E+00
60.00	9.498E−02	1.689E−01	2.638E−01	3.798E−01	5.167E−01	6.746E−01	8.534E−01	1.053E+00
70.00	8.422E−02	1.497E−01	2.339E−01	3.368E−01	4.584E−01	5.985E−01	7.572E−01	9.345E−01
80.00	7.598E−02	1.351E−01	2.111E−01	3.040E−01	4.137E−01	5.403E−01	6.837E−01	8.438E−01
90.00	6.948E−02	1.235E−01	1.931E−01	2.780E−01	3.784E−01	4.943E−01	6.255E−01	7.721E−01
100.0	6.421E−02	1.142E−01	1.784E−01	2.570E−01	3.498E−01	4.569E−01	5.783E−01	7.139E−01
150.0	4.796E−02	8.531E−02	1.334E−01	1.921E−01	2.616E−01	3.418E−01	4.327E−01	5.343E−01
200.0	3.958E−02	7.040E−02	1.101E−01	1.586E−01	2.160E−01	2.822E−01	3.573E−01	4.413E−01
250.0	3.446E−02	6.131E−02	9.586E−02	1.381E−01	1.881E−01	2.459E−01	3.113E−01	3.846E−01
300.0	3.103E−02	5.520E−02	8.631E−02	1.244E−01	1.694E−01	2.214E−01	2.804E−01	3.464E−01
400.0	2.674E−02	4.757E−02	7.439E−02	1.072E−01	1.460E−01	1.909E−01	2.418E−01	2.987E−01
500.0	2.420E−02	4.306E−02	6.733E−02	9.704E−02	1.322E−01	1.728E−01	2.189E−01	2.705E−01
600.0	2.255E−02	4.012E−02	6.275E−02	9.044E−02	1.232E−01	1.611E−01	2.040E−01	2.521E−01
700.0	2.141E−02	3.810E−02	5.959E−02	8.589E−02	1.170E−01	1.530E−01	1.938E−01	2.395E−01
800.0	2.060E−02	3.665E−02	5.732E−02	8.262E−02	1.126E−01	1.472E−01	1.864E−01	2.304E−01
900.0	1.999E−02	3.558E−02	5.564E−02	8.020E−02	1.093E−01	1.429E−01	1.810E−01	2.236E−01
1000.	1.953E−02	3.476E−02	5.436E−02	7.835E−02	1.068E−01	1.396E−01	1.768E−01	2.185E−01

Material: Polystyrene

Ion	Na	Mg	Al	Si	P	S	Cl	Ar
(E/A_1) / MeV				$(-\mathrm{d}E/\rho\mathrm{d}\ell)$ / MeV cm^2 mg^{-1}				
0.025	5.234E+00	5.449E+00	5.647E+00	5.843E+00	6.072E+00	6.259E+00	6.496E+00	6.642E+00
0.030	5.850E+00	6.079E+00	6.293E+00	6.505E+00	6.750E+00	6.957E+00	7.208E+00	7.369E+00
0.040	6.992E+00	7.253E+00	7.503E+00	7.745E+00	8.021E+00	8.265E+00	8.540E+00	8.724E+00
0.050	8.036E+00	8.337E+00	8.623E+00	8.897E+00	9.205E+00	9.483E+00	9.782E+00	9.986E+00
0.060	8.999E+00	9.343E+00	9.666E+00	9.973E+00	1.031E+01	1.063E+01	1.095E+01	1.117E+01
0.070	9.896E+00	1.028E+01	1.064E+01	1.098E+01	1.135E+01	1.170E+01	1.205E+01	1.230E+01
0.080	1.073E+01	1.116E+01	1.157E+01	1.194E+01	1.234E+01	1.272E+01	1.309E+01	1.336E+01
0.090	1.150E+01	1.199E+01	1.243E+01	1.284E+01	1.328E+01	1.369E+01	1.409E+01	1.438E+01
0.100	1.221E+01	1.275E+01	1.325E+01	1.370E+01	1.417E+01	1.462E+01	1.504E+01	1.535E+01
0.150	1.475E+01	1.562E+01	1.642E+01	1.714E+01	1.787E+01	1.855E+01	1.917E+01	1.964E+01
0.200	1.608E+01	1.722E+01	1.829E+01	1.926E+01	2.025E+01	2.118E+01	2.204E+01	2.274E+01
0.250	1.680E+01	1.812E+01	1.937E+01	2.053E+01	2.171E+01	2.285E+01	2.391E+01	2.480E+01
0.300	1.718E+01	1.862E+01	2.001E+01	2.131E+01	2.264E+01	2.393E+01	2.514E+01	2.618E+01
0.400	1.746E+01	1.906E+01	2.063E+01	2.210E+01	2.363E+01	2.513E+01	2.654E+01	2.780E+01
0.500	1.744E+01	1.913E+01	2.080E+01	2.238E+01	2.404E+01	2.568E+01	2.722E+01	2.861E+01
0.600	1.729E+01	1.903E+01	2.076E+01	2.242E+01	2.416E+01	2.589E+01	2.753E+01	2.900E+01
0.700	1.706E+01	1.884E+01	2.061E+01	2.231E+01	2.412E+01	2.592E+01	2.762E+01	2.917E+01
0.800	1.680E+01	1.859E+01	2.040E+01	2.213E+01	2.398E+01	2.584E+01	2.759E+01	2.918E+01
0.900	1.651E+01	1.832E+01	2.015E+01	2.190E+01	2.379E+01	2.568E+01	2.747E+01	2.909E+01
1.000	1.622E+01	1.804E+01	1.987E+01	2.164E+01	2.355E+01	2.547E+01	2.729E+01	2.894E+01
1.500	1.477E+01	1.657E+01	1.841E+01	2.019E+01	2.215E+01	2.414E+01	2.601E+01	2.773E+01
2.000	1.348E+01	1.522E+01	1.702E+01	1.877E+01	2.071E+01	2.270E+01	2.458E+01	2.629E+01
2.500	1.236E+01	1.405E+01	1.579E+01	1.749E+01	1.939E+01	2.135E+01	2.320E+01	2.489E+01
3.000	1.140E+01	1.302E+01	1.470E+01	1.635E+01	1.820E+01	2.011E+01	2.192E+01	2.358E+01
4.000	9.853E+00	1.134E+01	1.290E+01	1.444E+01	1.617E+01	1.798E+01	1.970E+01	2.129E+01
5.000	8.658E+00	1.003E+01	1.147E+01	1.291E+01	1.453E+01	1.623E+01	1.786E+01	1.937E+01
6.000	7.716E+00	8.983E+00	1.032E+01	1.167E+01	1.318E+01	1.478E+01	1.632E+01	1.775E+01
7.000	6.955E+00	8.130E+00	9.377E+00	1.064E+01	1.206E+01	1.355E+01	1.501E+01	1.637E+01
8.000	6.330E+00	7.423E+00	8.588E+00	9.772E+00	1.110E+01	1.251E+01	1.389E+01	1.519E+01
9.000	5.809E+00	6.830E+00	7.921E+00	9.036E+00	1.029E+01	1.162E+01	1.293E+01	1.416E+01
10.00	5.367E+00	6.324E+00	7.350E+00	8.403E+00	9.583E+00	1.084E+01	1.208E+01	1.327E+01
15.00	3.904E+00	4.629E+00	5.413E+00	6.232E+00	7.142E+00	8.119E+00	9.105E+00	1.007E+01
20.00	3.090E+00	3.673E+00	4.305E+00	4.973E+00	5.711E+00	6.505E+00	7.318E+00	8.130E+00
25.00	2.574E+00	3.062E+00	3.593E+00	4.158E+00	4.777E+00	5.446E+00	6.136E+00	6.836E+00
30.00	2.218E+00	2.639E+00	3.098E+00	3.588E+00	4.123E+00	4.700E+00	5.301E+00	5.917E+00
40.00	1.757E+00	2.091E+00	2.454E+00	2.844E+00	3.268E+00	3.724E+00	4.204E+00	4.701E+00
50.00	1.470E+00	1.750E+00	2.053E+00	2.380E+00	2.734E+00	3.114E+00	3.516E+00	3.936E+00
60.00	1.274E+00	1.516E+00	1.779E+00	2.062E+00	2.368E+00	2.696E+00	3.044E+00	3.410E+00
70.00	1.130E+00	1.345E+00	1.578E+00	1.830E+00	2.101E+00	2.392E+00	2.700E+00	3.025E+00
80.00	1.021E+00	1.215E+00	1.425E+00	1.652E+00	1.897E+00	2.159E+00	2.438E+00	2.732E+00
90.00	9.340E−01	1.111E+00	1.304E+00	1.512E+00	1.736E+00	1.976E+00	2.231E+00	2.500E+00
100.0	8.637E−01	1.028E+00	1.206E+00	1.399E+00	1.606E+00	1.827E+00	2.063E+00	2.312E+00
150.0	6.466E−01	7.696E−01	9.034E−01	1.048E+00	1.203E+00	1.369E+00	1.546E+00	1.733E+00
200.0	5.342E−01	6.360E−01	7.467E−01	8.663E−01	9.948E−01	1.132E+00	1.279E+00	1.434E+00
250.0	4.656E−01	5.544E−01	6.510E−01	7.553E−01	8.675E−01	9.875E−01	1.115E+00	1.251E+00
300.0	4.194E−01	4.995E−01	5.866E−01	6.807E−01	7.818E−01	8.901E−01	1.005E+00	1.128E+00
400.0	3.617E−01	4.308E−01	5.060E−01	5.873E−01	6.746E−01	7.681E−01	8.678E−01	9.736E−01
500.0	3.276E−01	3.901E−01	4.583E−01	5.319E−01	6.111E−01	6.959E−01	7.862E−01	8.821E−01
600.0	3.053E−01	3.637E−01	4.272E−01	4.959E−01	5.698E−01	6.488E−01	7.331E−01	8.226E−01
700.0	2.900E−01	3.455E−01	4.058E−01	4.711E−01	5.413E−01	6.164E−01	6.965E−01	7.816E−01
800.0	2.790E−01	3.323E−01	3.904E−01	4.532E−01	5.208E−01	5.931E−01	6.702E−01	7.520E−01
900.0	2.709E−01	3.227E−01	3.790E−01	4.400E−01	5.056E−01	5.758E−01	6.507E−01	7.302E−01
1000.	2.646E−01	3.153E−01	3.704E−01	4.299E−01	4.940E−01	5.627E−01	6.358E−01	7.135E−01

Material: Polytetrafluoroethylene (Teflon)

Ion	Li	Be	B	C	N	O	F	Ne
(E/A_1) / MeV				$(-\mathrm{d}E/\rho\mathrm{d}\ell)$ / MeV cm^2 mg^{-1}				
0.025	1.603E+00	1.976E+00	2.267E+00	2.498E+00	2.696E+00	2.869E+00	3.020E+00	3.160E+00
0.030	1.750E+00	2.173E+00	2.509E+00	2.779E+00	3.008E+00	3.207E+00	3.380E+00	3.539E+00
0.040	1.999E+00	2.518E+00	2.939E+00	3.287E+00	3.579E+00	3.834E+00	4.053E+00	4.250E+00
0.050	2.196E+00	2.808E+00	3.312E+00	3.735E+00	4.091E+00	4.403E+00	4.670E+00	4.909E+00
0.060	2.352E+00	3.052E+00	3.636E+00	4.133E+00	4.554E+00	4.924E+00	5.241E+00	5.523E+00
0.070	2.474E+00	3.255E+00	3.916E+00	4.486E+00	4.973E+00	5.401E+00	5.769E+00	6.095E+00
0.080	2.568E+00	3.421E+00	4.156E+00	4.798E+00	5.349E+00	5.838E+00	6.256E+00	6.629E+00
0.090	2.640E+00	3.556E+00	4.360E+00	5.069E+00	5.685E+00	6.234E+00	6.705E+00	7.125E+00
0.100	2.694E+00	3.665E+00	4.531E+00	5.305E+00	5.983E+00	6.591E+00	7.116E+00	7.584E+00
0.150	2.799E+00	3.952E+00	5.044E+00	6.070E+00	7.012E+00	7.882E+00	8.654E+00	9.359E+00
0.200	2.774E+00	4.014E+00	5.229E+00	6.406E+00	7.524E+00	8.584E+00	9.546E+00	1.044E+01
0.250	2.705E+00	3.986E+00	5.268E+00	6.535E+00	7.764E+00	8.951E+00	1.005E+01	1.109E+01
0.300	2.623E+00	3.921E+00	5.240E+00	6.560E+00	7.860E+00	9.133E+00	1.032E+01	1.146E+01
0.400	2.454E+00	3.751E+00	5.101E+00	6.474E+00	7.853E+00	9.225E+00	1.052E+01	1.178E+01
0.500	2.295E+00	3.572E+00	4.924E+00	6.317E+00	7.732E+00	9.155E+00	1.050E+01	1.183E+01
0.600	2.151E+00	3.400E+00	4.740E+00	6.136E+00	7.566E+00	9.017E+00	1.040E+01	1.176E+01
0.700	2.023E+00	3.238E+00	4.560E+00	5.949E+00	7.384E+00	8.848E+00	1.025E+01	1.163E+01
0.800	1.908E+00	3.088E+00	4.387E+00	5.764E+00	7.196E+00	8.665E+00	1.007E+01	1.147E+01
0.900	1.804E+00	2.949E+00	4.224E+00	5.584E+00	7.008E+00	8.477E+00	9.886E+00	1.129E+01
1.000	1.711E+00	2.821E+00	4.070E+00	5.412E+00	6.824E+00	8.289E+00	9.696E+00	1.110E+01
1.500	1.358E+00	2.310E+00	3.425E+00	4.660E+00	5.991E+00	7.399E+00	8.768E+00	1.015E+01
2.000	1.127E+00	1.952E+00	2.946E+00	4.073E+00	5.311E+00	6.641E+00	7.950E+00	9.283E+00
2.500	9.650E−01	1.690E+00	2.581E+00	3.609E+00	4.757E+00	6.006E+00	7.249E+00	8.527E+00
3.000	8.452E−01	1.490E+00	2.295E+00	3.237E+00	4.300E+00	5.472E+00	6.650E+00	7.870E+00
4.000	6.807E−01	1.209E+00	1.879E+00	2.679E+00	3.600E+00	4.632E+00	5.690E+00	6.800E+00
5.000	5.730E−01	1.020E+00	1.593E+00	2.285E+00	3.092E+00	4.007E+00	4.961E+00	5.972E+00
6.000	4.969E−01	8.848E−01	1.385E+00	1.994E+00	2.709E+00	3.527E+00	4.393E+00	5.317E+00
7.000	4.401E−01	7.835E−01	1.227E+00	1.770E+00	2.411E+00	3.149E+00	3.939E+00	4.789E+00
8.000	3.960E−01	7.046E−01	1.104E+00	1.594E+00	2.174E+00	2.845E+00	3.570E+00	4.355E+00
9.000	3.606E−01	6.415E−01	1.005E+00	1.451E+00	1.981E+00	2.595E+00	3.265E+00	3.993E+00
10.00	3.316E−01	5.896E−01	9.230E−01	1.333E+00	1.821E+00	2.387E+00	3.009E+00	3.688E+00
15.00	2.398E−01	4.260E−01	6.656E−01	9.598E−01	1.310E+00	1.718E+00	2.174E+00	2.679E+00
20.00	1.903E−01	3.380E−01	5.279E−01	7.603E−01	1.036E+00	1.357E+00	1.718E+00	2.121E+00
25.00	1.591E−01	2.826E−01	4.412E−01	6.351E−01	8.647E−01	1.131E+00	1.432E+00	1.768E+00
30.00	1.374E−01	2.442E−01	3.813E−01	5.487E−01	7.467E−01	9.759E−01	1.235E+00	1.525E+00
40.00	1.092E−01	1.942E−01	3.032E−01	4.363E−01	5.936E−01	7.753E−01	9.810E−01	1.211E+00
50.00	9.158E−02	1.628E−01	2.543E−01	3.660E−01	4.979E−01	6.501E−01	8.225E−01	1.015E+00
60.00	7.941E−02	1.412E−01	2.206E−01	3.175E−01	4.321E−01	5.641E−01	7.137E−01	8.808E−01
70.00	7.049E−02	1.253E−01	1.958E−01	2.820E−01	3.837E−01	5.011E−01	6.340E−01	7.825E−01
80.00	6.367E−02	1.132E−01	1.769E−01	2.548E−01	3.467E−01	4.528E−01	5.730E−01	7.072E−01
90.00	5.827E−02	1.036E−01	1.619E−01	2.332E−01	3.174E−01	4.146E−01	5.247E−01	6.477E−01
100.0	5.389E−02	9.584E−02	1.498E−01	2.157E−01	2.937E−01	3.836E−01	4.854E−01	5.993E−01
150.0	4.037E−02	7.180E−02	1.122E−01	1.617E−01	2.202E−01	2.877E−01	3.642E−01	4.498E−01
200.0	3.337E−02	5.936E−02	9.281E−02	1.337E−01	1.821E−01	2.380E−01	3.013E−01	3.722E−01
250.0	2.909E−02	5.176E−02	8.093E−02	1.166E−01	1.588E−01	2.076E−01	2.629E−01	3.248E−01
300.0	2.622E−02	4.665E−02	7.295E−02	1.051E−01	1.432E−01	1.872E−01	2.370E−01	2.929E−01
400.0	2.263E−02	4.027E−02	6.297E−02	9.075E−02	1.236E−01	1.616E−01	2.047E−01	2.529E−01
500.0	2.051E−02	3.649E−02	5.706E−02	8.225E−02	1.120E−01	1.465E−01	1.856E−01	2.293E−01
600.0	1.913E−02	3.404E−02	5.323E−02	7.672E−02	1.045E−01	1.367E−01	1.731E−01	2.139E−01
700.0	1.818E−02	3.235E−02	5.059E−02	7.292E−02	9.935E−02	1.299E−01	1.646E−01	2.034E−01
800.0	1.750E−02	3.114E−02	4.870E−02	7.020E−02	9.564E−02	1.250E−01	1.584E−01	1.958E−01
900.0	1.700E−02	3.024E−02	4.730E−02	6.819E−02	9.290E−02	1.215E−01	1.539E−01	1.902E−01
1000.	1.661E−02	2.956E−02	4.624E−02	6.665E−02	9.081E−02	1.187E−01	1.504E−01	1.859E−01

Material: Polytetrafluoroethylene (Teflon)

Ion	Na	Mg	Al	Si	P	S	Cl	Ar
(E/A_1) / MeV				$(-\mathrm{d}E/\rho\mathrm{d}\ell)$ / MeV cm^2 mg^{-1}				
0.025	3.269E+00	3.392E+00	3.506E+00	3.618E+00	3.732E+00	3.835E+00	3.958E+00	4.048E+00
0.030	3.662E+00	3.795E+00	3.919E+00	4.040E+00	4.163E+00	4.276E+00	4.407E+00	4.504E+00
0.040	4.406E+00	4.561E+00	4.705E+00	4.843E+00	4.982E+00	5.116E+00	5.258E+00	5.369E+00
0.050	5.102E+00	5.284E+00	5.450E+00	5.607E+00	5.763E+00	5.916E+00	6.072E+00	6.194E+00
0.060	5.754E+00	5.967E+00	6.159E+00	6.337E+00	6.513E+00	6.686E+00	6.857E+00	6.991E+00
0.070	6.367E+00	6.612E+00	6.833E+00	7.034E+00	7.233E+00	7.428E+00	7.616E+00	7.764E+00
0.080	6.942E+00	7.222E+00	7.473E+00	7.701E+00	7.924E+00	8.142E+00	8.349E+00	8.512E+00
0.090	7.482E+00	7.798E+00	8.081E+00	8.337E+00	8.587E+00	8.829E+00	9.056E+00	9.236E+00
0.100	7.987E+00	8.341E+00	8.659E+00	8.945E+00	9.221E+00	9.488E+00	9.738E+00	9.936E+00
0.150	9.996E+00	1.056E+01	1.106E+01	1.152E+01	1.196E+01	1.238E+01	1.276E+01	1.307E+01
0.200	1.128E+01	1.204E+01	1.273E+01	1.337E+01	1.398E+01	1.456E+01	1.510E+01	1.555E+01
0.250	1.208E+01	1.299E+01	1.385E+01	1.463E+01	1.541E+01	1.615E+01	1.683E+01	1.743E+01
0.300	1.257E+01	1.360E+01	1.458E+01	1.549E+01	1.640E+01	1.728E+01	1.809E+01	1.881E+01
0.400	1.304E+01	1.422E+01	1.537E+01	1.646E+01	1.756E+01	1.864E+01	1.965E+01	2.057E+01
0.500	1.317E+01	1.444E+01	1.569E+01	1.689E+01	1.811E+01	1.933E+01	2.048E+01	2.152E+01
0.600	1.315E+01	1.447E+01	1.579E+01	1.705E+01	1.837E+01	1.967E+01	2.091E+01	2.205E+01
0.700	1.305E+01	1.441E+01	1.577E+01	1.708E+01	1.845E+01	1.982E+01	2.112E+01	2.233E+01
0.800	1.291E+01	1.429E+01	1.568E+01	1.702E+01	1.843E+01	1.985E+01	2.120E+01	2.245E+01
0.900	1.274E+01	1.414E+01	1.554E+01	1.691E+01	1.836E+01	1.981E+01	2.120E+01	2.248E+01
1.000	1.256E+01	1.396E+01	1.538E+01	1.676E+01	1.824E+01	1.972E+01	2.113E+01	2.244E+01
1.500	1.160E+01	1.300E+01	1.444E+01	1.584E+01	1.738E+01	1.892E+01	2.041E+01	2.178E+01
2.000	1.070E+01	1.207E+01	1.349E+01	1.488E+01	1.641E+01	1.797E+01	1.947E+01	2.085E+01
2.500	9.889E+00	1.122E+01	1.261E+01	1.397E+01	1.548E+01	1.703E+01	1.852E+01	1.989E+01
3.000	9.180E+00	1.047E+01	1.181E+01	1.314E+01	1.463E+01	1.615E+01	1.762E+01	1.897E+01
4.000	8.003E+00	9.203E+00	1.046E+01	1.171E+01	1.312E+01	1.458E+01	1.599E+01	1.729E+01
5.000	7.076E+00	8.191E+00	9.366E+00	1.054E+01	1.187E+01	1.326E+01	1.460E+01	1.585E+01
6.000	6.334E+00	7.369E+00	8.467E+00	9.573E+00	1.082E+01	1.213E+01	1.341E+01	1.460E+01
7.000	5.727E+00	6.692E+00	7.719E+00	8.760E+00	9.936E+00	1.117E+01	1.239E+01	1.353E+01
8.000	5.225E+00	6.126E+00	7.088E+00	8.070E+00	9.178E+00	1.035E+01	1.150E+01	1.259E+01
9.000	4.803E+00	5.647E+00	6.551E+00	7.478E+00	8.524E+00	9.631E+00	1.073E+01	1.177E+01
10.00	4.444E+00	5.237E+00	6.089E+00	6.966E+00	7.954E+00	9.005E+00	1.005E+01	1.105E+01
15.00	3.244E+00	3.849E+00	4.504E+00	5.190E+00	5.958E+00	6.782E+00	7.618E+00	8.433E+00
20.00	2.571E+00	3.058E+00	3.588E+00	4.149E+00	4.772E+00	5.445E+00	6.135E+00	6.822E+00
25.00	2.143E+00	2.552E+00	2.997E+00	3.471E+00	3.995E+00	4.561E+00	5.148E+00	5.740E+00
30.00	1.848E+00	2.201E+00	2.585E+00	2.997E+00	3.449E+00	3.938E+00	4.448E+00	4.968E+00
40.00	1.466E+00	1.745E+00	2.050E+00	2.378E+00	2.735E+00	3.121E+00	3.526E+00	3.947E+00
50.00	1.229E+00	1.462E+00	1.717E+00	1.991E+00	2.289E+00	2.610E+00	2.949E+00	3.304E+00
60.00	1.066E+00	1.268E+00	1.489E+00	1.727E+00	1.984E+00	2.261E+00	2.554E+00	2.862E+00
70.00	9.467E−01	1.127E+00	1.322E+00	1.533E+00	1.761E+00	2.006E+00	2.266E+00	2.540E+00
80.00	8.556E−01	1.018E+00	1.195E+00	1.386E+00	1.591E+00	1.812E+00	2.047E+00	2.294E+00
90.00	7.836E−01	9.325E−01	1.094E+00	1.269E+00	1.457E+00	1.659E+00	1.874E+00	2.100E+00
100.0	7.251E−01	8.629E−01	1.013E+00	1.174E+00	1.349E+00	1.535E+00	1.733E+00	1.943E+00
150.0	5.443E−01	6.480E−01	7.606E−01	8.823E−01	1.013E+00	1.153E+00	1.302E+00	1.460E+00
200.0	4.506E−01	5.364E−01	6.298E−01	7.307E−01	8.392E−01	9.552E−01	1.079E+00	1.210E+00
250.0	3.932E−01	4.682E−01	5.498E−01	6.379E−01	7.327E−01	8.341E−01	9.421E−01	1.057E+00
300.0	3.546E−01	4.223E−01	4.959E−01	5.755E−01	6.611E−01	7.526E−01	8.501E−01	9.537E−01
400.0	3.063E−01	3.648E−01	4.285E−01	4.973E−01	5.713E−01	6.505E−01	7.349E−01	8.246E−01
500.0	2.777E−01	3.308E−01	3.885E−01	4.510E−01	5.181E−01	5.900E−01	6.667E−01	7.480E−01
600.0	2.591E−01	3.086E−01	3.626E−01	4.209E−01	4.836E−01	5.507E−01	6.223E−01	6.983E−01
700.0	2.463E−01	2.934E−01	3.447E−01	4.001E−01	4.598E−01	5.236E−01	5.917E−01	6.640E−01
800.0	2.371E−01	2.825E−01	3.318E−01	3.852E−01	4.427E−01	5.042E−01	5.697E−01	6.394E−01
900.0	2.303E−01	2.744E−01	3.224E−01	3.743E−01	4.301E−01	4.898E−01	5.535E−01	6.212E−01
1000.	2.252E−01	2.683E−01	3.151E−01	3.659E−01	4.204E−01	4.789E−01	5.412E−01	6.073E−01

Material: Propane

Ion	Li	Be	B	C	N	O	F	Ne
(E/A_1) / MeV				$(-\mathrm{d}E/\rho\mathrm{d}\ell)$ / MeV cm^2 mg^{-1}				
0.025	3.332E+00	4.135E+00	4.766E+00	5.255E+00	5.720E+00	6.114E+00	6.408E+00	6.674E+00
0.030	3.612E+00	4.515E+00	5.239E+00	5.811E+00	6.340E+00	6.792E+00	7.134E+00	7.439E+00
0.040	4.056E+00	5.152E+00	6.053E+00	6.786E+00	7.441E+00	8.008E+00	8.448E+00	8.836E+00
0.050	4.373E+00	5.649E+00	6.721E+00	7.610E+00	8.391E+00	9.073E+00	9.611E+00	1.009E+01
0.060	4.592E+00	6.030E+00	7.261E+00	8.302E+00	9.212E+00	1.001E+01	1.065E+01	1.121E+01
0.070	4.739E+00	6.313E+00	7.690E+00	8.877E+00	9.916E+00	1.083E+01	1.158E+01	1.223E+01
0.080	4.835E+00	6.519E+00	8.024E+00	9.345E+00	1.051E+01	1.155E+01	1.240E+01	1.314E+01
0.090	4.893E+00	6.667E+00	8.281E+00	9.723E+00	1.101E+01	1.216E+01	1.311E+01	1.396E+01
0.100	4.924E+00	6.771E+00	8.476E+00	1.002E+01	1.142E+01	1.268E+01	1.374E+01	1.468E+01
0.150	4.880E+00	6.928E+00	8.912E+00	1.080E+01	1.258E+01	1.426E+01	1.573E+01	1.709E+01
0.200	4.713E+00	6.834E+00	8.940E+00	1.099E+01	1.297E+01	1.489E+01	1.661E+01	1.823E+01
0.250	4.519E+00	6.663E+00	8.827E+00	1.097E+01	1.306E+01	1.511E+01	1.698E+01	1.877E+01
0.300	4.326E+00	6.468E+00	8.657E+00	1.084E+01	1.300E+01	1.514E+01	1.710E+01	1.900E+01
0.400	3.970E+00	6.070E+00	8.263E+00	1.048E+01	1.271E+01	1.495E+01	1.701E+01	1.903E+01
0.500	3.659E+00	5.698E+00	7.862E+00	1.008E+01	1.233E+01	1.461E+01	1.672E+01	1.881E+01
0.600	3.390E+00	5.360E+00	7.483E+00	9.680E+00	1.193E+01	1.422E+01	1.636E+01	1.847E+01
0.700	3.157E+00	5.055E+00	7.129E+00	9.295E+00	1.153E+01	1.382E+01	1.596E+01	1.809E+01
0.800	2.952E+00	4.781E+00	6.802E+00	8.932E+00	1.114E+01	1.342E+01	1.556E+01	1.770E+01
0.900	2.773E+00	4.533E+00	6.501E+00	8.590E+00	1.077E+01	1.303E+01	1.517E+01	1.730E+01
1.000	2.613E+00	4.309E+00	6.223E+00	8.271E+00	1.042E+01	1.266E+01	1.478E+01	1.690E+01
1.500	2.031E+00	3.450E+00	5.115E+00	6.952E+00	8.924E+00	1.102E+01	1.304E+01	1.508E+01
2.000	1.663E+00	2.875E+00	4.335E+00	5.981E+00	7.783E+00	9.728E+00	1.163E+01	1.356E+01
2.500	1.411E+00	2.465E+00	3.759E+00	5.244E+00	6.891E+00	8.693E+00	1.047E+01	1.231E+01
3.000	1.228E+00	2.159E+00	3.318E+00	4.666E+00	6.178E+00	7.849E+00	9.522E+00	1.126E+01
4.000	9.798E−01	1.735E+00	2.690E+00	3.822E+00	5.115E+00	6.564E+00	8.047E+00	9.601E+00
5.000	8.194E−01	1.455E+00	2.266E+00	3.239E+00	4.363E+00	5.636E+00	6.961E+00	8.365E+00
6.000	7.071E−01	1.256E+00	1.961E+00	2.813E+00	3.805E+00	4.937E+00	6.132E+00	7.408E+00
7.000	6.238E−01	1.109E+00	1.732E+00	2.489E+00	3.376E+00	4.394E+00	5.480E+00	6.648E+00
8.000	5.594E−01	9.941E−01	1.554E+00	2.236E+00	3.037E+00	3.960E+00	4.955E+00	6.030E+00
9.000	5.080E−01	9.026E−01	1.411E+00	2.031E+00	2.763E+00	3.606E+00	4.523E+00	5.519E+00
10.00	4.660E−01	8.279E−01	1.294E+00	1.863E+00	2.536E+00	3.313E+00	4.163E+00	5.090E+00
15.00	3.341E−01	5.932E−01	9.263E−01	1.334E+00	1.816E+00	2.375E+00	2.998E+00	3.686E+00
20.00	2.637E−01	4.683E−01	7.310E−01	1.052E+00	1.432E+00	1.871E+00	2.366E+00	2.914E+00
25.00	2.195E−01	3.900E−01	6.087E−01	8.759E−01	1.192E+00	1.557E+00	1.968E+00	2.427E+00
30.00	1.891E−01	3.359E−01	5.245E−01	7.546E−01	1.026E+00	1.340E+00	1.695E+00	2.091E+00
40.00	1.496E−01	2.659E−01	4.153E−01	5.976E−01	8.128E−01	1.061E+00	1.342E+00	1.656E+00
50.00	1.250E−01	2.222E−01	3.471E−01	4.996E−01	6.797E−01	8.874E−01	1.122E+00	1.385E+00
60.00	1.082E−01	1.923E−01	3.004E−01	4.324E−01	5.883E−01	7.681E−01	9.717E−01	1.199E+00
70.00	9.583E−02	1.704E−01	2.662E−01	3.833E−01	5.216E−01	6.810E−01	8.616E−01	1.063E+00
80.00	8.641E−02	1.536E−01	2.401E−01	3.457E−01	4.705E−01	6.144E−01	7.774E−01	9.595E−01
90.00	7.898E−02	1.404E−01	2.195E−01	3.160E−01	4.302E−01	5.618E−01	7.109E−01	8.775E−01
100.0	7.295E−02	1.297E−01	2.027E−01	2.920E−01	3.975E−01	5.191E−01	6.570E−01	8.110E−01
150.0	5.441E−02	9.678E−02	1.513E−01	2.179E−01	2.967E−01	3.877E−01	4.908E−01	6.061E−01
200.0	4.486E−02	7.979E−02	1.247E−01	1.797E−01	2.447E−01	3.198E−01	4.049E−01	5.001E−01
250.0	3.903E−02	6.943E−02	1.086E−01	1.564E−01	2.130E−01	2.784E−01	3.526E−01	4.355E−01
300.0	3.512E−02	6.248E−02	9.770E−02	1.408E−01	1.917E−01	2.506E−01	3.174E−01	3.921E−01
400.0	3.024E−02	5.380E−02	8.413E−02	1.212E−01	1.651E−01	2.159E−01	2.734E−01	3.378E−01
500.0	2.735E−02	4.866E−02	7.610E−02	1.097E−01	1.494E−01	1.953E−01	2.474E−01	3.056E−01
600.0	2.547E−02	4.532E−02	7.088E−02	1.022E−01	1.392E−01	1.819E−01	2.304E−01	2.847E−01
700.0	2.418E−02	4.302E−02	6.728E−02	9.696E−02	1.321E−01	1.727E−01	2.188E−01	2.703E−01
800.0	2.325E−02	4.136E−02	6.469E−02	9.324E−02	1.270E−01	1.661E−01	2.104E−01	2.599E−01
900.0	2.256E−02	4.014E−02	6.277E−02	9.048E−02	1.233E−01	1.611E−01	2.041E−01	2.523E−01
1000.	2.203E−02	3.920E−02	6.131E−02	8.837E−02	1.204E−01	1.574E−01	1.994E−01	2.464E−01

Material: Propane

Ion	Na	Mg	Al	Si	P	S	Cl	Ar
(E/A_1) / MeV				$(-\mathrm{d}E/\rho\mathrm{d}\ell)$ / MeV cm^2 mg^{-1}				
0.025	6.899E+00	7.191E+00	7.454E+00	7.717E+00	8.040E+00	8.294E+00	8.625E+00	8.813E+00
0.030	7.695E+00	8.003E+00	8.287E+00	8.569E+00	8.913E+00	9.193E+00	9.540E+00	9.748E+00
0.040	9.160E+00	9.507E+00	9.835E+00	1.015E+01	1.054E+01	1.086E+01	1.124E+01	1.147E+01
0.050	1.048E+01	1.088E+01	1.126E+01	1.161E+01	1.204E+01	1.240E+01	1.280E+01	1.307E+01
0.060	1.169E+01	1.214E+01	1.257E+01	1.297E+01	1.343E+01	1.384E+01	1.427E+01	1.456E+01
0.070	1.278E+01	1.330E+01	1.378E+01	1.422E+01	1.473E+01	1.518E+01	1.564E+01	1.596E+01
0.080	1.378E+01	1.436E+01	1.490E+01	1.539E+01	1.594E+01	1.644E+01	1.694E+01	1.728E+01
0.090	1.469E+01	1.534E+01	1.594E+01	1.649E+01	1.708E+01	1.763E+01	1.816E+01	1.853E+01
0.100	1.551E+01	1.623E+01	1.690E+01	1.750E+01	1.814E+01	1.874E+01	1.931E+01	1.971E+01
0.150	1.836E+01	1.948E+01	2.051E+01	2.144E+01	2.239E+01	2.329E+01	2.410E+01	2.473E+01
0.200	1.981E+01	2.123E+01	2.257E+01	2.379E+01	2.504E+01	2.623E+01	2.732E+01	2.821E+01
0.250	2.054E+01	2.217E+01	2.372E+01	2.516E+01	2.663E+01	2.806E+01	2.937E+01	3.048E+01
0.300	2.091E+01	2.268E+01	2.438E+01	2.597E+01	2.761E+01	2.921E+01	3.069E+01	3.198E+01
0.400	2.110E+01	2.305E+01	2.495E+01	2.673E+01	2.859E+01	3.042E+01	3.213E+01	3.365E+01
0.500	2.096E+01	2.301E+01	2.502E+01	2.692E+01	2.892E+01	3.090E+01	3.276E+01	3.443E+01
0.600	2.068E+01	2.278E+01	2.486E+01	2.684E+01	2.893E+01	3.102E+01	3.297E+01	3.474E+01
0.700	2.033E+01	2.246E+01	2.459E+01	2.662E+01	2.878E+01	3.094E+01	3.296E+01	3.480E+01
0.800	1.994E+01	2.210E+01	2.426E+01	2.632E+01	2.852E+01	3.074E+01	3.281E+01	3.470E+01
0.900	1.955E+01	2.171E+01	2.389E+01	2.597E+01	2.821E+01	3.046E+01	3.257E+01	3.449E+01
1.000	1.915E+01	2.132E+01	2.350E+01	2.560E+01	2.786E+01	3.013E+01	3.227E+01	3.423E+01
1.500	1.727E+01	1.939E+01	2.156E+01	2.365E+01	2.594E+01	2.827E+01	3.046E+01	3.247E+01
2.000	1.566E+01	1.771E+01	1.981E+01	2.185E+01	2.411E+01	2.641E+01	2.859E+01	3.059E+01
2.500	1.430E+01	1.626E+01	1.829E+01	2.027E+01	2.246E+01	2.472E+01	2.685E+01	2.882E+01
3.000	1.315E+01	1.503E+01	1.697E+01	1.888E+01	2.101E+01	2.320E+01	2.528E+01	2.721E+01
4.000	1.131E+01	1.303E+01	1.482E+01	1.660E+01	1.858E+01	2.063E+01	2.260E+01	2.443E+01
5.000	9.914E+00	1.149E+01	1.314E+01	1.480E+01	1.664E+01	1.856E+01	2.042E+01	2.215E+01
6.000	8.822E+00	1.027E+01	1.180E+01	1.334E+01	1.506E+01	1.686E+01	1.861E+01	2.026E+01
7.000	7.945E+00	9.286E+00	1.071E+01	1.215E+01	1.375E+01	1.544E+01	1.709E+01	1.865E+01
8.000	7.227E+00	8.473E+00	9.799E+00	1.115E+01	1.265E+01	1.424E+01	1.580E+01	1.729E+01
9.000	6.629E+00	7.791E+00	9.032E+00	1.030E+01	1.171E+01	1.321E+01	1.469E+01	1.610E+01
10.00	6.124E+00	7.213E+00	8.377E+00	9.576E+00	1.091E+01	1.232E+01	1.372E+01	1.507E+01
15.00	4.454E+00	5.278E+00	6.166E+00	7.096E+00	8.122E+00	9.220E+00	1.033E+01	1.143E+01
20.00	3.526E+00	4.188E+00	4.905E+00	5.663E+00	6.495E+00	7.389E+00	8.305E+00	9.227E+00
25.00	2.937E+00	3.492E+00	4.094E+00	4.735E+00	5.435E+00	6.188E+00	6.968E+00	7.762E+00
30.00	2.530E+00	3.009E+00	3.530E+00	4.086E+00	4.692E+00	5.344E+00	6.023E+00	6.721E+00
40.00	2.003E+00	2.383E+00	2.796E+00	3.239E+00	3.720E+00	4.236E+00	4.779E+00	5.343E+00
50.00	1.675E+00	1.993E+00	2.338E+00	2.710E+00	3.111E+00	3.542E+00	3.997E+00	4.474E+00
60.00	1.450E+00	1.725E+00	2.024E+00	2.347E+00	2.694E+00	3.066E+00	3.461E+00	3.876E+00
70.00	1.286E+00	1.530E+00	1.795E+00	2.081E+00	2.389E+00	2.719E+00	3.069E+00	3.438E+00
80.00	1.161E+00	1.381E+00	1.620E+00	1.879E+00	2.157E+00	2.454E+00	2.770E+00	3.104E+00
90.00	1.062E+00	1.263E+00	1.482E+00	1.719E+00	1.973E+00	2.245E+00	2.534E+00	2.840E+00
100.0	9.812E−01	1.168E+00	1.370E+00	1.589E+00	1.824E+00	2.075E+00	2.343E+00	2.625E+00
150.0	7.335E−01	8.730E−01	1.025E+00	1.189E+00	1.365E+00	1.553E+00	1.753E+00	1.966E+00
200.0	6.054E−01	7.207E−01	8.462E−01	9.817E−01	1.127E+00	1.283E+00	1.449E+00	1.625E+00
250.0	5.272E−01	6.278E−01	7.371E−01	8.553E−01	9.823E−01	1.118E+00	1.263E+00	1.416E+00
300.0	4.747E−01	5.653E−01	6.638E−01	7.703E−01	8.848E−01	1.007E+00	1.138E+00	1.276E+00
400.0	4.090E−01	4.871E−01	5.721E−01	6.640E−01	7.628E−01	8.685E−01	9.811E−01	1.101E+00
500.0	3.701E−01	4.408E−01	5.178E−01	6.010E−01	6.905E−01	7.862E−01	8.882E−01	9.966E−01
600.0	3.448E−01	4.107E−01	4.824E−01	5.600E−01	6.434E−01	7.327E−01	8.278E−01	9.289E−01
700.0	3.274E−01	3.899E−01	4.581E−01	5.317E−01	6.109E−01	6.957E−01	7.861E−01	8.821E−01
800.0	3.148E−01	3.750E−01	4.405E−01	5.114E−01	5.876E−01	6.691E−01	7.561E−01	8.484E−01
900.0	3.055E−01	3.639E−01	4.275E−01	4.963E−01	5.703E−01	6.495E−01	7.339E−01	8.235E−01
1000.	2.984E−01	3.555E−01	4.176E−01	4.848E−01	5.570E−01	6.344E−01	7.169E−01	8.045E−01

Material: Silicon dioxide

Ion	Li	Be	B	C	N	O	F	Ne
(E/A_1) / MeV				$(-\mathrm{d}E/\rho\mathrm{d}\ell)$ / MeV cm^2 mg^{-1}				
0.025	1.481E+00	1.894E+00	2.237E+00	2.522E+00	2.767E+00	2.982E+00	3.170E+00	3.340E+00
0.030	1.600E+00	2.058E+00	2.443E+00	2.767E+00	3.047E+00	3.293E+00	3.508E+00	3.702E+00
0.040	1.800E+00	2.337E+00	2.798E+00	3.196E+00	3.541E+00	3.847E+00	4.116E+00	4.357E+00
0.050	1.961E+00	2.571E+00	3.099E+00	3.564E+00	3.970E+00	4.333E+00	4.653E+00	4.942E+00
0.060	2.091E+00	2.770E+00	3.361E+00	3.887E+00	4.349E+00	4.766E+00	5.135E+00	5.469E+00
0.070	2.197E+00	2.938E+00	3.590E+00	4.174E+00	4.690E+00	5.158E+00	5.573E+00	5.950E+00
0.080	2.280E+00	3.080E+00	3.790E+00	4.429E+00	4.997E+00	5.514E+00	5.973E+00	6.392E+00
0.090	2.347E+00	3.198E+00	3.963E+00	4.656E+00	5.274E+00	5.839E+00	6.341E+00	6.801E+00
0.100	2.399E+00	3.296E+00	4.112E+00	4.856E+00	5.523E+00	6.135E+00	6.680E+00	7.180E+00
0.150	2.520E+00	3.576E+00	4.582E+00	5.536E+00	6.419E+00	7.245E+00	7.991E+00	8.682E+00
0.200	2.526E+00	3.664E+00	4.781E+00	5.867E+00	6.901E+00	7.888E+00	8.796E+00	9.650E+00
0.250	2.488E+00	3.670E+00	4.853E+00	6.022E+00	7.156E+00	8.255E+00	9.279E+00	1.026E+01
0.300	2.432E+00	3.638E+00	4.861E+00	6.085E+00	7.287E+00	8.465E+00	9.572E+00	1.064E+01
0.400	2.302E+00	3.521E+00	4.786E+00	6.072E+00	7.359E+00	8.639E+00	9.852E+00	1.104E+01
0.500	2.170E+00	3.379E+00	4.657E+00	5.972E+00	7.305E+00	8.644E+00	9.921E+00	1.118E+01
0.600	2.046E+00	3.233E+00	4.508E+00	5.835E+00	7.192E+00	8.566E+00	9.882E+00	1.118E+01
0.700	1.932E+00	3.092E+00	4.355E+00	5.681E+00	7.049E+00	8.443E+00	9.783E+00	1.111E+01
0.800	1.829E+00	2.958E+00	4.203E+00	5.521E+00	6.892E+00	8.297E+00	9.650E+00	1.100E+01
0.900	1.735E+00	2.833E+00	4.057E+00	5.362E+00	6.729E+00	8.137E+00	9.498E+00	1.086E+01
1.000	1.649E+00	2.716E+00	3.917E+00	5.207E+00	6.565E+00	7.972E+00	9.335E+00	1.070E+01
1.500	1.321E+00	2.242E+00	3.321E+00	4.515E+00	5.804E+00	7.164E+00	8.499E+00	9.851E+00
2.000	1.102E+00	1.905E+00	2.871E+00	3.965E+00	5.168E+00	6.457E+00	7.738E+00	9.046E+00
2.500	9.471E−01	1.656E+00	2.525E+00	3.527E+00	4.645E+00	5.860E+00	7.079E+00	8.335E+00
3.000	8.318E−01	1.464E+00	2.252E+00	3.172E+00	4.212E+00	5.354E+00	6.512E+00	7.713E+00
4.000	6.725E−01	1.193E+00	1.852E+00	2.638E+00	3.542E+00	4.552E+00	5.596E+00	6.693E+00
5.000	5.676E−01	1.009E+00	1.575E+00	2.258E+00	3.052E+00	3.952E+00	4.896E+00	5.897E+00
6.000	4.931E−01	8.775E−01	1.372E+00	1.974E+00	2.681E+00	3.488E+00	4.347E+00	5.265E+00
7.000	4.374E−01	7.783E−01	1.218E+00	1.756E+00	2.391E+00	3.121E+00	3.906E+00	4.752E+00
8.000	3.940E−01	7.009E−01	1.097E+00	1.584E+00	2.160E+00	2.825E+00	3.547E+00	4.329E+00
9.000	3.592E−01	6.388E−01	1.000E+00	1.444E+00	1.970E+00	2.581E+00	3.248E+00	3.975E+00
10.00	3.306E−01	5.877E−01	9.198E−01	1.328E+00	1.813E+00	2.377E+00	2.997E+00	3.676E+00
15.00	2.398E−01	4.259E−01	6.655E−01	9.596E−01	1.310E+00	1.717E+00	2.174E+00	2.681E+00
20.00	1.907E−01	3.387E−01	5.288E−01	7.617E−01	1.038E+00	1.360E+00	1.722E+00	2.127E+00
25.00	1.596E−01	2.835E−01	4.427E−01	6.372E−01	8.676E−01	1.135E+00	1.437E+00	1.775E+00
30.00	1.380E−01	2.453E−01	3.829E−01	5.511E−01	7.500E−01	9.802E−01	1.241E+00	1.533E+00
40.00	1.099E−01	1.953E−01	3.050E−01	4.389E−01	5.971E−01	7.799E−01	9.869E−01	1.218E+00
50.00	9.221E−02	1.639E−01	2.560E−01	3.685E−01	5.014E−01	6.547E−01	8.283E−01	1.022E+00
60.00	8.002E−02	1.423E−01	2.223E−01	3.200E−01	4.354E−01	5.685E−01	7.193E−01	8.878E−01
70.00	7.108E−02	1.264E−01	1.975E−01	2.844E−01	3.870E−01	5.053E−01	6.394E−01	7.892E−01
80.00	6.424E−02	1.142E−01	1.785E−01	2.571E−01	3.498E−01	4.569E−01	5.781E−01	7.136E−01
90.00	5.882E−02	1.046E−01	1.635E−01	2.354E−01	3.204E−01	4.185E−01	5.297E−01	6.538E−01
100.0	5.442E−02	9.678E−02	1.513E−01	2.179E−01	2.966E−01	3.874E−01	4.903E−01	6.052E−01
150.0	4.082E−02	7.261E−02	1.135E−01	1.635E−01	2.227E−01	2.909E−01	3.683E−01	4.549E−01
200.0	3.377E−02	6.008E−02	9.394E−02	1.353E−01	1.843E−01	2.409E−01	3.050E−01	3.768E−01
250.0	2.947E−02	5.242E−02	8.197E−02	1.181E−01	1.609E−01	2.103E−01	2.663E−01	3.290E−01
300.0	2.657E−02	4.727E−02	7.392E−02	1.065E−01	1.451E−01	1.897E−01	2.402E−01	2.968E−01
400.0	2.295E−02	4.083E−02	6.386E−02	9.204E−02	1.254E−01	1.639E−01	2.076E−01	2.565E−01
500.0	2.081E−02	3.703E−02	5.791E−02	8.346E−02	1.137E−01	1.487E−01	1.883E−01	2.327E−01
600.0	1.942E−02	3.455E−02	5.404E−02	7.790E−02	1.061E−01	1.388E−01	1.758E−01	2.172E−01
700.0	1.846E−02	3.285E−02	5.138E−02	7.407E−02	1.009E−01	1.319E−01	1.672E−01	2.066E−01
800.0	1.778E−02	3.164E−02	4.948E−02	7.133E−02	9.718E−02	1.271E−01	1.610E−01	1.989E−01
900.0	1.727E−02	3.074E−02	4.808E−02	6.930E−02	9.443E−02	1.235E−01	1.564E−01	1.933E−01
1000.	1.689E−02	3.005E−02	4.701E−02	6.776E−02	9.232E−02	1.207E−01	1.529E−01	1.890E−01

Material: Silicon dioxide

Ion	Na	Mg	Al	Si	P	S	Cl	Ar
(E/A_1) / MeV				$(-\mathrm{d}E/\rho\mathrm{d}\ell)$ / MeV cm^2 mg^{-1}				
0.025	3.478E+00	3.623E+00	3.754E+00	3.880E+00	4.000E+00	4.111E+00	4.234E+00	4.333E+00
0.030	3.859E+00	4.019E+00	4.165E+00	4.303E+00	4.433E+00	4.556E+00	4.688E+00	4.796E+00
0.040	4.556E+00	4.749E+00	4.923E+00	5.086E+00	5.238E+00	5.384E+00	5.534E+00	5.658E+00
0.050	5.183E+00	5.412E+00	5.616E+00	5.806E+00	5.982E+00	6.154E+00	6.322E+00	6.463E+00
0.060	5.753E+00	6.018E+00	6.256E+00	6.474E+00	6.678E+00	6.876E+00	7.066E+00	7.224E+00
0.070	6.275E+00	6.578E+00	6.849E+00	7.097E+00	7.329E+00	7.554E+00	7.768E+00	7.946E+00
0.080	6.757E+00	7.096E+00	7.401E+00	7.680E+00	7.940E+00	8.193E+00	8.431E+00	8.630E+00
0.090	7.205E+00	7.578E+00	7.917E+00	8.225E+00	8.515E+00	8.796E+00	9.058E+00	9.280E+00
0.100	7.623E+00	8.029E+00	8.400E+00	8.738E+00	9.057E+00	9.366E+00	9.652E+00	9.896E+00
0.150	9.316E+00	9.891E+00	1.042E+01	1.090E+01	1.136E+01	1.181E+01	1.222E+01	1.258E+01
0.200	1.045E+01	1.119E+01	1.188E+01	1.251E+01	1.311E+01	1.370E+01	1.424E+01	1.471E+01
0.250	1.119E+01	1.206E+01	1.288E+01	1.365E+01	1.439E+01	1.511E+01	1.578E+01	1.637E+01
0.300	1.168E+01	1.265E+01	1.358E+01	1.445E+01	1.531E+01	1.614E+01	1.692E+01	1.763E+01
0.400	1.221E+01	1.332E+01	1.440E+01	1.543E+01	1.646E+01	1.747E+01	1.843E+01	1.931E+01
0.500	1.244E+01	1.364E+01	1.482E+01	1.595E+01	1.710E+01	1.823E+01	1.931E+01	2.031E+01
0.600	1.250E+01	1.376E+01	1.501E+01	1.621E+01	1.745E+01	1.868E+01	1.985E+01	2.094E+01
0.700	1.247E+01	1.377E+01	1.507E+01	1.632E+01	1.763E+01	1.892E+01	2.016E+01	2.132E+01
0.800	1.238E+01	1.371E+01	1.504E+01	1.634E+01	1.769E+01	1.903E+01	2.033E+01	2.154E+01
0.900	1.225E+01	1.360E+01	1.496E+01	1.628E+01	1.767E+01	1.906E+01	2.039E+01	2.164E+01
1.000	1.211E+01	1.347E+01	1.485E+01	1.618E+01	1.760E+01	1.902E+01	2.039E+01	2.167E+01
1.500	1.126E+01	1.263E+01	1.404E+01	1.541E+01	1.690E+01	1.840E+01	1.985E+01	2.121E+01
2.000	1.042E+01	1.177E+01	1.316E+01	1.452E+01	1.602E+01	1.754E+01	1.901E+01	2.038E+01
2.500	9.668E+00	1.098E+01	1.233E+01	1.367E+01	1.515E+01	1.666E+01	1.813E+01	1.949E+01
3.000	8.996E+00	1.027E+01	1.158E+01	1.289E+01	1.434E+01	1.583E+01	1.728E+01	1.863E+01
4.000	7.875E+00	9.058E+00	1.030E+01	1.153E+01	1.292E+01	1.434E+01	1.574E+01	1.704E+01
5.000	6.986E+00	8.087E+00	9.246E+00	1.041E+01	1.172E+01	1.308E+01	1.441E+01	1.565E+01
6.000	6.270E+00	7.294E+00	8.380E+00	9.478E+00	1.071E+01	1.200E+01	1.327E+01	1.446E+01
7.000	5.682E+00	6.638E+00	7.655E+00	8.690E+00	9.853E+00	1.107E+01	1.228E+01	1.342E+01
8.000	5.193E+00	6.087E+00	7.042E+00	8.019E+00	9.117E+00	1.027E+01	1.143E+01	1.251E+01
9.000	4.780E+00	5.620E+00	6.518E+00	7.442E+00	8.480E+00	9.578E+00	1.067E+01	1.172E+01
10.00	4.428E+00	5.218E+00	6.066E+00	6.941E+00	7.924E+00	8.966E+00	1.001E+01	1.101E+01
15.00	3.246E+00	3.851E+00	4.506E+00	5.194E+00	5.962E+00	6.785E+00	7.625E+00	8.446E+00
20.00	2.578E+00	3.067E+00	3.598E+00	4.162E+00	4.788E+00	5.461E+00	6.157E+00	6.851E+00
25.00	2.152E+00	2.562E+00	3.009E+00	3.487E+00	4.014E+00	4.583E+00	5.175E+00	5.773E+00
30.00	1.857E+00	2.212E+00	2.599E+00	3.013E+00	3.469E+00	3.961E+00	4.476E+00	5.002E+00
40.00	1.475E+00	1.757E+00	2.063E+00	2.394E+00	2.754E+00	3.143E+00	3.553E+00	3.978E+00
50.00	1.237E+00	1.473E+00	1.730E+00	2.006E+00	2.307E+00	2.631E+00	2.974E+00	3.332E+00
60.00	1.074E+00	1.278E+00	1.501E+00	1.741E+00	2.001E+00	2.280E+00	2.577E+00	2.888E+00
70.00	9.548E−01	1.136E+00	1.334E+00	1.547E+00	1.777E+00	2.024E+00	2.287E+00	2.564E+00
80.00	8.635E−01	1.027E+00	1.206E+00	1.399E+00	1.606E+00	1.829E+00	2.066E+00	2.317E+00
90.00	7.913E−01	9.414E−01	1.105E+00	1.281E+00	1.472E+00	1.675E+00	1.892E+00	2.122E+00
100.0	7.324E−01	8.715E−01	1.023E+00	1.186E+00	1.362E+00	1.551E+00	1.751E+00	1.964E+00
150.0	5.505E−01	6.553E−01	7.693E−01	8.924E−01	1.025E+00	1.166E+00	1.317E+00	1.477E+00
200.0	4.561E−01	5.430E−01	6.376E−01	7.397E−01	8.495E−01	9.670E−01	1.092E+00	1.225E+00
250.0	3.983E−01	4.743E−01	5.569E−01	6.462E−01	7.423E−01	8.450E−01	9.544E−01	1.071E+00
300.0	3.594E−01	4.280E−01	5.026E−01	5.833E−01	6.700E−01	7.628E−01	8.617E−01	9.667E−01
400.0	3.107E−01	3.700E−01	4.346E−01	5.044E−01	5.795E−01	6.599E−01	7.456E−01	8.365E−01
500.0	2.818E−01	3.357E−01	3.943E−01	4.577E−01	5.259E−01	5.989E−01	6.767E−01	7.593E−01
600.0	2.631E−01	3.134E−01	3.682E−01	4.274E−01	4.911E−01	5.593E−01	6.320E−01	7.092E−01
700.0	2.502E−01	2.981E−01	3.501E−01	4.065E−01	4.671E−01	5.320E−01	6.011E−01	6.746E−01
800.0	2.410E−01	2.871E−01	3.372E−01	3.915E−01	4.499E−01	5.124E−01	5.790E−01	6.498E−01
900.0	2.341E−01	2.789E−01	3.277E−01	3.805E−01	4.372E−01	4.980E−01	5.627E−01	6.316E−01
1000.	2.289E−01	2.728E−01	3.204E−01	3.720E−01	4.275E−01	4.870E−01	5.503E−01	6.176E−01

Material: Sodium iodide (modelled by NeXe)

Ion	Li	Be	B	C	N	O	F	Ne
(E/A_1) / MeV				$(-\mathrm{d}E/\rho\mathrm{d}\ell)$ / MeV cm^2 mg^{-1}				
0.025	1.572E+00	1.032E+00	1.181E+00	1.300E+00	1.399E+00	1.490E+00	1.572E+00	1.652E+00
0.030	1.764E+00	1.139E+00	1.315E+00	1.455E+00	1.569E+00	1.672E+00	1.764E+00	1.850E+00
0.040	2.123E+00	1.311E+00	1.542E+00	1.729E+00	1.880E+00	2.010E+00	2.123E+00	2.226E+00
0.050	2.452E+00	1.439E+00	1.720E+00	1.954E+00	2.146E+00	2.311E+00	2.452E+00	2.576E+00
0.060	2.743E+00	1.539E+00	1.861E+00	2.137E+00	2.369E+00	2.571E+00	2.743E+00	2.895E+00
0.070	2.998E+00	1.618E+00	1.977E+00	2.290E+00	2.557E+00	2.793E+00	2.998E+00	3.178E+00
0.080	3.220E+00	1.683E+00	2.073E+00	2.419E+00	2.718E+00	2.986E+00	3.220E+00	3.429E+00
0.090	3.417E+00	1.737E+00	2.154E+00	2.529E+00	2.858E+00	3.155E+00	3.417E+00	3.652E+00
0.100	3.593E+00	1.781E+00	2.224E+00	2.625E+00	2.981E+00	3.305E+00	3.593E+00	3.853E+00
0.150	4.244E+00	1.917E+00	2.452E+00	2.955E+00	3.417E+00	3.849E+00	4.244E+00	4.609E+00
0.200	4.656E+00	1.966E+00	2.560E+00	3.132E+00	3.669E+00	4.181E+00	4.656E+00	5.103E+00
0.250	4.924E+00	1.971E+00	2.603E+00	3.222E+00	3.814E+00	4.385E+00	4.924E+00	5.435E+00
0.300	5.094E+00	1.955E+00	2.610E+00	3.260E+00	3.892E+00	4.508E+00	5.094E+00	5.657E+00
0.400	5.266E+00	1.896E+00	2.574E+00	3.260E+00	3.940E+00	4.614E+00	5.266E+00	5.901E+00
0.500	5.319E+00	1.828E+00	2.512E+00	3.214E+00	3.921E+00	4.628E+00	5.319E+00	5.999E+00
0.600	5.315E+00	1.759E+00	2.443E+00	3.152E+00	3.873E+00	4.601E+00	5.315E+00	6.024E+00
0.700	5.281E+00	1.693E+00	2.372E+00	3.083E+00	3.811E+00	4.551E+00	5.281E+00	6.009E+00
0.800	5.229E+00	1.631E+00	2.302E+00	3.011E+00	3.742E+00	4.490E+00	5.229E+00	5.970E+00
0.900	5.167E+00	1.571E+00	2.234E+00	2.939E+00	3.670E+00	4.421E+00	5.167E+00	5.917E+00
1.000	5.099E+00	1.516E+00	2.169E+00	2.868E+00	3.597E+00	4.350E+00	5.099E+00	5.855E+00
1.500	4.730E+00	1.284E+00	1.883E+00	2.542E+00	3.246E+00	3.985E+00	4.730E+00	5.490E+00
2.000	4.375E+00	1.113E+00	1.660E+00	2.273E+00	2.941E+00	3.650E+00	4.375E+00	5.121E+00
2.500	4.056E+00	9.830E−01	1.483E+00	2.053E+00	2.682E+00	3.358E+00	4.056E+00	4.779E+00
3.000	3.775E+00	8.813E−01	1.340E+00	1.871E+00	2.463E+00	3.105E+00	3.775E+00	4.473E+00
4.000	3.310E+00	7.334E−01	1.127E+00	1.591E+00	2.117E+00	2.697E+00	3.310E+00	3.957E+00
5.000	2.946E+00	6.312E−01	9.759E−01	1.386E+00	1.858E+00	2.384E+00	2.946E+00	3.545E+00
6.000	2.656E+00	5.563E−01	8.630E−01	1.231E+00	1.658E+00	2.138E+00	2.656E+00	3.212E+00
7.000	2.419E+00	4.989E−01	7.755E−01	1.110E+00	1.499E+00	1.939E+00	2.419E+00	2.937E+00
8.000	2.222E+00	4.534E−01	7.057E−01	1.011E+00	1.369E+00	1.776E+00	2.222E+00	2.707E+00
9.000	2.057E+00	4.163E−01	6.485E−01	9.306E−01	1.262E+00	1.640E+00	2.057E+00	2.511E+00
10.00	1.915E+00	3.856E−01	6.009E−01	8.628E−01	1.171E+00	1.524E+00	1.915E+00	2.343E+00
15.00	1.435E+00	2.857E−01	4.456E−01	6.407E−01	8.711E−01	1.137E+00	1.435E+00	1.766E+00
20.00	1.160E+00	2.302E−01	3.592E−01	5.165E−01	7.024E−01	9.172E−01	1.160E+00	1.429E+00
25.00	9.802E−01	1.945E−01	3.035E−01	4.365E−01	5.936E−01	7.750E−01	9.802E−01	1.209E+00
30.00	8.539E−01	1.693E−01	2.644E−01	3.803E−01	5.172E−01	6.751E−01	8.539E−01	1.054E+00
40.00	6.871E−01	1.361E−01	2.126E−01	3.060E−01	4.162E−01	5.432E−01	6.871E−01	8.479E−01
50.00	5.812E−01	1.150E−01	1.797E−01	2.587E−01	3.519E−01	4.595E−01	5.812E−01	7.172E−01
60.00	5.075E−01	1.004E−01	1.568E−01	2.258E−01	3.072E−01	4.011E−01	5.075E−01	6.263E−01
70.00	4.530E−01	8.952E−02	1.399E−01	2.015E−01	2.742E−01	3.581E−01	4.530E−01	5.591E−01
80.00	4.111E−01	8.118E−02	1.269E−01	1.827E−01	2.487E−01	3.249E−01	4.111E−01	5.074E−01
90.00	3.777E−01	7.454E−02	1.165E−01	1.678E−01	2.285E−01	2.985E−01	3.777E−01	4.663E−01
100.0	3.505E−01	6.914E−02	1.081E−01	1.557E−01	2.120E−01	2.769E−01	3.505E−01	4.327E−01
150.0	2.657E−01	5.233E−02	8.182E−02	1.179E−01	1.606E−01	2.098E−01	2.657E−01	3.281E−01
200.0	2.213E−01	4.354E−02	6.810E−02	9.814E−02	1.337E−01	1.747E−01	2.213E−01	2.734E−01
250.0	1.940E−01	3.815E−02	5.967E−02	8.600E−02	1.172E−01	1.532E−01	1.940E−01	2.397E−01
300.0	1.756E−01	3.452E−02	5.399E−02	7.782E−02	1.060E−01	1.386E−01	1.756E−01	2.169E−01
400.0	1.525E−01	2.997E−02	4.687E−02	6.757E−02	9.206E−02	1.204E−01	1.525E−01	1.885E−01
500.0	1.388E−01	2.727E−02	4.266E−02	6.151E−02	8.381E−02	1.096E−01	1.388E−01	1.716E−01
600.0	1.300E−01	2.553E−02	3.994E−02	5.758E−02	7.846E−02	1.026E−01	1.300E−01	1.607E−01
700.0	1.239E−01	2.434E−02	3.807E−02	5.489E−02	7.480E−02	9.781E−02	1.239E−01	1.532E−01
800.0	1.196E−01	2.348E−02	3.673E−02	5.296E−02	7.217E−02	9.438E−02	1.196E−01	1.479E−01
900.0	1.164E−01	2.285E−02	3.575E−02	5.154E−02	7.024E−02	9.186E−02	1.164E−01	1.439E−01
1000.	1.140E−01	2.237E−02	3.500E−02	5.046E−02	6.877E−02	8.993E−02	1.140E−01	1.409E−01

Material: Sodium iodide (modelled by NeXe)

Ion	Na	Mg	Al	Si	P	S	Cl	Ar
(E/A_1) / MeV				$(-\mathrm{d}E/\rho\mathrm{d}\ell)$ / MeV cm^2 mg^{-1}				
0.025	1.725E+00	1.800E+00	1.872E+00	1.942E+00	2.007E+00	2.071E+00	2.134E+00	2.199E+00
0.030	1.930E+00	2.011E+00	2.089E+00	2.166E+00	2.237E+00	2.309E+00	2.380E+00	2.452E+00
0.040	2.319E+00	2.410E+00	2.498E+00	2.583E+00	2.663E+00	2.745E+00	2.826E+00	2.911E+00
0.050	2.685E+00	2.788E+00	2.885E+00	2.978E+00	3.065E+00	3.153E+00	3.240E+00	3.332E+00
0.060	3.026E+00	3.146E+00	3.256E+00	3.358E+00	3.452E+00	3.546E+00	3.638E+00	3.735E+00
0.070	3.335E+00	3.477E+00	3.604E+00	3.720E+00	3.825E+00	3.928E+00	4.025E+00	4.128E+00
0.080	3.611E+00	3.777E+00	3.925E+00	4.059E+00	4.178E+00	4.293E+00	4.401E+00	4.511E+00
0.090	3.860E+00	4.049E+00	4.219E+00	4.371E+00	4.508E+00	4.638E+00	4.758E+00	4.879E+00
0.100	4.085E+00	4.297E+00	4.487E+00	4.660E+00	4.814E+00	4.961E+00	5.095E+00	5.229E+00
0.150	4.946E+00	5.258E+00	5.546E+00	5.810E+00	6.052E+00	6.283E+00	6.494E+00	6.701E+00
0.200	5.522E+00	5.915E+00	6.283E+00	6.625E+00	6.945E+00	7.250E+00	7.533E+00	7.809E+00
0.250	5.921E+00	6.381E+00	6.817E+00	7.226E+00	7.613E+00	7.983E+00	8.331E+00	8.670E+00
0.300	6.199E+00	6.713E+00	7.206E+00	7.673E+00	8.119E+00	8.548E+00	8.953E+00	9.348E+00
0.400	6.522E+00	7.118E+00	7.697E+00	8.253E+00	8.792E+00	9.316E+00	9.818E+00	1.031E+01
0.500	6.671E+00	7.322E+00	7.960E+00	8.577E+00	9.184E+00	9.780E+00	1.035E+01	1.092E+01
0.600	6.731E+00	7.420E+00	8.099E+00	8.760E+00	9.417E+00	1.006E+01	1.069E+01	1.131E+01
0.700	6.739E+00	7.454E+00	8.163E+00	8.856E+00	9.550E+00	1.024E+01	1.091E+01	1.156E+01
0.800	6.717E+00	7.451E+00	8.181E+00	8.897E+00	9.620E+00	1.034E+01	1.104E+01	1.173E+01
0.900	6.675E+00	7.423E+00	8.170E+00	8.904E+00	9.648E+00	1.039E+01	1.111E+01	1.183E+01
1.000	6.621E+00	7.379E+00	8.138E+00	8.885E+00	9.648E+00	1.041E+01	1.115E+01	1.189E+01
1.500	6.271E+00	7.047E+00	7.835E+00	8.619E+00	9.429E+00	1.024E+01	1.105E+01	1.183E+01
2.000	5.893E+00	6.665E+00	7.455E+00	8.245E+00	9.070E+00	9.904E+00	1.073E+01	1.154E+01
2.500	5.534E+00	6.292E+00	7.072E+00	7.856E+00	8.681E+00	9.518E+00	1.035E+01	1.117E+01
3.000	5.205E+00	5.945E+00	6.710E+00	7.481E+00	8.297E+00	9.129E+00	9.958E+00	1.077E+01
4.000	4.642E+00	5.340E+00	6.067E+00	6.805E+00	7.592E+00	8.400E+00	9.209E+00	1.000E+01
5.000	4.185E+00	4.842E+00	5.530E+00	6.232E+00	6.984E+00	7.761E+00	8.542E+00	9.310E+00
6.000	3.810E+00	4.428E+00	5.078E+00	5.746E+00	6.463E+00	7.207E+00	7.959E+00	8.699E+00
7.000	3.497E+00	4.079E+00	4.695E+00	5.329E+00	6.013E+00	6.725E+00	7.447E+00	8.160E+00
8.000	3.232E+00	3.782E+00	4.366E+00	4.970E+00	5.622E+00	6.303E+00	6.996E+00	7.683E+00
9.000	3.006E+00	3.527E+00	4.080E+00	4.656E+00	5.278E+00	5.930E+00	6.597E+00	7.258E+00
10.00	2.810E+00	3.304E+00	3.830E+00	4.380E+00	4.975E+00	5.599E+00	6.240E+00	6.877E+00
15.00	2.130E+00	2.521E+00	2.942E+00	3.386E+00	3.870E+00	4.382E+00	4.914E+00	5.451E+00
20.00	1.728E+00	2.051E+00	2.400E+00	2.773E+00	3.178E+00	3.609E+00	4.061E+00	4.523E+00
25.00	1.463E+00	1.738E+00	2.038E+00	2.358E+00	2.706E+00	3.079E+00	3.471E+00	3.874E+00
30.00	1.275E+00	1.516E+00	1.778E+00	2.060E+00	2.366E+00	2.693E+00	3.039E+00	3.398E+00
40.00	1.026E+00	1.220E+00	1.432E+00	1.660E+00	1.907E+00	2.172E+00	2.454E+00	2.748E+00
50.00	8.676E−01	1.032E+00	1.211E+00	1.405E+00	1.614E+00	1.838E+00	2.076E+00	2.327E+00
60.00	7.576E−01	9.014E−01	1.058E+00	1.227E+00	1.409E+00	1.604E+00	1.812E+00	2.032E+00
70.00	6.764E−01	8.048E−01	9.445E−01	1.095E+00	1.258E+00	1.432E+00	1.618E+00	1.814E+00
80.00	6.139E−01	7.305E−01	8.572E−01	9.941E−01	1.142E+00	1.299E+00	1.468E+00	1.646E+00
90.00	5.642E−01	6.713E−01	7.879E−01	9.137E−01	1.049E+00	1.194E+00	1.349E+00	1.512E+00
100.0	5.236E−01	6.231E−01	7.313E−01	8.482E−01	9.739E−01	1.108E+00	1.252E+00	1.404E+00
150.0	3.972E−01	4.728E−01	5.551E−01	6.440E−01	7.395E−01	8.417E−01	9.506E−01	1.066E+00
200.0	3.310E−01	3.941E−01	4.628E−01	5.370E−01	6.167E−01	7.020E−01	7.930E−01	8.894E−01
250.0	2.902E−01	3.456E−01	4.059E−01	4.711E−01	5.411E−01	6.161E−01	6.960E−01	7.808E−01
300.0	2.627E−01	3.129E−01	3.676E−01	4.266E−01	4.901E−01	5.581E−01	6.305E−01	7.074E−01
400.0	2.283E−01	2.719E−01	3.194E−01	3.708E−01	4.261E−01	4.852E−01	5.483E−01	6.153E−01
500.0	2.079E−01	2.476E−01	2.909E−01	3.378E−01	3.882E−01	4.421E−01	4.996E−01	5.607E−01
600.0	1.946E−01	2.319E−01	2.725E−01	3.164E−01	3.636E−01	4.142E−01	4.680E−01	5.253E−01
700.0	1.856E−01	2.211E−01	2.598E−01	3.016E−01	3.467E−01	3.949E−01	4.463E−01	5.009E−01
800.0	1.791E−01	2.134E−01	2.507E−01	2.911E−01	3.346E−01	3.811E−01	4.308E−01	4.835E−01
900.0	1.743E−01	2.077E−01	2.440E−01	2.834E−01	3.257E−01	3.710E−01	4.193E−01	4.707E−01
1000.	1.706E−01	2.033E−01	2.389E−01	2.774E−01	3.189E−01	3.633E−01	4.106E−01	4.609E−01

Material: Tissue-equivalent gas (methane based)

Ion	Li	Be	B	C	N	O	F	Ne
(E/A_1) / MeV				$(-\mathrm{d}E/\rho\mathrm{d}\ell)$ / MeV cm^2 mg^{-1}				
0.025	2.663E+00	3.295E+00	3.789E+00	4.173E+00	4.521E+00	4.828E+00	5.063E+00	5.278E+00
0.030	2.892E+00	3.605E+00	4.174E+00	4.625E+00	5.025E+00	5.377E+00	5.651E+00	5.897E+00
0.040	3.261E+00	4.129E+00	4.840E+00	5.421E+00	5.925E+00	6.371E+00	6.724E+00	7.037E+00
0.050	3.535E+00	4.549E+00	5.395E+00	6.101E+00	6.708E+00	7.249E+00	7.682E+00	8.065E+00
0.060	3.734E+00	4.881E+00	5.855E+00	6.682E+00	7.394E+00	8.029E+00	8.543E+00	8.998E+00
0.070	3.875E+00	5.138E+00	6.232E+00	7.175E+00	7.990E+00	8.721E+00	9.318E+00	9.846E+00
0.080	3.973E+00	5.334E+00	6.535E+00	7.589E+00	8.506E+00	9.332E+00	1.001E+01	1.062E+01
0.090	4.038E+00	5.481E+00	6.778E+00	7.932E+00	8.946E+00	9.866E+00	1.063E+01	1.131E+01
0.100	4.080E+00	5.590E+00	6.969E+00	8.214E+00	9.320E+00	1.033E+01	1.118E+01	1.194E+01
0.150	4.092E+00	5.801E+00	7.445E+00	9.005E+00	1.046E+01	1.183E+01	1.303E+01	1.413E+01
0.200	3.977E+00	5.764E+00	7.532E+00	9.254E+00	1.090E+01	1.249E+01	1.393E+01	1.528E+01
0.250	3.829E+00	5.645E+00	7.474E+00	9.283E+00	1.104E+01	1.277E+01	1.435E+01	1.586E+01
0.300	3.678E+00	5.498E+00	7.356E+00	9.213E+00	1.104E+01	1.286E+01	1.453E+01	1.614E+01
0.400	3.391E+00	5.186E+00	7.057E+00	8.956E+00	1.086E+01	1.277E+01	1.454E+01	1.628E+01
0.500	3.138E+00	4.887E+00	6.741E+00	8.645E+00	1.057E+01	1.253E+01	1.436E+01	1.616E+01
0.600	2.917E+00	4.611E+00	6.436E+00	8.328E+00	1.026E+01	1.224E+01	1.409E+01	1.592E+01
0.700	2.724E+00	4.361E+00	6.148E+00	8.019E+00	9.946E+00	1.192E+01	1.379E+01	1.564E+01
0.800	2.553E+00	4.135E+00	5.880E+00	7.723E+00	9.635E+00	1.161E+01	1.347E+01	1.533E+01
0.900	2.403E+00	3.929E+00	5.632E+00	7.444E+00	9.336E+00	1.130E+01	1.316E+01	1.502E+01
1.000	2.269E+00	3.741E+00	5.402E+00	7.181E+00	9.049E+00	1.100E+01	1.285E+01	1.470E+01
1.500	1.774E+00	3.016E+00	4.472E+00	6.080E+00	7.810E+00	9.647E+00	1.142E+01	1.321E+01
2.000	1.459E+00	2.524E+00	3.807E+00	5.257E+00	6.846E+00	8.560E+00	1.024E+01	1.195E+01
2.500	1.241E+00	2.170E+00	3.311E+00	4.624E+00	6.084E+00	7.678E+00	9.259E+00	1.088E+01
3.000	1.082E+00	1.905E+00	2.930E+00	4.125E+00	5.470E+00	6.953E+00	8.442E+00	9.983E+00
4.000	8.659E−01	1.535E+00	2.382E+00	3.390E+00	4.544E+00	5.837E+00	7.162E+00	8.550E+00
5.000	7.257E−01	1.289E+00	2.011E+00	2.878E+00	3.884E+00	5.023E+00	6.211E+00	7.468E+00
6.000	6.271E−01	1.115E+00	1.743E+00	2.503E+00	3.392E+00	4.407E+00	5.480E+00	6.625E+00
7.000	5.539E−01	9.851E−01	1.541E+00	2.217E+00	3.012E+00	3.926E+00	4.902E+00	5.951E+00
8.000	4.973E−01	8.841E−01	1.383E+00	1.993E+00	2.711E+00	3.540E+00	4.435E+00	5.402E+00
9.000	4.520E−01	8.034E−01	1.257E+00	1.812E+00	2.467E+00	3.226E+00	4.051E+00	4.947E+00
10.00	4.150E−01	7.374E−01	1.153E+00	1.663E+00	2.266E+00	2.964E+00	3.729E+00	4.564E+00
15.00	2.983E−01	5.297E−01	8.273E−01	1.192E+00	1.624E+00	2.127E+00	2.687E+00	3.307E+00
20.00	2.358E−01	4.188E−01	6.539E−01	9.413E−01	1.282E+00	1.677E+00	2.121E+00	2.615E+00
25.00	1.966E−01	3.492E−01	5.451E−01	7.845E−01	1.068E+00	1.395E+00	1.765E+00	2.178E+00
30.00	1.695E−01	3.011E−01	4.701E−01	6.765E−01	9.204E−01	1.202E+00	1.521E+00	1.877E+00
40.00	1.343E−01	2.387E−01	3.728E−01	5.364E−01	7.297E−01	9.528E−01	1.205E+00	1.487E+00
50.00	1.123E−01	1.997E−01	3.119E−01	4.490E−01	6.108E−01	7.974E−01	1.009E+00	1.245E+00
60.00	9.726E−02	1.729E−01	2.701E−01	3.889E−01	5.291E−01	6.908E−01	8.739E−01	1.078E+00
70.00	8.623E−02	1.533E−01	2.395E−01	3.449E−01	4.693E−01	6.128E−01	7.753E−01	9.569E−01
80.00	7.779E−02	1.383E−01	2.161E−01	3.112E−01	4.236E−01	5.532E−01	7.000E−01	8.639E−01
90.00	7.113E−02	1.265E−01	1.977E−01	2.847E−01	3.874E−01	5.060E−01	6.404E−01	7.904E−01
100.0	6.573E−02	1.169E−01	1.827E−01	2.631E−01	3.581E−01	4.678E−01	5.920E−01	7.308E−01
150.0	4.909E−02	8.732E−02	1.365E−01	1.966E−01	2.677E−01	3.498E−01	4.429E−01	5.469E−01
200.0	4.051E−02	7.206E−02	1.127E−01	1.623E−01	2.210E−01	2.888E−01	3.657E−01	4.517E−01
250.0	3.527E−02	6.274E−02	9.810E−02	1.414E−01	1.925E−01	2.516E−01	3.186E−01	3.936E−01
300.0	3.175E−02	5.649E−02	8.833E−02	1.273E−01	1.734E−01	2.266E−01	2.870E−01	3.545E−01
400.0	2.736E−02	4.868E−02	7.612E−02	1.097E−01	1.494E−01	1.953E−01	2.474E−01	3.057E−01
500.0	2.476E−02	4.406E−02	6.890E−02	9.930E−02	1.353E−01	1.768E−01	2.240E−01	2.768E−01
600.0	2.307E−02	4.105E−02	6.420E−02	9.254E−02	1.261E−01	1.648E−01	2.088E−01	2.580E−01
700.0	2.191E−02	3.898E−02	6.097E−02	8.787E−02	1.197E−01	1.565E−01	1.983E−01	2.450E−01
800.0	2.107E−02	3.750E−02	5.864E−02	8.453E−02	1.152E−01	1.506E−01	1.907E−01	2.357E−01
900.0	2.045E−02	3.640E−02	5.693E−02	8.205E−02	1.118E−01	1.461E−01	1.851E−01	2.288E−01
1000.	1.998E−02	3.556E−02	5.561E−02	8.016E−02	1.092E−01	1.428E−01	1.809E−01	2.235E−01

Material: Tissue-equivalent gas (methane based)

Ion	Na	Mg	Al	Si	P	S	Cl	Ar
(E/A_1) / MeV				$(-\mathrm{d}E/\rho\mathrm{d}\ell)$ / MeV cm^2 mg^{-1}				
0.025	5.468E+00	5.677E+00	5.878E+00	6.078E+00	6.312E+00	6.503E+00	6.746E+00	6.880E+00
0.030	6.118E+00	6.333E+00	6.551E+00	6.766E+00	7.015E+00	7.226E+00	7.481E+00	7.630E+00
0.040	7.326E+00	7.561E+00	7.813E+00	8.057E+00	8.334E+00	8.580E+00	8.856E+00	9.027E+00
0.050	8.428E+00	8.693E+00	8.982E+00	9.258E+00	9.566E+00	9.845E+00	1.014E+01	1.033E+01
0.060	9.437E+00	9.738E+00	1.007E+01	1.038E+01	1.072E+01	1.104E+01	1.136E+01	1.157E+01
0.070	1.036E+01	1.070E+01	1.108E+01	1.143E+01	1.181E+01	1.216E+01	1.251E+01	1.274E+01
0.080	1.122E+01	1.160E+01	1.202E+01	1.242E+01	1.283E+01	1.322E+01	1.360E+01	1.385E+01
0.090	1.200E+01	1.242E+01	1.290E+01	1.334E+01	1.379E+01	1.422E+01	1.463E+01	1.491E+01
0.100	1.271E+01	1.318E+01	1.372E+01	1.420E+01	1.470E+01	1.516E+01	1.561E+01	1.591E+01
0.150	1.531E+01	1.606E+01	1.689E+01	1.763E+01	1.838E+01	1.909E+01	1.974E+01	2.022E+01
0.200	1.677E+01	1.774E+01	1.883E+01	1.983E+01	2.082E+01	2.178E+01	2.265E+01	2.334E+01
0.250	1.758E+01	1.870E+01	1.998E+01	2.118E+01	2.238E+01	2.354E+01	2.461E+01	2.550E+01
0.300	1.803E+01	1.924E+01	2.067E+01	2.201E+01	2.337E+01	2.469E+01	2.592E+01	2.696E+01
0.400	1.838E+01	1.970E+01	2.132E+01	2.284E+01	2.441E+01	2.596E+01	2.741E+01	2.867E+01
0.500	1.838E+01	1.976E+01	2.148E+01	2.312E+01	2.482E+01	2.652E+01	2.811E+01	2.951E+01
0.600	1.823E+01	1.963E+01	2.142E+01	2.313E+01	2.493E+01	2.672E+01	2.840E+01	2.989E+01
0.700	1.801E+01	1.941E+01	2.124E+01	2.300E+01	2.486E+01	2.672E+01	2.847E+01	3.003E+01
0.800	1.774E+01	1.913E+01	2.100E+01	2.279E+01	2.469E+01	2.660E+01	2.840E+01	3.001E+01
0.900	1.745E+01	1.884E+01	2.072E+01	2.253E+01	2.447E+01	2.641E+01	2.825E+01	2.989E+01
1.000	1.715E+01	1.853E+01	2.042E+01	2.224E+01	2.421E+01	2.618E+01	2.805E+01	2.971E+01
1.500	1.565E+01	1.698E+01	1.886E+01	2.070E+01	2.270E+01	2.473E+01	2.666E+01	2.838E+01
2.000	1.431E+01	1.558E+01	1.742E+01	1.922E+01	2.120E+01	2.322E+01	2.515E+01	2.687E+01
2.500	1.314E+01	1.437E+01	1.615E+01	1.790E+01	1.983E+01	2.182E+01	2.372E+01	2.542E+01
3.000	1.213E+01	1.332E+01	1.503E+01	1.672E+01	1.861E+01	2.055E+01	2.241E+01	2.407E+01
4.000	1.048E+01	1.160E+01	1.318E+01	1.477E+01	1.653E+01	1.837E+01	2.013E+01	2.173E+01
5.000	9.207E+00	1.026E+01	1.173E+01	1.320E+01	1.486E+01	1.658E+01	1.825E+01	1.977E+01
6.000	8.196E+00	9.187E+00	1.055E+01	1.193E+01	1.348E+01	1.510E+01	1.667E+01	1.812E+01
7.000	7.378E+00	8.317E+00	9.590E+00	1.088E+01	1.233E+01	1.385E+01	1.534E+01	1.672E+01
8.000	6.704E+00	7.596E+00	8.785E+00	9.998E+00	1.136E+01	1.279E+01	1.420E+01	1.552E+01
9.000	6.141E+00	6.990E+00	8.104E+00	9.247E+00	1.052E+01	1.188E+01	1.322E+01	1.447E+01
10.00	5.665E+00	6.474E+00	7.521E+00	8.600E+00	9.805E+00	1.108E+01	1.236E+01	1.356E+01
15.00	4.088E+00	4.742E+00	5.543E+00	6.382E+00	7.313E+00	8.311E+00	9.321E+00	1.030E+01
20.00	3.216E+00	3.763E+00	4.410E+00	5.095E+00	5.850E+00	6.662E+00	7.496E+00	8.323E+00
25.00	2.667E+00	3.137E+00	3.681E+00	4.259E+00	4.894E+00	5.578E+00	6.287E+00	7.002E+00
30.00	2.290E+00	2.704E+00	3.173E+00	3.675E+00	4.224E+00	4.815E+00	5.432E+00	6.061E+00
40.00	1.807E+00	2.142E+00	2.514E+00	2.914E+00	3.348E+00	3.815E+00	4.307E+00	4.816E+00
50.00	1.510E+00	1.792E+00	2.103E+00	2.438E+00	2.800E+00	3.190E+00	3.602E+00	4.032E+00
60.00	1.306E+00	1.552E+00	1.822E+00	2.112E+00	2.425E+00	2.762E+00	3.118E+00	3.492E+00
70.00	1.159E+00	1.378E+00	1.616E+00	1.874E+00	2.152E+00	2.449E+00	2.765E+00	3.098E+00
80.00	1.046E+00	1.244E+00	1.459E+00	1.692E+00	1.943E+00	2.211E+00	2.496E+00	2.797E+00
90.00	9.566E−01	1.138E+00	1.335E+00	1.548E+00	1.778E+00	2.023E+00	2.284E+00	2.560E+00
100.0	8.844E−01	1.052E+00	1.235E+00	1.432E+00	1.644E+00	1.871E+00	2.112E+00	2.367E+00
150.0	6.619E−01	7.878E−01	9.247E−01	1.073E+00	1.232E+00	1.402E+00	1.582E+00	1.774E+00
200.0	5.468E−01	6.510E−01	7.643E−01	8.867E−01	1.018E+00	1.159E+00	1.309E+00	1.468E+00
250.0	4.765E−01	5.674E−01	6.662E−01	7.730E−01	8.878E−01	1.011E+00	1.141E+00	1.280E+00
300.0	4.293E−01	5.112E−01	6.003E−01	6.966E−01	8.001E−01	9.109E−01	1.029E+00	1.154E+00
400.0	3.702E−01	4.408E−01	5.178E−01	6.009E−01	6.903E−01	7.860E−01	8.880E−01	9.962E−01
500.0	3.352E−01	3.992E−01	4.689E−01	5.443E−01	6.253E−01	7.120E−01	8.044E−01	9.026E−01
600.0	3.124E−01	3.721E−01	4.371E−01	5.074E−01	5.830E−01	6.639E−01	7.501E−01	8.417E−01
700.0	2.967E−01	3.534E−01	4.152E−01	4.820E−01	5.538E−01	6.307E−01	7.126E−01	7.996E−01
800.0	2.854E−01	3.400E−01	3.994E−01	4.637E−01	5.328E−01	6.068E−01	6.856E−01	7.694E−01
900.0	2.771E−01	3.301E−01	3.878E−01	4.502E−01	5.173E−01	5.891E−01	6.657E−01	7.470E−01
1000.	2.707E−01	3.225E−01	3.789E−01	4.398E−01	5.054E−01	5.756E−01	6.505E−01	7.300E−01

Material: Tissue-equivalent gas (propane based)

Ion	Li	Be	B	C	N	O	F	Ne
(E/A_1) / MeV				$(-\mathrm{d}E/\rho\mathrm{d}\ell)$ / MeV cm^2 mg^{-1}				
0.025	2.700E+00	3.338E+00	3.839E+00	4.229E+00	4.586E+00	4.900E+00	5.141E+00	5.361E+00
0.030	2.933E+00	3.654E+00	4.230E+00	4.687E+00	5.096E+00	5.456E+00	5.736E+00	5.988E+00
0.040	3.311E+00	4.189E+00	4.909E+00	5.496E+00	6.008E+00	6.463E+00	6.822E+00	7.141E+00
0.050	3.589E+00	4.618E+00	5.475E+00	6.189E+00	6.805E+00	7.354E+00	7.793E+00	8.182E+00
0.060	3.789E+00	4.955E+00	5.944E+00	6.782E+00	7.503E+00	8.146E+00	8.667E+00	9.127E+00
0.070	3.930E+00	5.214E+00	6.325E+00	7.283E+00	8.110E+00	8.851E+00	9.455E+00	9.988E+00
0.080	4.026E+00	5.409E+00	6.631E+00	7.702E+00	8.634E+00	9.473E+00	1.016E+01	1.077E+01
0.090	4.090E+00	5.555E+00	6.874E+00	8.048E+00	9.080E+00	1.001E+01	1.079E+01	1.148E+01
0.100	4.129E+00	5.662E+00	7.064E+00	8.330E+00	9.455E+00	1.048E+01	1.135E+01	1.211E+01
0.150	4.134E+00	5.863E+00	7.528E+00	9.110E+00	1.058E+01	1.198E+01	1.320E+01	1.432E+01
0.200	4.014E+00	5.820E+00	7.607E+00	9.349E+00	1.102E+01	1.263E+01	1.408E+01	1.545E+01
0.250	3.864E+00	5.698E+00	7.545E+00	9.373E+00	1.115E+01	1.290E+01	1.450E+01	1.602E+01
0.300	3.711E+00	5.548E+00	7.424E+00	9.300E+00	1.115E+01	1.298E+01	1.467E+01	1.630E+01
0.400	3.421E+00	5.232E+00	7.121E+00	9.037E+00	1.096E+01	1.289E+01	1.468E+01	1.643E+01
0.500	3.166E+00	4.930E+00	6.802E+00	8.723E+00	1.067E+01	1.264E+01	1.449E+01	1.630E+01
0.600	2.942E+00	4.652E+00	6.493E+00	8.403E+00	1.036E+01	1.235E+01	1.422E+01	1.606E+01
0.700	2.747E+00	4.400E+00	6.203E+00	8.090E+00	1.004E+01	1.203E+01	1.391E+01	1.577E+01
0.800	2.575E+00	4.170E+00	5.932E+00	7.792E+00	9.722E+00	1.171E+01	1.359E+01	1.546E+01
0.900	2.423E+00	3.962E+00	5.681E+00	7.510E+00	9.419E+00	1.140E+01	1.327E+01	1.514E+01
1.000	2.288E+00	3.773E+00	5.449E+00	7.244E+00	9.129E+00	1.109E+01	1.296E+01	1.482E+01
1.500	1.788E+00	3.040E+00	4.509E+00	6.131E+00	7.876E+00	9.730E+00	1.152E+01	1.332E+01
2.000	1.470E+00	2.544E+00	3.837E+00	5.300E+00	6.902E+00	8.630E+00	1.032E+01	1.204E+01
2.500	1.250E+00	2.187E+00	3.337E+00	4.660E+00	6.131E+00	7.739E+00	9.330E+00	1.097E+01
3.000	1.090E+00	1.919E+00	2.952E+00	4.156E+00	5.511E+00	7.006E+00	8.504E+00	1.006E+01
4.000	8.721E−01	1.546E+00	2.399E+00	3.414E+00	4.576E+00	5.879E+00	7.212E+00	8.609E+00
5.000	7.307E−01	1.298E+00	2.025E+00	2.898E+00	3.911E+00	5.058E+00	6.253E+00	7.517E+00
6.000	6.314E−01	1.123E+00	1.754E+00	2.520E+00	3.415E+00	4.436E+00	5.515E+00	6.667E+00
7.000	5.576E−01	9.916E−01	1.551E+00	2.232E+00	3.032E+00	3.951E+00	4.933E+00	5.988E+00
8.000	5.005E−01	8.899E−01	1.392E+00	2.006E+00	2.729E+00	3.563E+00	4.463E+00	5.435E+00
9.000	4.549E−01	8.086E−01	1.265E+00	1.823E+00	2.483E+00	3.246E+00	4.075E+00	4.976E+00
10.00	4.176E−01	7.421E−01	1.160E+00	1.673E+00	2.280E+00	2.983E+00	3.752E+00	4.591E+00
15.00	3.001E−01	5.329E−01	8.325E−01	1.199E+00	1.634E+00	2.139E+00	2.703E+00	3.326E+00
20.00	2.373E−01	4.214E−01	6.578E−01	9.470E−01	1.289E+00	1.687E+00	2.133E+00	2.630E+00
25.00	1.978E−01	3.513E−01	5.484E−01	7.892E−01	1.074E+00	1.404E+00	1.776E+00	2.190E+00
30.00	1.705E−01	3.029E−01	4.729E−01	6.805E−01	9.257E−01	1.209E+00	1.530E+00	1.887E+00
40.00	1.351E−01	2.401E−01	3.749E−01	5.395E−01	7.339E−01	9.582E−01	1.212E+00	1.496E+00
50.00	1.130E−01	2.008E−01	3.137E−01	4.515E−01	6.142E−01	8.019E−01	1.014E+00	1.252E+00
60.00	9.780E−02	1.739E−01	2.716E−01	3.910E−01	5.320E−01	6.947E−01	8.788E−01	1.084E+00
70.00	8.671E−02	1.542E−01	2.409E−01	3.468E−01	4.719E−01	6.162E−01	7.796E−01	9.622E−01
80.00	7.822E−02	1.391E−01	2.173E−01	3.130E−01	4.259E−01	5.562E−01	7.038E−01	8.687E−01
90.00	7.152E−02	1.272E−01	1.987E−01	2.862E−01	3.896E−01	5.088E−01	6.439E−01	7.948E−01
100.0	6.609E−02	1.175E−01	1.837E−01	2.645E−01	3.601E−01	4.703E−01	5.952E−01	7.348E−01
150.0	4.936E−02	8.779E−02	1.372E−01	1.977E−01	2.692E−01	3.517E−01	4.452E−01	5.498E−01
200.0	4.072E−02	7.244E−02	1.132E−01	1.632E−01	2.222E−01	2.904E−01	3.677E−01	4.541E−01
250.0	3.545E−02	6.307E−02	9.862E−02	1.421E−01	1.935E−01	2.529E−01	3.203E−01	3.956E−01
300.0	3.192E−02	5.678E−02	8.879E−02	1.279E−01	1.743E−01	2.278E−01	2.885E−01	3.564E−01
400.0	2.750E−02	4.893E−02	7.651E−02	1.103E−01	1.502E−01	1.963E−01	2.487E−01	3.072E−01
500.0	2.489E−02	4.428E−02	6.925E−02	9.980E−02	1.360E−01	1.777E−01	2.251E−01	2.782E−01
600.0	2.319E−02	4.126E−02	6.453E−02	9.300E−02	1.267E−01	1.656E−01	2.098E−01	2.593E−01
700.0	2.202E−02	3.918E−02	6.127E−02	8.831E−02	1.203E−01	1.573E−01	1.993E−01	2.462E−01
800.0	2.118E−02	3.768E−02	5.894E−02	8.495E−02	1.157E−01	1.513E−01	1.917E−01	2.369E−01
900.0	2.056E−02	3.658E−02	5.721E−02	8.246E−02	1.123E−01	1.469E−01	1.861E−01	2.299E−01
1000.	2.008E−02	3.573E−02	5.589E−02	8.055E−02	1.097E−01	1.435E−01	1.818E−01	2.246E−01

Material: Tissue-equivalent gas (propane based)

Ion	Na	Mg	Al	Si	P	S	Cl	Ar
(E/A_1) / MeV				$(-\mathrm{d}E/\rho\mathrm{d}\ell)$ / MeV cm^2 mg^{-1}				
0.025	5.555E+00	5.769E+00	5.974E+00	6.180E+00	6.421E+00	6.617E+00	6.866E+00	7.003E+00
0.030	6.214E+00	6.434E+00	6.657E+00	6.877E+00	7.134E+00	7.350E+00	7.613E+00	7.765E+00
0.040	7.436E+00	7.677E+00	7.934E+00	8.185E+00	8.471E+00	8.723E+00	9.008E+00	9.183E+00
0.050	8.551E+00	8.821E+00	9.117E+00	9.400E+00	9.718E+00	1.000E+01	1.031E+01	1.051E+01
0.060	9.573E+00	9.878E+00	1.022E+01	1.054E+01	1.089E+01	1.121E+01	1.154E+01	1.175E+01
0.070	1.051E+01	1.086E+01	1.124E+01	1.160E+01	1.198E+01	1.234E+01	1.270E+01	1.294E+01
0.080	1.138E+01	1.176E+01	1.219E+01	1.259E+01	1.302E+01	1.341E+01	1.380E+01	1.406E+01
0.090	1.217E+01	1.260E+01	1.308E+01	1.352E+01	1.399E+01	1.442E+01	1.484E+01	1.512E+01
0.100	1.289E+01	1.337E+01	1.391E+01	1.440E+01	1.490E+01	1.538E+01	1.583E+01	1.614E+01
0.150	1.553E+01	1.628E+01	1.712E+01	1.788E+01	1.864E+01	1.936E+01	2.002E+01	2.050E+01
0.200	1.698E+01	1.795E+01	1.906E+01	2.007E+01	2.109E+01	2.206E+01	2.295E+01	2.365E+01
0.250	1.777E+01	1.890E+01	2.020E+01	2.141E+01	2.263E+01	2.381E+01	2.490E+01	2.580E+01
0.300	1.821E+01	1.944E+01	2.088E+01	2.223E+01	2.361E+01	2.495E+01	2.620E+01	2.725E+01
0.400	1.855E+01	1.988E+01	2.151E+01	2.305E+01	2.464E+01	2.621E+01	2.767E+01	2.894E+01
0.500	1.856E+01	1.993E+01	2.167E+01	2.332E+01	2.504E+01	2.675E+01	2.836E+01	2.976E+01
0.600	1.840E+01	1.980E+01	2.160E+01	2.333E+01	2.514E+01	2.695E+01	2.865E+01	3.015E+01
0.700	1.817E+01	1.957E+01	2.142E+01	2.319E+01	2.507E+01	2.695E+01	2.871E+01	3.028E+01
0.800	1.790E+01	1.930E+01	2.117E+01	2.298E+01	2.490E+01	2.683E+01	2.864E+01	3.026E+01
0.900	1.761E+01	1.900E+01	2.089E+01	2.272E+01	2.467E+01	2.664E+01	2.849E+01	3.014E+01
1.000	1.731E+01	1.868E+01	2.059E+01	2.243E+01	2.441E+01	2.640E+01	2.828E+01	2.995E+01
1.500	1.580E+01	1.712E+01	1.902E+01	2.086E+01	2.288E+01	2.493E+01	2.687E+01	2.860E+01
2.000	1.444E+01	1.570E+01	1.756E+01	1.937E+01	2.137E+01	2.341E+01	2.535E+01	2.708E+01
2.500	1.325E+01	1.448E+01	1.627E+01	1.803E+01	1.999E+01	2.199E+01	2.390E+01	2.561E+01
3.000	1.223E+01	1.341E+01	1.514E+01	1.685E+01	1.875E+01	2.070E+01	2.257E+01	2.425E+01
4.000	1.057E+01	1.168E+01	1.328E+01	1.487E+01	1.665E+01	1.850E+01	2.027E+01	2.187E+01
5.000	9.277E+00	1.032E+01	1.181E+01	1.329E+01	1.495E+01	1.669E+01	1.837E+01	1.990E+01
6.000	8.256E+00	9.246E+00	1.062E+01	1.201E+01	1.356E+01	1.519E+01	1.678E+01	1.823E+01
7.000	7.430E+00	8.369E+00	9.650E+00	1.095E+01	1.240E+01	1.394E+01	1.544E+01	1.682E+01
8.000	6.750E+00	7.642E+00	8.838E+00	1.006E+01	1.142E+01	1.287E+01	1.429E+01	1.561E+01
9.000	6.182E+00	7.032E+00	8.152E+00	9.301E+00	1.059E+01	1.195E+01	1.329E+01	1.456E+01
10.00	5.702E+00	6.512E+00	7.565E+00	8.650E+00	9.861E+00	1.115E+01	1.243E+01	1.364E+01
15.00	4.113E+00	4.769E+00	5.574E+00	6.418E+00	7.353E+00	8.356E+00	9.371E+00	1.036E+01
20.00	3.235E+00	3.784E+00	4.434E+00	5.123E+00	5.881E+00	6.697E+00	7.535E+00	8.366E+00
25.00	2.682E+00	3.155E+00	3.701E+00	4.283E+00	4.921E+00	5.608E+00	6.320E+00	7.037E+00
30.00	2.304E+00	2.719E+00	3.191E+00	3.696E+00	4.247E+00	4.841E+00	5.460E+00	6.092E+00
40.00	1.818E+00	2.154E+00	2.528E+00	2.930E+00	3.366E+00	3.836E+00	4.330E+00	4.841E+00
50.00	1.518E+00	1.802E+00	2.115E+00	2.451E+00	2.816E+00	3.207E+00	3.621E+00	4.053E+00
60.00	1.314E+00	1.561E+00	1.832E+00	2.124E+00	2.439E+00	2.777E+00	3.135E+00	3.511E+00
70.00	1.165E+00	1.385E+00	1.625E+00	1.884E+00	2.163E+00	2.463E+00	2.780E+00	3.115E+00
80.00	1.051E+00	1.250E+00	1.467E+00	1.701E+00	1.953E+00	2.223E+00	2.510E+00	2.812E+00
90.00	9.619E−01	1.144E+00	1.343E+00	1.557E+00	1.787E+00	2.034E+00	2.296E+00	2.573E+00
100.0	8.892E−01	1.058E+00	1.241E+00	1.440E+00	1.653E+00	1.881E+00	2.123E+00	2.380E+00
150.0	6.654E−01	7.920E−01	9.297E−01	1.078E+00	1.238E+00	1.409E+00	1.591E+00	1.784E+00
200.0	5.497E−01	6.544E−01	7.683E−01	8.913E−01	1.024E+00	1.165E+00	1.316E+00	1.475E+00
250.0	4.790E−01	5.703E−01	6.697E−01	7.771E−01	8.924E−01	1.016E+00	1.147E+00	1.287E+00
300.0	4.315E−01	5.138E−01	6.034E−01	7.002E−01	8.042E−01	9.156E−01	1.034E+00	1.160E+00
400.0	3.720E−01	4.431E−01	5.204E−01	6.040E−01	6.939E−01	7.900E−01	8.925E−01	1.001E+00
500.0	3.369E−01	4.012E−01	4.713E−01	5.470E−01	6.284E−01	7.156E−01	8.085E−01	9.071E−01
600.0	3.140E−01	3.740E−01	4.393E−01	5.099E−01	5.859E−01	6.672E−01	7.539E−01	8.459E−01
700.0	2.982E−01	3.552E−01	4.173E−01	4.844E−01	5.565E−01	6.338E−01	7.161E−01	8.036E−01
800.0	2.869E−01	3.417E−01	4.014E−01	4.660E−01	5.354E−01	6.098E−01	6.890E−01	7.732E−01
900.0	2.785E−01	3.317E−01	3.897E−01	4.524E−01	5.198E−01	5.920E−01	6.690E−01	7.507E−01
1000.	2.721E−01	3.241E−01	3.807E−01	4.420E−01	5.079E−01	5.784E−01	6.536E−01	7.335E−01

Material: Liquid water

Ion	Li	Be	B	C	N	O	F	Ne
(E/A_1) / MeV				$(-\mathrm{d}E/\rho\mathrm{d}\ell)$ / MeV cm^2 mg^{-1}				
0.025	2.626E+00	3.272E+00	3.773E+00	4.154E+00	4.490E+00	4.778E+00	4.992E+00	5.182E+00
0.030	2.840E+00	3.565E+00	4.142E+00	4.593E+00	4.984E+00	5.321E+00	5.575E+00	5.797E+00
0.040	3.191E+00	4.061E+00	4.776E+00	5.358E+00	5.860E+00	6.298E+00	6.637E+00	6.931E+00
0.050	3.461E+00	4.463E+00	5.304E+00	6.009E+00	6.616E+00	7.152E+00	7.578E+00	7.948E+00
0.060	3.665E+00	4.790E+00	5.749E+00	6.568E+00	7.276E+00	7.907E+00	8.418E+00	8.865E+00
0.070	3.817E+00	5.052E+00	6.122E+00	7.049E+00	7.854E+00	8.578E+00	9.171E+00	9.693E+00
0.080	3.927E+00	5.258E+00	6.431E+00	7.460E+00	8.360E+00	9.173E+00	9.847E+00	1.044E+01
0.090	4.004E+00	5.419E+00	6.684E+00	7.809E+00	8.799E+00	9.700E+00	1.045E+01	1.112E+01
0.100	4.056E+00	5.542E+00	6.890E+00	8.103E+00	9.179E+00	1.016E+01	1.100E+01	1.174E+01
0.150	4.102E+00	5.803E+00	7.432E+00	8.968E+00	1.039E+01	1.173E+01	1.290E+01	1.398E+01
0.200	3.998E+00	5.787E+00	7.551E+00	9.262E+00	1.089E+01	1.246E+01	1.388E+01	1.521E+01
0.250	3.853E+00	5.675E+00	7.505E+00	9.311E+00	1.107E+01	1.278E+01	1.435E+01	1.585E+01
0.300	3.702E+00	5.529E+00	7.391E+00	9.250E+00	1.108E+01	1.289E+01	1.456E+01	1.617E+01
0.400	3.413E+00	5.215E+00	7.091E+00	8.994E+00	1.090E+01	1.281E+01	1.459E+01	1.633E+01
0.500	3.158E+00	4.912E+00	6.772E+00	8.680E+00	1.061E+01	1.257E+01	1.440E+01	1.621E+01
0.600	2.934E+00	4.634E+00	6.463E+00	8.358E+00	1.030E+01	1.227E+01	1.413E+01	1.598E+01
0.700	2.739E+00	4.381E+00	6.172E+00	8.045E+00	9.974E+00	1.195E+01	1.383E+01	1.569E+01
0.800	2.567E+00	4.152E+00	5.901E+00	7.747E+00	9.660E+00	1.163E+01	1.351E+01	1.538E+01
0.900	2.415E+00	3.944E+00	5.650E+00	7.465E+00	9.357E+00	1.132E+01	1.319E+01	1.506E+01
1.000	2.280E+00	3.756E+00	5.418E+00	7.199E+00	9.068E+00	1.101E+01	1.287E+01	1.474E+01
1.500	1.782E+00	3.026E+00	4.484E+00	6.093E+00	7.823E+00	9.659E+00	1.144E+01	1.324E+01
2.000	1.465E+00	2.533E+00	3.817E+00	5.269E+00	6.859E+00	8.571E+00	1.026E+01	1.198E+01
2.500	1.247E+00	2.179E+00	3.322E+00	4.636E+00	6.097E+00	7.691E+00	9.279E+00	1.091E+01
3.000	1.087E+00	1.913E+00	2.940E+00	4.137E+00	5.484E+00	6.967E+00	8.463E+00	1.001E+01
4.000	8.706E−01	1.542E+00	2.392E+00	3.403E+00	4.560E+00	5.854E+00	7.187E+00	8.584E+00
5.000	7.299E−01	1.296E+00	2.020E+00	2.891E+00	3.900E+00	5.042E+00	6.237E+00	7.503E+00
6.000	6.310E−01	1.122E+00	1.752E+00	2.516E+00	3.408E+00	4.427E+00	5.506E+00	6.660E+00
7.000	5.575E−01	9.911E−01	1.549E+00	2.230E+00	3.029E+00	3.945E+00	4.928E+00	5.986E+00
8.000	5.005E−01	8.898E−01	1.391E+00	2.004E+00	2.727E+00	3.560E+00	4.461E+00	5.436E+00
9.000	4.550E−01	8.087E−01	1.265E+00	1.823E+00	2.482E+00	3.245E+00	4.076E+00	4.979E+00
10.00	4.178E−01	7.423E−01	1.161E+00	1.673E+00	2.280E+00	2.983E+00	3.753E+00	4.595E+00
15.00	3.004E−01	5.335E−01	8.332E−01	1.200E+00	1.636E+00	2.142E+00	2.707E+00	3.332E+00
20.00	2.376E−01	4.219E−01	6.587E−01	9.483E−01	1.291E+00	1.689E+00	2.137E+00	2.635E+00
25.00	1.981E−01	3.518E−01	5.492E−01	7.904E−01	1.076E+00	1.406E+00	1.779E+00	2.195E+00
30.00	1.708E−01	3.034E−01	4.737E−01	6.817E−01	9.274E−01	1.212E+00	1.533E+00	1.892E+00
40.00	1.354E−01	2.406E−01	3.757E−01	5.406E−01	7.354E−01	9.602E−01	1.215E+00	1.499E+00
50.00	1.132E−01	2.013E−01	3.144E−01	4.525E−01	6.156E−01	8.037E−01	1.017E+00	1.255E+00
60.00	9.803E−02	1.743E−01	2.723E−01	3.920E−01	5.333E−01	6.963E−01	8.809E−01	1.087E+00
70.00	8.692E−02	1.545E−01	2.415E−01	3.477E−01	4.731E−01	6.178E−01	7.816E−01	9.646E−01
80.00	7.842E−02	1.394E−01	2.179E−01	3.138E−01	4.270E−01	5.577E−01	7.056E−01	8.709E−01
90.00	7.171E−02	1.275E−01	1.993E−01	2.870E−01	3.906E−01	5.102E−01	6.456E−01	7.969E−01
100.0	6.627E−02	1.178E−01	1.842E−01	2.653E−01	3.611E−01	4.716E−01	5.969E−01	7.368E−01
150.0	4.950E−02	8.805E−02	1.376E−01	1.983E−01	2.700E−01	3.527E−01	4.466E−01	5.514E−01
200.0	4.085E−02	7.266E−02	1.136E−01	1.637E−01	2.229E−01	2.913E−01	3.688E−01	4.555E−01
250.0	3.557E−02	6.328E−02	9.894E−02	1.426E−01	1.942E−01	2.538E−01	3.213E−01	3.969E−01
300.0	3.203E−02	5.698E−02	8.909E−02	1.284E−01	1.749E−01	2.285E−01	2.894E−01	3.576E−01
400.0	2.760E−02	4.910E−02	7.678E−02	1.107E−01	1.507E−01	1.970E−01	2.496E−01	3.083E−01
500.0	2.498E−02	4.444E−02	6.950E−02	1.002E−01	1.365E−01	1.784E−01	2.259E−01	2.792E−01
600.0	2.327E−02	4.141E−02	6.477E−02	9.335E−02	1.272E−01	1.663E−01	2.106E−01	2.602E−01
700.0	2.210E−02	3.933E−02	6.151E−02	8.865E−02	1.208E−01	1.579E−01	2.000E−01	2.472E−01
800.0	2.126E−02	3.783E−02	5.916E−02	8.528E−02	1.162E−01	1.519E−01	1.924E−01	2.378E−01
900.0	2.064E−02	3.672E−02	5.743E−02	8.278E−02	1.128E−01	1.475E−01	1.868E−01	2.308E−01
1000.	2.016E−02	3.588E−02	5.611E−02	8.088E−02	1.102E−01	1.441E−01	1.825E−01	2.255E−01

Material: Liquid water

Ion	Na	Mg	Al	Si	P	S	Cl	Ar
(E/A_1) / MeV				$(-\mathrm{d}E/\rho\mathrm{d}\ell)$ / MeV cm^2 mg^{-1}				
0.025	5.352E+00	5.542E+00	5.724E+00	5.905E+00	6.120E+00	6.294E+00	6.522E+00	6.642E+00
0.030	5.998E+00	6.193E+00	6.390E+00	6.583E+00	6.810E+00	7.000E+00	7.237E+00	7.369E+00
0.040	7.203E+00	7.420E+00	7.649E+00	7.868E+00	8.118E+00	8.338E+00	8.590E+00	8.739E+00
0.050	8.300E+00	8.551E+00	8.820E+00	9.073E+00	9.352E+00	9.604E+00	9.875E+00	1.004E+01
0.060	9.298E+00	9.590E+00	9.905E+00	1.020E+01	1.051E+01	1.080E+01	1.110E+01	1.128E+01
0.070	1.021E+01	1.054E+01	1.091E+01	1.125E+01	1.161E+01	1.194E+01	1.226E+01	1.247E+01
0.080	1.104E+01	1.142E+01	1.184E+01	1.223E+01	1.263E+01	1.300E+01	1.336E+01	1.359E+01
0.090	1.181E+01	1.223E+01	1.271E+01	1.314E+01	1.358E+01	1.400E+01	1.439E+01	1.466E+01
0.100	1.250E+01	1.298E+01	1.351E+01	1.399E+01	1.448E+01	1.494E+01	1.537E+01	1.566E+01
0.150	1.513E+01	1.585E+01	1.666E+01	1.740E+01	1.813E+01	1.882E+01	1.945E+01	1.993E+01
0.200	1.668E+01	1.762E+01	1.869E+01	1.966E+01	2.063E+01	2.155E+01	2.240E+01	2.308E+01
0.250	1.756E+01	1.866E+01	1.993E+01	2.110E+01	2.228E+01	2.341E+01	2.445E+01	2.532E+01
0.300	1.804E+01	1.926E+01	2.068E+01	2.201E+01	2.334E+01	2.465E+01	2.586E+01	2.689E+01
0.400	1.843E+01	1.976E+01	2.138E+01	2.291E+01	2.447E+01	2.601E+01	2.746E+01	2.872E+01
0.500	1.844E+01	1.983E+01	2.156E+01	2.321E+01	2.491E+01	2.660E+01	2.819E+01	2.960E+01
0.600	1.829E+01	1.970E+01	2.150E+01	2.322E+01	2.502E+01	2.681E+01	2.850E+01	3.001E+01
0.700	1.805E+01	1.947E+01	2.132E+01	2.309E+01	2.495E+01	2.681E+01	2.857E+01	3.015E+01
0.800	1.778E+01	1.920E+01	2.107E+01	2.287E+01	2.478E+01	2.669E+01	2.850E+01	3.013E+01
0.900	1.748E+01	1.889E+01	2.079E+01	2.261E+01	2.455E+01	2.650E+01	2.834E+01	3.000E+01
1.000	1.718E+01	1.858E+01	2.048E+01	2.232E+01	2.428E+01	2.626E+01	2.813E+01	2.982E+01
1.500	1.567E+01	1.702E+01	1.891E+01	2.076E+01	2.276E+01	2.479E+01	2.672E+01	2.846E+01
2.000	1.432E+01	1.562E+01	1.747E+01	1.928E+01	2.126E+01	2.328E+01	2.521E+01	2.694E+01
2.500	1.315E+01	1.441E+01	1.619E+01	1.795E+01	1.989E+01	2.188E+01	2.378E+01	2.549E+01
3.000	1.214E+01	1.336E+01	1.508E+01	1.678E+01	1.867E+01	2.061E+01	2.247E+01	2.415E+01
4.000	1.050E+01	1.164E+01	1.324E+01	1.483E+01	1.659E+01	1.843E+01	2.020E+01	2.181E+01
5.000	9.226E+00	1.030E+01	1.178E+01	1.326E+01	1.492E+01	1.664E+01	1.832E+01	1.986E+01
6.000	8.218E+00	9.233E+00	1.061E+01	1.199E+01	1.354E+01	1.516E+01	1.675E+01	1.822E+01
7.000	7.401E+00	8.362E+00	9.641E+00	1.094E+01	1.239E+01	1.392E+01	1.542E+01	1.682E+01
8.000	6.728E+00	7.640E+00	8.835E+00	1.006E+01	1.142E+01	1.286E+01	1.428E+01	1.561E+01
9.000	6.166E+00	7.033E+00	8.153E+00	9.304E+00	1.059E+01	1.195E+01	1.330E+01	1.457E+01
10.00	5.690E+00	6.516E+00	7.569E+00	8.656E+00	9.867E+00	1.115E+01	1.244E+01	1.365E+01
15.00	4.112E+00	4.777E+00	5.583E+00	6.430E+00	7.367E+00	8.371E+00	9.392E+00	1.039E+01
20.00	3.237E+00	3.792E+00	4.444E+00	5.135E+00	5.896E+00	6.715E+00	7.557E+00	8.394E+00
25.00	2.686E+00	3.162E+00	3.710E+00	4.294E+00	4.935E+00	5.624E+00	6.340E+00	7.063E+00
30.00	2.307E+00	2.725E+00	3.199E+00	3.705E+00	4.259E+00	4.856E+00	5.479E+00	6.114E+00
40.00	1.821E+00	2.159E+00	2.534E+00	2.938E+00	3.376E+00	3.847E+00	4.344E+00	4.859E+00
50.00	1.521E+00	1.806E+00	2.120E+00	2.458E+00	2.824E+00	3.217E+00	3.633E+00	4.067E+00
60.00	1.317E+00	1.565E+00	1.836E+00	2.129E+00	2.445E+00	2.785E+00	3.145E+00	3.522E+00
70.00	1.168E+00	1.388E+00	1.629E+00	1.889E+00	2.169E+00	2.470E+00	2.789E+00	3.125E+00
80.00	1.054E+00	1.254E+00	1.471E+00	1.706E+00	1.959E+00	2.229E+00	2.517E+00	2.821E+00
90.00	9.644E−01	1.147E+00	1.346E+00	1.561E+00	1.792E+00	2.040E+00	2.303E+00	2.581E+00
100.0	8.917E−01	1.061E+00	1.245E+00	1.444E+00	1.657E+00	1.886E+00	2.130E+00	2.387E+00
150.0	6.674E−01	7.944E−01	9.325E−01	1.082E+00	1.242E+00	1.413E+00	1.596E+00	1.789E+00
200.0	5.514E−01	6.565E−01	7.707E−01	8.942E−01	1.027E+00	1.169E+00	1.320E+00	1.480E+00
250.0	4.806E−01	5.722E−01	6.719E−01	7.796E−01	8.954E−01	1.019E+00	1.151E+00	1.291E+00
300.0	4.329E−01	5.156E−01	6.054E−01	7.026E−01	8.070E−01	9.187E−01	1.038E+00	1.164E+00
400.0	3.734E−01	4.447E−01	5.223E−01	6.061E−01	6.963E−01	7.929E−01	8.957E−01	1.005E+00
500.0	3.381E−01	4.027E−01	4.730E−01	5.490E−01	6.308E−01	7.183E−01	8.115E−01	9.105E−01
600.0	3.152E−01	3.754E−01	4.410E−01	5.119E−01	5.881E−01	6.697E−01	7.567E−01	8.491E−01
700.0	2.993E−01	3.566E−01	4.189E−01	4.862E−01	5.587E−01	6.362E−01	7.189E−01	8.067E−01
800.0	2.880E−01	3.430E−01	4.030E−01	4.678E−01	5.375E−01	6.122E−01	6.917E−01	7.763E−01
900.0	2.796E−01	3.330E−01	3.912E−01	4.542E−01	5.219E−01	5.944E−01	6.717E−01	7.537E−01
1000.	2.732E−01	3.254E−01	3.823E−01	4.438E−01	5.100E−01	5.808E−01	6.563E−01	7.365E−01

Material: Water vapor

Ion	Li	Be	B	C	N	O	F	Ne
(E/A_1) / MeV				$(-\mathrm{d}E/\rho\mathrm{d}\ell)$ / MeV cm^2 mg^{-1}				
0.025	2.388E+00	2.938E+00	3.350E+00	3.652E+00	3.922E+00	4.155E+00	4.323E+00	4.476E+00
0.030	2.599E+00	3.224E+00	3.707E+00	4.071E+00	4.388E+00	4.659E+00	4.856E+00	5.033E+00
0.040	2.949E+00	3.715E+00	4.329E+00	4.816E+00	5.229E+00	5.587E+00	5.853E+00	6.084E+00
0.050	3.221E+00	4.119E+00	4.856E+00	5.459E+00	5.970E+00	6.416E+00	6.759E+00	7.054E+00
0.060	3.429E+00	4.451E+00	5.304E+00	6.019E+00	6.625E+00	7.160E+00	7.580E+00	7.943E+00
0.070	3.584E+00	4.718E+00	5.683E+00	6.505E+00	7.207E+00	7.830E+00	8.326E+00	8.758E+00
0.080	3.697E+00	4.929E+00	5.999E+00	6.924E+00	7.719E+00	8.430E+00	9.004E+00	9.505E+00
0.090	3.778E+00	5.095E+00	6.260E+00	7.281E+00	8.168E+00	8.965E+00	9.617E+00	1.019E+01
0.100	3.833E+00	5.222E+00	6.472E+00	7.583E+00	8.557E+00	9.439E+00	1.017E+01	1.081E+01
0.150	3.892E+00	5.500E+00	7.035E+00	8.477E+00	9.804E+00	1.105E+01	1.212E+01	1.310E+01
0.200	3.802E+00	5.500E+00	7.172E+00	8.792E+00	1.033E+01	1.181E+01	1.313E+01	1.437E+01
0.250	3.672E+00	5.404E+00	7.144E+00	8.860E+00	1.052E+01	1.215E+01	1.363E+01	1.504E+01
0.300	3.534E+00	5.275E+00	7.048E+00	8.817E+00	1.056E+01	1.228E+01	1.386E+01	1.538E+01
0.400	3.269E+00	4.990E+00	6.781E+00	8.597E+00	1.041E+01	1.224E+01	1.393E+01	1.559E+01
0.500	3.032E+00	4.712E+00	6.491E+00	8.316E+00	1.016E+01	1.203E+01	1.378E+01	1.551E+01
0.600	2.824E+00	4.455E+00	6.208E+00	8.024E+00	9.879E+00	1.177E+01	1.355E+01	1.531E+01
0.700	2.640E+00	4.219E+00	5.939E+00	7.737E+00	9.587E+00	1.149E+01	1.328E+01	1.506E+01
0.800	2.478E+00	4.005E+00	5.687E+00	7.461E+00	9.299E+00	1.119E+01	1.299E+01	1.478E+01
0.900	2.334E+00	3.809E+00	5.453E+00	7.199E+00	9.019E+00	1.091E+01	1.270E+01	1.449E+01
1.000	2.206E+00	3.631E+00	5.235E+00	6.951E+00	8.751E+00	1.062E+01	1.241E+01	1.420E+01
1.500	1.730E+00	2.937E+00	4.350E+00	5.908E+00	7.582E+00	9.358E+00	1.108E+01	1.281E+01
2.000	1.426E+00	2.464E+00	3.712E+00	5.122E+00	6.665E+00	8.327E+00	9.959E+00	1.162E+01
2.500	1.215E+00	2.122E+00	3.235E+00	4.515E+00	5.936E+00	7.487E+00	9.028E+00	1.061E+01
3.000	1.060E+00	1.866E+00	2.867E+00	4.034E+00	5.347E+00	6.792E+00	8.246E+00	9.753E+00
4.000	8.501E−01	1.506E+00	2.336E+00	3.323E+00	4.453E+00	5.717E+00	7.016E+00	8.378E+00
5.000	7.134E−01	1.267E+00	1.975E+00	2.826E+00	3.813E+00	4.930E+00	6.097E+00	7.332E+00
6.000	6.172E−01	1.097E+00	1.714E+00	2.461E+00	3.335E+00	4.331E+00	5.387E+00	6.514E+00
7.000	5.456E−01	9.700E−01	1.517E+00	2.183E+00	2.965E+00	3.863E+00	4.825E+00	5.859E+00
8.000	4.901E−01	8.712E−01	1.363E+00	1.963E+00	2.671E+00	3.487E+00	4.369E+00	5.324E+00
9.000	4.457E−01	7.922E−01	1.239E+00	1.786E+00	2.432E+00	3.180E+00	3.994E+00	4.879E+00
10.00	4.094E−01	7.274E−01	1.137E+00	1.640E+00	2.235E+00	2.924E+00	3.679E+00	4.504E+00
15.00	2.947E−01	5.234E−01	8.175E−01	1.178E+00	1.605E+00	2.102E+00	2.656E+00	3.270E+00
20.00	2.333E−01	4.143E−01	6.468E−01	9.312E−01	1.268E+00	1.659E+00	2.099E+00	2.588E+00
25.00	1.946E−01	3.457E−01	5.397E−01	7.766E−01	1.057E+00	1.382E+00	1.748E+00	2.157E+00
30.00	1.679E−01	2.983E−01	4.657E−01	6.701E−01	9.117E−01	1.191E+00	1.507E+00	1.859E+00
40.00	1.332E−01	2.366E−01	3.695E−01	5.318E−01	7.234E−01	9.445E−01	1.195E+00	1.474E+00
50.00	1.114E−01	1.981E−01	3.094E−01	4.453E−01	6.058E−01	7.910E−01	1.001E+00	1.235E+00
60.00	9.651E−02	1.716E−01	2.681E−01	3.859E−01	5.250E−01	6.855E−01	8.673E−01	1.070E+00
70.00	8.560E−02	1.522E−01	2.378E−01	3.424E−01	4.659E−01	6.084E−01	7.697E−01	9.499E−01
80.00	7.725E−02	1.374E−01	2.146E−01	3.091E−01	4.206E−01	5.493E−01	6.951E−01	8.579E−01
90.00	7.065E−02	1.256E−01	1.963E−01	2.827E−01	3.849E−01	5.026E−01	6.361E−01	7.851E−01
100.0	6.530E−02	1.161E−01	1.815E−01	2.614E−01	3.558E−01	4.647E−01	5.882E−01	7.261E−01
150.0	4.881E−02	8.682E−02	1.357E−01	1.955E−01	2.662E−01	3.478E−01	4.403E−01	5.438E−01
200.0	4.030E−02	7.168E−02	1.121E−01	1.615E−01	2.199E−01	2.873E−01	3.638E−01	4.494E−01
250.0	3.510E−02	6.244E−02	9.763E−02	1.407E−01	1.916E−01	2.504E−01	3.171E−01	3.917E−01
300.0	3.161E−02	5.624E−02	8.793E−02	1.267E−01	1.726E−01	2.256E−01	2.857E−01	3.529E−01
400.0	2.725E−02	4.848E−02	7.581E−02	1.093E−01	1.488E−01	1.945E−01	2.464E−01	3.045E−01
500.0	2.467E−02	4.389E−02	6.864E−02	9.893E−02	1.348E−01	1.762E−01	2.232E−01	2.758E−01
600.0	2.299E−02	4.091E−02	6.398E−02	9.222E−02	1.256E−01	1.642E−01	2.081E−01	2.571E−01
700.0	2.184E−02	3.886E−02	6.077E−02	8.759E−02	1.193E−01	1.560E−01	1.976E−01	2.442E−01
800.0	2.101E−02	3.738E−02	5.847E−02	8.427E−02	1.148E−01	1.501E−01	1.902E−01	2.350E−01
900.0	2.040E−02	3.629E−02	5.676E−02	8.182E−02	1.115E−01	1.457E−01	1.846E−01	2.282E−01
1000.	1.993E−02	3.546E−02	5.546E−02	7.995E−02	1.089E−01	1.424E−01	1.804E−01	2.230E−01

Material: Water vapor

Ion	Na	Mg	Al	Si	P	S	Cl	Ar
(E/A_1) / MeV				$(-\mathrm{d}E/\rho\mathrm{d}\ell)$ / MeV cm^2 mg^{-1}				
0.025	4.616E+00	4.777E+00	4.935E+00	5.095E+00	5.290E+00	4.155E+00	5.652E+00	5.752E+00
0.030	5.195E+00	5.356E+00	5.524E+00	5.692E+00	5.897E+00	4.659E+00	6.280E+00	6.391E+00
0.040	6.301E+00	6.470E+00	6.657E+00	6.842E+00	7.060E+00	5.587E+00	7.478E+00	7.603E+00
0.050	7.337E+00	7.526E+00	7.740E+00	7.946E+00	8.183E+00	6.416E+00	8.633E+00	8.767E+00
0.060	8.298E+00	8.518E+00	8.767E+00	9.003E+00	9.265E+00	7.160E+00	9.757E+00	9.901E+00
0.070	9.189E+00	9.443E+00	9.736E+00	1.001E+01	1.030E+01	7.830E+00	1.084E+01	1.100E+01
0.080	1.001E+01	1.031E+01	1.065E+01	1.095E+01	1.128E+01	8.430E+00	1.189E+01	1.207E+01
0.090	1.078E+01	1.111E+01	1.150E+01	1.185E+01	1.222E+01	8.965E+00	1.288E+01	1.309E+01
0.100	1.148E+01	1.186E+01	1.230E+01	1.269E+01	1.310E+01	9.439E+00	1.384E+01	1.406E+01
0.150	1.416E+01	1.479E+01	1.550E+01	1.614E+01	1.678E+01	1.105E+01	1.792E+01	1.831E+01
0.200	1.575E+01	1.660E+01	1.758E+01	1.846E+01	1.934E+01	1.181E+01	2.093E+01	2.152E+01
0.250	1.666E+01	1.768E+01	1.886E+01	1.995E+01	2.103E+01	1.215E+01	2.304E+01	2.382E+01
0.300	1.717E+01	1.830E+01	1.964E+01	2.088E+01	2.213E+01	1.228E+01	2.448E+01	2.542E+01
0.400	1.760E+01	1.885E+01	2.038E+01	2.183E+01	2.331E+01	1.224E+01	2.613E+01	2.731E+01
0.500	1.765E+01	1.896E+01	2.060E+01	2.217E+01	2.380E+01	1.203E+01	2.692E+01	2.825E+01
0.600	1.754E+01	1.887E+01	2.059E+01	2.223E+01	2.395E+01	1.177E+01	2.727E+01	2.870E+01
0.700	1.734E+01	1.868E+01	2.044E+01	2.214E+01	2.392E+01	1.149E+01	2.738E+01	2.888E+01
0.800	1.710E+01	1.844E+01	2.023E+01	2.196E+01	2.379E+01	1.119E+01	2.735E+01	2.890E+01
0.900	1.684E+01	1.817E+01	1.998E+01	2.173E+01	2.359E+01	1.091E+01	2.723E+01	2.881E+01
1.000	1.656E+01	1.789E+01	1.971E+01	2.147E+01	2.336E+01	1.062E+01	2.705E+01	2.866E+01
1.500	1.517E+01	1.645E+01	1.828E+01	2.005E+01	2.198E+01	9.358E+00	2.580E+01	2.747E+01
2.000	1.391E+01	1.515E+01	1.693E+01	1.868E+01	2.059E+01	8.327E+00	2.441E+01	2.608E+01
2.500	1.280E+01	1.400E+01	1.573E+01	1.743E+01	1.931E+01	7.487E+00	2.308E+01	2.473E+01
3.000	1.183E+01	1.300E+01	1.467E+01	1.632E+01	1.815E+01	6.792E+00	2.184E+01	2.347E+01
4.000	1.025E+01	1.135E+01	1.291E+01	1.445E+01	1.618E+01	5.717E+00	1.969E+01	2.125E+01
5.000	9.023E+00	1.006E+01	1.151E+01	1.295E+01	1.457E+01	4.930E+00	1.789E+01	1.938E+01
6.000	8.044E+00	9.029E+00	1.037E+01	1.172E+01	1.324E+01	4.331E+00	1.637E+01	1.780E+01
7.000	7.250E+00	8.184E+00	9.435E+00	1.070E+01	1.212E+01	3.863E+00	1.509E+01	1.645E+01
8.000	6.594E+00	7.482E+00	8.652E+00	9.846E+00	1.118E+01	3.487E+00	1.398E+01	1.528E+01
9.000	6.045E+00	6.891E+00	7.988E+00	9.114E+00	1.037E+01	3.180E+00	1.302E+01	1.427E+01
10.00	5.580E+00	6.387E+00	7.419E+00	8.483E+00	9.670E+00	2.924E+00	1.219E+01	1.338E+01
15.00	4.037E+00	4.688E+00	5.480E+00	6.310E+00	7.230E+00	2.102E+00	9.218E+00	1.019E+01
20.00	3.180E+00	3.724E+00	4.365E+00	5.043E+00	5.791E+00	1.659E+00	7.423E+00	8.245E+00
25.00	2.639E+00	3.107E+00	3.646E+00	4.219E+00	4.849E+00	1.382E+00	6.231E+00	6.941E+00
30.00	2.268E+00	2.679E+00	3.145E+00	3.643E+00	4.187E+00	1.191E+00	5.387E+00	6.011E+00
40.00	1.792E+00	2.124E+00	2.493E+00	2.890E+00	3.321E+00	9.445E−01	4.274E+00	4.780E+00
50.00	1.497E+00	1.778E+00	2.086E+00	2.419E+00	2.779E+00	7.910E−01	3.575E+00	4.003E+00
60.00	1.296E+00	1.541E+00	1.808E+00	2.096E+00	2.407E+00	6.855E−01	3.096E+00	3.468E+00
70.00	1.150E+00	1.367E+00	1.605E+00	1.860E+00	2.136E+00	6.084E−01	2.746E+00	3.077E+00
80.00	1.038E+00	1.235E+00	1.449E+00	1.680E+00	1.929E+00	5.493E−01	2.480E+00	2.779E+00
90.00	9.502E−01	1.130E+00	1.326E+00	1.538E+00	1.766E+00	5.026E−01	2.269E+00	2.543E+00
100.0	8.787E−01	1.045E+00	1.227E+00	1.423E+00	1.633E+00	4.647E−01	2.099E+00	2.352E+00
150.0	6.581E−01	7.834E−01	9.195E−01	1.067E+00	1.225E+00	3.478E−01	1.574E+00	1.764E+00
200.0	5.440E−01	6.476E−01	7.604E−01	8.822E−01	1.013E+00	2.873E−01	1.302E+00	1.460E+00
250.0	4.742E−01	5.647E−01	6.631E−01	7.694E−01	8.836E−01	2.504E−01	1.136E+00	1.274E+00
300.0	4.273E−01	5.089E−01	5.976E−01	6.935E−01	7.966E−01	2.256E−01	1.024E+00	1.149E+00
400.0	3.687E−01	4.391E−01	5.157E−01	5.985E−01	6.876E−01	1.945E−01	8.845E−01	9.923E−01
500.0	3.339E−01	3.978E−01	4.672E−01	5.423E−01	6.230E−01	1.762E−01	8.016E−01	8.994E−01
600.0	3.114E−01	3.709E−01	4.357E−01	5.057E−01	5.810E−01	1.642E−01	7.476E−01	8.389E−01
700.0	2.958E−01	3.523E−01	4.139E−01	4.805E−01	5.521E−01	1.560E−01	7.104E−01	7.975E−01
800.0	2.846E−01	3.390E−01	3.983E−01	4.623E−01	5.313E−01	1.501E−01	6.837E−01	7.683E−01
900.0	2.763E−01	3.292E−01	3.867E−01	4.490E−01	5.159E−01	1.457E−01	6.639E−01	7.458E−01
1000.	2.700E−01	3.217E−01	3.779E−01	4.387E−01	5.041E−01	1.424E−01	6.488E−01	7.281E−01

6.8. TABLES: RANGES OF SIXTEEN IONS IN LIQUID WATER

Range or average path length travelled for slowing-down from initial energy E to $E_0 = 0.025$ MeV/u.

Material: Liquid water								
Ion	Li	Be	B	C	N	O	F	Ne
(E/A_1) / MeV	$[\rho R(E)-\rho R(E_0)]$ / mgcm^{-2}							
0.025	0.000E+00	0.000E+00	0.000E+00	0.000E+00	0.000E+00	0.000E+00	0.000E+00	0.000E+00
0.030	1.283E−02	1.319E−02	1.393E−02	1.375E−02	1.482E−02	1.589E−02	1.804E−02	1.827E−02
0.040	3.612E−02	3.689E−02	3.872E−02	3.802E−02	4.081E−02	4.363E−02	4.939E−02	4.995E−02
0.050	5.720E−02	5.806E−02	6.061E−02	5.920E−02	6.333E−02	6.751E−02	7.624E−02	7.696E−02
0.060	7.686E−02	7.753E−02	8.054E−02	7.832E−02	8.353E−02	8.882E−02	1.001E−01	1.008E−01
0.070	9.558E−02	9.583E−02	9.910E−02	9.597E−02	1.021E−01	1.083E−01	1.217E−01	1.224E−01
0.080	1.137E−01	1.133E−01	1.166E−01	1.125E−01	1.194E−01	1.263E−01	1.417E−01	1.423E−01
0.090	1.313E−01	1.302E−01	1.334E−01	1.282E−01	1.357E−01	1.433E−01	1.605E−01	1.609E−01
0.100	1.487E−01	1.466E−01	1.496E−01	1.433E−01	1.513E−01	1.594E−01	1.782E−01	1.784E−01
0.150	2.345E−01	2.260E−01	2.265E−01	2.138E−01	2.231E−01	2.329E−01	2.582E−01	2.568E−01
0.200	3.209E−01	3.036E−01	3.000E−01	2.797E−01	2.889E−01	2.991E−01	3.292E−01	3.254E−01
0.250	4.101E−01	3.821E−01	3.730E−01	3.443E−01	3.527E−01	3.625E−01	3.965E−01	3.898E−01
0.300	5.028E−01	4.625E−01	4.469E−01	4.089E−01	4.159E−01	4.248E−01	4.623E−01	4.523E−01
0.400	6.999E−01	6.302E−01	5.988E−01	5.405E−01	5.433E−01	5.493E−01	5.926E−01	5.754E−01
0.500	9.133E−01	8.081E−01	7.576E−01	6.763E−01	6.735E−01	6.754E−01	7.237E−01	6.983E−01
0.600	1.143E+00	9.968E−01	9.239E−01	8.172E−01	8.074E−01	8.043E−01	8.569E−01	8.226E−01
0.700	1.390E+00	1.197E+00	1.098E+00	9.636E−01	9.455E−01	9.364E−01	9.928E−01	9.489E−01
0.800	1.655E+00	1.408E+00	1.280E+00	1.116E+00	1.088E+00	1.072E+00	1.132E+00	1.078E+00
0.900	1.936E+00	1.630E+00	1.471E+00	1.273E+00	1.235E+00	1.212E+00	1.274E+00	1.209E+00
1.000	2.234E+00	1.864E+00	1.670E+00	1.437E+00	1.387E+00	1.355E+00	1.420E+00	1.343E+00
1.500	3.984E+00	3.207E+00	2.791E+00	2.346E+00	2.221E+00	2.132E+00	2.204E+00	2.060E+00
2.000	6.160E+00	4.839E+00	4.125E+00	3.408E+00	3.179E+00	3.013E+00	3.083E+00	2.855E+00
2.500	8.758E+00	6.759E+00	5.673E+00	4.624E+00	4.263E+00	4.000E+00	4.057E+00	3.731E+00
3.000	1.177E+01	8.968E+00	7.436E+00	5.997E+00	5.475E+00	5.094E+00	5.131E+00	4.689E+00
4.000	1.901E+01	1.424E+01	1.161E+01	9.210E+00	8.287E+00	7.609E+00	7.575E+00	6.853E+00
5.000	2.783E+01	2.063E+01	1.663E+01	1.305E+01	1.162E+01	1.056E+01	1.042E+01	9.350E+00
6.000	3.817E+01	2.811E+01	2.249E+01	1.751E+01	1.547E+01	1.396E+01	1.367E+01	1.218E+01
7.000	4.999E+01	3.666E+01	2.918E+01	2.258E+01	1.983E+01	1.779E+01	1.732E+01	1.536E+01
8.000	6.326E+01	4.626E+01	3.668E+01	2.827E+01	2.471E+01	2.207E+01	2.138E+01	1.887E+01
9.000	7.795E+01	5.688E+01	4.499E+01	3.455E+01	3.010E+01	2.678E+01	2.584E+01	2.271E+01
10.00	9.402E+01	6.851E+01	5.407E+01	4.143E+01	3.599E+01	3.193E+01	3.070E+01	2.690E+01
15.00	1.942E+02	1.410E+02	1.108E+02	8.436E+01	7.273E+01	6.401E+01	6.090E+01	5.279E+01
20.00	3.261E+02	2.365E+02	1.855E+02	1.410E+02	1.212E+02	1.064E+02	1.007E+02	8.677E+01
25.00	4.881E+02	3.538E+02	2.773E+02	2.106E+02	1.809E+02	1.585E+02	1.496E+02	1.285E+02
30.00	6.789E+02	4.919E+02	3.855E+02	2.926E+02	2.511E+02	2.200E+02	2.073E+02	1.777E+02
40.00	1.142E+03	8.273E+02	6.480E+02	4.916E+02	4.218E+02	3.693E+02	3.475E+02	2.973E+02
50.00	1.710E+03	1.238E+03	9.693E+02	7.351E+02	6.307E+02	5.521E+02	5.191E+02	4.437E+02
60.00	2.376E+03	1.720E+03	1.346E+03	1.021E+03	8.757E+02	7.666E+02	7.203E+02	6.154E+02
70.00	3.136E+03	2.269E+03	1.776E+03	1.346E+03	1.155E+03	1.011E+03	9.497E+02	8.110E+02
80.00	3.985E+03	2.883E+03	2.256E+03	1.710E+03	1.467E+03	1.284E+03	1.206E+03	1.030E+03
90.00	4.919E+03	3.559E+03	2.784E+03	2.110E+03	1.810E+03	1.584E+03	1.488E+03	1.270E+03
100.0	5.935E+03	4.294E+03	3.359E+03	2.546E+03	2.183E+03	1.911E+03	1.794E+03	1.531E+03
150.0	1.211E+04	8.759E+03	6.851E+03	5.189E+03	4.449E+03	3.893E+03	3.653E+03	3.116E+03
200.0	1.993E+04	1.441E+04	1.127E+04	8.535E+03	7.315E+03	6.400E+03	6.005E+03	5.121E+03
250.0	2.913E+04	2.106E+04	1.647E+04	1.247E+04	1.069E+04	9.349E+03	8.771E+03	7.478E+03
300.0	3.952E+04	2.857E+04	2.234E+04	1.691E+04	1.449E+04	1.268E+04	1.189E+04	1.014E+04
400.0	6.313E+04	4.563E+04	3.567E+04	2.700E+04	2.314E+04	2.024E+04	1.898E+04	1.618E+04
500.0	8.982E+04	6.492E+04	5.075E+04	3.841E+04	3.291E+04	2.878E+04	2.699E+04	2.300E+04
600.0	1.189E+05	8.591E+04	6.716E+04	5.083E+04	4.354E+04	3.808E+04	3.571E+04	3.043E+04
700.0	1.497E+05	1.082E+05	8.459E+04	6.402E+04	5.484E+04	4.796E+04	4.497E+04	3.832E+04
800.0	1.820E+05	1.316E+05	1.028E+05	7.783E+04	6.666E+04	5.829E+04	5.466E+04	4.657E+04
900.0	2.155E+05	1.557E+05	1.217E+05	9.211E+04	7.889E+04	6.898E+04	6.468E+04	5.510E+04
1000.	2.498E+05	1.805E+05	1.411E+05	1.068E+05	9.145E+04	7.995E+04	7.497E+04	6.387E+04

Material: Liquid water

Ion	Na	Mg	Al	Si	P	S	Cl	Ar
(E/A_1) / MeV				$[\rho R(E)-\rho R(E_0)]$ / mgcm^{-2}				
0.025	0.000E+00	0.000E+00	0.000E+00	0.000E+00	0.000E+00	0.000E+00	0.000E+00	0.000E+00
0.030	2.033E−02	2.051E−02	2.236E−02	2.249E−02	2.404E−02	2.414E−02	2.551E−02	2.863E−02
0.040	5.547E−02	5.606E−02	6.113E−02	6.155E−02	6.590E−02	6.619E−02	7.006E−02	7.865E−02
0.050	8.529E−02	8.627E−02	9.409E−02	9.477E−02	1.016E−01	1.020E−01	1.082E−01	1.215E−01
0.060	1.115E−01	1.128E−01	1.230E−01	1.239E−01	1.329E−01	1.335E−01	1.416E−01	1.591E−01
0.070	1.351E−01	1.367E−01	1.490E−01	1.501E−01	1.610E−01	1.617E−01	1.717E−01	1.929E−01
0.080	1.568E−01	1.586E−01	1.728E−01	1.740E−01	1.866E−01	1.874E−01	1.991E−01	2.236E−01
0.090	1.770E−01	1.789E−01	1.948E−01	1.961E−01	2.103E−01	2.112E−01	2.243E−01	2.520E−01
0.100	1.959E−01	1.980E−01	2.154E−01	2.168E−01	2.324E−01	2.333E−01	2.479E−01	2.784E−01
0.150	2.799E−01	2.821E−01	3.059E−01	3.070E−01	3.287E−01	3.294E−01	3.498E−01	3.924E−01
0.200	3.524E−01	3.540E−01	3.826E−01	3.829E−01	4.090E−01	4.090E−01	4.338E−01	4.859E−01
0.250	4.196E−01	4.202E−01	4.525E−01	4.516E−01	4.813E−01	4.803E−01	5.087E−01	5.688E−01
0.300	4.842E−01	4.835E−01	5.190E−01	5.166E−01	5.493E−01	5.469E−01	5.783E−01	6.454E−01
0.400	6.104E−01	6.065E−01	6.475E−01	6.413E−01	6.791E−01	6.733E−01	7.097E−01	7.895E−01
0.500	7.351E−01	7.278E−01	7.732E−01	7.628E−01	8.047E−01	7.950E−01	8.355E−01	9.267E−01
0.600	8.604E−01	8.492E−01	8.986E−01	8.834E−01	9.288E−01	9.148E−01	9.590E−01	1.061E+00
0.700	9.870E−01	9.717E−01	1.025E+00	1.004E+00	1.053E+00	1.034E+00	1.082E+00	1.194E+00
0.800	1.115E+00	1.096E+00	1.152E+00	1.126E+00	1.178E+00	1.154E+00	1.204E+00	1.327E+00
0.900	1.246E+00	1.222E+00	1.281E+00	1.249E+00	1.303E+00	1.274E+00	1.327E+00	1.460E+00
1.000	1.379E+00	1.350E+00	1.412E+00	1.374E+00	1.430E+00	1.395E+00	1.451E+00	1.593E+00
1.500	2.080E+00	2.025E+00	2.099E+00	2.025E+00	2.090E+00	2.023E+00	2.090E+00	2.280E+00
2.000	2.849E+00	2.762E+00	2.842E+00	2.725E+00	2.795E+00	2.689E+00	2.765E+00	3.003E+00
2.500	3.687E+00	3.563E+00	3.645E+00	3.478E+00	3.549E+00	3.398E+00	3.480E+00	3.766E+00
3.000	4.598E+00	4.428E+00	4.510E+00	4.285E+00	4.354E+00	4.152E+00	4.237E+00	4.573E+00
4.000	6.641E+00	6.357E+00	6.425E+00	6.064E+00	6.118E+00	5.797E+00	5.882E+00	6.318E+00
5.000	8.983E+00	8.553E+00	8.590E+00	8.063E+00	8.092E+00	7.626E+00	7.704E+00	8.242E+00
6.000	1.163E+01	1.102E+01	1.101E+01	1.029E+01	1.028E+01	9.643E+00	9.704E+00	1.035E+01
7.000	1.458E+01	1.375E+01	1.368E+01	1.273E+01	1.267E+01	1.185E+01	1.188E+01	1.263E+01
8.000	1.784E+01	1.676E+01	1.661E+01	1.541E+01	1.528E+01	1.424E+01	1.424E+01	1.510E+01
9.000	2.142E+01	2.004E+01	1.979E+01	1.830E+01	1.810E+01	1.682E+01	1.679E+01	1.776E+01
10.00	2.531E+01	2.358E+01	2.323E+01	2.142E+01	2.113E+01	1.960E+01	1.951E+01	2.060E+01
15.00	4.939E+01	4.535E+01	4.424E+01	4.040E+01	3.951E+01	3.633E+01	3.586E+01	3.755E+01
20.00	8.114E+01	7.373E+01	7.152E+01	6.492E+01	6.317E+01	5.780E+01	5.675E+01	5.908E+01
25.00	1.203E+02	1.085E+02	1.049E+02	9.485E+01	9.202E+01	8.394E+01	8.213E+01	8.516E+01
30.00	1.666E+02	1.495E+02	1.442E+02	1.300E+02	1.259E+02	1.146E+02	1.119E+02	1.157E+02
40.00	2.796E+02	2.491E+02	2.397E+02	2.155E+02	2.082E+02	1.892E+02	1.841E+02	1.895E+02
50.00	4.184E+02	3.712E+02	3.566E+02	3.201E+02	3.090E+02	2.805E+02	2.726E+02	2.799E+02
60.00	5.813E+02	5.143E+02	4.938E+02	4.428E+02	4.273E+02	3.877E+02	3.764E+02	3.858E+02
70.00	7.671E+02	6.774E+02	6.502E+02	5.827E+02	5.622E+02	5.099E+02	4.948E+02	5.066E+02
80.00	9.747E+02	8.596E+02	8.249E+02	7.389E+02	7.127E+02	6.465E+02	6.271E+02	6.415E+02
90.00	1.203E+03	1.060E+03	1.017E+03	9.106E+02	8.784E+02	7.967E+02	7.726E+02	7.899E+02
100.0	1.451E+03	1.278E+03	1.226E+03	1.097E+03	1.058E+03	9.600E+02	9.307E+02	9.512E+02
150.0	2.958E+03	2.598E+03	2.492E+03	2.229E+03	2.150E+03	1.950E+03	1.890E+03	1.929E+03
200.0	4.862E+03	4.268E+03	4.091E+03	3.659E+03	3.529E+03	3.201E+03	3.101E+03	3.164E+03
250.0	7.101E+03	6.230E+03	5.972E+03	5.339E+03	5.149E+03	4.670E+03	4.524E+03	4.614E+03
300.0	9.626E+03	8.442E+03	8.091E+03	7.234E+03	6.975E+03	6.326E+03	6.127E+03	6.248E+03
400.0	1.536E+04	1.347E+04	1.291E+04	1.154E+04	1.112E+04	1.009E+04	9.767E+03	9.956E+03
500.0	2.184E+04	1.915E+04	1.834E+04	1.640E+04	1.580E+04	1.433E+04	1.388E+04	1.414E+04
600.0	2.889E+04	2.532E+04	2.426E+04	2.168E+04	2.090E+04	1.895E+04	1.835E+04	1.869E+04
700.0	3.638E+04	3.188E+04	3.054E+04	2.730E+04	2.631E+04	2.385E+04	2.309E+04	2.353E+04
800.0	4.422E+04	3.875E+04	3.712E+04	3.317E+04	3.197E+04	2.898E+04	2.806E+04	2.858E+04
900.0	5.233E+04	4.585E+04	4.392E+04	3.924E+04	3.782E+04	3.429E+04	3.319E+04	3.381E+04
1000.	6.065E+04	5.314E+04	5.090E+04	4.548E+04	4.383E+04	3.973E+04	3.846E+04	3.918E+04

Journal of the ICRU Vol 5 No 1 (2005) Report 73
Oxford University Press
doi:10.1093/jicru/ndi014

REFERENCES

Abdesselam, M., Stoquert, J., Guillaume, G., Hageali, M., Grob, J. and Siffert, P. (1991) 'Stopping power of C and Al ions in solids.' Nucl. Instrum. Meth. B **61**, 385–393.

Abdesselam, M., Stoquert, J., Guillaume, G., Hageali, M., Grob, J. and Siffert, P. (1992) 'Stopping power of O-16, Ti-48 and Ag-108 ions in C and Al between 0.5 and 3. MeV/u.' Nucl. Instrum. Meth. B **72**, 293–301.

Agostinelli, S., Allison, J., Amako, K., Apostolakis, J., Araujo, H., Arce, P., Asai, M., Axen, D., Banerjee, S., Barrand, G., Behner, F., Bellagamba, L., Boudreau, J., Broglia, L., Brunengo, A., Burkhardt, H., Chauvie, S., Chuma, J., Chytracek, R., Cooperman, G., Cosmo, G., Degtyarenko, P., Dell'Acqua, A., Depaola, G., Dietrich, D., Enami, R., Feliciello, A., Ferguson, C., Fesefeldt, H., Folger, G., Foppiano, F., Forti, A., Garelli, S., Giani, S., Giannitrapani, R., Gibin, D., Cadenas, J. J. G., Gonzalez, I., Abril, G. G., Greeniaus, G., Greiner, W., Grichine, V., Grossheim, A., Guatelli, S., Gumplinger, P., Hamatsu, R., Hashimoto, K., Hasui, H., Heikkinen, A., Howard, A., Ivanchenko, V., Johnson, A., Jones, F. W., Kallenbach, J., Kanaya, N., Kawabata, M., Kawabata, Y., Kawaguti, M., Kelner, S., Kent, P., Kimura, A., Kodama, T., Kokoulin, R., Kossov, M., Kurashige, H., Lamanna, E., Lampen, T., Lara, V., Lefebure, V., Lei, F., Liendl, M., Lockman, W., Longo, F., Magni, S., Maire, M., Medernach, E., Minamimoto, K., de Freitas, P. M., Morita, Y., Murakami, K., Nagamatu, M., Nartallo, R., Nieminen, P., Nishimura, T., Ohtsubo, K., Okamura, M., O'Neale, S., Oohata, Y., Paech, K., Perl, J., Pfeiffer, A., Pia, M. G., Ranjard, F., Rybin, A., Sadilov, S., Di Salvo, E., Santin, G., Sasaki, T., Savvas, N., Sawada, Y., Scherer, S., Seil, S., Sirotenko, V., Smith, D., Starkov, N., Stoecker, H., Sulkimo, J., Takahata, M., Tanaka, S., Tcherniaev, E., Tehrani, E. S., Tropeano, M., Truscott, P., Uno, H., Urban, L., Urban, P., Verderi, M., Walkden, A., Wander, W., Weber, H., Wellisch, J. P., Wenaus, T., Williams, D. C., Wright, D., Yamada, T., Yoshida, H. and Zschiesche, D. (2003) 'GEANT4 — a simulation toolkit.' Nucl. Instrum. Meth. A **506**, 250–303.

Ahlen, S. P. (1978) 'Z_1^7 stopping-power formula for fast heavy ions.' Phys. Rev. A **17**, 1236–1239.

Ahlen, S. P. (1980) 'Theoretical and experimental aspects of the energy loss of relativistic heavily ionizing particles.' Rev. Mod. Phys. **52**, 121–173.

Ahlen, S. P. and Tarlé, G. (1983) 'Observation of large deviations from the Bethe–Bloch formula for relativistic uranium ions.' Phys. Rev. Lett. **50**, 1110–1113.

Al-Bedri, M. B. and Harris, S. J. (1975) 'Energy straggling of fission fragments in gases and solids.' Nucl. Instrum. Meth. **124**, 125–130.

Alanko, T., Hyvonen, J., Kyllonen, V., Laitinen, P., Matilainen, A., Räisänen, J. and Virtanen, A. (2001) 'Polycarbonate, Mylar and Havar stopping powers for 1.0–3.25 MeV/nucleon Ar-40-ions.' J. Phys. Condens. Matter **13**, 10777–10784.

Alanko, T., Trzaska, W. H., Lyapin, V., Räisänen, J., Tiourine, G. and Virtanen, A. (2002) 'Simultaneous wide-range stopping power determination for several ions.' Nucl. Instrum. Meth. B **190**, 60–63.

Ali, S. P. and Gallaher, D. F. (1974) 'Electronic stopping power of channelled ions in a model incorporating Pauli principle.' J. Phys. C **7**, 2434–2446.

Allison, S. K. (1958) 'Experimental results on charge-changing collisions of hydrogen and helium atoms and ions at kinetic energies above 0.2 keV.' Rev. Mod. Phys. **30**, 1137–1168.

Allison, S. K., Cuevas, J. and Garcia-Munos, M. (1962) 'Partial atomic stopping power of gaseous hydrogen for hydrogen beams.' Phys. Rev. **127**, 792–798.

Amsel, G., Battistig, G. and L'Hoir, A. (2003) 'Small angle multiple scattering of fast ions, physics, stochastic theory and numerical calculations.' Nucl. Instrum. Meth. B **201**, 325–388. Available on www.mfm.kfki.hu/ms.

Andersen, H. H. (1991) Accelerators and stopping power experiments. In: *Interaction of Charged Particles with Solids and Surfaces*, vol. B 271 of *NATO ASI Series*. Gras-Marti, A., Urbassek, H. M., Arista, N. R. and Flores, F., Eds. (New York: Plenum) p. 145.

Andersen, H. H. and Bøttiger, J. (1971) 'Multiple scattering of heavy ions of keV energies transmitted through thin carbon films.' Phys. Rev. B **4**, 2105–2111.

Andersen, H. H. and Sigmund, P., Eds. (2002) 'Stopping of heavy ions — STOP 01.' Nucl. Instrum. Meth. B **195**.

Andersen, H. H. and Ziegler, J. F. (1977) Hydrogen stopping powers and ranges in all elements. In: *The Stopping and Ranges of Ions in Matter*, vol. 2, Ziegler, J. F., Ed. (New York: Pergamon) pp. 1–207.

Andersen, H. H., Garfinkel, A. F., Hanke, C. C. and Sørensen, H. (1966) 'Stopping power of aluminium for 5–12 MeV protons and deuterons.' Mat. Fys. Medd. Dan. Vid. Selsk. **34**, 1–24.

Andersen, H. H., Simonsen, H. and Sørensen, H. (1969) 'An experimental investigation of charge-dependent deviations from the Bethe stopping power formula.' Nucl. Phys. A **125**, 171–175.

© International Commission on Radiation Units and Measurements 2005

Andersen, H. H., Bøttiger, J. and Knudsen, H. (1972) 'Multiple scattering of heavy ions of keV energies transmitted through thin, polycrystalline gold foils.' Radiat. Eff. **13**, 203–207.

Andersen, H. H., Bøttiger, J., Knudsen, H., Petersen, P. M. and Wohlenberg, T. (1974) 'Multiple scattering of heavy ions of keV energies transmitted through thin films.' Phys. Rev. A **10**, 1568–1577.

Andersen, H. H., Besenbacher, F. and Knudsen, H. (1978) 'Stopping power and straggling of 65–500 keV Lithium ions in H_2, He, CO_2, N_2, O_2, Ne, Ar, Kr, and Xe.' Nucl. Instrum. Meth. **149**, 121–127.

Andersen, H. H., Besenbacher, F. and Goddiksen, P. (1980) 'Stopping power and straggling of 80–500 keV Lithium ions in C, Al, Ni, Cu, Se, Ag, and Te.' Nucl. Instrum. Meth. **168**, 75–80.

Andersen, L. H., Hvelplund, P., Knudsen, H., Møller, S. P., Pedersen, J. O. P., Uggerhøj, E., Elsener, K. and Morenzoni, E. (1989) 'Measurement of the Z_1^3 contribution to the stopping power using MeV protons and antiprotons — the Barkas effect.' Phys. Rev. Lett. **62**, 1731–1734.

Angulo, C., Delbar, T., Graulich, J.-S. and Leleux, P. (2000) 'Stopping powers of ions at 1 MeV per nucleon.' Nucl. Instrum. Meth. B **170**, 21–27.

Anne, R., Herault, J., Bimbot, R., Gauvin, H., Bastin, G. and Hubert, F. (1988) 'Multiple angular scattering of heavy ions (^{16,17}O, ^{40}Ar, ^{86}Kr and ^{100}Mo) at intermediate energies (20–90 MeV/u).' Nucl. Instrum. Meth. B **34**, 295–308.

Anthony, J. M. (1983) 'Heavy ion energy straggling.' Nucl. Instrum. Meth. **218**, 803–809.

Anthony, J. M. and Lanford, W. A. (1982) 'Stopping power and effective charge of heavy ions in solids.' Phys. Rev. A **25**, 1868–1879.

Antolak, A., Handy, B., Morse, D. and Pontau, A. (1991) 'Energy loss and straggling measurements of ions in solid absorbers.' Nucl. Instrum. Meth. B **59**, 13–17.

Araujo, L. L., Grande, P. L., Behar, M. and dos Santos, J. H. R. (2002) 'Random stopping power and energy straggling of O-16 ions into amorphous Si target.' Nucl. Instrum. Meth. B **190**, 79–83.

Arbó, D. G., Gravielle, M. S. and Miraglia, J. E. (2000) 'Second-order Born collisional stopping of ions in a free-electron gas.' Phys. Rev. A **62**, 032901–1–7.

Arista, N. R. (2002) 'Energy loss of heavy ions in solids: non-linear calculations for slow and swift ions.' Nucl. Instrum. Meth. B **195**, 91–105.

Arista, N. R. and Lifschitz, A. F. (1999) 'Nonlinear calculation of stopping powers for protons and antiprotons in solids: the Barkas effect.' Phys. Rev. A **59**, 2719–2722.

Arista, N. R. and Lifschitz, A. F. (2002) 'Non-linear calculation of antiproton stopping powers at finite velocities using the extended Friedel sum rule.' Nucl. Instrum. Meth. B **193**, 8–14.

Arnau, A. and Echenique, P. M. (1989) 'Stopping power of an electron gas for partially stripped ions.' Nucl. Instrum. Meth. B **42**, 165–170.

Arnau, A., Echenique, P. M. and Ritchie, R. H. (1988) 'Stopping power of slow ions in metals and insulators.' Nucl. Instrum. Meth. B **33**, 138–141.

Arnold, R. C. and Meyer-Ter-Vehn, J. (1987) 'Inertial confinement fusion driven by heavy-ion beams.' Repts. Prog. Phys. **50**, 559–606.

Arstila, K. (2000) 'An experimental method for precise determination of electronic stopping powers for heavy ions.' Nucl. Instrum. Meth. B **168**, 473–483.

Arstila, K., Keinonen, J. and Tikkanen, P. (1995) 'Stopping power for low-velocity heavy ions: (0.01–0.9) MeV/nucleon Si ions in 18 ($Z = 13$–79) metals.' Nucl. Instrum. Meth. B **101**, 321–326.

Ashley, J. C., Ritchie, R. H. and Brandt, W. (1972) 'Z_1^3 effect in the stopping power of matter for charged particles.' Phys. Rev. B **5**, 2393–2397.

Ashley, J. C., Ritchie, R. H., Echenique, P. M. and Nieminen, R. M. (1986) 'Nonlinear calculations of the energy loss of slow ions in an electron gas.' Nucl. Instrum. Meth. B **15**, 11–13.

Azevedo, G. M., Grande, P. L. and Schiwietz, G. (2000) 'Impact-parameter dependent energy loss of screened ions.' Nucl. Instrum. Meth. B **164–165**, 203–211.

Azevedo, G. M., Grande, P. L., Behar, M., Dias, J. F. and Schiwietz, G. (2001) 'Giant Barkas effect observed for light ion channeling in Si.' Phys. Rev. Lett. **86**, 1482–1485.

Baklitsky, B. E., Parilis, E. S. and Ferleger, V. K. (1973) 'Dependence of inelastic energy loss on the atomic number of the ions.' Radiat. Eff. **19**, 155–160.

Balashov, V. V., Bibikov, A. V. and Bodrenko, I. V. (1997) 'Effect of charge exchange on the energy distribution of fast multiply charged ions propagating through matter.' Zh. Eksp. Teor. Fiz. **111**, 2226–2236 [English translation: JETP **84**, 1215–1220 (1997)].

Barkas, W. H., Dyer, J. N. and Heckman, H. H. (1963) 'Resolution of the Σ^--mass anomaly.' Phys. Rev. Lett. **11**, 26–28.

Baudin, K., Brunelle, A., Chabot, M., Della-Negra, S., Depauw, J., Gardès, D., kansson, P. H., LeBeyec, Y., Billebaud, A., Fallavier, M., Remillieux, J., Poizat, J. C. and Thomas, J. P. (1994) 'Energy loss by MeV carbon clusters and fullerene ions in solids.' Nucl. Instrum. Meth. B **94**, 341–344.

Bauer, P. (1987) 'How to measure absolute stopping cross sections by backscattering and by transmission methods. Part I. Backscattering.' Nucl. Instrum. Meth. B **27**, 301–314.

Bauer, P., Kastner, F., Arnau, A., Salin, A., Fainstein, P. D., Ponce, V. H. and Echenique, P. M. (1992) 'Phase effect in the energy loss of H projectiles in Zn targets — experimental evidence and theoretical explanation.' Phys. Rev. Lett. **69**, 1137–1139.

Bearden, J. A. and Burr, A. F. (1967) 'Reevaluation of X-Ray Atomic Energy Levels.' Rev. Mod. Phys. **39**, 125–142.

Ben-Hamu, D., Baer, A., Feldman, H., Levin, J., Heber, O., Amitay, Z., Vager, Z. and Zajfman, D. (1997) 'Energy loss of fast clusters through matter.' Phys. Rev. A **56**, 4786–4794.

Bentini, G., Bianconi, M., Nipoti, R., Malaguti, F. and Verondini, E. (1991) 'Random and channeling stopping power of nitrogen in silicon in the 700–1500 keV range.' Nucl. Instrum. Meth. B **53**, 1–6.

Bentini, G., Bianconi, M. and Nipoti, R. (1993) 'Energy loss and equilibrium charge distribution of nitrogen ions transmitted through thin silicon crystals.' Nucl. Instrum. Meth. B **80–81**, 33–36.

Benton, E. V. and Henke, R. P. (1969) 'Heavy particle range-energy relations for dielectric nuclear track detectors.' Nucl. Instrum. Meth. **67**, 87–92.

Berger, M. J. and Paul, H. (1995) *Stopping Powers, Ranges, and Straggling*; *Atomic and Molecular Data for Radiotherapy and Radiation Research*. IAEA-TECDOC-799, Chap. 7 (Vienna: IAEA), pp. 415–545.

Bergsmann, M., Hörlsberger, P., Kastner, F. and Bauer, P. (1998) 'Electronic stopping power of protons and He ions in a dilute electron gas of a metal.' Phys. Rev. B **58**, 5139–5144.

Bergsmann, M., Raab, W., Schrenk, G., Kastner, F., No, R. D. M., Arnau, A., Salin, A., Bauer, P. and Echenique, P. M. (2000) 'Phase effect in stopping of H ions in Mg.' Phys. Rev. B **62**, 3153–3159.

Berkowitz, J. (1979) *Photoabsorption, Photoionization and Photoelectron Spectroscopy* (New York: Academic Press).

Berkowitz, J. (2002) *Atomic and Molecular Photoabsorption. Absolute Total Cross Sections* (San Diego: Academic Press).

Bertulani, C. A. and Baur, G. (1988) 'Electromagnetic processes in relativistic heavy-ion collisions.' Phys. Rep. **163**, 299–408.

Besenbacher, F., Heinemeier, J., Hvelplund, P. and Knudsen, H. (1978) 'Influence of spatial correlation between target atoms on the scattering of energetic ions: multiple scattering in molecular gases.' Phys. Rev. A **18**, 2470–2481.

Besenbacher, F., Andersen, J. U. and Bonderup, E. (1980) 'Straggling in energy loss of energetic hydrogen and helium ions.' Nucl. Instrum. Meth. **168**, 1–15.

Besenbacher, F., Bøttiger, J., Graversen, O. and Hansen, J. L. (1981) 'Stopping power of solid argon for helium ions.' Nucl. Instrum. Meth. **188**, 657–667.

Bethe, H. (1930) 'Zur Theorie des Durchgangs schneller Korpuskularstrahlen durch Materie.' Ann. Physik **5**, 324–400.

Bethe, H. (1932) 'Bremsformel für Elektronen relativistischer Geschwindigkeit.' Z. Phys. **76**, 293–299.

Bethe, H. A. (1953) 'Moliere's theory of multiple scattering.' Phys. Rev. **89**, 1256–1266.

Betz, H. D. (1972) 'Charge states and charge-changing cross sections of fast heavy ions penetrating through gaseous and solid media.' Rev. Mod. Phys. **44**, 465–539.

Betz, H. D. and Grodzins, L. (1970) 'Charge states and excitation of fast heavy ions passing through solids: a new model for the density effect.' Phys. Rev. Lett. **25**, 211–214.

Bhalla, C. P. and Bradford, J. N. (1968) 'Oscillating behavior of electron stopping power.' Phys. Lett. A **27**, 318–319.

Bhalla, C. P., Bradford, J. N. and Reese, G. (1970) Critical examination of modified Firsov theory of inelastic energy loss in atomic collisions. In: *Atomic Collisions in Solids*, Palmer, D. W., Thompson, M. W. and Townsend, P. D., Eds. (Amsterdam: North Hollan) p. 361.

Bianchi, L., Fernandez, B., Gastebois, J., Gillibert, A., Mittig, W. and Barrette, J. (1989) 'SPEG — an energy-loss spectrometer for GANIL.' Nucl. Instrum. Meth. A **276**, 509–520.

Bichsel, H. (2002) 'Shell corrections in stopping powers.' Phys. Rev. A **65**, 052709–1–11.

Bichsel, H., Hiraoka, T. and Omata, K. (2000) 'Aspects of fast-ion dosimetry.' Radiat. Res. **153**, 208.

Bierman, D. J., Turkenburg, W. C. and Bhalla, C. P. (1972) 'Inelastic energy losses in small-angle scattering of energetic particles.' Physica **60**, 357–374.

Bimbot, R. (1992) 'Compilation, measurements and tabulation of heavy ion stopping data.' Nucl. Instrum. Meth. B **69**, 1–9.

Bimbot, R. (1999) Cyclotrons and their applications. In: *From the Discovery of Radioactivity to the Production of Radioactive Beams*, Baron, E. and Lieuvin, M., Eds. (Bristol: Institute of Physics Publishing) pp. 5–12.

Bimbot, R., della Negra, S., Gardès, D., Gauvin, H., Fleury, A. and Hubert, F. (1978) 'Stopping power measurements for 4–5 MeV/nucleon ^{16}O,^{40}Ar, ^{63}Cu and ^{84}Kr in C, Al, Ni, Ag and Au.' Nucl. Instrum. Meth. **153**, 161–169.

Bimbot, R., Gardès, D., Geissel, H., Kitahara, T., Armbruster, P., Fleury, A. and Hubert, F. (1980) 'Stopping power measurements for 3–5 MeV/nucleon ^{86}Kr, ^{136}Xe, ^{208}Pd and ^{238}U in solids.' Nucl. Instrum. Meth. **174**, 231–236.

Bimbot, R., Gauvin, H., Orliange, I., Anne, R., Bastin, G. and Hubert, F. (1986) 'Stopping powers of solids for ^{40}Ar and ^{40}Ca ions at intermediate energies (20–80 MeV/u).' Nucl. Instrum. Meth. B **17**, 1–10.

Bimbot, R., Cabot, C., Gardès, D., Gauvin, H., Hingmann, R., Orliange, I., De Reilhac, L. and Hubert, F. (1989a) 'Stopping power of gases for heavy ions: gas–solid effect I. 2–13 MeV/u Ne and Ar projectiles.' Nucl. Instrum. Meth. B **44**, 1–18.

Bimbot, R., Cabot, C., Gardès, D., Gauvin, H., Orliange, I., DeReilhac, L., Subotic, K. and Hubert, F. (1989b) 'Stopping power of gases for heavy ions: gas–solid effect II. 2–6 MeV/u Cu, Kr and Ag projectiles.' Nucl. Instrum. Meth. B **44**, 19–34.

Bimbot, R., Barbey, S., Benfoughal, T., Clapier, F., Mirea, M., Pauwels, N., Pierre, S., Rivet, M. F., Fares, G., Hachem, A., Anne, R., Georget, Y., Hue, R. and Tribouillard, C. (1996) 'Stopping powers of gases for very heavy ions.' Nucl. Instrum. Meth. B **107**, 9–14.

Bimbot, R., Khoumri, A., Fahli, A., Barbey, S., Benfoughal, T., Mirea, M., Hachem, A., Fares, G., Anne, E., Delagrange, H., Tribouillard, C., Georget, Y. and Foy, J. C. (2000) 'Stopping powers of gases for 40 MeV/u tellurium ions.' Nucl. Instrum. Meth. B **170**, 329–335.

Bird, J. R. and Williams, J. S. (1989) *Ion Beams for Material Analysis* (New York: Academic Press).

Blazevic, A., Bohlen, H. G. and Oertzen, W. V. (2000) 'Charge-state changing processes for Ne ions passing through thin carbon foils.' Phys. Rev. A **61**, 032901–1–6.

Blazevic, A., Bohlen, H. G. and von Oertzen, W. (2002) 'Stopping power of swift neon ions in dependence on the charge state in the non-equilibrium regime.' Nucl. Instrum. Meth. B **190**, 64–68.

Bloch, F. (1933a) 'Bremsvermögen von Atomen mit mehreren Elektronen.' Z. Phys. **81**, 363–376.

Bloch, F. (1933b) 'Zur Bremsung rasch bewegter Teilchen beim Durchgang durch Materie.' Ann. Physik **16**, 285–320.

Bohr, N. (1913) 'On the theory of the decrease of velocity of moving electrified particles on passing through matter.' Philos. Mag. **25**, 10–31.

Bohr, N. (1915) 'On the decrease of velocity of swiftly moving electrified particles in passing through matter.' Philos. Mag. **30**, 581–612.

Bohr, N. (1940) 'Scattering and stopping of fission fragments.' Phys. Rev. **58**, 654–655.

Bohr, N. (1941) 'Velocity–range relation for fission fragments.' Phys. Rev. **59**, 270–275.

Bohr, N. (1948) 'The penetration of atomic particles through matter.' Mat. Fys. Medd. Dan. Vid. Selsk. **18**(8), 1–144.

Bohr, N. and Lindhard, J. (1954) 'Electron capture and loss by heavy ions penetrating through matter.' Mat. Fys. Medd. Dan. Vid. Selsk. **28**(7), 1–31.

Bonderup, E. (1967) 'Stopping of swift protons evaluated from statistical atomic model.' Mat. Fys. Medd. Dan. Vid. Selsk. **35**(17), 1–20.

Bonderup, E. and Hvelplund, P. (1971) 'Stopping power and energy straggling for swift protons.' Phys. Rev. A **4**, 562–589.

Booth, N. E., Cabrera, B. and Fiorini, E. (1996) 'Low-temperature particle detectors.' Ann. Rev. Nucl. Part. Sci. **46**, 471–532.

Booth, W. and Grant, I. S. (1965) 'The energy loss of oxygen and chlorine ions in solids.' Nucl. Phys. **63**, 481–495.

Bothe, W. (1921) 'Theorie der Zerstreuung der α-Strahlen über kleine Winkel.' Z. Phys. **4**, 300.

Bøttiger, J. and Bason, F. (1969) 'Energy loss of heavy ions along low-index directions in gold single crystals.' Radiat. Eff. **2**, 105.

Brandt, W. and Kitagawa, M. (1982) 'Effective stopping-power charges of swift ions in condensed matter.' Phys. Rev. B **25**, 5631–5637.

Brandt, W., Ratkowski, A. and Ritchie, R. H. (1974) 'Energy loss of swift proton clusters in solids.' Phys. Rev. Lett. **33**, 1325–1328.

Brice, D. K. (1972) 'Three-parameter formula for the electronic stopping cross section at nonrelativistic velocities.' Phys. Rev. A **6**, 1791–1805.

Bridwell, L. B., Cowern, N. E. B., Read, P. M. and Sofield, C. J. (1986) 'Measurement of polarization, Bloch and charge exchange contributions to the stopping power of C and O ions in carbon.' Nucl. Instrum. Meth. B **13**, 123–126.

Brière, M. and Biersack, J. (1992) 'Energy loss straggling of MeV ions in thin solid films.' Nucl. Instrum. Meth. B **64**, 693–700.

Briggs, J. S. and Pathak, A. P. (1974) 'The stopping power of solids for low-velocity channelled heavy ions.' J. Phys. C **7**, 1929–1936.

Broude, C., Engelstein, P., Popp, M. and Tandon, P. N. (1972) 'Dependence of the Doppler shift lifetime method on slowing environment.' Phys. Lett. B **39**, 185–187.

Brunelle, A., Della-Negra, S., Depauw, J., Joret, H., LeBeyec, Y. and Wien, K. (1989) 'Equilibrium charge state of fast heavy ions in solids. Measurements of post-ionization effects.' Nucl. Instrum. Meth. B **43**, 484–489.

Brunelle, A., Della-Negra, S., Depauw, J., Jacquet, D., LeBeyec, Y. and Pautrat, M. (1997) *MeV Cluster Interactions with Solids: Explosion, Charge States and Secondary Emission*. Technical Report IPNO-DRE-97-35, Institut de Physique Nucleaire, Orsay.

Bryant, P. J. and Johnsen, K. (1993) *The Principles of Circular Accelerators and Storage Rings* (Cambridge: Cambridge University Press).

Bulgakov, Y. V., Nikolaev, V. S. and Shulga, V. I. (1974) 'The experimental determination of the impact parameter dependenceof inelastic energy loss of channeled ions.' Phys. Lett. A **46**, 477–478.

Burenkov, A. F., Komarov, F. F. and Fedotov, S. A. (1992a) 'The ion charge fluctuation effect on impurity depth distributions for high-energy ion implantation — the backward transport equation-based simulation.' Phys. Stat. Sol. B **169**, 33–49.

Burenkov, A. F., Komarov, F. F. and Fedotov, S. A. (1992b) 'The ion charge state fluctuation effect during high energy ion implantation: Monte-Carlo simulation.' Nucl. Instrum. Meth. B **67**, 35.

Burenkov, A. F., Komarov, F. F. and Fedotov, S. A. (1992c) 'The transport equation approach for the simulation of charge state fluctuation effects during ion implantation into solids.' Nucl. Instrum. Meth. B **67**, 30–34.

Bussmann, U., Hecking, N., Heidemann, K. F. and TeKaat, E. (1986) 'Ranges and electronic stopping powers of 1–24 MeV ^{12}C and ^{14}N ions in Si targets from optical reflectivity measurements on bevelled samples.' Nucl. Instrum. Meth. B **15**, 105–108.

Calera-Rubio, J., Gras-Marti, A. and Arista, N. R. (1994) 'Stopping power of low-velocity ions in solids — inhomogeneous electron-gas model.' Nucl. Instrum. Meth. B **93**, 137–141.

Chabot, M., Nectoux, M., Gardès, D., Maynard, G. and Deutsch, C. (1998) 'Charge state dependence of the stopping power for chlorine ions interacting with a cold gas and a plasma (1.5 MeV/u).' Nucl. Instrum. Meth. A **415**, 571–575.

Cheshire, I. M. and Poate, J. M. (1970) Shell effects in low-energy atomic collisions. In: *Atomic Collisions in Solids*. Palmer, D. W., Thompson, M. W. and Townsend, P. D., Eds. (Amsterdam: North Holland) pp. 351–360.

Cheshire, I. M., Dearnaley, G. and Poate, J. M. (1968) 'The Z_1-dependence of electronic stopping.' Phys. Lett. A **27**, 304–305.

Chu, W. K. (1976) 'Calculation of energy straggling for protons and helium ions.' Phys. Rev. A **13**, 2057–2060.

Chu, W. K. and Powers, D. (1972a) 'Calculations of mean excitation energy for all elements.' Phys. Lett. A **40**, 23–24.

Chu, W. K. and Powers, D. (1972b) 'On the Z_2 dependence of stopping cross sections for low energy alpha particles.' Phys. Lett. A **38**, 267–268.

Chu, W. K., Bourland, P. D., Wang, K. H. and Powers, D. (1968) 'Range and dE/dx of C, N, O, F, and Ne in Be and C from 500 keV to 2 MeV.' Phys. Rev. **175**, 342–353.

Chukreev, F. E. (1992) *Program 'POTAUS'*. Available on www.nea.fr/html/dbprog.

Clementi, E. and Roetti, C. (1974) 'Roothaan-Hartree-Fock atomic wave functions.' At. Data Nucl. Data Tables **14**, 177.

Cowern, N. E. B., Sofield, C. J., Freeman, J. M. and Mason, J. P. (1979) 'Energy straggling of 3–36-MeV C ions in aluminum.' Phys. Rev. A **19**, 111–115.

Cowern, N. E. B., Trehan, P. N., Sofield, C. J., Bridwell, L. B. and Ferguson, S. M. (1983a) 'Energy-straggling measurements with energetic C ions in Al and Ag.' Nucl. Instrum. Meth. **206**, 595–598.

Cowern, N. E. B., Woods, C. J. and Sofield, C. J. (1983b) 'The gas–solid density effect for MeV/u ions: charge changing cross sections and the effective charge.' Nucl. Instrum. Meth. **216**, 287–292.

Cowern, N. E. B., Read, P. M., Sofield, C. J., Bridwell, L. B., Huxtable, G. and Miller, M. (1984a) 'Charge state dependence of dE/dx for ions in very thin targets.' Nucl. Instrum. Meth. B **2**, 112–115.

Cowern, N. E. B., Read, P. M., Sofield, C. J., Bridwell, L. B. and Lucas, M. W. (1984b) 'Charge-changing energy loss, higher-order Z_1 dependence, and pre-equilibrium behavior in the stopping power for energetic ions in solids.' Phys. Rev. A **30**, 1682–1691.

Craseman, B., Karim, K. R. and Chen, M. H. (1987) 'Resource note: theoretical atomic-electron binding energies.' At. Data Nucl. Data Tables **36**, 355–374.

Cruz, S. A., Vargas, C. and Brice, D. K. (1979) 'Critical analysis of the modified Firsov model. Sensitivity to the choice of atomic wavefunctions.' Radiat. Eff. Lett. **43**, 79–84.

Cuevas, J., Garcia-Munos, M., Torres, P. and Allison, S. K. (1964) 'Partial atomic and ionic stopping powers of gaseous hydrogen for helium and hydrogen beams.' Phys. Rev. A **135**, 335–345.

Datz, S., Krause, H. F., Vane, C. R., Knudsen, H., Grafström, P. and Schuch, R. H. (1996) 'Effect of nuclear size on the stopping power of ultrarelativistic heavy ions.' Phys. Rev. Lett. **77**, 2925–2928.

Datz, S., Martin, F. W., Moak, C. D., Appleton, B. R. and Bridwell, L. B. (1972) 'Charge-changing collisions of channeled oxygen ions in gold.' Radiat. Eff. **12**, 163–169.

Datz, S., DelCampo, J. G., Dittner, P. F., Miller, P. D. and Biggerstaff, J. A. (1977) 'Higher-order Z_1 effects and effects of screening by bound K electrons on the electronic stopping of channeled ions.' Phys. Rev. Lett. **38**, 1145–1148.

Daw, M. S. and Baskes, M. I. (1984) 'Embedded-atom method — derivation and application to impurities, surfaces, and other defects in metals.' Phys. Rev. B **29**, 6443–6453.

de Ferrariis, L. and Arista, N. R. (1984) 'Classical and quantum-mechanical treatments of the energy loss of charged particles in dilute plasmas.' Phys. Rev. A **29**, 2145–2159.

Dedkov, G. V. (1995) 'The interatomic interaction potentials in radiation physics.' Phys. Stat. Sol. A **149**, 453–514.

Dehmer, J. L., Inokuti, M. and Saxon, R. P. (1975) 'Systematics of dipole oscillator-strength distributions for atoms of the first and second row.' Phys. Rev. A **12**, 102–121.

Della-Negra, S., LeBeyec, Y., Monart, B., Standing, K. and Wien, K. (1987) 'Measurement of the average equilibrium charge of fast heavy ions in a solid by H^+ emission at the exit surface.' Phys. Rev. Lett. **58**, 17–20.

Deutsch, C., Maynard, G. and Minoo, H. (1983) 'Ions stopping in dense and hot matter.' J. Phys. **44**, (C8), 67–92.

Deutsch, C., Maynard, G., Bimbot, R., Gardes, D., Dellanegra, S., Dumail, M., Kubica, B., Richard, A., Rivet, M. F., Servajean, A., Fleurier, C., Sanba, A., Hoffmann, D. H. H., Weyrich, K. and Wahl, H. (1989) 'Ion beam–plasma interaction — a standard model approach.' Nucl. Instrum. Meth. A **278**, 38–43.

Diwan, P. K., Kumar, S., Singh, G. and Singh, L. (2001a) 'Energy loss of heavy ions in gases: a comparative study.' Radiat. Meas. **33**, 193–202.

Diwan, P. K., Sharma, A. and Kumar, S. (2001b) 'Stopping power for heavy ions ($3 \leq Z \leq 35$) in solids at energies $\sim$0.5–2.5 MeV/n.' Nucl. Instrum. Meth. B **174**, 267–273.

Echenique, P. M., Nieminen, R. M. and Ritchie, R. H. (1981) 'Density functional calculation of stopping power of an electron gas for slow ions.' Solid State Commun. **37**, 779–781.

Echenique, P. M., Nieminen, R. M., Ashley, J. C. and Ritchie, R. H. (1986) 'Nonlinear stopping power of an electron gas for slow ions.' Phys. Rev. A **33**, 897–904.

Echenique, P. M., Arnau, A., Peñalba, M. and Nagy, I. (1991) 'Stopping power of low velocity ions in solids.' Nucl. Instrum. Meth. B **56–57**, 345–347.

Eckardt, J. C., Lantschner, G. H., Jakas, M. M. and Ponce, V. H. (1984) 'The correlation between inelastic energy-loss and scattering angle in transmission experiments.' Nucl. Instrum. Meth. B **230**, 168–172.

Eckstein, W. (1991) *Computer Simulation of Ion–Solid Interactions* (Berlin: Springer-Verlag).

Efken, B., Hahn, D., Hilscher, D. and Wüstefeld, G. (1975) 'Energy loss and energy loss straggling of N, Ne, and Ar ions in thin targets.' Nucl. Instrum. Meth. **129**, 219–225.

Egelhof, P. (1999) 'High resolution calorimetric low-temperature detectors for application in atomic and nuclear physics.' Adv. Solid State Phys. **39**, 61.

Eichler, J. (1985) 'Relativistic Eikonal theory of electron capture.' Phys. Rev. A **32**, 112–121.

Eichler, J. and Meyerhof, W. E. (1995) *Relativistic Atomic Collisions* (San Diego: Academic Press).

Eisen, F. H. (1968) 'Channeling of medium-mass ions through silicon.' Can. J. Phys. **46**, 561–572.

El-Hoshi, A. H. and Gibbons, J. F. (1968) 'Periodic dependence of the electronic stopping cross section for energetic heavy ions in solids.' Phys. Rev. **173**, 454–460.

Eppacher, C., Muiño, R. D., Semrad, D. and Arnau, A. (1995) 'Stopping power of lithium for hydrogen projectiles.' Nucl. Instrum. Meth. B **96**, 639–642.

Eriksson, L., Davies, J. A. and Jespersgaard, P. (1967) 'Range measurements in oriented tungsten single crystals (0.1–1.0 MeV). I. Electronic and nuclear stopping powers.' Phys. Rev. **161**, 219–234.

Esbensen, H. (1976) *Contributions to detailed perturbation theory for slowing-down of charged particles*, Ph.D. thesis, Aarhus University.

Esbensen, H. and Sigmund, P. (1990) 'Barkas effect in a dense medium: stopping power and wake field.' Ann. Physics **201**, 152–192.

Eyeberger, L. (1999) 'SWIMS, Sigmund and Winterbon multiple scattering of ion beams'. Available on www.nea.fr/abs/html/ests0682.html.

Falcone, G., Gras-Marti, A., Sigmund, P., Smend, F., Ahlert, J., Schumacher, M., Rullhusen, P. and Ziegeler, L. (1981) 'Stopping of slow recoil atoms in gases.' Z. Physik A **301**, 101–107.

Fano, U. (1963) 'Penetration of protons, alpha particles, and mesons.' Ann. Rev. Nucl. Sci. **13**, 1–66.

Fano, U. and Lichten, W. (1965) 'Interpretation of Ar^+–Ar collisions at 50 keV.' Phys. Rev. Lett. **14**, 627–629.

Fastrup, B., Hvelplund, P. and Sautter, C. A. (1966) 'Stopping cross section in carbon of 0.1–1.0 MeV atoms with $6 < Z_1 < 20$.' Mat. Fys. Medd. Dan. Vid. Selsk. **35**(10), 1–28.

Fermi, E. and Amaldi, E. (1934) 'Le orbite degli elementi.' Mem. Accad. Italia **6**, 119–149.

Fermi, E. and Teller, E. (1947) 'The capture of negative mesotrons in matter.' Phys. Rev. **72**, 399–408.

Finnemann, J. (1968) *En redegørelse for resultaterne af beregninger over spredning af elektroner med lav energi på afskærmede Coulombfelter*, Master's thesis, Aarhus University.

Firsov, O. B. (1957) 'Interaction energy of atoms for small nuclear separations.' Zh. Eksp. Teor. Fiz. **32**, 1464–1469 [English translation: Sov. Phys. JETP **5**, 1192–1196 (1957)].

Firsov, O. B. (1959) 'A qualitative interpretation of the mean electron excitation energy in atomic collsions.' Zh. Eksp. Teor. Fiz. **36**, 1517–1523 [English translation: Sov. Phys. JETP **9**, 1076–1080 (1959)].

Flamm, L. and Schumann, R. (1916) 'Die Geschwindigkeitsabnahme der α-Strahlen in Materie.' Ann. Physik **50**, 655.

Fleurier, C., Mathias, J., Damax, B., Pellicer, J., Bonnet, A., Gardès, D. and Kubica, B. (1991) 'Fast valve for ion beam–plasma interaction.' Nucl. Instrum. Meth. B **61**, 236–238.

Folger, H., Ed. (1989) *Heavy Ion Targets and Related Phenomena*, vol. 282 of *Nucl. Instrum. Meth. A* (Nucl. Instrum. Methods B).

Folger, H. (1999) 'Aspects of the historical development of targetry for heavy ions of 0.05–2000 A·MeV at GSI.' Nucl. Instrum. Meth. A **438**, 131–151.

Forster, J. S., Ward, D., Andrews, H. R., Ball, G. C., Costa, G. J., Davies, W. G. and Mitchell, I. V. (1976) 'Stopping power measurements for ^{19}F, ^{24}Mg, ^{27}Al, ^{32}S and ^{35}Cl at energies 0. 2 to 3. 5 MeV/nucleon in Ti, Fe, Ni, Cu, Ag and Au.' Nucl. Instrum. Meth. **136**, 349–359.

Franzke, B. (1987) 'The heavy-ion storage and cooler ring project ESR at GSI.' Nucl. Instrum. Meth. B **24/25**, 18–25.

Frey, C. M., Dollinger, G., Bergmaier, A., Faestermann, T. and Maier-Komor, P. (1996) 'Charge state dependence of the stopping power of 1 MeV/A ^{58}Ni ions.' Nucl. Instrum. Meth. B **107**, 31–35.

Fuggle, J. C. and Mårtensson, N. (1980) 'Core-level binding energies in metals.' J. Elect. Spect. Rel. Phenomena **21**, 275–281.

Gardès, D., Servajean, A., Kubica, B., Fleurier, C., Hong, D., Deutsch, C. and Maynard, G. (1992) 'Stopping of multicharged ions in dense and fully ionized hydrogen.' Phys. Rev. A **46**, 5101–5111.

Gardès, D., Chabot, M., Nectoux, M., Maynard, G., Deutsch, C. and Roudskoi, I. (1998) 'Experimental study of stopping power for high Z ion in hydrogen.' Nucl. Instrum. Meth. A **415**, 698–702.

Gardès, D., Chabot, M., Nectoux, M., Maynard, G., Deutsch, C. and Belyaev, G. (2001) 'Experimental analysis of the stopping cross sections and of the charge changing processes for Clq+ projectiles at the maximum of the stopping power.' Nucl. Instrum. Meth. A **464**, 253–256.

Gauvin, H., Bimbot, R., Herault, J., Anne, R., Bastin, G. and Hubert, F. (1987) 'Stopping powers of solids for ^{16}O ions at intermediate energies (20–95 MeV/u).' Nucl. Instrum. Meth. B **28**, 191–194.

Gauvin, H., Bimbot, R., Herault, J., Kubica, B., Anne, R., Bastin, G. and Hubert, F. (1990) 'Stopping powers of solids for $^{84,86}Kr$, ^{100}Mo and $^{129,132}Xe$ ions at intermediate energies (20–45 MeV/u) and the charge state distributions at equilibrium.' Nucl. Instrum. Meth. B **47**, 339–350.

Geissel, H. (1982) 'Untersuchungen zur Abbremsung von Schwerionen in Materie im Energiebereich von (0,5–10) MeV/U.' GSI-Report **82–12**, 21–29.

Geissel, H. (1997) 'Relativistische exotische Kerne als Projektilstrahlen — Neue Perspektiven zum Studium der Kerneigenschaften.' GSI Report **97–03**, 1, habilitation thesis.

Geissel, H. and Scheidenberger, C. (1998) 'Slowing down of relativistic heavy ions and new applications.' Nucl. Instrum. Meth. B **136–138**, 114–124.

Geissel, H., Güttner, K., Hofmann, S. and Münzenberg, G. (1977) 'Energy loss and straggling of alpha particles in thin homogeneous Ne-111 scintillator foils.' Nucl. Instrum. Meth. **144**, 465–468.

Geissel, H., Armbruster, P., Kitahara, T., Kraft, G., Spieler, H. and Güttner, K. (1980) 'Energy loss and energy straggling of heavy particles.' Nucl. Instrum. Meth. **170**, 217–219.

Geissel, H., Laichter, Y., Schneider, W. F. W. and Armbruster, P. (1982) 'Energy loss and energy loss straggling of fast heavy ions in matter.' Nucl. Instrum. Meth. **194**, 21–29.

Geissel, H., Laichter, Y., Albrecht, R., Kitahara, T., Klabunde, J., Strehl, P. and Armbruster, P. (1983a) 'A time-of-flight method for stopping power measurements of bunched ion beams.' Nucl. Instrum. Meth. **206**, 609–612.

Geissel, H., Laichter, Y., Schneider, W. F. W. and Armbruster, P. (1983b) 'Energy loss straggling of 1.4–10 MeV/u heavy ions in gases.' Nucl. Instrum. Meth. **215**, 329–335.

Geissel, H., Lennard, W. N., Andrews, H. R., Jackson, D. P., Mitchell, I. V., Philips, D. and Ward, D. (1985)

'Energy-angle distribution measurements for $0.8\,v_0$ ^{20}Ne and ^{209}Bi ions.' Nucl. Instrum. Meth. B **12**, 38–42.

Geissel, H., Lennard, W. N., Andrews, H. R., Ward, D. and Phillips, D. (1984) 'Problems of interpreting energy loss data for non-zero emergent angles.' Phys. Lett. A **106**, 371–373.

Geissel, H., Armbruster, P., Behr, K. H., Brunle, A., Burkard, K., Chen, M., Folger, H., Franczak, B., Keller, H., Klepper, O., Langenbeck, B., Nickel, F., Pfeng, E., Pfützner, M., Roeckl, E., Rykaczewski, K., Schall, I., Schardt, D., Scheidenberger, C., Schmidt, K. H., Schröter, A., Schwab, T., Sümmerer, K., Weber, M. and Münzenberg, G. (1992a) 'The GSI projectile fragment separator (FRS) — a versatile magnetic system for relativistic heavy-ions.' Nucl. Instrum. Meth. B **70**, 286–297.

Geissel, H., Beckert, K., Bosch, F., Eickhoff, H., Franczak, B., Franzke, B., Jung, M., Klepper, O., Moshammer, R., Münzenberg, G., Nickel, F., Nolden, F., Schaaf, U., Scheidenberger, C., Spätke, P., Steck, M., Sümmerer, K. and Magel, A. (1992b) 'First storage and colling of secondary heavy-ion beams at relativistic energies.' Phys. Rev. Lett. **68**, 3412–3415.

Geissel, H., Münzenberg, G. and Riisager, K. (1995) 'Secondary exotic nuclear beams.' Ann. Rev. Nucl. Part. Sci. **45**, 163–203.

Geissel, H., Weick, H., Scheidenberger, C., Bimbot, R. and Gardès, D. (2002) 'Experimental studies of heavy-ion slowing down in matter.' Nucl. Instrum. Meth. B **195**, 3–54.

Gemmell, D. S. (1974) 'Channeling and related effects in motion of charged particles through crystals.' Rev. Mod. Phys. **46**, 129–227.

Glazov, L. and Sigmund, P. (1997) 'Energy-loss spectra of charged particles in the presence of charge exchange.' Nucl. Instrum. Meth. B **125**, 110–115.

Glazov, L. and Sigmund, P. (2000) 'Energy-loss spectra of charged particles in the presence of charge exchange: addendum on ^{6}Li spectra.' Nucl. Instrum. Meth. B **170**, 39–44.

Glazov, L. G. (2000) 'Energy-loss spectra of swift ions.' Nucl. Instrum. Meth. B **161**, 1–8.

Glazov, L. G. (2002a) 'Frozen-charge stopping of ions in the Bethe regime.' Nucl. Instrum. Meth. B **195**, 118–132.

Glazov, L. G. (2002b) 'Multiple-peak structures in energy-loss spectra of swift ions.' Nucl. Instrum. Meth. B **193**, 56–65.

Glazov, L. G. and Sigmund, P. (2003) 'Nuclear stopping in transmission measurements.' Nucl. Instrum. Meth. B **207**, 240–256.

Glazov, L. G., Sigmund, P. and Schinner, A. (2002) 'Statistics of heavy-ion stopping.' Nucl. Instrum. Meth. B **195**, 183–187.

Golovchenko, J. A., Goland, A. N., Rosner, J. S., Thorn, C. E., Wegner, H. E., Knudsen, H. and Moak, C. D. (1981) 'Charge state dependence of channeled ion energy loss.' Phys. Rev. B **23**, 957–966.

Gombas, P. (1956) Statistische Behandlung des Atoms. In: *Handbuch der Physik*, vol. 36, Flügge, S., Ed. (Berlin: Springer) pp. 109–231.

Goppelt-Langer, P., Yamamoto, S., Aoki, Y., Takeshita, H. and Naramoto, H. (1996) 'Stopping-powers and straggling of N-15 ions for nuclear reaction analysis at 6.385 MeV.' Nucl. Instrum. Meth. B **118**, 7–10.

Goudsmit, S. and Saunderson, J. L. (1940) 'Multiple scattering of electrons.' Phys. Rev. **57**, 24–29.

Grahmann, H. and Kalbitzer, S. (1976) 'Nuclear and electronic stopping powers of low energy ions with $Z \leq 10$ in silicon.' Nucl. Instrum. Meth. **132**, 119.

Grande, P. L. and Schiwietz, G. (1991) 'Impact-parameter dependence of electronic energy loss and straggling of incident bare ions on H and He atoms by using the coupled-channel method.' Phys. Rev. A **44**, 2984–2992.

Grande, P. L. and Schiwietz, G. (1998) 'Impact-parameter dependence of the electronic energy loss of fast ions.' Phys. Rev. A **58**, 3796–3801.

Grande, P. L. and Schiwietz, G. (2000) 'CasP version 1.1.' Available on www.hmi.de/people/schiwietz/casp.html 451.

Grande, P. L. and Schiwietz, G. (2001) 'CasP version 1.2.' Available on www.hmi.de/people/schiwietz/casp.html 451.

Grande, P. L. and Schiwietz, G. (2002) 'The unitary convolution approximation for heavy ions.' Nucl. Instrum. Meth. B **195**, 55–63.

Grande, P. L., Araujo, L. L., DeAzevedo, G. M., Behar, M., Dias, J. F., DosSantos, J. H. R. and Schiwietz, G. (2002) 'Energy loss under channeling conditions.' Nucl. Instrum. Meth. B **195**, 172–177.

Gras-Marti, A. (1985) 'Increased energy losses in off-beam directions for MeV protons traversing thin films.' Nucl. Instrum. Meth. B **9**, 1–5.

Green, D. W., Cooper, J. N. and Harris, J. C. (1955) 'Stopping cross sections of metals for protons of energies from 400 to 1000 keV.' Phys. Rev. **98**, 466–470.

Groeneveld, K. O., Meckbach, W. and Sellin, I. A., eds. (1984) *Forward Electron Ejection in Ion Collisions*, vol. 213 *Lecture Notes in Physics* (Berlin: Springer).

Habs, D., Kester, O., Rudolph, K., Thirolf, P., Hinderer, G., Nolte, E., Bollen, G., Raimbault-Hartmann, H., Ravn, H., Ames, F., Liljeby, L., Rensfelt, K. G., Schwalm, D., Hahn, R. V., Repnow, R., Schempp, A., Ratzinger, U., Duppen, P. V., Huyse, M. and Walter, G. (1996) 'The REX-ISOLDE project.' Nucl. Instrum. Meth. B **126**, 218–223.

Hahn, R. L., Toth, K. S., Ferguson, R. L. and Plasil, F. (1981) 'Energy loss and straggling of 7.3 MeV/nucleon ^{84}Kr ions in Ni, Aland Ti.' Nucl. Instrum. Meth. **180**, 581–588.

Hahn, Y. (1987) 'Resonant transfer and excitation, dielectronic recombination and related processes: a unified approach.' Comm. At. Mol. Phys. **19**, 99.

Harikumar, V., Pathak, A. P., Sharma, S. K., Kumar, S., Nath, N., Kabiraj, D. and Avasthi, D. K. (1996) 'Energy loss of MeV heavy ions in carbon.' Nucl. Instrum. Meth. B **108**, 223–226.

Harikumar, V., Pathak, A. P., Nath, N., Kumar, S., Sharma, S. K., Hui, S. K. and Avasthi, D. K. (1997) 'Stopping Power of Carbon for Si, Fe, Ni and Cu Ions Using the ERDA Technique.' Nucl. Instrum. Meth. B **129**, 143–146.

Henke, B. L., Gullikson, E. M. and Davies, J. C. (1993) 'X-ray interactions: photoabsorption, scattering, transmission, and reflection at $E = 50$–$30{,}000$ eV, $Z = 1$–92.' At. Data Nucl. Data Tables **54**, 181–342.

Herault, J., Bimbot, R., Gauvin, H., Kubica, B., Anne, R., Bastin, G. and Hubert, F. (1991) 'Stopping powers of gases for heavy ions (O, Ar, Kr, Xe) at intermediate energy (20–100 MeV/u). Vanishing of the gas-solid effect.' Nucl. Instrum. Meth. B **61**, 156–166.

Hill, K. W. and Merzbacher, E. (1974) 'Polarization in distant Coulomb collisions of charged particles with atoms.' Phys. Rev. A **9**, 156–165.

Hiraoka, T. and Bichsel, H. (2000) 'Stopping power and range tables for carbon, nitrogen, neon, silicon and argon ions in various dosimetric materials.' Medical Standard Dose, Chiba, Japan **5 (Suppl. 1)**, 1.

Hoffmann, I., Jäger, E. and Müller-Jahreis, U. (1976) 'Z_1-dependence of electronic energy straggling of light ions.' Radiat. Eff. **31**, 57.

Hohenberg, P. and Kohn, W. (1964) 'Inhomogeneous electron gas.' Phys. Rev. **136**, B864–B871.

Hooton, B. W., Freeman, J. M. and Kane, P. P. (1975) 'Small angle multiple scattering of 12–40 MeV heavy ions from thin foils.' Nucl. Instrum. Meth. **124**, 29–39.

Hubert, F., Fleury, A., Bimbot, R. and Gardès, D. (1980) 'Range and stopping power tables for 2.5–100 MeV/nucleon heavy ions in solids.' Ann. Physique. **5 S**, 3–213.

Hubert, F., Bimbot, R. and Gauvin, H. (1989) 'Semi-empirical formulae for heavy ion stopping powers in solids in the intermediate energy range.' Nucl. Instrum. Meth. B **36**, 357–363.

Hubert, F., Bimbot, R. and Gauvin, H. (1990) 'Range and stopping-power tables for 2.5–500 MeV nucleon heavy ions in solids.' At. Data Nucl. Data Tables **46**, 1–213.

Hvelplund, P. (1968) *Besvarelse af Aarhus Universitets prisopgave i fysik for aaret 1968* (Aarhus: Institute of Physics).

Hvelplund, P. (1971) 'Energy loss and straggling of 100–500 keV atoms with $2 \leq Z_1 \leq 12$ in various gases.' Mat. Fys. Medd. Dan. Vid. Selsk. **38**(4), 1–25.

Hvelplund, P. (1975) 'Energy loss and straggling of 100–500 keV $_{90}$Th, $_{82}$Pb, $_{80}$Hg, and $_{64}$Gd in H_2.' Phys. Rev. A **11**, 1921–1927.

Hvelplund, P. and Fastrup, B. (1968) 'Stopping cross sections in carbon of 0.2–1.5 MeV atoms with $21 \leq Z_1 \leq 39$.' Phys. Rev. **165**, 408–414.

Hvelplund, P., Bjørnelund, S. K., Knudsen, H. and Tawara, H. (1992) 'Electron capture in collisions between medium velocity multiply charged ions and H and H_2.' Phys. Scr. **45**, 231–237.

Ichihara, A., Shirai, T. and Eichler, J. (1993) 'Cross sections for electron capture in relativistic atomic collisions.' At. Data Nucl. Data Tables **55**, 63–79.

ICRU. (1984) *Stopping Powers for Electrons and Positrons*. ICRU Report 37 (Bethesda, MD: ICRU).

ICRU. (1993) *Stopping Powers and Ranges for Protons and Alpha Particles*. ICRU Report 49 (Bethesda, MD: ICRU).

Inokuti, M., Dehmer, J. L., Baer, T. and Hanson, J. D. (1981) 'Oscillator-strength moments, stopping powers, and total inelastic-scattering cross sections of all atoms through strontium.' Phys. Rev. A **23**, 95–109.

Itoh, A., Tsuchida, H., Majima, T., Yogo, A. and Ogawa, A. (1999) 'Equilibrium charge distributions of lithium ions emerging from a carbon foil.' Nucl. Instrum. Meth. B **159**, 22–27.

IUPAP. (1987) *Symbols, Units, Nomenclature and Fundamental Constants in Physics* (International Union of Pure and Applied Physics).

Ivanchenko, V. N., Giani, S., Pia, M. G., Urban, L., Nieminen, P. and Mancinelly, G. CERN (1999) 'Geant4 simulation of energy losses of ions.' Technical Report. Available on www.ge.infn.it/geant4/papers/CERN-99-300.ps.

Jackson, D. P. (1980) 'Comparison of ion backscattering models.' J. Nucl. Mater. **93/94**, 507–511.

Jackson, J. D. and McCarthy, R. L. (1972) 'Z^3 corrections to energy loss and range.' Phys. Rev. B **6**, 4131–4141.

Jacobsen, K. W., Nørskov, J. K. and Puska, M. J. (1987) 'Interatomic interactions in the effective-medium theory.' Phys. Rev. B **35**, 7423–7442.

Janni, J. F. (1982) 'Proton range-energy tables, 1 keV–10 GeV, part 2. elements.' At. Data Nucl. Data Tables **27**, 341–529.

Jensen, J. and Sigmund, P. (2000) 'Electronic stopping of swift pastially stripped molecules and clusters.' Phys. Rev. A **61**, 032903–1–14.

Jiang, W., Grötzschel, R., Pilz, W., Schmidt, B. and Möller, W. (1999) 'Random and channeling stopping powers and charge-state distributions in silicon for 0.2–1.2 MeV/u positive heavy ions.' Phys. Rev. B **59**, 226–234.

Jokinen, J. (1997) 'Stopping powers of C, Al and Cu for use in ERDA analyses withprobing MeV energy Au-197 ions.' Nucl. Instrum. Meth. B **124**, 447–452.

Kabachnik, N. M. (1993) 'Screening and antiscreening in the semiclassical description of ionization in fast ion-atom collisions.' J. Phys. B **26**, 3803–3814.

Kalbitzer, S., Oetzmann, H., Grahmann, H. and Feuerstein, A. (1976) 'Simple universal fit formula to experimental nuclear stopping power data.' Z. Phys. A.-Hadrons Nuclei **278**, 223–224.

Kaneko, T. (1988) 'Energy loss and straggling accompanied by charge exchange.' Nucl. Instrum. Meth. B **33**, 151–154.

Kaneko, T. (1990) 'Energy loss and straggling of heavy ions in matter.' Nucl. Instrum. Meth. B **48**, 83–86.

Kaneko, T. (1999) 'Energy-loss of swift boron and carbon clusters in solids.' Nucl. Instrum. Meth. B **153**, 15–20.

Kelley, J. G., Sellers, B. and Hanser, F. A. (1973) 'Energy-loss and stopping-power measurements between 2 and 10 MeV/amu for ^{12}C, ^{14}N, and ^{16}O in silicon.' Phys. Rev. B **8**, 103–106.

Kessel'man, V. S. (1971a) 'Oscillatory dependence on the atomic number of the projectile atom for the stopping power due to inelastic collisions.' Zh. Tekh. Fiz. **42**, 1161.

Kessel'man, V. S. (1971b) 'Stopping power of crystals for inelastic collisions with oscillatory dependence on ion charge.' Zh. Tekh. Fiz. **42**, 1161 [English translation: Sov. Phys. Techn. Phys. **16**, 1346 (1972)].

Kienlin, A. V., Azgui, F., Böhmer, W., Djotni, K., Egelhof, P., Henning, W., Kraus, G., Meier, J. and Shepard, K. W.

(1996) 'High resolution detection of energetic heavy ions with a calorimetric low temperature detector.' Nucl. Instrum. Meth. A **368**, 815–818.

Kim, Y. K. and Cheng, K. T. (1980) 'Stopping power for partially stripped ions.' Phys. Rev. A **22**, 61–67.

Kimura, K., Hasegawa, M. and Mannami, M. (1987) 'Energy loss of MeV light ions specularly reflected from a SnTe(001) surface.' Phys. Rev. B **36**, 7–12.

Kishinevskii, L. M. (1962) 'Cross sections for inelastic atomic collisions.' Izv. Akad. NAUK SSSR **26**, 1410 [English translation: Bull. Acad. Sci. USSR Phys. Ser. **20**, 1433–1438 (1963)].

Knipp, J. and Teller, E. (1941) 'On the energy loss of heavy ions.' Phys. Rev. **59**, 659–669.

Knudsen, H. and Andersen, H. H. (1976) 'Multiple scattering of MeV gold and carbon-ions in carbon and gold targets.' Nucl. Instrum. Meth. **136**, 199–201.

Knudson, A. R., Burghalter, P. G. and Nagel, D. J. (1974) 'Vacancy configurations of argon projectile ions in solids.' Phys. Rev. A **10**, 2118–2122.

Kohn, W. and Sham, L. J. (1965) 'Self-consistent equations including exchange and correlation effects.' Phys. Rev. **140**, A1133–A1138.

Komarov, F. F. (1979) 'Comment on "Critical analysis of the modified Firsov model. Sensitivity to the choice of atomic wave functions" by S. A. Cruz, C. Vargas and D. K. Brice.' Radiat. Eff. Lett. **43**, 139.

Komarov, F. F. and Kumakhov, M. A. (1973) 'Electronic energy loss of ions in the modified Firsov theory.' Phys. Stat. Sol. B **58**, 389–400.

Konac, G., Kalbitzer, S., Klatt, C., Niemann, D. and Stoll, R. (1998a) 'Energy loss and straggling of H and He ions of keV energies in Si and C.' Nucl. Instrum. Meth. B **138**, 159–165.

Konac, G., Klatt, C. and Kalbitzer, S. (1998b) 'Universal fit formula for electronic stopping of all ions in carbon and silicon.' Nucl. Instrum. Meth. B **146**, 106–113.

Krist, T., Mertens, P. and Biersack, J. P. (1984) 'Nuclear stopping power for particles transmitted through thin foils in the beam direction.' Nucl. Instrum. Meth. B **2**, 177–181.

Kumar, S., Sharma, S. K., Nath, N., Harikumar, V., Pathak, A. P., Kabiraj, D. and Avasthi, D. K. (1996) 'Stopping power of carbon for heavy ions up to copper.' Radiat. Eff. Def. Solids **139**, 197–206.

Kumar, V. H. and Pathak, A. P. (1993) 'Z_1-oscillations in the stopping powers of silicon and tungsten for low-velocity channelled heavy-ions.' J. Phys. Condens. Matter **5**, 3163–3168.

Lamb, W. E. (1940) 'Passage of uranium fission fragments through matter.' Phys. Rev. **58**, 696–702.

Land, D. J. and Brennan, J. G. (1976) 'Sensitivity of the electronic stopping power to the shell structure of the target material.' Nucl. Instrum. Meth. **132**, 89.

Land, D. J., Brennan, J. G., Simons, D. G. and Brown, M. D. (1977) 'Comparison of theoretical models for the electronic stopping power of low-velocity heavy ions.' Phys. Rev. A **16**, 492–499.

Land, D. J., Simons, D. G., Brennan, J. G. and Glass, G. A. (1985) 'Range distributions and electronic stopping power of nitrogen ions in solids.' Nucl. Instrum. Meth. B **10/11**, 234–236.

Landau, L. (1944) 'On the energy loss of fast particles by ionization.' J. Phys. USSR **8**, 201.

Lantschner, G. H., Eckardt, J. C., Jakas, M. M., Capuj, N. E. and Ascolani, H. (1987) 'Variation of peak energy for energy loss with angle of observation.' Phys. Rev. A **36**, 4667.

Lassen, N. O. (1951a) 'Total charges of fission fragments as functions of the pressure in the stopping gas.' Mat. Fys. Medd. Dan. Vid. Selsk. **26**(12), 1–19.

Lassen, N. O. (1951b) 'The total charges of fission fragments in gaseous and solid stopping media.' Mat. Fys. Medd. Dan. Vid. Selsk. **26**(5), 1–28.

Latta, B. M. and Scanlon, P. J. (1976) 'Average electronic energy loss in the modified Firsov theory.' Phys. Stat. Sol. B **74**, 711–719.

LBL (2002) 'Atomic scattering factors.' Available on www-cxro.lbl.gov/optical_constants/asf.html.

Lennard, W. N. and Geissel, H. (1987) 'Energy loss and energy loss straggling for heavy ions.' Nucl. Instrum. Meth. B **27**, 338–343.

Lennard, W. N., Jackman, T. E. and Phillips, D. (1980) 'The charge state equilibration distance for phosphorous ions in carbon.' Phys. Lett. A **79**, 309–310.

Lennard, W. N., Andrews, H. R., Freeman, M., Mitchell, I. V., Phillips, P., Walker, D. A. S. and Ward, D. (1982) 'Time-of-flight system for slow heavy ions.' Nucl. Instrum. Meth. **203**, 565–570.

Lennard, W. N., Geissel, H., Jackson, D. and Phillips, D. (1986a) 'Electronic stopping values for low velocity ions ($9 \leq Z_1 \leq 92$) in carbon targets.' Nucl. Instrum. Meth. B **13**, 127–132.

Lennard, W. N., Geissel, H., Phillips, D. and Jackson, D. P. (1986b) 'Heavy-ion straggling: possible evidence for inner-shell excitation.' Phys. Rev. Lett. **57**, 318–320.

Lifschitz, A. F. and Arista, N. (1998) 'Velocity-dependent screening in metals.' Phys. Rev. A **57**, 200–207.

Lindhard, J. (1954) 'On the properties of a gas of charged particles.' Mat. Fys. Medd. Dan. Vid. Selsk. **28**(8), 1–57.

Lindhard, J. (1965) 'Influence of crystal lattice on motion of energetic charged particles.' Mat. Fys. Medd. Dan. Vid. Selsk. **34**(14), 1–64.

Lindhard, J. (1976) 'The Barkas effect — or Z_1^3, Z_1^4-corrections to stopping of swift charged particles.' Nucl. Instrum. Meth. **132**, 1–5.

Lindhard, J. (1985) 'On the theory of energy loss distributions for swift charged particles.' Phys. Scr. **32**, 72–80.

Lindhard, J. and Scharff, M. (1953) 'Energy loss in matter by fast particles of low charge.' Mat. Fys. Medd. Dan. Vid. Selsk. **27**(15), 1–31.

Lindhard, J. and Scharff, M. (1961) 'Energy dissipation by ions in the keV region.' Phys. Rev. **124**, 128–130.

Lindhard, J. and Sørensen, A. H. (1996) 'On the relativistic theory of stopping of heavy ions.' Phys. Rev. A **53**, 2443–2456.

Lindhard, J. and Winther, A. (1964) 'Stopping power of electron gas and equipartition rule.' Mat. Fys. Medd. Dan. Vid. Selsk. **34**(4), 1–22.

Lindhard, J., Nielsen, V., Scharff, M. and Thomsen, P. V. (1963a) 'Integral equations governing radiation effects.' Mat. Fys. Medd. Dan. Vid. Selsk. **33**(10), 1.

Lindhard, J., Scharff, M. and Schiøtt, H. E. (1963b) 'Range concepts and heavy ion ranges.' Mat. Fys. Medd. Dan. Vid. Selsk. **33**(14), 1.

Lindhard, J., Nielsen, V. and Scharff, M. (1968) 'Approximation method in classical scattering by screened coulomb fields.' Mat. Fys. Medd. Dan. Vid. Selsk. **36**(10), 1–32.

Livingston, M. S. and Bethe, H. A. (1937) 'Nuclear physics. C. Nuclear dynamics, experimental.' Rev. Mod. Phys. **9**, 245–390.

Lo, H. H. and Fite, W. L. (1969) 'Electron-capture and loss cross sections for fast heavy particles passing through gases.' At. Data **1**, 305–328.

Lu, X., Xia, Z., Zheng, T. and Shen, Y. (2000) 'Stopping powers of C, Al, Ti, Cu, Nb and Ag for ^{16}O and ^{19}F ions.' Nucl. Instrum. Meth. B **168**, 287–293.

Mabong, S., Maynard, G. and Katsonis, K. (1996) 'Parametric potential for modelling of highly charged heavy ions.' Laser Particle Beams **14**, 575–586.

Maier-Komor, P., Dollinger, G. and Körner, H. J. (1999) 'Reproducibility and simplification of the preparation procedure for carbon stripper foils by laser plasma ablation deposition.' Nucl. Instrum. Meth. A **438**, 73–78.

Mann, R., Hagmann, S. and Weitzel, L. (1988) 'Cusp-electrons used for velocity measurements of heavy ion projectiles.' Nucl. Instrum. Meth. B **34**, 403–406.

Martin, F. W. and Northcliffe, L. C. (1962) 'Energy loss and effective charge of He, C, and Ar ions below 10 MeV/amu in gases.' Phys. Rev. **128**, 1166–1174.

Marwick, A. D. and Sigmund, P. (1975) 'Small-angle multiple scattering of ions in the screened Coulomb region. 2. Lateral spread.' Nucl. Instrum. Meth. **126**, 317–323.

Mayer, J. W., Eriksson, L. and Davies, J. A. (1970) *Ion Implantation in Semiconductors. Silicon and Germanium* (New York: Academic Press).

Maynard, G., Katsonis, K. and Mabong, S. (1996) 'Average atom model for swift heavy ions in dense matter.' Nucl. Instrum. Meth. B **107**, 51–55.

Maynard, G., Gardès, D., Chabot, M., Nectoux, M. and Deutsch, C. (1998a) 'Effective stopping-power charges of swift heavy ions in gases.' Nucl. Instrum. Meth. B **146**, 88–94.

Maynard, G., Katsonis, K., Zwicknagel, G., Mabong, S., Chabot, M., Gardès, D. and Kurilenkov, Y. K. (1998b) 'Nonlinear effects in stopping of partially ionized swift heavy ions.' Nucl. Instrum. Meth. A **415**, 687–692.

Maynard, G., Chabot, M. and Gardès, D. (2000) 'Density effect and charge dependent stopping theories for heavy ions in the intermediate velocity regime.' Nucl. Instrum. Meth. B **164–165**, 139–146.

Maynard, G., Katsonis, K., Deutsch, C., Zwicknagel, G., Chabot, M. and Gardès, D. (2001a) 'Modeling of swift heavy ions interaction with dense matter.' Nucl. Instrum. Meth. A **464**, 86–92.

Maynard, G., Zwicknagel, G., Deutsch, C. and Katsonis, K. (2001b) 'Diffusion-transport cross section and stopping power of swift heavy ions.' Phys. Rev. A **63**, 052903–1–14.

Maynard, G., Deutsch, C., Dimitriou, K., Katsonis, K. and Sarrazin, M. (2002a) 'Evaluation of the energy deposition profile for swift heavy ions in dense plasmas.' Nucl. Instrum. Meth. B **195**, 188–215.

Maynard, G., Sarrazin, M., Katsonis, K. and Dimitriou, K. (2002b) 'Quantum and classical stopping cross-sections of swift heavy ions derived from the evolution with time of the Wigner function.' Nucl. Instrum. Meth. B **193**, 20–25.

McGuire, E. J. (1983) 'Extraction of shell corrections from Born-approximation stopping-power calculations in Al.' Phys. Rev. A **28**, 49–52.

Medenwaldt, R., Møller, S. P., Uggerhøj, E., Worm, T., Hvelplund, P., Knudsen, H., Elsener, K. and Morenzoni, E. (1991) 'Measurement of the stopping power of silicon for antiprotons between 0.2 and 3 MeV.' Nucl. Instrum. Meth. B **58**, 1–5.

Mertens, P. (1978) 'Energy loss of light 300 keV ions in thin metal foils.' Nucl. Instrum. Meth. **149**, 149–153.

Mertens, P. (1987) 'How to measure absolute stopping cross sections by backscattering and by transmission methods. Part II. Transmission.' Nucl. Instrum. Meth. B **27**, 315–322.

Mertens, P. and Krist, T. (1982) 'Energy Loss of 300-keV He^+ and N^+ in 150- to 800-Å Carbon Foils.' Phys. Rev. B **25**, 5591–5597.

Meyer, L. (1971) 'Plural and multiple scattering of low-energy heavy particles in solids.' Phys. Stat. Sol. B **44**, 253–268.

Mikkelsen, H. H. and Flyvbjerg, H. (1992) 'Exact stopping cross section of the quantum harmonic oscillator for a penetrating point charge of arbitrary strength.' Phys. Rev. A **45**, 3025–3031.

Mikkelsen, H. H. and Sigmund, P. (1989) 'Barkas effect in electronic stopping power: rigorous evaluation for the harmonic oscillator.' Phys. Rev. A **40**, 101–116.

Molière, G. (1947) 'Theorie der Streuung schneller geladener Teilchen I. Einzelstreuung am abgeschirmten Coulomb-Feld.' Z. Naturforsch. **2a**, 133–145.

Molière, G. (1948) 'Theorie der Streuung schneller geladener Teilchen. II. Mehrfach- und Vielfachstreuung.' Z. Naturforsch. **3a**, 78–97.

Møller, S. P. (1998) *Experimental investigations of stopping power and straggling for very low and very high energy particles of positive and negative charge*, Ph.D. thesis, University of Aarhus.

Møller, S. P., Uggerhøj, E., Bluhme, H., Knudsen, H., Mikkelsen, U., Paludan, K. and Morenzoni, E. (1997) 'Direct measurement of the stopping power for antiprotons of light and heavy targets.' Phys. Rev. A **56**, 2930–2939.

Møller, S. P., Csete, A., Ichioka, T., Knudsen, H., Uggerhoj, U. I. and Andersen, H. H. (2002) 'Antiproton stopping at low energies: confirmation of velocity-proportional stopping power.' Phys. Rev. Lett. **88**, 193201–1–4.

Mukherji, S. and Nayak, A. (1979) 'Calculation of heavy ion ranges in complex media.' Nucl. Instrum. Meth. **159**, 421–431.

Närmann, A. and Sigmund, P. (1994) 'Statistics of energy loss and charge exchange of penetrating

particles: Higher moments and transients.' Phys. Rev. A **49**, 4709–4715.

Nath, N., Dahinval, O. P., Bhagwat, A., Avasthi, D. K., Harikumar, V. and Pathak, A. P. (1994) 'Electronic stopping power measurements using secondary beams.' Surf. Coat. Technol. **66**, 231–234.

Neuwirth, W. and Both, G. (1985) 'Aggregates of atoms and their stopping cross sections.' Nucl. Instrum. Meth. B **12**, 67–72.

Neuwirth, W., Hauser, U. and Kühn, E. (1969) 'Energy loss of charged particles in matter. I. Experimental method and velocity dependence of the energy loss of lithium ions.' Z. Phys. **220**, 241–264.

Niemann, D., Konac, G. and Kalbitzer, S. (1996) 'Stopping power measurements of ^{1}H, ^{4}He and ^{14}N in Si in the energy range of 0.02–1 MeV/amu.' Nucl. Instrum. Meth. B **118**, 11–18.

Nikolaev, V. S. and Dmitriev, I. S. (1968) 'On the equilibrium charge distributions of heavy elemental ion beams.' Phys. Lett. A **28**, 277–278.

NIST. (2001) 'Fundamental physical constants.' Technical Report, National Institute of Standards and Technology. Available on http://physics.nist.gov/cuu/Constants/.

Northcliffe, L. C. (1960) 'Energy loss and effective charge of heavy ions in aluminum.' Phys. Rev. **120**, 1744–1757.

Northcliffe, L. C. (1963) 'Passage of heavy ions through matter.' Ann. Rev. Nucl. Sci. **13**, 67–102.

Northcliffe, L. C. and Schilling, R. F. (1970) 'Range and stopping power tables for heavy ions.' Nucl. Data Tables A**7**, 233–463.

Oddershede, J. and Sabin, J. R. (1984) 'Orbital and whole-atom proton stopping power and shell corrections for atoms with $Z < 36$.' At. Data Nucl. Data Tables **31**, 275–297.

Oddershede, J., Sabin, J. R. and Sigmund, P. (1983) 'Predicted Z_2-structure and gas-solid difference in low-velocity stopping power of light ions.' Phys. Rev. Lett. **51**, 1332–1335.

Ogawa, H., Katayama, I., Ikegami, H., Haruyama, Y., Aoki, A., Tosaki, M., Fukuzawa, F., Yoshida, K., Sugai, I. and Kaneko, T. (1991) 'Direct measurement of fixed-charge stopping power for 32-MeV He^{3+} in a charge-state nonequilibrium region.' Phys. Rev. B **43**, 11370–11376.

Ogawa, H., Katayama, I., Sugai, I., Haruyama, Y., Aoki, A., Tosaki, M., Fukuzawa, F., Yoshida, K. and Ikegami, H. (1992a) 'Charge state dependent energy loss of light ions.' Nucl. Instrum. Meth. B **69**, 108–112.

Ogawa, H., Katayama, I., Sugai, I., Haruyama, Y., Tosaki, M., Aoki, A., Yoshida, K. and Ikegami, H. (1992b) 'Charge state dependent energy loss of high velocity carbon ions in the charge state non-equilibrium region.' Phys. Lett. A **167**, 487–492.

Ogawa, H., Katayama, I., Sugai, I., Haruyama, Y., Saito, M., Yoshida, K., Tosaki, M. and Ikegami, H. (1993) 'Charge state dependent energy loss of high velocity oxygen ions in the charge state non-equilibrium region.' Nucl. Instrum. Meth. B **82**, 80–84.

Ogawa, H., Katayama, I., Sugai, I., Haruyama, Y., Saito, M., Yoshida, K. and Tosaki, M. (1996a) 'Energy loss of high velocity Li-6^{2+} ions in carbon foils in charge state non-equilibrium region.' Nucl. Instrum. Meth. B **115**, 66–69.

Ogawa, H., Sakamoto, N., Katayama, I., Haruyama, Y., Saito, M., Yoshida, K., Tosaki, M., Susuki, Y. and Kimura, K. (1996b) 'Measurement of energy losses of 10-MeV neutral hydrogen atoms in carbon foils.' Phys. Rev. A **54**, 5027–5030.

Ogawa, H., Sakamoto, N., Katayama, I., Haruyama, Y., Saito, M., Yoshida, K., Tosaki, M., Susuki, Y. and Kimura, K. (1997) 'Energy loss of 10 MeV/amu atomic helium in carbon.' Nucl. Instrum. Meth. B **132**, 36–40.

Ormrod, J. H. (1968) 'Low-energy electronic stopping cross sections in nitrogen and argon.' Can. J. Phys. **46**, 497–502.

Ormrod, J. H. and Duckworth, H. E. (1963) 'Stopping cross sections in carbon for low-energy atoms with $Z \leq 12$.' Can. J. Phys. **41**, 1424–1442.

Ormrod, J. H., MacDonald, J. R. and Duckworth, H. E. (1965) 'Some low-energy atomic stopping cross sections.' Can. J. Phys. **43**, 275–284.

Ouichaoui, S. and Bouzid, B. (2002) 'Energy loss straggling of swift heavy ions below 100 MeV/u.' Nucl. Instrum. Meth. B **193**, 36–42.

Ouichaoui, S., Hourani, E., Rosier, L., Bimbot, R., Beaumevieille, H., Bouzid, B. and Mammeri, S. (2000) 'Energy loss straggling of swift heavy ions in metal foils at $E/A \sim 2$ MeV/u.' Nucl. Instrum. Meth. B **164–165**, 259–267.

Palik, E. D. (1985) *Handbook of Optical Constants*, vol. 1, *Academic Press Handbook Series* (Orlando: Academic Press).

Palik, E. D. (1991) *Handbook of Optical Constants of Solids*, vol. 2, *Academic Press Handbook series* (Boston: Academic Press).

Palik, E. D. (1996) *Handbook of Optical Constants of Solids*, vol. 3, *Academic Press Handbook series* (Boston: Academic Press).

Palik, E. D. (2000) *Electronic Handbook of Optical Constants of Solids–version 1.0* (SciVision: Academic Press).

Pathak, A. P. (1974a) 'The Z_1 oscillations in stopping power of metals for low velocity channeled heavy-ions.' J. Phys. F **4**, 1883–1888.

Pathak, A. P. (1974b) 'Z_2 dependence of electronic stopping power of low-velocity channeled heavy-ions.' J. Phys. C **7**, 3239–3244.

Pathak, A. P. (1980) 'Systematic study of channeling stopping-power oscillations for low-velocity heavy ions.' Phys. Rev. B **22**, 96–98.

Paul, H. (2003) 'Stopping power for light ions.' Available on www.exphys.uni-linz.ac.at/stopping.

Paul, H. and Schinner, A. (2001) 'An empirical approach to the stopping power of solids and gases for ions from ^{3}Li to ^{18}Ar.' Nucl. Instrum. Meth. B **179**, 299–315.

Paul, H. and Schinner, A. (2002) 'An empirical approach to the stopping of solids and gases for ions from Li to Ar, part II.' Nucl. Instrum. Meth. B **195**, 166–174.

Paul, H. and Schinner, A. (2003a) 'Empirical stopping power tables for ions from ^{3}Li to ^{18}Ar and from 0.001 to 1000 MeV/nucleon in solids and gases.' At. Data Nucl. Data Tables **85**, 377.

Paul, H. and Schinner, A. (2003b) 'Judging the reliability of stopping power tables and programs for heavy ions.' Nucl. Instrum. Meth. B **209**, 252–258.

Peñalba, M., Arnau, A. and Echenique, P. M. (1992) 'Z_1 oscillations in slow channeled ion stopping power.' Nucl. Instrum. Meth. B **67**, 66–68.

Pierce, T. E. and Blann, M. (1968) 'Stopping powers and ranges of 5–90-MeV S^{32}, Cl^{35}, Br^{79}, and I^{127} ions in H_2, He, N_2, and Kr: a semiempirical stopping power theory for heavy ions in gases and solids.' Phys. Rev. **173**, 390–405.

Pietsch, W., Hauser, U. and Neuwirth, W. (1976) 'Stopping powers from the inverted doppler shift attenuation method: *Z*-oscillations: Bragg's rule or chemical effects; solid and liquid state effects.' Nucl. Instrum. Meth. **132**, 79–87.

Pollock, R. E. (1991) 'Storage rings for nuclear physics.' Ann. Rev. Nucl. Part. Sci. **41**, 357–388.

Porat, D. I. and Ramavataram, K. (1961) 'The rate of energy loss and ranges of carbon and oxygen ions in solids.' Proc. Phys. Soc. **77**, 97–102.

Posselt, M. (1994) 'Crystal-TRIM and its application to investigations on channeling effects during ion implantation.' Radiat. Eff. Def. Solids **130**, 87–119.

Powers, D., Lodhi, A. S., Lin, W. K. and Cox, H. L. (1973) 'Molecular effects in the energy loss of alpha particles in gaseous media.' Thin Sol. Films **19**, 205–215.

Powers, D., Olson, H. G. and Gowda, R. (1984) 'Molecular stopping powers and effect of chemical bonding in gaseous amine compounds.' J. Appl. Phys. **55**, 1274–1277.

Price, J. L., Simons, D. G., Stern, S. H., Land, D. J., Guardala, N. A., Brennan, J. G. and Stumborg, M. F. (1993) 'Stopping powers of the noble gases for (0.3–10)-MeV nitrogen ions.' Phys. Rev. A **47**, 2913–2918.

Rauhala, E. and Räisänen, J. (1990) 'Stopping powers of ^{7}Li, ^{11}B, ^{12}C, ^{14}N and ^{16}O ions in $C_{16}H_{14}O_3$ polycarbonate.' Phys. Rev. B **42**, 3877–3880.

Ray, E., Kirsch, R., Mikkelsen, H. H., Poizat, J. C. and Remillieux, J. (1992) 'Slowing down of hydrogen clusters in thin foils.' Nucl. Instrum. Meth. B **69**, 133–141.

Read, P. M. (1984) *Projectile Charge Dependence of Heavy Ion Stopping*, Ph.D. thesis, University of Salford.

Read, P., Sofield, C., Cowern, N. and Bridwell, L. (1987) 'Stopping powers for energetic ions in carbon targets.' Nucl. Instrum. Meth. B **29**, 583–586.

Reynolds, H. K., Dunbar, D. N. F., Wenzel, W. A. and Whaling, W. (1953) 'The stopping cross section of gases for protons, 30–600 keV.' Phys. Rev. **92**, 742.

Robinson, M. T. and Torrens, I. M. (1974) 'Computer simulation of atomic-displacement cascades in solids in the binary-collision approximation.' Phys. Rev. B **9**, 5008–5024.

Roth, M., Stöckl, C., Suss, W., Iwase, O., Gericke, D. O., Bock, R., Hoffmann, D. H. H., Geissel, M. and Seelig, W. (2000) 'Energy loss of heavy ions in laser-produced plasmas.' Europhys. Lett. **50**, 28–34.

Rozet, J. P., Stephan, C. and Vernhet, D. (1996) 'ETACHA: a program for calculating charge states at GANIL energies.' Nucl. Instrum. Meth. B **107**, 67–70.

Ryssel, H. and Ruge, I. (1986) *Ion Implantation* (Chichester: John Wiley).

Salamon, M. H., Ahlen, S. P., Tarlé, G. and Crebbin, K. C. (1981) 'Measurement of higher-order corrections to stopping power for relativistic Ne, Ar, and Fe beams.' Phys. Rev. A **23**, 73–76.

Santry, D. and Werner, R. (1991) 'Measured stopping powers of ^{12}C and ^{14}N ions in thin elemental foils.' Nucl. Instrum. Meth. B **53**, 7–14.

Santry, D. and Werner, R. (1992) 'Measured stopping powers of ^{16}O and ^{19}F ions in thin elemental films.' Nucl. Instrum. Meth. B **69**, 167–173.

Scheidenberger, C., Geissel, H., Mikkelsen, H. H., Nickel, F., Brohm, T., Folger, H., Irnich, H., Magel, A., Mohar, M. F., Münzenberg, G., Pfützner, M., Roeckl, E., Schall, I., Schardt, D., Schmidt, K. H., Schwab, W., Steiner, M., Stöhlker, T., Sümmerer, K., Vieira, D. J., Voss, B. and Weber, M. (1994) 'Direct observation of systematic deviations from the Bethe stopping theory for relativistic heavy ions.' Phys. Rev. Lett. **73**, 50–53.

Scheidenberger, C., Geissel, H., Mikkelsen, H. H., Nickel, F., Czajkowski, S., Folger, H., Irnich, H., Münzenberg, G., Schwab, W., Stöhlker, T., Suzuki, T. and Voss, B. (1996) 'Energy-loss straggling experiments with relativistic heavy ions in solids.' Phys. Rev. Lett. **77**, 3987–3990.

Scheidenberger, C., Stöhlker, T., Meyerhof, W. E., Geissel, H., Mokler, P. H. and Blank, B. (1998) 'Charge states of relativistic heavy ions in matter.' Nucl. Instrum. Meth. B **142**, 25.

Scheidenberger, C., Bollen, G., Bosch, F., Casares, A., Geissel, H., Kholomeev, A., Münzenberg, G., Weick, H. and Wollnik, H. (2000) 'Gross properties of exotic nuclei investigated at storage rings and ion traps.' AIP Conf. Proc. **512**, 275.

Schinner, A. and Sigmund, P. (2000) 'Polarization effect in stopping of swift partially screened heavy ions: perturbative theory.' Nucl. Instrum. Meth. B **164–165**, 220–229.

Schiøtt, H. E. (1966) 'Range-energy relations for low-energy ions.' Mat. Fys. Medd. Dan. Vid. Selsk. **35**(9), 1–20.

Schiwietz, G. (1990) 'Coupled-channel calculation of stopping powers for intermediate-energy light ions penetrating atomic H and He targets.' Phys. Rev. A **42**, 296–306.

Schiwietz, G. and Grande, P. L. (2001) 'Improved charge-state formulas.' Nucl. Instrum. Meth. B **175–177**, 125–131.

Schmelmer, O., Dollinger, G., Frey, C. M., Bergmaier, A. and Karsch, S. (1998a) 'Charge dependent energy loss of 60 MeV $^{58}Ni^{q+}$ ions in argon gas.' Nucl. Instrum. Meth. B **146**, 95–100.

Schmelmer, O., Dollinger, G., Frey, C. M., Bergmaier, A. and Karsch, S. (1998b) 'Energy straggling of 60 MeV ^{58}Ni ions in thin carbon foils and gases.' Nucl. Instrum. Meth. B **145**, 261–270.

Schopper, H. (1993) *Advances of Accelerator Physics and Technology* (Singapore: World Scientific Press).

Schramm, R. and Betz, H. D. (1992) 'Problems concerning the effective charge of swift heavy ions traversing gaseous and solid targets.' Nucl. Instrum. Meth. B **69**, 123–126.

Schulz, F. and Brandt, W. (1982) 'Effective charge of low velocity ions in matter: a comparison of theoretical predictions with data derived from energy-loss measurements.' Phys. Rev. B **26**, 4864–4870.

Schwab, T., Geissel, H., Armbruster, P., Gillibert, A., Mittig, W., Olson, R. E., Winterbon, K. B., Wollnik, H. and Munzenberg, G. (1990) 'Energy and angular distributions for Ar-ions penetrating solids.' Nucl. Instrum. Meth. B **48**, 69–74.

Sevier, K. D. (1972) *Low Energy Electron Spectrometry* (New York: Wiley).

Sharma, A., Diwan, P. K., Kumar, S., Sharma, S. K., Mittal, V. K., Rao, S. V. S. N., Sannakki, B., Ghosh, S. and Avasthi, D. K. (2002) 'dE/dx measurements for heavy ions with $Z = 6$–29 in polycarbonate.' Nucl. Instrum. Meth. B **194**, 7–14.

Sharma, A., Fettouhi, A., Schinner, A. and Sigmund, P. (2004a) 'Stopping of swift ions in compounds.' Nucl. Instrum. Meth. B **218**, 19–28.

Sharma, A., Fettouhi, A., Schinner, A. and Sigmund, P. (2004b) 'Electronic stopping of swift ions in compounds.' in preparation.

Sharma, S. K., Kumar, S., Yadav, J. S. and Sharma, A. P. (1995) 'Stopping power of heavy ions in solids: a comparative study.' Appl. Radiat. Isot. **46**, 39–52.

Shen, W., Wang, B., Feng, J., Zhan, W., Zhu, Y. and Feng, E. (1989) 'Total reaction cross section for heavy-ion collisions and its relation to the neutron excess degree of freedom.' Nucl. Instrum. Meth. A **282**, 247.

Shima, K., Ishihara, T. and Mikumo, T. (1982) 'Empirical formula for the average charge-state of heavy ions behind various foils.' Nucl. Instrum. Meth. **200**, 605–608.

Shima, K., Kuno, N., Yamanouchi, M. and Tawara, H. (1992) 'Equilibrium charge fractions of ions of $Z = 4$–92 emerging from a carbon foil.' At. Data Nucl. Data Tables **51**, 173–241.

Shnidman, R., Tapphorn, R. M. and Geller, K. N. (1973) 'Recoil fraction technique for measuring nuclear and electronic stopping powers.' Appl. Phys. Lett. **22**, 551–553.

Sidenius, G. (1974) 'Systematic stopping cross section measurements with low energy ions in gases.' Mat. Fys. Medd. Dan. Vid. Selsk. **39**(4), 1–32.

Sidenius, G., Andersen, N., Sigmund, P., Besenbacher, F., Heinemeier, J., Hvelplund, P. and Knudsen, H. (1976) 'Effect of molecular geometry on multiple scattering of heavy energetic particles.' Nucl. Instrum. Meth. **134**, 597–599.

Sigmund, P. (1975) Energy loss of charged particles in solids. In: *Radiation Damage Processes in Materials*, NATO Advanced Study Institutes Series, Dupuy, C. H. S. Ed. (Leyden: Noordhoff) pp. 3–117.

Sigmund, P. (1976) 'Energy loss and angular spread of ions traversing matter.' Ann. Israel Phys. Soc. **1**, 69–120.

Sigmund, P. (1978) 'Statistics of particle penetration.' Mat. Fys. Medd. Dan. Vid. Selsk. **40**(5), 1–36.

Sigmund, P. (1982) 'Kinetic theory of particle stopping in a medium with internal motion.' Phys. Rev. A **26**, 2497–2517.

Sigmund, P. (1991) Statistics of charged-particle penetration. In: *Interaction of Charged Particles with Solids and Surfaces*, vol. 271 of *NATO ASI Series*, Gras-Marti, A., Urbassek, H. M., Arista, N. and Flores, F., Eds. (New York: Plenum Press) pp. 73–144.

Sigmund, P. (1992) 'Statistical theory of charged-particle stopping and straggling in the presence of charge exchange.' Nucl. Instrum. Meth. B **69**, 113–122.

Sigmund, P. (1994) 'Analysis of charge-dependent stopping of swift ions.' Phys. Rev. A **50**, 3197–3201.

Sigmund, P. (1996) 'Low-velocity limit of Bohr's stopping-power formula.' Phys. Rev. A **54**, 3113–3117.

Sigmund, P. (1997) 'Charge-dependent electronic stopping of swift nonrelativistic heavy ions.' Phys. Rev. A **56**, 3781–3793.

Sigmund, P. (1998) 'Stopping power in perspective.' Nucl. Instrum. Meth. B **135**, 1–15.

Sigmund, P. (2000a) 'Shell correction in Bohr stopping theory.' Eur. Phys. J. D **12**, 111–116.

Sigmund, P. (2000b) 'Stopping power: wrong terminology.' ICRU News **1**, 17.

Sigmund, P. (2004) *Stopping of Heavy Ions. A Theoretical Approach*, vol. 204, *Springer Tracts Mod. Physics* (Berlin: Springer).

Sigmund, P. and Fu, D.-J. (1982) 'Energy loss straggling of a point charge penetrating a free-electron gas.' Phys. Rev. A **25**, 1450.

Sigmund, P. and Glazov, L. (1998) 'Energy loss and charge exchange: statistics and atomistics.' Nucl. Instrum. Meth. B **136–38**, 47–54.

Sigmund, P. and Glazov, L. G. (2003) 'Interplay of charge exchange and projectile excitation in the stopping of swift heavy ions.' Europ. Phys. J. D **23**, 211–215.

Sigmund, P. and Haagerup, U. (1986) 'Bethe stopping theory for a harmonic oscillator and Bohr's oscillator model of atomic stopping.' Phys. Rev. A **34**, 892–910.

Sigmund, P. and Schinner, A. (2000) 'Binary stopping theory for swift heavy ions.' Eur. Phys. J. D **12**, 425–434.

Sigmund, P. and Schinner, A. (2001a) 'Binary theory of antiproton stopping.' Eur. Phys. J. D **15**, 165–172.

Sigmund, P. and Schinner, A. (2001b) 'Effective charge and related/unrelated quantities in heavy-ion stopping.' Nucl. Instrum. Meth. B **174**, 535–540.

Sigmund, P. and Schinner, A. (2001c) 'Nonperturbative theory of charge-dependent heavy-ion stopping.' Phys. Scr. **T92**, 222–224.

Sigmund, P. and Schinner, A. (2001d) 'Resolution of the frozen-charge paradox in stopping of channeled heavy ions.' Phys. Rev. Lett. **86**, 1486–1489.

Sigmund, P. and Schinner, A. (2002a) 'Barkas effect, shell correction, screening and correlation in collisional energy-loss straggling of an ion beam.' Eur. Phys. J. D **23**, 201–209.

Sigmund, P. and Schinner, A. (2002b) 'Binary theory of electronic stopping.' Nucl. Instrum. Meth. B **195**, 64–90.

Sigmund, P. and Schinner, A. (2002c) 'Binary theory of light-ion stopping.' Nucl. Instrum. Meth. B **193**, 49–55.

Sigmund, P. and Schinner, A. (2003) 'Anatomy of the Barkas effect.' Nucl. Instrum. Meth. B **212**, 110–117.

Sigmund, P. and Winterbon, K. B. (1974) 'Small-angle multiple scattering of ions in the screened Coulomb region, I. Angular distributions.' Nucl. Instrum. Meth. **119**, 541–557.

Sigmund, P. and Winterbon, K. B. (1975) 'Erratum.' Nucl. Instrum. Meth. **125**, 491.

Sigmund, P. and Winterbon, K. B. (1985) 'Energy loss spectrum of swift charged particles penetrating a layer of material.' Nucl. Instrum. Meth. B **12**, 1–16.

Sigmund, P., Fettouhi, A. and Schinner, A. (2003) 'Material dependence of electronic stopping.' Nucl. Instrum. Meth. B **209**, 19–25.

Sillanpää, J., Vainonen-Ahlgren, E., Haussalo, P. and Keinonen, J. (1999) 'Stopping of 5–100 keV Helium in Molybdenum, Chromium, Copper and Nickel.' Nucl. Instrum. Meth. B **142**, 1–8.

Skoog, R. (1975) 'Elastic interaction of atomic projectiles in an amorphous target.' Radiat. Eff. **27**, 53–58.

Slater, J. C. (1955) 'One-electron energies of atoms, molecules and solids.' Phys. Rev. **98**, 1039–1045.

Smith, F. M., Birnbaum, W. and Barkas, W. H. (1953) 'Measurements of meson masses and related quantities.' Phys. Rev. **91**, 765–766.

Sofield, C. J., Cowern, N. E. B., Petty, R. J., Freeman, J. M. and Mason, J. P. (1978) 'Charge-exchange effects in the energy-loss straggling of ^{16}O ions in Al.' Phys. Rev. A **17**, 859–867.

Sørensen, A. H. (1990) 'Barkas effect at low velocities.' Nucl. Instrum. Meth. B **48**, 10–13.

Sørensen, A. H. (2002) 'Stopping of relativistic hydrogen- and heliumlike heavy ions.' Nucl. Instrum. Meth. B **195**, 106–117.

Sørensen, A. H. (2003) 'Stopping of relativistic ions; the pair production and bremsstrahlung channels.' AIP Conf. Proc. **680**, 102–105. [The energy loss to bremsstrahlung is here erroneously estimated to dominate over the loss to pair production for very highvalues of γ (beyond 10^4); see Sørensen (2004) for details.]

Sørensen, A. H. (2005) 'Energy loss of relativistic heavy ions due to pair production and emission of bremsstrahlung.' Nucl. Instrum. Meth. B **230**, 12–16.

Spahn, G. and Groeneveld, K. O. (1975) 'Angular straggling of heavy and light ions in thin solid foils.' Nucl. Instrum. Meth. **123**, 425–429.

Sternheimer, R. M., Seltzer, S. M. and Berger, M. J. (1982) 'Density effect for the ionization loss of charged particles in various substances.' Phys. Rev. B **26**, 6067.

Steward, P. (1968) *Stopping power and range for any nucleus in the specific energy interval 0.01- to 500-MeV/amu in any nongaseous material*, Ph.D. thesis, University of California, Berkeley, uCRL-18127.

Steward, P. G. and Wallace, R. (1966) 'Calculation of stopping power and range-energy values for any heavy ion in nongaseous media.' Technical Report UCRL-17314, University of California, Berkeley.

Stobbe, M. (1930) 'Zur Quantenmechanik Photoelektrischer Prozesse.' Ann. Physik **7**, 661–715.

Stritt, N., Jolie, J., Jentschel, M., Börner, H. G. and Lehmann, H. (1999) 'Slowing down of atoms in metals studied by the Doppler-broadened γ-ray line shapes produced after thermal-neutron capture in Fe and Cr crystals.' Phys. Rev. B **60**, 6476–6483.

Symon, K. (1948) *Fluctuations in energy lost by high energy charged particles in passing through matter*, Ph.D. thesis, Harvard University.

Tai, H., Bichsel, H., Wilson, H., Shin, J. L., Cucinotta, A. and Badavi, F. F. (1997) 'Comparison of stopping power and range data bases for radiation transport studies.' Technical Report NASA Technical paper 3644, Langley Research Center, Hampton, VA.

Takahashi, T., Awaya, Y., Tonuma, T., Kumagai, H., Izumo, K., Hashizume, A., Uchiyama, S. and Hitachi, A. (1979) 'Energy straggling of C and He Ions in metal foils.' Nucl. Instrum. Meth. **166**, 587–589.

Talman, J. D. (1978) 'Numerical Fourier and Bessel transforms in logarithmic variables.' J. Comput. Phys. **29**, 35–48.

Tarlé, G. and Solarz, M. (1978) 'Evidence for higher-order contributions to the stopping power of relativistic iron nuclei.' Phys. Rev. Lett. **41**, 483–486.

Teplova, Y. A., Nikolaev, V. S., Dimitriev, I. S. and Fateeva, L. N. (1962) 'Slowing down of multicharged ions in solids and gases.' Zh. Eksp. Teor. Fiz. **42**, 44–60 [English translation: Sov. Phys. JETP **15**, 31–41 (1962)].

Thwaites, D. I. (1983) 'Bragg's rule of stopping power additivity: a compilation and summary of results.' Radiat. Res. **95**, 495–518.

Thwaites, D. I. (1984) 'Current status of physical state effects on stopping power.' Nucl. Instrum. Meth. B **12**, 84–89.

Thwaites, D. I. (1987) 'Review of stopping powers in organic materials.' Nucl. Instrum. Meth. B **27**, 293–300.

Thwaites, D. I. (1992) 'Departures from Bragg's rule of stopping power additivity for ions in dosimetric and related materials.' Nucl. Instrum. Meth. B **69**, 53–63.

Tilinin, I. S. (1995) 'Quasiclassical expression for inelastic energy losses in atomic particle collisions below the Bohr velocity.' Phys. Rev. A **51**, 3058–3065.

Titeica, S. (1937) 'Sur les fluctuations de parcours des rayons corpusculaires.' Bull. Soc. Roumaine Phys. **38**, 81.

Tofterup, A. L. (1983) 'Relativistic binary-encounter and stopping theory: general expressions.' J. Phys. B **16**, 2997–3003.

Tomaschko, C., Brandl, D., Kügler, R., Schurr, M. and Voit, H. (1995) 'Energy loss of MeV carbon cluster ions in matter.' Nucl. Instrum. Meth. B **103**, 407–411.

Trzaska, W. H., Lyapin, V., Alanko, T., Mutterer, M., Räisänen, J., Tjurin, G. and Wojdyr, M. (2002) 'New approach to energy loss measurements.' Nucl. Instrum. Meth. B **195**, 147–165.

Tschalär, C. (1968) 'Straggling distributions of large energy losses.' Nucl. Instrum. Meth. **61**, 141–156.

Valdes, J. E. and Arista, N. R. (1994) 'Energy-loss effects in multiple-scattering distributions of ions in matter.' Phys. Rev. A **49**, 2690–2696.

Vavilov, P. V. (1957) 'Ionization losses of high-energy heavy particles.' Zh. Eksp. Teor. Fiz. **32**, 920–923 [English translation: Sov. Phys. JETP **5**, 749–751 (1957)].

Villari, A. C. C. (2001) 'The accelerated ISOL technique and the SPIRAL project.' Nucl. Phys. A **693**, 465–476.

Vollmer, O. (1974) 'Der einfluss der ladungsfluktuationen auf die energieverlustverteilung geladener teilchen.' Nucl. Instrum. Meth. **121**, 373–377.

Ward, D., Andrews, H. R., Mitchell, I. V., Lennard, W. N., Walker, R. B. and Rud, N. (1979) 'Systematics for the

Z_1-oscillation in stopping powers of varioussolid materials.' Can. J. Phys. **57**, 645–656.

Weick, H., Geissel, H., Scheidenberger, C., Attallah, F., Baumann, T., Cortina, D., Hausmann, M., Lommel, B., Münzenberg, G., Nankov, N., Nickel, F., Radon, T., Schatz, H., Schmidt, K., Stadlmann, J., Sümmerer, K., Winkler, M. and Wollnik, H. (2000) 'Slowing down of relativistic few-electron heavy ions.' Nucl. Instrum. Meth. B **164–165**, 168–179.

Weick, H., Sørensen, A. H., Geissel, H., Maier, M., Münzenberg, G., Nankov, N. and Scheidenberger, C. (2002) 'Stopping power of partially ionized relativistic heavy ions.' Nucl. Instrum. Meth. B **193**, 1–7.

Weijers, T. D. M., Duck, B. C. and O'Connor, D. J. (2004) 'The development of a stopping power predictor for ions with energies of 0.1–1.0 MeV/u in elemental targets.' Nucl. Instrum. Meth. B **215**, 35–47.

Weyl, P. K. (1953) 'The energy loss of hydrogen, helium, nitrogen, and neon ions in gases.' Phys. Rev. **91**, 289–296.

White, W. and Mueller, R. M. (1969) 'Electronic stopping cross sections of ^{1}H, ^{4}He particles in Cr, Mn, Fe, Co, Ni, and Cu at energies near 100 keV.' Phys. Rev. **187**, 499–503.

Whitlow, H. J., Timmers, H., Elliman, R. G., Weijers, T. D. M., Zhang, Y. and O'Connor, D. J. (2002) 'Measurement and unceretainties of energy loss in silicon over a wide Z_1 range using time of flight detector telescopes.' Nucl. Instrum. Meth. B **195**, 133–146.

Whitton, J. L. (1974) 'The dependence of electronic stopping cross-section of K-42 an different target materials.' Can. J. Phys. **52**, 12–16.

Williams, E. J. (1939) 'Concerning the scattering of fast electrons and of cosmic-ray particles.' Proc. Roy. Soc. A **169**, 531–572.

Williams, E. J. (1940) 'Multiple scattering of fast electrons and alpha-particles, and "curvature" of cloud tracks due to scattering.' Phys. Rev. **58**, 292–306.

Williams, G. (1995) 'Electron binding energies.' Available on http://xray.uu.se/hypertex/EBindEnergies.html.

Wilson, W. D., Haggmark, L. G. and Biersack, J. P. (1977) 'Calculations of nuclear stopping, ranges and straggling in the low-energy region.' Phys. Rev. B **15**, 2458–2468.

Winter, H. (2002) 'Collisions of atoms and ions with surfaces under grazing incidence.' Phys. Rep. **367**, 387–582.

Winterbon, K. B. (1968) 'Z_1 oscillations in stopping of atomic particles.' Can. J. Phys. **46**, 2429–2433.

Winterbon, K. B. (1972) 'Heavy-ion range profiles and associated damage distributions.' Radiat. Eff. **13**, 215–226.

Winterbon, K. B. (1977) 'Electronic energy loss and charge-state fluctuations of swift ions.' Nucl. Instrum. Meth. **144**, 311–315.

Winterbon, K. B., Sigmund, P. and Sanders, J. B. (1970) 'Spatial distribution of energy deposited by atomic particles in elastic collisions.' Mat. Fys. Medd. Dan. Vid. Selsk. **37**(14), 1–73.

Woods, C. J., Sofield, C. J., Cowern, N. E. B., Murrell, M. and Draper, J. (1984) 'Comparison of charge-changing cross sections in gaseous and solid targets.' J. Phys. B **17**, 867–878.

Wu, Z. Q., Lu, X. T., Jin, C. W. and Zheng, T. (1994) 'Energy straggling measurements of O-16 and F-19 ions in Au and CaF_2.' Chinese Phys. Lett. **11**, 605–608.

Xia, Y. Y. and Tan, C. (1986) '4-Parameter formulas for the electronic stopping cross-section of low-energy ions in solids.' Nucl. Instrum. Meth. B **13**, 100–106.

Yamamura, Y. and Misuno, Y. (1985) 'ACAT.' Technical Report IPPJ-AM-40, Institute of Plasma Physics, Nagoya University.

Yang, Q. (1994) 'Partial stopping power and straggling effective charges of heavy ions in condensed matter.' Phys. Rev. A **49**, 1089–1095.

Yang, Q. and MacDonald, R. J. (1993) 'Energy loss and straggling of heavy ions in condensed matter.' Nucl. Instrum. Meth. B **83**, 303–310.

Yang, Q., Li, T., O'Connor, D. J., Macdonald, R. J., Ophel, T. R., Hay, H. J., Cockayne, D. J. H. and Sikorski, A. (1993) 'Energy loss straggling of MeV C-12 and O-16 ions in carbon.' Nucl. Instrum. Meth. B **83**, 439–448.

Yarlagadda, B. S., Robinson, J. E. and Brandt, W. (1978) 'Effective-charge theory and the electronic stopping power of solids.' Phys. Rev. B **17**, 3473–3483.

Zhang, Y., Possnert, G. and Weber, W. J. (2002) 'Measurement of electronic stopping power of swift heavy ions using high-resolution time-of-flight spectrometer.' Appl. Phys. Lett. **80**, 4662–4664.

Zhang, Y. W. (2002) 'High-precision measurement of electronic stopping powers for heavy ions using high-resolution time-of-flight spectrometry.' Nucl. Instrum. Meth. B **196**, 1–15.

Zheng, T., Lu, Z., Zhai, Y., Xia, Z., Shen, D., Wang, Z. and Zhao, Q. (1998) 'Stopping power for MeV ^{12}C ions in solids.' Nucl. Instrum. Meth. B **135**, 169–174.

Ziegler, J. F. (1977) *Helium: Stopping Powers and Ranges in all Elemental Matter*, vol. 4, *The Stopping and Ranges of Ions in Matter* (Elmsford, NY: Pergamon Press).

Ziegler, J. F. (1980) 'The stopping and ranges of ions in matter.' In: '*Handbook of Stopping Cross-sections for Energetic Ions in all Elements*.' vol. 5, *The Stopping and Ranges of Ions in Matter*, Ziegler, J. F., Ed. (New York: Pergamon), pp. 1–432.

Ziegler, J. F. (1998) 'RBS/ERD simulation problems: stopping powers, nuclear reactions and detector resolution.' Nucl. Instrum. Meth. B **136–138**, 141–146.

Ziegler, J. F. (2001) 'The stopping and range of ions in matter'. Available on www.srim.org/, version SRIM-2000.40.

Ziegler, J. F. (2003) 'The stopping and range of ions in matter'. Available on www.srim.org/, version SRIM-2003.

Ziegler, J. F. and Manoyan, J. M. (1988) 'The stopping of ions in compounds.' Nucl. Instrum. Meth. B **35**, 215–228.

Ziegler, J. F., Biersack, J. P. and Littmark, U. (1985) The stopping and range of ions in solids. In: *The Stopping and Ranges of Ions in Matter*, vol. 1, Ziegler, J. F., Ed. (New York: Pergamon) pp. 1–319.

Zielinski, M., Kaletta, E., Neuwirth, W. and Bharuth-Ram, K. (1988) 'The energy loss of carbon ions in carbon.' South Afr. J. Phys. **11**, 13.